THE PHYSICAL REVIEW

VOLUME 91 *Second Series* NUMBER 5

SEPTEMBER 1, 1953

Published for the

AMERICAN PHYSICAL SOCIETY

by the

AMERICAN INSTITUTE OF PHYSICS
Incorporated

LANCASTER, PA., AND NEW YORK, N. Y.

PHYSICAL REVIEW

A journal of [illegible] founded by E. L. Nichols in 1893

Published by the American Institute of Physics
for the
AMERICAN PHYSICAL SOCIETY

Officers

President

ENRICO FERMI
Institute for Nuclear Studies
University of Chicago
Chicago 37, Illinois

Vice-President

H. A. BETHE
Cornell University
Ithaca, New York

Secretary

K. K. DARROW
Bell Telephone Laboratories
Office:
Columbia University
New York 27, New York

Treasurer

G. B. PEGRAM
Columbia University
New York 27, New York

Local Secretary
for the Pacific Coast

J. KAPLAN
University of California
Angeles
Los Angeles, California

Managing Editor

S. A. GOUDSMIT
Brookhaven National Laboratory
Upton, Long Island
New York

BOARD OF EDITORS

Associate Editors

1952–1954

W. P. ALLIS
I. G. BRICKWEDDE
W. B. FRETTER
GOTTFRIED HERZBERG
E. W. LAVARENZ
ARNOLD NORDSIECK

The Physical Review

Entered as second-class matter [illegible]

Acceptance for mailing at special rate [illegible]

NOW AVAILABLE

THE PHYSICAL REVIEW INDEX
1921-1950

The thirty-year cumulative index is published in
two volumes: AUTHOR INDEX, 543 pp.
SUBJECT INDEX, 498 pp.

This extremely useful index has been carefully prepared under the direction of Professor J. W. Buchta, who was Assistant Editor of The Physical Review, 1930-50.

This undertaking was made financially feasible through the assistance of the U. S. Office of Naval Research.

Order blank with prices:

AMERICAN INSTITUTE OF PHYSICS
57 East 55th Street, N. Y. 22, N. Y.

Please send .... copies (2 vols. each) in accordance with items checked hereunder. Remittance is made herewith.

Stiff paper binding—1 copy, 2 vols.	( )	**$14.00**
Cloth Binding —1 copy, 2 vols.	( )	**$16.00**

Special price for one copy only (2 vols.) to a member of The American Physical Society.

( ) I am a member of The American Physical Society.

Stiff paper binding—1 copy, 2 vols.	( )	**$10.00**
Cloth Binding —1 copy, 2 vols.	( )	**$12.00**

ADDRESS:

Name: (Please Print) .....

Street and No. .....

City and Postal District .....

State or Country .....

SIGNED: .....

THE
PHYSICAL REVIEW

A journal of experimental and theoretical physics established by E. L. Nichols in 1893

SECOND SERIES, VOL. 91, NO. 5 SEPTEMBER 1, 1953

Two-Fluid Models of Superconductivity with Application to Isotope Effects*†

PAUL M. MARCUS, *Department of Physics, Carnegie Institute of Technology, Pittsburgh, Pennsylvania*

AND

E. MAXWELL, *Cryogenics Section, National Bureau of Standards, Washington, D. C.*

(Received April 30, 1953)

A general form of the two-fluid model of a superconductor, which includes all previous forms, is set up and the underlying assumptions examined in the light of the lattice vibration theory of superconductivity. Thermodynamic relations are derived and their consistency with the observed isotope effects indicated. Specialization to the α model of Casimir and Gorter permits fitting recent precise critical field data and evaluation of the parameter α characterizing different superconductors. Comparison is made with Koppe's form of the two-fluid model, which is shown not to fit all the data, and simplified and limiting forms of his equations are given.

1. INTRODUCTION

THE two-fluid model of a superconductor was proposed originally to describe the second-order phase transition and the temperature dependence of both the thermodynamic functions and the critical field curve. This it succeeded in doing in a remarkably simple way.[1] The model has acquired fresh support in recent years by its success in interpreting other properties of superconductors. In particular the temperature dependence of the penetration depth is correctly predicted,[2] and the model may be extended to describe behavior in a magnetic field, leading to a theory of the surface energy between normal and superconducting phases and to the field dependence of the penetration depth.[3]

Additional support for the model, in that it is consistent with the observed effects of the change of isotopic mass on the electronic entropy, has been pointed out by one of us[4] and will be developed further here.

Other recent papers which make use of the model will be referred to at appropriate points. (See references 5, 23, and 24.)

One of the purposes of this paper is to refine the the comparison of the two-fluid model with measured values by taking advantage of recent precise critical field data. In particular, the observed deviations from the parabolic law may be brought within the framework of the model by using a more general form of the model containing an adjustable parameter, different for each superconductor.

We also take the occasion to develop the two-fluid model in full generality and to examine the underlying phenomenological assumptions and show these are plausible in the light of the usual band description of electrons in metals and the lattice vibration interaction theory of superconductivity. The resulting general representation of the equilibrium properties of superconductors affords an illuminating example of a second-order phase transition which has a particularly simple, explicit, and apparently quite accurate representation. Thus the dependence of the various thermodynamic functions on an inner parameter which measures the gradually increasing degree of condensation below the transition may be examined in detail.

* Work begun at the University of Illinois, Urbana, Illinois, and supported there by the U. S. Office of Naval Research.

† Supported in part by Office of Scientific Research, Air Research and Development Command.

[1] C. J. Gorter and H. B. G. Casimir, Physik. Z. **35**, 963 (1934). An electrodynamic two-fluid model had been suggested by H. London, Nature **133**, 497 (1934).

[2] Daunt, Miller, Pippard, and Shoenberg, Phys. Rev. **74**, 842 (1948).

[3] L. Landau and V. Ginsburg, J. Exptl. Theoret. Phys. (U.S.S.R.) **20**, 1064 (1950); A. B. Pippard, Proc. Roy. Soc. (London) **A203**, 210 (1950); J. Bardeen (to be published); also Phys. Rev. **81**, 1070 (1951).

[4] E. Maxwell, Phys. Rev. **87**, 1126 (1952); Physics Today **5**, 14 (1952).

Section 2 contains the general formulation of the model, presented with reference to the lattice vibration theory and the underlying statistical basis for the model afforded by that theory. Particular attention is paid to the assumption that the condensation process takes place essentially for electrons close to the Fermi level and to the effect of condensation on the lattice contribution to the free energy. The interrelations of the various thermodynamic quantities are given in detail, since they contain all previous relations for special forms of the model.

Section 3 shows how the general form of the model leads plausibly to the invariance of various reduced quantities to change of isotopic mass and discusses the necessary assumption that the temperature dependent part of the lattice contribution to the free energy must be independent of the degree of condensation.

Section 4 first analyzes the requirements on the general form of the model which follow from the condition that the transition be second order, with no discontinuous changes in degree of condensation. Arguments are given for the conclusion that the effective number of normal electrons approaches 0 at 0°K. The α model of Casimir and Gorter is shown to be a plausible assumption satisfying the requirements obtained previously, and with sufficient flexibility to represent present data adequately; α is then evaluated from experimental data for tin, mercury, thallium, and indium. The need for precise measurements in fixing α is emphasized, since all values are quite close to the simple parabolic case. The Koppe-Heisenberg form of the model with its unique prediction for the reduced quantities of all superconductors is compared both with the α model and with the experimental values. It is shown not to fit all of the experimental data and also markedly deviates from the α model at very low temperatures. The equations for this model are given in detail in Appendix II in substantially simplified form which reduces them to tabulated functions. It is noted that fundamental justification for any of these forms of the model has not yet been established.

2. GENERAL FORMULATION OF THE TWO-FLUID MODEL

The phenomenological formulation of the model postulates a mixture of two electronic phases in the superconductor when in the superconducting state. One is a degenerate Fermi gas, the "normal" phase, and the other a condensed phase with no temperature excitation (hence no entropy), the "superconducting" phase, and they are assumed to be in equilibrium with each other (and the lattice). The degree of condensation is measured by a parameter ω, which by definition takes only values from 0 to 1 as the temperature falls below the transition temperature T_c (in zero magnetic field). The free energy and internal energy of the system decreases by the condensation energy $-\beta\omega$ where β is a constant, as the condensation proceeds. We may think of ω as measuring the "degree of superconductivity," or the "fraction of superconducting electrons" (relative to the number at 0°K), or as a long-range order parameter in the electron distribution, but it is essentially introduced as a measure of the condensation energy.[5]

The normal phase electrons are assumed to show the temperature excitation of the degenerate Fermi gas, specific heat γT per mole, but the effective number of normal electrons will be assumed proportional to a function of the degree of condensation, $K(\omega)$, where $K(0)=1$ and $K(1)=0$.[6] This dependence on ω is not surprising if we anticipate the statistical explanation of the model,[7] and note that in the ordinary band picture of a metal the effective number of electrons is determined by the density of states at the Fermi surface. This density may be expected to alter strongly in the development of the superconducting state as is specifically indicated by calculations based on the theory introducing interactions of electrons with lattice vibrations.

On the basis of these assumptions, a reasonable form for the Helmholtz free energy per mole of the metal in the superconducting state is

$$F_s(T,\omega)=U_0-\beta\omega-\tfrac{1}{2}\gamma T^2K(\omega)+F_L(T), \qquad (2.1)$$

where two further assumptions have been introduced. First, the zero-point energy of the electron distribution and of the lattice vibrations or internal energy of the metal per mole at 0°K, U_0, is assumed unaltered as electrons transfer from the normal to the superconducting phase, except for the part specifically taken into account by the condensation energy, $-\beta\omega$. Thus the model does not imply that each electronic phase separately builds up its own degenerate Fermi distribution with rapidly changing total numbers of electrons below T_c. Rather the condensation is concerned with processes taking place at the surface of the single Fermi distribution of all the electrons which alter electron energies very slightly near that surface, but no change occurs in the vast bulk of the electrons in the interior of the Fermi sphere whose energies make up the large zero-point energy.

Second, the temperature dependent lattice contribution to the free energy, $F_L(T)$, is assumed independent of ω, i.e., unchanged by the transition to the superconducting state. Although the lattice vibration theory of superconductivity specifically assumes that a strong interaction between electrons and lattice vibrations sets

[5] In view of the direct physical interpretation of ω in the statistical picture, it seems advisable to retain it as the fundamental parameter rather than use the parameter $x=1-\omega$ advocated by P. L. Bender and C. J. Gorter, Physica **18**, 597 (1952), p. 600, on the basis of the analogy with the two-fluid model of liquid helium. In fact the effective number of normal electrons is not proportional to $1-\omega$, as shown by Eq. (2.1).

[6] A discussion is given later (Sec. 4), of the significance of and evidence for the assumption $K(1)=0$.

[7] A plausible statistical basis for the two-fluid model will be developed in detail elsewhere by one of us (P. M. M.).

in at the transition, this is consistent with the assumption about $F_L(T)$ if we assume that the important interactions are only with the short wavelength vibrations at the top of the frequency distribution. At the low temperature of the transition (compared to the Debye temperature), these short wavelengths are not excited being present only in the zero-point oscillation, hence change of ω will affect only the zero-point energies, not $F_L(T)$, and will be absorbed in the condensation energy, $-\beta\omega$.[8]

In fact, the success of the model in accounting for the observed thermodynamic properties will be support for the assumption that the important interactions are with short wavelength zero-point oscillations. In particular, the correct prediction of the behavior under change of isotopic mass will be significant because $F_L(T)$ depends strongly on lattice mass, as will be brought out later (Sec. 3).

In the normal state (unstable in the absence of a magnetic field for $T<T_c$), the free energy corresponding to (1) is

$$F_n(T)=U_0-\tfrac{1}{2}\gamma T^2+F_L(T). \tag{2.2}$$

The equilibrium value of ω, ω_e at any temperature is determined by minimizing F_s, yielding the implicit equation for ω_e as a function of T,

$$K'(\omega_e)=-2\beta/\gamma T^2=K'(0)(T_c/T)^2. \tag{2.3}$$

In the right hand form of Eq. (2.3), ω_e has been set equal to zero at the transition temperature, T_c, thereby assuming that the transition is second order and no abrupt change of ω occurs at T_c.

The critical field H_c at any T is related to the free energy difference by

$$\begin{aligned} H_c^2V_m/8\pi &= F_n(T)-F_s(T,\omega_e) && \text{(a)}\\ &= \beta\omega_e-\tfrac{1}{2}\gamma T^2[1-K(\omega_e)], && \text{(b)} \end{aligned} \tag{2.4}$$

on neglecting penetration effects, so that the Gibbs free energy of the superconducting phase in the field is obtained from F_s simply by adding the term $H^2V_m/8\pi$ per mole,[9] where V_m is the molar volume.

Since by definition $\omega_e=1$ at $T=0$, Eq. (2.4) gives

$$\beta=H_0^2V_m/8\pi, \tag{2.5}$$

where H_0 is the critical field at 0°K. Putting Eq. (2.5) in Eq. (2.3) gives

$$\gamma=-H_0^2V_m/T_c^2 4\pi K'(0), \tag{2.6}$$

a generalization of Kok's relation, derived originally for the case of a parabolic critical field,[10] for which case, as will be shown later, $K'(0)=-\frac{1}{2}$.

Substitution of Eq. (2.6) and Eq. (2.5) in Eq. (2.4) gives the critical field curve, which is, in reduced form,

$$h^2=\omega_e+t^2[1-K(\omega_e)]/K'(0), \tag{2.7}$$

where

$$h=H_c/H_0; \quad t=T/T_c. \tag{2.8}$$

Differentiating Eq. (2.7), and using Eq. (2.3), gives the simple formula for the slope of the reduced field curve:[11]

$$dh/dt=h/t-\omega_e/ht, \tag{2.9}$$

which reduces at the transition temperature where $t=1$, $h=\omega_e=0$, to

$$(dh/dt)_{t=1}=-[-(d\omega_e/dt)_{t=1}]^{\frac{1}{2}}. \tag{2.10}$$

Substitution of Eq. (2.10) in Eq. (2.6) gives

$$\gamma=\left(\frac{dH}{dT}\right)^2_{T=T_c}\frac{V_m}{4\pi K'(0)(d\omega_e/d't)_{t=1}}, \tag{2.11}$$

a formula permitting γ to be determined from the initial slope of the critical field curve once the model is fixed, i.e., once $K(\omega)$ is known.

Finally, using Eq. (2.4), the entropy differences are

[8] In the Debye approximation the lattice zero-point energy included in U_0 is $(9/8)h\nu_mN$, where $\nu_m=kT/\theta$ is the maximum lattice frequency and N the atom density (per mole). The temperature dependent part of the lattice free energy is $F_L(T)=-\frac{1}{5}\pi^4NkT(T/\theta)^3$. Condensation energies in the electron distribution and decreases in the zero-point energies of lattice vibrations cannot really be distinguished, since we are dealing with an interaction in which the energy is not uniquely assigned to either. A further argument that the significant interactions are with short wavelength vibrations has been given by J. Bardeen, Phys. Rev. **81**, 1070 (1951), namely that the transition temperature of films or colloids, 5×10^{-6} cm in dimension, is essentially the same as for bulk material. Hence the long wavelength part of the vibrational spectrum, comparable with 5×10^{-6} cm or greater, which is affected by the small size, is not important for the interaction producing the condensation.

[9] See, for example, P. M. Marcus, Phys. Rev. **88**, 373 (1952), Eq. (3.5) with $\Phi=0$.

[10] J. A. Kok, Physica **1**, 1103 (1934). Bender and Gorter (reference 5) also give an equation equivalent to Eq. (2.6) [their Eq. (12)], in which the function $r(x, T)$, $x=1-\omega$, replaces our $K(\omega)$. The additional generality implied in introducing T explicitly in r does not lead in a simple way to a critical field curve expressed in pure reduced form, as required to explain the isotope effects (Sec. 3), and is not in accord with a statistical picture based on a mean potential which varies with ω (see reference 25). A relation like Eq. (2.6) may, in fact, be established without a model, simply in terms of the form of $h(t)$ near $t=0$ see Eq. (2.7)), by assuming that the entropy difference S_n-S_s (given by Eq. (2.12)) is dominated by a linear term in t, as $t\to0$, which comes from the normal state electronic entropy. This assumption leads to the form $h(t)=1-t^2q(t)$ where $q(0)$ is finite (and $q(1)=1$), and gives $\gamma=H_0^2V_mq(0)/2\pi T_c^2$. It is not necessary to assume the derivatives of $q(t)$ exist at $t=0$, as is done by A. Sommerfeld, Z. Physik **118**, 467 (1941), which in fact is not generally possible for the two fluid model. Compare also Lock, Pippard, and Shoenberg, Proc. Cambridge Phil. Soc. **47**, 811 (1951), p. 818.

[11] Equation (2.9) also follows as a direct consequence of the identity:

$$F_n-F_s=\beta\omega_e+\tfrac{1}{2}T\partial/(\partial T)_V(F_n-F_s),$$

a form not unlike the Gibbs-Helmholtz equation which is obtained by using Eq. (2.12a) in Eq. (2.4). Equation (2.9) could then be used to obtain $\omega_e(t)$ directly from $h(t)$. Equation (2.7) would then give the corresponding value of $K(\omega_e)$, provided that $K'(0)$ is known. Alternatively, differentiating h^2 leads to the simple relation $K(\omega_e)=1-K'(0)[d(h^2)/d(t^2)]$ which also permits evaluating $K(\omega_e)$ from experimental data. If $K(1)=0$, then $K'(0)=1/[d(h^2)/d(t^2)]_{t=0}$. Arguments for $K(1)=0$ are given in Sec. 4, and this is shown to be equivalent to lack of a linear term in S_s, the assumption used in (see reference 10).

given by

$$\left.\begin{aligned} S_n-S_s &= -[\partial(F_n(T)-F_s(T,\omega))/\partial T]_{\nu,\omega=\omega_e} \quad \text{(a)} \\ &= -[\partial(F_n(T)-F_s(T,\omega_e))/\partial T]_{\nu} \quad \text{(b)} \\ &= \gamma T[1-K(\omega_e)], \quad \text{(c)} \end{aligned}\right\} \quad (2.12)$$

which evidently satisfies the requirements of the third law of thermodynamics. Note that ω does not have to be held constant in the differentiation if it has its equilibrium value, ω_e, since $[\partial F_s(T,\omega)/\partial\omega]_{\omega=\omega_e}=0$. Equation (2.12) may also be written in terms of the electronic entropies in the two states as

$$S_n^{\text{elect}}=\gamma T; \quad S_s^{\text{elect}}=\gamma T K(\omega_e). \quad (2.13)$$

Correspondingly the specific heats (all at constant volume) are given by

$$\begin{aligned} C_n^{\text{elect}}/\gamma T &= 1, \quad \text{(a)} \\ C_s^{\text{elect}}/\gamma T &= K(\omega_e)+(K'(0)/t)(d\omega_e/dt) \quad \text{(b)} \\ &= K(\omega_e)-2[K'(0)]^2/t^4K''(\omega_e), \quad \text{(c)} \end{aligned} \quad (2.14)$$

and the discontinuity in specific heat at T_c is then

$$[(C_s-C_n)/\gamma T_c]_{t=1}=-K'(0)(dh/dt)^2_{t=1}. \quad (2.15)$$

Another useful result which follows from Eq. (2.9) may be mentioned here. On making use of the limiting form

$$h\underset{t\to 0}{\longrightarrow}1+t^2/2K'(0),$$

it can be shown that

$$\omega_e\underset{t\to 0}{\longrightarrow}1-t^4/4[K'(0)]^2. \quad (2.16)$$

3. RELATION TO ISOTOPE EFFECTS

The implications of the generalized two-fluid model with respect to isotopic change of lattice mass, M, are obtained from the assumption that $K(\omega)$ is a function characteristic of the electron distribution and independent of M. In addition, γ, the electronic specific heat coefficient in the normal state, a function of the electron distribution and interatomic potential, is plausibly assumed independent of M. The assumption about $K(\omega)$ is not entirely obvious since the lattice vibrations, which depend on M, interact with the electron distribution. However, change of M affects the amplitudes of zero-point oscillations (and the frequencies, although not the wave numbers), hence, may reasonably be thought to affect the strength of the interaction but not the manner of alteration of the electron distribution when the condensation starts, i.e., not the particular way the mean potential alters as the electrons condense. In other words the distortion of the mean potential, or mean energy function for individual electrons, and the consequent effective number of normal electrons, is conceived to depend only on the extent to which the electronic wave functions have altered as a result of condensation, and this extent is measured by the single parameter ω. The distortion is the same even though the same value of ω may be obtained at different T, depending on the strength of the interaction with the lattice vibrations, e.g., as is brought about by change of M.[12] Thus, β or H_0 and T_c are dependent on M, but we assume $K(\omega)$, and γ are not. Hence, ω_e, determined by Eq. (2.3), and $K'(0)$, are functions only of reduced temperature and not of M.

The immediate result of this assumption is that the reduced critical field curve, given by Eq. (2.7), is invariant to change of M, as are the ratio H_0/T_c by Eq. (2.6),[13] and the initial slope of the critical field curve, $(dH/dT)_{T_c}$ by Eq. (2.11) or Eq. (2.10). These conclusions are in agreement with experiment.[14,15] In addition, the reduced electronic entropy and specific heat are invariant functions of reduced temperature, as shown by (2.13), (2.14), (2.15), and as indicated previously for the α model,[4] and termed the similarity property.

Now if the temperature-dependent lattice contribution to the free energy, $F_L(T)$, were a function of ω as well as of T, these conclusions about invariance with respect to M would not follow, since the derivation of Eq. (2.7), depending on Eq. (2.4), would turn up terms involving $F_L(T,\omega)$ which could not be written in reduced form.[16] This means the critical field curve could not be given in purely reduced form, in contradiction to its observed invariance with respect to M. Thus the initial assumption that $F_L(T)$ is independent of ω is supported.

4. SPECIAL FORMS OF K(ω) AND EXPERIMENTAL COMPARISONS

Although $K(\omega)$, the effective number of normal electrons (relative to the normal state), cannot be determined without a detailed theory of the interaction producing the electron condensation, some information about $K(\omega)$ follows from the condition that the phase transition be a second-order transition (an assumption already used in the general analysis of Sec. 2). Thus ω must shown no sudden jumps at T_c or at lower T (note all considerations are for zero magnetic field). It will follow that the α model of Casimir and Gorter is a permissible and plausible choice to represent $K(\omega)$ which then permits systematic and satisfactory repre-

[12] For example, Bardeen's interaction term in the Hamiltonian is assumed proportional to the lattice vibration amplitudes [Phys. Rev. **80**, 567 (1950), Eq. (2.6)], and this makes the interaction energy, or H_0^2 [Eq. (4.26)], proportional to M^{-1}, as observed in the isotope shift.

[13] Note that the relation between γ and $q(0)$ in reference 10 established without any model shows that the invariance of H_0/T_c to change of M follows directly from the invariance of $h(t)$ and γ, and is thus not an independent test of the model.

[14] E. Maxwell, Phys. Rev. **86**, 235 (1952).

[15] Lock, Pippard, and Shoenberg, Proc. Cambridge Phil. Soc. **47**, 811 (1951).

[16] The critical field curve becomes

$$h^2=\omega_e+\beta^2\frac{[1-K(\omega_e)]}{K'(0)}-\beta^2\frac{[1-K(\omega_e)]}{\beta K(0)}\frac{\partial F_L(T,\omega_e)}{\partial\omega_e}+\frac{1}{\beta}[F_L(T,0)-F_L(T,\omega_e)].$$

sentation of the measured values of thermodynamic properties.

By definition ω takes values only in the restricted, positive range from 0 to 1, and β, the condensation energy, is an intrinsically positive quantity, as shown by Eq. (2.5). Then $K(\omega)$ must decrease as ω increases from 0, for if $K(\omega)$ increased with ω, finite values of ω would be favorable at all T since $F_s(T,\omega)$, as given by Eq. (2.1), would then decrease. Also $K(0)=1$, since by definition $\omega=0$ in the normal state, corresponding to F_n given by Eq. (2.2).

Evidently values of $\omega>0$ will not be favorable as long as $(\partial F_s(T,\omega)/\partial\omega)_{\omega=0}>0$. The transition point, given by

$$(\partial F_s(T_c,\omega)/\partial\omega)_{\omega=0}=-\beta-\tfrac{1}{2}\gamma T_c^2K'(0)=0, \quad (4.1)$$

marks the beginning of the temperature range in which finite values of ω are favorable. However, if a finite jump increase in ω at T_c is not to be favorable, we must have

$$(\partial^2F_s(T_c,\omega)/\partial\omega^2)_{\omega=0}=-\tfrac{1}{2}\gamma T_c^2K''(0)>0, \quad (4.2)$$

since the second derivative will dominate the change of F_s with ω at T_c. From Eq. (4.1) or Eq. (2.3), $K'(0)<0$, and from Eq. (4.2), $K''(0)<0$.

The same arguments apply at any $T<T_c$ if no finite jumps in ω are to occur and lead to the general conditions:[17]

$$K'(\omega)<0; \quad K''(\omega)<0; \quad 0\leq\omega\leq1. \quad (4.3)$$

A further interesting general result is that ω_s must be a monotonically increasing function of t as t decreases, since by Eq. (4.3) $K'(\omega)$ is negative and decreasing as ω increases, and by Eq. (2.3) which gives ω_s as a function of t, $K'(\omega_s)$ monotonically decreases (algebraically) as t decreases.

In addition to the conditions Eq. (4.3) on $K(\omega)$, $K(0)=1$ as noted above and it is reasonable to take $K(1)=0$. The latter implies that the effective number of normal electrons vanishes at 0°K, a conclusion for which there is some evidence from the specific heat and from the behavior of the high-frequency losses. Thus if $K(1)$ is finite, there will be a linear term in the specific heat of the superconducting phase.[18] Since no linear term has been observed, this is also evidence that $K(1)=0$. Pippard[19] has shown that the losses in tin at 3-cm wavelength approach zero at 0°K, hence $K(\omega)$ should approach zero at 0°K, since it is plausible that the same $K(\omega)$ enters into the effective number of normal electrons determining both the specific heat and the Ohmic conductivity (at sufficiently low frequencies —at higher frequencies excited electrons produced by internal photoeffect might be expected to produce additional Ohmic currents).

Now a general function that satisfies the boundary conditions $K(0)=1$, $K(1)=0$ can be given in the form

$$K(\omega)=(1-\omega)^{\alpha(\omega)}. \quad (4.4)$$

$\alpha(\omega)$ might be reasonably expected to be a slowly varying function of ω, since the boundary conditions at $\omega=0$, 1 are automatically satisfied for any finite α (which is positive at $\omega=1$). The conditions Eq. (4.3) will now give restrictions on the slowness of variation of $\alpha(\omega)$, namely on its derivatives, but it will be sufficient here to show that constant α provides enough flexibility to reproduce the measured values. This is the original model of Casimir and Gorter,[1] conveniently termed the α model. The conditions, Eq. (4.3) then require[20]

$$0<\alpha<1. \quad (4.5)$$

The general relations of Sec. 2 reduce to special forms for the α model. These are tabulated briefly for

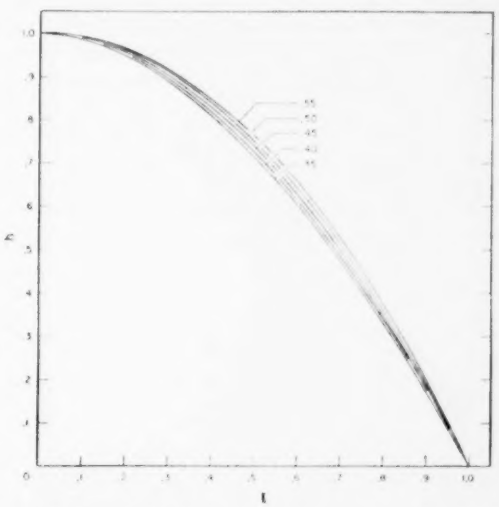

FIG. 1. Reduced critical field curves according to the α model for various values of α.

[17] The argument is really repeated at $\omega=\omega_s$ for each $t<1$, at which $(\partial F_s(T,\omega_s)/\partial\omega)=0$, but this covers $0\leq\omega\leq1$. Conditions similar to (4.3) are obtained by Landau and Lifshitz at the Curie point of a general order-disorder transformation, also by consideration of expansions in powers of the order parameter. See L. Landau and E. Lifshitz, *Statistical Physics* (Oxford University Press, London, 1938), e.g., p. 207, Eq. (69.5).

[18] If $K(1)$ were finite it would follow from Eq. (2.13) that S_s^{elect} would contain a linear term (plus higher order terms). Consequently C_s^{elect} would also contain a linear term. Otherwise stated a linear term in Eq. (2.14b) would arise only from $K(1)\neq0$, since, as a consequence of Eq. (2.16), the term $[K'(0)/t](d\omega_s/dt)\rightarrow0$ as $t\rightarrow0$.

[19] A. B. Pippard, Proc. Roy. Soc. (London) **A203**, 98 (1950).

[20] In a certain sense a superconductor with larger α may be regarded as more strongly superconducting since $\alpha\rightarrow1$ tends to convert the second-order transition into the stronger first-order type. Smaller α makes the transition less abrupt (possibly non-superconductors can be interpreted as having $\alpha<0$). α measures how strongly the electron condensation affects the mean potential acting on all electrons, but does not measure the size of the condensation energy which is what determines T_c. It will be readily seen that α is given by $-K'(0)$, the rate at which the effective number of normal electrons decreases as the condensation process starts.

reference in Appendix I together with the special simple case $\alpha=\frac{1}{2}$ which leads to the well-known parabolic critical field law and has a special place in the theory.

The significance of the case $\alpha=\frac{1}{2}$ with its particularly simple formulas is shown by the reduced critical field curves in Fig. 1. The curves cross at $t=0$ and 1, and all have zero slope at $t=0$. In fact the curves for the general case with arbitrary $K(\omega)$ are all parabolic for small t, although with different curvatures, since the temperature-dependent part of (2.4) is then dominated by the term $-\frac{1}{2}\gamma T^2$ which arises from the Fermi-Dirac statistics.[21] In addition the curves are rather insensitive to change of α around $\frac{1}{2}$; thus a 20 percent change from 0.5 to 0.4 produces a maximum deviation in h values of only 5 percent. The curves therefore all tend to look parabolic, and rather good precision (of the order of a few tenths of a percent), only recently attained, is required to fix α more exactly from experimental data.

Curves showing the deviations from the parabolic case, $h_\frac{1}{2}-h_\alpha$, plotted in Fig. 2 against t^2, are convenient for analyzing the experimental results.[22] Some of the experimental data for tin, thallium, indium, and mercury are shown in Fig. 2, for purposes of comparison. The general trend of these data is consistent with the form suggested by the α model in the measured range of temperature. The fact that tin, thallium, and indium appear to be characterized by the same value of α (0.38) is probably without significance. The internal consistency of the data is good, as indicated by the relatively small scatter. Nevertheless the degree of convexity of the experimental curves, and consequently the appropriate α, is sensitive to small changes in the value of H_0 used for normalization. H_0 is obtained by an extrapolation procedure which involves fitting the data to some smooth function, in the case of Fig. 2, a cubic equation. However with another and equally reasonable choice of smoothing function it was observed that the indium and thallium points shifted down to the neighborhood of the $\alpha=0.45$ curve while the tin points continued to cluster around $\alpha=0.40$. Nevertheless the curves are definitely convex in spite of the fact that α cannot be precisely specified. For mercury, however, the data are very closely parabolic. A fuller discussion of these and other experimental matters will appear in another paper.[22]

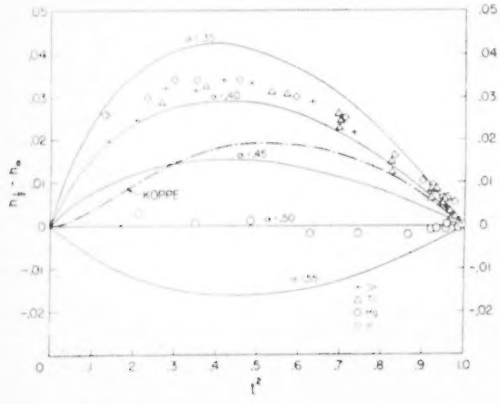

FIG. 2. Plots of the deviation of the critical fields from parabolic form for the α model, the K model, and the experimental data.

Also plotted in Fig. 2 are the predicted values given by an interesting special form of the two-fluid model due to Koppe[23] which has been used in two recent papers to compare with experimental results.[24] Koppe obtains a unique form for $K(\omega)$ and the various thermodynamic functions by means of a statistical assumption derived from Heisenberg's theory of superconductivity. Koppe's curve is not inconsistent with the indium and thallium data, if we take into account the uncertainties in H_0 discussed above. There would appear to be a small, but not very serious disagreement with the tin data. For these three metals both the Koppe model and the α model are plausible descriptions at temperatures above 1°K. The mercury data are, however, accurately parabolic and hence conflict with Koppe's model which predicts a universal (nonparabolic) critical field curve for all superconductors. The parabolic behavior was first observed both in a mercury sample contained in a glass capillary and later confirmed for a single-crystal free rod, thus minimizing the possibility of secondary effects due to strain.

No single value of α will fit Koppe's curve, as shown by Fig. 3 where the equivalent α values, i.e., the values of constant α giving the same h at that t, are plotted against t. [These are not quite the values of $\alpha(\omega)$ that would occur in a representation of Koppe's curve in the form Eq. (4.4).] The difference from the α model is particularly marked at low t, where Koppe's values for the effective number of normal electrons, n_s, proportional to $K(\omega)$, decrease more rapidly than any α model and the decrease is, in fact, exponential as shown by (II.18). Analysis of electronic specific heat and thermal conductivity measurements should be useful here, since they depend directly on n_s, whereas h is rather insensitive to n_s at low t (all curves becoming parabolic with zero slope at $t=0$; Koppe's curve has also the same curvature as the simple parabola of the case $\alpha=\frac{1}{2}$). (See remarks under footnote 26.)

Koppe's equations follow from the assumption that the density of electron states (in energy) has a discontinuity at the Fermi level (for 0°K), ϵ_0, remaining the same below ϵ_0, but being reduced by the factor $(1-\omega)$ above ϵ_0. This is qualitatively deduced from Heisenberg's picture of a condensation of a portion ω of the electrons at the Fermi surface resulting from Coulomb

[21] $K(1)=0$ and $(1-\omega_s)/t^2\to 0$ as $t\to 0$ as in reference 19.
[22] E. Maxwell and O. S. Lutes (to be published).
[23] H. Koppe, Ann. Physik (6), **1**, 405 (1947).
[24] Reference 5 and Worley, Zemansky, and Boorse, Phys. Rev. **87**, 1142(L) (1952).

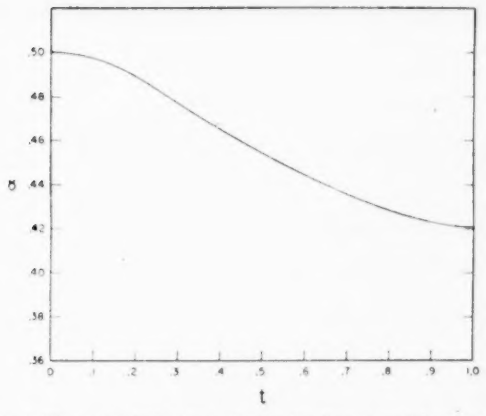

FIG. 3. The equivalent values of α for the Koppe model expressed as a function of t.

interactions between electrons.[25] The density of states is thus not defined at the Fermi level because of the discontinuity, but it is not surprising that the statistical calculation gives for $K(\omega)$ a value close to the geometric mean of the two values above and below the discontinuity, namely $(1-\omega)^{\frac{1}{2}}$. Koppe's formulas may be obtained in simplified form by evaluating the Fermi-Dirac integrals differently (without the usual integration by parts), and in fact reduced to tabulated functions, so that it seems worth while to repeat some of them here, and they are listed in Appendix II.[26] Goodman has independently obtained simplifications of Koppe's equation similar to those given here (Cambridge thesis, unpublished).

In view, on the one hand, of the recent successes of the lattice vibration interaction theory and, on the other hand, of various severe criticisms of the Heisenberg theory, it would seem that the original basis for Koppe's assumptions is very doubtful. His resulting value for $K(\omega)$ is, however, quite reasonable, although it is quantitatively in disagreement with experimental results for mercury. The greater flexibility of the α model permits fairly accurate characterization of all the measurements, although it too has as yet no fundamental justification.

It is noteworthy that Koppe has made a definite and quite simple statistical assumption in deriving his results, thus going one stage further back than the discussion of the α model given above. However a similar, although not as simple, statistical assumption could easily be introduced to obtain the α model[27] and eventually the lattice vibration theory may derive some statistical basis of this kind. Meanwhile the adequacy of the α model should be tested by additional measurements, both on more superconductors, and at lower temperatures where the predictions of the two models above differ substantially with regard to the effective number of normal electrons.

The authors are indebted to Dr. J. Bardeen for helpful comment and discussion.

APPENDIX I

Tabulated Relations for the α Model

		General α	Case $\alpha=\frac{1}{2}$	
$K(\omega)$	=	$(1-\omega)^{\alpha}$	$(1-\omega)^{\frac{1}{2}}$	(I.1)
$K'(0)$	=	$-\alpha$	$-\frac{1}{2}$	(I.2)
ω_c	=	$1-t^{2/(1-\alpha)}$	$1-t^4$	(I.3)
$K(\omega_c)$	=	$t^{2\alpha/(1-\alpha)}$	t^2	(I.4)
h^2	=	$1-t^2/\alpha+(1/\alpha-1)t^{2/(1-\alpha)}$	$(1-t^2)^2$	(I.5)
$(dh/dt)_{t=1}$	=	$[2/(1-\alpha)]^{\frac{1}{2}}$	2	(I.6)
γ	=	$H_0^2V_m/T_c^2 4\pi\alpha$	$H_0^2V_m/T_c^2 2\pi$	(I.7)
γ	=	$(dH/dT)^2_{T=T_c}V_m(1-\alpha)/8\pi\alpha$	$(dH/dT)^2_{T=T_c}V_m/8\pi$	(I.8)
$S_s^{\text{elect}}/\gamma T$	=	$t^{2\alpha/(1-\alpha)}$	t^2	(I.9)
$C_s^{\text{elect}}/\gamma T$	=	$t^{2\alpha/(1-\alpha)}(1+\alpha)/(1-\alpha)$	$3t^2$	(I.10)
$(C_s-C_n)/\gamma T_c$	=	$2\alpha/(1-\alpha)$	2	(I.11)

[25] The relation of Koppe's theory to a more general statistical treatment of the superconducting condensation will be given in more detail separately (see reference 7). This treatment relates the condensation to the usual band theory of metals by introducing a mean potential for any of the electrons, which depends on and which determines the quantum levels over which all the electrons are distributed according to the Fermi-Dirac statistics. The treatment is qualitatively linked to the lattice vibration interaction theory.

[26] Preliminary reports of thermal conductivity measurements at very low t do indicate an exponential form for the effective number of normal electrons; B. B. Goodman, Cambridge thesis (unpublished) also Report on Oxford Conference for Very Low Temperature Physics (1951); Proc. Phys. Soc. (London) **A66**, 217 (1953); J. G. Daunt *et al.*, Proceedings of Schenectady Cryogenics Conference (1952). Thus while the α model may be adequate for $t>0.3$, a form of $K(\omega)$ like that of Koppe's may be better at lower t, although it should be noted that Koppe predicts the same exponential for all superconductors, as shown by (II.18).

[27] Assume the density of states for energies greater than ϵ_0 is reduced by a factor $g(\omega)$ rather than $(1-\omega)$. Then for each α, $g(\omega)$ can be determined to give $K(\omega)=(1-\omega)^{\alpha}$. (II.1), (II.2) are simply modified by replacing by $1-g(\omega)$ wherever ω appears explicitly. (II.4), (II.5) have similar, although slightly different, replacements.

APPENDIX II

Simplified and Limiting Forms of Koppe's Model

$$K(\omega)=(1-\omega)(1+3a^2/\pi^2\omega) + (6\omega/\pi^2)f(1/(1+e^a), \quad \text{(II.1)}$$

$$\omega=a/\ln(1+e^a), \quad \text{(II.2)}$$

$$f(x)=-\int_0^x dx\,\ln(1-x)/x=\sum_{n=1}^{\infty}x^n/n^2, \quad \text{(II.3)}$$

$$K'(\omega)=-1+3a^2(1-2\omega)/\pi^2\omega^2 + (6/\pi^2)f[1/(1+e^a)], \quad \text{(II.4)}$$

$$K''(\omega)=-(6a/\pi^2\omega)(da/d\omega). \quad \text{(II.5)}$$

Together with Eqs. (2.3)–(2.15), (II.1)–(II.5) permit simple numerical calculation of the various thermodynamic functions and the critical field curve. The function $f(x)$ has been discussed and tabulated by Mitchell.[28] In the present application the complete range of interest is $0\leqslant x\leqslant 0.5$ for which the series converges rapidly; in the worst case, $x=0.5$, only 8 terms are required for four place accuracy.

Of particular interest are the limiting forms of the functions in (II.1)–(II.5) and various other functions, as t approaches 1 and 0, since these permit direct comparison with the α model. Thus, when

$$t\to 1, \quad \omega_e\to 0, \quad a_e\to 0, \quad \text{(II.6)}$$

$$a\cong\omega(1+\omega/2)\ln 2+O(\omega^3), \quad \text{(II.7)}$$

$$K(\omega)\cong K(0)+\omega K'(0)+(\omega^2/2)K''(0)+O(\omega^3) \quad \text{(II.8)}$$

$$=1-(\omega/2)-(3/\pi^2)(\ln^2 2)\omega^2+O(\omega^3),$$

$$\omega_e\cong(\pi^2/6\ln^2 2)(1-t)+O[(1-t)^2], \quad \text{(II.9)}$$

$$[(C_e-C_n)/\gamma T_c]_{t=1}=(\pi^2/12\ln^2 2)=1.7118; \quad \text{(II.10)}$$

and similarly when

$$t\to 0, \quad \omega_e\to 1, \quad a_e\to\infty, \quad \text{(II.11)}$$

$$(1-\omega)\cong(e^{-a}/a)+O(e^{-2a}/a), \quad \text{(II.12)}$$

$$K(\omega)\cong e^{-a}(3a/\pi^2+6/\pi^2+1/a)+O(ae^{-2a}), \quad \text{(II.13)}$$

$$K'(\omega)=-1-3a^2/\pi^2+6e^{-a}/\pi^2+O(ae^{-2a}), \quad \text{(II.14)}$$

$$a_e\cong(c/t)(1-t^2+O(t^4)+O(e^{-a_e}/a_e), \quad \text{(II.15)}$$

where

$$c=(\pi^2/6)^{\frac{1}{2}}=1.2826, \quad \text{(II.16)}$$

$$\omega_e=1-(t/c)e^{-c/t}[1+tc+(1+c^2/2)t^2 + O(t^3)]+O(e^{-2a_e}/a_e), \quad \text{(II.17)}$$

$$K(\omega_e)=(e^{-c/t}/2ct)[1+(c+2/c)t+(3+c^2/2)t^2 + O(t^3)]+O(a_e e^{-2a_e}). \quad \text{(II.18)}$$

[28] K. Mitchell, Phil. Mag. **40**, 351 (1949). $f(x)$ is tabulated over $x=-1.00(0.01)1.00:9D$ and over $x=0.000(0.001)0.500:9D$.

The Field Emission Initiated Vacuum Arc. I. Experiments on Arc Initiation*

W. P. Dyke, J. K. Trolan, E. E. Martin, and J. P. Barbour
Physics Department, Linfield College, McMinnville, Oregon

(Received March 30, 1953)

It is known that electrical breakdown between metal electrodes can be initiated by field emission. The present work concerns a further study of that initiation process under conditions of excellent vacuum and a clean cathode surface.

As the field current density from the single crystal tungsten emitter is continuously increased, the normal emission is terminated by an explosive vacuum arc. Since this breakdown occurs in less than a microsecond, the experimental observations were obtained by use of pulse electronic techniques. The magnitude of the electric field, current density, and work function at the cathode were simultaneously determined prior to breakdown. From this investigation it has been established that:

(1) the vacuum arc was initiated at a critical value of the field current density of the order of 10^6 amperes/cm^2;

(2) breakdown was predictable and not random; in fact easily recognizable conditions preceding arc formation have been established; at current densities just below the critical value, an electron emission process was observed, which apparently involved both high electric fields and high temperatures;

(3) arc formation did not require cathode bombardment by material from the anode or from residual gases;

(4) breakdown was independent of the applied microsecond voltage in the range $5<V<60$ kv, provided the critical current density was not exceeded;

(5) the current during arc exceeded the initiating field current by a factor of at least 100.

INTRODUCTION

HIGH field current densities are known to initiate electrical breakdown between metal electrodes in vacuum[1] but the mechanisms involved in the initiation of that breakdown have not been well understood. The present work concerns a further study of the problem and is one of a series of investigations concerned with phenomena accompanying field emission of electrons at very large current densities.

Field emission was recognized as an initiating factor for the breakdown of static potentials of the order of 10 kv between metal electrodes in vacuum in earlier experiments.[2–4] When the static potential was increased to the order of 100 kv, electrical breakdown was increasingly dependent on total voltage[4] in contrast with its dependence on electric field at lower voltages. In other experiments,[1,5,6] when high voltages were applied for short time intervals, breakdown was dependent on the electric field at the cathode. In some experiments, breakdown was thought to be initiated by various mechanisms involving anode material;[3,4,7,8] however, more recently, positive ion emission coefficients have been found insufficient[9] for a proposed particle interchange mechanism.[4] Adsorbed gas on the cathode surface[5] and residual gas in the experimental tube[3] have been considered in other proposed explanations for breakdown. Few of those earlier experiments were favored by the high vacuum and clean surfaces available through recently developed techniques.[10,11] Electrical breakdown generally was observed at calculated values of the electric field about an order of magnitude less than that required theoretically[12] for appreciable field emission. It was supposed in most cases that the electric field was intensified in the vicinity of surface irregularities[13] which could not be resolved by optical microscopy. Arcing at electrical contacts on closure in air was recently recognized as being initiated by field emission at voltages less than 100 volts.[14,15]

Neither electrical breakdown nor appreciable field emission was observed for values of the electric field less than those for which field emission is predicted theoretically when very high vacuum and smooth, clean electrode surfaces were obtained. Under such conditions and with static potentials less than 20 kv, the field current density from a tungsten single crystal followed the value predicted by the wave mechanical field emission theory[12] up to a current density of the order of 10^6 amperes/cm^2.[1,16] At larger direct current densities, electrical breakdown was observed.[1] Under similar experimental conditions when microsecond potentials up to 30 kv were used, the field current density in-

* Most of the support for this work was extended by the U. S. Office of Naval Research; in part it was supported by the U. S. Air Force through the Microwave Laboratory of the University of California.

[1] W. P. Dyke and J. K. Trolan, Phys. Rev. **89**, 799 (1953).
[2] A. J. Ahearn, Phys. Rev. **50**, 238 (1936).
[3] W. H. Bennett, Phys. Rev. **39**, 182 (1932); **40**, 416 (1932).
[4] J. G. Trump and R. J. Van de Graaff, J. Appl. Phys. **18**, 327 (1947).
[5] W. Kilpatrick, Report of University of California Radiation Laboratory (unpublished).
[6] D. H. Goodman and D. H. Sloan, Phys. Rev. **82**, 575 (1951).
[7] W. H. Bennett, Phys. Rev. **45**, 891 (1934).
[8] Lawrence Cranberg, J. Appl. Phys. **23**, 518 (1952).
[9] Webster, Van de Graaff, and Trump, J. Appl. **23**, 264 (1952).
[10] R. T. Bayard and D. Alpert, Rev. Sci. Instr. **21**, 6, 571 (1950).
[11] W. B. Nottingham, Abstracts of Field Emission Seminar, Linfield College, 1952 (unpublished).
[12] A. Sommerfeld and H. Bethe, *Handbuch der Physik* (J. Springer, Berlin, 1933), Vol. 24, No. 2, p. 441.
[13] W. Schottky, Z. Physik **14**, 80 (1923).
[14] L. H. Germer, J. Appl. Phys. **22**, 955 (1951); **22**, 1133 (1951).
[15] L. H. Germer and J. L. Smith, J. Appl. Phys. **23**, 553 (1952).
[16] R. H. Haefer, Z. Physik **116**, 604 (1940).

creased with applied potential in the manner predicted by the theory (when space charge effects were recognized) up to a critical current density J_x in the range $10^7 < J_x < 10^8$ amperes/cm².[1] Upon a further increase in current density, the normal field emission was terminated by a low-impedance vacuum arc which altered the emitter geometry. Evidence indicated that the vacuum arc was caused by thermal effects when the emitter was heated by a current density-dependent process, the resistive mechanism being one possibility.[2,17]

It was recognized that resistive heating would provide an upper limit for the current densities emitted stably and it was desirable to show whether or not the densities obtained in reference 1 corresponded to that limit. Calculations are presented in Part II of the present work for the temperature rise expected in a typical field emitter due to the resistive process when the simultaneous dissipation of heat by conduction is considered.

In Part I are presented several experiments concerning arc initiation under conditions of excellent vacuum and a clean tungsten cathode surface. The evidence[1] indicated that electrical breakdown under such conditions was not dependent on bombardment of the cathode by positive ions; however that evidence was largely indirect and by no means complete. The contribution of such cathode bombardment was evaluated by more direct methods in the present work in order to (1) determine whether or not yet larger current densities desired for several experiments were physically attainable, and (2) better identify the mechanisms fundamental to arc initiation. Bombardment of the cathode was minimized when the production of ions was limited by use of very high vacuum and clean electrode surfaces. Bombardment of the cathode by chemically active ions, if appreciable, was recognized[18] from its effect on the emission pattern from the clean tungsten emitter, which pattern was viewed in a modified Mueller projection tube.[19] In one experiment, bombardment of the cathode by ions formed at the anode was precluded by use of a voltage pulse whose time duration was short compared with the ion transit times.

In a second experiment, the arc formation was observed with various voltages up to 60 kv of microsecond duration to determine whether or not (1) large field current densities were emitted stably at high voltages, and (2) breakdown depended on total voltage in the manner reported by Trump and Van de Graaff[4] under other experimental conditions. No such effect was observed when voltages were applied for short time intervals by Kilpatrick,[5] Sloan and Goodman,[6] and by Dyke and Trolan;[1] however the voltages used in reference 1 were low, i.e., $5 < V < 32$ kv.

A third experiment is described in which the normal field current prior to arc was compared by direct measurement with the current during arc. The magnitude of the latter was previously inferred[1] from the voltage wave shape through circuit analysis.

Anomalies in the pre-arc performance of the field emitter were observed which showed that electrical breakdown is predictable and not random under the present experimental conditions.

EXPERIMENTAL METHODS

Field emission is known to initiate the electrical breakdown whose study is the subject of the present work. It therefore appeared logical that the mechanisms involved in the initiation of that breakdown could best be identified by an experimental method which permitted a simultaneous determination of the values of the variables fundamental to field emission, i.e., current density J, electric field F, and work function ϕ. These variables are related in the theoretical expression:[12]

$$J = 1.55 \times 10^{-6} (F^2/\phi) \exp[-6.85 \times 10^7 \phi^{\frac{1}{2}} f(y)/F], \quad (1)$$

where J is in amperes/cm², F is in volts/cm, and ϕ is in electron volts.

In many of the earlier experiments, unresolved surface geometry of the emitter precluded accurate calculation of both F and J. When field currents were identified, use was made of the empirical relationship[20] between current I and voltage V:

$$I = C \exp(-B/V), \quad (2)$$

which is an adequate procedure provided that C and B are constants as supposed by the authors of Eq. (2), who noted the rigorous experimental conditions required for that purpose (very high vacuum and clean surfaces). Under experimental conditions which are less favorable but more frequently reported in earlier work, significant time-dependent changes in both C and B are expected in view of the recent field emission literature. These result from changes in ϕ due to surface contamination[11,16,18,19] and from changes in F due both to the growth of crystallites of impurities on the emitting surface[16] and to the surface migration of the emitter material.[21] A plausible combination of these effects results in a change in J in excess of a factor of 10^4 at constant voltage. Use of Eq. (1) when experimental conditions are such that C and B are not constant could result in failure (1) to identify field currents as such, and (2) to identify the mechanism by which field emission initiates electrical breakdown.

The transition between the normal field emission and the vacuum arc was studied previously[1] with improved field emission techniques[22] through which the values of electric field and current density were known accurately prior to breakdown. Those techniques were again used

[17] E. W. Mueller, Z. Physik **106**, 132 (1937).
[18] J. A. Becker, Bell System Tech. J. **30**, 907 (1951).
[19] E. W. Mueller, Z. Physik **106**, 541 (1937).
[20] R. A. Millikan and C. C. Lauritsen, Proc. Nat. Acad. Sci. U. S. **14**, 1 (1928).
[21] E. W. Mueller, Z. Physik **126**, 642 (1949).
[22] Dyke, Trolan, Dolan, and Barnes, J. Appl. Phys. **24**, 570 (1953).

in the present paper and in addition the values of the work function of the emitting surface were known from previously published data for clean tungsten,[23] when the cleanliness of the present emitting surfaces was determined by analysis of the electron emission pattern obtained in a Mueller projection tube.

Since the vacuum arc is initiated in less than a microsecond,[1] it was necessary to record the present data during individual time intervals of that order. Voltage was applied as a pulse of microsecond duration; voltage and current were recorded as oscillographs by previously published methods[1] and data were taken on an individual pulse basis. From measurements of the oscillographs, the current-voltage relationship was determined. A photograph of the electron emission pattern was taken during each microsecond current pulse.

The present experiments were conducted in the modified Mueller projection tube, shown in Fig. 1. Electrons diverged from the field cathode C and impinged on the anode, a phosphor screen P, where the enlarged electron emission pattern was viewed. The screen, a thin layer of willemite (1 mg/cm^2) was deposited on the inner surface of one hemisphere of the Pyrex envelope by the lacquer flow method. In order to provide a low-impedance anode which would conduct arc currents of the order of 100 amperes without significant anode potential drop, a thin layer of aluminum (1500A), connected electrically to the anode inseal A, was evaporated onto the inner surface of the phosphor and on the remaining inner surfaces of the Pyrex flask. The aluminum film was transparent to primary field electrons with energies used herein;[24] it was relatively opaque to lower-energy secondary electrons, to light, and to negative ions, thus limiting emission pattern aberrations due to those causes. Since the aluminum film shielded the cathode from stray fields due to charges which accumulate on insulating surfaces, it was possible to calculate the cathode electric field accurately from the measured potential and emitter geometry by previously described techniques.[22]

By use of the experimental tube in Fig. 1, it was possible to observe a series of electron emission patterns which were exposed during individual microsecond intervals at successively increased values of the applied potential during the transition from the normal field emission to the vacuum arc. From the emission patterns it was possible to detect surface contaminants, crystallite growth, and surface migration or other geometric change at the cathode. It was also possible to monitor residual pressure of chemically active gases and to detect gap traversal by anode ions.

Pressures of chemically active gases of the order of 10^{-12} mm of Hg which were used in most of the present work were obtained by methods discussed in references 1 and 11.

[23] M. H. Nichols, Phys. Rev. **57**, 297 (1940).
[24] D. W. Epstein and L. Pensak, RCA Rev. **7**, 5 (1946).

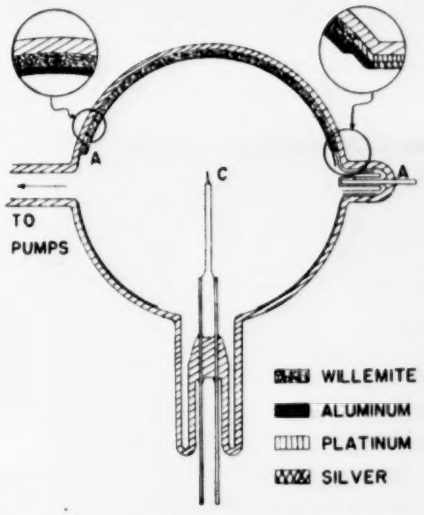

FIG. 1. Experimental field emission tube. (C), field cathode; (A), aluminum-backed-willemite anode.

Two changes in the voltage pulser of reference 1 are noted. In the present work, ½-microsecond pulses were obtained from an artificial line, while shorter pulses were obtained from a 70-ohm coaxial cable. For high-voltage microsecond operation, a 100-kv, 100-ampere pulse transformer, supplied by the University of California Radiation Laboratory, was used.

RESULTS AND CONCLUSIONS

1. Coincident Anomalies in the Current Pulse and Emission Pattern Which Mark the Onset of Breakdown

The experimental data from emitter 0–38 were recorded as shown in Fig. 2. Each emission pattern photograph and the oscillographs of the current and voltage waves with which it was coincident were obtained during a single-microsecond interval of operation. From those and other similar data from the same emitter, the current-voltage relationship for its combined direct current and pulsed operation was plotted in Fig. 3. In that figure, the several experimental points which are lettered correspond to the data with the same letters in Fig. 2. These data are typical of that from each of fifteen emitters which were tested.

The present study of electrical breakdown will consider the data at the large current extremity of the graph in Fig. 3; however, a brief parenthetical comment on the rest of the data in that figure may be instructive. The graph departs from linearity at C, such departure being similar to that observed for other emitters.[1] The departure was assumed to be an effect of space charge on the cold cathode emission. Figure 13 of reference 1 described the probable effect of the space charge upon the surface distribution of the field current density. That result is qualitatively confirmed by a

comparison of the emission patterns in Figs. 2(C) and 2(D). The former was taken at the largest current for which space charge was negligible; the latter corresponds to a marked space-charge influence. As may be seen from the corresponding emission pattern, Fig. 2(D), space charge resulted in a relatively uniform current density (except in the high work function (110) crystal directions) over an increased emitting area including most of the emitter hemisphere. The correlation between current density, crystallographic direction and emitting areas on the surface of such hemispherical single crystal tungsten field emitters is described elsewhere.[17,25] A more quantitative analysis of the effects of space charge on field emission will be submitted for publication at a later date.

Marked changes in the normal performance of the field emitter were observed just prior to electrical breakdown. Anomalies appeared both in the current wave shape and in the emission pattern during a 30 percent increase in current density to the critical value J_x at which arc resulted. However, if arc was avoided by keeping the current density below J_x, those pre-arc anomalies, and the entire performance of the emitter at all lower current densities were reproducible and reversible.

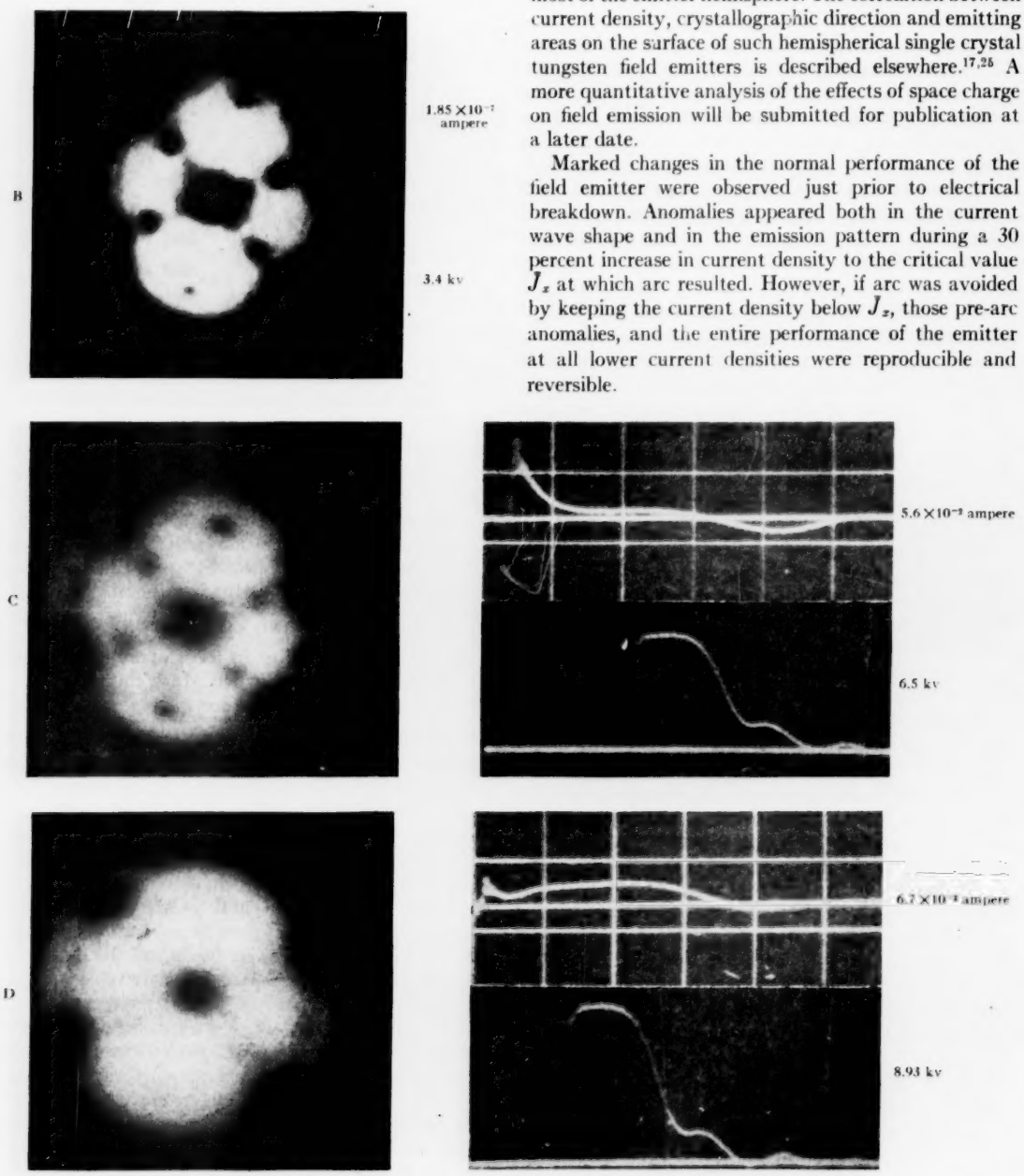

FIG. 2. Typical experimental data as recorded for emitter 0–38 including emission pattern photographs (left) and corresponding current and voltage oscillographs (right) at various current and voltage levels. Data are lettered corresponding to points with the same letter on the graph of Fig. 3. Direct current operation at (B), pulsed operation at (C), (D), (E), and (F). Peculiarities at the leading and trailing edges of the current pulse were due to circuitry, not field emission.

[25] I. N. Stranski and R. Suhrmann, Ann. Physik 1, 153 (1947).

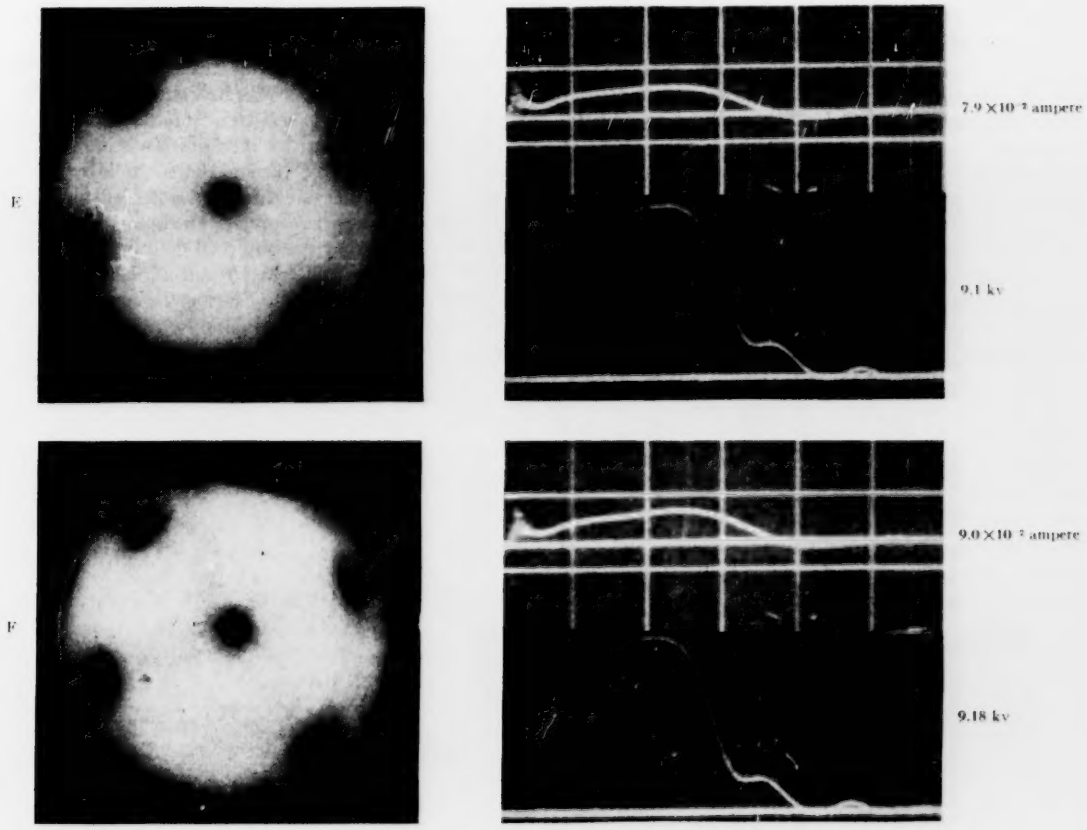

FIG. 2.—*Continued.*

One of the pre-arc anomalies in emitter performance was an increase in current with time while voltage was held constant [Fig. 2(F)]. That anomaly, previously[1] called "tilted current pulse" and abbreviated as "tilt" hereafter, was not characteristic of the cold cathode field emitter. The normal field current was constant when voltage was constant as was expected from Eq. (1). Such a normal current pulse is shown in Fig. 2(D), which was typical of that obtained from lower currents.

With the tilt there appeared simultaneously an anomaly in the emission pattern, a "ring" of electron emission concentric with and external to the normal pattern [Fig. 2(F)]. Evidently the ring was not due to electron emission under the influence of electric field alone, since the increase in ring intensity during the series of patterns 2(D) through 2(F) was considerably greater than that expected from Eq. (1) for the 3 percent increase in applied potential during the series. The expected change in current density was a factor of 1.6, while the observed change in intensity in the ring was in excess of an order of magnitude, based on an estimate aided by a densitometric analysis of the photographic negatives of the emission patterns.[26]

[26] Dyke, Trolan, Dolan, and Grundhauser (to be published).

Electrical breakdown in the form of an explosive vacuum arc occurred when the applied potential was increased 1 percent to 2 percent above the value for which ring and tilt were observed for each of four emitters which were so tested. Ring and tilt were thus identified with the onset of electrical breakdown. An important observation is that electrical breakdown was predictable and not random as often supposed.

Since electrical breakdown was predictable, it was avoided to prevent the usual emitter damage which accompanies breakdown [Figs. 5(C) and 7], in order to obtain the electron micrographs of emitter 0-38 shown in Figs. 4(A) and 4(B). From those micrographs the emitter geometry was determined as an aid to the calculation of both electric field and current density.[22] The emitter was stable during ring and tilt, as judged from the reproducibility of its performance (including ring and tilt) as shown in Figs. 2 and 3.

Ring and tilt were observed at a critical value of the current density in the range for which electrical breakdown was observed for other emitters.[1] The critical density $J_s = 6 \times 10^7$ amperes/cm^2 for the present emitter was calculated from Eq. (7) of reference 1. J_s was approximately the average current density through the

emitter cross section XX in Fig. 4(D), that profile of the emitter being an enlargement of Fig. 4(B). Further support is thus added to the previous observation[1] that electrical breakdown is initiated by a current density dependent mechanism under the present experimental conditions.

It will be shown in Part II of this paper that emitter temperature approaching the melting point of tungsten is expected from the resistive generation of heat during the emission of current densities approximately equal to the observed values of J_x. It is presently supposed that the ring and tilt, and the electrical breakdown which they precede, were initiated by thermal effects accompanying that temperature increase. It follows from the resistive mechanism that the emitter temperature increases with time during microsecond intervals of operation and from the theory of Guth and Mullin[27] that such a temperature increase would cause a corresponding increase of current density with time. This effect is presumed to account for the tilted current pulse. Since the ring and tilt occur simultaneously, and since neither can be accounted for by cold cathode field emission alone, as noted above, it is probable that both effects are due to electron emission at high field and high temperature.

Available evidence indicates that the temperature required for ring and tilt was near the melting point of tungsten. Evaporated emitter material appeared to be the source of the positive ions which are required to neutralize space charge during the large increase in current accompanying the transition from field emission to vacuum arc.[1] Temperatures in excess of the melting point are required for the observed deformation of the cathode during arc [Figs. 5(C) and 7]. Furthermore, the increase in ring intensity during the series of Figs. 2(D) through 2(F) was considerably greater than the current density increase predicted theoretically[27] for temperatures less than 2000°K to which the theory is limited. When the emitter was heated to 2100°K from an external heat source (its support filament) the emitter was stable during the emission of microsecond current densities less than $J_x/3$ and no evidence of ring and tilt was then observed. Presumably temperatures greater than 2100°K are required for those effects.

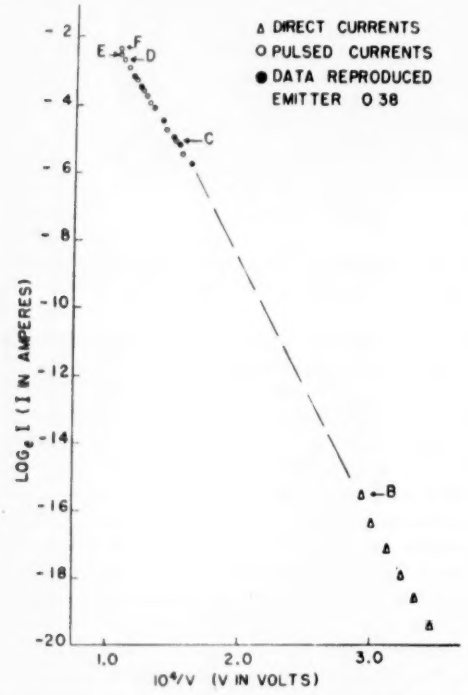

FIG. 3. Current-voltage relationship for combined direct current and pulsed operation of emitter 0-38. Data at (B), (C), (D), (E), and (F), correspond to the data at the same letters in Fig. 2. Space-charge effects were observed at currents above (C); anomalies in the normal emission preceding electrical breakdown were observed from (D) to (F).

[27] E. Guth and C. J. Mullin, Phys. Rev. **61**, 339 (1942).

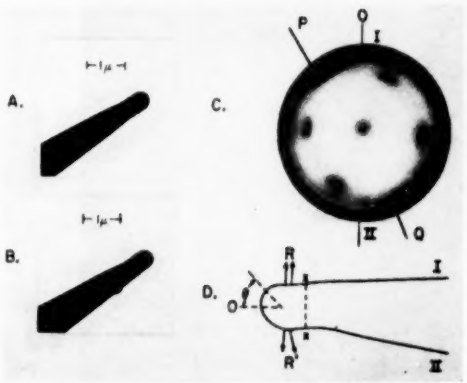

FIG. 4. (A) and (B), electron micrographs of two profiles of emitter 0-38 at 90° with respect to each other; (C), an emission pattern photograph from emitter 0-38 identical with Fig. 2(F). (D), an enlargement of (B), shows ring emitting area RR', minimum emitter cross section XX where current density was maximum; sides I and II correspond to those sides of the pattern at (C). θ, the polar angle for the approximate hemispherical emitter tip was measured relative to the apex.

It is important to note that the resistive generation of heat, together with the predicted[27] increase of current density with temperature, combine in a regenerative process yielding further increases in both current density and temperature. If, as supposed, the resistive mechanism produces an increase in temperature to a value near the melting point of tungsten, further increases in temperature by the regenerative process would lead to emitter instability, particularly in view of the large electrical force on the emitter tip. The tilt is regarded as evidence of that regenerative process. Emitter instability accompanied electrical breakdown [Fig. 5(C)].

The area from which the ring emission originated was located in the approximate region RR' [Fig. 4(D)]. That profile of the emitter is an enlargement of Fig. 4(B). Observed crystallographic detail in the ring at P and Q, Fig. 4(C), corresponds to (110) crystal faces[17,23,25] found at $\theta=\pi/2$ [Fig. 4(D_7)]; however the extent of the region RR' along the emitter shank is uncertain. It was not possible to use measurements of the dimension of the emission pattern ring to determine the area RR' since the magnification in the θ direction in that part of the emission pattern was quite small due to the large radii of curvature at the corresponding surfaces. This difficulty precluded calculation of the magnitude of the current density from the area RR' in the present experiment.

The electric field was calculated by the methods of reference 22 for surfaces where space-charge effects were negligible. By this method the field at R, Fig. 4(C), was 5.7×10^7 v/cm and that at R' was 6.3×10^7 v/cm when the applied potential was 9.2 kv, the value for which ring and tilt were observed. With the same potential, the electric field at the emitter apex was 7.4×10^7 v/cm. The latter field was calculated from Eq. (1) and the observed value of the current density since space charge near the apex precluded use of the methods in reference 22. Apparently the difference in fields between R and R' accounts for the observed difference in ring intensity in the emission pattern, Fig. 4(C), at the corresponding points I and II whose work functions are similar.

It may be concluded from this section that electrical breakdown was predictable under the experimental conditions used in this work. Easily recognizable conditions (i.e., ring and tilt) which precede arc formation have been established and these appear to be due to electron emission from the cathode in the presence of high electric field and high temperature.

Electrical breakdown occurred at a critical current density J_x of the order of 10^8 amperes/cm^2 for the microsecond field emission from clean tungsten in high vacuum. Breakdown apparently resulted from thermal effects when the emitter was resistively heated.

2. Arc Formation Without Cathode Bombardment from Ions Formed at the Anode

The electrical breakdown described in the previous section was apparently initiated by thermal effects when the emitter was resistively heated. The contribution of other heat sources appeared negligible. One such source, the bombardment of the cathode by positive ions, was intentionally minimized. High vacuum and, in some cases,[1] well-outgassed electrodes of high melting point were used to minimize the production of positive ions by field electrons. Direct evidence was obtained from the field emission patterns (Fig. 2) that bombardment by chemically active ions (and residual gas) was negligible prior to breakdown. Other evidence indicating that ion bombardment was negligible is seen

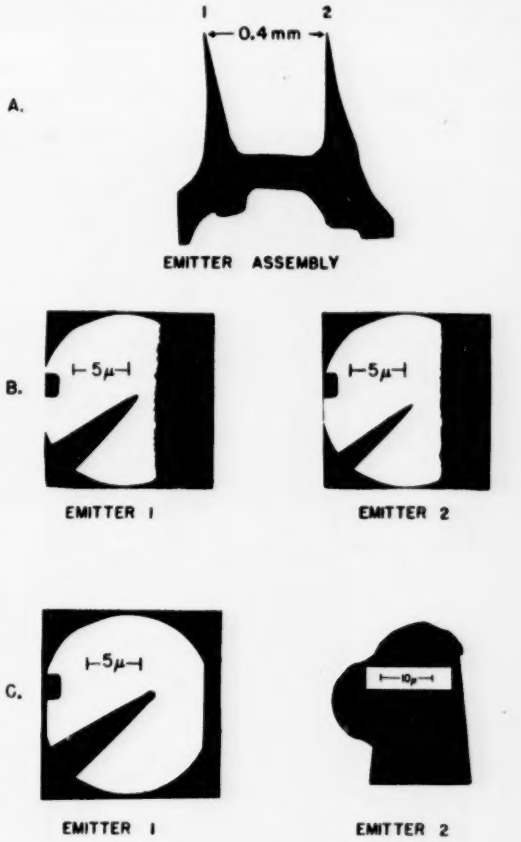

FIG. 5. (A), optical micrograph of twin emitter assembly showing emitter No. 1 and emitter No. 2 as marked. (B) electron micrographs before use. (C) electron micrographs after use.

from the observed dependence of the breakdown on current density. Breakdown due to ion bombardment might more logically be expected to depend on total voltage,[4] but this was not observed under the present conditions.

Although the evidence against the initiation of the present breakdown by positive ion bombardment of the cathode was considerable, it was nevertheless largely indirect. It was recognized that bombardment of the cathode by chemically inactive ions might not be recognized through their effects, if any, on the emission pattern. That method would be particularly ineffective for detecting ion bombardment along the emitter shank for reasons which precluded an accurate evaluation of the current density in those areas in the preceding section of this paper. Furthermore, the useful features of the emission pattern were destroyed during the vacuum arc [see Fig. 6(D)] and any contribution of ion bombardment of the cathode at that time must be judged by other means. Experiments described in this and in the following sections of the present paper

were performed to better evaluate such heating mechanisms prior to and during the breakdown process.

Experiments are described in this section in which vacuum arcs were observed when gap traversal by ions or clusters formed at the anode was precluded by use of a voltage pulse whose time duration was short compared with the gap transit times of the material in question. A suitable combination[28,29] was a $\frac{1}{2}$-micro-

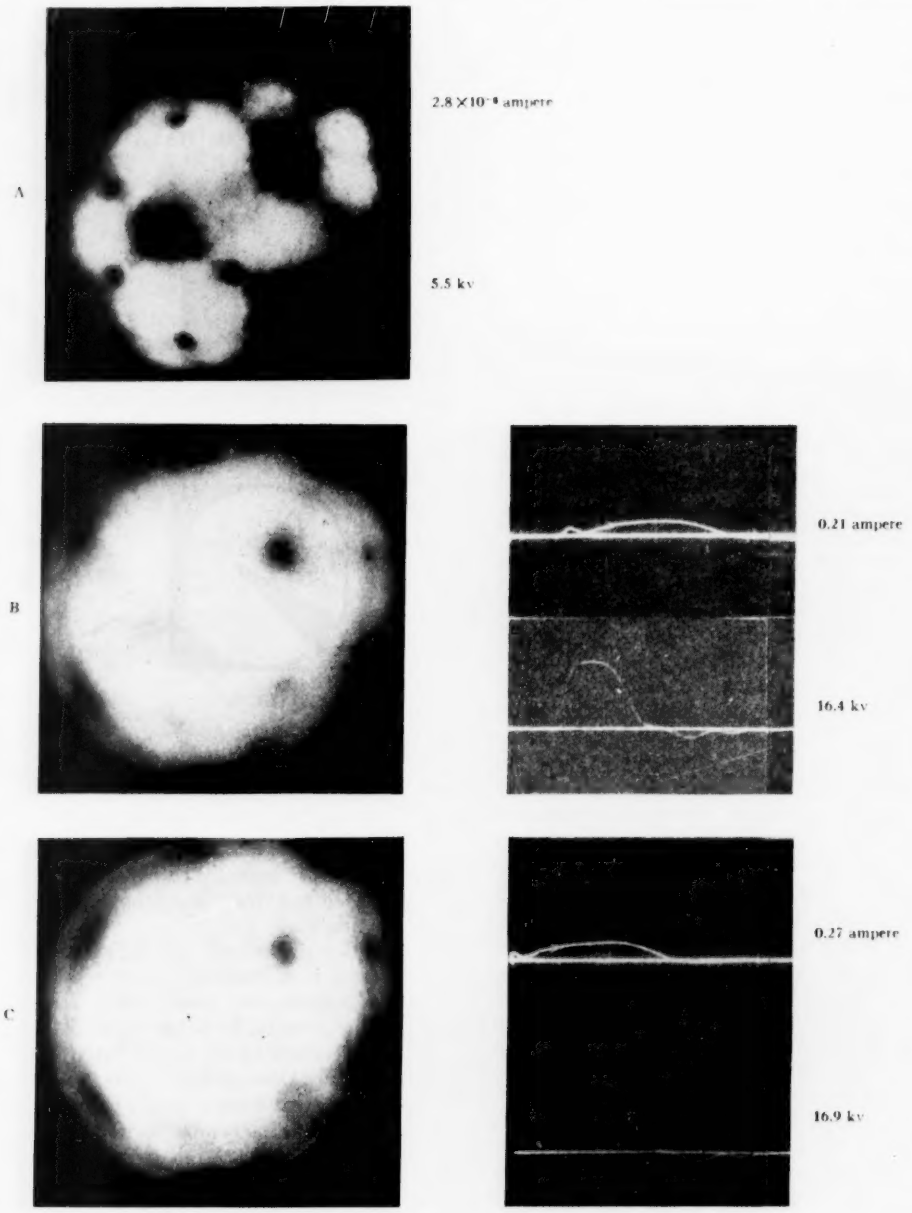

FIG. 6. Experimental data as recorded during the operation of the twin cathode shown in Fig. 5. (A) the combined emission pattern of both cathodes during direct current operation. (B) the combined pattern with current and voltage oscillographs during pulsed operation with space charge but without pre-arc anomalies. (C) ring observed concentric with emission pattern from cathode No. 2; total current trace from both cathodes "tilted." (D) photographs obtained during vacuum arc. (E) the emission pattern from the surviving cathode (No. 1) during direct current operation after the arc of cathode No. 2.

[28] K. R. Spangenberg, *Vacuum Tubes* (McGraw-Hill Book Company, Inc., New York, 1948).
[29] George Barnes (to be published).

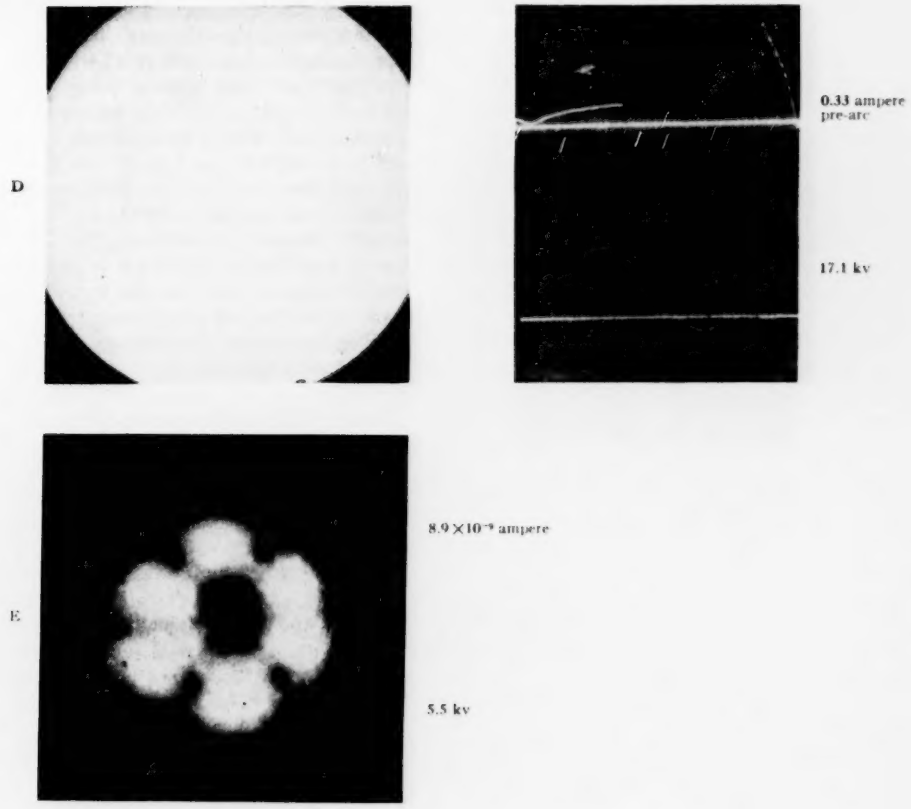

FIG. 6.—*Continued.*

second voltage pulse and 8.5-cm electrode spacing (Fig. 1) with voltages below 10 kv. Such an arrangement excluded gap transit during the pulse time by ions which were expected from sources such as aluminum from the anode or oxygen or nitrogen adsorbed thereon.

Thus operated, ring, tilt, and the electrical breakdown of emitter X-62 resulted at $\bar{J}_z=4\times10^7$ amperes/cm^2, the corresponding values of current I and voltage V being $I=0.07$ ampere, $V=8.8$ kv. The value of $\bar{J}_z$ for this emitter was judged from its electrical behavior using Eq. (1) and the methods of reference 1. By this method, $\bar{J}_z$ was known within a factor of 3 and it is noteworthy that this value was in the range for which breakdown was observed for other emitters.[1]

The data from other emitters were similar when a pulse length of 5×10^{-8} second was used, and that period was considerably shorter than gap transit time of the ions and clusters noted above.

It is concluded that ring, tilt, and arc formation do not require the bombardment of the cathode by ions or clusters from the anode material or from its adsorbed gases under the present experimental conditions.

3. Arc Formation With Microsecond Potentials of Large Magnitude

Effects due to bombardment of the cathode by positive ions would be expected to increase with the applied potential because of increased ion energies. Although that mechanism was judged negligible in the experiments just described, it was postulated to account for the "voltage effect" observed by Trump and Van de Graaff[4] at higher voltages and under experimental conditions different from those used herein. More recently, however, positive ion emission coefficients have been found insufficient[9] for the proposed particle exchange mechanism.[4]

It was therefore desirable to observe arc formation with the present techniques and at higher voltages than those used previously.[1] For voltages in the range 50 to 100 kv an emitter of tip radius of the order of 10^{-4} cm was required. Quite by chance such an emitter, X-62-*A*, was formed in the experimental tube from emitter X-62 when the tip of the latter was increased in radius to 1.3×10^{-4} cm during the vacuum arc described in the preceding experiment.

It was thus possible to measure J_s at widely different voltages, i.e., 8.8 kv and 60.1 kv, other experimental conditions being identical. At the higher voltage, the critical current density J_s was identified by the ring and tilt, avoiding an arc in order to obtain electron micrographs of the emitter. The resulting value of J_s was known, within 20 percent, and it is significant that its magnitude, $J_s = 2.5 \times 10^7$ amperes/cm^2, was in close agreement with that which initiated the low-voltage arc in the same tube, i.e., $J_s = 4 \times 10^7$ amperes/cm^2. Both values are in the range found for other emitters.

The experimental results were similar when microsecond potentials up to 50 kv were applied to several field emitters in the point-to-plane type tubes of reference 1, the electrode spacing being 0.2 cm to 1.0 cm in various cases.

Cathode bombardment was not excluded by reason of ion transit time at the higher voltages described in this section. However, the breakdown did not appear to be initiated by that process. Arc initiation evidently depended on current density; no voltage effect was observed for the electrical breakdown of microsecond potential under the present experimental conditions, the total voltage range being $5 < V < 60$ kv when previous data[1] were included. It appears that the initiation of breakdown was again due to thermal effects accompanying resistive heating.

It should be noted that the present data from each emitter were obtained from a total of about two hundred individual microsecond current pulses. It is not known whether or not other processes would initiate breakdown if the cathode were repeatedly pulsed for long periods of time at the present voltage levels.

The importance of clean surfaces and high vacuum should be emphasized. Under less favorable conditions, breakdown was not predictable and occurred generally at lower levels of operation.

4. On the Bombardment of the Cathode by Ions During an Arc

Bombardment of the cathode by ions formed at the anode or in the residual gas was judged negligible during an arc or during its initiation based on evidence presented in the foregoing sections. Part of that evidence was indirect. The field emission pattern from clean tungsten is not sensitive to the small amounts of helium which are known to diffuse into evacuated Pyrex envelopes from the atmosphere.[20] Ion bombardment of a cathode during its arc could not be detected from its field emission pattern since the useful features of the pattern were then destroyed [see Fig. 6(D) for example]. Evidence on the magnitude of the bombardment of the cathode by ions formed from inert gas prior to arc or from any source during arc is provided in the following experiment.

[20] Saul Dushman, *Scientific Foundation of Vacuum Technique* (John Wiley and Sons, Inc., New York, 1949), p. 531.

Use of a field cathode to monitor the effects of ions during an arc at another cathode appeared feasible. A spacing between cathodes which was small [Fig. 5(A)], compared to their spacing from a common anode (Fig. 1) provided similar probabilities for the bombardment of each cathode by ions from the anode. With an anode to cathode spacing of 4 cm and a microsecond applied potential of 17 kv, gap traversal by ions was possible during the pulse time. The cathodes had nearly identical geometries [Fig. 5(B)] and hence nearly equal values of electric field and current density for a common value of the applied potential. This arrangement was chosen for reasons which follow.

If a vacuum arc was initiated by a current density dependent mechanism, as supposed, breakdown should occur first at that cathode with the greatest current density. If the arc involved primarily cathode phenomena, it was recognized that an arc at one cathode might not cause an arc at the other. In this event examination of the emission pattern of the surviving cathode would yield direct evidence concerning the magnitude of cathode bombardment by chemically active ions from the anode or the residual gas during arc at the other cathode. On the other hand, if an arc at one cathode initiated an arc at the other at a lower current density than that for which arc was expected at the latter cathode, then ion bombardment would be suspected.

Two needle-shaped tungsten field emitters on a common support filament [Fig. 5(A)] were fabricated by previously described techniques.[22] The two emitters had nearly identical cone angles after their simultaneous electrolytic etch in normal NaOH [Fig. 5(B)]. When the emitters were simultaneously heated in the experimental tube during the outgassing procedure both emitter tips were shaped into approximate hemispheres of nearly equal radii by the surface migration of tungsten-on-tungsten.[21] Electron micrographs of each emitter were obtained after the experiment [Fig. 5(C)]. That shown for emitter No. 1 was also approximately the geometry of emitter No. 2 before its arc, as will be argued in the following.

When operated in a Mueller projection tube (Fig. 1), emitter No. 2 supplied two-thirds of the total field current. The ratio of currents from the two cathodes was determined by a densitometric analysis of the photograph of their combined emission pattern prior to arc [Fig. 6(C)]. The result was consistent with the current ratio found from a comparison of the total current from both cathodes prior to arc [Fig. 6(A)] with the current from the single surviving cathode No. 1 after arc [Fig. 6(E)], the comparison being made at a common value of the applied potential.

The performance of the twin cathode during the transition from field emission [Figs. 6(A) to 6(C)], to the vacuum arc [Fig. 6(D)] is significant. Figure 6(A) taken at a small continuous current level shows the

overlapping emission patterns from the two emitters. Oscillographs of the combined current from both emitters and of their common applied microsecond potential during operation at a relatively high field current density are shown in Fig. 6(B) [space-charge effects are comparable to those shown in Fig. 2(C)]. In Fig. 6(C), ring and tilt are apparent; however, the ring is concentric with the pattern from emitter No. 2. No ring appears concentric with the pattern from emitter No. 1. This observation is consistent with the supposition that ring and tilt are initiated at a critical current density, since the current density from cathode No. 2 was larger than that from cathode No. 1 by a factor of two, as noted above. Ring and tilt and the entire pre-arc performance of the twin emitter were reversible and reproducible as was the case for emitter 0-38 described earlier. No contamination of either cathode was observed prior to arc.

During arc initiation, Fig. 6(D), the current and voltage wave shapes were similar to those described in more detail in reference 1. Arc was initiated (at cathode No. 2 only) after the total field current from both cathodes had reached approximately the peak value expected during the microsecond interval [compare with 6(C)]. Arc was initiated abruptly, the current increasing during arc by a factor of approximately 100 judged from the corresponding decrease in voltage and the known pulser impedance. No emission pattern detail was observed during arc [Fig. 6(D)].

The emission pattern immediately following arc, Fig. 6(E), shows only emission from cathode No. 1. No emission was then obtained from cathode No. 2 whose geometry was altered by arc as shown in Fig. 5(C). It is significant that emitter No. 1 did not arc or suffer detectable geometric change during the electrical breakdown of its companion, although the electric fields at the two cathodes differed by only a few percent and their current densities differed by only a factor of two prior to arc. During later tests, cathode No. 1 exhibited ring and tilt at a current just twice that which it sustained without damage during the arc at its neighbor. In that case, ring and tilt were observed at a critical current density $\bar{J}_z = 5 \times 10^7$ amperes/cm^2 in the range reported for other emitters. (For other data on this emitter 2X4, see Table I, Part II of this paper.) This result provides direct evidence that the energy added to cathode No. 1 by positive ion bombardment during the arc at cathode No. 2 was not large compared with that supplied to cathode No. 1 by the resistive mechanism.

Further evidence supporting this conclusion is seen from the negligible contamination exhibited by cathode No. 1 as the result of the arc at its neighbor. The emission pattern, Fig. 6(E) taken immediately after that arc, and without any further treatment such as heating to remove contaminants, indicates only the most minute contamination on the (110) crystal face

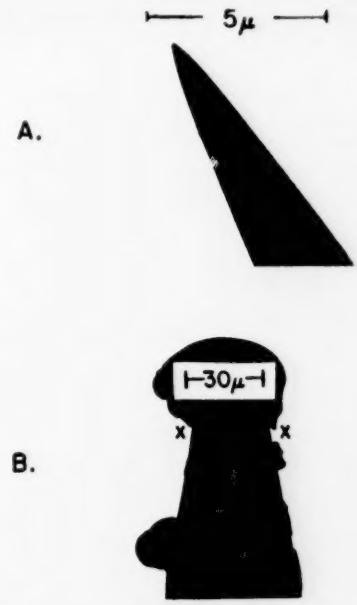

FIG. 7. Electron micrographs of emitter 0-61 before use (A) and after vacuum arc (B).

(central nonemitting area). That contaminant was probably tungsten[21] evaporated from the tip of emitter No. 2 during its arc (evaporated emitter material was postulated in reference 1 as a source of positive ions required to neutralize space charge during the large current increase accompanying the arc).

This experiment provides direct evidence that electrical breakdown involved primarily cathode phenomena under the present experimental conditions. Breakdown was dependent on current density but apparently independent of the effects of positive ions from anode or residual gas sources. Breakdown again occurred at a critical current density for which appreciable resistive heating was predicted.

5. Direct Measurement of the Current During Vacuum Arc

The current during a vacuum arc was previously[1] judged by indirect evidence to be of the order of 100 amperes under present experimental conditions. The arc current was measured directly in the present work.

Use was made of the ring and tilt to identify the largest stable microsecond pre-arc field current $I_z = 0.1$ ampere for emitter 0-61. Arc was thus avoided during that initial measurement permitting the later decrease in sensitivity of the current measuring circuit[1] required for an accurate measurement of the total current I_a during arc. For the same emitter $I_a = 46$ amperes. The low-impedance feature of the present vacuum arc is noteworthy.

The arc current of 46 amperes corresponds to a cur-

rent density of 8.7×10^6 amperes/cm^2 at the cross section XX of the emitter profile in Fig. 7(B). That current density is about equal to the value required to raise the tip of the emitter 7(B) to its melting point in one microsecond in view of the calculations presented in Part II of this paper. The heat of fusion is small, and no large amount of material was vaporized during arc judged from the electron micrographs of Fig. 7. The evidence indicates that the resistive mechanism was adequate to account for the heat required by the observed emitter deformation during arc. Apparently energy was not supplied by other mechanisms at a rate large compared with that of the resistive mechanism.

PHYSICAL REVIEW VOLUME 91, NUMBER 5 SEPTEMBER 1, 1953

The Field Emission Initiated Vacuum Arc. II. The Resistively Heated Emitter*

W. W. Dolan, W. P. Dyke, and J. K. Trolan
Physics Department, Linfield College, McMinnville, Oregon
(Received March 30, 1953)

Electrical breakdown between clean metal electrodes in high vacuum was observed when the field current density at the single crystal tungsten cathode exceeded a critical value of the order of 10^8 amperes/cm^2. At current densities just below the critical value, an electron emission process was observed which apparently involved both high temperature and high electric field. Calculations are presented for the emitter temperature increase due to the resistive mechanism for both the steady state and the transient solution. Emitter geometries used for the calculations approximated those obtained from electron micrographs of several emitters. The calculations show that the resistive heating was sufficient to melt the emitter at the critical current density, assuming the accepted value of the physical constants for the polycrystalline metal.

IN Part I of this paper evidence has been presented showing that the interruption of the microsecond field emission from the tungsten emitter by the occurrence of a vacuum arc is dependent principally upon current density J under conditions of clean emitter surfaces and excellent vacuum. It also has been pointed out that the experimentally observed values of the critical current density $\bar{J}_x$ for arc initiation lie in the range $10^7<\bar{J}_x<10^8$ amperes/cm^2 for microsecond operation, with the suggestion that heating of the emitter by a current density dependent mechanism may be the initiating factor of the breakdown. The purpose of this part of the paper is to present an analysis of the heat flow problem when an emitter of idealized geometry approximating those used in actual operation is heated resistively. The current density dependent mechanism proposed by Nottingham[1] is briefly considered. A comparison will be made between values of the current density for which an arbitrary large temperature increase is predicted by resistive heating and experimental values of $\bar{J}_x$.

A mathematical analysis of the resistive generation of heat and its simultaneous dissipation by conduction, using physical constants for the polycrystalline metal, was made possible when electron micrographs had revealed the geometry of the emitter,[2] whose shape in the present experiments was a cone whose half-angle was in the range 2.75° to 15.5°, with a hemispherical tip of radius between 1.5×10^{-5} and 1.5×10^{-4} cm. Although this geometry does not lend itself directly to any simple coordinate system, it may be closely approximated by a portion of a cone bounded by concentric spherical surfaces, orthogonal to the cone, for which ordinary spherical coordinates are suitable. Figure 1 shows a comparison between the idealized geometry and that of several typical emitters. The point $u=m$ is chosen to correspond to the position of maximum current density, which may be expected at the "neck" of constricted emitters [see Sec. XX of Fig. 4(D), Part I], or in the case of emitters without constriction, at a distance from the vertex of the emitter about equal to the radius of its hemispherical tip.

The flow lines for both electric current and heat are assumed to follow the radial coordinate curves of the system. Heat radiation is supposed negligible. Consideration of the resistive generation of heat, together with the usual laws of heat conduction, leads to the differential equation

$$u^4\partial^2T/\partial u^2+2u^3\partial T/\partial u-\alpha^2u^4\partial T/\partial t=b. \qquad (1)$$

Here u is the distance in cm from the vertex of the cone, T is temperature in degrees centigrade, t is time in seconds; $\alpha^2=c\delta/\kappa$, where c is specific heat, δ is density, and κ is thermal conductivity; b is defined by

* Support for this work was extended by the U. S. Air Force through the Microwave Laboratory of the University of California, and by the U. S. Office of Naval Research.
[1] W. B. Nottingham, Phys. Rev. **59**, 906 (1941).
[2] Dyke, Trolan, Dolan, and Barnes, J. Appl. Phys. **24**, 570 (1953).

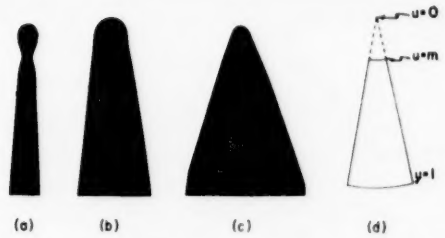

FIG. 1. A comparison between the geometry of typical field emitters (a, b, c) and the idealized conical geometry (d) used in heat flow calculations.

the equation

$$b=\frac{-I^2\rho}{4\pi^2(4.18\kappa)(1-\cos v_0)^2}, \tag{2}$$

with I indicating electric current, ρ the resistivity, and v_0 the interior half-angle of the cone. Equation (1) overlooks the variation of the physical constants with temperature which if included would unreasonably complicate the solution. The use of values for intermediate temperatures is a satisfactory alternative.

If the term involving t in Eq. (1) is omitted, a steady-state solution $s(u)$, useful in the general case, is obtained,

$$s(u)=b/u^2+c_1/u+c_2, \tag{3}$$

where c_1 and c_2 are constants of integration. For the general equation (1), the method of separation of variables may be used. A solution of the form

$$T=U(u)\theta(t)+s(u) \tag{4}$$

is assumed. $\theta(t)$ has the usual exponential form appearing in Eq. (8) below and the function $U(u)$ must satisfy the equation

$$\frac{d^2U}{du^2}+\frac{2}{u}\frac{dU}{du}+k^2U=0, \tag{5}$$

k being arbitrary. Boundary conditions are based on the assumptions of zero temperature at a relatively great distance $u=l$ from the apex of the emitter, and no heat flow through the apex where $u=m$, that is,

$$U(l)=0, \quad dU/du\big]_{u=m}=0. \tag{6}$$

A related problem treated in Churchill[3] suggests a solution of Eq. (5) satisfying the first of conditions (6), namely,

$$U=(a/u)\sin(k(l-u)),$$

where a is arbitrary. To satisfy the second of conditions (6) requires the relation

$$\tan(k(l-m))=-mk, \tag{7}$$

an equation with infinitely many solutions k_n. The functions $\sin(k_n(l-u))$ are orthogonal for all values of k_n so that they may serve as a basis for the series expansion needed below.

The solution (4) now takes the form

$$T=\frac{1}{u}\sum_{n=1}^{\infty}\exp(-k_n^2t/\alpha^2)A_n\sin(k_n(l-u))+s(u). \tag{8}$$

Clearly T approaches the steady-state value $s(u)$ when $t\to\infty$, and the coefficients A_n must be so chosen that $T=0$ when $t=0$, i.e., the function $-us(u)$ must be expanded in a series of the orthogonal functions $\sin(k_n(l-u))$. A process analogous to that used in the usual Fourier series development leads to an evaluation of the coefficients in the form

$$A_n=\frac{1}{M_n}\int_m^l xs(x)\sin(k_n(l-x))dx, \tag{9}$$

where

$$M_n=\int_m^l\sin^2(k_n(l-x))dx$$

$$=\frac{l-m}{2}-\frac{1}{4k_n}\sin(2k_n(l-m)). \tag{10}$$

The procedure for writing the series (8) is now straightforward. The roots k_n of Eq. (7) are obtained by successive approximations, and thereafter the values M_n, A_n, and the exponential factors of (8) are computed. If the experimental current is drawn for short intervals of time, many terms are necessary to get the desired convergence of the series (80 terms in the present case of microsecond pulses). Computation of steady-state temperatures on the other hand is relatively simple. The physical constants for the tungsten emitter used are those tabulated by Worthing and Halliday.[4] For resistivity ρ and specific heat c, which vary considerably with temperature, intermediate values $\rho=50\times10^{-6}$ ohm cm and $c=0.045$ cal/g°C have been arbitrarily chosen for the present examples; a further comment on a possible dependence of resistivity on current density appears below. The value of l is taken as one millimeter, which approximates the usual length of the emitters used, and is large compared with the radius at the apex. The value of m varies with cone angle in such a way as to make the cross-section radius where $u=m$ equal to the true emitter radius. The value of the cone angle, within broad limits exceeding those encountered in practice, makes relatively little difference to the results in terms of permissible current density, not more than a factor of 3 between half-angles of 5° and 20°. In the calculation of Eq. (11) an arbitrary angle of $\arctan\frac{1}{5}$ (approximately 11°) is assumed.

[3] R. V. Churchill, *Fourier Series and Boundary Value Problems* (McGraw-Hill Book Company, Inc., New York, 1941), pp. 113–114.

[4] A. G. Worthing and D. Halliday, *Heat* (John Wiley and Sons, Inc., New York, 1948), p. 496.

The maximum steady-state temperature, which occurs at $u=m$, may be expressed by the relation

$$T_{max}=9.5\times10^{-4}J^2r^2 \text{ deg C}, \quad (11)$$

where J is current density in amperes/cm^2, and r is emitter radius in cm. If T_{max} is to be held at less than 1000°C, an arbitrary value used for illustration, it is clear that the product J^2r^2 must not exceed 10^6. Thus in the range of radii from 10^{-4} to 10^{-5} cm, J for direct current operation may reach corresponding values of 10^7 to 10^8 amperes/cm^2 under the conditions here described. It should be noted that while the permissible J varies inversely as the radius, the total current involves emitting area and so varies directly as radius.

The temperature rise-time indicated by the calculation of the series in Eq. (8) is such that the steady state is closely approached in 10^{-5} sec, and about one-fourth of the temperature increase is to be expected in a microsecond. Since T is proportional to J^2, microsecond operation should permit about twice as large a current density as can be sustained in the steady state, and shorter pulses offer the possibility of attaining still higher levels.

The analysis for a cylindrical emitter is useful in comparison with the foregoing because it represents a limiting case for very small cone angles. In cylindrical coordinates the equation corresponding to Eq. (1) is

$$\partial^2T/\partial u^2-\alpha^2\partial T/\partial t=-a, \quad (12)$$

where T, t, and α have the same significance as before; u is the length coordinate along the cylindrical wire, and a is defined by the relation

$$a=I^2\rho/4.18\pi^2\kappa v_0^4, \quad (13)$$

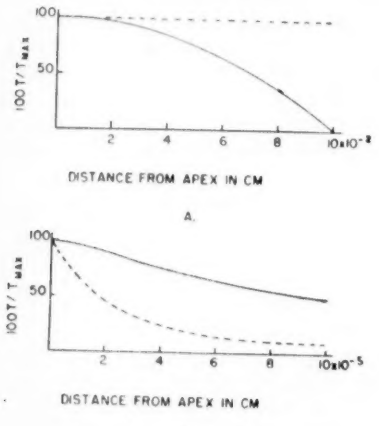

FIG. 2. A comparison between steady-state temperature gradients (solid curves) in the idealized field emitters of (A) cylindrical and (B) conical geometries, the latter assuming an emitter tip radius of 10^{-5} cm. Dotted curves are corresponding gradients if heat conduction is neglected, adjusted to arbitrary maxima.

v_0 being the radius of the wire. The steady-state solution is

$$T=-\tfrac{1}{2}au^2+c_1u+c_2. \quad (14)$$

If the origin is chosen so that $u=0$ at the emitting end of the wire, and $u=l$ at the cool end, the boundary conditions are: (1) $T=0$ when $u=l$, (2) $dT/du=0$ when $u=0$. By use of these conditions, Eq. (14) becomes

$$T=\tfrac{1}{2}a(l^2-u^2). \quad (15)$$

If the emitter is one millimeter long as in the conical case, the maximum value of T found where $u=0$ is given by the relation,

$$T_{max}=2.45\times10^{-7}J^2 \text{ deg C}, \quad (16)$$

which may be compared with Eq. (11) for the cone. The temperature in the present case is independent of radius.

Equation (16) immediately gives a limiting value of J of about 10^5 amperes/cm^2 for operation at 1000°C in the steady state, which is a factor of several hundred less than the level permitted by conical emitters of typical radius. Although the temperature in conical emitters is not very sensitive to changes in cone angle within the stated limits, the change is very rapid as the angle approaches zero, and it may be shown that Eq. (16) is the limit of Eq. (11) under such conditions.

A comparison of temperature gradients for the cylindrical and conical cases in the steady state is instructive. Figure 2 shows such a comparison, with the dotted curves indicating the corresponding gradients if heat conduction is neglected. The latter curves reach no steady state and are arbitrarily adjusted to the same maxima. It is observed that while the temperature in the conical case decreases to one-half of its maximum in a distance of ten emitter radii from the apex, the same fraction is reached for the cylinder at a distance of several thousand radii.

Details of the transient case for a cylindrical wire will not be included. The procedure is straightforward, except that the boundary conditions do not permit expansion of the steady-state function in ordinary Fourier series; however, a series of terms in the orthogonal functions $\cos(2n-1)\pi u/2l$ is permissible and the solution is given explicitly by the expression

$$T=\frac{a}{2}(l^2-u^2)-\frac{16al^2}{\pi^3}\sum_{n=1}^{\infty}\frac{(-1)^{n-1}}{(2n-1)^3}\times\exp[-(2n-1)^2Ct]\cos\left(\frac{(2n-1)\pi u}{2l}\right), \quad (17)$$

where C represents the quantity $\pi^2/4l^2\alpha^2$.

In experimental work[5] direct current operation of emitters has been observed at current densities in excess of 10^6 amperes/cm^2 as compared with predicted values for the conical case of approximately 10^7 am-

[5] W. P. Dyke and J. K. Trolan, Phys. Rev. **89**, 799 (1953).

TABLE I. A comparison between observed experimental current densities $\bar{J}_z$ required to initiate arc for several emitters (Column B) and current densities J_R (Column C) for which the calculated temperature reaches 3000°C in the corresponding pulse times.

A Emitter number	B $\bar{J}_z$ (amp/cm²)	C J_R (amp/cm²)	D V_{max} (kv)	E Radius of the emitter tip (cm)	F Half-angle of the emitter cone (degrees)	G Pulse length (μsec)	H[a] Tube type, electrode spacing (cm), anode material
O-38	6×10^7	7.0×10^7	9.2	2.4×10^{-5}	5	1	S, 4.5, ABW
X-62[b]	4×10^7	2.4×10^7	8.8		10	½	S, 8.5, ABW
X-62-A	3×10^7	2.5×10^7	60.1	1.5×10^{-4}	10	1	S, 8.5, ABW
Q-1	4×10^7	7.1×10^7	4.9	1.5×10^{-5}	3	1	PTP, 1, Moly.
Q-29	7×10^7	7.4×10^7	14.2	3.2×10^{-5}	6	1	S, 8.5, ABW
O-54	1×10^8	2.7×10^8	16.1	2.0×10^{-5}	16	1	S, 4.5, ABW
2-X-4	5×10^7	5.8×10^7	13.3	3.8×10^{-5}	6	1[c]	S, 4.5, ABW

[a] Experimental tube type S is shown in Fig. 1; type PTP, i.e., point-to-plane, is shown in reference 5; ABW, aluminum-backed willemite.

[b] Electron micrographs of this emitter were not available; hence $\bar{J}_z$ was calculated from its electrical behavior with the aid of Eq. (1) of Part I. In this case, $\bar{J}_z$ was known within a factor of 3. For the other emitters, electron micrographs were available and $\bar{J}_z$ was known within ±10 percent.

peres/cm². Larger experimental current densities may yet be obtained for the steady state since the limitation imposed in reference 5 was not due to the cathode.

Table I exhibits the comparison of the maximum current densities J_R predicted by the resistive process (Column C) with the values of the critical current density $\bar{J}_z$ observed experimentally during the microsecond operation for several emitters (Column B). Methods for calculating the value of $\bar{J}_z$ were presented in Part I. J_R was arbitrarily defined as that current density required to raise the emitter temperature to 3000°K in a time equal to the duration of the experimental current pulse. For all emitters except X-62 the tip radius and cone angle were obtained from electron micrographs, and the resulting values of the experimental current densities are correct within 20 percent. The critical current density showed approximately the expected dependence on radius and cone angle. It will be noted that electrical breakdown depended on current density. It was independent of voltage, total current, anode material, and gap spacing.

With regard to the assumed values of the physical constants for tungsten, it may be pointed out that recent work by Ignateva and Kalashnikov[6] suggests that for impulse operation at values of J above 10^6 amperes/cm², the resistivity of some metals may be increased by a considerable factor. The reference notes an increase by a factor of 2 in resistivity of tungsten at the largest current density reported, i.e., 4×10^6 amperes/cm². Current densities two orders of magnitude larger were observed in the present work, and the increase of resistivity with current density, if any, must be less than an order of magnitude for $J<10^8$ amperes/cm² unless it is later shown that the physical constants for the polycrystalline metal are inapplicable to the small single crystals used herein.

The heating process suggested by Nottingham,[1] a quantitative analysis of which has not been made, is based on the suggestion that emitted electrons must be replaced in the metal at their respective energy levels by electrons supplied at the top Fermi level. The energy lost in the replacement process was assumed to heat the emitter. The analysis of this mechanism requires knowledge of (1) the energy distribution of the emitted electrons under conditions of simultaneously high field and high temperature, and (2) the spatial distribution of the heating within the emitter. The former is presently under study and he lattter is in question.[7] The effect of this heating mechanism would be small, according to preliminary analysis, unless it can be shown that the average energy per electron given to the metal is about 1 ev and that this energy is released within a distance from the emitter tip which is small compared to the emitter radius.

The resistive heating process provides adequate emitter temperature increase to support the suppositions in Part I which were advanced to account for the observed ring and tilt prior to arc formation. Thus, no other source is required for the generation of the heat which presumably initiated the observed electrical breakdown.

The experimental data for Table I were supplied by the authors of Part I. The continued interest of Professor J. E. Henderson of the Physics Department, University of Washington, is appreciated.

[6] L. A. Ignateva and S. G. Kalashnikov, Zhur. Eksptl. i Teort. Fiz. **22**, 385 (1952).

[7] G. M. Fleming and J. E. Henderson, Phys. Rev. **59**, 907 (1941).

The Rapid Separation of He^3 from He^4 by the "Heat Flush" Method*

T. SOLLER, W. M. FAIRBANK,† AND A. D. CROWELL
Amherst College, Amherst, Massachusetts

(Received May 25, 1953)

A practical method is decribed for separating the He^3 which occurs in well helium from the liquefied mixture using the "heat flush" technique. Approximately 2 liters/hr of liquid can be processed, a rate considerably in excess of any previous separations. When the separated isotope is finally withdrawn at room temperature, the concentration of He^3 is approximately 0.5 percent. This concentration corresponds to an enrichment factor of 3×10^4, which is an order of magnitude greater than enrichment factors reported previously in the literature.

I. INTRODUCTION

THE peculiar superfluid properties of liquid helium below the λ point have been the object of intense experimental and theoretical investigation since their discovery in 1937. In 1947 it was discovered that the rare isotope He^3 apparently does not exhibit these superfluid properties.[1] This seemed to lend evidence to the idea proposed by London in 1938[2] that the transformation of He I into the superfluid He II is analogous to the degeneration which occurs at low temperatures in a perfect Bose-Einstein gas. He^3, obeying the Fermi-Dirac statistics, would not undergo such a transition.

Experiments on the properties of He^3 and solutions of He^3 in He^4 have been made more difficult because of the small quantities of He^3 which have been generally available. Since He^3 occurs in ordinary well helium gas only to the extent of 1.5 parts in 10^7,[3,4] separation of He^3 by conventional methods is prohibitively slow.[5–7] However, the fact that He^3 does not participate in the superfluid flow of He^4 makes possible a very rapid separation of the two isotopes in the liquid phase.[8,9] Lane, Fairbank, *et al.*[8,9] have demonstrated that if heat is applied at one end of a vessel containing liquid helium below the λ point and refrigeration at the other end, the He^3 flows with the normal liquid away from the heater and toward the cold end of the tube. They called this method of separation a "heat flush method." Other investigators[10–12] have thus enriched the concentration of He^3 in relatively small samples of liquid by factors up to 5000.

This paper reports essentially complete removal of the He^3 at a higher enrichment factor than has been previously obtained in a single step, as well as the development of a method for performing this separation inside the helium cryostat at about the rate of liquefaction.

II. APPARATUS AND EXPERIMENTAL PROCEDURE

The apparatus shown in Fig. 1 was designed to be suspended below the main liquid reservoir in a Collins type liquefier built at Amherst College. A and B are copper spheres, of volume 700 cc and 1000 cc, respectively. Both bulbs can be filled with liquid helium through valves V_1 and V_2. The temperature of the liquid in bulb B can be reduced by pumping through tube T_4, and the liquid in A is simultaneously cooled because of the good thermal contact with B afforded by the thin copper cup C separating the two liquids. A small tube T_1 leads from the bottom of C to an external Toeppler pump.

The procedure in performing a separation is as follows:

(1) The bulbs are filled with liquid, using the four carbon resistors R_1 through R_4 to indicate when the bulbs are empty and when they are full.[13]

(2) Valves V_1 and V_2 are closed.

(3) The temperature of the liquid in both spheres is reduced to below the λ point by pumping through T_4.

(4) Heat is applied to the liquid in A by means of heater H_1 at the top of A, while the liquid in B is maintained below the λ point by continued pumping on B. This produces a "heat flush," causing the He^3 to collect at the bottom of C in the small tube D which is the coldest part of the vessel A. Upon application of a quantity of heat equal to or greater than that required to raise the temperature of the liquid in A from absolute zero to the temperature actually existing in A, all of

* This work has been assisted by the Research Corporation and the U. S. Office of Naval Research.

† Now at Duke University, Durham, North Carolina.

[1] Daunt, Probst, Johnston, Aldrich, and Nier, Phys. Rev. **72**, 502 (1947).

[2] F. London, Phys. Rev. **54**, 947 (1938); J. Phys. Chem. **43**, 49 (1939).

[3] L. T. Aldrich and A. C. Nier, Phys. Rev. **74**, 1590 (1948).

[4] J. H. Coon, Phys. Rev. **75**, 1355 (1949).

[5] McInteer, Aldrich, and Nier, Phys. Rev. **74**, 946 (1948).

[6] A. Andrew and W. R. Smythe, Phys. Rev. **74**, 496 (1948).

[7] Schuette, Zucker, and Watson, Rev. Sci. Instr. **21**, 1016 (1950).

[8] Lane, Fairbank, Aldrich, and Nier, Phys. Rev. **73**, 256 (1948).

[9] B. V. Rollin and J. Hatton, Phys. Rev. **74**, 508 (1948).

[10] K. W. Taconis, Ned. Tydschr. Natuurk. **16**, 101 (1950).

[11] B. N. Eselson and B. G. Lazerev, Doklady Adad. Sci. (U.S.S.R.) **20**, 748 (1950).

[12] B. V. Rollin and J. Hatton, Phys. Rev. **74**, 508 (1948).

[13] We have found that a very simple and effective way of measuring the height of liquid is to observe the change in current flowing in a composition resistor of nominal value of 300 ohms when it becomes wet with liquid, with a constant voltage of 10 volts applied to the circuit. The response is both rapid and large, the current changing by at least a factor of two.

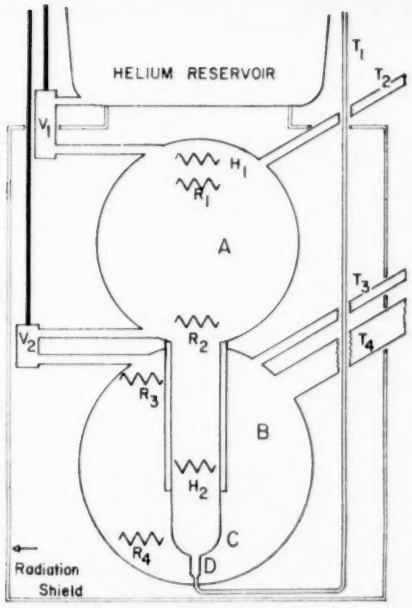

FIG. 1. Schematic diagram of He^3 separator. V_1V_2 values; H_1H_2 heaters; $R_1R_2R_3R_4$ carbon resistors; T_1 tube to Toeppler pump; T_2T_3 tubes to manometers; T_4 tube to pump.

the He^3 originally present will be collected in the small tube D.[14]

(5) The He^3 is now removed from D by opening a valve between tube T_1 and an external Toeppler pump of one-liter capacity. As evaporation takes place from the surface of the liquid in T_1, a second "heat flush" stage of separation takes place, since the surface is cooled by the evaporation, and consequently there is a flow of heat (and with it, of He^3) from D to the evaporating surface. The valve is left open until a total of 1000 cc of gas at approximately 20-mm Hg pressure have been collected in the Toeppler pump at room temperature.

(6) After drawing off the sample into the Toeppler pump, the "waste" He^4 in A is drained into B, which by this time has been sufficiently emptied by continual pumping to accept the liquid from A. Bulb A may now be refilled from the reservoir by opening V_1, and the previous process repeated from step 3.

An alternative method of producing the heat flush after the first filling is to fill bulb A very slowly by just cracking V_1. In this case the liquid evaporates on leaving V_1, and recondenses on the surface of the liquid remaining in A. If this liquid is maintained below the λ point, this recondensation is a heating process, and thus performs the same function as heater H_1. Both methods of flushing work satisfactorily.

[14] Reynolds, Fairbank, Lane, McInteer, and Nier, Phys. Rev. **76**, 64 (1949).

III. RESULTS

(1) A single flush yields 20–25 cc of gas at NTP, of which approximately $\frac{1}{2}$ percent is He^3 corresponding to an enrichment factor of 3×10^4. The He^3 concentration is determined by differential pressure measurements between the sample and pure He^4, above the λ point, assuming the validity of Raoult's Law.[15–19]

(2) Within experimental error of measurement, all of the He^3 originally present in the liquid was collected in the Toeppler pump, assuming an original concentration of He^3 of 1.5×10^{-7}.

(3) With the apparatus described, it is possible to perform approximately 3 complete flushes per hour, thus keeping up with a liquefaction rate of somewhat over 2 liters/hour.

IV. DISCUSSION

Several factors must be carefully considered in the design of the draw-off tube T_1 in order to assure that He^3 will travel from D to the surface of the liquid in T_1. In the first place, the size of the tube in this region must be kept to a minimum so that the amount of heat removed in the evaporation will be sufficient to flush all of the He^3 from D. Also, heat conduction down the tube T_1 from the warm upper end to the liquid surface in T_1 must be minimized. This is accomplished by anchoring T_1 at a point a short distance above the liquid surface to a copper strip making contact with the main reservoir at 4°K. Furthermore, the rate at which the Toeppler pump withdraws the gas must be considerably greater than the rate at which the creeping film evaporates in T_1, in order to prevent undue dilution of the He^3–He^4 mixture. To accomplish this, the diameter of the tube T_1 above the anchor point is made much larger than at the bottom.

The enrichment factor of 3×10^4 is not necessarily the maximum attainable since it has not as yet been determined that it is necessary to draw off as large a volume of gas as here reported in order to collect all of the He^3. Also, it should be possible to collect in C the He^3 resulting from several fillings of A before withdrawing the sample into the Toeppler pump thus speeding up the entire process considerably when large amounts are to be processed. In order to hold the He^3 in C during step 6, heater H_2 is turned on during this draining. Experiments to date using this multiple flush method have not been as effective in recovering all of the He^3 originally present as when it is removed

[15] Fairbank, Reynolds, Lane, McInteer, Aldrich, and Nier, Phys. Rev. **74**, 345 (1948).
[16] Eselson, Lazarev, and Alekseevski, J. Exptl. Theoret. Phys. (U.S.S.R.) **20**, 1055 (1950).
[17] J. G. Daunt and C. V. Heer, Phys. Rev. **86**, 205 (1952).
[18] Abraham, Osborne, and Weinstock, Phys. Rev. **80**, 366 (1950).
[19] H. S. Sommers, Jr., Phys. Rev. **88**, 113 (1952).

after each cycle, probably because of a certain amount of backdiffusion of He^3 into the liquid being drained from A to B.

For larger-scale operation, there is no reason why the present design of separator should not be scaled up to take care of any given larger available rate of liquefaction. The number of flushes which can be performed per hour is limited by the rate at which heat can be transferred from A to B, consequently the critical dimension is the area of the cup C.

It should also be observed that with careful design, at least 50 percent of the liquid helium processed remains as a "by-product," and can be used for other cryogenic experiments.

PHYSICAL REVIEW VOLUME 91, NUMBER 5 SEPTEMBER 1, 1953

The Magnetoresistance of Bismuth Crystals at Low Temperatures

P. B. ALERS AND R. T. WEBBER
U. S. Naval Research Laboratory, Washington, D. C.

(Received January 22, 1953)

Using bismuth monocrystals at 4.2°K, the magnetoresistive behavior of the metal has been investigated in fields ranging to 100 000 gauss. The crystals were mounted transverse to the field with the principal crystalline axis parallel to the specimen axis. It is observed that the magnetoresistance oscillates at twice the frequency of the susceptibility oscillations of the de Haas-van Alphen effect. The resistance oscillation is separated into two frequency components, one twice the other, and each component is related to a group of electrons having a certain effective mass. The group which is thought to be primarily responsible for the de Haas-van Alphen effect produces magnetoresistance oscillations of small amplitude and of the same frequency. The other group yields larger amplitude resistance oscillations of twice this frequency. Resistance minima have been found at fields of 23.2, 12.5, 8.8 and 6.5 kilogauss when the field is perpendicular to a binary axis of the crystal. The results are discussed in terms of the theory of Davydov and Pomeranchuk, and yield a degeneracy temperature of about 210°K.

INTRODUCTION

IN general, when a metal is placed in a magnetic field, its resistance is observed to increase. This increase is usually monotonic, having at first a roughly quadratic dependence on field which gradually becomes linear as the field is increased.[1] As a function of temperature,[2–5] the effect is proportional to $1/\rho$, where ρ is the resistivity. Thus, at helium temperatures one should expect the magnetoresistance to be quite large. It is at these temperatures that anomalies in the magnetoresistive behavior of bismuth[6] have been observed, and similar, though much weaker, effects in zinc[7] and tin.[8] The bismuth anomalies are such as to suggest that the magnetoresistance contains an oscillatory component, and the proposal has been made[9] that this is linked to the susceptibility oscillations of the de Haas-van Alphen effect.[10] Indeed, the discovery of such behavior in bismuth prompted de Haas and van Alphen to make their original investigation of the susceptibility.

The experiments reported here were undertaken to extend existing data to higher fields and to attempt to establish an experimental correlation between the anomalies in the magnetoresistance and those of the susceptibility.

PREPARATION OF SPECIMENS

The magnetoresistive effect in bismuth is quite sensitive to impurities, especially at low temperatures, and care was taken to obtain pure material and prevent contamination during the process of growing single crystals. The bismuth used in crystals 4 through 7 was obtained from the Cerro de Pasco Copper Company and was stated by them to be 99.999 percent pure. The work of Shoenberg and Uddin[11] on the de Haas-van Alphen effect indicated that small amounts (~0.01 percent) of certain impurities affected the susceptibility oscillations considerably, and it appears that the same is true for the magnetoresistance. For crystal No. 3, reported earlier,[12] Johnson & Matthey bismuth (Lot No. 2824) was used and the crystals grown less carefully. We have concluded, in the light of subsequent

[1] P. Kapitza, Proc. Roy. Soc. (London) **A119**, 358 (1928); **A123**, 292 (1929).
[2] D. K. C. MacDonald and K. Sarginson, Repts. Progr. Phys. **15**, 249 (1952) give a resume of the work done on magnetoresistance and the Hall effect, with an extensive bibliography.
[3] E. Justi and H. Scheffers, Physik. Z. **39**, 105 (1938).
[4] M. Kohler, Physik. Z. **39**, 9 (1938).
[5] J. W. Blom, Physica **16**, 144–182 (1950). The second article (pp. 152–170) gives a discussion of the Kohler diagram and its application to gallium.
[6] de Haas, Blom, and Schubnikow, Physica **2**, 907 (1935); see also L. W. Schubnikow and W. J. de Haas, Proc. Acad. Sci. Amsterdam **33**, 130, 363, and 418 (1930).
[7] N. M. Nachimovich, J. Phys. (U.S.S.R.) **6**, 111 (1942).
[8] E. S. Borovik, Doklady Akad. Nauk. (S.S.S.R.) **69**, 767 (1949).
[9] W. J. de Haas, Nature **127**, 335 (1931).
[10] W. J. de Haas and P. M. van Alphen, Leiden Comm. **212a** (1930) and **220b** (1932).
[11] D. Shoenberg and M. Z. Uddin, Proc. Roy. Soc. (London) **A156**, 687 (1936).
[12] P. B. Alers and R. T. Webber, Phys. Rev. **84**, 863 (1951).

TABLE I. Orientations and resistance ratios of the bismuth crystals. θ is the angle between the trigonal axis and the specimen axis, and $R_{4.2°K}/R_{0°C}$ is the ratio of resistance in zero field at 4.2°K to the resistance at 0°C.

Crystal no.	θ	$\frac{R_{4.2°K}}{R_{0°C}}$
3	9.0°	4.8×10^{-3}
4	3.1°	4.1×10^{-3}
5	12.9°	3.9×10^{-3}
6	5.1°	2.2×10^{-3}
7*a*	1.4°	2.7×10^{-3}
7*b*	1.4°	2.1×10^{-3}
de Haas *et al.*[a]	0°	3×10^{-3}

[a] See reference 6.

results, that some "active" impurity was present in this crystal which served to distort and attenuate the effects to a considerable degree.

Crystals 4 through 7 were grown in a furnace of the type described by Schubnikow,[13] where the bismuth was in contact only with glass and a flux of silicone oil (Dow-Corning 550). The prime feature of this type of furnace is that the walls of the mold surrounding the specimen can move, thus preventing the strains which are caused by a rigid mold when the bismuth expands on solidification. Since a particular crystal orientation was desired, seeding was accomplished by placing a crystal at one end of the mold and allowing the molten bismuth to come in contact with a freshly cleaved face. Thus, as crystallization began, the specimen took the orientation of the seed. Repeated recrystallizations served to increase the purity of the portion of the crystal which was ultimately used.

As an index of purity, a resistance ratio consisting of the resistance at 4.2°K divided by the resistance at 0°C was calculated for each crystal. This served to indicate the degree to which various physical and chemical impurities were present. From this, the magnetic behavior could usually be inferred, although, as indicated above, particular kinds of chemical impurities could apparently be present in very small amounts and have a disastrous effect on the magnetoresistance.

Bismuth has a rhombohedral crystal structure with threefold symmetry about the principal axis and binary symmetry perpendicular to the principal axis.[14] In these experiments, all the specimens used had their axes parallel to the principal axis. In no case was the parallelism exact, however, the angle varying from 1° to 13°, but the magnetoresistive effect does not seem to be a strong function of this angle so long as it is small.

Table I gives a survey of the characteristics of each crystal, showing its resistance ratio and the angle between the trigonal axis and the specimen axis.

EXPERIMENTAL TECHNIQUE

Magnetic fields continuously variable to 100 000 gauss were provided by a Bitter-type solenoid. The opening in the coil was 1 in. in diameter, and since a conventional glass Dewar assembly would have occupied a prohibitive amount of space, a metal Dewar[15] was employed. This gave a low-temperature working space $\frac{1}{2}$ in. in diameter.

The crystal was mounted transverse to the field on a small brass plate. Current and potential leads were attached by a spot-welding technique, and current flow was along the axis of the rod, thus being perpendicular to the field. The crystal was rotated about its axis by means of a gear arrangement and a shaft leading through the top of the cryostat. Rotation, therefore, changed the angle between one of the binary axes of the crystal and the field. The variation of resistance with this angle was measured by observing the potential drop across the crystal with a recording potentiometer, while a timing motor turned the crystal. Because of symmetry, a sweep of 60° was all that was necessary to produce a complete curve, since this represented the resistance variation as the field was successively parallel, perpendicular, and again parallel to some binary axis. The angle ϕ describes this orientation and for the sake of symmetry in the presentation of the curves is set equal to zero, when the field is perpendicular to a binary axis.

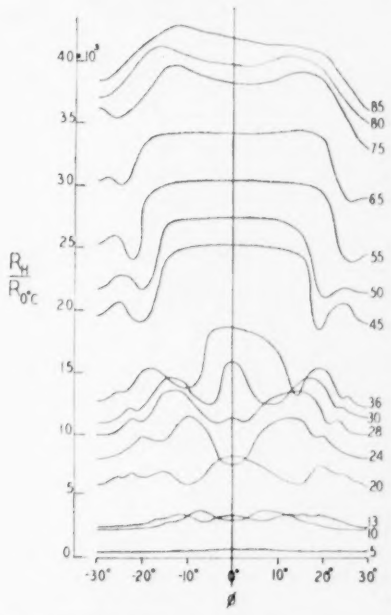

FIG. 1. Resistance as a function of angle between a binary axis and the field for Bi crystal No. 6 at 4.2°K. Parameter is H in kilogauss, and $\phi=0$ for field perpendicular to binary axis.

[13] L. W. Schubnikow, Koninkl. Ned. Akad. Wetenschap. Proc. **33**, 327 (1930); Leiden Comm. **207b**.

[14] G. W. C. Kaye, Proc. Roy. Soc. (London) **A170**, 561 (1939). In particular note Fig. 1, p. 562, and Fig. 4(c), p. 568. For heat flow F substitute current flow I.

[15] W. E. Henry and R. L. Dolecek, Rev. Sci. Instr. **21**, 496 (1950).

EXPERIMENTAL RESULTS

The rotation curves for a typical crystal (No. 6) are shown in Fig. 1. It is seen that at low fields the variation is approximately sinusoidal, becoming more complicated as the field is increased. Strong variations with angle, however, die out above 30 kilogauss and the resistance becomes almost constant, falling off only at the ends of the sweep. It is thought that the lopsided appearance of the highest curves is due to some impurity effect,

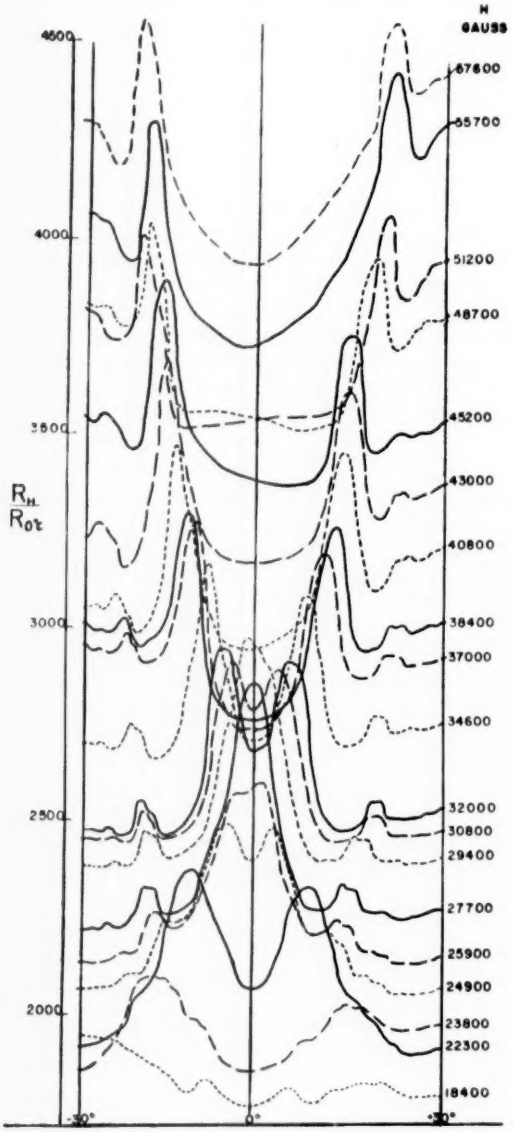

FIG. 2. Resistance as a function of angle between a binary axis and the field for Bi crystal No. 3 at 4.2°K. $H > 18\,000$ gauss. $\phi = 0$ for field perpendicular to binary axis.

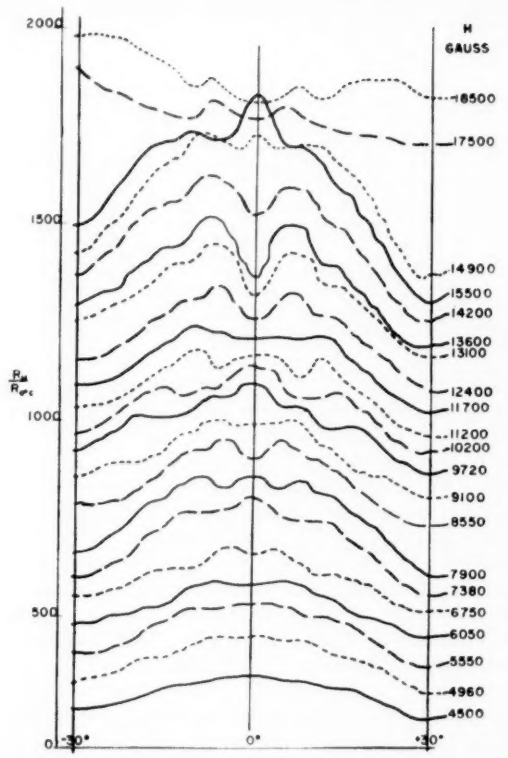

FIG. 3. Resistance as a function of angle between a binary axis and the field for Bi crystal No. 3 at 4.2°K. $H < 18\,000$ gauss. $\phi = 0$ for field perpendicular to binary axis.

since the resistance *vs* field curve for this crystal is also irregular at these fields.

In Figs. 2 and 3, the rotation diagrams for crystal No. 3 are shown for comparison. Apart from the fact that the resistances are much lower, it can be seen that for low fields the curves are similar in character to those of No. 6, while for high fields, they are quite different. It would thus appear that for bismuth at least, a slight amount of certain impurities can alter completely the behavior of the resistance in high magnetic fields. It might be suggested that the low-temperature magnetoresistance of some metals could provide an extremely sensitive test for the presence of certain contaminants.

In Fig. 4, the variation of resistance with field at $\phi = 0°$ (i.e., with H perpendicular to both the trigonal and binary axes) is shown. By comparison with Table I, it can be seen that successively higher curves have lower values for their resistance ratios. Assuming that a lower zero-field ratio indicated higher purity,[16] one sees that the small irregularities in the curves tend to die out as purity increases, while the anomalous be-

[16] See, for example, D. K. C. MacDonald and K. Mendelssohn, Proc. Roy. Soc. (London) **A202**, 103 (1950).

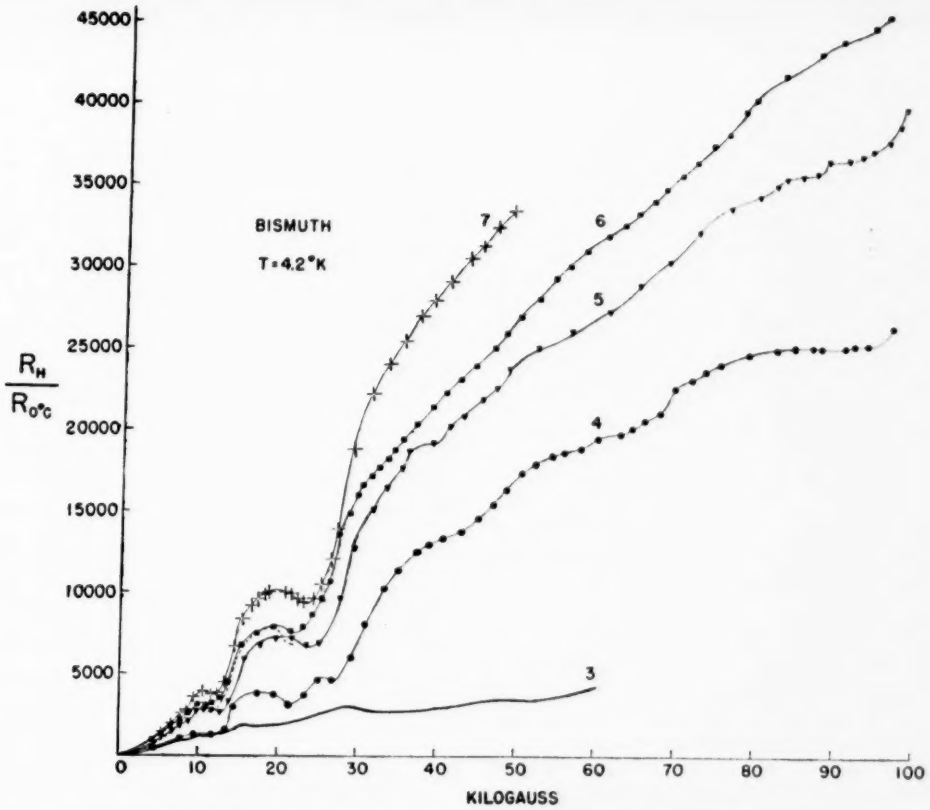

FIG. 4. Resistance as a function of field for $\phi=0$ and θ as given in Table I. The dotted curve lying for the most part between the curves for specimens 5 and 6 is the work of de Haas, Blom, and Schubnikow.[6]

havior at low fields is somewhat enhanced. The dotted curve represents the work of de Haas, Blom, and Schubnikow,[6] and curve No. 3 is that for crystal No. 3 reported earlier.[12] A close inspection of the curve for crystal No. 7a reveals a slightly anomalous variation in resistance below 10 000 gauss. In order to bring this out more distinctly, another specimen cut from the same crystal as 7a was investigated in the 0–18 000 gauss range. This crystal (No. 7b) had the lowest zero-field resistance ratio of all ($R_{4.2°K}/R_{0°C}=2.1\times10^{-3}$), and the anomalies in question are clearly visible; this curve appears as Fig. 5.

DISCUSSION

From inspection of the foregoing data, one can draw several conclusions. First, there seems to be no saturation effect in any of the resistances as far as the fields were carried. In addition, there appears to be a marked change in behavior in the region of 30 kilogauss. Below this field, the curves are somewhat depressed, and contain anomalies of considerable size, while above it the resistance follows a fairly linear course. Finally, as should be expected of bismuth, the relative increase in resistance is enormous compared with that of other metals. For the highest fields, the resistance had increased by a factor of about 24 million over its resistance in zero field and at 4.2°K.

The results have their primary application, however, in attempting to establish a correlation between the de Haas-van Alphen effect and the oscillatory com-

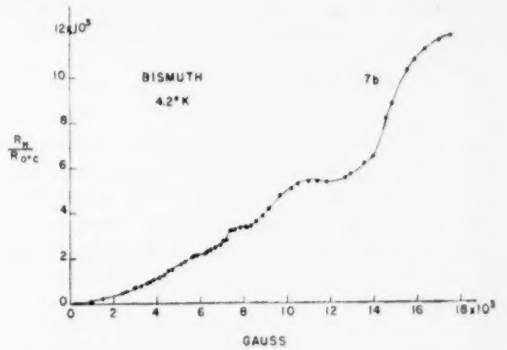

FIG. 5. Resistance as a function of field for Bi crystal No. 7b, showing behavior in fields below 18 000 gauss. $\phi=0$.

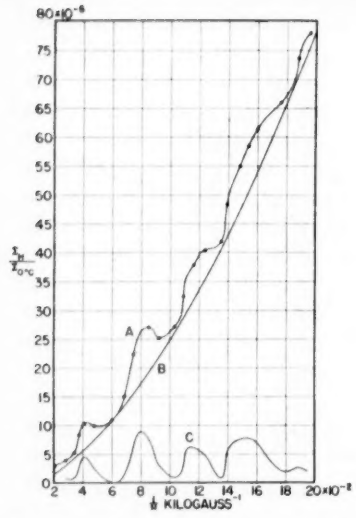

FIG. 6. Normalized conductivity of crystals (7a and 7b) plotted against reciprocal field. Curve *A* shows the experimental data, curve *B* the monotonic increase of conductivity, and curve *C* the oscillating component of conductivity.

ponent of the magnetoresistance. In Fig. 6, we have taken the data for crystal No. 7b, normalized them so as to match the data for crystal No. 7a in the region of 9000 gauss, and then taken the reciprocal of the composite data to give the conductivity of a general specimen. When this is plotted against the reciprocal of the field, we obtain a curve which can be arbitrarily separated into two parts; one representing a steady decrease in conductivity with increasing field, and the other a roughly sinusoidal variation of conductivity with field. The monotonic portion obeys a power law, being proportional to $(1/H)^{1.66}$, while the sinusoidal conductivity is of substantially constant frequency in $1/H$.

Such a procedure allows us to apply the same type of analysis as was employed by Shoenberg[17] in discussions of the de Haas-van Alphen effect. The susceptibility of a metal which exhibits the de Haas-van Alphen effect is of the following form:

$$x = A + B \sin\left(\frac{2\pi E_0}{\beta^* H} + \delta\right). \tag{1}$$

A and B are terms which depend on both the temperature and field. β^* is a double effective Bohr magneton, containing the effective mass, m^*, δ is an adjustable phase factor, and E_0 is the "chemical potential," the energy between the nearest Brillouin zone boundary and the overlapping constant energy surface. The degeneracy temperature T_0 is defined from $T_0 = E_0/k$.

If the argument of the sine in Eq. (1) is equated to an integer times π, one obtains values of the reciprocal field for which the sine is zero; i.e., where the oscillating component of the susceptibility crosses the $1/H$ axis. When these values of $1/H$ are then plotted against their corresponding integers, a straight line is obtained whose slope is equal to $2E_0/\beta^*$, and whose intercept for $1/H = 0 (H = \infty)$ gives the value of δ. Proceeding by analogy, a similar plot (Fig. 7) was made for the magnetoresistance, with the important difference that the fields for which the conductivity was a maximum were employed. A line drawn through the points obtained in this way was found to be nearly parallel to the line drawn by extrapolation of Shoenberg's susceptibility data[17] to our orientation. However, the fact that the maxima in conductivity correspond to the zeros of the oscillating susceptibility would imply that the resistance oscillates at a double frequency, at least at this temperature and in this range of fields.

A theoretical discussion of this phenomenon was given by Achieser[18] in 1939, and by Davydov and Pomeranchuk[19] in 1940. The latter authors were concerned primarily with the effect in bismuth, and used the data of de Haas *et al.*[6] and the results of Shoenberg's[17] susceptibility measurements published in 1939. Their calculations indicated that resistance minima should occur at fields $H_{\min}$ given by the following relation:

$$H_{\min} = \frac{E_0}{\beta^*} \frac{1}{(n+\frac{1}{2})}, \tag{2}$$

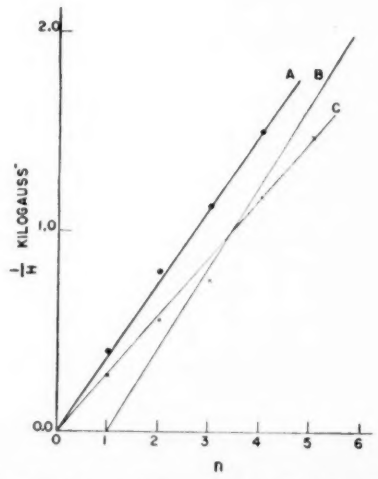

FIG. 7. Plot similar to that employed by Shoenberg in discussing the de Haas-van Alphen effect. Points on curve *A* represent the reciprocal fields at which the oscillating conductivity of specimens 7a and 7b goes through a maximum. Curve *B* is the line drawn from the cross-over points in Shoenberg's long-period susceptibility curves (see reference 17). The points on curve *C* are taken from the data for the relatively impure crystal No. 3.

[17] D. Shoenberg, Proc. Roy. Soc. (London) **A170**, 341 (1939).

[18] A. Achieser, Compt. rend. (U.R.S.S.) **23**, 874 (1939).

[19] B. Davydov and I. Pomeranchuk, J. Phys. (U.S.S.R.) **2**, 147 (1940).

TABLE II. Fields at which resistance minima occur, calculated from (2) using (n) and $(n+\frac{1}{2})$. Experimental observations are given for comparison. Two "series" of anomalies are observed, each corresponding to a value of β^*.

$E_0 = 2.9 \times 10^{-14}$ erg $(T_0 = 210°\text{K})$.

	$\beta_1^* = 1.18 \times 10^{-18}$ erg/gauss				$\beta_2^* = 2.37 \times 10^{-18}$ erg/gauss		
n	$H_{(n+\frac{1}{2})}$ calc	H_n calc	H obs	n	$H_{(n+\frac{1}{2})}$ calc	H_n calc	H obs
0	48.8	∞	—	0	24.4	∞	—
1	16.2	24.4	23.2	1	8.1	12.2	12.5
2	9.7	12.2	12.5	2	4.9	6.1	6.5
3	7.0	8.1	8.8				
4	5.4	6.1	6.5				

where, as before, E_0 is the "chemical potential," and $\beta^* = eh/m^*c$, a double effective Bohr magneton.

The effective mass, in general, is a tensor quantity, and is related, in momentum space, to the axes of the constant energy ellipsoid. In the case of bismuth, we have three identical ellipsoids, whose centers coincide and which are inclined at an angle of 120° with each other. For the crystal orientation considered in these experiments, namely, both the trigonal axis and a binary axis perpendicular to the field, one ellipsoid has its long axis parallel to the field, and the other ellipsoids are at angles of $\pm 120°$ on either side. This means that the magnetic field, acting on the electrons with momenta perpendicular to it, produces the most marked effect on those electrons having a small effective mass. Owing to the angles between the ellipsoids, and also to the fact that they are extremely long and thin, the electrons separate into two groups; one with an effective mass m_1^* and the other with an effective mass $m_2^* = \frac{1}{2}m_1^*$. This gives rise to two values of β^*, and thus to two magnetoresistive "series."

Using more recent (1952) values of E_0 and the effective masses deduced by Shoenberg[20] from his measurements of the de Haas-van Alphen effect, we have calculated the fields at which minima in the magnetoresistance should occur, and compared the results with experimental data. The calculations have been made using the $(n+\frac{1}{2})$ equation of Davydov and Pomeranchuk and also using (n). The $(n+\frac{1}{2})$ term arises in the theoretical treatment when the wave equation is reduced to that of an harmonic oscillator, for the case in which collisions are not considered. A much better agreement with experiment is obtained, however, when (n) alone is used, as can be seen in Table II. H is given in kilogauss.

It should be pointed out that the component of oscillation due to the electrons associated with β_2^* is the component which matches the oscillation frequency of the susceptibility. It is this group of electrons which is primarily responsible for the de Haas-van Alphen effect in bismuth in this range of fields.

The larger amplitude of the second and fourth maxima of curve C in Fig. 6 leads us to believe that there is a small-amplitude magnetoresistance oscillation of this frequency. The other group of electrons, associated with β_1^*, which gives rise to the double frequency component, is contributed by the ellipsoids which are inclined at $\pm 120°$ from the long-period de Haas-van Alphen ellipsoid. Susceptibility oscillations associated with the β_1^* electrons were found by Shoenberg[17] for some orientations of the crystal in the magnetic field.

The angle sweeps of Figs. 1–3 can be interpreted as reflecting the variations of effective mass which the conduction electrons undergo as the angle between the field and a binary axis is changed. Curves of similar complexity have been observed previously,[21] and it is possible that this implies anomalous field dependence as well. Gallium, however, which has strong angular anisotropy, was exhaustively investigated by Blom[8] in fields up to 20 kilogauss, and while a somewhat unusual behavior was observed, nothing resembling oscillations was found.

Studies[22,23] of the thermal conductivity of bismuth in a magnetic field indicate that the heat transport due to the electrons is practically zero at helium temperatures; indeed, a magnetoresistive effect in the thermal conductivity did not become appreciable until temperatures of the order of 60°K were reached. This may be explained by the very small number of conduction electrons in bismuth, so that the low-temperature thermal conductivity is almost entirely due to the lattice.

In metals such as aluminum or zinc, oscillations of the order of magnitude reported here would probably not be observed. This is based on the assumption that the oscillating conductivity would have an amplitude proportional to that of the oscillating susceptibility, and that the constant of proportionality is roughly the same for all metals. It then follows that the oscillating component would make such a negligible contribution to the total conductivity of most metals that it would be unobservable, except in the case of bismuth and possibly antimony and graphite.

The authors wish to thank Jules R. de Launay and Ted G. Berlincourt of the Cryogenics Branch for their helpful and illuminating discussions and suggestions. In addition, they gratefully acknowledge the help of A. H. Mister and F. G. Thorne, who operated the Bitter magnets and provided much assistance in the experimental runs.

Note added in proof: Since the completion of this paper, the magnetic susceptibility of our crystal No. 7b has been measured in fields up to 25 kilogauss by Dr. T. G. Berlincourt of this laboratory. A preliminary report of these measurements is published in Phys. Rev. **91**, 1277 (1953).

[20] D. Shoenberg, Trans. Roy. Soc. (London) **245**, 1 (1952).

[21] E. Justi and H. Scheffers, Physik. Z. **37**, 700 (1936).
[22] de Haas, Gerritsen, and Capel, Physica **3**, 1143 (1936).
[23] S. Shalyt, J. Phys. (U.S.S.R.) **8**, 315 (1944).

Electronic Structure of *F* Centers: Hyperfine Interactions in Electron Spin Resonance

A. F. Kip, C. Kittel, R. A. Levy, and A. M. Portis
Department of Physics, University of California, Berkeley, California
(Received May 18, 1953)

It is shown that the observed width of the microwave electron spin resonance absorption lines associated with *F* centers in KCl, NaCl, and KBr crystals can be attributed to hyperfine interactions between the *F*-center electron and the nuclear magnetic moments of the ions adjacent to the *F* center. The width arises from the distribution of nuclear moment components. Theoretical calculations of the width are in good agreement with observation provided that the *F*-center wave function is treated as a linear combination of atomic orbitals; wave functions calculated on continuum models are shown to be unsatisfactory. The theory is confirmed by a comparison of observations on *F* centers in crystals of $K^{39}Cl$ and $K^{41}Cl$. If the width is attributed to interactions with the nearest sets of K and Cl ions, the experiments lead directly to quantitative values of the electronic charge density at the K and Cl nuclei: one finds $|\Psi(K)|^2=0.70\times10^{24}$ cm^{-3} and $|\Psi(Cl)|^2=0.12\times10^{24}$ cm^{-3}.

I. INTRODUCTION

IN this paper we show that the shape and width of microwave spin resonance absorption lines associated with *F* centers in alkali halide crystals are caused by hyperfine interactions and find a natural explanation on a molecular orbital model of an *F* center.[1] The line width is attributed to the hyperfine interactions between the *F*-center electron and the nuclear magnetic moments of the ions adjacent to the *F* center. This explanation is supported, as shown below, both by theoretical calculations and by a comparison of observations on *F* centers in crystals of $K^{39}Cl$ and in $K^{41}Cl$. The molecular orbital model[2] describes an *F* center, which is an electron attached to a halogen ion vacancy (Fig. 1), by a linear combination of atomic orbitals (LCAO), each representing the extra electron in an atomic state on an atom in the cluster bounding the vacancy. The electron will interact through the *s* components of the atomic orbitals with the nuclear spins of the cluster of alkali atoms. We shall see below that the envelope of the intensity distribution of the hyperfine components of the spin resonance line is approximately Gaussian, and we shall calculate the half-width of the distribution.

Our interest in the *F*-center problem arose from the observation by Hutchison and Noble[3] that the width of the electron spin resonance absorption line in a KCl crystal colored by the addition of the order of 10^{18} excess K atoms per cm^3 was 49 oersteds between points of maximum slope in absorption. The line shape was reported to be Gaussian, so that the full width at half-maximum absorption is presumably about 56 oersteds. The observed shape and width are in marked disagreement with the theory of dipolar interactions. The theoretical magnetic dipolar width[4] for the actual *F* center concentration, assuming *F* centers distributed at random in the crystal lattice, is of the order of 0.1 oersted, and the theoretical line shape is Lorentzian.

Prompted by the above discrepancy, we investigated experimentally the spin resonance line associated with *F* centers in KCl crystals colored additively at various concentrations and quenching rates and also colored at room temperature by 2.5-Mev electron bombardment and by 250-kev x-ray irradiation. Microwave measurements were made at room and liquid nitrogen temperatures. In all of our measurements on KCl the line shape was approximately Gaussian, and the width was in very close agreement with the value observed by Hutchison and Noble. Our observations suggest then that the width of the resonance line is not caused by interactions between the *F* centers, but rather by the interactions of an *F*-center electron with its immediate environment in the crystal. The dominant interaction of this type is the hyperfine interaction between the *F*-center electron and the nuclear magnetic moments of the ions adjacent to the *F* center.

Most of the theoretical calculations of wave functions of *F* centers have treated the crystal as a homogeneous dielectric continuum,[5] with the electron moving in a

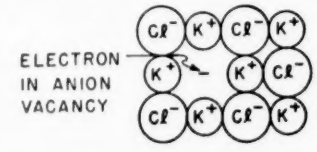

FIG. 1. *F* center in KCl. The ionic radii are drawn approximately to scale, but the distortion of the lattice near the *F* center is not included.

[1] A preliminary account of this work was given by C. Kittel, Bull. Am. Phys. Soc. **28**, No. 2, 21 (1953).

[2] T. Muto, Progr. Theoret. Phys. **4**, 243 (1949); T. Inui and Y. Uemura, Progr. Theoret. Phys. **5**, 252, 395 (1950); see also a related calculation by S. R. Tibbs, Trans. Faraday Soc. **35**, 1471 (1939).

[3] C. A. Hutchison, Jr. and G. A. Noble, Phys. Rev. **87**, 1125 (1952); earlier resonance experiments on *F*-centers are reported by C. A. Hutchison, Jr., Phys. Rev. **75**, 1769 (1949); E. E. Schneider and T. S. England, Physica **17**, 221 (1951); M. Tinkham and A. F. Kip, Phys. Rev. **83**, 657 (1951).

[4] For N electrons/cm^3 distributed at random on a simple cubic lattice, $\Delta H\approx N\times10^{-19}$ oersteds, provided that the fractional population is less than 0.01; this estimate uses the theory developed by C. Kittel and E. Abrahams, Phys. Rev. **90**, 238 (1953). Hutchison and Noble calculate values using an incorrect theory of the line width for random population.

[5] Typical of calculations of this character are those of S. R. Tibbs, Trans. Faraday Soc. **35**, 1471 (1939); J. H. Simpson, Proc. Roy. Soc. (London) **A197**, 269 (1949); L. Pincherle, Proc. Phys. Soc. (London) **A64**, 648 (1951); J. A. Krumhansl and N. Schwartz, Phys. Rev. **89**, 1154 (1953); C. I. Pekar, J. Exptl. Theoret. Phys. **16**, 335 (1946); **17**, 868 (1947); **19**, 746 (1949); **20**, 510 (1950).

central field. Such calculations take no account of the singularities in the potential which occur at the nuclei of the ions adjacent to the F center. We should not expect such wave functions to give correct estimates of the hyperfine interactions, and in fact we shall find that the calculated line width using Simpson's wave functions for NaCl is only of the order of several oersteds. Further, it was shown earlier by Kahn and Kittel[6] that the central field model is unable to account for the observed g value of the F-center resonance, and they proposed instead a molecular orbital model which gives correctly the order of magnitude of the observed Δg. It will be seen below that their model gives quite satisfactory values for the line width in KCl.

II. ELEMENTARY THEORY FOR KCl

We represent the F center, following Kahn and Kittel, by the molecular orbital

$$\Psi=(1/6)^{\frac{1}{2}}\sum_{i=1}^{6}\psi_i; \tag{1}$$

here ψ_i is the wave function of the valence electron when on the ith of the six K^+ ions bounding the anion vacancy. Taking the ψ_i as normalized, then Ψ will be normalized apart from overlap integrals which we neglect for the present; the results of Secs. III and IV below do not involve this assumption. On a free potassium atom ψ_i would be a $4s$ function, but in the crystal the state becomes electrically polarized[6] by the unsymmetrical crystal field which exists near the vacancy. We denote the fractional effective s character[7] of ψ_i by ξ, in the sense that in the crystal the value of $|\psi_i(0)|^2$ at a nucleus is equal to ξ times the free atom value of $|\psi_{4s}(0)|^2$; here $\xi\leqq 1$. We have then for the part of the Hamiltonian describing the hyperfine interaction with the alkali atom nuclei of spin I:

$$\mathcal{H}'=\tfrac{1}{6}\xi A\mathbf{S}\cdot\sum\mathbf{I}_i, \tag{2}$$

where $A\mathbf{S}\cdot\mathbf{I}$ is the interaction in the free atom. For K^{39}, the most abundant (93 percent) isotope of potassium, the coupling constant A has the value 0.0077 cm^{-1}, according to Fox and Rabi.[8]

When the Zeeman energy of the system is large in comparison with the hyperfine coupling we may treat the latter as a small perturbation on the Zeeman energy levels. In the representation in which M_s, $m_I(1)$, $m_I(2)$, $\cdots$, $m_I(6)$ are diagonal, the diagonal matrix elements of $\mathcal{H}'$ are

$$(M_s m_I(1)\cdots m_I(6)|\mathcal{H}'|M_s m_I(1)\cdots m_I(6))=\tfrac{1}{6}\xi^2 A M_s M_I. \tag{3}$$

The interaction of an rf field in the x direction with the system is described by the term

$$\mathcal{H}_{rf}=-(g\mu_B S_x+g_n\mu_n\sum I_{xi})H_x, \tag{4}$$

where g_n, μ_n refer to the nuclei. As $g_n\mu_n/g\mu_B$ is of the order of 10^{-3}, the transitions induced by H_x in which the nuclear spins change orientation are much weaker than those in which the electron spins change orientation; the nuclear transitions are neglected. We are thus led to the approximate selection rule $\Delta M_s=\pm 1$; $\Delta M_I=0$. The absorption frequencies are given by

$$h\omega=g\mu_B H_0+\tfrac{1}{6}\xi A M_I. \tag{5}$$

For six nuclei each of spin $\frac{3}{2}$ the maximum value of $\frac{1}{6}AM_I$ is $\frac{3}{2}A$, or 0.0115 cm^{-1}. This is equivalent (for $g=2$) to 123 oersteds: thus the effect of the hyperfine interaction is to spread out the transition over a region 123ξ oersteds to either side of the central Zeeman frequency.

The shape of the resulting line will be determined by the distribution of M_I values. As each nucleus has four possible values of m_I, there will be $4^6=4096$ arrangements of the six spins. These are distributed as follows among the several M_I values:

M_I	9	8	7	6	5	4	3	2	1	0
No. of arrangements	1	6	21	56	120	216	336	456	546	580

The negative values of M_I are distributed in the same fashion as the positive values. A Gaussian curve of the same integrated line strength and adjusted to fit at $M_I=0$ gives an excellent fit all the way along the envelope, the deviations being less than 2 percent of the central value. The envelope of the hyperfine lines therefore may be considered to be Gaussian to a good approximation, in agreement with the experimental result.

The width of the envelope at half-maximum is $1.12\xi A$, or, for potassium, 92ξ oersteds. The observed width of the F-center line is 54 ± 2 oersteds, suggesting that $\xi\cong 0.6$, which means that the atomic orbitals have 0.6 s character. Values of ξ are expected to be of the order of one-half, from considerations of the electrostatic polarization of the potassium atom towards the interior of the negative ion vacancy. We note that a mixture of s and p_z orbitals has its maximum dipole moment when the coefficients of the s and p_z parts are equal. Values of this order are also required[6] to account for the g shift. One should expect that higher angular momenta will also be present and that the electron may penetrate beyond the first shell of K ions. For these various reasons we may consider the measure 0.6 of

[6] A. H. Kahn and C. Kittel, Phys. Rev. **89**, 315 (1953).

[7] The components of higher orbital angular momenta mixed in this way into the ground state are almost completely quenched, and the states contribute to the hyperfine interaction only through the electron spin. The spin contribution in the potassium $4p$ level is less than 0.1 of the orbital contribution, and further, the total hyperfine splitting in p states in potassium and lighter alkali atoms is only about 0.1 of the corresponding s-state splitting. Thus the quenched p state hyperfine interaction may be in potassium of the order of only 0.01 of the s state interaction. We therefore neglect here the hyperfine splitting from the $4p$ and higher states. In Cs and Rb it may be worth while to include the p state effects.

[8] M. Fox and I. Rabi, Phys. Rev. **48**, 746 (1935); for a tabulation for alkali atoms, see J. B. M. Kellogg and S. Millman, Revs. Modern Phys. **18**, 323 (1946).

the s character of the atomic orbitals to be quite reasonable and consistent with other evidence.

We now compare the value of the effective coupling constant deduced from the observed line width with estimates made using the conventional theoretical model of the F-center ground state as a 1s state in a central field. Simpson[9] has calculated on this basis the wave function in NaCl, and we may safely consider that the wave function in KCl would be closely similar. Taking $|\Psi|^2$ at the center of a sodium ion from this wave function, the coupling constant works out as 1.4×10^{-5} cm^{-1} between the F-center electron and an individual K nucleus. The observed line width, however, points to a coupling constant,

$$\tfrac{1}{6}\xi A = 77\times10^{-5}\text{ cm}^{-1},$$

about 50 times larger. We therefore conclude that the central potential does not give an adequate representation of the actual wave function, whereas the molecular orbital model discussed above leads quite naturally to interactions of the correct order of magnitude.

III. GENERAL THEORY

It is of interest to derive general expressions for the mean-square and mean-fourth frequency deviations of electron spin resonance lines in the presence of hyperfine interactions. The generalization of the above results consist in the application of the method of sums to interactions with a mixture of atoms with various nuclear moments and nuclear spins. The generalization will enable us to consider conveniently the effect on the line width of interactions with the anions beyond the first shell of cations bounding the vacancy. The first anion shell in KCl has $4^{12}\cong17\times10^6$ spin arrangements, so that it is impractical to enumerate the arrangements individually.

We have the perturbation Hamiltonian,

$$\mathcal{H}=\sum_i a_i\mathbf{S}\cdot\mathbf{I}_i, \tag{6}$$

where[10]

$$a_i=\frac{-16\pi}{3}\frac{\mu_B\mu_i}{I_i}|\Psi(i)|^2. \tag{7}$$

Here μ_i is the magnetic moment of nucleus i; I_i is the spin of nucleus i; and $\Psi(i)$ is the value of the normalized electron wave function at the position of nucleus i. The absorption frequencies are

$$\hbar\omega=g_e\mu_BH_0+\sum a_iI_i^z, \tag{8}$$

according to Eq. (5). Thus the mean-square deviation from the central frequency is

$$\langle(\hbar\Delta\omega)^2\rangle_{Av}=\langle(g_e\mu_B\Delta H)^2\rangle_{Av}=\langle\textstyle\sum_i(a_iI_i^z)^2\rangle_{Av}, \tag{9}$$

or

$$\langle(\Delta H)^2\rangle_{Av}=\langle\textstyle\sum_i(h_iI_i^z)^2\rangle_{Av}=\sum_i h_i^2\langle m_i^2\rangle_{Av}, \tag{10}$$

where

$$h_i=(8\pi\mu_i/3I_i)|\Psi(i)|^2, \tag{11}$$

and m_i is the value of I_i^z. Similarly,

$$\langle(\Delta H)^4\rangle_{Av}=\sum h_i^4\langle m_i^4\rangle_{Av}. \tag{12}$$

Now

$$\langle m_i^2\rangle_{Av}=\tfrac{1}{3}I_i(I_i+1),$$

so that

$$\langle(\Delta H)^2\rangle_{Av}=\tfrac{1}{3}\sum h_i^2I_i(I_i+1)$$
$$=\frac{64\pi^2}{27}\sum\mu_i^2\frac{I_i+1}{I_i}|\Psi(i)|^4. \tag{13}$$

This is the most useful result of the theory.

We note that

$$\langle m_i^4\rangle=\tfrac{1}{5}I_i(I_i+1)[I_i(I_i+1)-\tfrac{1}{3}], \tag{14}$$

so that if all the nuclei are similar and the h_i are equal,

$$\frac{\langle m_i^4\rangle^{\frac{1}{2}}}{\langle m_i^2\rangle^{\frac{1}{2}}}=\left\{\frac{9}{5}\frac{[I_i(I_i+1)-\frac{1}{3}]}{I_i(I_i+1)}\right\}^{\frac{1}{2}}. \tag{15}$$

For a Gaussian line this ratio should be equal to $(3)^{\frac{1}{2}}=1.32$. For spin $\frac{3}{2}$, as in K^{39} and K^{41}, it is actually equal to 1.13. The discrepancy is not significant as the actual line has a finite cutoff, while the Gaussian has not. The explicit determination of the envelope for a special case in Sec. II gave a shape close to Gaussian.

IV. ANALYSIS OF RESULTS WITH $K^{39}Cl$ AND $K^{41}Cl$

In Sec. II above we saw that hyperfine interactions appear to account for the width of the spin resonance line associated with F centers in KCl. A critical test of this hypothesis is provided by the comparison of line widths in natural KCl with $K^{41}Cl$. The isotope abundances in natural potassium are: K^{39}, 93.08 percent; K^{40}, 0.012 percent; K^{41}, 6.91 percent. The ratio of the magnetic moments $\mu(41)/\mu(39)$ is 0.550, or $\mu(41)/\langle\mu(\text{natural})\rangle_{\text{rms}}=0.563$, so that if the hyperfine interactions are principally with the potassium ions bordering the anion vacancy, the resonance line should be appreciably sharper for F centers in $K^{41}Cl$ than in natural KCl. It would be naive, however, to expect that the line width would be exactly in the ratio of the moments, as the ground-state energy calculations by Inui and Uemura[2] suggest that the neighboring Cl^- ions do bear a part of the wave function.

We obtained through the courtesy of the Stable Isotopes Division of the U. S. Atomic Energy Commission the loan of 1.8 grams of powdered $K^{41}Cl$, in which the K^{41} had been concentrated electromagnetically at Oak Ridge. The potassium isotope abundances reported for the specimen are: K^{39}, 0.789 percent; K^{40}, 0.002 percent; K^{41}, 99.21 percent. We fused the powder in a procelain crucible and then colored the resulting specimen by x-ray irradiation at room temperature with 250-kev x-rays.

[9] J. H. Simpson, Proc. Roy. Soc. (London) **A197**, 269 (1949).
[10] E. Fermi and E. Segrè, Z. Physik **82**, 729 (1933).

TABLE I. Data on nuclear magnetic moments relevant to the present paper.

Isotope	Natural abundance (percent)	Spin	Magnetic moment (nuclear magnetons)	Hyperfine coupling constant, ground state of free atom (cm^{-1})
Na^{23}	100.	3/2	2.217	0.0296
K^{39}	93.08	3/2	0.391	0.00770
K^{41}	6.91	3/2	0.215	0.00424
$\langle K(natural)\rangle_{rms}$	···	3/2	(0.382)	(0.00752)
Rb^{87}	27.85	3/2	2.750	0.114
Cs^{133}	100.	7/2	2.577	0.0767
Cl^{35}	75.4	3/2	0.822	···
Cl^{37}	24.6	3/2	0.684	···
$\langle Cl(natural)\rangle_{rms}$	···	3/2	(0.790)	···
Br^{79}	50.52	3/2	2.11	···
Br^{81}	49.48	3/2	2.27	···
$\langle Br(natural)\rangle_{rms}$	···	3/2	(2.189)	···

Microwave spin resonance measurements on the colored $K^{41}Cl$ specimen gave a line width of 36 ± 2 oersteds, as compared with 54 ± 2 oersteds for the colored natural KCl specimen. If only the first set of K^+ ions bordering the vacancy shared in the F-center wave function we should expect a width of 31 oersteds in the $K^{41}Cl$. The extent of the agreement is a convincing indication that the line width is actually caused by hyperfine interactions, but the small discrepancy between the observed and calculated values suggests that the Cl^- ions also share in the F-center wave function.

We shall now analyze the data for potassium chloride on the following simplifying assumptions:

(1) The F-center wave function overlaps only the six nearest neighbor K ions and the twelve next nearest neighbor Cl ions.

(2) The F-center wave function at the nuclei has the same density in $K^{39}Cl$ and in $K^{41}Cl$.

(3) Isotopic mixtures are treated using root-mean-square values of the magnetic moments (Table I); this procedure is rigorously correct.

(4) The resonance line shape is treated as if it were Gaussian, so that the width at half-maximum absorption is taken as 2.35 times the root-mean-square width.

(5) Hyperfine interaction is the only significant source of line broadening.

We have from Eq. (13), the ratio of the K moments, and the observed widths:

$$\begin{aligned} 530&=7.5h^2(\mathrm{K})+15h^2(\mathrm{Cl});\\ 235&=(7.5)(0.317)h^2(\mathrm{K})+15h^2(\mathrm{Cl}). \end{aligned} \tag{16}$$

Here K denotes natural potassium. Then

$$h(\mathrm{K})=7.56 \text{ oersteds}; \quad h(\mathrm{Cl})=2.57 \text{ oersteds}. \tag{17}$$

Using Eqs. (11) and (17), we find for the charge densities at the nuclei:

$$\begin{aligned} |\Psi(\mathrm{K})|^2&=0.70\times10^{24}\ \mathrm{cm}^{-3};\\ |\Psi(\mathrm{Cl})|^2&=0.12\times10^{24}\ \mathrm{cm}^{-3}. \end{aligned} \tag{18}$$

These are to be considered as approximate experimental values of the electron densities at the nuclei of the nearest K and Cl ions bordering the F center. It is seen that the Cl ions play a much smaller role than do the K ions. By contrast with the above values, continuum wave functions give values of the order of 0.02×10^{24} cm^{-3} for $|\Psi(\mathrm{K})|^2$. It would seem reasonable to judge the accuracy of future wave function calculations by the extent of the agreement of the calculated $|\Psi|^2$ values with the values given in Eq. (18).

We can calculate $|\psi(0)|^2$ for the $4s$ state of a free potassium atom by use of Eq. (7) and the experimental coupling constant obtained from atomic beam results.[8] We find $|\psi(0)|^2=7.5\times10^{24}$ cm^{-3}. This may be compared with $6|\Psi(\mathrm{K})|^2=4.2\times10^{24}$ cm^{-3} from Eq. (18); the comparison means, in general agreement with the earlier estimate, that the F-center wave function on the nearest K ions has 56 percent of the s character that one would have with a linear combination of $4s$ atomic orbitals on the potassium atoms only. This high percentage tells us that the wave function must be strongly localized in the immediate vicinity of the anion vacancy. If the wave function covered a large number of K atoms equally, we note that the line width would diminish proportional to $(1/N)^{\frac{1}{2}}$, where N is the number of atoms involved. It seems likely that, by analogy with metallic potassium, the overlap effects in the normalization integral are considerable and act to increase the charge density at the nuclei. The nearest neighbor distance between K ions is roughly the same in the metal as in KCl.

V. F CENTERS IN NaCl AND KBr

We have now under way a substantial program to investigate F, V, and other centers in the alkali halides, alkaline earth salts, and other crystals, including situations (such as with zero nuclear spin) where the hyperfine interactions may be small enough to give a sharp resonance line and situations (as in cesium and rubidium salts) where the cation hyperfine interaction may be large enough to enable individual hyperfine components to be resolved, provided the nearest neighbor shell of cations does not contribute significantly to the interaction. The only other F-center measurements we are able to report at present are for NaCl, where the width is 162 oersteds, and for KBr, where the width is 146 oersteds. The NaCl and KBr crystals were measured at the temperature of liquid nitrogen. The NaCl was colored by bombardment with 2.5-Mev electrons from the electron linear accelerator stage of the Berkeley synchrotron.[11] The KBr was colored additively.

We shall now try to understand approximately these two widths, considering first the width in NaCl. We shall suppose for the purpose of the estimate that the contributions of the Cl ions in NaCl to the mean-square

[11] We are indebted to Mr. George MacFarland and Mr. Duane Mosier of the University of California Radiation Laboratory for the electron bombardments.

line width is the same as in KCl, and that the contribution of the Na ions is related to that of the K ions by the ratio of the hyperfine coupling constants in the free atom. According to Table I, this ratio is 296/75 = 3.94. On these assumptions the calculated mean-square width in NaCl is, from Eq. (16),

$$(7.5)(3.94)^2(7.5)^2+(15)(2.7)^2\cong 6500, \qquad (19)$$

which corresponds to a calculated width at half-maximum absorption of 190 oersteds. The observed width in NaCl is 162 oersteds. The agreement is generally satisfactory in view of the sweeping nature of the assumptions on which the estimate is based.

In making an estimate for KBr, we assume that the contribution of the K ions is the same as in KCl. It is assumed further that the contribution of the Br ions is related to that of the Cl ions by the ratio of the coupling constants. The ratio of the coupling constants is estimated in an indirect way from the coupling constants of atomic Rb and K, these atoms being isoelectronic with the Br^{2-} and Cl^{2-} ions. We consider Rb^{87}, as it has a spin of $\frac{3}{2}$. All the other nuclei involved have also spins of $\frac{3}{2}$. The relevant data are given in Table I. The coupling constant ratio $Rb^{87}/K^{39}=14.8$; as we are interested in an estimate of the coupling constant ratio $\langle Br\rangle_{rms}/\langle Cl\rangle_{rms}$ we must multiply 14.8 by the magnetic moment ratio $\langle Br\rangle_{rms}/Rb^{87}=0.80$ and also by the magnetic moment ratio $K^{39}/\langle Cl\rangle_{rms}=0.50$ In this way we have as a rough estimate the coupling constant ratio $\langle Br\rangle_{rms}/\langle Cl\rangle_{rms}\approx 5.9$. The mean-square line width on this basis would be, from Eq. (16),

$$7.5(7.5)^2+15(2.7)^2(5.9)^2\approx 4200 \qquad (20)$$

which corresponds to a calculated width at half-maximum absorption of about 153 oersteds. The observed width in KBr is 146 oersteds.

VI. EXPERIMENTAL

With the exception of the $K^{41}Cl$, measurements were made on single crystals obtained from the Harshaw Chemical Company. For KCl and KBr, measurements were also made on polycrystalline pellets fused from material obtained from the J. T. Baker Chemical Company. These pellets contained less than 0.0001 percent of paramagnetic impurities. In the absence of coloration of the samples no resonance absorption was observed. By varying the irradiation time for the electron and x-ray bombarded samples, and by varying the temperature of the furnace and quenching rate for the additively colored specimens, it was possible to obtain measurements over a range of F-center concentrations from 5×10^{16} to $10^{18}/cm^3$, as determined spectroscopically from the strength of the optical absorption in the F band.

The samples were mounted on blocks cut from Styrofoam and placed at the center (the region of lowest E and highest H field) of a rectangular cavity resonant for the TE_{102} mode at approximately 8950 Mc/sec. The samples were rectangular in shape, nearly filling the cavity cross section. The sample thickness was adjusted to reduce the unloaded Q of the cavity to about $\frac{2}{3}$ of its value in the absence of the sample; the sample volume was generally of the order of 1 cm^3.

A 2K39 reflex Klystron amplitude modulated at 6 kc/sec was employed as the microwave source. The variation in power reflected from the cavity was detected by a specially selected 1N23 crystal placed in one arm of a magic-tee bridge. The 6-kc/sec signal was amplified by a narrow-band low-noise amplifier at a voltage gain of about 10^4. The resonance envelope was detected in a lock-in mixer and presented on the screen of a long persistence cathode-ray oscilloscope, whose horizontal deflection was made to vary linearly with the magnetic field. The field was swept at a rate compatible with a band pass of about 0.1 cps. Field markers obtained from a rotating flux meter bridge were superimposed on the oscilloscope trace. The experimental data were obtained from photographs of the oscilloscope presentation.

For reasons discussed more fully in the following paper, it was found possible to make more accurate measurements on the dispersion envelope than on the absorption. We present in Table II our measurements of g values and of full width between points of maximum dispersion. The dispersion curves were closely Gaussian; we present also for comparison the equivalent (calculated) full width at half-maximum absorption for the corresponding absorption curves. Our results on g value, shape, and width were found to be characteristic only of the particular alkali halide investigated and independent of the concentration of F centers, method of preparation, or temperature at which the resonance was observed.

The g values may presumably be interpreted along the lines suggested by Kahn and Kittel[6] for KCl, but we are not able at this time to give a detailed discussion of the differences among the g values of the several salts; this must await the calculation of very good wave functions for the ground and excited states. Configuration interaction might be expected to play a significant part in the g value.

We should emphasize the great importance (to accurate line width determinations) of saturation

TABLE II. Summary of experimental results on F-center resonance.

Crystal	g	Observed full width between points of maximum dispersion (oersteds)	Equivalent full width between points of half-maximum absorption (oersteds)
KCl	1.995	61	54
$K^{41}Cl$	1.995	40	36
KBr	1.980	162	146
NaCl	1.987	180	162

effects. It is very easily possible to make serious errors through their neglect. The following paper by A. M. Portis discusses the saturation effects in detail.

VII. CONCLUSION

From the experiments and calculations described above it appears that one may with some confidence attribute to hyperfine interactions the width of the electron spin resonance line arising from F centers in alkali halide crystals. It appears further than an F-center wave function which is a linear combination of polarized atomic orbitals will give a fair quantitative representation of the hyperfine interactions. It is also possible to make reasonable empirical estimates of the line widths on the basis of the results for $K^{39}Cl$ and $K^{41}Cl$, together with the free atom hyperfine coupling constants for the atoms under consideration. Our interpretation of the observed resonance line is also supported in detail by observations by Portis and Kip[12] on the rf saturation behavior of the resonance.

We are glad to acknowledge again our indebtedness to the U. S. Atomic Energy Commission for the provision of the $K^{41}Cl$. We thank the U. S. Naval Radiological Defense Laboratory, San Francisco, for the x-ray irradiations and the University of California Radiation Laboratory for the electron bombardments. The planning of the $K^{41}Cl$ experiment was assisted greatly by the generous advice and encouragement of Professor E. Segrè. We have profitted from discussions with L. W. Alvarez, I. Estermann, W. D. Knight, and F. Seitz. This research was supported in part by the U. S. Office of Naval Research.

[12] A. M. Portis and A. F. Kip, Bull. Am. Phys. Soc. **28**, No. 2, 9 (1953); A. M. Portis (following paper), Phys. Rev. **91**, 1071 (1953).

PHYSICAL REVIEW VOLUME 91, NUMBER 5 SEPTEMBER 1, 1953

Electronic Structure of F Centers: Saturation of the Electron Spin Resonance

A. M. PORTIS
Department of Physics, University of California, Berkeley, California

(Received May 18, 1953)

It is shown that the unusual observed saturation behavior of the microwave electron spin resonance associated with F centers in KCl, NaCl, and KBr crystals can be accounted for if the overall width is ascribed to interaction between the F-center electrons and the nuclear magnetic moments of the ions adjacent to the F centers. The measured saturation factor gives for F centers in KCl a spin-lattice relaxation time of 2.5×10^{-5} sec at room temperature. The observed saturation behavior in which only the absorption saturates is in marked disagreement with the Kramers-Kronig relations. However it is shown, that the Kramers-Kronig relations are not applicable to saturated systems. Expressions which avoid the use of these relations are presented for saturable systems.

I. INTRODUCTION

IT is shown in this paper that the unusual saturation behavior of the microwave spin resonance absorption and dispersion associated with F centers in alkali halide crystals can be accounted for if the over-all width is caused by hyperfine interaction.[1] The details of the saturation behavior of a system depend markedly on the nature of the broadening mechanism. If the broadening arises from dipolar interaction between like spins or from interaction with the radiation field, then the thermal equilibrium of the spin system will be preserved during resonance absorption. This will also be true if the line width comes from some mechanism which is external to the spin system but is fluctuating rapidly compared with the time associated with a spin transition. This first case we call the *homogeneous* case. The consequence of homogeneous broadening is that the energy absorbed from the microwave field is distributed to all the spins and thermal equilibrium of the spin system is maintained through resonance. In an effort to understand the observed saturation results, our measurements were first compared with the behavior expected for this kind of broadening. This comparison is shown in Fig. 1. The observed and the theoretical behavior for a simple line of the observed shape were fitted so as to have the same slope at low microwave fields. It can be seen that the simple theory completely fails to account for our saturation results.

In attempting to account for our results we realized that if the line width were to come from variations in the local magnetic fields the physical response of the system would be markedly different. For this second case, which we call the inhomogeneous case, energy will be transferred only to those spins whose local fields satisfy the resonance condition. Further, the processes for spin-spin interaction will be slow as compared with the direct interaction of the spins with the lattice, since in order for spins in different local fields to come to equilibrium, energy will have to be transferred to the lattice. It is useful for this case to think of spin packets

[1] A preliminary account of this work was given by A. M. Portis and A. F. Kip, Bull. Am. Phys. Soc. **28**, No. 2, 9 (1953).

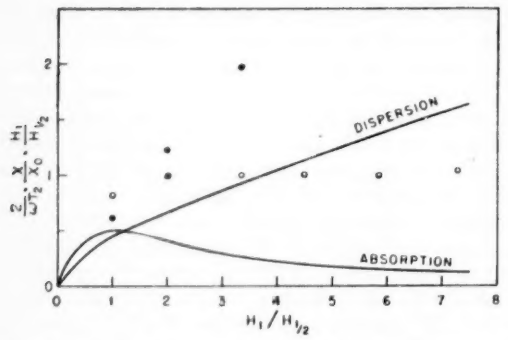

FIG. 1. Comparison between the observed saturation behavior of F centers in KCl and the simple theory of Sec. II.

having little or no interaction with each other and of width given by the simple dipole-dipole interaction. Then the over-all response of the spin system will be a superposition of the individual responses of the spin packets. It is clear that the broadening of the spin resonance in alkali halides where the width is from the distribution in hyperfine fields is of the inhomogeneous type. The excellent agreement between our results and the predicted saturation behavior for this case is shown in Sec. V.

By studying the way in which the system saturates at high-microwave fields it is possible to determine the spin-lattice relaxation time. Of course, for a steady-state experiment, one does not obtain directly the spin lattice relaxation time, T_1, but rather the product T_1T_2, where T_2 is the time associated with the width of the spin packets. This case is closely related to one considered by Bloembergen, Purcell, and Pound[2] where the over-all width comes from inhomogeneities in the applied magnetic field. At high-microwave fields the relation between absorption and dispersion deviated from the relationship developed by Kramers and Kronig.[3] This deviation has led here to a re-examination of the derivation of these relations. It has been found that certain assumptions made in the derivation regarding the behavior of the complex susceptibility are not valid for saturable systems. This problem is discussed in Sec. VI and Appendix I, where a scheme which introduces the Kramers-Kronig relations only in a restricted way is presented.

II. THE ELEMENTARY THEORY OF SATURATION

We consider here the saturation behavior of a system for which the broadening is of the *homogeneous* type. For simplicity we consider single electron spins so that only on the application of an external magnetic field is the spin degeneracy lifted. We then have two states per electron of frequency separation:

$$\omega_0 = g(e/2mc)H_0, \tag{1}$$

where g is the spectroscopic splitting factor and H_0 the applied magnetic field. These spin levels are not perfectly defined but are somewhat broadened. Sources of *homogeneous* broadening include:

(*a*) Dipolar interaction between like spins;
(*b*) Spin-lattice relaxation;
(*c*) Interaction with the radiation field;
(*d*) Motion of carriers in the microwave field;
(*e*) Diffusion of excitation through the sample;
(*f*) Motionally narrowed fluctuations in the local field.

We define N^+ to be the number of spins in the higher-energy spin state and N^- the number in the lower-energy state. For the entire spin system in thermal equilibrium we have

$$N^+/N^- = \exp(-\hbar\omega_0/kT_s), \tag{2}$$

where T_s is the effective spin temperature. If the spin system is in thermal equilibrium with the lattice at some temperature T_l,

$$N^+ = N_0^+, \quad N^- = N_0^-,$$

and

$$N_0^+/N_0^- = \exp(-\hbar\omega_0/kT_l). \tag{3}$$

We consider now the deviations of the spin system from equilibrium with the lattice under the interaction of the spin system with the radiation field and with the lattice. If we let $n = N^- - N^+$:

$$dn/dt = (dn/dt)_{rf} + (dn/dt)_{sl}, \tag{4}$$

where $(dn/dt)_{rf}$ and $(dn/dt)_{sl}$ give the rate of change of the difference in populations from interaction with the radiation field and spin-lattice interaction respectively.

The rate of change of the difference in populations from interaction with the radiation field at a frequency ω is given by

$$(dn/dt)_{rf} = -\tfrac{1}{4}\pi\gamma^2 H_1^2 g(\omega-\omega_0)n, \tag{5}$$

where γ is the magnetomechanical ratio, H_1 the maximum amplitude of the microwave magnetic field, and $g(\omega-\omega_0)$ the normalized shape factor for the transition. Following Bloembergen,[2] we take for the interaction with the lattice:

$$(dn/dt)_{sl} = (n_0 - n)/T_1, \tag{6}$$

where $n_0 = N_0^- - N_0^+ \simeq (\hbar\omega_0/2kT_l)N$ and T_1 is the spin-lattice relaxation time.

If the microwave power incident on the sample is varying slowly as compared with T_1, we obtain a quasi-steady state condition for which

$$dn/dt \cong 0,$$

and

$$n = n_0/[1+\tfrac{1}{4}\pi\gamma^2 H_1^2 T_1 g(\omega-\omega_0)]. \tag{7}$$

For the case where the microwave power is amplitude modulated at a frequency high compared with $1/T_1$,

[2] Bloembergen, Purcell, and Pound, Phys. Rev. **73**, 679 (1948).
[3] R. de L. Kronig, J. Opt. Soc. Am. **12**, 547 (1926); H. A. Kramers, Atti congr. intern. fis. Como **2**, 545 (1927).

n will not be able to follow the variations in microwave power over a modulation cycle but will respond to the average power. These two cases are examined in detail in Appendix II.

We are concerned here with the rate at which energy is absorbed from the radiation field:

$$P_a = -\tfrac{1}{2}h\omega(dn/dt)_{\mathrm{rf}}. \tag{8}$$

Substituting from Eqs. (5) and (7), we find that

$$P_a = \tfrac{1}{2}\omega\left\{\tfrac{1}{2}\omega_0\left(\frac{\gamma^2 h n_0}{2\omega_0}\right)\cdot\frac{\pi g(\omega-\omega_0)}{1+\tfrac{1}{4}\pi\gamma^2 H_1^2 T_1 g(\omega-\omega_0)}\right\}. \tag{9}$$

Noting that the complex part of the rf susceptibility is defined by

$$P_a = \tfrac{1}{2}\omega\chi'' H_1^2, \tag{10}$$

and that the static spin susceptibility,

$$\chi_0 = \gamma^2 h n_0/2\omega_0, \tag{11}$$

we have

$$\chi''(\omega) = \tfrac{1}{2}\chi_0\omega_0\frac{\pi g(\omega-\omega_0)}{1+\tfrac{1}{4}\pi\gamma^2 H_1^2 T_1 g(\omega-\omega_0)}. \tag{12}$$

We define T_2 such that at the line center

$$g(0) = T_2/\pi. \tag{13}$$

Then

$$\chi''(\omega_0) = \tfrac{1}{2}\chi_0\omega_0 T_2\frac{1}{1+\tfrac{1}{4}\gamma^2 H_1^2 T_1 T_2}. \tag{14}$$

The expression derived in Appendix I for the real part of the rf susceptibility is

$$\chi'(\omega) = \tfrac{1}{2}\chi_0\omega_0\frac{1}{1+\tfrac{1}{4}\pi\gamma^2 H_1^2 T_1 g(\omega-\omega_0)} \times\int_0^\infty\frac{2\omega' g(\omega'-\omega_0)}{\omega'^2-\omega^2}d\omega'. \tag{15}$$

III. THE GENERAL THEORY OF SATURATION

We considered in Sec. II the saturation behavior for *homogeneous* broadening of the spin levels. However, as in spin resonance from F centers in alkali halides, the over-all width may be caused by factors which do not maintain the spin system in equilibrium. Here one must take the results of Sec. II as applying to a spin packet of width approximately $1/T_2$. These lines must be then assembled under an envelope the shape of which is given by the details of the inhomogeneous broadening as illustrated in Fig. 2. The distinction between homogeneous and inhomogeneous broadening is that the inhomogeneous broadening must come from interactions outside the spin system and must be slowly varying over the time required for a spin transition. Examples of inhomogeneous broadening include:

(*a*) Hyperfine interaction,
(*b*) Anisotropy broadening,
(*c*) Dipolar interaction between spins with different Larmor frequencies,
(*d*) Inhomogeneities in the applied magnetic field.

The distribution in local fields is given by $h(\omega-\omega_0)$, which is normalized so that

$$\int_0^\infty h(\omega-\omega_0)d\omega = 1.$$

We define T_2^* so that at the center of the distribution

$$h(0) = T_2^*/\pi. \tag{16}$$

Then we obtain in the general case for the absorption

$$\chi''(\omega) = \tfrac{1}{2}\chi_0\int_0^\infty\frac{\pi\omega' g(\omega-\omega')}{1+\tfrac{1}{4}\pi\gamma^2 H_1^2 T_1 g(\omega-\omega')}h(\omega'-\omega_0)d\omega'. \tag{17}$$

The dispersion is given by

$$\chi'(\omega) = \tfrac{1}{2}\chi_0\int_0^\infty\frac{\omega' h(\omega'-\omega_0)d\omega'}{1+\tfrac{1}{4}\pi\gamma^2 H_1^2 T_1 g(\omega-\omega')} \times\int_0^\infty\frac{2\omega'' g(\omega''-\omega')d\omega''}{\omega''^2-\omega^2}. \tag{18}$$

As is shown in Appendix I, if the over-all broadening is large compared with the width of the spin packets, these expressions simplify to

$$\chi''(\omega) = \tfrac{1}{2}\chi_0\omega h(\omega-\omega_0)\int_0^\infty\frac{\pi g(\omega-\omega')}{1+\tfrac{1}{4}\pi\gamma^2 H_1^2 T_1 g(\omega-\omega')}d\omega', \tag{19}$$

$$\chi'(\omega) = \tfrac{1}{2}\chi_0\int_0^\infty\frac{2\omega'^2 h(\omega'-\omega_0)}{\omega'^2-\omega^2}d\omega'. \tag{20}$$

We note that the absorption line does not change shape on saturation since the integral in Eq. (19) will not be a function of ω. The details of the way in which

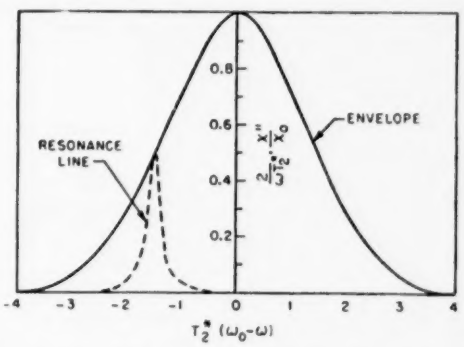

FIG. 2. Diagram illustrating the distinction between the resonance line for a spin packet and the envelope caused by inhomogeneous broadening.

$\chi''(\omega)$ changes in amplitude depend on the form of the shape function $g(\omega-\omega')$. As will be shown in Sec. V the observed behavior of the spin resonance is in good agreement with these results and allows further the determination of the shape of $g(\omega-\omega')$ even though it is masked by the over-all broadening.

IV. EXPERIMENTAL PROCEDURE

The experiments described in this and the preceding paper were performed at a frequency of approximately 8590 Mc/sec corresponding to a resonance field of about 3200 oersteds. A 2K39 reflex klystron nominally delivering 250 mw of microwave power was employed as the microwave source. The power was 100 percent modulated at 6 kc/sec by a microwave gyrator.[4] A simplified block diagram of the resonance equipment is shown in Fig. 3. The equipment for Pound stabilization, power monitoring, and power modulation of the microwave oscillator is not shown. The signal detected by a 1N23 crystal in the arm to the right of the magic-tee bridge is proportional to the difference in power reflected from the variable probe and the resonant cavity. In practice the bridge was first balanced by adjusting the position and depth of the variable probe until no microwave power reached the detecting crystal. The bridge was then unbalanced until about 1 μw of microwave power reached the detecting crystal.

One can unbalance the bridge in one of two ways, either by translating the probe along the guide or by decreasing the depth of its penetration into the guide. Translating the probe makes the bridge sensitive to variations in cavity frequency giving a signal at the crystal proportional to the dispersion. Raising the probe makes the bridge sensitive to variations in cavity Q giving a signal proportional to the absorption.

After unbalancing the bridge by raising the probe, the position of the probe along the guide was always readjusted for minimum power to the crystal in order to avoid a mixture of absorption and dispersion. In this way the amplitudes of the absorption and dispersion signals were compared over a range of 20 db in microwave power. After each power change the unbalance of the bridge was readjusted in order to maintain the same power on the detecting crystal. Using this procedure, it can easily be shown that the detected absorption and dispersion signals are proportional to $H_1\chi''$ and $H_1\chi'$ respectively.

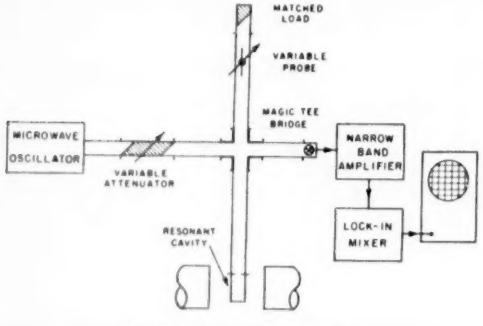

FIG. 3. Microwave apparatus.

[4] C. L. Hogan, Bell System Tech. J. **31**, 1 (1952).

The microwave field in the cavity was calculated from measurements of the loaded Q of the cavity, the voltage standing wave ratio in the cavity arm, and the power incident on the cavity. The power reflection coefficient of the cavity,

$$|\Gamma|^2=[(\beta-1)/(\beta+1)]^2, \tag{21}$$

where β is the voltage standing wave ratio and is equal to Q_e/Q_u, the ratio of the external Q to the unloaded Q of the cavity. It can be shown that the condition for optimum sensitivity is

$$\delta^2|\Gamma|^2/\delta Q_e\delta Q_u=0. \tag{22}$$

From differentiation of Eq. (21) it follows that for optimum sensitivity, assuming square law detection, the coupling iris should be chosen so that one-third of the incident power is reflected from the cavity. Since

$$1/Q_l=1/Q_u+1/Q_e, \tag{23}$$

where Q_l is the loaded Q, a measurement of Q_l and β will suffice to determine the unloaded Q of the cavity. If P is the power incident on the cavity it can be shown that

$$H_1^2=32\pi Q_u(1-|\Gamma|^2)P/\omega V, \tag{24}$$

where V is the volume of the resonant cavity.

V. ANALYSIS OF RESULTS IN KCl

The saturation results in crystals of KCl, KBr, and NaCl were qualitatively similar and further work is in progress. We will describe here only the results on KCl, for which a detailed study has been made at room temperature. Since at ordinary power levels the dispersion signal is nearly five times as strong as the absorption signal, the former was used for the analysis of line shape. Figure 4 presents a comparison of the results obtained for KCl with the theoretical Gaussian and Lorentz line shapes. As shown the line is essentially Gaussian in shape, in good agreement with the theory of hyperfine interaction as presented in the preceding paper. It was found further that the line width and line shape of both the absorption and dispersion were independent of the microwave power level.

Figure 5 presents the saturation results for KCl as a function of H_1. The parameters plotted are the peak absorption and dispersion signals, suitably normalized. H_1 is the value of the microwave field such that the saturation parameter at the line center,

$$S(\omega_0, H_1)=1/(1+\tfrac{1}{4}\gamma^2H_1^2T_1T_2)=\tfrac{1}{2}. \tag{25}$$

The results are compared with the theory of Sec. III with $g(\omega-\omega')$ taken to be Lorentz in shape.

It is clear from Fig. 1 that the results cannot be explained in any way on the basis of the simple theory of Sec. II. Equation (12) of that section gives for the absorption signal at the line center:

$$\frac{2}{\omega_0 T_2}\frac{\chi''(\omega_0)}{\chi_0}\frac{H_1}{H_{\frac{1}{2}}}=\frac{1}{1+(H_1/H_{\frac{1}{2}})^2}\frac{H_1}{H_{\frac{1}{2}}}. \tag{26}$$

For large H_1, on this basis, the absorption signal should go as $H_{\frac{1}{2}}/H_1$, as contrasted with the signal obtained, which is independent of H_1. Further, the theory of Sec. II predicts for a Gaussian line a flattening of the central portion of the line and a nearly twofold increase in line width over the range investigated. Neither of these effects was observed.

However, based on the theory of Sec. III, no change in line width or line shape should be expected. The saturation broadens and reduces the intensity of the absorption of the individual spin packets, but as long as the packets are narrow as compared with the inhomogeneous broadening of the resonance, this effect

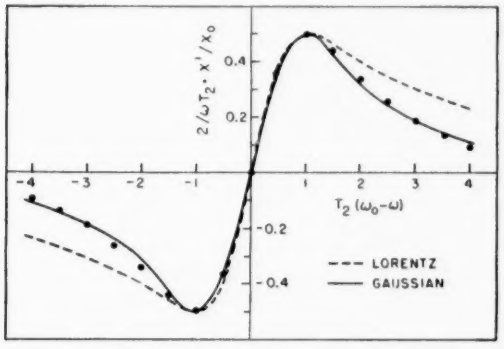

FIG. 4. Line shape (dispersion curve) of F centers in KCl.

will be reflected only in a reduction in the intensity of the absorption. As shown in Appendix I, the dispersion is not affected by the saturation of the spin packets, in agreement with the observations on KCl.

From Eq. (19), the peak absorption signal for the composite line is

$$\frac{2}{\omega T_2^*}\frac{\chi''(\omega_0)}{\chi_0}\frac{H_1}{H_{\frac{1}{2}}}=\int_0^\infty \frac{g(\omega-\omega')d\omega'}{1+(H_1/H_{\frac{1}{2}})^2\pi[g(\omega-\omega')/T_2]}\frac{H_1}{H_{\frac{1}{2}}}. \tag{27}$$

We wish to determine the form of $g(\omega-\omega')$ such that $\chi''(\omega_0)$ will behave in the observed way as a function of H_1. We require that for $H_1>H_{\frac{1}{2}}$

$$\int_0^\infty \frac{g(\omega-\omega')d\omega'}{1+(H_1H_{\frac{1}{2}})^2\pi[g(\omega-\omega')/T_2]}\frac{H_1}{H_{\frac{1}{2}}}\cong 1. \tag{28}$$

If $g(\omega-\omega')$ represents a Lorentz line, that is

$$g(\omega-\omega')=(T_2/\pi)[1/1+T_2^2(\omega-\omega')^2], \tag{29}$$

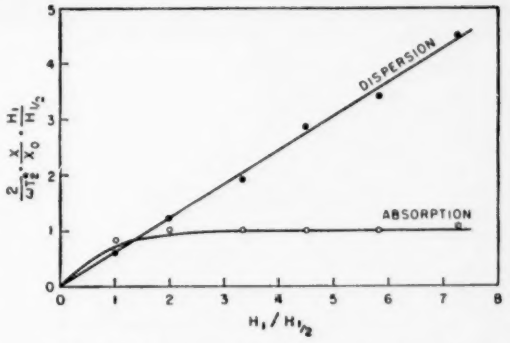

FIG. 5. Saturation behavior of F centers in KCl.

then the left side of Eq. (28) is equal to

$$\{1/[1+(H_1/H_{\frac{1}{2}})^2]^{\frac{1}{2}}\}(H_1/H_{\frac{1}{2}}), \tag{30}$$

which for large H_1 satisfies the required condition. If $g(\omega-\omega')$ were taken as cutting off more sharply in the wings than a Lorentz line, then the left side of Eq. (28) would be decreasing for $H_1>H_{\frac{1}{2}}$, in contrast with the observed behavior. On this basis we must conclude that the spin packets are very closely Lorentz in shape. This result is in good agreement with the arguments of Anderson[5] and the rigorous calculations of Kittel and Abrahams[5] of the frequency moments for dipolar broadening from paramagnetic ions randomly distributed on a simple cubic lattice. The result of Kittel and Abrahams is that, for a fractional magnetic population of less than 0.01, the resonance line is very nearly Lorentz with a half-width at half-maximum intensity,

$$\Delta H=5.3g\mu_B N, \tag{31}$$

where N is the concentration of paramagnetic ions. Substituting for N, the concentration of F centers in the sample studied as determined from the strength of the optical absorption in the F band, the value $2.9\times10^{17}/\text{cm}^3$, we obtain for the half-width of the spin packets:

$$\Delta H=0.028 \text{ oersted}.$$

Comparing this with the half-width at half-maximum intensity for the over-all line of 27 oersteds, it is clear that the assumption made that the packets be narrow as compared with the over-all line width is well justified.

From a study of the saturation behavior it is possible to estimate the spin-lattice relaxation time. The saturation parameter at the line center is defined as

$$S(\omega_0, H_1)=\chi''(\omega_0, H_1)/\chi''(\omega_0, 0). \tag{32}$$

For $H_1>H_{\frac{1}{2}}$ we find

$$S(\omega_0, H_1)\cong 0.012/H_1.$$

However, as shown in Appendix II, the form of the saturation factor will depend to some extent on whether $\omega_m T_1$ is less than or greater than unity, where ω_m is the

[5] P. W. Anderson, Phys. Rev. **82**, 342 (1952); C. Kittel and E. Abrahams, Phys. Rev. **90**, 238 (1953).

frequency of the modulation envelope of the microwaves. Since for F centers in KCl at room temperature,

$$\omega_m T_1 \sim 1,$$

one can at best make an estimate of T_1. Taking the saturation factor at the line center,

$$S(\omega_0, H_1) \simeq \frac{1.6}{\gamma (T_1 T_2)^{\frac{1}{2}}} \frac{1}{H_1},$$

we obtain

$$T_1 T_2 = 5.7 \times 10^{-11} \text{ sec}^2.$$

From the known concentration of F centers

$$T_2 = 1/\gamma \Delta H = 2.3 \times 10^{-6} \text{ sec}.$$

This gives for the spin-lattice relaxation time at room temperature

$$T_1 = 2.5 \times 10^{-5} \text{ sec}.^{6}$$

VI. ON THE KRAMERS-KRONIG RELATIONS

The Kramers-Kronig relations[3] give the form of the dispersion if the absorption is known for all frequencies and, conversely, the absorption if the dispersion is known,

$$\chi'(\omega) = \frac{2}{\pi} \int_0^\infty \frac{\omega' \chi''(\omega')}{\omega'^2 - \omega^2} d\omega', \tag{33}$$

$$\chi''(\omega) = -\frac{2}{\pi} \omega \int_0^\infty \frac{\chi'(\omega')}{\omega'^2 - \omega^2} d\omega'. \tag{34}$$

Our experimental results are in strong contradiction with the above relations. We find that at high power levels χ' is independent of power level but χ'' decreases in amplitude with increasing microwave power. Neither the absorption nor the dispersion vary in shape or width. This strong discrepany led to a re-examination of the validity of these relations. Their derivation is presented clearly by Van Vleck,[7] and it is his presentation which will be examined here. The usual procedure is to define a complex susceptibility,

$$\chi(\omega') = \chi'(\omega') - i\chi''(\omega'), \tag{35}$$

where ω' is a complex frequency. One then integrates the function

$$\chi(\omega')/(\omega' - \omega),$$

where ω is real, along the real frequency axis closing the contour around the lower half of the complex frequency plane. Since for physically realizable systems the absorption is an even function of the frequency and the dispersion an odd function, and further stipulating that there be no singularities in the lower half of the complex plane, the relations Eqs. (33) and (34) are obtained.

It is in particular the stipulation that the complex susceptibility be analytic over the lower half of the complex frequency plane which we wish to examine here. Van Vleck establishes this condition on the basis of the linearity of the system. In considering the behavior of the complex dielectric constant, he expresses the electric polarization of the system in terms of a Fourier integral over the spectrum of the electrical disturbance by introducing a dielectric constant which is a function of frequency. It is concluded then that the dielectric constant can have no singularities in the lower half of the complex frequency plane, since if this were not the case one would have a response of the system preceding the arrival of the electrical disturbance. This situation is closely related to the impossibility of having exponentially increasing solutions for the response of a physical system in the absence of any excitation. We show here that if the system is nonlinear the treatment of Van Vleck does not apply, nor are his conclusions about the behavior of the system in the absence of any excitation valid. The susceptibility will in fact have singularities in the lower half of the complex frequency plane. The existence of these singularities is contingent on the presence of excitation, and it is in this important respect that linear and nonlinear systems differ. It does not follow then that for nonlinear systems the presence of singularities in the lower half of the complex frequency plane has as a consequence that there will be exponentially increasing solutions in the absence of excitation. Further, the response cannot precede the disturbance since it is the disturbance which creates the singularities.

Taking the results of Appendix I for the complex susceptibility in the simple case,

$$\chi(\omega) = \tfrac{1}{2}\chi_0 \omega_0 \frac{\left\{ \int_0^\infty [2\omega' g(\omega' - \omega_0)/(\omega'^2 - \omega^2)] d\omega' \right\} - i\pi g(\omega - \omega_0)}{1 + (H_1/H_2)^2 [\pi g(\omega - \omega_0)/T_2]}, \tag{36}$$

the complex susceptibility will have simple poles in the complex frequency plane for

$$[\pi g(\omega - \omega_0)/T_2]^{\frac{1}{2}} (H_1/H_2) = \pm i. \tag{37}$$

These poles must occur in conjugate complex pairs, from which it follows that if H_1 is nonvanishing there will be poles in the lower half of the complex frequency plane. The residues at these poles will be of order $(H_1/H_2)^2$, so that for low power levels they can be disregarded. However, as has been seen at high power levels, the presence of these poles may profoundly alter the relation between χ' and χ'' so that their presence cannot be neglected. It does not seem possible in

[6] An estimate of the spin-lattice relaxation time from the hyperfine interaction, using the results of Waller for Raman processes [Z. Physik **79**, 370 (1932)], yields a value about ten times greater than this. However, because of the roughness of the estimate a more exact calculation might still be profitable.

[7] J. H. Van Vleck, Massachusetts Institute of Technology Radiation Laboratory Technical Report 735, 1945 (unpublished).

general to obtain an analytical expression, for example, for a saturated disperion line from a knowledge of the form of the saturated absorption line. It is possible on physical grounds to circumvent this problem as is done in Appendix I. It is required, however, that the form of the absorption in the absence of saturation be known.

As an example of the above considerations, we examine the solutions of the Bloch equations[8] for the behavior of a paramagnetic system in crossed constant and rotating magnetic fields. The importance of the Bloch equations here is that they yield expressions for the absorption and dispersion for any H_1 without the need for introducing the Kramers-Kronig relations. We obtain for a rotating microwave field of amplitude H_1

$$\chi'(\omega)=\tfrac{1}{2}\chi_0\omega_0 T_2\{T_2(\omega_0-\omega)/[1+s+T_2^2(\omega_0-\omega)^2]\}, \quad (38)$$

$$\chi''(\omega)=\tfrac{1}{2}\chi_0\omega_0 T_2\{1/[1+s+T_2^2(\omega_0-\omega)^2]\}, \quad (39)$$

where $s=\gamma^2H_1^2T_1T_2$.

$$\chi(\omega)=\chi'(\omega)-i\chi''(\omega)=-\tfrac{1}{2}\chi_0\omega_0\frac{\omega-[\omega_0-(i/T_2)]}{\{\omega-[\omega_0-(i/T_2)(1+s)^{\frac{1}{2}}]\}\{\omega-[\omega_0+(i/T_2)(1+s)^{\frac{1}{2}}]\}}. \quad (40)$$

The complex susceptibility will have poles at

$$\omega=\omega_0\pm(i/T_2)(1+s)^{\frac{1}{2}}.$$

The residue at the pole in the lower half of the complex plane is

$$-\tfrac{1}{4}\chi_0\omega_0[1-(1+s)^{-\frac{1}{2}}],$$

which is of order $(H_1/H_{\frac{1}{2}})^2$.

If one substitutes the expression of Eq. (39) for the absorption into Eq. (33), one does not obtain the expression of Eq. (38) for a nonvanishing microwave field. The solutions of the Bloch equation are then not in agreement with the Kramers-Kronig relations. They are, however, completely consistent with our Eqs. (12) and (15), which were derived using the Kramers-Kronig relations in only a very restricted way.

I wish to acknowledge my indebtesness to Professor A. F. Kip and Professor C. Kittel for their stimulating direction and invaluable contributions during the course of this work. I have benefited in addition from discussions with Professor W. D. Knight and Professor W. A. Nierenberg. This work was supported in part by the U. S. Office of Naval Research and was carried out during the tenure of a fellowship from the U. S. Atomic Energy Commission.

APPENDIX I. DERIVATION OF THE SUSCEPTIBILITY EXPRESSIONS

In the absence of saturation we have, from Eq. (12),

$$\chi''(\omega)=\tfrac{1}{2}\pi\chi_0\omega_0 g(\omega-\omega_0).$$

Since we are dealing here with an unsaturated system, we can obtain the unsaturated dispersion from Eq. (33), the first of the Kramers-Kronig relations. Then

$$\chi'(\omega)=\tfrac{1}{2}\chi_0\omega_0\int_0^\infty\frac{2\omega' g(\omega'-\omega_0)}{\omega'^2-\omega^2}d\omega'.$$

The saturation is introduced through Eq. (7), which gives the way in which the difference in populations of the spin levels decreases with increasing microwave power. Then, for arbitrary microwave field strength

$$\chi''(\omega)=\tfrac{1}{2}\chi_0\omega_0\frac{\pi g(\omega-\omega_0)}{1+\frac{1}{4}\pi\gamma^2H_1^2T_1 g(\omega-\omega_0)}, \quad (12)$$

$$\chi'(\omega)=\tfrac{1}{2}\chi_0\omega_0\frac{\int_0^\infty[2\omega' g(\omega'-\omega_0)/(\omega'^2-\omega^2)]d\omega'}{1+\frac{1}{4}\pi\gamma^2H_1^2T_1 g(\omega-\omega_0)}. \quad (15)$$

In the general case with both homogeneous and inhomogeneous broadening, we assemble the response of the spin packets under an envelope of shape $h(\omega-\omega_0)$. We obtain

$$\chi''(\omega)=\tfrac{1}{2}\chi_0\int_0^\infty\frac{\pi\omega' g(\omega-\omega')}{1+\frac{1}{4}\pi\gamma^2H_1^2T_1 g(\omega-\omega')}h(\omega'-\omega_0)d\omega', \quad (17)$$

$$\chi'(\omega)=\tfrac{1}{2}\chi_0\int_0^\infty\frac{\omega' h(\omega'-\omega_0)d\omega'}{1+\frac{1}{4}\pi\gamma^2H_1^2T_1 g(\omega-\omega')}\times\int_0^\infty\frac{2\omega'' g(\omega''-\omega')}{\omega''^2-\omega^2}d\omega''. \quad (18)$$

For the case where the spin packets are narrow compared with the over-all line width, $g(\omega-\omega')$ will be appreciably different from zero only for $\omega'\sim\omega$. Since $h(\omega'-\omega_0)$ is slowly varying over this region, we obtain from Eq. (17)

$$\chi''(\omega)=\tfrac{1}{2}\chi_0\omega h(\omega-\omega_0)\int_0^\infty\frac{\pi g(\omega-\omega')d\omega'}{1+\frac{1}{4}\pi\gamma^2H_1^2T_1 g(\omega-\omega')}. \quad (19)$$

To obtain Eq. (20), we first reverse the order of integration of Eq. (18)

$$\chi'(\omega)=\tfrac{1}{2}\chi_0\int_0^\infty\frac{2\omega''d\omega''}{\omega''^2-\omega^2}\times\int_0^\infty\frac{\omega' h(\omega'-\omega_0)g(\omega''-\omega')}{1+\frac{1}{4}\pi\gamma^2H_1^2T_1 g(\omega-\omega')}d\omega'. \quad (41)$$

[8] F. Bloch, Phys. Rev. **70**, 460 (1946).

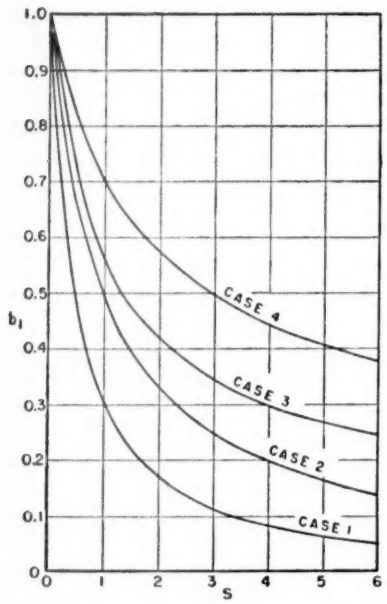

FIG. 6. Variation of the saturation parameter as a function of microwave power.

The contribution of the denominator in the integral over ω' will be of order T_2^*/T_2, so that we neglect it under the assumptions being made in this treatment. Then

$$\chi'(\omega)=\tfrac{1}{2}\chi_0\int_0^\infty \frac{2\omega''d\omega''}{\omega''^2-\omega^2}\int_0^\infty \omega' h(\omega'-\omega_0)g(\omega''-\omega')d\omega'.$$

Since $h(\omega'-\omega_0)$ is slowly varying in the vicinity of $\omega''\sim\omega'$, where $g(\omega''-\omega')$ is appreciable, and since

$$\int_0^\infty g(\omega''-\omega')d\omega'=1,$$

we obtain finally

$$\chi'(\omega)=\tfrac{1}{2}\chi_0\int_0^\infty \frac{2\omega''^2 h(\omega''-\omega_0)}{\omega''^2-\omega^2}d\omega''. \qquad (20)$$

It should be observed that this is just the dispersion that one obtains from the Kramers-Kronig relations for an absorption of shape $h(\omega-\omega_0)$.

APPENDIX II

Saturation Behavior for Power Modulated Microwaves

We have treated the microwave power level as varying slowly enough compared with T_1 so that we could consider the spin system as being in a quasi-steady state. However if ω_m, the frequency of power modulation of the microwaves, is of the order of or greater than $1/T_1$, the saturation behavior is somewhat altered. We consider here four cases:

Case 1. Homogeneous broadening and $\omega_m T_1<1$. The system will follow the variations in microwave power. Or if we take the saturation factor

$$S(\omega, H_1)=\chi''(\omega, H_1)/\chi''(\omega, 0),$$

the saturation factor will be periodic at the frequency ω_m.

Case 2. Homogeneous broadening and $\omega_m T_1>1$. For this case the system will not follow the variations in microwave power but will saturate at the average power level.

Case 3. Inhomogeneous broadening and $\omega_m T_1<1$. Here we will saturate spin packets individually rather than transferring power at once to the whole spin system. However, the spin packets will individually follow the periodic variations in power level.

Case 4. Inhomogeneous broadening and $\omega_m T_1>1$.

If the microwave field is power modulated, the power in the signal at the detecting crystal is given by

$$P_s=F\chi_0\omega_0 T_2 S(\omega_0, H_1)[1+\sin(\omega$$

where P is the power incident on the microwave cavity and F is a factor which depends on the Q of the cavity, the filling factor for the sample, and the conversion loss of the detecting crystal. Since the detected signal is amplified by a narrow band amplifier and detected by a lock-in mixer, in the Fourier expansion of P_s:

$$P_s=F\chi_0\omega_0 T_2 P\sum_n a_n\cos(n\omega_m t)+b_n\sin(n\omega_m t),$$

the observed signal will be proportional to b_1. Our result is that for

Case 1: $b_1=(2/s^2)[(1+s)/(1+2s)^{\frac{1}{2}}]$;

Case 2: $b_1=1/(1+s)$;

Case 3: $b_1\simeq(1+0.60s)/(1+s)^{\frac{1}{2}}$;

Case 4: $b_1=1/(1+s)^{\frac{1}{2}}$,

where $s=\frac{1}{4}\gamma^2 H_1^2 T_1 T_2$.

These functions are plotted in Fig. 6 and behave in the expected way, with Case 1 saturating the most rapidly and Case 4 the most slowly.

Electron Multiplication in Silicon and Germanium

K. G. McKay and K. B. McAfee
Bell Telephone Laboratories, Murray Hill, New Jersey

(Received May 29, 1953)

Electron multiplication in silicon and germanium has been studied in the high fields of wide p-n junctions for voltages in the prebreakdown region. Multiplication factors as high as eighteen have been observed at room temperature. Carriers injected by light, alpha particles, or thermal-generation are multiplied in the same manner. The time required for the multiplication process is less than 2×10^{-8} second. Approximately equal multiplication factors are obtained for injected electrons and injected holes. The multiplication increases rapidly as "breakdown voltage" is approached. The data are well represented by ionization rates computed by conventional avalanche theory. In very narrow junctions, no observable multiplication occurs before Zener emission sets in, as previously reported. It is incidentally determined that the efficiency of ionization by alpha particles bombarding silicon is 3.6 ± 0.3 electron volts per electron-hole pair produced.

INTRODUCTION

ELECTRON multiplication in gases in the prebreakdown Townsend avalanche has been known for years; however, the corresponding charge multiplication in solids has not been as clearly recognized. The increased dark current observed in some insulators prior to breakdown has been attributed to strong field emission from the electrode[1] while current multiplication in semiconductors is normally caused by transistor action, i.e., the control of electron flow by the presence of positive holes or vice versa. The purpose of this paper is to describe experiments that demonstrate that charge carriers, injected into a p-n junction, can multiply under high field conditions. This multiplication appears to be an avalanche formation, and it occurs in both silicon and germanium. Previous measurements[2] of carriers injected by photons into very narrow germanium junctions have shown no charge multiplication. Subsequent measurements on those junctions of carriers injected either by photons or alpha particles have confirmed the earlier measurements, particularly in the prebreakdown region. For such junctions the slope of the current-voltage characteristic in the breakdown region is in essential agreement with the Zener theory of internal field emission.[3] The absence of multiplication is also implicit in the Zener theory.

The measurements to be described in the present paper were undertaken to examine in detail the portion of the current-voltage characteristic just below the "breakdown" or "voltage-limiting" region. The germanium junctions presently to be described differ in an important manner from those previously studied in having a broader space-charge region. The observation of charge carrier multiplication leads to the possibility of avalanche breakdown in broad junctions and Zener internal field emission in junctions which are too narrow to support appreciable multiplication.

[1] A. von Hippel, Phys. Rev. **54**, 1096 (1938).
[2] McAfee, Ryder, Shockley, and Sparks, Phys. Rev. **83**, 650 (1951).
[3] C. Zener, Proc. Roy. Soc. (London) **145**, 523 (1934).

SAMPLE CHARACTERISTICS

Although current multiplication has now been observed in a large number of junctions, in the following we shall concentrate on just two particular crystals—one of silicon and one of germanium. The crystals were fabricated by pulling from the melt with the axis of the seed parallel to the 111 crystal direction. The melt at the start contained p-type impurity. Halfway through growth the n-type impurity was added. The units were cut from the crystals so that they were bisected by the p-n junction whose plane was normal to the rod axis. In all of the measurements to be considered here, the individual rods from a given crystal had essentially identical properties, so only one of each will be specified. The physical dimensions, donor and acceptor impurities, and the resistivities are given in Table I.

CURRENT-VOLTAGE CHARACTERISTICS

Figure 1 shows the room temperature current-voltage characteristics of the junctions plotted on a log-log scale. The germanium junction exhibits an excellent saturation characteristic followed by the now familiar breakdown region.[2] The silicon reverse characteristic does not saturate as well, and the reverse current is much larger than it should be, based on the observed forward current and Shockley's theory of the p-n junction. However, this seems typical of well-behaved silicon junctions, and McAfee has proposed that this is due to spontaneous electron-hole pair generation within the space-charge region itself. Shockley and Read have shown that this is theoretically possible.[4]

Figure 2 shows the breakdown regions on a greatly expanded voltage scale to permit a measurement of the

Table I. Samples characteristics.

Crystal	Length cm	Width cm	Donor	Acceptor	$\bar{\rho}_n$ ohm-cm	$\bar{\rho}_p$ ohm-cm
Ge	1	0.1	Arsenic	Gallium	0.0066	0.27
Si	1	0.1	Phosphorus	Boron	0.024	0.006

[4] W. Shockley and W. T. Read, Jr., Phys. Rev. **87**, 835 (1952).

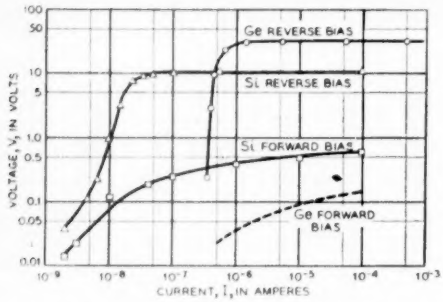

FIG. 1. Current *vs* voltage characteristics for the germanium and silicon *p-n* junctions.

slope $d(\ln V)/d(\ln I)$ in this region. The measured slopes for the germanium and silicon junctions, respectively, are 0.0013 and 0.00070. These slopes are at least a factor of ten smaller than those predicted by Shockley's modification of the Zener theory of internal field emission.[2]

CAPACITY-VOLTAGE CHARACTERISTICS

Figure 3 shows the variation of junction capacitance as a function of applied reverse voltage V as measured on an audio-frequency bridge. From the capacity per unit area, C/A, we obtain the effective width W of the space-charge region simply through the relation

$$W=\frac{\kappa}{4\pi C/A},$$

where κ = dielectric constant = 16 for germanium and 12 for silicon. However, additional information can be derived from the functional form of the capacity variation with voltage. If we increase the voltage in Fig. 3 by the built-in voltage $(2\psi_i)$ for applied voltage equal to zero, we find that $\log(C/A)$ *vs* $\log(V+2\psi_i)$ yields a good straight line. For both the germanium and silicon junctions, the slope of that line is given by $C\sim(V+2\psi_i)^{-\frac{1}{3}}$, which is the relationship derived for a linear gradient of impurity concentration across a junction.[5] The growth processes for both junctions were

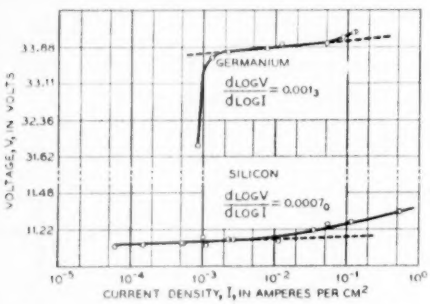

FIG. 2. Enlarged I/V characteristics, showing the details in the breakdown region.

[5] W. Shockley, Bell System Tech. J. **28**, 435 (1949).

such that a near-linear gradient was to be expected. The capacity variation confirms this expectation and permits the assertion that the electric field is a maximum at the center of the junction and decreases parabolically with distance from the center. The maximum field is

$$E_{\max}=1.5E_{\text{av}}=1.5(V+2\psi_i)W^{-1}.$$

Figures 4 and 5 show W and $E_{\max}$ plotted as a function of V as obtained from these relations. These data serve to establish the basic electrical features of these junctions.

PHOTOENHANCEMENT

It has been demonstrated by Goucher[6] that when light falls on a germanium reverse-biased *p-n* junction, unit quantum yield is obtained and that, within wide limits, this is independent of the bias voltage. Our measurements show significant departures from this relation as the bias voltage approaches breakdown. The measurements were made by measuring the voltage and current through a nonilluminated junction

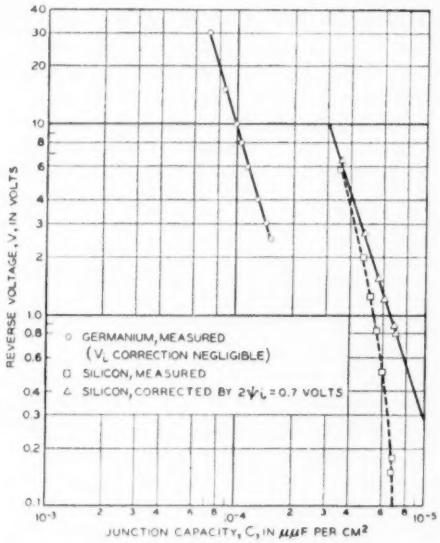
GERMANIUM, MEASURED
(V_L CORRECTION NEGLIGIBLE)
SILICON, MEASURED
SILICON, CORRECTED BY $2\psi_L$ = 0.7 VOLTS
REVERSE VOLTAGE, V, IN VOLTS
JUNCTION CAPACITY, C, IN $\mu\mu$F PER CM²

FIG. 3. Measured variation of junction capacity with applied voltage.

with a type K potentiometer. The junction was then illuminated, the junction voltage readjusted to the previous value, and the new current determined. The change in current was ascribed to photoconduction. Figure 6 shows a plot of photocurrent *vs* applied voltage for the silicon junction. The light was filtered by a monochromator and wavelengths above and below the long-wave limit for silicon were used. By normalizing the photocurrents at low voltages where the induced

[6] Goucher, Pearson, Sparks, Teal, and Shockley, Phys. Rev. **81**, 637 (1951).

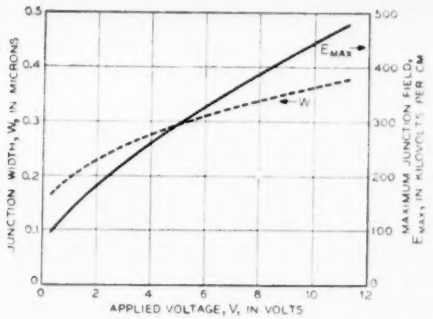

FIG. 4. Variation of junction width W and maximum junction field E_{max} with applied voltage V for the silicon junction

currents are very nearly voltage-independent, we see that the yield curves are essentially independent of exciting wavelength. Moreover, the normalized curves are independent of the intensity of the light over the measured range of 100:1. The photo yield curves for the germanium junction were very similar in shape to those for silicon if the voltage scale was multiplied everywhere by about a factor of three. To check the absolute yield, a light spot of a known intensity was used on the germanium junction. At a low reverse bias of 3 volts this yielded a quantum efficiency of 0.65. An estimate of the width of the light spot, together with the diffusion lengths in the sample, corrects this to approximately unity quantum yield. At a bias of 33.9 volts, the photocurrent had increased by a factor of ten to give an apparent quantum yield of 6.5 and a corrected yield of about 10.

It is of importance to know whether the photo-enhancement at high voltages is the same for injected holes as for injected electrons. This was determined by scanning the junction in a direction parallel to the sample axis with a small spot of light. This is essentially the same as the technique described by Goucher[6] to measure diffusion lengths. The two solid curves of Fig. 7 are typical of the germanium sample. The light spot was small enough to guarantee that when scanning on the n side we were indeed injecting holes into the barrier and not electrons generated by scattered light over the p side. The two curves are essentially identical

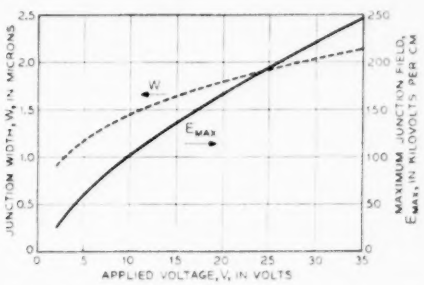

FIG. 5. Variation of junction width W and maximum junction field E_{max} with applied voltage V for the germanium function.

in shape and, if normalized to the same maximum current, are alike. The same is true of curves measured at other biases. If multiplication of injected electrons did occur and multiplication of injected holes did not occur, the yield at the higher bias would follow the lower curve on the n side and the upper curve on the p side as shown by the dotted line. This is clearly not the case.

ALPHA-BOMBARDMENT CONDUCTIVITY

The measurements described above are all dc measurements; they cannot ascertain the time scale at

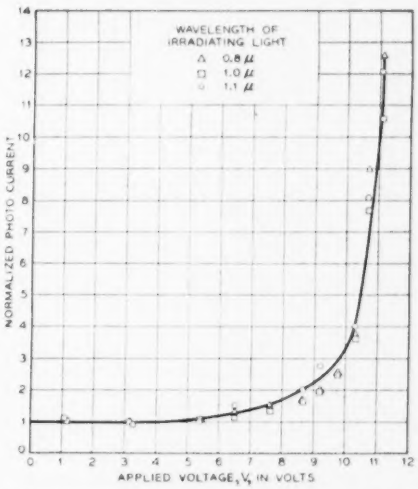

FIG. 6. Variation of photocurrent with applied junction voltage for light of various frequencies illuminating the silicon junction. The ordinate scales have been normalized by setting the photocurrent equal to unity at low voltages.

which the enhancement takes place. In particular, they cannot distinguish between essentially instantaneous multiplication in the junction and a form of transistor action established by an n-p-n-p structure. It was thus desirable to measure the time scale of the action and to study the enhancement by using an entirely different form of current injection. These objectives were achieved by bombarding the junction with alpha particles from polonium and measuring the charge produced per alpha particle. The charge pulse is transformed to a voltage pulse, amplified on a wide-band, high-gain amplifier and displayed on an oscilloscope. The details of the equipment have been published previously.[7] It should be noted that an absolute determination of charge is obtained in this measurement.

Figure 8 shows the variation of the charge collected in units of e, the charge on an electron, as a function of applied voltage for both silicon and germanium junctions. The three sets of points for silicon were taken on three different junctions of somewhat different dimen-

[7] K. G. McKay, Phys. Rev. **84**, 829 (1951).

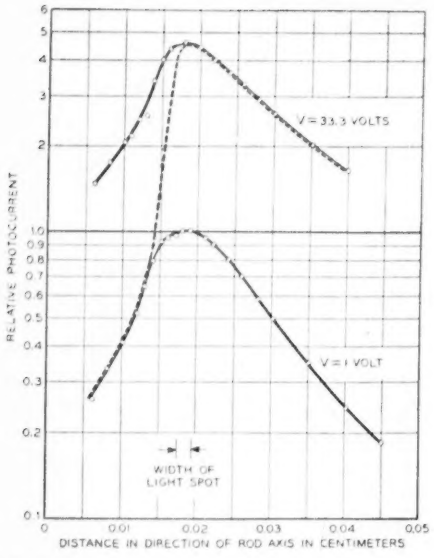

FIG. 7. Photoresponse of the germanium junction as a function of distance from junction of light spot for two different values of applied voltage. The dotted curve represents the expected response if holes injected by light did not multiply in junction.

sions which were cut from the same single crystal. The dots and squares correspond to measurements taken by photographing the oscilloscope traces and carefully measuring the negatives. The circles and crosses correspond to visual observations of the oscilloscope and thus are not as accurate. Thus within the accuracy of the visual measurements there is no significant difference between the three sets of points for silicon. As will be shown later, these results agree with the photoenhancement measurements.

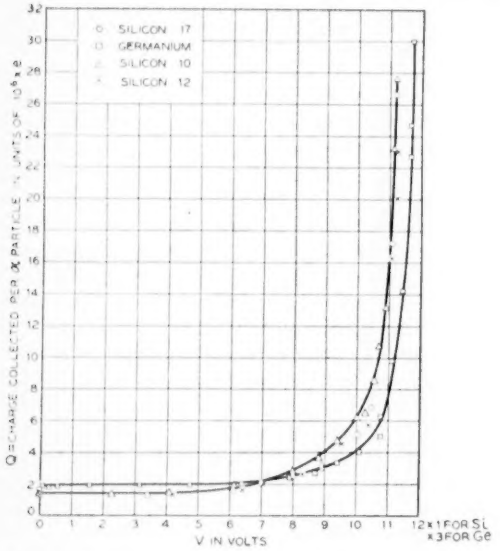

FIG. 8. Charge Q collected per alpha particle incident on junction of applied voltage. Data are shown for three separate silicon junctions and the germanium junction. Silicon No. 10 is the junction used in all other figures.

The absolute yield values are of interest. The low field yield for germanium was 1.80×10^6 electronic charges per polonium alpha particle. This gives for the efficiency of ionization, $\epsilon=2.94\pm0.15$ ev/pair, where ϵ is defined as the energy of the bombarding particle divided by the number of electron hole pairs produced per particle. This value for ϵ compares well with the previously determined value of $\epsilon=3.0\pm0.3$ ev/pair as measured on several other germanium junctions in the low field region.[7] The corresponding value for silicon is $\epsilon=3.6\pm0.3$ ev/pair, for which a value has not previously been published.

By examining the individual pulses on a fast sweep, the pulse rise times could be studied. As previously described,[7] the rise time corresponds to the total time that the induced current is flowing across the junction. Careful studies were made on both silicon and germanium of the pulse rise times throughout the voltage ranges shown on Fig. 8. For all voltages, including those where the charge enhancement was greater than 15, pulses were observed with a rise time that was characteristic of the amplifier, i.e., the actual pulse rise time must be less than 0.02 μsec.

NORMALIZED YIELD CURVES

Figure 9 sums up the previous results. The photo yields and alpha-bombardment yields have been normalized to unity at low biases where they are voltage independent. The normalized voltage$=V/V_b$ where V_b, the breakdown voltage, is obtained from the current-voltage characteristics shown in Fig. 2. It should be emphasized that the normalizing voltage has not been determined simply by the voltage at which the charge enhancement became very large. The normalized curves are similar for the two junctions although showing a real difference for $0.6<$normalized voltage<0.95.

Another source of carriers which are injected into the junction is the saturation current itself, derived from the spontaneous thermal generation of electron-hole pairs. According to the previous results, this current also be multiplied in the high field region. If the linear portion of the saturation current in Fig. 1 is extrapolated to higher voltages and the difference between this and the actual current is plotted against normalized voltage, the result is a plot which follows the curves of Fig. 9. The multiplication so obtained is indeed somewhat less than that obtained by deliberate carrier injection. This is to be expected since the dc reverse current is made up partly of a volume current and partly of surface leakage which is strongly dependent on previous surface treatment. However, this result means that for these junctions, the "soft" knee observed in the transition from the saturation region

to the breakdown region, as shown in Fig. 1, can be attributed to multiplication in the junction of the saturation current.[8]

DISCUSSION

The experimental evidence that has been presented can be used to establish the following characteristics of the observed process:

(1) The agreement obtained in photoyield *versus* voltage with different values of the incident wavelength (Fig. 6) is sufficient to show that multiplication takes place in the same amount regardless of the depth within the semiconductor at which the charge carriers are produced. The longer wavelengths employed gave a penetration depth[9] for the light many times the dimensions of the sample while the shorter wavelength produced most of its charge carriers in the region near the surface.

The agreement, shown on Figs. 6 and 9, between the yield curves for various wavelengths of light together with those for alpha-bombardment conductivity, rules out the possibility that the increased induced current can result merely from an enhanced rate of production of carriers by the bombarding particle in the high field region.

(2) The absolute measurements of quantum yield both with light and with alpha bombardment, show that charge multiplication is really taking place in the junction.

(3) The rise-time measurements of the pulses produced by alpha particles show that this multiplication takes place in a time that is less than 2×10^{-8} second. Moreover, the values so obtained agree with those observed in the dc measurements. From this we conclude that the multiplication is not merely a consequence of a hook mechanism resulting from an *n-p-n-p* structure or a complex of traps such as are invoked in secondary photoconductivity. Rather, we conclude that we have *true* multiplication taking place in the high field of the barrier. Further evidence that the barriers studied are not pathological is obtained from the completely normal current-voltage characteristics of Fig. 1, the capacity-voltage characteristic of Fig. 3, and the diffusion length characteristic of Fig. 7. Moreover, the fact that such multiplication has been observed in many junctions rules out a mere freak configuration of impurities.

(4) In the diffusion length curves of Fig. 7, the holes or electrons that reach the barrier from a light spot a given distance from the barrier, remain essentially constant irrespective of the barrier voltage. Thus, the fact that the entire curve is unchanged in shape by

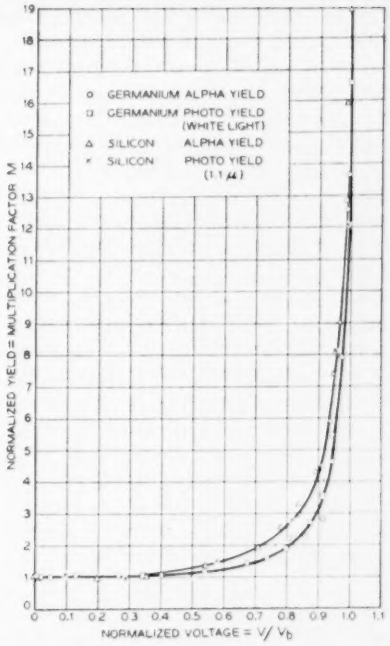
o GERMANIUM ALPHA YIELD
□ GERMANIUM PHOTO YIELD (WHITE LIGHT)
Δ SILICON ALPHA YIELD
× SILICON PHOTO YIELD (1.1 μ)
NORMALIZED YIELD = MULTIPLICATION FACTOR M
NORMALIZED VOLTAGE = V/ Vb

FIG. 9. Normalized yield curves of alpha bombardment and of photoconductivity for the silicon and germanium junctions from Fig. 8 and Fig. 6. Ordinate normalization was obtained by setting photo or alpha yield equal to unity for small applied voltage. Abscissa normalization was obtained by dividing the applied voltages by the breakdown voltages from Fig. 2.

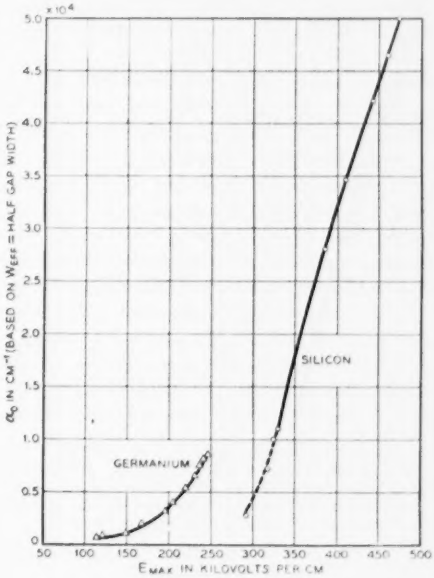

FIG. 10. Calculated ionization coefficients for germanium and silicon.

[8] Another method of carrier injection is by a point emitter. A point contact was set down 0.025 cm from the *p-n* junction in the *p* region of the germanium junction. Using the latter as collector in a conventional transistor circuit, the resultant current multiplication α of the injected electrons was measured. The variation in α with junction voltage showed essentially the same characteristic as that exhibited by the photoenhancement and the alpha-bombardment conductivity.

[9] H. Briggs, Phys. Rev. **77**, 727 (1950).

multiplication implies that both electrons and holes multiply at approximately the same rate. A correction term has been added to the diffusion equation to estimate the effect of applied field upon motion of the injected carriers. Using the measured resistivities this contribution proves to be negligible when compared with the diffusion term.

(5) The good agreement between the voltage at which the multiplication becomes very large and the onset of breakdown suggests that the two are closely connected.

One possible model of the multiplication process is that the production of an electron-hole pair by an incident electron can take place anywhere in the high field region of the barrier rather than at one singular point or on one singular plane. In that case we have a situation analogous to that of a gas discharge in which the walls and electrodes act only as sinks for charge carriers and both electrons and ions can ionize. This is the Townsend β process.[10] It can be shown[11] that for equal rates of ionization of electrons and positive holes and for a uniform field, we have simply

$$\alpha_0 = (1-M^{-1})/W_{eff}, \tag{1}$$

where α_0 = the rate of ionization, i.e., the number of electron-hole pairs produced by a carrier per cm path traveled in the direction of the field, M = the observed multiplication factor, and W_{eff} = the effective barrier width.

Actually the field distribution across the barrier is parabolic as determined from the capacity-voltage measurements. However, at this stage it is reasonable to assume a uniform field and an effective barrier width. The effective barrier width W_{eff} was chosen as one-half the actual barrier width as determined from capacity measurements, and the effective "uniform" field was taken equal to the maximum field existing at the center of the junction. For a given applied voltage, values of W and E_{max} were obtained from Figs. 4 and 5 and values of M from Fig. 8. Inserting these in Eq. (1), we get the values of α_0 shown in Fig. 10. These show that although the multiplication is a rapidly varying function of the field, no such violent variation is required of the rates of ionization. It should be observed that the use of Eq. (1) does not depend critically on the assumption that the ionization rates for electrons and holes are equal.

Although insufficient data are available to deduce values of α_0 theoretically, at least it can be shown that the values obtained are not unreasonable. The collision cross section for electron-hole pair production is not known as a function of the energy of an exciting electron or hole. However, the alpha-bombardment measurements set an upper limit to the minimum energy E_{min} required for pair production, while the energy gap E_G sets a lower limit. (If the lattice interaction is neglected, the lower limit will be $2E_G$.) Thus for germanium 0.7 ev$<E_{min}<$2.9 ev and for silicon $1.1<E_{min}<3.6$ ev. Shockley's theory of hot electrons in germanium[12] makes plausible the existence of electrons of several volts energy for fields of greater than 10^5 volts/cm. The reciprocal of α_0 is the mean free path for pair production in the direction of the applied field. The minimum value of α_0^{-1} obtained for silicon was 2000A corresponding to a barrier width $W=3750$A and an applied voltage of 11 volts. Thus sufficient energy is available within a mean free path α_0^{-1} to make pair production possible.

Using the measured values of α_0 for germanium, we can compute the expected multiplication for the narrow junctions in which the voltage limiting region was identified with Zener emission in an earlier publication.[2] For the highest voltages used, the calculated multiplication is less than 3 percent and hence negligible. This agrees with the experimental data. Thus it appears that, for very narrow junctions, appreciable multiplication can occur at very high fields and, before such fields are reached, internal field emission sets in. However, for wider junctions, the multiplication factor M may become infinite for fields below those required for field emission.

The junctions studied in the present work do not appear to be in any way unusual; they are uniform and well-behaved. It should be noted here that multiplication has been observed in junctions at least ten times as wide as these. Consequently the junction width and the impurity concentration do not appear to be critical. It is evident that although these experiments do not concern the region of breakdown itself, they must be taken into account in any theory of breakdown for these semiconductors.

ACKNOWLEDGMENT

We wish to express our appreciation to many of our colleagues at the Bell Telephone Laboratories who have contributed to this work. In particular we wish to acknowledge many stimulating discussions with W. Shockley who initiated the research. Thanks are also tendered to M. Sparks for his contributions to these studies. The crystals were grown by E. Buehler and R. Mikulyak. Valuable technical assistance was rendered by Miss C. Peffer and H. C. Meier.

[10] L. B. Loeb, *Fundamental Processes of Electrical Discharge in Gases* (John Wiley and Sons, Inc., New York, 1939).

[11] We are grateful to D. J. Rose for bringing Eq. (1) to our attention and for many helpful suggestions concerning the applicability of gas discharge theory to the present work.

[12] W. Shockley, Bell System Tech. J. **30**, 990 (1951).

Sublattice Effects in Magnetic Resonance*†

ROALD K. WANGSNESS
United States Naval Ordnance Laboratory, White Oak, Maryland
(Received May 28, 1953)

The resonance frequencies of a system containing two or four magnetic sublattices with different gyromagnetic ratios are calculated. It is found that in many cases the results reduce to the standard formulas of ferromagnetic and antiferromagnetic resonance; they are stated, however, in terms of an effective gyromagnetic ratio equal to the quotient of the net magnetic moment and the net angular momentum of the system. Line splitting due to the existence of several normal modes of nearly equal frequencies, and the effect of the sublattice structure upon the anisotropy contribution to the line width are also discussed. The calculated values of effective g values and line widths as a function of composition are compared with the experimental results for the nickel ferrite-aluminates.

INTRODUCTION

THE interpretation of the static magnetic properties of antiferromagnetic and ferrimagnetic materials is generally based upon the possibility of dividing the magnetic ions into two or more groups such that the magnetic moments within each group are parallel.[1] The assumed interactions among the magnetizations of these groups, or sublattices, then results in a magnetic structure in which the magnetizations of a given pair of sublattices have a definite orientation with respect to each other—usually either parallel or antiparallel. The predominant interaction in these materials can be taken to be of an antiferromagnetic nature,[1] i.e., leading to an antiparallel orientation, but there are other possibilities involving combinations of ferromagnetic and antiferromagnetic interactions which lead to magnetic structures of varying degrees of complexity.[2]

In time dependent problems, such as the magnetic resonance experiments which we shall consider, the existence of sublattices gives rise to observable effects which are sometimes of a rather unexpected kind. Above the Curie temperature, the observed resonance absorption is much like that found in other paramagnetics although there are indications that the short-range magnetic order resulting from the interactions affects the magnitude of the absorption.[3] Ferrimagnetic materials, such as the ferrites, have a macroscopic magnetization below the Curie temperature and resonance experiments on several of these[4] have been interpreted very successfully on this basis by the use of the results of the usual theory of ferromagnetic resonance.[5] The important role of the sublattices in the theory of antiferromagnetic resonance was first pointed out by Nagamiya and Kittel.[6] In essence, one regards the interacting sublattices as a coupled system whose normal modes and frequencies can be found by standard methods from the equations of motion. If $\mathbf{M}_1$ and $\mathbf{M}_2$ are the magnetizations of the sublattices, one finds in the simplest case that since the effective fields due to anisotropy have opposite signs for the two sublattices, the significant variables become $\mathbf{M}_1 \pm \mathbf{M}_2$ rather than the individual magnetizations. As a result, the effective field describing the interactions (the "exchange field") no longer drops out as it ordinarily does in the ferromagnetic case,[5] but usually forms the predominant part of the expression for the frequency. This method has since been generalized and applied to more complicated systems.[7–9]

A common feature of the above calculations is the assumption of the equality of the gyromagnetic ratios characteristic of the individual sublattices. Gyromagnetic ratios obtained from resonance experiments, however, are in general significantly different from the free electron spin value and the differences are primarily due to the varying contributions of the orbital angular momentum as determined by the crystalline potential.[10] Since the grouping into sublattices is usually determined by the different crystallographic sites available to the magnetic ions, one should assume that the gyromagnetic ratios of the various sublattices are actually different. We then have the possibility that a shift of magnetic ions from one type of site to another can change the resultant magnetic moment and angular momentum of the sample as a whole by different factors and thus alter the "effective" value of the sample gyromagnetic ratio. One of the purposes of this paper is to demonstrate that these effects do occur and that very small differences in the gyromagnetic ratios can affect the resonance behavior of the material in a profound and sometimes striking manner.

We shall confine ourselves to the determination of the

* Supported in part by the U. S. Office of Naval Research.
† A brief report of part of this work was given at the North Carolina meeting of the American Physical Society. [Phys. Rev. **91**, 206 (1953).]
[1] L. Néel, Ann. phys. **3**, 137 (1948).
[2] P. W. Anderson, Phys. Rev. **79**, 705 (1950); J. H. Van Vleck, J. phys. et radium **12**, 262 (1951); J. S. Smart, Phys. Rev. **86**, 968 (1952).
[3] R. K. Wangsness, Phys. Rev. **89**, 142 (1953).
[4] See footnote 2 of reference 8 for a partial list of references.
[5] C. Kittel, Phys. Rev. **73**, 155 (1948); J. H. Van Vleck, Phys. Rev. **78**, 266 (1950).
[6] T. Nagamiya, Prog. Theoret. Phys. **6**, 350 (1951); C. Kittel, Phys. Rev. **82**, 565 (1951).
[7] F. Keffer and C. Kittel, Phys. Rev. **85**, 329 (1952).
[8] R. K. Wangsness, Phys. Rev. **86**, 146 (1952).
[9] J. Ubbink, Phys. Rev. **86**, 567 (1952); Physica **19**, 9 (1953).
[10] C. Kittel, Phys. Rev. **76**, 743 (1949).

normal frequencies ω of the system basing the calculations entirely upon the classical equations of motion,

$$d\mathbf{M}_i/dt=\gamma_i\mathbf{M}_i\times\mathbf{H}_i, \tag{1}$$

in which damping is neglected. In these equations, $\mathbf{M}_i$ is the magnetization, γ_i the gyromagnetic ratio, and $\mathbf{H}_i$ the effective field for the ith sublattice. By using (1), we are implicitly assuming the magnetic ordering to be sufficient to give $\mathbf{M}_i$ a meaning. In principle, this would require the temperature to be nearly 0°K, but the results should be applicable as an approximation for higher temperatures provided that one recognizes that at a given finite temperature the approximation will be the poorer the lower the Curie temperature of the material. We shall first obtain the general result for a system comprising two magnetic sublattices and discuss a few of the important approximations and compare them with some interesting experimental data. Later, we extend our considerations to a system of four sublattices—a generalization which is found to increase the complexity of the possible resonance behavior.

TWO SUBLATTICES

The external static field H is assumed to be in the positive z direction. The molecular field coefficients describing the intra- and inter-sublattice interactions are λ_{11}, λ_{22}, and $\lambda_{12}=\lambda_{21}=\lambda$; they can be of either sign. We represent the common demagnetizing factors by N_x, N_y, N_z and the effective demagnetizing factors resulting from anisotropy[5] by N_{1x}, N_{1y}, $\cdots$, N_{2z}. The field on sublattice 1 can then be written as

$$\begin{aligned}\mathbf{H}_1=&H\mathbf{k}+\lambda_{11}\mathbf{M}_1+\lambda\mathbf{M}_2-N_x(M_{1x}+M_{2x})\mathbf{i}\\&-N_y(M_{1y}+M_{2y})\mathbf{j}-N_z(M_{1z}+M_{2z})\mathbf{k}\\&-N_{1x}M_{1x}\mathbf{i}-N_{1y}M_{1y}\mathbf{j}-N_{1z}M_{1z}\mathbf{k},\end{aligned} \tag{2}$$

with a similar expression for $\mathbf{H}_2$.

Combining (1) and (2), we find as before[8] that $M_{iz}\simeq\text{const}=M_i$. If we assume the other components to be proportional to $e^{i\omega t}$, we find from the secular equation that the normal frequencies are

$$\omega^2=F\pm[F^2-(A_xB_x-C_xD_x)(A_yB_y-C_yD_y)]^{\frac{1}{2}}, \tag{3}$$

where

$$\left.\begin{aligned}&F=\tfrac{1}{2}(A_xA_y+B_xB_y+C_xD_y+C_yD_x),\\&A_j=\gamma P+E_{j+},\\&B_j=\gamma Q_j+\delta(N_j-\lambda)\Delta+E_{j+},\\&C_j=\delta P+E_{j-},\\&D_j=\delta Q_j+\gamma(N_j-\lambda)\Delta+E_{j-},\\&E_{j\pm}=\tfrac{1}{2}(N_{1j}-N_{1z})\gamma_1M_1\pm\tfrac{1}{2}(N_{2j}-N_{2z})\gamma_2M_2,\\&P=H+(\lambda-N_z)M,\\&Q_j=H+(N_j-N_z)M,\quad j=x,y;\end{aligned}\right\} \tag{4}$$

and

$$M=M_1+M_2,\quad \Delta=M_1-M_2; \tag{5}$$

$$\gamma=\tfrac{1}{2}(\gamma_1+\gamma_2),\quad \delta=\tfrac{1}{2}(\gamma_1-\gamma_2). \tag{6}$$

As so often happens, this complicated general expression is not very helpful for understanding the effects due to the different gyromagnetic ratios, and we shall proceed at once to the consideration of several important cases of (3). We note first, however, that when $\gamma_1=\gamma_2$ the result reduces to that previously found,[8] and if δ is small, we can use the classifications introduced before as a guide for the simplification of (3). We shall further restrict ourselves for simplicity only to those cases of ordinary interest in which $\omega\approx\gamma H$ rather than to the range of very high frequencies in which the exchange field is predominant in determining the magnitude of ω.

THE FERROMAGNETIC FORMULA

For the present, we neglect the anisotropy fields by setting $E_j=0$. We shall also assume that the Curie temperature is large enough so that the molecular fields whose magnitudes are of the order of $|\lambda M_i|$ are very great compared to the external field H and the demagnetizing fields, i.e., $|\lambda|\gg N_{x,y,z}$. We then find from (4) that $A_j=\gamma P$, $B_j\simeq\gamma Q_j-\lambda\delta\Delta$, $C_j=\delta P$, and $D_j\simeq\delta Q_j-\lambda\gamma\Delta$. Since we also have $P\simeq\lambda M$, we see that we can get a good approximation to F by keeping only those terms which are of the order of the square of the exchange field. We finally find that

$$F\simeq\tfrac{1}{2}(\gamma P-\delta\lambda\Delta)^2 \tag{7}$$

and

$$\begin{aligned}R=&(A_xB_x-C_xD_x)(A_yB_y-C_yD_y)\\&=P^2(\gamma^2-\delta^2)^2Q_xQ_y.\end{aligned} \tag{8}$$

Upon comparing (7) and (8), we see that ordinarily we can expect that $R\ll F^2$. Thus we can get a good first approximation to ω^2 by expanding the radical in (3) in powers of R/F^2; we choose the minus sign in order that a result of the desired order of magnitude be obtained. We find that

$$\begin{aligned}\omega^2=&R/2F\\&=\gamma_{eff}^2[H+(N_x-N_z)M][H+(N_y-N_z)M],\end{aligned} \tag{9}$$

where

$$\gamma_{eff}=P(\gamma^2-\delta^2)/(\gamma P-\lambda\delta\Delta).$$

This becomes

$$\gamma_{eff}=(M_1+M_2)[(M_1/\gamma_1)+(M_2/\gamma_2)]^{-1}, \tag{10}$$

if we use (5), (6), and the approximation $P=\lambda M$.

Equation (9) retains the form of the resonance condition suitable for a ferromagnetic but the existence of the sublattice structure is shown by the replacement of the electron spin gyromagnetic ratio by the effective ratio given by (10). Equation (10) has a simple physical interpretation as it expresses γ_{eff} as the ratio of the resultant magnetic moment and the resultant angular momentum of the system. This result can also be written in terms of the g values of the sublattices and their angular momenta S_i. Equation (10) then yields the

following expression for the effective value of g:

$$g_{eff}=(g_1S_1+g_2S_2)/(S_1+S_2). \quad (11)$$

Equations (9) and (11) have also been found by Tsuya[11] by means of the quantum-mechanical analog of our calculation.

Equation (9) was not obtained by using explicitly the physical conditions appropriate to the ferrimagnetic case, and also does not contain any direct reference to the anisotropy and exchange fields which are known to have an important influence on the resonance condition for this case. It turns out to be more suitable for further discussion to consider another approximation to (3) in order to see how these effects enter. This procedure will, in addition, enable us to get a better understanding of the mechanism by which the different gyromagnetic ratios affect the frequencies and the dependence of the line width upon the sublattice structure.

THE FERRIMAGNETIC CASE

We shall restrict ourselves in what follows to the case in which the sample is a sphere so that $N_{x,y,z}=N=4\pi/3$. This corresponds to what is most often used experimentally, and also effects considerable simplification in the necessary algebra. Equation (4) shows that then N enters only in the combination λ-N which is approximately λ for materials with reasonable values of the Curie temperature.

In the ferrimagnetic case, the sublattices are antiparallel with M_1, say, parallel to H. The simplest way of introducing the effect of anisotropy is to assume that the z direction is also nearly the direction of a preferred axis of the crystal, so that the anisotropy field can be written as H_a for M_1 and $-H_a$ for M_2; in the notation of (2), this means that we assume that[8]

$$-N_{1z}M_1=N_{2z}M_2=H_a; \quad N_{1x,y}=N_{2x,y}=0. \quad (12)$$

Using these assumptions, we find from (4) that A_j, B_j, C_j, and D_j are all independent of j and equal, respectively, to

$$\left.\begin{aligned} A&=\gamma(H+\lambda M)+\delta H_a,\\ B&=\gamma H+\delta(H_a-\lambda\Delta),\\ C&=\delta(H+\lambda M)+\gamma H_a,\\ D&=\delta H+\gamma(H_a-\lambda\Delta). \end{aligned}\right\} \quad (13)$$

Since it is known[12] that in this case

$$\omega=\tfrac{1}{2}(A+B)\pm[\tfrac{1}{4}(A-B)^2+CD]^{\frac{1}{2}},$$

we need only substitute the expressions given in (13) into the above equation to find that for a ferrimagnetic sphere we have

$$\omega=\gamma H+\delta H_a+\tfrac{1}{2}\lambda(\gamma_2M_1+\gamma_1M_2) \pm\{(\gamma H_a+\delta H)[\gamma H_a+\delta H-\lambda(\gamma_2M_1-\gamma_1M_2)] +\tfrac{1}{4}\lambda^2(\gamma_2M_1+\gamma_1M_2)^2\}^{\frac{1}{2}}. \quad (14)$$

[11] N. Tsuya, Prog. Theoret. Phys. **7**, 263 (1952).
[12] Equation following (10) in reference 8.

The effect of assuming different magnitudes H_{a1} and H_{a2} for the anisotropy fields is merely the replacement of H by $H+H_{a-}$ and H_a by H_{a+} where $H_{a\pm}=\frac{1}{2}(H_{a1}\pm H_{a2})$; we shall not consider this further.

Before we go on to consider other approximations to (14), let us temporarily assume that $H_a=0$, so that (14) becomes

$$\omega=\gamma H+\tfrac{1}{2}\lambda(\gamma_2M_1+\gamma_1M_2) \pm\{\delta H[\delta H-\lambda(\gamma_2M_1-\gamma_1M_2)] +\tfrac{1}{4}\lambda^2(\gamma_2M_1+\gamma_1M_2)^2\}^{\frac{1}{2}}. \quad (15)$$

A comparable result in which anisotropy is included but different values of γ_i are not is[13]

$$\omega/\gamma=H+\tfrac{1}{2}\lambda(M_1+M_2)\pm\{H_a[H_a-\lambda(M_1-M_2)] +\tfrac{1}{4}\lambda^2(M_1+M_2)^2\}^{\frac{1}{2}}. \quad (16)$$

If we now compare (15) and (16), we see that the effect of having $\gamma_1\neq\gamma_2$ so that $\delta\neq0$ is to introduce an apparent anisotropy field into the system even if none were naturally present. The magnitude of this field is $\delta H/\gamma$. The existence of this anisotropy can be seen most clearly from the equations of motion themselves rather than from results derived from them. Suppose in Eqs. (1), we assume that $\gamma_1=\gamma_2=\gamma$, use (7), and omit all other terms. The equations of motion for this case then become

$$\left.\begin{aligned} d\mathbf{M}_1/dt&=\gamma\mathbf{M}_1\times\mathbf{H}+\gamma\mathbf{M}_1\times H_a\mathbf{k},\\ d\mathbf{M}_2/dt&=\gamma\mathbf{M}_2\times\mathbf{H}-\gamma\mathbf{M}_2\times H_a\mathbf{k}. \end{aligned}\right\} \quad (17)$$

If, on the other hand, we assume that $\gamma_1\neq\gamma_2$ and include only the external field $\mathbf{H}$, we find that we can write the equations of motion in the form

$$\left.\begin{aligned} d\mathbf{M}_1/dt&=\gamma\mathbf{M}_1\times\mathbf{H}+\mathbf{M}_1\times\delta\mathbf{H},\\ d\mathbf{M}_2/dt&=\gamma\mathbf{M}_2\times\mathbf{H}-\mathbf{M}_2\times\delta\mathbf{H}. \end{aligned}\right\} \quad (18)$$

Comparison of (17) and (18) clearly shows that if $\delta\neq0$ the direction of the external field becomes in effect a preferred direction to which we can ascribe an anisotropy field of magnitude $\delta H/\gamma$. These results tend to blur the distinction between the effects on the single crystal resonance of anisotropy and differing gyromagnetic ratio and to increase the difficulty of making an unambiguous determination of anisotropy from resonance experiments especially since the term $\delta H/\gamma$ can be comparable in magnitude to H_a.

We can approximate (14) in general by expanding the radical in inverse powers of its last term. In so doing we get a result which is independent of λ and has the following form:

$$\omega=\gamma_{eff}\{H+[(M_1-M_2)/(M_1+M_2)]H_a\}, \quad (19)$$

where γ_{eff} is again given by (10).

This result differs in an interesting way from the formula which is obtained for a sphere from the ferromagnetic formula; the term in the braces would be

[13] Equation (11) of reference 8.

simply $H+H_a$ rather than the more complicated term in (19). Thus the sublattice structure not only alters the effective gyromagnetic ratio but makes the shift in resonance frequency due to anisotropy also depend upon the exact distribution of magnetic ions.

In a polycrystalline material or a powder, we would not expect the term involving H_a to result in a shift of the line, but rather in a contribution ΔH to the line width due to an orientational broadening. The resonance condition would be simply

$$\omega=\gamma_{eff}H, \tag{20}$$

and from (19) we see that the order of magnitude of ΔH could be expected to be given by

$$\frac{\Delta H}{H_a}=\left|\frac{M_1-M_2}{M_1+M_2}\right|=\left|\frac{g_1S_1-g_2S_2}{g_1S_1+g_2S_2}\right|. \tag{21}$$

Hence if M_1 and M_2 were to be altered by temperature variation or changes in composition this should be reflected in the behavior of the line width.

We now proceed to the consideration of the resonance conditions for two special situations which can occur in ferrimagnetics. The first corresponds to the vanishing of the resultant angular momentum, i.e., $S=S_1+S_2=0$, or, equally well, $(M_1/\gamma_1)+(M_2/\gamma_2)=0$. If $\gamma_1\neq\gamma_2$, this does not mean the vanishing of the net magnetic moment. When $S=0$, Eq. (10) would predict that γ_{eff} would be infinite; the expansion leading to (19), however, would no longer be legitimate and we must find the value of ω for this case from the exact expression (14). If we continue to write $\omega=\gamma_{eff}H$, we find that

$$\gamma_{eff}(S=0)=\gamma-(-2\delta\gamma_2\lambda M_1/H)^{\frac{1}{2}}, \tag{22}$$

where we have again chosen the minus sign, neglected the ratio H_a/H, and assumed that $|\lambda M_1|\gg H$.

For the other case in which $M=0$, the first approximation for γ_{eff} as given by (10) predicts a value of zero. We find, however, that (14) becomes

$$\omega=\gamma H+\delta(H_a+H_E)\pm\{(\gamma H_a+\delta H)\times[\gamma(H_a+2H_E)+\delta H]+(\delta H_E)^2\}^{\frac{1}{2}}, \tag{23}$$

where we have let $-\lambda M_1=H_E$. We note in passing that if $\delta=0$, this reduces to the well-known antiferromagnetic resonance condition $\omega/\gamma=H\pm[H_a(H_a+2H_E)]^{\frac{1}{2}}$.[6] Since, generally, $H_E\gg H$ and H_a, if $\delta\neq0$, we can expand the radical in inverse powers of $(\delta H_E)^2$, and we find that (23) reduces to

$$\omega=\gamma_a H_a, \tag{24}$$

where

$$\frac{1}{\gamma_a}=\frac{1}{2}\left(\frac{1}{\gamma_1}-\frac{1}{\gamma_2}\right), \tag{25}$$

and where, as usual, the minus sign in (23) has been kept. This result, of course, also follows directly from (19). Equation (24) is independent of H, and since the frequency given by (24) will not ordinarily coincide with the fixed applied frequency of the apparatus, no resonance will be observed, so that in the language of (20), we can say that in effect

$$\gamma_{eff}(M=0)=0, \tag{26}$$

in agreement with the result given by (10).

If the plus sign before the radical of (14) is taken, the predominant term is $\frac{1}{2}\lambda(\gamma_2M_1+\gamma_1M_2)$; this gives us the following result for the frequency of resonance in the exchange field:

$$\omega_e=\lambda(\gamma_2M_1+\gamma_1M_2). \tag{27}$$

This agrees with the frequency found by Kaplan and Kittel[14] by a more specialized calculation.

A COMPARISON WITH EXPERIMENT

In this section we shall discuss in detail only some of the results of resonance experiments which have been performed at the Naval Ordnance Laboratory on a series of compounds known as nickel ferrite-aluminates.[15] These materials have the chemical formula $NiOFe_{2-x}Al_xO_3$, in which $0\leq x\leq2$. The resonance absorption was observed in small spheres of the sintered material; the frequency used was that corresponding to a wavelength of approximately 3 cm. Effective g values were found for each resonance by means of (20); the resulting values for liquid nitrogen temperature are shown in their dependence upon composition as open circles in Fig. 1.[16]

In order to calculate g_{eff} as a function of x from Eq. (11), it is necessary to know the distribution of the magnetic ions over the various lattice sites in order to find S_1 and S_2. A reasonable, although not unique, distribution of this kind has been deduced for the nickel ferrite-aluminates by McGuire[16] from measurements of

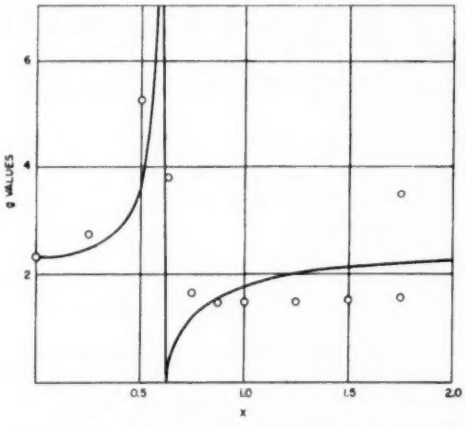

FIG. 1. g values vs composition for $NiOFe_{2-x}Al_xO_3$. Solid line is calculated values. Open circles are experimental points.

[14] J. Kaplan and C. Kittel, J. Chem. Phys. **21**, 760 (1953).
[15] Maxwell, Pickart, and Hall, Phys. Rev. **91**, 206 (1953); T. R. McGuire, Phys. Rev. **91**, 206 (1953).
[16] T. R. McGuire (private communication).

the saturation magnetization. The theoretical curve shown in Fig. 1 was calculated from (11) by the use of this distribution. All of the nickel ions with spin 1 and $g_1=2.3$ were taken as comprising sublattice 1, while all of the iron ions with spin 2.5 and $g_2=2.0$ formed sublattice 2; the grouping was done in this way so that the two sublattice formulas could be used although both the nickel and the iron are apparently distributed on both A and B sites—this point will be considered in more detail in the next section. The large g values have an upper limit of about 10 for $x=0.6$ as given by the more exact formula (22).

The general agreement between the curves is fairly statisfactory. The disagreement at the two points $x=0.5$ and 0.65 is probably due to a small deviation in composition in this region of rapid change of g_{eff}. For $x>1$, the two curves really have in common only the tendency toward lower values, although the experimental results have a slight trend toward a value near 2.3 which would be expected for nickel aluminate provided that the resonance were observable. Other than the inadequacy of the formula (11), a more likely reason for the discrepancy for $x>1$ is that the distribution of magnetic ions used for the calculations is not quite correct since this distribution is especially hard to determine for $x>1$ and is also apparently very sensitive to the exact heat treatment given the sample.[15,16]

The composition dependent contribution to the line width as given by (21) has also been calculated with the use of the same distribution. These values are shown as the solid line in Fig. 2 along with the experimental results[16] for the ratios $\Delta H(x)/\Delta H(0)$. The general agreement between the two curves is quite satisfactory especially in regard to the existence and location of the maximum and minimum. Better agreement than is observed can probably not be expected since no attempt has been made to allow for the contributions of the many other effects which can influence the line width; the remarks made above about the distribution for $x>1$ are equally applicable here.

A behavior which is qualitatively similar to that of Fig. 1 has been found for the variation of g with *temperature* in $Li_{0.5}Fe_{1.25}Cr_{1.25}O_4$ by van Wieringen.[17] As discussed in the introduction, the present theory cannot be expected to give an exact account of temperature dependence, but the general aspect of van Wieringen's curve can be understood on the same basis, namely, that the magnetic moment and angular momentum vanish at two different points.

FOUR SUBLATTICES

In order to make the specific calculations of the last section, the atoms were grouped into sublattices by gyromagnetic ratio rather than by the orthodox grouping according to the type of crystallographic site

[17] J. S. van Wieringen, Phys. Rev. **90**, 488 (1953).

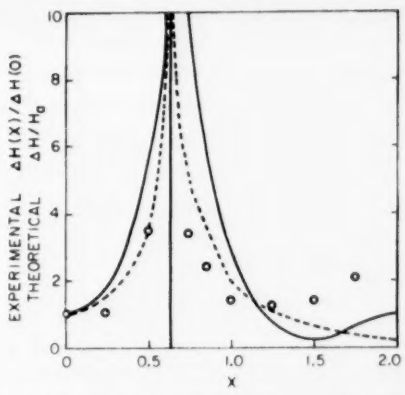

FIG. 2. Relative line widths vs composition for $NiOFe_{2-x}Al_xO_3$. Open circles are experimental points. Solid and dashed lines are values calculated from two- and four-sublattice formulas, respectively.

occupied. According to the distribution of ions which is indicated by the saturation magnetization, however, both the iron and nickel are distributed between the A and B sites of the spinel structure. As a result, in the specific case of the nickel ferrite-aluminates we are actually dealing with a system of four sublattices with the accompanying possibility of four different gyromagnetic ratios. The purpose of this section is to try to determine if our previous results are seriously affected by this situation.

One can proceed by using Eqs. (1) exactly as in the two sublattice case, but the secular determinant now has eight rows and columns and the complexity of the resulting expansion makes this method impractical. What we can do instead is to use a more approximate method whose utility has been demonstrated by Keffer and Kittel.[7] The basic idea is that if the total change of the magnetization can be described in terms of an angular velocity $\boldsymbol{\omega}$ then (1) can be written as

$$d\mathbf{M}_i/dt=\boldsymbol{\omega}\times\mathbf{M}_i=\gamma_i\mathbf{H}_i\times\mathbf{M}_i, \tag{28}$$

where we have explicitly taken into account the fact that the electron gyromagnetic ratio is negative so that γ_i now stands for its magnitude.

The specific case to which we shall first apply (28) is shown in Fig. 3. The *magnitudes* of the magnetizations of the sublattices are A, B, C, and D with corresponding gyromagnetic ratios γ_A, γ_B, γ_C, and γ_D. The magnetizations are assumed to precess about the external field H with the same angular velocity $\boldsymbol{\omega}$; we further assume the angles made by them with the direction of H to be small and, for definiteness, that $\phi_B>\phi_A>\phi_D>\phi_C$. The essential nature of the ferrimagnetic case has been included since A and B are assumed to be oppositely directed to C and D; we now let λ be the magnitude of the molecular field coefficient describing the interaction between these two groups. The magnitudes of the coupling coefficient between A and B will be written as

λ_1 and that for C and D as λ_2; we shall also explicitly assume that these couplings are of an antiferromagnetic nature.

If we neglect anisotropy and demagnetizing fields, the four equations obtained from (28) become

$$\begin{aligned}
\omega A\phi_A &= \gamma_A A[H\phi_A+\lambda C(\phi_A-\phi_C)+\lambda D(\phi_A-\phi_D)+\lambda_1 B(\phi_B-\phi_A)],\\
\omega B\phi_B &= \gamma_B B[H\phi_B+\lambda C(\phi_B-\phi_C)+\lambda D(\phi_B-\phi_D)-\lambda_1 A(\phi_B-\phi_A)],\\
\omega C\phi_C &= \gamma_C C[H\phi_C+\lambda A(\phi_A-\phi_C)+\lambda B(\phi_B-\phi_C)-\lambda_2 D(\phi_D-\phi_C)],\\
\omega D\phi_D &= \gamma_D D[H\phi_D+\lambda A(\phi_A-\phi_D)+\lambda B(\phi_B-\phi_D)+\lambda_2 C(\phi_D-\phi_C)].
\end{aligned} \tag{29}$$

The secular equation which results has the form

$$\omega^4+a_1\omega^3+a_2\omega^2+a_3\omega+a_4H=0, \tag{30}$$

where the coefficients a_i are rather long and involved functions of the external field, the molecular field coefficients, and the sublattice magnetizations.

The fact that we are looking for a solution of (30), however, such that $\omega\sim H$ enables us to obtain a suitable approximation from (30) rather easily. If we let H_E be the magnitude of the product of a molecular field coefficient and a magnetization, we can generally expect that $H_E\gg H$. If one then inspects the explicit expressions for the a_i, one finds that the order of magnitude of their largest terms are given by $a_1\sim H_E$, $a_2\sim H_E^2$, a_3 and $a_4\sim H_E^3$. Then the order of the terms in (30) are H^4, H_EH^3, $H_E^2H^2$, H_E^3H, and H_E^3H, respectively. Since the ratio H/H_E is so small, we can then approximate (30) by the equation

$$a_3\omega+a_4H=0 \tag{31}$$

and any fractional error made in finding ω from (31) will be of the order of the negligible term H/H_E.

Thus we have found that the four sublattice system also leads to an expression for ω of the form given in (20) where, of course,

$$\gamma_{\text{eff}}=-a_4/a_3.$$

Explicit evaluation of this expression, in which only terms of the order of H_E^3 are kept, yields the result that

$$\gamma_{\text{eff}}=\frac{A+B-C-D}{A/\gamma_A+B/\gamma_B-C/\gamma_C-D/\gamma_D}. \tag{32}$$

We see that to this approximation γ_{eff} is again independent of the λ's and is equal to the quotient of the net magnetization and the net angular momentum. In terms of g values, (32) becomes

$$g_{\text{eff}}=\frac{g_AS_A+g_BS_B-g_CS_C-g_DS_D}{S_A+S_B-S_C-S_D}. \tag{33}$$

In the specific ferrimagnetic case exemplified by the nickel ferrite-aluminates we have assumed that $g_A=g_C=g_1$, and $g_B=g_D=g_2$. Equation (33) is then seen to reduce at once to (11) since $S_1=S_A-S_C$ and $S_2=S_B-S_D$ for this case.

Now we have assumed a specific form of the normal precession mode in order to obtain (29). As Keffer and Kittel have shown[7] in the two sublattice case, we can assume that there are other possible modes which differ primarily in the sense of precession of the various sublattices. Such a possibility, analogous to that discussed by Keffer and Kittel, is shown in Fig. 4. Here we assume that A and B precess in phase as do C and D but that the sense of precession of these two groups is opposite. If one now writes down the equations similar to (29) as obtained from (28), one finds that the new equations are the same as (29) except that γ_C and γ_D are replaced by $-\gamma_C$ and $-\gamma_D$, respectively. The rest of the calculation would go as before with the net result that all of the algebraic signs in the denominator of (32) would be plus; the denominator of (33) would similarly have all plus signs, while the signs in both numerators would be unaltered.‡

The same sort of considerations would be valid for other assumed modes so that the above results can be generalized and correlated with the assumed direction of the angular velocity of a given sublattice with respect to H. For if we treat A, B, $\cdots$, γ_C, γ_D as all positive numbers, all of the possibilities are contained in the following extension of (33), namely, that

$$g_{\text{eff}}=\frac{g_AS_A+g_BS_B-g_CS_C-g_DS_D}{S_A\pm S_B\mp S_C\mp S_D}. \tag{34}$$

Here we have assumed A and B to be "up," and C and

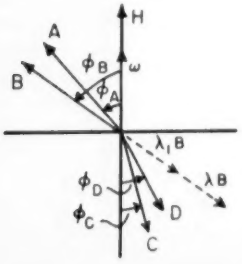

FIG. 3. Assumed normal mode for four sublattices. Dotted line indicates molecular fields ascribed to sublattice B.

‡ *Note added in proof.*—Dr. J. Smit of the Philips Research Laboratories has kindly pointed out to me that the relative angles of the sublattices in the mode assumed in Fig. 4 are not constants of the motion so that the derivation of this paragraph is apparently vitiated. If one continues to use the small angle approximation, however, and evaluates Eqs. (28) for various phases of the assumed motion, the resulting frequency is still found to be that discussed in this paragraph. Actually, of course, the question of the reality of these modes can only be answered by considering the solutions of the exact equations of motion.

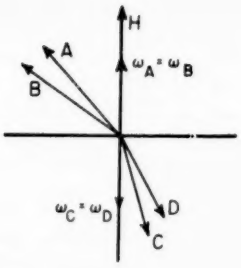

FIG. 4. Another assumed normal mode for four sublattices.

D "down." The signs in the denominator are chosen as follows: the upper sign applies if the assumed direction of the angular velocity of the sublattice is parallel to H (always the case for A since another choice will not lead to physically different values for g_{eff}), while the lower sign applies if the angular velocity is assumed to be antiparallel to H.

From (34), we see that if the angular momentum of one of the sublattices is small enough, then the frequencies of the two modes corresponding to different signs may be so close together that they both fall within the range of the apparatus. This is apparently the reason for the extra low-temperature peak observed in the nickel ferrite-aluminate with $x=1.75$. As shown in Fig. 1 the experimental value of g is 3.5; the value of g_{eff} calculated on this basis by using (11) with the denominator S_1-S_2 is 3.8. The agreement is sufficiently good to show that these other modes very likely can give rise to an apparent splitting of the low-temperature resonance curve with values of g_{eff} given by the various formulas contained in (34).

Anisotropy and the Line Width

We shall briefly consider the result of including an anisotropy field in the mode pictured in Fig. 3. For simplicity we shall assume the anisotropy field to have the same magnitude H_a for all four sublattices and is directed parallel to H for A and B, and antiparallel to H for C and D.

When the equations of motion are written down from (28) for this case, they are found to be the same as (29) except that H is replaced by $H+H_a$ in the first two, and by $H-H_a$ in the last two. In accord with our previous method of approximation we need only find what the inclusion of H_a does to the last term of (30). This is a straightforward but lengthy calculation; the result is that the frequency is given by

$$\omega=\gamma_{eff}\{H+[(A+B+C+D)/(A+B-C-D)]H_a\}, \quad (35)$$

where γ_{eff} is again given by (32).

For a polycrystalline material or a powder, we can expect to find from this result a contribution ΔH to the line width of magnitude

$$\frac{\Delta H}{H_a}=\left|\frac{A+B+C+D}{A+B-C-D}\right|. \quad (36)$$

We see that in the interesting case in which $\gamma_A=\gamma_C=\gamma_1$ and $\gamma_B=\gamma_D=\gamma_2$, Eq. (36) does not reduce to the result (21) which was found for the two sublattice case since the numerator of (36) does not become M_1-M_2. The relative line width calculated from (36) for the nickel ferrite-aluminates is shown as the dashed line in Fig. 2. The agreement with the experimental curve is definitely improved for values of x up to about 1.25, but the minimum which was previously found for $x>1$ no longer appears. Very likely the disagreement with experiment for $x>1$ is due to the use of a distribution for the ions which is not exact as we have previously discussed.

CONCLUSION

Both the theoretical considerations given above and the limited comparison with experiment indicate that the expressions for the effective gyromagnetic ratio given by (10) and (32) as well as their natural extension to more complex situations are accurately applicable to systems containing sublattices. If a system can be adequately described in terms of only two sublattices, then one has the possibility of actually being able to determine the magnetizations of the individual sublattices, and thence the ionic distribution by using both the measured values of the saturation magnetization and effective g values for the sample as a whole. For systems of more sublattices, these two values are not sufficient to determine the ion distributions completely, but comparison of experimental g values with those calculated from an assumed distribution will provide a useful check on the accuracy of the distribution. Equations (21) and (36) will be helpful when one is considering the contributions of other effects to the line width because their use will enable one to separate the contributions dependent upon the sublattice structure from the total observed widths.

I wish to thank Dr. L. R. Maxwell, Dr. T. R. McGuire, and Dr. J. S. Smart for some interesting discussions of this work.

Mobility of Interstitial Atoms in a Face-Centered Metal

H. B. HUNTINGTON
Physics Department, Rensselaer Polytechnic Institute, Troy, New York
(Received April 27, 1953)

Calculation of the energies of interstitial atoms in copper have been carried through in some detail using a free-electron model and approximating the repulsion of closed shells with a Born-Mayer potential. Alternate choices of constants in this potential have been employed to explore the extent of the associated uncertainty. Results show that interstitials require an activation energy of about ¼ ev or less for motion. Applications to various current experiments are pointed out.

CURRENT interest in radiation damage in metals has indicated the importance of the behavior of interstitial atoms. Earlier theoretical study[1] had tended to discount the role of interstitials as a mechanism for diffusion because of the large amount of energy needed in their creation but had indicated that if formed their mobility might be high. Under radiation by energetic massive particles large numbers[2] of lattice displacements consisting of vacancies and displaced interstitial atoms result. There is evidence from the low-temperature annealing of this damage[3] that there exists a mechanism (perhaps several) for atom motion with low activation energy.

Accordingly this paper is an attempt to study the interstitial atom in a metal such as copper in more detail and with particular emphasis on the relative energy difference between the two equilibrium configurations for the interstitial atom since this difference is the activation energy for interstitial motion. The general procedure follows that of I. The copper metal is represented by a lattice of positive point ions immersed in a uniform, compensating distribution of electrons. Each ion repels its neighbors according to an exponential potential, involving two semi-empirical constants, which represents the repulsion of closed shells after the Born-Mayer treatment. This treatment is, however, more detailed and differs from I at three points. In the first place, the form of the exponential repulsion of the closed shells of copper has been revised to fit with more recent findings. Secondly, the electrostatic potential of the interstitial position has been evaluated, whereas formerly it was assumed to be zero. Lastly, the method has been altered to consider the relaxation of neighbors *before* the redistribution of electron charge. The effect of the latter, always difficult to estimate, is greatly reduced and the reliability of the method is thereby improved. It should be emphasized that such a technique is not limited to the treatment of individual interstitials but should prove useful for treating more complex lattice defects such as may be generated in metals by radiation damage or cold work.

A. THE EXPONENTIAL CLOSED-SHELL REPULSION

1. Constructing the Potential

Besides I, other papers[4,5] have employed exponential repulsive potentials for copper. The common features have been to use the elastic moduli to determine the constants in the formula. The variation of compressibility with pressure and behavior of the Hartree wave functions for the copper atom have also been invoked to substantiate the final result. Since different authors have come up with somewhat different expressions, it appears worth while to investigate critically the causes for these divergences.

Let the interaction energy of two adjacent ions be written $U(r)=Ae^{(r-r_0)/\rho}$, where r_0 is the equilibrium separation, A gives the interaction energy at this distance, and r_0/ρ is a dimensionless number whose magnitude is a measure of the rigidity of the repulsion. Contributions to the elastic constants for the face-centered lattice from the close range forces may be computed[6] from the equations

$$(c_{11}'+2c_{12}')/3=(6/9)N[r^2U'']_{r_0}, \tag{1}$$

$$c_{44}'=\tfrac{1}{2}N[r^2U''+3rU']_{r_0}, \tag{2}$$

$$c_{11}'-c_{12}'=\tfrac{1}{2}N[r^2U''+7rU']_{r_0}, \tag{3}$$

where N is number of ions per unit volume. Primed elastic constants are corrected for the effects of long-range forces. The nature of these corrections will be discussed below.

The bulk modulus of copper is 13.9×10^{11} dynes/cm^2. Values for the shear moduli given by Goens and Weerts[7] and by Lazarus[8] are in close agreement for $c_{11}-c_{12}=4.7\times10^{11}$ dynes/cm^2 and $c_{44}=7.5\times10^{11}$ dynes/cm^2. With the model that is used here to represent the metal, namely, nearly free electrons and a lattice of singly charged ions, the long-range forces are the elec-

[1] H. B. Huntington and F. Seitz, Phys. Rev. **61**, 315 (1942); hereafter called I.
[2] F. Seitz, Discussions Faraday Soc. No. 5, 271 (1949).
[3] C. J. Dienes in *Annual Review of Nuclear Science* (Annual Reviews, Inc., Stanford, 1953), Vol. II; Marx, Cooper and Henderson, Phys. Rev. **88**, 106 (1952); A. W. Overhauser, Phys. Rev. **90**, 393 (1953); R. R. Eggleston, Bull. Am. Phys. Soc. **27**, No. 6, 9 (1952).
[4] C. Zener, Acta Cryst. **3**, 346 (1950).
[5] G. J. Diennes, Phys. Rev. **86**, 228 (1952).
[6] K. Fuchs, Proc. Roy. Soc. (London) **A153**, 622 (1936).
[7] E. Goens and J. Weerts, Physik. Z. **37**, 321 (1936).
[8] D. Lazarus, Phys. Rev. **76**, 545 (1949).

trostatic interactions and the pressure of the electron gas. The latter will contribute to the bulk modulus, while the former will affect the shear moduli.

The actual bulk modulus will be

$$(c_{11}+2c_{12})/3=N(\hbar k_m)^2/5m^*+(c_{11}'+2c_{12}')/3, \quad (4)$$

where the first term on the right is the bulk modulus of the electron gas. The value for m^*, the effective electron mass, was taken to be $1.47m$ in accord with low-temperature measurements of specific heat.[9] In establishing the values used for A and ρ in his work, Zener[4] omitted Eq. (1) because of uncertainty of the correction term in Eq. (4). Besides the lack of supporting theoretical evidence for the value of m^*, this model of the free-electron metal as used by Fuchs[6] was relatively unsuccessful in explaining the cohesion of copper. Nevertheless, it turns out that the contribution to the bulk modulus from the compression of a gas of free electrons is only about 20 percent of the experimental bulk modulus so that the remaining contribution to the bulk modulus from the short-range forces is fairly well known.

In his work on copper,[6] Fuchs calculated the electrostatic contributions to the shear constants arising from distorting a lattice of positive point charges in a uniform negative charge distribution. They[10] are $(c_{11}-c_{12})_{\text{elec}}=0.57$ and $(c_{44})_{\text{elec}}=2.57$ in units of 10^{11} dynes/cm^2. Though these terms are relatively small, they affect c_{44} much more than $c_{11}-c_{12}$ and so alter the anisotropy ratio $2c_{44}/(c_{11}-c_{12})$. As Zener has remarked, the r_0/ρ is quite sensitive to this ratio. Since the electron density does not stay uniform with elastic shear distortion but changes to neutralize in part the electrostatic stored energy in the distorted point lattice, the terms calculated by Fuchs represent an upper limit for this effect. Zener,[4] in his consideration of this point, concluded that electron compensation made the electrostatic contributions negligible, but he made no direct calculation on this point.

In Appendix A, a variational calculation has been carried out on an approximate model to determine what fraction of the electrostatic terms is really operative. A shear distortion of the angle between two cubic axes in a face-centered cubic lattice has the effect of decreasing the distances between atoms in the (110) direction and increasing the distances in the (1-10) direction, so an effective charge deformation is generated in a criss-cross pattern with a period of $d/\sqrt{2}$, where d is the lattice constant. The variational calculation using a very simple form of modulation shows a reduction of 25 percent in the electrostatic energy of deformation. Since more elaborate methods should give greater reduction, it seems reasonable to put these contributions to the elastic constants at one-half their value for the uniform electron distribution.

TABLE I. Data for determining A and ρ. All values are given in units of 10^{11} dynes/cm^2.

	$\frac{1}{3}(c_{11}+2c_{12})$	$c_{11}-c_{12}$	c_{44}
Experimental elastic constants	13.9	4.7	7.5
Contributions from long-range forces	2.6	0.28	1.28
Primed quantities	11.3	4.42	6.22

All these considerations are summarized in Table I and can now be applied to determining A and (r_0/ρ).

With values of the primed shear constants as obtained in Appendix A together with the correction to the primed bulk modulus given in Eq. (4), Eqs. (1)–(3) can be solved by the least-squares method to give $(r_0/\rho)=14.9$ and $A=0.056$ ev, with a relative deviation less than 6 percent in every case.

In the corresponding expression developed by Zener,[4] the value of r_0/ρ was some 10 percent lower. In addition to using the ratio of the shear constants, Zener also adduced supporting evidence from two other sources, one arising from the exponential behavior of the d electrons for the Cu^+ ion in the Hartree-Foch solution[11] at a radial distance corresponding to mid-point between ions in the metal and the second from the change of compressibility of copper with pressure as determined by Bridgman[12] and Lazarus.[13] The treatment of the pressure data was reviewed by the author taking into account the effect of the electron gas on the compressibility and variation of compressibility with pressure and using the condition of equilibrium in a somewhat different manner. We obtained essentially the same result as Zener. A formula for $U(r)$ closely resembling his was adopted for subsequent work:

$$U_a(r)=0.053\exp[13.9(r_0-r)/r_0]\text{ev per ion pair.} \quad (5a)$$

Since the treatment of the elastic data given above called for a somewhat larger value of r_0/ρ, it was decided to bracket this value by carrying out alternate calculations with a function[14] of considerably larger r_0/ρ,

$$U_b(r)=0.038\exp[17.2(r_0-r)/r_0]\text{ ev per ion pair.} \quad (5b)$$

2. Repulsive Energies for Interstitial Configurations

Interstitial atoms in face-centered lattices have two equilibrium configurations as depicted in Fig. 1. Con-

[9] See F. Seitz, *Modern Theory of Solids* (McGraw-Hill Book Company, Inc., New York, 1940); Estermann, Friedberg, and Goldman, Phys. Rev. **87**, 582 (1952).

[10] See N. F. Mott and H. Jones, *The Theory and Properties of Metals and Alloys* (Oxford University Press, London, 1936), pp. 147–150.

[11] D. R. Hartree and W. Hartree, Proc. Roy. Soc. (London) **A157**, 490 (1936).

[12] P. W. Bridgman, Proc. Am. Acad. Arts Sci. **77**, 198 (1949).

[13] See reference 8.

[14] This potential is quite close to the one used by Huntington and Seitz in I and displayed as curve (2) in Fig. 1 of that paper. The values quoted in connection with this curve on p. 317 of I are in error. Corrected, they should read: $\rho=0.284$ in Bohr units (not angstroms), and $A=5.64\times10^4$ ry per ion pair (where the factor 10^4 was inadvertently omitted). A curve based on these values was used in the actual calculations. However, this curve was obtained using rather different shear constants and incorporating the full value of the electrostatic terms.

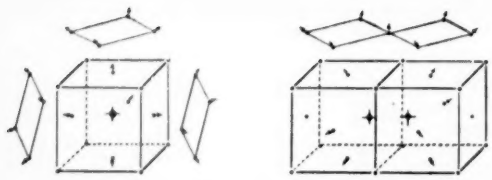

FIG. 1. B and C configurations for an interstitialcy.

figuration B (following notation of I, Fig. 2) represents the interstitial atom at the cube center and the associated disturbance has spherical symmetry. In configuration C two atoms appear on opposite sides of a vacant lattice site and the accompanying disturbance has only cylindrical symmetry. The procedure is to consider the relaxation of nearest neighbors, 6 for B and 8 for C, and in addition the relaxation of each quartet of ions most directly opposing the motion of each of the nearest neighbors. This brings the number of neighbors considered up to 30 for B and 36 for C. The relaxation of outermost ions which were not considered in I lowers the energy in each case by amounts of at least $\frac{1}{2}$ ev.

For configuration B, the origin of coordinates is put at the interstitial ion. The outward displacements of the nearest neighbors is given by a vector of the type $\frac{1}{2}\epsilon d$, 0, 0, where d is the lattice constant. The displacements of the ions at the positions of type $(d, \frac{1}{2}d, 0)$ is taken to be outward from the next neighbors and to be represented by vectors $\delta d/\sqrt{2}$, $\delta d/\sqrt{2}$, 0. The first part of the calculation consists in treating each nearest neighbor and the four ions against which it is pushed as forming a complex whose energy is minimized with respect to δ for each value of ϵ. The interaction of these complexes with the interstitial ion is then minimized with respect to ϵ.

For configuration C, the origin of coordinates is put at the empty site and the two ions flanking this position have coordinates $\pm(1-\lambda)d/2$, 0, 0. The eight next neighbors at $(\pm d/2, \pm d/2, 0)$ and $(\pm d/2, 0, \pm d/2)$ are given outward displacements of the type $\lambda\nu d/2$, $\nu d/2$, 0. The displacements of the more remote ions at positions $(d, d, 0)$, $(d/2, d, d/2)$, and $(0, d, 0)$ are all assumed to point outward from the next neighbors and are given magnitudes $\eta_1 d/\sqrt{2}$, $\eta_2 d/\sqrt{2}$, and $\eta_3 d/\sqrt{2}$, respectively. The procedure here is to assume an approximate value for $\lambda(\lambda=0.4)$ and for different values of ν to find the minimum values for the η's, taking into account only interaction with the 28 remote neighbors. The interaction of the interstitials with the complexes formed around the eight next neighbors is next minimized with respect to ν. The final step is to vary λ and to compute the energy of the configuration at the minimum values for all parameters, taking care to count all interactions only once.

TABLE II. Summary of closed-shell repulsive terms.

Configuration B	$U_a(r)$	$U_b(r)$
Minimizing value for ϵ	0.21	0.23
Minimizing value for δ	0.03_2	0.04_9
Energy minimum	4.34	4.85
Configuration C		
Minimizing value for λ	0.42	0.39
Minimizing value for ν	0.15	0.17
Minimizing value for η_1, η_2, η_3	(0.03_6, 0.023, 0.008)	(0.045, 0.028, 0.014)
Energy minimum	4.43 ev	4.74 ev

In each case, the energy is calculated from the normal lattice plus isolated "interstitial" ion as zero potential. It is to be noted that the ions whose relaxation was most important were not always those nearest the defect. For the B configuration, ions at the $(d/2, d/2, d/2)$ positions were passed over because the effect of ion repulsion was less important for them than for $(d, d/2, 0)$ neighbors. In configuration C, a similar remark holds for neighbors at the $(d/2, d/2, 0)$ positions. The final results of these calculations are given in Table II for configurations B and C.

From Table II one can judge how critical the choice of repulsive potential turns out to be for these configurations. With U_b, the "harder" potential, the level of both B and C configurations is raised by about $\frac{1}{2}$ ev. For U_b also, the B configuration lies higher by about 0.10 ev; whereas for U_a the difference is reversed. In both cases this difference is too small to imply much physical significance.

B. ELECTROSTATIC TERMS

The interstitial configurations at this stage where the electrons are uniformly distributed may be considered as consisting of point ions introduced into the lattice (one positive ion for Configuration B and two positive and one negative for Configuration C), a number of large dipoles which arise from the displacements of the nearest neighbors and a larger number of smaller dipoles because of the displacements of the more distant ions. The electrostatic energies associated with these configurations are subdivided into the following terms: (1) the lattice potential at the points where the ions are introduced, (2) the Coulombic interaction of these ions (for C configuration only), (3) ion-large dipole interactions (must treat dipoles as finite), (4) large dipole-dipole interactions, (5) large dipole-lattice interactions, (6) ion-small dipole interactions, (7) large-small dipole interactions, (8) small-small dipole interactions, (9) small dipole-lattice interactions. These quantities are evaluated by assuming that the ions are situated at the equilibrium positions determined in Sec. A. Since the closed shell repulsive forces treated there vary much more rapidly with distance than the electrostatic forces, this seems to be a reasonable approximation. Moreover, in a metal the electrons will tend to shield the ions to an extent that is difficult to determine, and so the electrostatic forces are less effec-

TABLE III. Electrostatic terms (all energy values in e^2/d).

Term	Configuration B Formula	With U_a	With U_b	Configuration C Formula	With U_a	With U_b
(1) Lattice potential	$V_e(d/2, 0, 0)$	−0.303	−0.303	$2V_e\{d(1-\lambda)/2, 0, 0\}-V_e(0)$	4.390	4.218
(2) Ion-ion				$-3/(1-\lambda)$	−5.175	−4.918
(3) Ion-large dipole	$+12[(1+\epsilon)^{-1}-1]$	−2.088	−2.244		−1.440	−1.640
(4) Large-large dipole	$10.5\epsilon^2$	0.464	0.556	$12.58\nu^2$	0.283	0.363
(5) Large dipole-lattice	$12.6\epsilon^2$	0.555	0.660	$19.5\nu^2$	0.439	0.565
(6) Ion-small dipoles	18.2δ	−0.582	−0.728		−0.266	−0.33
(7) Large-small dipoles	$-11.2\epsilon\delta$	−0.075	−0.103		−0.046	−0.07
(8) Small-small dipoles	$216\delta^2$	0.222	0.346		0.062	0.10
(9) Small dipole-lattice	$203\delta^2$	0.208	0.325		0.113	0.18
Total		−1.599	−1.491		−1.640	−1.53

tive in determining the equilibrium positions of the ions than might appear on the basis of uniform electron distribution. In Table III below are given the values for the various electrostatic terms.

For the calculation of the lattice potential the Ewald[15] method is used,

$$V_e(x)=e[\pi/4d+(\pi\Omega)^{-1}\sum_l' h_l^{-2}\exp-(\pi h_l/s)^2 +\sum_n|r-R_n|^{-1}\{1-\phi(s|r-R_n|)\}-\pi/s^2\Omega], \quad (6)$$

where the R_n are the translation vectors of the lattice, the h_l are the translation vectors of the reciprocal lattice, and s is an arbitrary parameter whose choice is governed by the need to have both series converge sufficiently rapidly. (In this work $s=\pi/d$ was chosen.) The symbol $\phi(x)$ stands for the error function. The first term inside the square bracket, namely $\pi/4d$, is introduced to take into account the dipole layer at the surface of a large spherical lattice. The derivation of this term, which does not appear to have been developed elsewhere, is given in Appendix B. The $V_e(0)$ is the potential at a lattice site when the ion at that position is missing. It is $-3.80_0e/d$, and is obtained by omitting from Eq. (6) the term for which $R_n=r$ in the second summation and adding a term $2s/\pi^{\frac{1}{2}}$.

In many cases of dipole-dipole interactions, the formula for infinitessimal dipoles proved to be sufficiently accurate, namely,

$$V_{d-d}=\tfrac{1}{2}\sum_{ij}[(\mathbf{D}_i\cdot\mathbf{D}_j)/r^3-3(\mathbf{D}_i\cdot\mathbf{r}_{ij})(\mathbf{D}_j\cdot\mathbf{r}_{ij})/r_{ij}^5], \quad (7)$$

where the $\mathbf{D}_i$ are the dipole moments and r_{ij} their mutual separations. Since the displacements are somewhat different according to whether U_a or U_b is used, results are given separately for both.

The dipole lattice term is the increase in electrostatic energy when an ion is displaced from its equilibrium position. It can be adequately approximated for our use by $ex^2/2r_s^3=8.4(e/d)(x/d)^2$, where x is the displacement from equilibrium.

In Table III formulas have been given, where possible, for the various electrostatic terms as functions of the displacement parameters. Such formulas were more difficult to use in configuration C because of its greater complexity and lower symmetry. For the terms involving the smaller dipoles, the multiple values of η made formulas impractical. In general, no accuracy is claimed for the last figure of the numbers in this table.

From Table III it can be observed that the reduction in energy throughout was greater with the U_b than with U_a, because in general U_b forced the greater displacements, hence the greater effective polarization. Because the electrostatic disturbance associated with the interstitial alone is less concentrated for configuration C, the lowering of the electrostatic energy is here considerably greater. When the effective polarizations of first the large and then the small dipoles are successively introduced, the $B-C$ difference is continually reduced to a value of about 0.04 e^2/d in the final total. Somewhat fortuitously perhaps the final values for the $B-C$ difference appear to be independent of the force law used to within the accuracy of the calculation.

The calculations so far are referred for zero potential to the isolated ion and the regular lattice. The energy to form an isolated ion is the sum of the cohesive energy plus the ionization of the atom minus the work function of the metal which is regained as the freed electron is returned to the lattice. For copper these quantities total about 7.2 ev. Also, for copper, the e^2/d unit is 4.0 ev. The summary of the results obtained so far, under the assumption of uniform electron distribution, is given in Table IV, where the results of Tables II and III are combined with the 7.2 ev for forming the isolated ion.

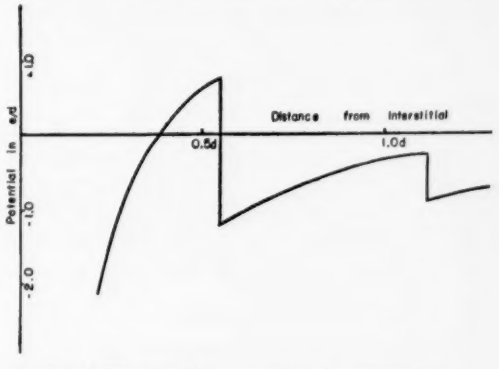

FIG. 2. Electrostatic potential for B configuration.

[15] P. P. Ewald, Ann. physik **49**, 1, 117 (1916); **64**, 253 (1921); Z. Kryst. **56**, 129 (1921).

TABLE IV. Summary of results. All energies are in ev.

Configuration	B		C	
Closed-shell force law	(a)	(b)	(a)	(b)
Closed-shell repulsion (Table II)	4.34	4.85	4.43	4.74
Electrostatic terms (Table III)	−6.40	−5.96	−6.56	−6.12
Formation of isolated ion	7.2	7.2	7.2	7.2
Energy on basis of uniform distribution	5.14	6.09	5.07	5.82

Table IV shows the calculated values for the interstitial configurations to be about 0.9 ev higher on the basis of U_b as compared with U_a, but the value for the $B-C$ difference is considerably less, 0.07 ev for U_a and 0.24 ev for U_b. On the basis of either force law, the configuration of lower symmetry C is favored as the equilibrium state.

C. VARIATION OF THE ELECTRON DISTRIBUTION

The study of the effect of the redistribution of electron density injects some calculational difficulties into what has been up to now a straightforward attack based on an easily applied model. We shall proceed by a simple variational approach and choose trial functions,

$$\psi_k(x) = V^{-\frac{1}{2}} e^{i\mathbf{k}\cdot\mathbf{r}} F(r), \tag{8}$$

where all the wave functions[16] are modulated by the same function F which depends only upon distance from the interstitial ion. The value of $F(r)$ is more than one near the interstitial ion and infinitesimally less than one elsewhere, so that the total number of electrons is conserved. V stands for the volume of the metal. The theory of a very similar case has been worked in I, and the analysis there shows that three terms enter into the variational calculation:

(1) The interaction of the change in charge distribution with the potential field of the defect. This field includes the contribution from the displacement dipoles as well as that from the interstitial ion.

(2) An increase in the kinetic energy arising from the modulation, which can be reduced to

$$-(\hbar^2/2m^*)\int F(r)\nabla^2 F(r)d\tau.$$

(3) The self-energy of the change in charge distribution.

The considerations governing the choice of the function $F(r)$ rested not so much on physical grounds as on mathematical convenience since the evaluation of three terms above in convenient closed forms was most desirable. The function chosen for configuration B was

$$F(r) = (1+B\cos 2br)^{\frac{1}{2}} \quad \text{for} \quad r<\pi/4b, \tag{9}$$

where the quantity B is determined to be 0.340 $(bd)^3$ by the condition that the interstitial defect appears electrically neutral at large distances in the metal. Beyond $r=\pi/4b$, $F(r)-1$ is of the order of $1/N$, where N is total number of atoms.

(1) For calculating (1), the interstitial potential is approximately $-e/r$ and the displacement dipoles are replaced by dipole spherical shells of equal total strength, so that one has a potential as shown in Fig. 2 of a Coulomb attraction with steps at the position of the dipole layers. For the choice $\epsilon=0.20$ and $\delta=0.032$, these potential steps turn out to be $V_1=1.98e/d$ for $r_1=0.55d$ and $V_2=0.61e/d$ at $r_2=1.12d$. Qualitatively their effect is to repel the neutralizing electronic charge so that it is spread over a greater volume than would be the case if the dipoles were not there. The expression for this interaction using trial function (9) is

$$[-2.43bd+4.21G(\xi_1)+1.30G(\xi_2)]e^2/d, \tag{10}$$

where $\xi_1=2br_1$, $\xi_2=2br_2$ and $G(\xi)=(\xi^2-2)\sin\xi+2\xi\cos\xi$.

(2) For the change in kinetic energy one can integrate by parts to get

$$-\frac{\hbar^2}{2m^*}\frac{4}{\Omega_0}\int_0^{b\pi/4} F(r)(\nabla^2 F(r))r^2dr$$

$$=\frac{2\pi\hbar^2}{m^*\Omega_0}\left[\left(\frac{\pi}{4b}\right)^2 Bb+\frac{(Bb)^2}{(2b)^3}\int_0^{\pi/2}\frac{\sin^2 xx^2dx}{1+B\cos x}\right]. \tag{11}$$

Because of the widely spread charge, B turns out to be small[17] and can be dropped from the denominator of the integral. This can be evaluated and itself shown to be negligible compared with the first term.

(3) The potential of the change in electron charge distribution ϕ_e can be found from Poisson's equation,

$$\nabla^2\phi_e(r) = (4eB/\Omega_0)\cos 2br,$$

to be

$$\phi_e(r) = \phi_e(\pi/4b)+4.26eb[4/\pi+\cos\xi_1-2\sin\xi_1/\xi_1]. \tag{12}$$

The value for the self-potential term is

$$(e/2\Omega_0)\int\phi_e(r)B\cos(2br)d\tau = 0.91be^2. \tag{13}$$

In Table V is given the results of minimizing the sum of Eqs. (10), (11), and (13) with respect to b. The table shows that the variation of the electron distribution in the above manner lowers the energy by $0.223e^2/d$ or 0.89 ev. This number serves to give the order of magnitude of the energy gain but may be too small for many reasons. As in any variational calculation, the arbitrarily chosen trial function can usually be improved. A radial function which decreases less rapidly at larger distances than the cosine might effectively shield out the farther dipoles. Further gains could be introduced by departure from spherical symmetry; i.e., let

[16] The validity of the subsequent results may be challenged because the trial functions are not orthogonal. There is indication, however, that this is not a serious shortcoming.

[17] The fractional error introduced by neglecting the nonothogonality of the trial functions is proportional to B, which is of the order of 0.01.

$F=F(r, \theta, \phi)$. Aside from these considerations associated with the variational procedure, there are still the electron correlation effects which would tend to reduce the self-potential term [see Eq. (13), which amounts to about +1.2 ev in the above reckoning]. From these considerations one estimates roughly that the energy gain from variation for configuration B will lie between 1.0 ev to 2.0 ev, which, when combined with the results of the preceding sections, yields an activation energy for interstitial diffusion bracketed between 3.8 ev to 5.1 ev. This seems to be well outside the range of experimental values for copper.

The application of a variational attack on configuration C does not appear warranted in view of the necessary complication. One expects that the energy lowering in such a process would be about the same as for configuration B, though perhaps somewhat smaller. There are two reasons why electron redistribution might be expected to be less effective for C. First, the departure from spherical symmetry might be expected to increase the change in the kinetic energy of the electron wave functions that is caused by the modulation. A second and more important reason is that the C configuration is slightly more spread out than the B, for example, 8 near neighbors and 28 next nearest as compared with 6 near neighbors and 24 next-nearest neighbors. It has already been pointed out that largely as a result of this spreading, the C configuration has a considerably lower electrostatic energy than B. The relaxations of the first and second neighbors reduces this difference markedly. Likewise, the modulation of the electron distribution might be expected to decrease the difference somewhat further and to favor B over C—perhaps by about 10 percent of the total energy lowering.

D. CONCLUSIONS

The results of this calculation indicate that once an interstitial atom is formed, it is relatively mobile because of the small activation energy required for it to jump from one equilibrium position to another. The calculation indicates an average value for this energy of about $\frac{1}{4}$ ev, with the less symmetrical configuration C as the more probable equilibrium position, though the reverse possibility that C is a saddle point cannot be definitely ruled out. Wherever a large nonequilibrium number of interstitials exists in the lattice, motion of interstitials will be important. On the other hand, the calculation shows that interstitial diffusion in copper is ordinarily unimportant because the energy to form an interstitial, while less than originally estimated (see I), is still greater by a considerable amount than the activation energy experimentally observed.

The possibility of mobile interstitials has bearing on the results of some current experiments. Recently the measurement[18] of changes in resistance found in the annealing of cold-worked wires of gold, silver, and copper at fixed temperatures for fixed periods of time has been reported, indicating clearly that at least two distinct atomic mechanisms are operative in the anneal. For one the activation energy is about $\frac{1}{4}$ ev or less, for the other the energy values fall around $\frac{3}{4}$ ev, for these metals. Manintveld has proposed that the second mechanism corresponds to the motion of single vacancies. We should like to suggest that the first effect can be attributed to the annealing out of interstitials formed by the cold work.

[18] J. A. Manintveld, Nature **169**, 623 (1952).

TABLE V. Variation of electron distribution. (Energies in units of e^2/d.)

$-1.52\ bd$	−0.517	$(bd)_{\min}=0.34$
$4.21\ G(\xi_1)$	0.076	$B=0.013$
$1.30\ G(\xi_2)$	0.160	
ΔKE Eq (11)	0.058	
Total energy gain	−0.223	

Recent work[19] at the University of Illinois has shown similar results from the study of resistance changes in radiation-damaged wires of copper, silver, gold, nickel, and tantalum. The investigators found at low temperatures activation energies for anneal in the range of 0.2 to 0.3 ev for all of these metals. More recent measurements reported on copper[20] from widely different sources agree on another activation energy for anneal of 0.68 ev but indicated that the situation is complex at lower energies. One explanation for this complexity may be that multiple vacancies formed along the track of the fast particle may require about the same energy for motion as the interstitials. (At still lower energy, the direct recombination of nearby vacancies and interstitials might be expected.) Experiments[21] with very rapid quenching of pure gold wires from high temperatures reveal an activation energy of 0.4 ev. Since the presence of interstitials after quench is unlikely, it would seem that this effect might arise from coupled vacancies[22] which result from a large density of vacancies frozen in from high temperature.

By way of interpretation, it is tempting to assign the 0.68 ev energy in copper to the motion for single vacancies. On the other hand, it is difficult to decide from theory or experiments performed so far, whether the interstitial or the coupled vacancy has the lower energy for motion or which plays the more important role in the radiation-induced changes in resistance.

The author wishes to thank Dr. G. J. Dienes and Dr. J. B. Sampson for their valuable suggestions and constructive criticisms.

APPENDIX A

The amount by which the electrostatic energy of the elastic deformation in shear of a point lattice is reduced by the motion

[19] Marx, Cooper, and Henderson, Phys. Rev. **88**, 106 (1952).
[20] A. W. Overhauser, Bull. Am. Phys. Soc. **27**, No. 6, 8 (1952); R. R. Eggleston, Bull. Am. Phys. Soc. **27**, No. 6, 9 (1952).
[21] J. W. Kauffman and J. S. Koehler, Phys. Rev. **88**, 149 (1952).
[22] Calculations by J. H. Bartlett and G. J. Dienes, Phys. Rev. **89**, 848 (1953), show that the energy for motion of paired vacancies should always be less than the energy for motion of a single vacancy.

of the electrons can be estimated for a particular model by a variational procedure. By an extension along the (110) direction and a compression along the (1–10) direction, a shear without dilation may be produced. If the electron distribution is maintained uniform, the potential in regions lying between ions along the (110) direction will be decreased. Between ions along the (1–10) direction, the potential will be increased. We shall approximate this potential distribution by two mutually perpendicular standing waves,

$$V(x, y) = V_0[\cos(lx) - \cos(ly)], \tag{A1}$$

where x is measured in the (110) direction and y is measured in the (1–10) direction, and $l = 2\sqrt{2}\pi/d$ (d is the lattice constant). For our purpose it will be sufficient to consider only one of the terms in Eq. (A1). If one chooses $V_0 = 4\pi ea/\bar{P}\Omega$, where Ω is the volume per ion, then one can consider that V is the result of a varying charge distribution caused by superimposing standing waves of the form

$$\rho(x) = (e/\Omega)a\cos(lx), \tag{A2}$$

where a is seen to be the fractional variation of charge density. The stored energy per unit volume for such a charge distribution is given by

$$\tfrac{1}{2}\int_\Omega \rho(x)V(x, 0)d\tau = \frac{\pi}{\Omega}\left(\frac{ae}{l}\right)^2. \tag{A3}$$

This stored energy may be decreased by modulating the uniform electron distribution. One takes for the wave functions of the electrons in the electrostatic field

$$\psi_k' = \psi_k[1 + b\cos(lx)], \tag{A4}$$

where the ψ_k are the orthogonal, normalized electron wave functions corresponding to the original uniform distribution. Though the new wave functions are not strictly orthogonal nor normalized these defects are not serious since terms in b^2 will be neglected ($b \sim a \ll 1$). The electron charge density is now altered by

$$\Delta\rho(x) = -(e/\Omega)2b\cos(lx). \tag{A5}$$

Correspondingly, a change in potential occurs,

$$\Delta V(x) = -(8\pi be/\bar{P}\Omega)\cos(lx). \tag{A6}$$

The quantity b is determined by minimizing the sum of three terms: (1) a kinetic energy term $\hbar^2\bar{P}^2b^2/4m^*$ per electron (where m^* is the effective mass of the conduction electrons), (2) a potential term

$$\int_\Omega V(x)\rho(x)d\tau,$$

and (3) a self-potential term

$$\tfrac{1}{2}\int_\Omega \Delta V(x)\rho(x)d\tau.$$

Accordingly this sum can be written

$$E = [(\hbar l)^2/4m^* + 4\pi e^2/\bar{P}\Omega]b^2 - 4\pi abe^2/\bar{P}\Omega, \tag{A7}$$

with

$$b_{\min} = \frac{a}{2}\left[1 + \frac{(\hbar l)^2}{4m^*}\frac{\bar{P}\Omega}{4\pi e^2}\right]^{-1} \simeq 0.123a, \tag{A8}$$

where m^*/m is taken equal to 1.47. It follows that

$$\frac{E_{\min}}{4\pi e^2/\bar{P}\Omega} = -\left(\frac{a}{2}\right)^2\left[1 + \frac{(\hbar l)^2}{4m^*}\frac{\bar{P}\Omega}{4\pi e^2}\right]^{-1} \simeq -0.062a^2. \tag{A9}$$

On comparing this result with the total stored energy, Eq. (A3), which is $\pi(ae)^2/\Omega^2$, one finds that this very simple trial wave function lowers the electrostatic energy to 75 percent of its original value. Presumably more detailed variations could lower this value substantially. In addition, the effect of electron-electron correlations of any sort will tend to decrease the self-potential term and subsequently $E_{\min}$ still further. For these reasons, we have subtracted off from the experimental values of the shear moduli only $\frac{1}{2}$ the electrostatic contributions as computed by Fuchs for the uniform electron distribution,

$$c'_{11} - c'_{12} = 4.7 - \tfrac{1}{2}(0.57) = 4.42\times10^{11}\ \text{dynes/cm}^2, \tag{A10}$$
$$c'_{44} = 7.5 - \tfrac{1}{2}(2.57) = 6.22\times10^{11}\ \text{dynes/cm}^2.$$

APPENDIX B

The calculation of the electrostatic energy associated with taking an ion from infinity and putting it at an interstitial position cannot be found directly from an application of the usual Ewald method since this procedure is based on the assumption of an infinite lattice filling all space. From a physical standpoint, the difficulty arises from the unspecified dipole surface layer which raises or lowers the potential of the whole lattice by an arbitrary constant. In the text the actual dipole layer of the metal is used in incorporating the work function value into the 7.19 ev, the energy for compressing the electron gas. The actual dipole layer gives the lattice a positive bias of a few tenths ev[23] as compared to a surface situation made up of s spheres, or atomic polyhedra, where the electron distribution goes sharply from average value to zero at the polyhedra surfaces. There are two problems here: (1) to determine what surface conditions would give the reference potential of the usual Ewald function (without the $\pi e/4d$ term) and (2) to calculate the potential change in going from this surface condition to that of the atomic polyhedra.

The first question can be answered by realizing that the space summation in the Ewald calculation, which can be made to predominate by the choice of a small value for s, is equivalent to the Coulomb potential of a collection of point charges, whose magnitudes depend only on distance, immersed in a compensating uniform charge distribution of opposite sign. Such radial symmetry implies a fundamental condition, where the compensating charge stops at the surface of a sphere just large enough to enclose the exact amount of uniformly distributed charge needed to compensate the enclosed point charges.

We have not been able to demonstrate in a formal manner that the potential difference from the surface condition of the large sphere to that of the close-packed duodecahedra of the face-centered lattice is $e\pi/4d$, but a process of induction makes it seem likely. First we calculated the potentials associated with the dipole layers which arise when the polyhedron surface is cut in turn by planes (100), (110), and (111) at the proper positions to ensure electrical neutrality. These potentials turned out to be respectively 1/12, 1/6, and 1/36 in units of $\pi e/d$. Single directions, however, intercept infinitesimal area on the large sphere. To average over solid angle, one must include deviations from the exact Miller indices. As a result, the tangent plane to the sphere makes in these cases small angles s/L with the crystal planes, where s is the distance between atom planes and L the interval of periodicity along the tangent plane. The potential of the resulting dipole layer is found from Poisson's equation,

$$\nabla^2 V_s = 4\pi(4e/d^3)\tfrac{1}{2}(1 - 2x/s). \tag{B1}$$

The second factor on the right is the uniform charge density in the interior. The factor $\frac{1}{2}$ enters because regions of charge overlap and charge deficit are spread equally over the tangent plane. These regions are wedge-shaped, and the final factor takes into account their linear decreases in cross section with distance from the surface as measured by the variable x. The dipole layer potential is then obtained from Eq. (B1) integrated twice with respect to x from $-s/2$ to $s/2$, namely,

$$V_s = (2\pi e/3d)(s/d)^2.$$

When one adds this quantity to the results already found for the surface potential in the exact direction of the Miller indices, one obtains in each case ($e\pi/4d$).

A similar procedure has been applied to calculating the surface potential in a simple cubic lattice in (100), (110), and (111) directions. In each case the results were ($e\pi/6d$). For the b.c.c. lattice, different results were obtained in different directions. Possibly the situation is more complex here because the atomic polyhydra have two different kinds of faces.

[23] See work function calculations on sodium by J. Bardeen, Phys. Rev. **49**, 653 (1936).

The Electronic and Lattice Specific Heats in W, Mo, and Re*

M. HOROWITZ AND J. G. DAUNT
Department of Physics and Astronomy, Ohio State University, Columbus, Ohio

(Received May 11, 1953)

Calorimetric measurements have been made in the temperature range 1°K to 77°K on W, Mo, and Re. At the lowest temperatures for W and Mo the specific heat could be resolved into a lattice T^3 function together with an electric term, γT. It was found that at the lowest temperatures (a), for W, $\theta=250$°K to 380°K and $\gamma=(1.8\pm0.7)\times10^{-4}$ cal/mole-deg^2 (b), for Mo, $\theta=445$°K and $\gamma=(5.1\pm0.4)\times10^{-4}$ cal/mole-deg^2. These new measurements on tungsten indicate the need for revising previously quoted data.

The measured lattice specific heat of tungsten agreed approximately with the theoretical computations made by Fine. The measured lattice specific heat of molybdenum varied with temperature in the manner predicted by Fine for the body-centered cubic lattice of tungsten. The measured electronic specific heat of tungsten was in moderate agreement with the theoretical computation of Manning and Chodorow, and the measured electronic specific heats of W and Mo were considerably less than those of most other transition elements except Cr, a result which may be approximately explained by assuming a d band similar to that calculated by Slater. The question of the d-band shape is discussed in detail in the light of recent experimental results.

Pure rhenium powder has been measured in the temperature range 68°K to 77°K. At these temperatures the Debye temperature θ was found equal to 262°K.

I. INTRODUCTION

HAVING developed a satisfactory semi-automatic recording calorimeter for low temperature specific heat measurements,[1] it was considered of interest to extend its use to measurements of the specific heats of W and Mo and Re. These metals were of interest in view of the fact that previous measurements had indicated that both the lattice and electronic specific heats in W might be anomalous[2] and in view of the fact that no very low temperature measurements had been previously made on Mo or Re.

The interest in obtaining satisfactory experimental information on the lattice specific heats in metals stems from the fact that in recent years a number of detailed computations have been made of the normal modes of vibration in crystals of various structures. Our previous observations[1] on an f.c.c. structure, namely Pb, showed remarkable agreement between the experimental results and the theoretical predictions. It was therefore considered of interest to extend, as we have done, our measurements to some b.c.c. structures, as represented by W and Mo.

The determination of the electronic energy spectrum in metals is of primary importance in understanding many of their properties, and it is possible to make at least a partial approach to this determination by assessing the electronic density of states through measurements of the electronic specific heats. By making calorimetric measurements of the over-all specific heat of a metal at sufficiently low temperature, it is possible to assess the separate contributions due to the lattice and due to the electron system. It is possible therefore to obtain a great deal of information regarding diverse properties of metals from an extended and intercorrelated study of their specific heats, and the results which we report below on W, Mo, and Re are discussed in their relationship to previous data which has been gathered for other transition elements.

II. THE SPECIMENS

a. The Tungsten Specimens

Two different specimens of tungsten were employed in order to provide a check on the possible effects on their specific heats of the metallurgical processes involved in their fabrication. The first was in the form of a cylindrical rod 1.585 cm in diameter, 7.31 cm long, and of mass 271.17 grams, formed by sintering. The rod was obtained from the Fansteel Corporation, with a stated purity of 99.9 percent. It was actually the same specimen which had been previously measured by Silvidi and Daunt[2] in the liquid helium temperature region and by Horowitz[3] in the liquid hydrogen temperature region. The second specimen was formed from tungsten wire of diameter 0.0501 cm, also obtained from the Fansteel Corporation and having a stated purity of 99.9 percent. The tungsten wire was cut in pieces 5.72 cm long and packed in a cylindrical copper container of height 5.96 cm and diameter 4.44 cm, the total mass of tungsten being 790.7 grams, that of the copper container being 219.0 grams, and that of the soft solder used to seal the container being 7.3 grams. 4.84×10^{-6} moles of helium gas were introduced at room temperature into the container for exchange purposes, and the container then was sealed off. In computing the specific heats, appropriate corrections were always made for the heat capacities of the various

* Assisted by a contract between the U. S. Atomic Energy Commission and The Ohio State University Research Foundation.

[1] Horowitz, Silvidi, Malaker, and Daunt, Phys. Rev. **88**, 1182 (1952).

[2] A. A. Silvidi and J. G. Daunt, Phys. Rev. **77**, 125 (1950).

[3] M. Horowitz, Master-of-Science thesis, Ohio State University, 1950 (unpublished).

TABLE I. Data on specific heat of tungsten.

T°K	ΔT°K	C_p cal/mole-deg
Wire at liquid hydrogen temperatures		
20.13	0.313	0.0813
19.84	0.310	0.0866
19.51	0.322	0.0803
19.17	0.338	0.0637
18.86	0.284	0.0626
18.57	0.306	0.0604
18.26	0.306	0.0592
18.02	0.188	0.0454
17.83	0.160	0.0431
17.67	0.169	0.0494
17.50	0.144	0.0518
16.83	0.154	0.0466
16.68	0.145	0.0373
16.53	0.142	0.0345
16.40	0.137	0.0400
16.30	0.0798	0.0418
16.24	0.112	0.0423
16.14	0.0913	0.0425
16.04	0.0983	0.0399
15.94	0.1020	0.0385
15.84	0.1200	0.0395
15.73	0.0932	0.0348
15.64	0.0862	0.0414
15.54	0.0836	0.0402
15.47	0.0813	0.0332
15.37	0.1090	0.0325
15.27	0.0810	0.0321
15.19	0.0982	0.0350
Wire at liquid helium temperatures		
4.180	0.185	0.00257
4.021	0.158	0.00243
3.750	0.130	0.00185
3.607	0.108	0.00170
3.474	0.0885	0.00143
3.341	0.103	0.00162
3.262	0.0858	0.00134
3.185	0.0809	0.00134
3.102	0.0660	0.00122
2.483	0.0506	0.000933
2.387	0.0360	0.000781
2.340	0.0344	0.000848
2.290	0.0268	0.000763
2.125	0.0253	0.000622
2.059	0.0254	0.000656
Rod at liquid helium temperatures		
4.043	0.465	0.00197
2.922	0.240	0.000913
2.733	0.182	0.000896
2.717	0.145	0.000983
2.503	0.169	0.000758
2.270	0.100	0.000599

foreign materials in the specimen and of the heater and thermometer elements.

b. The Molybdenum Specimen

The molybdenum specimen, obtained from the Fansteel Corporation, of purity 99.9 percent, was in the form of a cylinder of height 6.37 cm and diameter 4.11 cm, the total mass being 825.7 grams.

c. The Rhenium Specimen

High purity rhenium powder was obtained on loan from the Department of Chemistry of the University of Tennessee through the kindness of Dr. A. D. Melaven. 107.9 grams of this rhenium powder, of stated purity 99.8 percent, were placed in a copper container of mass 84.9 grams together with 1.02×10^{-5} moles of helium gas for exchange purposes, and the container was sealed off at room temperature. 4.8 grams of solder were used in sealing up the container.

III. EXPERIMENTAL PROCEDURES

The specific heats of all the specimens were measured using the same adiabatic calorimeter as described previously by us.[1] The electrical heaters on the specimens were wound from manganin wire of diameter 0.0079 cm. All the measurements of temperature, except those on the tungsten rod, were made using 10-ohm carbon radio resistors, as we have successfully

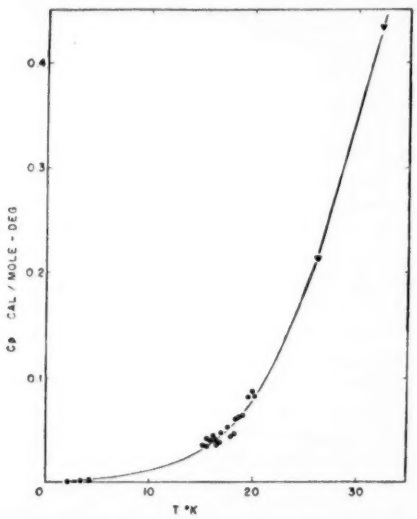

FIG. 1. The specific heat of tungsten below 32°K. ● Our observations. ▼ Lange (reference 6).

employed previously[1] and as have been described by Clement and Quinnell[4] and by Brown, Zemansky, and Boorse.[5] The resistance thermometer used with the tungsten rod specimen was a leaded phosphor-bronze wire of diameter 0.00508 cm and resistance 17.0 ohms at 0°C.

The same semi-automatic temperature recording system was employed as that used previously by us in specific heat measurements on Pb,[1] a system which we have found provides high accuracy of measurement. In the measurements the temperature differences between the specimen and its surroundings were always kept less than 0.3°K, a feature which minimized unwanted heat flows to and from the specimen.

[4] J. R. Clement and E. H. Quinnell, Rev. Sci. Instr. **23**, 213 (1952).
[5] Brown, Zemansky, and Boorse, Phys. Rev. **84**, 1050 (1951).

IV. RESULTS

Our results for C_p for tungsten, molybdenum, and rhenium are given in Tables I, II, and III respectively. The temperature given in the first columns is the average temperature of each measurement and ΔT is the observed temperature rise.

A graph showing the specific heat of tungsten in the range 1°K to 32°K is given in Fig. 1. The points shown in the figure for temperatures below 21°K are taken from our present results and those above 21°K are from Lange's measurements made in 1924.[6] It will be seen that a smooth curve, showing no indications of any anomalies, can be drawn through all the points. Moreover, the measurements reported here in the liquid hydrogen temperature range are in general agreement with unpublished data obtained earlier by one of us.[7]

Our results below 5°K are graphically displayed in Fig. 2 which plots C_v/T *versus* T^2 and it will be seen

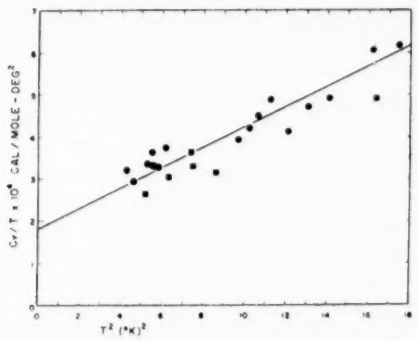

FIG. 2. C_v/T *versus* T^2 for tungsten below 5°K. ● Our observations on wire specimen. ■ Our observations on rod specimen.

that, although there is some scatter, these results do not refute the possibility which one expects theoretically that C_v/T should be a linear function of T^2. These results, together with the previous measurements[3] in the liquid hydrogen temperature range, indicate that there is no systematic difference in the specific heats of the two different forms of tungsten used.

Our results for molybdenum are shown in Fig. 3, which plots C_v/T *versus* T^2. If these results, together with the earlier measurements of Simon and Zeidler,[8] are plotted on a more extensive temperature scale than that given in Fig. 3, it will be found that a smooth curve with no indications of anomalies can describe all the data.

The results for rhenium in the temperature range 68°K to 77°K are shown in Fig. 4. We were unable to obtain satisfactory specific heat measurements in the liquid helium and liquid hydrogen temperature range on the rhenium specimen owing, it is thought, to the rather long relaxation times necessary for the establishment of temperature equilibrium in the powder.

V. INTERPRETATION OF RESULTS

a. Tungsten

If it is supposed that at sufficiently low temperatures the specific heat can be written as[9]

$$C_p = C_v = 464.4(T/\theta)^3 + \gamma T \text{ cal/mole-deg}, \quad (1)$$

where the first term represents the lattice specific heat and the second term that of the electrons, then a plot of C_v/T *versus* T^2 should yield a straight line, the intercept of which with the ordinate axis should yield the numerical value of γ.

TABLE II. Data on specific heat of molybdenum.

T°K	ΔT°K	C_p cal/mole-deg
10.445	0.488	0.0125
9.910	0.574	0.0107
9.429	0.263	0.00915
9.179	0.344	0.00880
4.873	0.0915	0.00293
4.769	0.0824	0.00295
4.603	0.0831	0.00259
4.495	0.0618	0.00279
3.478	0.0689	0.00200
2.980	0.0688	0.00162
2.878	0.0618	0.00148
2.741	0.0543	0.00153
2.523	0.0503	0.00145
2.412	0.0467	0.00141
1.420	0.0229	0.000742
1.392	0.0233	0.000724
1.365	0.0149	0.000742
1.339	0.0141	0.000692

TABLE III. Data on specific heat of rhenium.

T°K	ΔT°K	C_p cal/mole-deg
At liquid nitrogen temperatures		
77.1	0.363	3.29
76.9	0.285	3.49
71.9	0.885	3.27
70.9	0.785	3.35
70.2	0.369	3.37
70.0	0.317	3.10
69.7	0.388	3.19
69.4	0.373	3.23
69.0	0.303	3.23
68.6	0.335	3.26
68.0	0.267	3.15

[6] F. Lange, Z. Physik. Chem. **110**, 343 (1924).

[7] This earlier work by M. Horowitz (see reference 3) was undertaken partly to investigate the possible influence of an externally applied magnetic field on the specific heat of W between 10°K and 20°K. No evidence of any influence of fields up to 5200 gauss was observed.

[8] F. Simon and W. Zeidler, Z. Physik. Chem. **123**, 383 (1926).

[9] For the range of temperature discussed in this paper ($T<80$°K), C_p is equal to C_v in metals with high accuracy. The largest difference between C_p and C_v occurring in the present work is for Re at 75°K where the difference amounts only to 0.1 percent of C_p. In the discussion that follows, therefore, C_p and C_v are used indiscriminately.

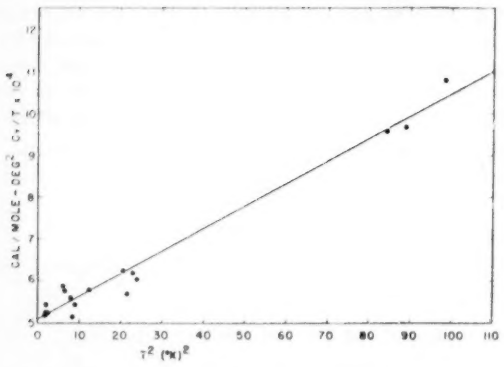

FIG. 3. C_v/T *versus* T^2 for molybdenum below 10°K.

Such a plot of C_v/T *versus* T^2 from our results on tungsten is shown in Fig. 2. Here it will be seen that, if a straight line drawn through the observed points, then a numerical value of γ of 1.8×10^{-4} cal/mole-deg^2 can be obtained. Owing, unfortunately, to the scatter of the points, the value of γ cannot be stated with an accuracy greater than $\pm0.7\times10^{-4}$ cal/mole-deg^2. Our results indicate, however, that the value of γ could not be much greater than 2.5×10^{-4} cal/mole-deg^2, a value which is very much smaller than that reported previously by Silvidi and Daunt.[2] Owing to the more accurate semiautomatic temperature recording instrumentation used for our present observations, we feel that the present results are the more trustworthy.

In order to describe the variation of the lattice

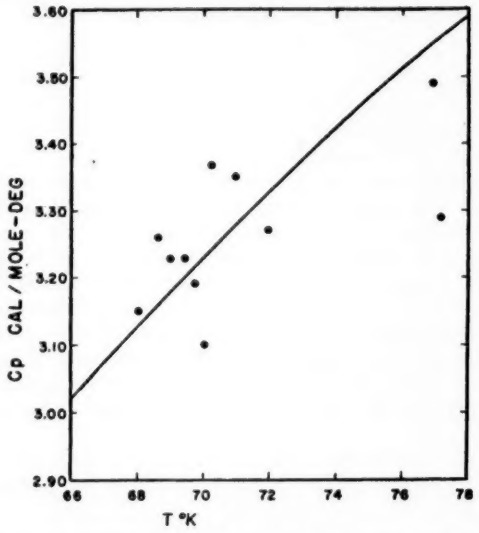

FIG. 4. The specific heat of rhenium at liquid nitrogen temperatures. ● Our observations. ——— Fitted Debye curve ($\theta=262$°K).

specific heat with temperature, we have computed the characteristic Debye θ temperatures corresponding to each measured point. In doing this the electronic specific heat was first subtracted off the observed total specific heat, and then the Debye θ value obtained by comparing the remainder with the tabulated Debye function.[10] The results of these computations for tungsten are shown in Fig. 5, in which the values due

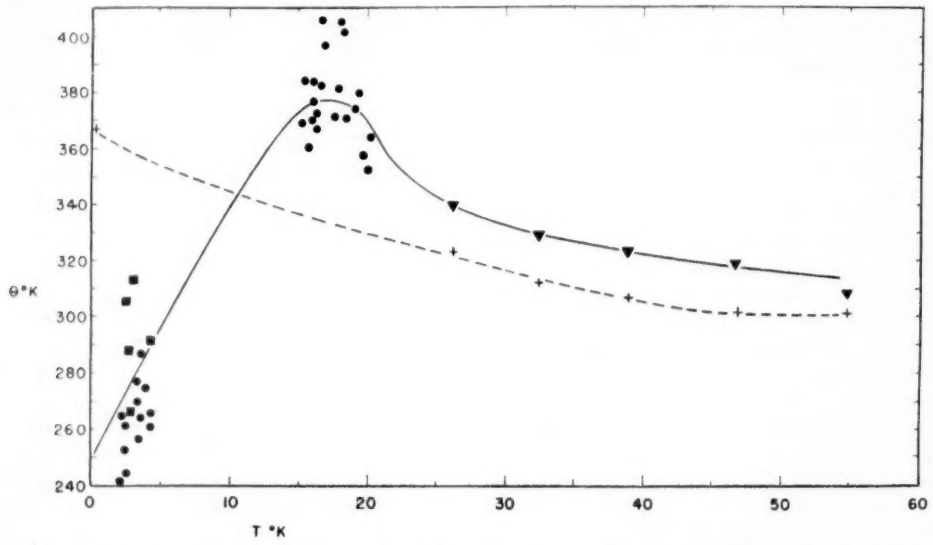

FIG. 5. Debye temperature for tungsten below 55°K. ● Our observations on wire specimen. ■ Our observations on rod specimen. ▼ Lange (reference 6). – – – + – – – Theory (fine, atomic model, reference 20). —Best fit measured points.

[10] P. Debye, Ann. Physik 39, 789 (1912).

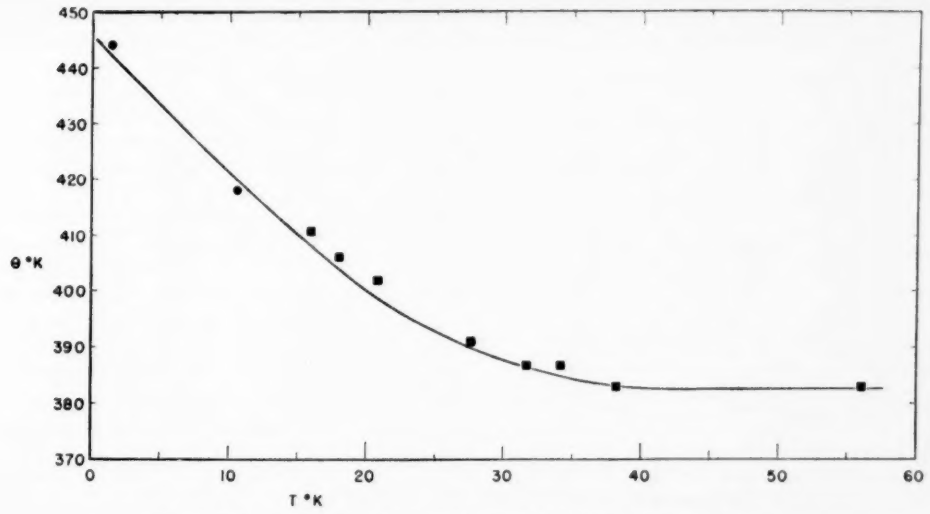

FIG. 6. Debye temperatures for molybdenum below 60°K. ● Our observations. ■ Simon and Zeidler (reference 8).

to Lange[6] in the temperature range 25°K to 55°K are also included. Our results for the tungsten rod and for the tungsten wire specimen, indicated by the squares and circles respectively, show some scatter. In the helium temperature range, where the scatter is most apparent, it must be remembered that relatively small variations in the chosen γ value will yield large variations in the Debye θ value.[11] The scatter, therefore, is a reflection of the uncertainty in the γ value for the electronic specific heat. In Fig. 5 the full curve indicates the best fit through the measured points and shows that the Debye θ value rises from a value of about 250°K at absolute zero to a maximum at about 18°K of approximately 375°K and then falls slowly and continuously to an approximately temperature independent value of 320°K at 55°K. This variation of the Debye θ values with temperature follows the general predictions given by Blackman[12] and is discussed in more detail in Sec. VI.

b. Molybdenum

The curve for C_v/T *versus* T^2 for molybdenum shown in Fig. 3 appears adequately linear to enable an estimate to be made of the electronic γ value by linear extrapolation to the absolute zero. By so doing we assess the γ value to be 5.1×10^{-4} cal/mole-deg$^2\pm0.4\times10^{-4}$ cal/mole-deg^2.

The Debye θ values for the lattice specific heat of molybdenum have been computed from the observed results in the manner described above for tungsten and the smoothed results are shown in Fig. 6. In obtaining the data for Fig. 6 we used both our own results described in this paper and the specific heat data above 15°K previously reported by Simon and Zeidler.[8] The curve in Fig. 6 indicates that the Debye θ value has its highest value at about 445°K at the absolute zero and that as the temperature increases the θ value decreases monotonically and appears to reach a steady temperature independent value of about 383°K at 55°K.

c. Rhenium

The points of Fig. 4 show the observed values of C_v for rhenium as a function of temperature, and the full curve represents what would be expected from Debye's theory for a θ value of 262°K. This value of $\theta=262$°K is somewhat lower than the value obtained by Meissner[13] of 310°K from resistance measurements. It is in agreement, however, with the value of 275°K which can be

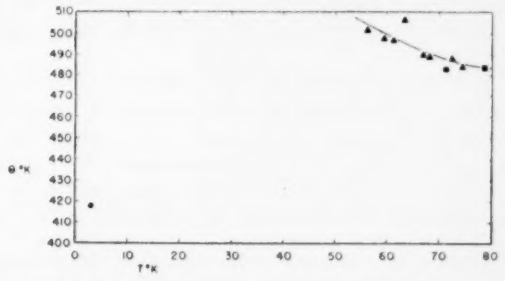

FIG. 7 Debye temperatures for chromium below 80°K. ● Estermann, Friedberg, and Goldman (reference 17). ▲ Anderson (reference 16). ■ Simon and Ruhemann (reference 15).

[11] If, for example, a value of $\gamma=2.5\times10^{-4}$ cal/mole-deg^2 were chosen instead of 1.8×10^{-4} cal/mole-deg^2, then the θ values would increase and center about 380°K.

[12] M. Blackman, Repts. Progr. Phys. 8, 11 (1941).

[13] W. Meissner, *Handbuch der experimentalphysik* (Akademische Verlagsgisellschaft, Leipzig, 1935), Vol. 11/2, p. 50.

TABLE IV. Calorimetric data for the transition elements.

No. of valence electrons	4	5	6	7	8	9	10
Element	Ti	V	Cr	Mn	Fe	Co	Ni
Crystal structure	h.c.p.	b.c.c.	b.c.c.	complex	b.c.c.	f.c.c.	f.c.c.
γ cal/mole-deg$^2\times10^4$	8.0(1.1)[a]	15(22.2)	3.80	42	12.0	12.0	17.4
θ°K	280	326	418	410[b]	464	443	413
Melting point °K	2073	1988	2070	1533	1812	1768	1728
Element	Zr	Nb	Mo	Tc	Ru	Rh	Pd
Crystal structure	h.c.p.	b.c.c.	b.c.c.	h.c.p.	h.c.p.	f.c.c.	f.c.c
γ cal/mole-deg$^2\times10^4$	6.92(3.92)[c]	21	5.1	–	3.04	–	31.0
θ°K	265	254	445	–	426	370	275
Melting point °K	1973	2223	2893	–	2723	2239	1828
Element	Hf	Ta	W	Re	Os	Ir	Pt
Crystal structure	h.c.p.	b.c.c.	b.c.c.	h.c.p.	h.c.p.	f.c.c.	f.c.c.
γ cal/mole-deg$^2\times10^4$	–	14.1	1.8–2.5	4.6	2.7	–	16.0
θ°K	213	264	250–380	262	256	285	233
Melting point °K	2480	3123	3673	3713	2973	2727	2046

[a] Value of 1.1 obtained from magnetic measurements on superconducting Ti.[28]
[b] 410°K given by Elson *et al.* (reference 31). Shomate (reference 32) and Kelly (J. Am. Chem. Soc. **61**, 203 (1939)), from measurements above 54°K, give $\theta = 344$°K.
[c] Value of 3.92 obtained from magnetic measurements on superconducting Zr.[29]

deduced from the recent calorimetric observations of Cobble, Smith, and Oliver.[14]

Owing to the relatively small range of temperature over which we took our measurements, no significant estimate can be made of the possible variation of θ with temperature.

VI. DISCUSSION

a. The Lattice Specific Heats of W, Mo, and Cr

It is of interest to consider together the lattice specific heats of W, Mo, and Cr since they all fall in the same group VI of the Periodic Table and since they are all b.c.c. structures.

Whereas the experimental data on W and Mo is reported above (see Figs. 5 and 6), that on Cr has previously been given by Simon and Ruhemann[15] and by Anderson[16] for temperatures above 55°K and by Estermann, Friedberg, and Goldman[17] for the liquid helium temperature range only. Unfortunately, no data are available for the temperature range between 4°K and 55°K. Figure 7 shows the Debye θ values as a function of temperature for Cr taken from these references.

In a previous paper, reporting measurements of the specific heat of Pb, we showed that there was excellent agreement between the measured lattice specific heat over a broad range of temperature from 1°K to 80°K and the computed values of the same quantity, the computations being made by Leighton[18] from estimates of the normal modes of vibration of the lattice. Leighton himself showed that for another f.c.c. structure, namely Ag, the agreement between theory and experiment was satisfactory.[19] It is considered of interest therefore to compare such theoretical computations for b.c.c. structures as there are of the variation of θ with temperature, with our experimental results.

The only detailed computations of the normal modes of vibration for a b.c.c. structure are those of Fine[20] for W. These computations are based on the known elastic constants of single crystals of W, as measured by Bridgman.[21] The results of these calculations are shown by the broken curve of Fig. 5. It will be seen that the curve starts from a value of 367°K at 0°K and falls monotonically with increasing temperature to a constant value of approximately 300 at 55°K.

Although the elastic constants for Mo are known,[22] it is not immediately possible to make the necessary computations in view of the fact that the crystal is elastically markedly nonisotropic.[23] The elastic constants for single crystals of Cr are not known.

A computation of the θ value for Mo, using Debye's theory, however, can be made using the known elastic constants[22] and the measured compressibility, and this yields a value of 495°K. This is somewhat larger than our measured values, even at the lowest temperatures.

The comparison between the theory and experiment for the lattice specific heat in W shown in Fig. 5 indicates considerable disagreement at temperatures below

[14] Private communication from Dr. J. W. Cobble [J. Am. Chem. Soc. (to be published)].
[15] F. Simon and M. Ruhemann, Z. Physik. Chem. **129**, 321 and 338 (1927).
[16] C. T. Anderson, J. Am. Chem. Soc. **59**, 488 (1937).
[17] Estermann, Friedberg, and Goldman, Phys. Rev. **87**, 582 (1952) and Phys. Rev. **85**, 375 (1952).
[18] R. B. Leighton, Revs. Modern Phys. **20**, 165 (1948).
[19] The apparent deviations at about 6°K reported by Leighton have subsequently been essentially removed by the more recent experimental observations of the specific heat of Ag by Keesom and Perlman in this temperature region. [See P. H. Keesom and N. Pearlman, Phys. Rev. **88**, 141 (1952).]
[20] P. C. Fine, Phys. Rev. **56**, 355 (1939).
[21] P. W. Bridgman, Proc. Nat. Acad. Sci. U. S. **10**, 411 (1924).
[22] M. J. Druyvesteyn, Physica **8**, 439 (1941).
[23] For a recent discussion of anisotropy in metals see W. Boas and J. K. Mackenzie. Progr. Metal Phys. **2**, 90 (1950).

about 20°K. This disagreement however may not be as serious as it appears. As pointed out in Sec. V above, there is a considerable latitude in the choice of the γ value and in consequence there is also considerable latitude in the chioce of the appropriate θ value in the liquid helium temperature range. If, for example, the correct γ value were 2.5×10^{-4} cal/mole-deg,[2] instead of the value of 1.8×10^{-4} chosen earlier, then the θ values would all be considerably increased, and would center about 380°K. This would be in agreement with the theoretical value of Fine.

On the other hand the measurements on Cr, shown in Fig. 7, indicate that the θ values at the lowest temperature fall considerably below what one might expect by extrapolation of the higher temperature values. The apparent maximum in the θ *versus* T curves in Cr and W may therefore be real and may indicate the necessity for further refinement of the theory. The measured θ values for Mo, as shown in Fig. 6, increase monotonically with decreasing temperature to the lowest possible temperatures of observation. It seems therefore that it may not be possible to represent the variation of the lattice specific heat with temperature in these three very similar b.c.c. structures by any general function.

b. The Electronic Specific Heats

Measurement of the electronic specific heats is of interest in that it provides information on the values of the density of states, $N(E)$. The relation between the electronic specific heat, C_{el}, and $N(E)$ is

$$C_{el}=\gamma T=\tfrac{2}{3}\pi^2k^2N(E)T \text{ cal/deg-cm}^3, \qquad (2)$$

where $N(E)$ is the number of electronic energy states per unit energy range per cm³ at the Fermi level.

In the transition metals, a large contribution to C_{el} is provided by the positive holes in the d band, as was first pointed out by Mott.[24] It is of interest therefore to discuss the evaluations of γ and hence of $N(E)$ for the transition series of metals in order to obtain some picture of the shape of the d bands. The γ values which we have observed in W and Mo are set out, together with those of other transition metals in Table IV. This table, which represents a section of the Periodic Table also displays other measured parameters of interest for each element. The data used in this table have been taken mostly from previous partial compilations by author (J.G.D.),[25–27] which give the references to the original sources. New data have been included as follows: Ti,[28] Zr,[29] Cr,[17] Ru,[30] Os.[30] The γ values quoted in the table for Re, Ru, and Os are somewhat doubtful since it is not certain how reversible were the magnetic superconductive transition curves from which the γ values were computed. It would be of value to have calorimetric measurements carried out on the elements of doubtful γ value listed above, as well as on Tc, Rh, Hf, and Ir.

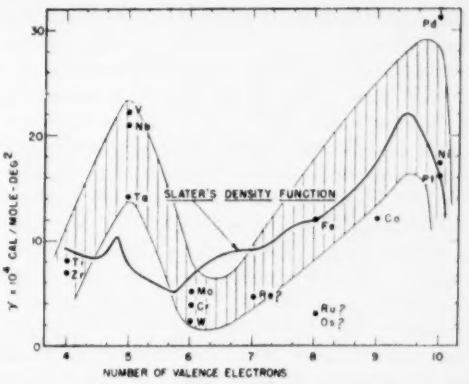

FIG. 8. Electronic specific heats of the transition elements.

All the known experimental results (with the exception of the γ value for Mn) are plotted in Fig. 8 as a function of the total number, n, of "valence" electrons. As is indicated by the shaded areas, the γ values, and hence the $N(E)$ curve, show two distinct maxima as the d band is steadily filled up. Moreover, this general picture is probably valid for all three series of transition elements.

The first maximum occurs for $n=5$, i.e., for V, Nb, and Ta, and the second maximum is at the end of the series for Ni, Pd, and Pt. The value of $\gamma=42\times10^{-4}$ cal/mole-deg² obtained by Elson, Grayson-Smith, and Wilhelm[31] from measurements in the relatively high temperature range of from 15°K to 22°K seems to lie well outside these considerations, and remains unexplained.[32]

It is of interest to note the low minimum exhibited at $n=6$ for Cr, Mo, and W and to compare the measured γ value for W with the value of 4.8×10^{-4} cal/mole-deg² computed by Manning and Chodorow[33] from a d-band structure computation.

[24] N. F. Mott, Proc. Phys. Soc. (London) **47**, 571 (1935). See also N. F. Mott and H. Jones, *The Theory of the Properties of Metals and Alloys* (Oxford University Press, London, 1936).
[25] A. A. Silvidi and J. G. Daunt, Phys. Rev. **77**, 125 (1950).
[26] J. G. Daunt, Phys. Rev. **80**, 911 (1950).
[27] J. G. Daunt and T. S. Smith, Phys. Rev. **88**, 309 (1952).
[28] Smith, Gager, and Daunt, Phys. Rev. **89**, 654 (1953).
[29] T. S. Smith and J. G. Daunt, Phys. Rev. **88**, 1172 (1952).
[30] B. B. Goodman, Nature **167**, 111 (1951).
[31] Elson, Grayson-Smith, and Wilhelm, Can. J. Research **18**, 82 (1940).
[32] These measurements were made on so-called "powdered manganese" of unstated purity and of unstated phase. It is possible to have both the α and γ phases stable at low temperatures; [see, e.g., C. H. Shomate, J. Chem. Phys. **13**, 326 (1945)]. The stability of the latter being assisted on an admixture of impurities. The specific heat of the α phase is known to be anomalous (see Shomate above), due probably to the transition to antiferromagnetism at about 100°K as observed by Shull [C. G. Shull and M. K. Wilkinson, Phys. Rev. **86**, 599 (1952)], and this may be a contributory factor in the apparent high γ value. It would be of value to have calorimetric measurements made in the liquid helium temperature region both on α and γ Mn.
[33] M. F. Manning and M. I. Chodorow, Phys. Rev. **56**, 787 (1939).

The probable shape of the $N(E)$ curve illustrated by the shaded areas of Fig. 8 confirms in broad outline the theoretical computation by Krutter[34] and by Slater[35] of the 3d band in Cu. Slater's curve is shown also in Fig. 8, normalized arbitrarily to fit the measured Fe point at $n=8$. Computations subsequently made of the energy band structure by Manning and Chodorow[33] for W, by Manning[36] for Fe (b.c.c.), and by Fletcher and Wohlfarth[37] for Ni also indicate the existence of a second maximum at the smaller n values. In the $N(E)$ curve given by the latter authors this is most marked.

In making such general $N(E)$ curves, as we have given in Fig. 8 by the shaded area, its very approximate nature must be borne in mind, since some modifications must be necessary in going from one crystal structure to another. It is very likely, however, that these modifications would not alter greatly the general picture of the maxima in the curves, but rather as a first approximation affect only the band width, as has been pointed out by Smoluchowski.[38]

The observed low values of γ for all three transition metals of Group 6, namely Cr, Mo, and W, may simply reflect the minimum existing here in the $N(E)$ curve. This view has also been adopted recently by Kriessman,[39] who supports it from his observation of the positive temperature coefficient of the magnetic susceptibility in these metals. An alternative explanation of the low γ values has been suggested by Estermann *et al.*[17] They noted Zener's observation[40] that Cr may be antiferromagnetic and hence have its d band split, as was shown to be a general requirement for antiferromagnetism in such metals by Slater,[41] into a filled half and an unfilled half. The filled half would not be able to contribute to the specific heat and hence a low γ value would result. Antiferromagnetism, with a Néel temperature of about 150°C, has indeed been observed by Shull and Wilkinson[42] from neutron diffraction studies. However, they observed no antiferromagnetism in either Mo or W even down to temperatures as low as 20°K, and hence one must conclude that the explanation put forward by Estermann *et al.*[17] for the low γ value of Cr is not generally operative for all the transition metals of Group 6.

One final point should be mentioned, namely the possibility of there being a third maximum in the $N(E)$ curve at $n=7$, i.e., for the Group 7 transition metals Mn, Tc, and Re. In the rough drawing of the $N(E)$ curve of Fig. 8 this possibility has not been included. It should be noted that, besides the unexplained high γ value for Mn,[32] the temperature coefficients of the magnetic susceptibility of Mn and Tc are negative.[43] This could mean, as pointed out by Kriessman,[39] that the γ values are passing through a maximum. Against this, however, the magnetic susceptibility of Re is known to be temperature independent,[44] thereby disposing of the requirement of a maximum in the $N(E)$ curve for this metal. Exact calorimetric measurements on these metals to liquid helium temperatures are therefore highly desirable.

This work was supported in part from funds granted to The Ohio State University by The Ohio State University Research Foundation for aid in fundamental research, for which we are grateful. Our thanks go also to Doctor B. Kaplan for his generous help during the experiments.

[34] H. M. Krutter, Phys. Rev. **48**, 664 (1935).
[35] J. C. Slater, Phys. Rev. **49**, 537 (1936).
[36] M. F. Manning, Phys. Rev. **63**, 190 (1943).
[37] G. C. Fletcher and E. P. Wohlfarth, Phil. Mag. **42**, 106 (1951).
[38] R. Smoluchowski, "Ferromagnetismet Antiferromagnetisme," Proc. Grenoble Conference, 241 (1950).
[39] C. J. Kriessman, Revs. Modern Phys. **25**, 122 (1953).
[40] C. Zener, Phys. Rev. **81**, 440 (1951).
[41] J. C. Slater, Phys. Rev. **82**, 538 (1951).
[42] C. G. Shull and M. K. Wilkinson, Phys. Rev. **86**, 599 (1952).
[43] C. M. Nelson, Ph.D. dissertation University of Tennessee, 1952 (unpublished). We are grateful to Doctor Nelson for allowing us to see the results of this work before its publication.
[44] N. Perakis and L. Capatos, J. phys. et radium **6**, 462 (1935). See also reference 43 for further confirmation.

Mechanism of Transition in Magnetite at Low Temperatures*

H. J. WILLIAMS, R. M. BOZORTH, AND MATILDA GOERTZ
Bell Telephone Laboratories, Murray Hill, New Jersey

(Received May 7, 1953)

When magnetite is cooled through −160°C it is known to undergo a transition (cubic to orthorhombic) that is influenced by the presence of a magnetic field. Our experiments are in agreement with the following mechanism of the transition: The orthorhombic c axis is parallel to one of the original cubic axes and is the axis of easiest magnetization. Generally, different regions of the original crystal will transform with their c axes lying along different cubic axes, and when no field is applied there are 6 different orientations which different regions assume. When a field is applied during cooling a c axis tends to lie along the original cubic axis that is nearest to the applied field, the a and b axes having less but different tendencies to lie parallel to the field.

Six magnetic crystal anisotropy constants are derived from torque curves measured in the (100) and (110) planes. From them magnetization curves are calculated for the [100] and [110] directions, and these are in agreement with experiment.

THE existence of a transition in magnetite at about 120°K was evident in 1929 from the work by Weiss and Forrer[1] and of Millar,[2] who made measurements of magnetization and of specific heat, respectively. A mechanism was proposed in 1939 by Verwey,[3] who suggested that below the transition the Fe^{++} and Fe^{+++} ions form an ordered lattice, while at higher temperatures disorder is produced by the movement of electrons between the iron ions.

As pointed out by Verwey and de Boer,[4] conductivity and x-ray measurements on magnetite indicate that it has the inverse spinel structure first determined in $MgFe_2O_4$ by Barth and Posnjak;[5] in magnetite eight Fe^{+++} ions occupy the tetrahedral or "A" positions, while eight Fe^{+++} and eight Fe^{++} occupy the sixteen octahedral or "B" positions in the cubic unit of structure. This has recently been confirmed by Shull, Wollan, and Koehler[6] using neutron diffraction. When ordering of the octahedral Fe^{+++} and Fe^{++} ions occurs at low temperatures, the structure loses its cubic symmetry. Although Verwey, Haayman, and Romeijn[7] described the symmetry of the proposed ordered structure as tetragonal, Bickford[8] pointed out that it is orthorhombic, and this has been confirmed by his own measurements[9] of the strains occurring during the transformation and by the x-ray measurements of Abrahams and Calhoun[10] ($a=5.912, b=5.945, c=8.388$A, at 78°K). The first detection of noncubic symmetry by x-rays was by Tombs and Rooksby[11] who interpreted their results as showing rhombohedral symmetry, but this appears to be inconsistent with the later x-ray work and with the results of Bickford[9] and of Williams and Bozorth.[12]

Li[13] first showed that the direction of easy magnetization in a single crystal below the transition temperature is influenced by the direction of the field present during the cooling through the transition. Verwey, Haayman, and Romeijn[7] interpreted Li's results as showing that the magnetic field caused one of the cubic axes to become the easy direction of the transformed crystal, and this interpretation has been strongly supported by Bickford's[8] and our results.[12] One of the orthorhombic axes was thus assumed to be parallel to one of the original cubic axes; the probable positions of the other axes and a method of checking them were worked our by Elizabeth A. Wood of these Laboratories and by L. R. Bickford during a discussion of the latter's strain gauge measurements and our preliminary torque measurements. The relative positions of the axes are shown in Fig. 1. This mode of transformation has now been confirmed by further measurements of Bickford[9] and by our present work.

Our work has been to measure the crystal anisotropy below the transition, which took place in the presence of a magnetic field oriented in various directions in the (100) and (110) planes of the crystal. (All indices refer to the original cubic axes.) The six anisotropy constants of the orthorhombic crystal were determined from the torque curves and show a high crystal anisotropy (see Fig. 7) of the same order as that deduced by Bickford[14] from his microwave measurements and from Domenicali's[15] magnetization curves. These magnetization curves, measured in the [100] and [110] directions in single crystals at low temperatures, are in accord with such curves calculated from our anisotropy constants.

* Reported in part at the Washington Conference, September, 1952. See reference 12.

[1] P. Weiss and R. Forrer, Ann. phys. [10], **12**, 279 (1929).
[2] R. W. Millar, J. Am. Chem. Soc. **51**, 215 (1929).
[3] E. J. W. Verwey, Nature **144**, 327 (1939).
[4] E. J. W. Verwey and J. H. de Boer, Rec. trav. chim. **55**, 531 (1936).
[5] T. F. W. Barth and E. Posnjak, Z. Krist. **82**, 325 (1932).
[6] Shull, Wollan, and Koehler, Phys. Rev. **84**, 912 (1951).
[7] Verwey, Haayman, and Romeijn, J. Chem. Phys. **15**, 181 (1947).
[8] L. R. Bickford, Phys. Rev. **78**, 449 (1950).
[9] L. R. Bickford, Revs. Modern Phys. **25**, 75 (1953).
[10] S. C. Abrahams and B. A. Calhoun, Acta Cryst. **6**, 105 (1953).
[11] N. C. Tombs and H. P. Rooksby, Acta Cryst. **4**, 474 (1951).
[12] H. J. Williams and R. M. Bozorth, Revs. Modern Phys. **75**, 79 (1953).
[13] C. H. Li, Phys. Rev. **40**, 1002 (1932).
[14] L. R. Bickford, Laboratory for Insulation Research, Massachusetts Institute of Technology Report 23, 1949 (unpublished).
[15] C. A. Domenicali, Phys. Rev. **78**, 458 (1950).

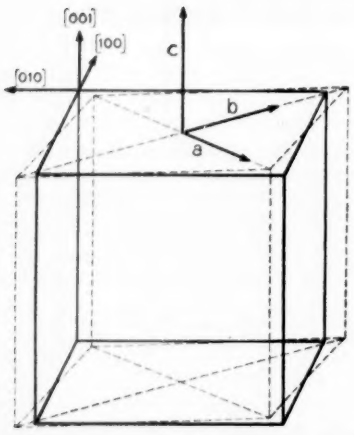

FIG. 1. Mode of transformation of cubic to orthorhombic crystal: orthorhombic c axis parallel to original cubic [100], orthorhombic a and b axes at 45° to other cubic axes.

The single anisotropy constant of cubic magnetite at room temperature was also determined and compared with the value determined by Bickford[8] from his experiments on microwave resonance. This constant can be compared with the high coercive force observed by Gottschalk[16] in finely powdered material.

EXPRESSIONS FOR ANISOTROPY

As shown in Fig. 1, the orthorhombic c axis in Fe_3O_4 is parallel to a cubic axis of the original crystal, and the a and b axes lie at about 45° to the cubic axes in the (001) plane. Accordingly we have chosen these orthorhombic axes to describe the magnetic anisotropy. The magnetic anisotropy energy density is then given to the second approximation by the relation

$$E=K_a\sin^2\theta_a+K_a'\sin^4\theta_a+K_b\sin^2\theta_b+K_b'\sin^4\theta_b+K_c\sin^2\theta_c+K_c'\sin^4\theta_c, \quad (1)$$

in which θ_a, θ_b, and θ_c are the angles between the direction of the saturation magnetization and the orthorhombic a, b, and c axes, respectively. Our early results showed that three constants are not sufficient. Cross products involving two θ's are neglected, but their inclusion might have led to better agreement between calculated and observed torque curves. It should be pointed out that our a and b axes may be interchanged with respect to the crystallographic axes, which by convention are such that the dimensions of the unit cell are $a<b<c$.

When the crystal transforms on cooling there will be six possible orientations which an orthorhombic crystal may have with respect to the original crystal axes. It is assumed in our study of a natural crystal that when no field is applied during cooling, various portions transform into all of the six possible orientations. When the crystal is heated again to room temperature, the magnetic data show that a single cubic crystal is again formed, consequently one crystal can be repeatedly cooled and heated through the transformation without deterioration.

The magnetic torque curves discussed below indicate that the direction of easy magnetization at low temperatures is the c axis. Consequently it is assumed that, when the specimen is cooled with a strong magnetic field parallel to a cubic axis, this becomes a c axis. In this case orthorhombic crystals of two orientations would be formed, corresponding to the 2 alternative positions of the a and b axes. (See the Appendix and Fig. 10.) When the cooling field is applied parallel to a cubic direction [110] there are 2 possible positions of the c axis, each with 2 positions of the a and b axes, or 4 positions in all, as shown in Fig. 11. Similarly, when the cooling field is parallel to [111] there are 6 positions to be considered, of which 3 are selected as being most probable because of energy considerations, as discussed below (see Fig. 12).

Measurements were made of the torque exerted on crystals of disk form cut parallel to (100) and (110) planes, when cooled in fields parallel to [001] in (100), and parallel to [001], [1$\bar{1}$0], and [1$\bar{1}$1] in (110). The expressions for the torque under these four conditions are derived in the Appendix and are as follows, where H_T designates the field present during the cooling through the transformation and θ is the angle measured in the given plane between the [001] direction and the saturating field used for measurement of torque:

(1) $H_T\|[001]$ in (100):

$$L_1=\tfrac{1}{4}(2K_a+2K_b-4K_c+3K_a'+3K_b'-4K_c')\sin2\theta+\tfrac{1}{8}(K_a'+K_b'+4K_c')\sin4\theta; \quad (2)$$

(2) $H_T\|[001]$ in (110):

$$L_2=(K_a-K_c+K_a'-K_c')\sin2\theta+\tfrac{1}{2}(K_a'+K_c')\sin4\theta; \quad (3)$$

(3) $H_T\|[1\bar{1}0]$ in (110):

$$L_3=\tfrac{1}{16}(-4K_a-4K_b+8K_c-5K_a'-5K_b'+12K_c')\times\sin2\theta+\tfrac{1}{32}(-7K_a'-7K_b'+4K_c')\sin4\theta; \quad (4)$$

(4) $H_T\|[1\bar{1}1]$ in (110):

$$L_4=(4K_a-4K_b+3K_a'-5K_b'+4K_c')(\sin2\theta)/24+(K_a'-7K_b'+12K_c')(\sin4\theta)/48+(4K_a-4K_b+5K_a'-5K_b')(\cos2\theta)(\sqrt{2}/12)+(-K_a'+K_b')(\cos4\theta)(\sqrt{2}/12). \quad (5)$$

These relations were used for determining the values of the 6 anisotropy constants from the data, as described below. These constants were then used for calculating torque curves for other orientations of H_T, when the symmetry does not prescribe uniquely the distribution of orthorhombic axes. For example, when H_T is applied in the (100) plane at an angle of say 40° to the [001]

[16] V. H. Gottschalk, Physics **6**, 127 (1935).

direction, it could not be predicted whether the c axes in all portions of the crystal would be parallel to [001] or whether some, on account of local fields, would be parallel to [010]. Theoretical curves can be fitted to experimental curves by assuming that a certain fraction of the specimen had c axes parallel to [001], the remainder parallel to [010].

Similarly torque curves were calculated for various orientations of H_T in the (110) plane. Here the positions of the a and b axes, as well as the c axes, are not generally prescribed by symmetry.

In accordance with Eq. (1), the anisotropy energies parallel to the a, b, and c axes are

$$E_a = K_b + K_c + K_b' + K_c',$$
$$E_b = K_c + K_a + K_c' + K_a',$$
$$E_c = K_a + K_b + K_a' + K_b'.$$

Since the c axis is found to be the direction of easy magnetization, the point of zero energy is taken in this direction:

$$E_c = 0.$$

EXPERIMENTAL

The specimens used for most of the torque measurements were cut from a natural crystal of excellent octahedral habit obtained from the Ward Natural Science Establishment. It analyzed 71.7 percent iron, close to the theoretical 73.6 percent. A qualitative spectral analysis showed vanadium as chief impurity, present to the extent of 0.01 to 0.3 percent, and traces of other elements. Also, a specimen of artificial magnetite grown by Dr. J. Smiltens was obtained through the kindness of Professor A. von Hippel of the Massachusetts Institute of Technology. This was closely stoichiometric in composition and showed a somewhat higher anisotropy at room temperature than the natural specimen. However, its magnetic anisotropy at $-196°$C was not affected by a field of 9000 oersteds present during cooling, whereas the natural crystal was so affected.

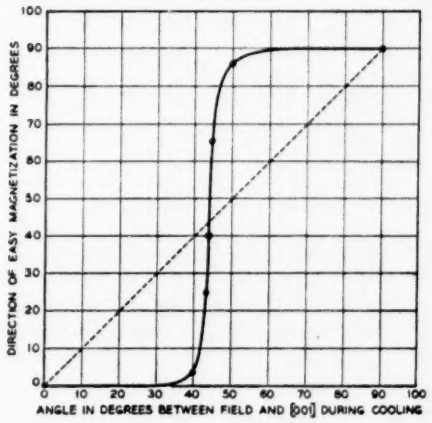

FIG. 2. (100) plane. Dependence of direction of easy magnetization on direction in which field was applied during cooling. Angles measured from [001].

The weight of the natural crystal disk cut in the (100) plane was 0.19 g; that cut in (110) was 0.165 g. The ratios of diameter to thickness were, respectively, 4.6 and 2.5. Measurement of the torque was carried out in the apparatus designed by Williams,[17] which could be read to 5 dyne-cm, corresponding to an anisotropy energy of 500 to 1000 erg/cm^3 in the specimens used. Field strengths of 9000 oersteds were used for measurement, and this was sufficiently high so that no correction was needed for the torque at saturation.

The specimen was imbedded in a brass disk and fixed in position by placing Scotch tape on it under slight pressure. This was placed in a Lucite cup, which was kept filled with liquid nitrogen for cooling through the transition and for measurement. The orientations of the crystals were first determined by x-rays, and later the directions of easy magnetization at room temperature were taken as [011] in (100) and [1$\bar{1}$1] in (110). As noted by Okamura and Ogawa,[18] the direction of easy magnetization shifts from [111] to [100] just above the transition point near $-140°$C, on cooling. This observation was used by Bickford[8] to explain the maximum in the curve of μ_0 *vs* temperature reported by Snoek[19] at about this temperature.

Torque curves were taken at room temperature, and at $-196°$C after cooling in zero field or in a field of 9000 oersteds in various directions in the plane of the specimen.

RESULTS

The torque curves at room temperature, for the (100) and (110) disks of the natural crystal, and the (110) artificial crystal, yielded the following values of the cubic anisotropy constant K: $-140\,000$, $-140\,000$, and $-127\,000$ ergs/cm^3, respectively. This may be compared with the average value $-112\,000$ derived by Bickford[8] from his microwave resonance measurements of several natural and artificial crystals. His lower values may be due to the fact that the field present during measurement was not sufficient to saturate, or the values for our natural crystal may be the result of the impurities it contains.

The effect of the direction of the field present during cooling on the resulting direction of easy magnetization, subsequently measured at $-196°$C, is shown for the (100) disk in Fig. 2. This shows that the easy direction coincides with that direction of the ⟨100⟩ form, namely [001], that is nearest to the direction of the field, until these two directions differ by about 40°. Apparently

[17] See R. M. Bozorth, *Ferromagnetism* (D. Van Nostrand Company, New York, 1951), p. 556 and 831.

[18] T. Okamura and S. Ogawa, Proc. Phys.-Math. Soc. Japan **23**, 363 (1941).

[19] J. L. Snoek, *New Developments in Magnetic Materials* (Elsevier Publishing Company, Inc., New York, 1947), p. 25.

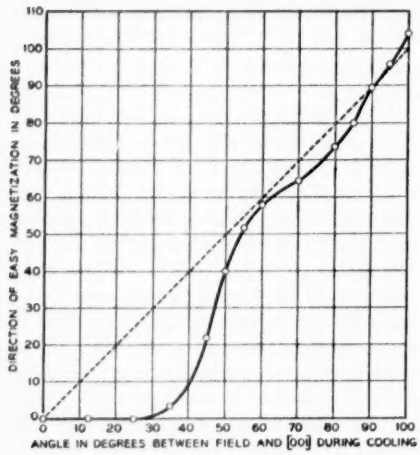

FIG. 3. (110) plane. Dependence of direction of easy magnetization on direction of field during cooling. Angles measured from [001].

some portions of the specimen then begin to have easy directions in the next-nearest ⟨100⟩ direction, [010], and the portions become about equal when the angle is 45°, as is to be expected. This supports the idea that the orthorhombic c axis, which is parallel to one of the original cubic axes, is the direction of easiest magnetization in the orthorhombic crystal.

Similar data for the (110) plane (Fig. 3) show that deviations of the easy direction from the nearest ⟨100⟩ direction occur when this direction is only about 30°, considerably less than the angle for the first deviation in the (100) plane. When the angle between H_T and [001], θ_T, reaches 55°, the c axes should be equally distributed along the 3 original cubic axes and the easy direction of the crystal, represented by θ_E, should be parallel to θ_T. They are observed to be parallel within about 3°. Between $\theta_T=55°$ and 90°, θ_E may be expected to be less than θ_T, and at $\theta_T=90°$ θ_E should equal θ_T, as observed. At $\theta_T=90°$ the easy direction is expected to become greater than θ_E, as observed, and the curve should continue symmetrically.

Torque curves for the (100) and (110) planes, measured after cooling in fields inclined at various angles to [001], are shown in Figs. 4, 5, and 6. The torque curve for the (110) specimen cooled in a field parallel to the [001] direction ($\theta_T=0$) should be especially noted. When measurements were made up to about $\theta=40°$, they were quite reproducible, but beyond this point the torque was found to decrease with time. After θ was increased slowly to 90°, allowing time for this drift to complete itself, the curve was again measured and was now completely reproducible over its entire extent, at a level considerably below the original one. It is believed that this is due to the shift, in the high applied field used during measurement, of those a axes which are originally at 90° to the (110) plane, to the alternative position lying in the plane, the related b axes shifting in the opposite sense. This orientation is energetically more favorable, as shown in Fig. 7, and is that considered in the Appendix, Case 2. Such a shift has also been noted by Bickford,[8] who found that in one of his specimens a field applied below the transition can switch a magnetic axis from one cubic axis to another.

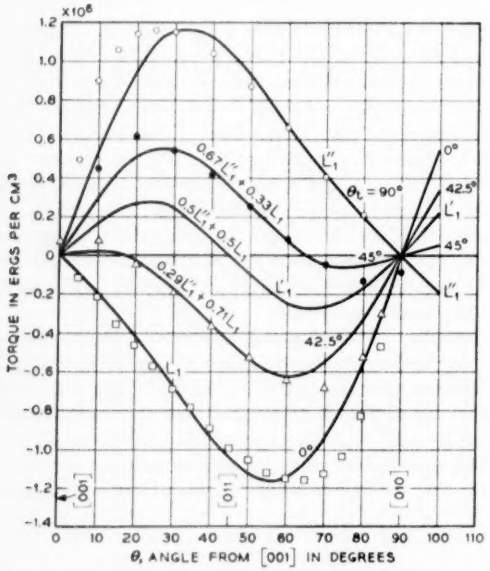

FIG. 4. Torque curves for (100) plane, obtained after cooling with magnetic field inclined at various angles θ_T to [001] direction. Points show experimental values, lines are theoretical curves.

DERIVATION OF CONSTANTS

The anisotropy constants, K_a to K_c', were derived from the following torque curves:

(100) plane, $H_T \| [001]$ (Fig. 4),

(110) plane, $H_T \| [001]$ (Fig. 5),

(110) plane, $H_T \| [1\bar{1}0]$ (Fig. 6),

(110) plane, $H_T \| [1\bar{1}1]$ (Fig. 5),

using the expressions for L_1 to L_4 [Eqs. (2)–(5)] and the additional expression

$$E_c = K_a + K_b + K_a' + K_b' = 0.$$

These curves were fitted to the data at $\theta=30°$ and $\theta=60°$ for L_1, L_2, and L_3, and $\theta=30°$, 60°, and 90° for L_4. With the further condition $E_c=0$ we then had 10 relations from which the six constants were derived using the method of least squares. The derived constants are, in ergs/cm³,

K_a:	890×10^3,	K_a':	-400×10^3,
K_b:	-620×10^3,	K_b':	120×10^3,
K_c:	370×10^3,	K_c':	620×10^3;

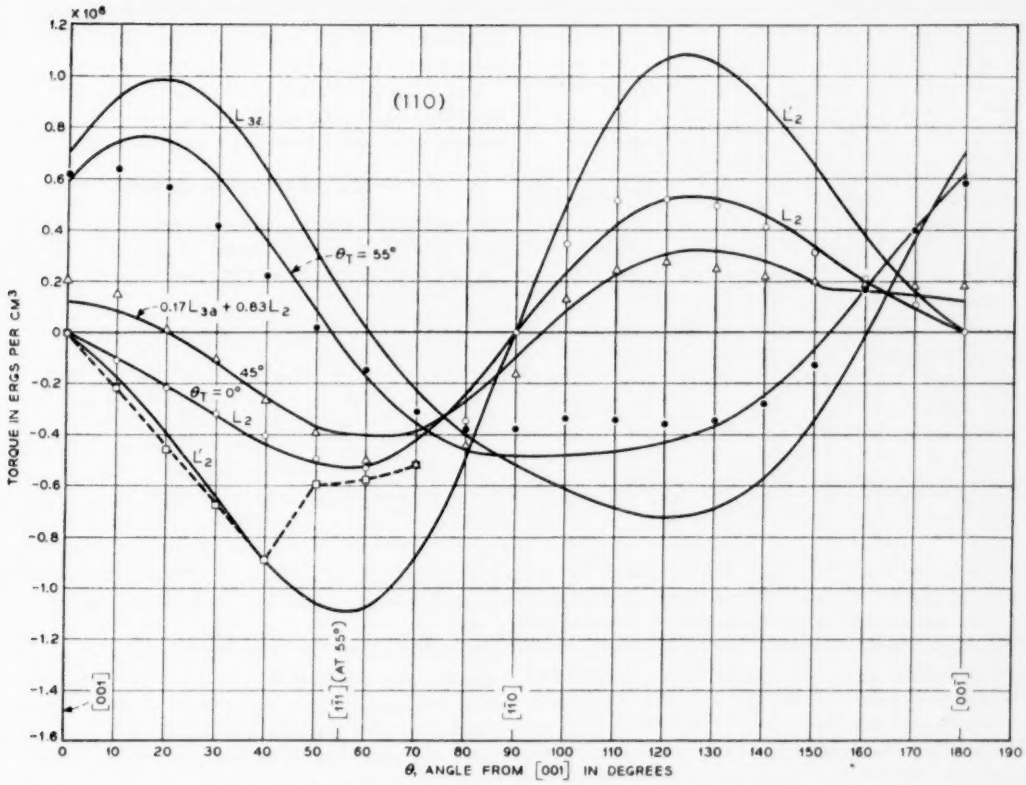

FIG. 5. Torque curves for (110) plane with cooling field applied at 0°, 45°, and 55° from [001]. Curves for 45° and 55° are combinations of L_2 and L_{3a} in different proportions (see text).

and the anisotropy energies parallel to the a, b, and c axes are, in ergs/cm³,

$$E_a = 490\times 10^3, \quad E_b = 1490\times 10^3, \quad E_c = 0.$$

The accuracy of the constants is not high—the probable error averages about 100×10^3,

The torque curves L_1 to L_4 were then calculated from the anisotropy constants and compared with the experimental curves. This comparison is shown in Figs. 4 to 6. There is some evidence that agreement would be improved slightly by the addition of a 6θ term that would come from higher terms in the expansion of E [Eq. (1)]. However, no attempt was made to improve the fit in this manner.

The torque curves obtained after cooling with H_T making various other angles to the axes were also calculated from the K's and compared with experiment, as shown in the same figures. These curves all have shapes that are accounted for by theory, and they are in fair quantitative agreement with the values of the K's selected.

In several cases the theory does not predict the fractions of the crystal that have transformed in two ways; in these cases curves can be fitted by assuming arbitrary fractions transformed in one way, the remaining transforming the alternate way. For example,

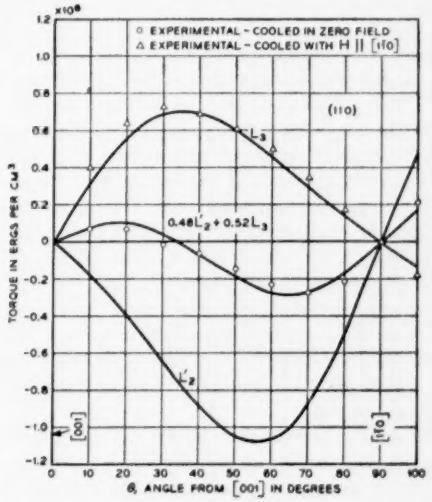

FIG. 6. Additional theoretical torque curves and observed points for (110) plane.

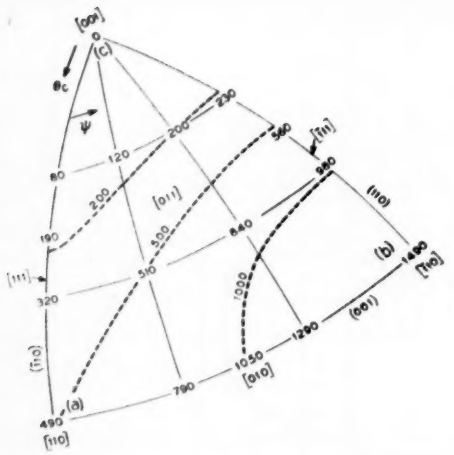

FIG. 7. Anisotropy energies, in 10^6 ergs/cm^3, in various directions in transformed orthorhombic crystal. Note both orthorhomibc axes (a, b, c) and original cubic axes ([100], etc.).

when H_T is applied 42.5° from [001] in (100), the experimental torque curve can be satisfied by assuming that in 71 percent of the specimen the c axis lies along [001] and in 29 percent along [010], as shown in Fig. 4. This distribution is probably caused by the local variations in the direction of the internal field, caused by local strains and imperfections.

In the (110) plane, with $\theta_T=45°$, the crystals transform so that the resultant torque curve is a combination of L_2 and L_{3a}, as shown in Fig. 5 and discussed in the Appendix. When $\theta_T>60°$ it appears that a third orientation is possible—that corresponding to L_3. When $\theta_T=80°$ the direction of easy magnetization lies at $\theta=65°$; by combining L_2, L_3, and L_{3a} the observed easy directions lying between $\theta=60°$ and 90° can thus be accounted for, and at 90° all portions of the crystal transform in accordance with L_3 of Fig. 6.

The torque curves measured in the (100) plane after cooling in zero field were found to be somewhat different in different experiments, perhaps because the crystal was not properly demagnetized before cooling. They agree with the theoretical expression L_{100} (Appendix, Case 5) in general character; the ⟨110⟩ are the easy and the ⟨100⟩ the hard directions in this plane, and the average amplitude is very close to that calculated from the constants K_a, $\cdots K_c'$, namely, 230×10^3 ergs/cm^3. It is at first thought surprising but is in accord with theory that a ⟨100⟩ direction, which in a single oriented orthorhombic crystal can become the easiest direction of all, will be the hard direction when all possible orientations are present.

The torque curve in the (110) plane after cooling in zero field also shows, in agreement with theory, that [001] is not as easy a direction as [1$\bar{1}$1]. The observed curve is not in agreement with equal distribution of the c axes among the three possible ⟨100⟩ directions, but indicates, as shown in Fig. 6, that 48 percent instead of 33 percent of the c axes lie parallel to [001]. This may also be due to imperfect demagnetization.

The anisotropy energies in various directions in the orthorhombic crystal are shown in Fig. 7. The highest energy, along the b axis, is 1.5×10^6 ergs/cm^3.

MAGNETIZATION CURVES

Domenicali[15] has measured the magnetization curves at −180°C for crystals cooled in zero field and magnetized in the [100] and [110] directions. These curves

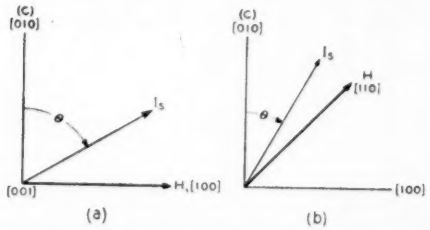

FIG. 8. Diagram for calculating magnetization curves from anisotropy energies: (a) $H\|[100]$, drawing magnetization I_s from direction of easy magnetization [010]; (b) $H\|[110]$.

can be calculated theoretically from our constants as follows: One-third of the crystal will transform with its c axis parallel or antiparallel to [100]. When the measuring field is applied parallel to [100] only a weak field, assumed to be negligible, will be required to orient its moment parallel to the field. In the other $\frac{2}{3}$ of the crystal the c axis will lie at 90° to the applied field H, and the spontaneous magnetization I_s will gradually be rotated from the c axis into the direction of H as its strength increases. The energy of anisotropy E plus the mutual magnetic energy between H and I_s is then

$$E_T=E-HI_s\sin\theta,$$

θ being defined as in Fig. 8(a). This is a minimum when $\partial E_T/\partial\theta=0$, or, since $L=-\partial E/\partial\theta$, we have

$$H=-L/(I_s\cos\theta).$$

The intensity of magnetization is

$$I_1=I_s\sin\theta.$$

In this case $L=L_1$ [Eq. (2) above]; this is an approximation only, for I_s may not be exactly in a (100) plane. For the crystal as a whole,

$$I_{100}=I_s/3+2I_1/3,$$

and I is easily calculated as $f(H)$.

When H is applied parallel to [110], H is inclined to the c axis by 45° for $\frac{2}{3}$ of the crystal, by 90° for $\frac{1}{3}$ of it. For $\frac{2}{3}$ of the crystal [see Fig. 8(b)],

$$H_1=-L_1/[I_s\sin(\tfrac{1}{4}\pi-\theta)],$$
$$I_1'=I_s\cos(\tfrac{1}{4}\pi-\theta).$$

For the other $\frac{1}{3}$ of the crystal we have [Fig. 8(a)]

$$H_2 = -L_2/(I_s \cos\theta),$$

and

$$I_2 = I_s \sin\theta.$$

The resultant curve for the whole crystal is then readily determined by evaluating $I_{110} = I_2/3 + 2I_1'/3$ for given values of $H = H_1 = H_2$.

The demagnetizing factor N for Domenicali's disk-shaped specimen can be calculated approximately from the dimensions, which have a ratio of length to thickness of 5. Using $N = 1.54$ and $I_s = 500$, the demagnetizing fields were added to the fields calculated above. The The resultant I, H curves are compared with Domenicali's measurements for $-180°$C in Fig. 9. Considering the fact that the anisotropy constants are those determined for $-196°$C and that hysteresis is not taken into account, the agreement is good.

The magnetization of finely powdered magnetitite at low temperature will take place entirely by domain rotation and not by boundary movement, and the coercive force can be calculated. If the magnetizing field is applied always parallel to the c axis, reversal of magnetization will take place by rotation of the magnetization vector in the (110) plane through the direction of the a axis, over an energy hump of 0.5×10^6 ergs/cm^3. To obtain the field necessary for this reversal,

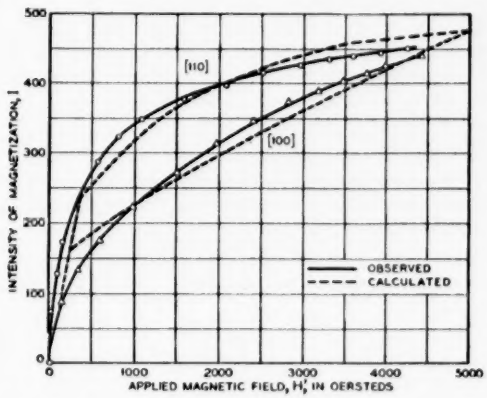

FIG. 9. Calculated magnetization curves for [001] and [110] directions at $-195°$C (broken lines) compared with Domenicali's observed curves (solid lines).

$-L_2$ is equated to the torque created by the applied field:

$$HI_s \sin\theta = -(K_a - K_c + K_a' - K_c') \sin 2\theta - \tfrac{1}{2}(K_a' + K_c') \sin 2\theta.$$

The largest value of H for the various values of θ, in this case the value for $\theta = 41°$, is the coercive force. We obtain

$$H_c = 1420 \text{ oersteds.}$$

No measurements of coercive force at this temperature have been reported for fine particles.

Similarly the coercive force of fine powder at room temperature may be calculated from the cubic anisotropy constant K. When crystals are oriented at random with respect to the magnetizing field we have[17]

$$H_c = 0.64|K|/I_s \approx 160.$$

This is to be compared with the highest observed value of Gottschalk, 127 oersteds, in particles ground to about 4-microns diameter. This particle size is rather large to show the fine-particle effect; it is possible that the particles observed are agglomerates of finer particles, or that they are under enough strain to account for the high coercive force.

We are glad to acknowledge the benefit of discussions with Dr. R. W. Hamming and Dr. J. W. Tukey on the evaluation of the constants. The derivations of the equations were checked by Miss B. B. Cetlin, and the calculations of the constants by least squares were carried out under the supervision of Miss C. L. Froelich, to whom we are indebted.

APPENDIX

Case 1: A disk cut parallel to a (100) plane is cooled in a field, H_T, parallel to the [001] direction lying in the plane. It is assumed that the orthorhombic c axis will be parallel to [001], the a and b axes inclined 45° to the plane. See Fig. 10. Let θ be the angle in the plane between the [001] direction and the direction of the field, H_m, applied during measurement. Then [see Eq. (1)] $\theta_c = \theta$, $\cos\theta_b = \cos\theta_a = (\sin\theta)/\sqrt{2}$ and the anisotropy energy is

$$E_1 = \tfrac{1}{4}(3K_a + 3K_b + 2K_c) + \tfrac{1}{32}(19K_a' + 19K_b' + 12K_c') + \tfrac{1}{8}(2K_a + 2K_b - 4K_c + 3K_a' + 3K_b' - 4K_c') \cos 2\theta + \tfrac{1}{32}(K_a' + K_b' + 4K_c') \cos 4\theta.$$

The torque in the plane, $L_1 = -\partial E/\partial\theta$, is given by Eq. (2) in the text. Since the a and b axes make the same angle with H_m, the torque on the two crystal

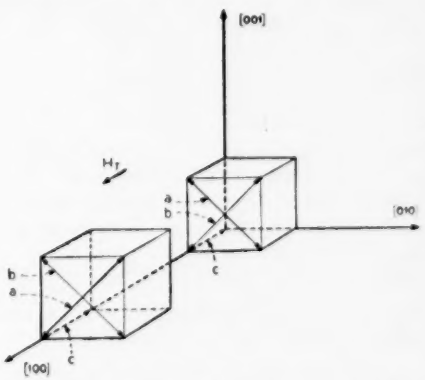

FIG. 10. Possible orientations of orthorhombic crystals resulting from cooling cubic crystal in field parallel to [100].

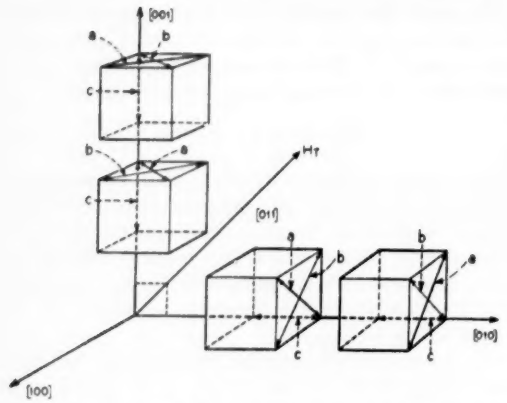

FIG. 11. Orientations of orthorhombic crystals when cooling field is parallel to [110].

positions (those with a and b axis interchanged) is the same.

When H_T is parallel to [011], it is assumed that the c axes are equally distributed between [001] and [010]. For half the crystal the torque is given by L_1 above, and for the other half θ is replaced by $(\theta+\frac{1}{2}\pi)$ so that $L_1''(\theta)=L_1(\theta+\frac{1}{2}\pi)$ as in Fig. 4. The sum of the two is then $\frac{1}{2}[L_1(\theta)+L_1(\theta+\frac{1}{2}\pi)]$ or $L_1'=\frac{1}{8}(K_a'+K_b'+4K_c')\times\sin4\theta$. This relation contains the same coefficient of $\sin4\theta$ as we have in L_1, but now the coefficient of $\sin2\theta$ is zero.

Case 2: The disk is cut parallel to (110) and cooled with H_T parallel to [001], and θ is measured in the plane from [001]. It is assumed that all portions of the crystal have c axes parallel to [001] and that just after cooling in half of the crystal the a axes lie in the (110) plane along $[1\bar{1}0]$, and in half the a axes are 90° to the plane, along [110], the b axes lying in the alternate positions. See Fig. 10. Experiments indicate, however, that after applying a strong field at $\theta=40°$ to 90° a rearrangement of axes takes place, and it is assumed that thereafter the a axes lie in the (110) plane throughout the crystal, the c axes remaining as before. For this case $\theta_c=\theta$, $\theta_b=\pi/2$ and $\theta_a=\pi/2-\theta$. Then

$$E_2=\tfrac{1}{2}(K_a+2K_b+K_c)+\tfrac{1}{8}(3K_a'+4K_b'+3K_c')+\tfrac{1}{2}(K_a-K_c+K_a'+K_c')\cos2\theta+\tfrac{1}{8}(K_a'+K_c')\cos4\theta,$$

and L_2 is given by Eq. (3) in the text. In the former case, with two orientations of crystals present, we must calculate the torque when the b axes lie in the plane. Now $\theta_c=\theta$, $\theta_b=\frac{1}{2}\pi-\theta$, and $\theta_a=\frac{1}{2}\pi$. The torque is

$$L_{2a}=(K_b-K_c+K_b'-K_c')\sin2\theta+\tfrac{1}{2}(K_b'+K_c')\sin4\theta,$$

and the torque for equal proportions of the two crystal orientations is

$$L_2'=\tfrac{1}{2}(L_2+L_{2a})=\tfrac{1}{2}(K_a+K_b-2K_c+K_a'+K_b'-2K_c')\times\sin2\theta+\tfrac{1}{4}(K_a'+K_b'+2K_c')\sin4\theta.$$

Case 3: When H_T is applied parallel to $[1\bar{1}0]$ in the (110) disk, the c axes are inclined 45° to the plane and to H_T, half above and half below ([100] and $[0\bar{1}0]$). Since each portion has the same torque we need calculate it only for one case; however, each c axis position is accompanied by two possible arrangements of a and b axes as shown in Fig. 11. In the one case, measuring θ from [001], we have $\cos\theta_a=(\sin\theta)/2+(\cos\theta)/\sqrt{2}$, $\cos\theta_b=(\sin\theta)/2-(\cos\theta)/\sqrt{2}$, $\cos\theta_c=(\sin\theta)/\sqrt{2}$, and

$$E_{3a}=\tfrac{1}{8}(5K_a+5K_b+6K_c)+(1/64)(15K_a'+15K_b'+11K_c')+\tfrac{1}{32}(-4K_a-4K_b+8K_c-5K_a'-5K_b'+12K_c')\cos2\theta+(-4K_a+4K_b-5K_a'+5K_b')(\sin2\theta)/8\sqrt{2}+(-7K_a'-7K_b'+4K_c')(\cos4\theta)/128+(K_a'-K_b')(\sin4\theta)/16\sqrt{2},$$

and

$$L_{3a}=(-4K_a-4K_b+8K_c-5K_a'-5K_b'+12K_c')(\sin2\theta)/16+(4K_a-4K_b+5K_a'-5K_b')(\cos2\theta)/4\sqrt{2}+(-7K_a'-7K_b'+4K_c')(\sin4\theta)/32+(-K_a'+K_b')(\cos4\theta)/4\sqrt{2}.$$

For the second position, L_{3b} is given by interchanging subscripts a and b in L_{3a}. Then $L_3=\frac{1}{2}(L_{3a}+L_{3b})$ and is given by Eq. (4) in the text.

Case 4: When H_T is applied parallel to $[1\bar{1}1]$ in (110), the c axes lie along original cubic axes, and so we have 3 possible positions, each equally inclined to H_T. However, each position of the c axis has 2 possible positions for its corresponding a and b axes. Of these the a axis is a direction of lower energy; therefore it is assumed that it will be oriented more nearly in the direction of the field used during cooling, as shown in Fig. 12. When the c axis lies in the plane of the disk, the a axes will also lie in the plane of the disk and the b axes perpendicular thereto. Then $\frac{1}{3}$ of the crystal has the torque L_2 and $\frac{2}{3}$ of the crystal the torque L_{3a} given above. The whole

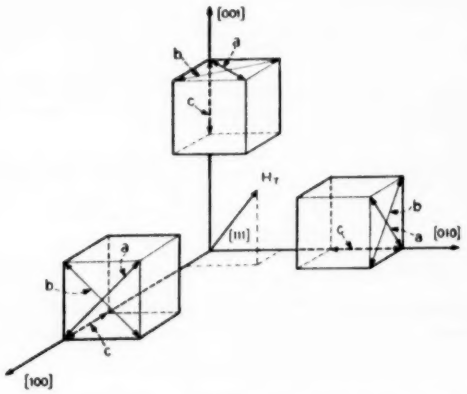

FIG. 12. Orientations of orthorhombic crystals when cooling field is parallel to [111].

torque is then

$$L_4 = \tfrac{1}{3}L_2 + \tfrac{2}{3}L_{3a},$$

given in Eq. (5) in the text. In this case, for the first time, cosine terms are present and the calculated and observed torque curves are less symmetrical—in the 0° to 180° range in θ no symmetry is present. In general $L \neq 0$ at $\theta = 0$.

Case 5: When no field is applied during cooling, the torque for the (100) plane is calculated in three parts, corresponding to three positions of the c axis: (1) regions having c axes parallel to [001], (2) regions having c axes parallel to [010], and (3) regions having c axes parallel to [100], perpendicular to the plane of measurement. The torque for the first 2 positions combined is described by L_1' (Case 1 of Appendix). For the third position there are two possible orientations of the a and b axes, 90° to each other in the (100) plane; for one of these $\theta_c = 90°$, $\theta_b = \frac{1}{4}\pi + \theta$, $\theta_a = \frac{1}{4}\pi - \theta$, and the corresponding energy and torque are

$$E_{3a} = \tfrac{1}{2}(K_a + K_b + 2K_c) + \tfrac{1}{8}(3K_a' + 3K_b' + 8K_c') + \tfrac{1}{2}(-K_a + K_b - K_a' + K_b') \sin 2\theta - \tfrac{1}{8}(K_a' + K_b') \cos 4\theta$$

and

$$L_{3a} = (K_a - K_b + K_a' - K_b') \cos 2\theta - \tfrac{1}{2}(K_a' + K_b') \sin 4\theta.$$

The energy, and torque L_{3b}, for the other orientation of position (3) are obtained by interchanging subscripts a and b in these expressions.

The result is then

$$L_{100} = \tfrac{1}{6}(4L_1' + L_{3a} + L_{3b}) = -\tfrac{1}{12}(K_a' + K_b' - 4K_c') \sin 4\theta.$$

Case 6: When no field is applied to the (110) specimen during cooling, $\frac{1}{3}$ of the specimen will have the torque L_2' (Case 2 above), $\frac{2}{3}$ will have L_3 (Case 3 above):

$$L_{110} = \tfrac{1}{3}(L_2 + 2L_3) = (-K_a' - K_b' + 4K_c')(\sin 2\theta)/24 + (-3K_a' - 3K_b' + 8K_c')(\sin 4\theta)/48.$$

PHYSICAL REVIEW VOLUME 91, NUMBER 5 SEPTEMBER 1, 1953

Deformation of Copper Single Crystals at 300°K and 78°K

T. H. BLEWITT
Oak Ridge National Laboratory, Oak Ridge, Tennessee

(Received April 20, 1953)

Single crystals of copper were deformed at 78°K and 300°K. There was slight temperature dependence of the critical shear stress in this range of temperature and for shear strains less than about 0.25 the stress-strain relationship was linear and independent of temperature. The linear relationship of the stress-strain curve persisted for higher strains at 78°K. The annealing at 300°K of crystals deformed at 78°K showed a decrease in electrical resistance accompanied by a phenomenon suggestive of strain aging. The magnitude of the recoverable resistance was dependent on the strain varying at a faster rate than a linear relationship. A measurable decrease in electrical resistance was not observed for strains less than about 0.30. These results are interpreted according to the theory of dislocations and indicate some modification to the theory of work hardening suggested by Mott.

I. INTRODUCTION

THERE has recently been considerable interest in the phenomena of low-temperature annealing of the electrical resistivity in cold-worked metals. The motivation for this work originates in an interesting paper presented by Seitz[1] at the Pittsburgh Conference on Plastic Deformation, in which Seitz pointed out that plastic deformation increased the number of vacant lattice sites in ionic crystals by about a hundredfold. He also pointed out that after about one hour at room temperature, the number of vacancies has decreased to the equilibrium number. Shortly thereafter a group of experimentalists at North American Aviation[2] found that metals, specifically copper and aluminum, irradiated by 36-Mev α particles at −160°C in the Berkeley cyclotron showed an apparent decrease in residual resistance on warming to room temperature. Since theoretical studies of Seitz[3] and others had indicated that vacant lattice sites and interstitial atoms should be formed by the bombardment of metals by high energy particles, the annealing effects observed by the North American Aviation, and more recently by a group at Illinois,[4] might be attributed to the movement of these defects. Thus, if metals showed a behavior similar to that observed by ionic crystals in that lattice vacancies or interstitial atoms were formed by plastic deformation then an annealing phenomenon in cold-worked metals similar to that observed in irradiated metals should be observed. With this in mind a group at Oak Ridge National Laboratory[5] made measurements on the effect of a room temperature warmup on the elec-

[1] F. Seitz, *Pittsburgh Conference on Plastic Deformation of Crystalline Solids, May, 1950*, U. S. Office of Naval Research Report NAVEXOS-P-834 (unpublished), p. 37
[2] Eggleston, Martin, and Tarpinian, Phys. Rev. **81**, 664 (1951).
[3] F. Seitz, Disc. Faraday Soc. No. 5, 271 (1949).
[4] Marx, Copper, and Henderson, Phys. Rev. **88**, 1006 (1952).
[5] Blewitt, Taylor, and Coltman, Phys. Rev. **82**, 769 (1951).

TABLE I. Qualitative analyses of impurities in copper metal.

	Sample 175-*B*	Sample 182-*B*	Sample 182-*A*
Group I as Ag	<1[a] ppm	<1[a] ppm	<1[a] ppm
Group IIa as As (As, Se, Te, Mo, Ge)	1.5	2.0	4.5
Group IIb as Pt (Pt, Au)	0.15	0.20	0.10
Group IIc as Sb (Sb, Sn)	<0.003	<0.003	0.01
Group III as Fe (Fe, P, Ga, Zr, Hf, W, Ta, Cr, In, RE's)	80	63	60
Group IV as Co (Co, Zn, Ni, Mn)	2.0	1.8	1.0
Group V as Ba (Ba, Sr, Ca, Mg)	<0.1	0.3	<0.1
Group VI as Na (K, Rb, Cs, Na)	200[b]	300[b]	200[b]

[a] Questionable—copper contaminated.
[b] Probably contamination external.

trical resistivity of polycrystalline copper and aluminum samples deformed at liquid nitrogen temperatures. A group at Delft[6] had simultaneously made similar and probably more extensive measurements. Considerable work has been done since these experiments from both a theoretical and experimental standpoint. In a recent paper Seitz[7] has described in some detail the manner by which vacancies are formed by moving dislocations and their possible contribution to work hardening. Measurements of the activation energy to recover the electrical resistivity at these relatively low temperatures have been made by the group at Delft[8] and by the group at North American Aviation.[9] Similar experiments are underway by a group at the General Electric Research Laboratory.[10]

The present paper describes the experiments which were performed by the Oak Ridge group using single crystals of copper, which seem to offer a more basic insight into the formation of mobile defects from deformation than do polycrystalline samples. The stress strain curves at 78°K and at 300°K are reported. Changes in the electrical resistivities and yield point at 78°K following a room temperature warmup are also reported and interpreted.

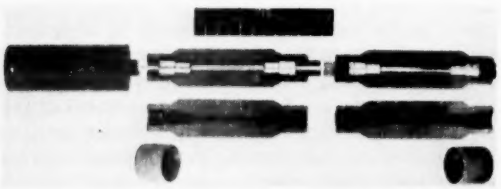

FIG. 1. The crucibles used in casting the samples showing the arrangement by which two crystals of the same orientation are grown.

[6] J. Molenaar and W. H. Aarts, Nature **166**, 690 (1950).
[7] F. Seitz, Advances in Physics **1**, 6.43 (1952).
[8] J. A. Manintveld, Nature **169**, 623 (1952).
[9] R. R. Eggleston, J. Appl. Phys. **23**, 1400 (1952).
[10] R. H. Pry, General Electric Research Laboratory (private communication).

II. EXPERIMENTAL PROCEDURE

A. Sample Preparation

The single crystals of copper were grown from high purity American Smelting and Refining copper by the Bridgman technique. Presumably the metal in its original condition was 99.999 percent copper. From an activation analysis,[11] the results of which are shown in Table I, it is clear that little if any impurity has been added during specimen preparation. The samples were grown in the shape of standard ASTM tensile specimen under high vacuum. Split AGOT graphite molds were used, and Fig. 1 shows the dimensions and physical arrangement of the molds and charging space. In addition to the ease in removing the samples, a split mold has the further advantage that repeated use of the same mold undoubtedly decreases the probability of introducing impurities from the mold. (In all cases two samples of the same orientation were prepared, by placing two crucibles in tandem with each other as is shown in Fig. 1.)

The potential probes used to measure the electrical resistivity consisted of No. 36 magnet wire sintered to the sample. The sintering was achieved by allowing the weight of crystals to be supported by the No. 36 copper wire and then annealing the assembly at a high temperature (1030°C) for 3 hours at a pressure of 10^{-5} mm or less. The sintering technique seemed to give a satisfactory bond, the cohesion being stronger than the wire. This technique has the advantage over welding or soldering in that it reduces the possibility of damaging the relatively fragile specimens and at the same time does not require the presence of any foreign material to secure a bond.

B. The Deformation Technique

The samples were deformed in an Instron Tensile Machine.[12] This is a screw machine with an amplidyne drive and a weighing system utilizing an SR-4 strain gauge to measure the elastic deformation of a stainless steel member. The machine was adapted for deformation at low temperatures.

The load was recorded directly and the elongation determined from the cross head motion. In all cases the cross head was driven at 0.020 in./min with the chart moving at 2 in./min so that each inch of chart represents 0.01 in. of cross head motion. Samples were gripped with split grips.

[11] G. W. Leddicotte and S. A. Reynolds, Nucleonics **8**, No. 3, 62 (1951).
[12] Instron Engineering Corporation, Quincy, Massachusetts.

In order to determine the reproducibility of this arrangement two samples of the same orientation were deformed at liquid nitrogen temperature. The resulting load-elongation curves were reproducible to $\pm\frac{1}{2}$ percent. While there is a very close agreement between the two curves it should be noted that this does not imply that absolute values of strain are this accurate. The assumption is made that there is no deformation in the shoulders of the specimens in using the cross head motion to determine the elongation. The determination of the elongation by direct means compared with the results from the above method indicates that shear strain is probably not in error by more than 0.04 anywhere on the stress strain curve.

C. The Measurement of Electrical Resistance

The electrical resistivity was determined by the potential drop method. A schematic drawing of the apparatus is shown in Fig. 2. Since the resistance of the samples was of the order of a few micro-ohms it was necessary to measure a relatively small potential drop. Consequently numerous precautions were taken to reduce thermal emf's to a minimum. In order to eliminate spurious potentials, readings were taken with the current flowing in both directions and the average of these conditions being taken as the real potential drop across the sample. In all cases potential drops were determined with two different currents flowing through the sample and the degree of reproducibility of these two determinations was used as a criterion of the reliability of the measurement.

The measurements were all made with the sample in the tensile machine. The following technique was used. The samples were loaded in the tensile machine and then cooled in a bath of boiling nitrogen and plastically deformed. The load was then released, 15 pounds being retained to insure good electrical contact. The resistance was then measured, the load released, and the sample allowed to warmup to about 300°K. Following a 16-hour anneal the samples were again cooled to 78°K and a tensile load of 15 pounds placed on the sample, and the resistance was again measured.

III. COMPUTATIONS

The computations of the shear stress and the shear strain were performed in the usual manner. For the case where the sample was in single slip, the resolved shear strain is given by[13]

$$S=\cos\lambda_i/\sin\chi_i-\cos\lambda_0/\sin\chi_0,$$

where λ_i is the angle between the tensile axis and the slip direction after the ith strain, χ_i is the angle between the tensile axis and the slip plane after the ith strain. The relation between χ_i, χ_0 (the original angle between the slip plane and tensile axis), and ϵ_i (the tensile elongation) is given by[13]

$$\epsilon_i=\sin\chi_0/\sin\chi_i.$$

A similar relationship is valid for λ_i, λ_0, and ϵ_i, namely

$$\epsilon_i=\sin\lambda_0/\sin\lambda_i.$$

It is assumed that duplex slip occurs when the angles λ_i and χ_i indicate that the specimen has rotated into the dodecahedral plane. The shear strain is then given by the following relationship:[14]

$$S=\left(\frac{\cos\lambda_D}{\sin\chi_D}-\frac{\cos\lambda_0}{\sin\chi_0}\right)+2.45\ln\left(\frac{1+\sqrt{2}\cot\delta_i}{1+\sqrt{2}\cot\delta_0}\right).$$

The angle δ_0 is the angle between the tensile axis at the point where it initially enters the dodecahedral plane and the (112) plane. For additional strains in a pure metal the tensile axis will remain in the dodecahedral plane and rotate towards the (112) plane. After the ith strain the angle δ_i is given by

$$\epsilon_i'=\sin\delta_0/\sin\delta_i,$$

where the tensile strain ϵ_i' is given by

$$\epsilon_i'=\epsilon_i/\epsilon_D,$$

ϵ_D being the tensile strain at which the tensile axis first enters the dodecahedral plane.

The shear stress in the region of single slip is given by[13]

$$\sigma_i=(F/A_0)\sin\chi_0\cos\lambda_i,$$

where F is the load and A_0 is the initial area.

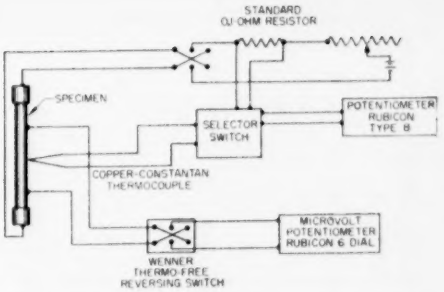

FIG. 2. Schematic diagram of the apparatus used to measure the electrical resistivity.

TABLE II. Effect of temperature on critical shear stress and orientation on the rate of work hardening.

Sample No.	Critical shear stress at 78°K kg/mm²	Critical shear stress at 300°K kg/mm²	Initial work hardening kg/mm²/unit strain	Ratio critical shear stress latent to active plane
142	0.219	0.218	12.84	0.554
158	0.276	0.278	15.4	0.808
175	0.254	0.257	18.86	0.904
182	0.200	0.325	14.3	0.806

[13] E. Schmid and W. Boas, *Plasticity of Crystals* (F. A. Hughes Company, London, 1950).

[14] R. Karnop and G. Sachs, Z. Physik **42**, 283 (1927).

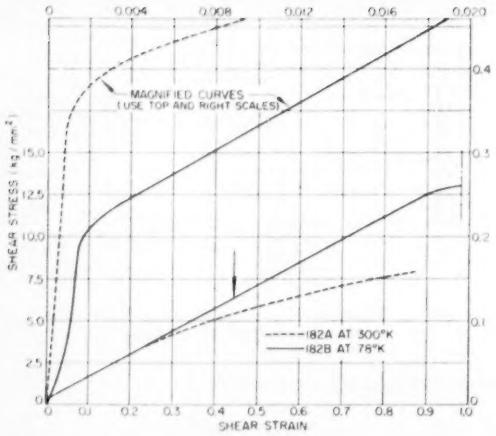

FIG. 3. Stress-strain curve of samples 182*A* and 182*B*. Sample 182*A* was deformed at 300°K and sample 182*B* at 78°K. The arrow denotes the strain at which the specimen axis enters the dodecahedral plane. The vertical dashed line denotes the strain at which a room temperature warmup was made and the resistance measured.

Upon the onset of double slip the equation must be modified and is given by

$$\sigma_i = (F/A_0)\epsilon_i \sin\chi' \cos\lambda',$$

where the angles χ' and λ' are given by

$$\sin\chi' = \cos 54°44' \cos(35°16' - \delta_i),$$
$$\cos\lambda' = \cos 30° \cos\delta_i.$$

IV. RESULTS

In addition to the data obtained on the low-temperature recovery of the electrical resistance, significant and somewhat surprising results were noted of the dependence of the rate of work hardening and the critical shear stress on the temperature. In Fig. 3 through Fig. 6 the stress-strain curves of various pairs of copper crystals are shown. In each figure the stress-strain relationships of two crystals of the same orientation are shown. One sample of each pair was deformed at 78°K, while the other was deformed at 300°K. In order to

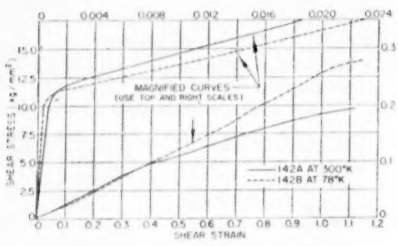

FIG. 4. Stress-strain curve of samples 142*A* and 142*B*. Sample 142*A* was deformed at 300°K and sample 142*B* at 78°K. The arrow denotes the strain at which the specimen axis enters the dodecahedral plane.

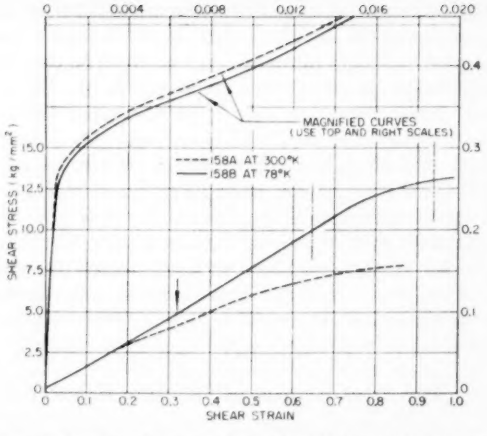

FIG. 5. Stress-strain curve of samples 158*A* and 158*B*. Sample 158*A* was deformed at 300°K and sample 158*B* at 78°K. The arrow denotes the strain at which the specimen axis enters the dodecahedral plane. The vertical dashed line denotes the strain at which a room temperature warmup was made and the resistance measured.

illustrate the transition from elastic to plastic strain the stress-strain curve for both samples has been shown on an expanded scale for small strains. The curve over the entire range to the ultimate critical shear stress is also shown in the same figure. In each of the figures the points where duplex slip should occur are indicated by vertical arrows and points where resistance measurements were made are indicated by dashed lines.

From these data (which is summarized in Table II) it would appear that the critical shear stress is independent of the temperature at least in the region from 78°K to 300°K, for with the exception of the pair of Fig. 3 (182*A* and *B*) each of the samples appears to

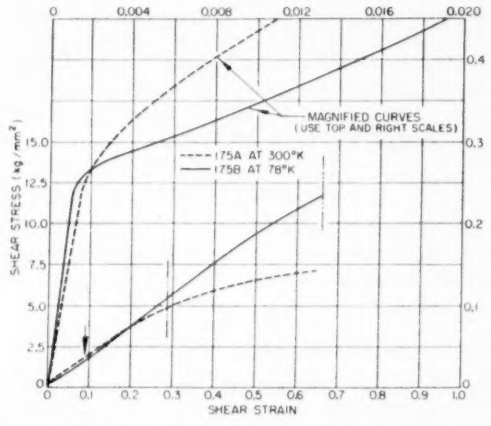

FIG. 6. Stress-strain curve of samples 175*A* and 175*B*. Sample 175*A* was deformed at 300°K and sample 175*B* at 78°K. The arrow denotes the strain at which the specimen axis enters the dodecahedral plane. The vertical dashed line denotes the strain at which a room temperature warmup was made and the resistance measured.

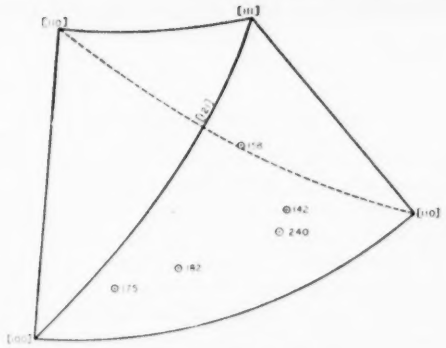

FIG. 7. Orientation of the copper crystals before deformation.

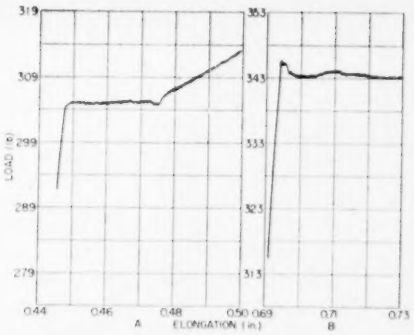

FIG. 8. The load-elongation curve of sample 158*B* after reloading. Curve *A* is that following the initial recovery in resistance. Curve *B* is that following the second recovery in resistance.

have, within experimental limits, the same critical shear stress. In the case of the 182 pair of samples, the one which was deformed at 78°K, 182*B*, has the lower critical shear stress. It should be noted that if an activation energy were associated with deformation that the converse should be expected. It is, however, not unreasonable that the apparent discrepancy arises as sample 182*A* was slightly deformed before the recorded deformation.

Evidence to support the viewpoint that the critical shear stress is independent of the temperature in the range from 78°K to 300°K, is apparent when the effect of temperature on the rate of work hardening is considered. From the data shown in Figs. 3 through 6 it is clear that for shear strains less than 0.25 the rate of work hardening is independent of temperature. For strains greater than 0.25 the rate of work hardening is less at 300°K than at 78°K. It is interesting to note that the elongation at which the stress-strain curves diverge is independent of the onset of duplex slip, as the point in question is observed to occur both prior to and after the onset of duplex slip. On the other hand there seems to be a decided orientation effect on the rate of work hardening. On consideration of the orientation of the crystals shown in Fig. 7 and the data of Table II, it seems that those crystals which have their specimen axis nearest the dodecahedral plane have the highest rate of work hardening and the lowest ultimate shear strain.[15]

The data pertaining to the recovery of electrical resistance by annealing at 300°K are shown in Table III. The data of the table may be summarized as follows. Upon deformation at 78°K followed by a 16-hour anneal at 300°K, the electrical resistance at 78°K is reduced by an amount which is dependent on the amount of deformation. No change in resistance is apparent for strains less than 0.25. This recovery of the resistance is apparently not associated with the recovery of hardness as upon reloading the sample at 78° an increase rather than a decrease in the yield point is observed. A discontinuity of small, but measurable, magnitude is apparent when the yield point is examined on an expanded scale. Such results are illustrated in Fig. 8 and Fig. 9. It appears that a definite strain aging phenomena is observed. This phenomenon was observed only in those regions where a recovery of electrical resistance was observed. For example, stopping the test of a sample, releasing the load, warming up, and then reloading did not result in the small maximum and the "easy flow" region for a strain less than 0.25. Similarly in most cases following a rest period at 78°K the anomolous yielding phenomena was not observed. A yielding was observed for an annealing period at 78°K when the strain was very large and approaching the ultimate strain.

TABLE III. The effect of isothermal annealing at 300°K on the electrical resistance of copper crystals plastically deformed at 78°K.

Sample No.	Shear strain	Shear stress kg/mm²	Resistance before anneal ohms ×10⁸	Resistance after anneal ohms ×10⁸	Percent change in resistance at 78°K	Change in resistivity ohm-cm ×10⁹
49	0.20		7.99	8.00	0	0
182	0.98	14.1	24.44	22.35	8.6	17.2
175	0.28	5.5	8.51	8.48	0.35	0.7
	0.66	11.7	12.80	12.39	3.7	7.4
158	0.65	10.2	12.07	11.89	1.5	3.0
	0.94	13.4	17.43	16.48	5.5	11.0

[15] G. Masing and T. Raffelsieper, Z. Metallkunde **41**, 65 (1950), also report an orientation dependence on the rate of work hardening in aluminum crystals.

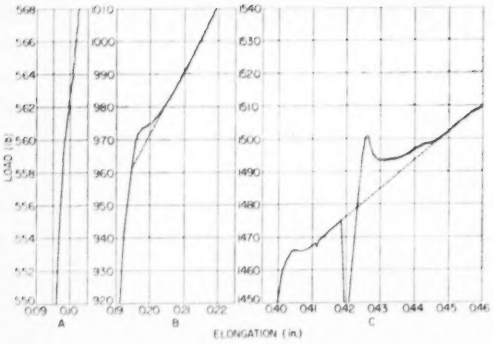

FIG. 9. The load-elongation curve of sample 200*A* ($\frac{7}{32}$-in. diameter) after reloading. Curve *A* is the reloading curve after a shear strain of 0.165 (shear stress 3.93 kg/mm²) and an anneal at 300°K for 1 hour. Curve *B* is that following a shear strain of 0.368 (shear stress 6.98 kg/mm²) following an anneal at 300°K for 1 hour. Curve *C* is that following a shear strain of 0.759 (shear stress 12.1). The first discontinuity arises from a one hour rest at 78°K. The load was then released and the sample annealed at 300°K for one hour and reloaded.

V. DISCUSSION

A. The Critical Shear Stress

It is reasonably clear from the data presented here that the critical shear stress is independent of temperature.[16] The results of other investigators[13,17] seem to indicate that the critical shear stress has a definite dependence on temperature for both hexagonal and cubic metals. In fact some effort has been made to explain this apparent temperature dependence by Andrade[17] and by Kochendörfer.[18]

More recently Mott,[19] using the concept of the Frank-Read[20] spinning dislocation, has pointed out that one should expect only a slight temperature effect which is directly proportional to the temperature dependence of the bulk modulus for pure and annealed metals.

He has further pointed out that impurity atoms would cause a hardening from the formation of a Cottrell atmosphere in the vicinity of Frank-Read generators. This latter hardening is strongly temperature-dependent,[21] and it would appear that the results of earlier investigators may be due to impurities. Experimentally a strong temperature effect has been observed on the critical shear stress of reactor-irradiated copper crystals and *MS* 80 α brass crystals,[22] which seem to support in some degree the above viewpoint.

B. The Stress Strain Curves

Koehler[23] and Mott[19] have recently given theoretical consideration to the mechanism of work hardening of metal crystals. Koehler's theory is primarily applicable for the region of small strains, where it has been assumed that hardening results from the fact that the Frank-Read generators lock and generators of shorter length must be used. Mott assumes that barriers to the motion of dislocations pile up a large number of dislocations and create a local stress, in a manner similar to that formulated in the original Taylor[24] theory, which locks the generator and causes work hardening. These barriers are assumed to be sessile dislocations when edge dislocations are generated, and lattice vacancies when screw dislocations are generated. Consider the data presented here in accordance with the theory suggested by Mott.

The relationship between stress and shear strain is interesting in that a linear relationship is observed during the first portion of the stress-strain curve at 300°K. The linear relationship seems to persist for higher strains at 78°K. It may be that at the zero point a linear relationship is preserved for the entire region of deformation by slip. In order to investigate this possibility, a pair of single crystals was deformed as described previously. In this case, one was deformed at 78°K and the other at 4.2°K. The results shown in Fig. 10, seem to substantiate the extrapolation to the zero point. The critical shear stress is nearly the same in both samples, and the stress strain curve at 4.2°K is linear as long as slip occurs. After an elongation of about 60 percent (shear strain of about 1.25) the sample deforms by a mechanism other than slip which has some of the characteristics of twinning, and it finally fractures by cleavage after an elongation of about 120 percent. There is a sharp transition between the region of slip and the region of apparent twinning. It would thus seem reasonable that the stress-strain relationship of copper is a linear one at the zero point.

Mott's treatment, on the other hand, indicates that the stress should be proportional to the square root of the strain. To obtain a linear relationship between stress and strain from this formulation, it is necessary that the length of the Frank-Read generator vary inversely with the strain. It would appear that this is a rather stringent requirement.

[16] The values reported in this paper are in close agreement with those reported by P. W. Neurath and J. S. Koehler, J. Appl. Phys. **22**, 621 (1951). It should be noted, however, that while the experimental technique was in general very different, specimens were prepared from similar materials in a similar manner to those described here.

[17] E. N. da C. Andrade, Phil. Mag. **43**, 1218 (1952).

[18] A. Kochendörfer, *Plastische Eigenschaften von Kristallen und metallischen Werkstoffen* (Verlag Julius Springer, Berlin, 1941).

[19] A. F. Mott, Phil. Mag. **43**, 1151 (1952).

[20] F. G. Frank and T. Read, *Pittsburgh Symposium on Plastic Deformation of Crystalline Solids, May, 1950*, U. S. Office of Naval Research Report NAVEXOS-P-834 (unpublished), p. 44.

[21] A. H. Cottrell and B. A. Bilby, Proc. Phys. Soc. (London) **A62**, 49 (1949).

[22] Unpublished data of Blewitt, Coltman, and Jamison give the following values of the critical shear stress of copper crystals irradiated for 6×10^{18} neutrons/cm²: 3.17 kg/mm at 300°K, 4.25 kg/mm² at 200°K, 6.30 kg/mm² at 78°K, and 7.78 kg/mm² at 4°K. R. E. Jamison also reports the following values for *MS* 80 brass crystals: 1.55 kg/mm² at 300°K and 3.07 kg/mm² at 78°K.

[23] J. S. Koehler, Phys. Rev. **86**, 52 (1952).

[24] G. I. Taylor, Proc. Phys. Soc. (London) **A145**, 362 (1934).

C. The Formation of Vacancies

It has been previously indicated that the low-temperature recovery of the electrical resistance has been interpreted to be the motion of vacant lattice sites formed by deformation.[25]

From the data of Table III and from the related data of strain aging, it appears as though very few defects are formed when the strain is small. Unfortunately, there is not sufficient evidence, due to the orientation dependence of the stress-strain curves, to decide the exact relationship between strain and the recoverable resistance. Since it has been proposed that those defects are formed by the interaction of a moving screw dislocation and a line dislocation lying in another plane, it would seem that either the number of moving screw dislocation or the number of dislocations with which it can interact must increase rapidly with the strain.

D. Temperature Dependence

It would further seem that the proposed dependence of the stress-strain relationship on the temperature might require some modification in the relatively low temperature regions where normal self-diffusion cannot occur, as it is quite apparent that the role attributed to vacant lattice sites in the hardening process must be modified. If these defects have been annihilated, as perhaps is suggested by the reduction in resistance, then following the annihilation or the motion of these defects to traps as the case may be, one should expect an accompanying reduction in hardness. Instead, a small but definite increase in resistance to flow is observed with the characteristics associated with strain aging. It seems that these vacant lattice sites have sufficient mobility at 300°K to move to dislocations, and hardening occurs in the manner suggested by Cottrell.[26] It is tempting to assume from the results in Figs. 3 through 6 that thermal fluctuations enable dislocations to break loose from the barriers restricting their motion. It appears that the activation energy for this process is dependent on the localized stress since a higher stress is required at lower temperatures. It may be that the mechanism proposed by Frank, which should be temperature-dependent, to explain the passage of slip lines through grain boundaries would be applicable here. That is, after Frank,[27] a stress concentration such as that in the vicinity of a dislocation "pile up" might result in the activation of a new generator with the help of thermal energy. As the temperature decreases, it is observed that the stress concentration must increase.

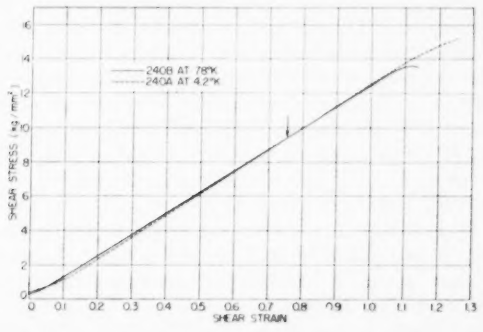

FIG. 10. Stress-strain curve of sample 240*A* and 240*B*. Sample 240*A* was deformed at 4.2°K and 240*B* at 78°K. The stress-strain curve of sample 240*A* considers only that part for which a slip mechanism is operative. A further tensile elongation of 0.60 was observed prior to brittle fracture.

[25] It is not clear that this interpretation should not be modified to some extent in view of recent unpublished data pertaining to the reactor bombardment of disordered Cu_3Au. It was found by Coltman and Blewitt, that the defects, apparently vacancies, formed by fast neutrons failed to induce diffusion and ordering at an appreciable rate below 0°C. It would appear that the activation energy for this process would certainly be no higher than for the motion of defects in copper. However, the defects moving at low temperatures in conformance with the earlier concepts will be arbitrarily termed vacancies with the reservation that further evidence is necessary to confirm this viewpoint.

VI. ACKNOWLEDGMENT

The author is indebted to Mrs. J. K. Redman for her assistance in making many of the measurements and for making the mathematical computations involved; to F. A. Sherrill for growing the crystals and determining their orientation, and to H. A. Mahlman for the activation analyses. He is also appreciative to R. R. Coltman, R. E. Jamison, and D. S. Billington for many helpful suggestions made in frequent discussions during the progress of the research.

Note added in proof.—F. D. Rossi[28] has independently obtained results on the deformation of copper crystals at 300°K which show that the rate of work hardening is dependent on the crystal orientation.

[26] A. H. Cottrell, *Bristol Conference on the Strength of Solids* (Physical Society, London, 1948), p. 30.

[27] F. G. Frank, *Pittsburgh Conference on the Plastic Deformation of Crystalline Solids, May, 1950*, U. S. Office of Naval Research Report NAVEXOS-P-834 (unpublished), p. 89.

[28] F. D. Rossi, Sylvania Electric Company, private communication.

Computation of Mean Debye Temperature of Cubic Crystals from Elastic Constants*

S. L. QUIMBY AND PAUL M. SUTTON†
Columbia University, New York, New York
(Received May 28, 1953)

An improved method is presented for computing the mean Debye characteristic temperature of cubic crystals from the elastic constants. It is based upon an evaluation of the distribution in solid angle of the roots of the cubic equation which describes the propagation of plane acoustic waves in the crystal, and otherwise employs a device due to Hopf and Lechner. The end result is given in simple closed expressions which present no computational difficulty. The uncertainty in the computed value of the mean Debye temperature due to the approximation made in the method is of the order 0.1 percent when the anisotropy factor of the crystal is as large as 4.

INTRODUCTION

THE mean Debye temperature, Θ_D, of a cubic crystal is given by the expression

$$\Theta_D=(h/k)v_m\{3N/4\pi V\}^{\frac{1}{3}}, \tag{1}$$

where N is the number of atoms in volume V of the crystal and v_m is defined by the formula

$$3/v_m^3=\sum_i(1/v_{mi}^3), \quad i=1,2,3, \tag{2}$$

in which the v_{mi} are the three velocities of propagation of plane elastic waves in the crystal, averaged over all directions in the crystal. A given direction of propagation in a cubic crystal is conveniently specified by its direction cosines, α, β, γ, with respect to the principal crystal axes. The corresponding propagation velocities are then given in terms of the elastic constants, c_{jk}, of the lattice by the expression

$$z_i=(\rho v_i^2-c_{44})/(c_{11}-c_{44}), \tag{3}$$

provided the z_i are the three real roots of the cubic equation,[1]

$$z^3-z^2+(1-K^2)\Gamma z-(1-3K^2+2K^3)\chi=0, \tag{4}$$

where

$$K=(c_{12}+c_{44})/(c_{11}-c_{44}), \quad \Gamma=\alpha^2\beta^2+\beta^2\gamma^2+\gamma^2\alpha^2,$$
$$\chi=\alpha^2\beta^2\gamma^2.$$

It follows immediately from Eqs. (2) and (3) that

$$\frac{3}{v_m^3}=\left[\frac{\rho}{c_{11}-c_{44}}\right]^{\frac{3}{2}}\int_0^{4\pi}\left[\sum_i\frac{1}{(C+z_i)^{\frac{1}{2}}}\right]\frac{d\Omega}{4\pi}, \tag{5}$$

where $C=c_{44}/(c_{11}-c_{44})$, and $d\Omega$ is an element of solid angle. The present paper is concerned with the evaluation of the integral in Eq. (5).

Hopf and Lechner[2] devised a method for the approximate evaluation of the integral which is, briefly, as follows: The function $f(z)=(C+z)^{-\frac{1}{2}}$ is replaced in the interval $0<z<1$ by a fifth degree polynomial in z. The coefficients of z in this polynomial are obtained by the Lagrange interpolation method. This amounts to forcing the representative function through the points $f(0)$, $f(1)$ and four equally spaced intermediate points. The sum in the integrand then appears as a series of sums of powers, up to the fifth, of the roots of the cubic Eq. (4), multiplied by numerical coefficients. But such sums of powers are directly expressible in terms of the coefficients of the cubic, which are constants apart from the quantities Γ and χ. Accordingly, the approximate evaluation of the integral requires only computation of the average values of various functions of the direction cosines, α, β, and γ. These averages are, of course, the same for all cubic crystals and are given by Hopf and Lechner.

Three defects in the foregoing method are apparent: first, it is extremely laborious, and the labor increases rapidly as higher powers of z are introduced in the representative functions;[3] second, no cognizance is taken of the actual range of values of the roots or of their distribution in solid angle; third, the method contains no means for ascertaining the accuracy of the result obtained. In accordance with Eq. (4), both the range and distribution of the roots depend solely on the quantity K. It is shown hereafter than if $K>1$, two of the roots are negative and the third is greater than

TABLE I. Values of the constant K, and the anisotropy factor, A, for various cubic crystals.[a]

	K	A		K	A		K	A
Fe	2.29	2.32	Ag	1.74	2.88	Al	1.13	1.18
Ni	2.12	2.63	Pb	1.64	3.89	W	1.01	1.01
Cu	2.09	3.21	Cu_3Au	1.63	2.52	NaCl	0.70	0.69
ZnS	1.98	1.16	Au	1.40	2.91	CaF_2	0.60	0.57
LiF	1.93	1.69	C	1.37	1.60	KI	0.38	0.37
MgO	1.79	1.42	NaBr	1.36	1.37	KCl	0.37	0.37

[a] Most of these are computed with values of the elastic constants tabulated by R. F. S. Hearmon, Revs. Modern Phys. **18**, 409 (1946).

* Publication assisted by the Ernest Kempton Adams Fund for Physical Research of Columbia University.
† Now at Corning Glass Works, Corning, New York.
[1] M. Born, *Atomtheorie des festen Zustandes*, Enc. Math. Wiss. (Teubner, Leipzig), Vol. 3, p. 648.
[2] L. Hopf and G. Lechner, Verhandl. deut. physik. Ges. **16**, 643 (1914).
[3] Fuchs has employed an eighth degree polynomial. See Proc. Roy. Soc. (London) **A153**, 622 (1936) and **A157**, 444 (1936).

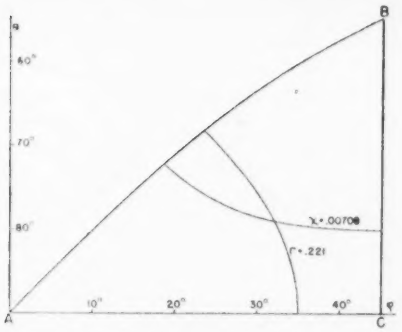

FIG. 1. The basic triangle, showing a line of constant Γ and a line of constant χ.

1 for all directions in the crystal; if $K<1$, all three roots lie between 0 and 1, but in general two lie close to 0 and the third close to 1. Approximate values of K for various cubic crystals are given in Table I: it will be noted that $K>1$ for all metals and many other crystals. Evidently, an approximation function fitted in the interval 0 to 1 is ill-suited to represent the behavior of these materials.

Obvious improvement in the method of Hopf and Lechner is gained if $f(z)$ is represented by a polynomial in the intervals in which the roots actually lie, as suggested by Durand.[4] But the accuracy of the result remains uncertain, and also the optimum degree of the polynomial to be employed, and the choice of the values of z to be used in the computation of its coefficients. A means for the removal of these uncertainties is suggested by the following analysis.

Let the integral in Eq. (5) be denoted by Y and written in the form

$$Y=\frac{1}{4\pi}\sum_i\int_{z_i}\frac{1}{(C+z_i)^4}\frac{d\Omega_i}{dz_i}dz_i, \tag{6}$$

where, now, $(d\Omega_i/dz_i)dz_i$ is the element of solid angle associated with values of the ith root lying between z_i and z_i+dz_i. Evidently, the values of z chosen for computation of the representative function should include those at which maxima in the functions $d\Omega_i/dz_i$ occur. Furthermore, if the three distribution functions, $d\Omega_i/dz_i$, are known, a direct measure of the accuracy of the approximate method follows from comparison of values of Y obtained when the true and representative functions are, respectively, inserted in the integrand. The optimum degree of the representative polynomial is then the lowest that yields a desired accuracy. Accordingly, the matters of immediate interest are, first, the specification of the ranges of the roots in terms of K, and second, the determination of the functions $d\Omega_i/dz_i$. Analytical expressions for the distribution functions in terms of K have not been obtained (otherwise no approximation would be necessary), but a numerical evaluation thereof for a particular crystal permits a satisfactory resolution of the questions raised in the foregoing.

[4] M. A. Durand, Phys. Rev. **50**, 449 (1936).

DESCRIPTION OF THE METHOD

Consider a unit vector drawn from the origin of a rectangular coordinate system whose axes lie parallel to the principal crystal axes. The direction of this vector may be specified by the polar coordinates, θ, φ, of its point of intersection with a unit sphere centered on the origin. In consequence of the crystal symmetry, the value of Y is 48 times the value of the integrals in Eq. (5) extended over the solid angle subtended by the right spherical triangle whose vertices lie at the points $\theta=90°$, $\varphi=0°$; $\theta=54°45'$ $(\cos^2\theta=\frac{1}{3})$, $\varphi=45°$; $\theta=90°$, $\varphi=45°$. Figure 1 is a plan drawing of this triangle, in which the abscissas are proportional to φ and the ordinates to the compliment of θ. Goens[5] has given closed expressions for the three roots of Eq. (4) at all points on the boundary of the triangle. Expressed in terms of K, these are as follows.

For the boundary AC,

$$z_1, z_2=\tfrac{1}{2}\{1\pm(\cos^2 2\varphi+K^2\sin^2 2\varphi)^{\frac{1}{2}}\},\quad z_3=0; \tag{7}$$

for the boundary AB,

$$z_1, z_2=\tfrac{1}{4}\{(K-1)\sin^2\psi+2[1\pm F(K)]\},$$
$$z_3=\tfrac{1}{2}(1-K)\sin^2\psi, \tag{8}$$

where

$$F(K)=\{-\tfrac{3}{4}(5K+3)(K-1)\sin^4\psi + (4K+3)(K-1)\sin^2\psi+1\}^{\frac{1}{2}},$$

and ψ is the polar angle measured along AB from A.

For the boundary BC the formulas are those of the boundary AB with θ substituted for ψ and z_2, z_3 interchanged. In these expressions z_1 is the root corresponding to the longitudinal wave, is always positive, and $z_1\gtrless 1$ according as $K\gtrless 1$. The roots z_2 and z_3 correspond to transverse waves, are negative or positive according as $K\gtrless 1$, and $|z_2|\gtrless|z_3|$.

The values of the roots at the points A, B and C are given in Table II. It will appear presently that these values determine the ranges of the roots. If $K>1$, the negative roots lie between $\frac{1}{2}(1-K)$ and 0, and the

TABLE II. Values of the roots of Eq. (4) at the vertices of the basic triangle, Fig. 1.

	A	B	C
Γ	0	1/3	1/4
χ	0	1/27	0
z_1	1	$\frac{1}{3}(1+2K)$	$\frac{1}{4}(1+K)$
z_2	0	$\frac{1}{3}(1-K)$	$\frac{1}{4}(1-K)$
z_3	0	$\frac{1}{3}(1-K)$	0

[5] E. Goens, Ann. phys. **29**, 279 (1937). Formulas appropriate to crystals of the tetragonal and hexagonal systems are also given.

positive root between 1 and $\frac{1}{3}(1+2K)$. If $K<1$, the smaller roots lie between 0 and $\frac{1}{2}(1-K)$, and the larger between $\frac{1}{3}(1+2K)$ and 1.

The computation of $d\Omega/dz$ for each of the three roots is based upon a graphical method for the solution of the cubic Eq. (4.)[6] The substitution $z=y+\frac{1}{3}$ reduces this equation to the form

$$y^3+py+q=0, \tag{9}$$

where

$$p=(1-K^2)\Gamma-\tfrac{1}{3},$$
$$q=\tfrac{1}{3}(1-K^2)\Gamma-(1-3K^2+2K^3)\chi-2/27. \tag{10}$$

In accordance with Eq. (9), p varies linearly with q for constant y. If p, q are regarded as the orthogonal coordinates of a point, then the curve $y=$ real constant is a straight line, such as the line AC of Fig. 2, which corresponds to $y=-\frac{1}{3}(z=0)$. The envelope of this family of lines is the discriminant curve of the cubic, the equation of which is

$$4p^3=-27q^2. \tag{11}$$

The discriminant is shown as the curve NOM of Fig. 2. All points corresponding to values of p and q that yield real roots of Eq. (9) lie on, or within the cusp of, this curve. Associated with a point on either branch of the discriminant is a double root corresponding to the tangent to that branch, and a single root corresponding to the tangent to the other branch, both tangents being drawn through the point. The three real roots associated with a given point within the cusp are those associated with the three tangents to the discriminant, drawn through the point. They are

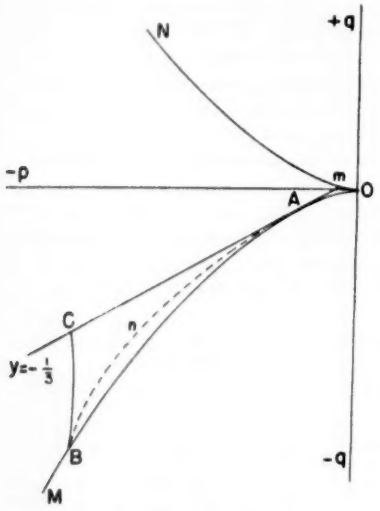

FIG. 2. Graphical solution of the reduced cubic, Eq. (9) (schematic).

[6] C. Runge, *Graphical Methods* (Columbia University Press, New York, 1912), p. 59.

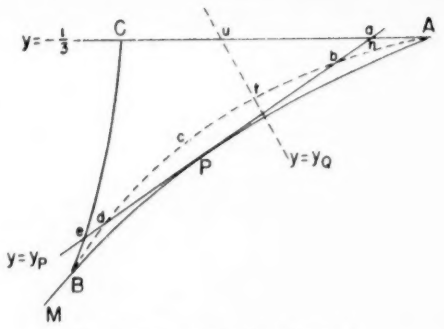

FIG. 3. Detail of Fig. 2 (schematic).

the respective double roots associated with the three tangent points on the discriminant. The values of the double roots at points on the discriminant are given by the expression

$$y=\pm(-p/3)^{\frac{1}{2}}, \tag{12}$$

where p is the abscissa of the point and the sign of y is same as that of the ordinate, q. It follows that, for different points within the cusp, the absolute values of the real roots are monotonically increasing functions of the absolute values of the abscissas of the points of tangency with the discriminant.

In virtue of Eqs. (10), the triangle of Fig. 1 can be mapped on the p–q space of Fig. 2. The p, q values corresponding to points A and B satisfy Eq. (11) and q is negative, hence both lie on OM. One root corresponding to point C and, by Eq. (7) to all points on AC, is $y=-\frac{1}{3}(z=0)$. Hence the line AC of Fig. 1 maps as the tangent AC of Fig. 2. The boundary AB of Fig. 1 maps as the dotted curve AnB of Fig. 2. (Not all values of p and q that yield real roots of Eq. (9) are consistent with Eqs. (10), because the ranges of possible values of Γ and χ are limited to $\frac{1}{3}$ and $1/27$, respectively.) Now Γ and χ may be regarded as curvilinear coordinates of points in the triangle ABC of Fig. 1. Hence, through Eqs. (10), every point in this triangle can be mapped in the triangular area $AnBC$ of Fig 2, *and vice versa*.

It should be noted that the triangle $AnBC$ of Fig. 2 corresponds to $K>1$. If $K<1$, the point A remains unaltered, but point C lies on Am and point B on AO. If $K=0$, C coincides with m and B with O; if $K=\frac{1}{3}$, C lies on the p-axis.

Earlier remarks concerning the signs of the roots and their ranges are immediate deductions from Fig. 2. For example, it is evident that, for $K>1$, the maximum positive root corresponds to the tangent to ON through B, and the negative root of greatest absolute value corresponds to the tangent through C to OM prolonged.

The reader should now imagine that Fig. 1 is modified by the addition, within the triangle, of a grid of coordinate lines of constant Γ and constant χ. (One each is shown in the figure.) It follows from the foregoing that to any area within the triangle $AnBC$ of Fig. 2 there

corresponds an area in the triangle ABC of Fig. 1, which can be mapped with the aid of this coordinate grid. The value of this area is proportional to $\int d\theta d\varphi$. Suppose, next, that the abscissa of every point of the grid is reduced in the ratio $\sin\theta$: 1. Then any area mapped on the shrunken grid is proportional to $\int \sin\theta d\theta d\varphi$, i.e. to the solid angle associated with that area. Hence to any area in the triangle of Fig. 2 there corresponds a solid angle measurable with a planimeter. This is the basis of the present method for measuring $d\Omega/dz$, which will now be described.

A portion of Fig. 2 is redrawn, schematically, in Fig. 3. Here ae is the line corresponding to the (negative) double root y_P on AM. It must be recalled that, in accordance with the present convention regarding the negative roots, $|z_2|>|z_3|$. Now for all points in the area $AnbaA$, tangent points of *both* tangents to AM lie between A and P, hence, by Eq. (12), *both* negative roots corresponding to such points are less than y_P. But for all points in the area $abcdeCa$ the tangent point of only one tangent, namely that corresponding to the smaller root, lies between A and P, i.e., only the root z_3 is less than y_P. Thus the solid angle, Ω, associated with roots z_2 less than y_P is that corresponding to the area $AnbaA$, while the solid angle associated with roots z_3 less than y_P is that corresponding to the area $AnbcdeCA$. Furthermore, let the dashed line, ut, be the tangent to ON corresponding to the (positive) double root y_Q. Then the solid angle associated with roots z_1 less than y_Q is that corresponding to the area $AntuA$.

Therefore, to obtain the solid angles Ω_1, Ω_2, Ω_3 associated, respectively, with roots z_1, z_2, z_3, less than preassigned values it is necessary only to plot the corresponding straight lines ae and ut on the shrunken grid of Fig. 1 and planimeter the appropriate areas. Curves of Ω_i as function of z_i are plotted, and graphical differentiation yields the functions $d\Omega_i/dz_i$.

The procedure described in the foregoing has been completed for the value $K=2.29$ of crystalline iron, with the result shown in Fig. 4. With regard to $d\Omega_3/dz_3$, separate analysis shows that, in the neighborhood of $z_3=0$,

$$\frac{d\Omega_3}{dz_3}=\frac{\pi}{8}\left\{\frac{1+K}{(1+2K)(1-K)z_3}\right\}^{\frac{1}{2}}.$$

Hence the contribution of this region to the quantity Y remains finite and computable.

The curves of Fig. 4 suggest that if a fifth degree polynomial is adopted to represent $f(z)$, then suitable values of z to be used for computing the coefficients of this polynomial are $\frac{1}{2}(1-K)$, $\frac{1}{3}(1-K)$, 0, 1, $\frac{1}{2}(1+K)$ and $\frac{1}{3}(1+2K)$. These lie at the termini of the resultant distribution function $\Sigma_i d\Omega_i/dz_i$, and at or near its three maxima. A significant computational advantage accrues from this choice of z values, for then an analytical solution of the resulting five simultaneous equations yields closed expressions for the polynomial coefficients and, with the aid of the averages of the appropriate functions of Γ and χ previously mentioned, a closed expression for the approximate value of Y itself, all in terms of the single parameter K. Thus, let $[f(z)]_K$ denote the representative polynomial given by the expression

$$[f(z)]_K=a_0+a_1z+a_2z^2+a_3z^3+a_4z^4+a_5z^5,$$

and

$$Y_R=\int_0^{4\pi}\{\sum_i [f(z_i)]_K\}d\Omega/4\pi. \tag{13}$$

Then

$$a_5=(1/x^2)\{2.25m_1/bd-9m_2/bcg+40.5m_3/cdf-9m_4/bcf+20.25m_5/ceg\},$$
$$a_4+(2+\tfrac{2}{3}x)a_5=(1/x)\{3m_1/bd+3m_2/xbc-40.5m_3/xdf-3m_4/bcf\},$$
$$a_3+2a_4+(x^2-x+3)a_5=(1/x)\{m_1/b+(m_2-m_4)/bc\},$$
$$a_2+(2-x)a_3+(x^2-3x+3)a_4+(2-x)(x^2-2x+2)a_5=(1/x)\{m_1-(m_4/b)\},$$
$$a_1+a_2+a_3+a_4+a_5=m_1,$$
$$a_0=m_0,$$

where

$$m_0=f(0), \quad m_3=f(\tfrac{2}{3}x)-m_0, \quad x=\tfrac{1}{2}(1-K), \quad d=3-2x,$$
$$m_1=f(1)-m_0, \quad m_4=f(1-x)-m_0, \quad b=1-x, \quad e=3-4x,$$
$$m_2=f(x)-m_0, \quad m_5=f(1-4x/3)-m_0, \quad c=1-2x, \quad f=3-5x,$$
$$g=3-7x.$$

Furthermore,

$$Y_R=-5a_5(16x^3be)/385+(5a_5+2a_4)(16x^2b^2)/21+(5a_5+4a_4+3a_3)(4x^2e)/105-(5a_5+4a_4+3a_3+2a_2)(4xb)/5+m_1+3m_0. \tag{14}$$

The curves of Fig. 4 appertain specifically to a crystal for which $K=2.29$. However, certain characteristics of these curves are independent of the value of K, and these both justify the application of Eq. (14) to crystals of arbitrary K and permit a facile computation of approximate distribution functions for such crystals. Thus, the maximum of $d\Omega_1/dz_1$ always lies at the value of z_1 corresponding to $\frac{3}{4}$ of the interval of z_1; the maximum of $d\Omega_2/dz_2$ always lies slightly beyond the value of

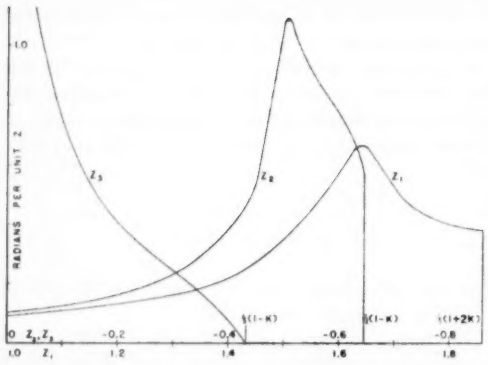

FIG. 4. The distribution functions for $K=2.29$.

z_2 corresponding to $\frac{2}{3}$ of the interval to z_2; the maximum of $d\Omega_3/dz_3$ always lies at $z_3=0$, and its minimum, which is zero, always lies at the value of z_3 corresponding to $\frac{2}{3}$ of the interval of z_2. Furthermore, the interval of z_1 is 4/3 that of z_2, irrespective of the value of K, and all three intervals are proportional to $|K-1|$. Lastly, the areas under all three curves must always equal $4\pi/48$. Hence the distribution curves for any cubic crystal are approximately those obtainable from Fig. 4 by altering the abscissas of all points in the ratio $|K-1|/(2.29-1)$ and altering their ordinates in the inverse ratio.

If the curves of Fig. 4 are replotted with a single scale of abscissas, so that those for z_2 and z_3 lie to the left of $z=0$, and that for z_1 lies to the right of $z=1$, then the distribution functions for crystals with $K<1$ are similar, in the above sense, to those obtained by reflection of the z_2 and z_3 curves in the plane $z=0$ and reflection of the z_1 curve in the plane $z=1$. The remarks of the preceding paragraph are applicable without modification to these curves.

IMPROVEMENT OF THE ACCURACY OF THE METHOD

The accuracy of a tentative set of distribution functions can be readily ascertained as follows. Consider the two expressions

$$(a)\quad \frac{1}{4\pi}\sum_i \int_{z_i} [f(z_i)]_R (d\Omega_i/dz_i)dz_i,$$

and

$$(b)\quad \frac{48}{4\pi}\sum_i \int_{z_i} [f(z_i)]_R (d\Omega_i/dz_i)_C dz_i. \qquad (15)$$

Here the range of each integral is the range of values of the indicated root of the cubic Eq. (4), $(d\Omega_i/dz_i)$ is the *true* distribution function for this root, and $(d\Omega_i/dz_i)_C$ the computed distribution function. Then (*a*) is identical with the quantity Y_R and is evaluated exactly by Eq. (14). The accuracy of the computed function follows by comparison of this figure with that obtained from expression (*b*) with the aid of a planimeter. The observed discrepancy is 0.23 percent for the functions of Fig. 4, and this is a reasonable estimate of the intrinsic inaccuracy of the graphical method employed. The procedure for obtaining the approximate distribution functions of other crystals from those of iron, described at the end of the preceding section, is verified by application of formulas (*a*) and (*b*) to the data of lead ($K=1.64$). The discrepancy is 3.3 percent.

The percent error in the computed mean Θ_D introduced by the substitution of Y_R for Y in Eq. (5) is one third of the percent difference between these two quantities. The difference itself is given by the expression

$$\frac{48}{4\pi}\sum_i \int_{z_i} \{f(z_i)-[f(z_i)]_R\}(d\Omega_i/dz_i)_C dz_i, \qquad (16)$$

evaluated with a planimeter. Clearly approximate distribution functions, such as those of lead cited in the preceding paragraph, are entirely adequate for use in the formula (16), since the error so computed is a few percent at most. A means is therefore available whereby the approximate value, Y_R, of Y for whatever crystal can be *corrected*, so that the residual error in the computed mean Θ_D due to the approximation is entirely negligible.

As z approaches $-C$, the function $f(z)$ approaches infinity, hence the representation afforded by $[f(z)]_R$ and the accuracy of the approximation become poorer. Now the minimum value of z, $z(\min)$, is $\frac{1}{2}(1-K)$ and $1+z(\min)/C=(c_{11}-c_{12})/2c_{44}=1/A$, where A is the anisotropy factor of the crystal. The correction, computed as a function of $1/A$ with formula (16), which is to be *added* to the value of Y_R obtained with Eq. (14), is given in Fig. 5. When the value of Y_R thus corrected is substituted for the integral in Eq. (5), the associated residual uncertainty in the computed mean Θ_D is of the order 0.1 percent, which is at least an order of magnitude less than that introduced by the experimental uncertainty in the difference factor $(c_{11}-c_{44})$ of Eq. (5).

APPLICATIONS OF THE METHOD

Grüneisen and Goens[7] devised an alternative method for the evaluation of v_m. In this method the vertices of the basic triangle are the points $\theta=0$; $\theta=90°$, $\varphi=0$;

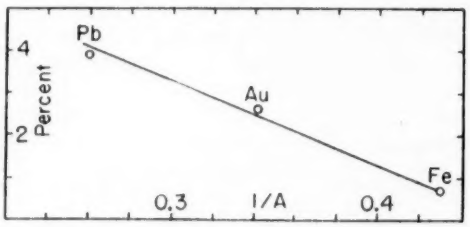

FIG. 5. Correction to be added to the value of Y_R computed with Eq. (14).

[7] E. Grüneisen and E. Goens, Z. Physik **26**, 255 (1924).

$\theta=90°$, $\varphi=45°$. Values of z_i at angular intervals of 15° on the boundary are computed with Eqs. (7) and (8); values at the same intervals on the meridians $\varphi=15°$, $\varphi=30°$ are obtained by solution of the cubic Eq. (4).[8] The corresponding mean velocities v_{mi} are computed with the trapezoidal formula, and then v_m with Eq. (2).

[8] A. Zavrotsky, *Tablas para la Resolucion de las Ecuaciones Cubicas* (Editorial Standard, Caracas, 1945), contains the real and complex roots of the reduced cubic [Eq. (9)] to six figures, for $-100<p,q<+100$, with the interval unity.

Röhl obtained by this method the mean Debye temperatures 158°K for gold and 212°K for silver at room temperature.[9] The present method *applied to Röhl's data*, yields the values 157.6°K and 211.3°K, respectively.

In conclusion, the authors gratefully acknowledge their indebtedness to the Watson Scientific Computing Laboratory of Columbia University for an especially prepared, six-place, differenced table of values of $x^{-\frac{1}{2}}$.

[9] H. Röhl, Ann. phys. **16**, 887 (1933).

PHYSICAL REVIEW VOLUME 91, NUMBER 5 SEPTEMBER 1, 1953

Deflection of High-Energy Electrons in Magnetized Iron*

STEPHAN BERKO AND FRANK L. HEREFORD
University of Virginia, Charlottesville, Virginia

(Received March 23, 1953)

High-energy electrons are scattered in magnetized iron. From a shift in the multiple scattering curves due to the reversal of the magnetic field, the effective field b_{eff} acting on electrons traversing ferromagnetic media is computed. Such an effective field is dependent on the short range forces between beam electrons and spin-aligned ferromagnetic electrons. The measurements show an effective field equal to the macroscopically measured flux density B.

THE question as to the effective magnetic field acting on charged particles traversing a ferromagnetic medium was first raised in connection with cosmic-ray deflection experiments.[1] The most complete theoretical discussion of the problem is given by Wannier,[2] who translated into quantum-mechanical language the objections, first raised by Swann[3] in classical terms, against the supposition that the effective field is necessarily equal to the macroscopically defined flux density B. Wannier's theoretical conclusions can be summed up as follows.

Since the magnetization in a ferromagnet is due to the electron spin, the macroscopically defined flux density B is the result of an average over all elementary dipoles (spin-aligned electrons). If a fast charged particle traverses the magnet, it is influenced at each point by a force due to the "true" field at this point. This true field, however, varies over a very wide range of magnitudes within regions of the order of a Compton wavelength around the spin-aligned electrons. The effective field b_{eff} is defined as an average field acting on the particle along its path. It can be shown that, although rare, close range interactions (corresponding to classical "head-on collisions") between the beam particle and the ferromagnetic electrons are decisive in determining this average. Only if all points in the magnet can be given equal statistical weight, will $b_{eff}=B$. Should short-range forces exist between beam particle and electrons, the effective field will be changed accordingly. This effect is described by introducing a "coincidence probability,"

$$p(r)=\frac{\text{(chance of finding the electron at } r \text{ if beam particle is also at } r)}{\text{(chance of finding the electron at } r \text{ if beam particle is far away)}}.$$

The average of the magnetization along the path of the beam particle is taken by first weighting the true magnetization at each point with this coincidence probability $p(r)$, a quantity dependent on the force between beam particle and electrons. Wannier has computed $p(r)$ for the case of Coulomb forces. The final result is expressed by $b_{eff}=B+2\pi M(p-1)$.

In this formula $p>1$ means attractive forces (for example positrons) $p<1$, replusive ones. It is seen that b_{eff} can be larger than B for the attractive case. The deviation of p from 1 occurs, however, at such low beam energies that it would be hardly verifiable experimentally. Should, however, short-range forces exist, the deviation of b_{eff} from B could be more pronounced than for the pure Coulomb case. An experiment on the effect-

* Supported by the Office of Ordnance Research, U. S. Army.
[1] B. Rossi, Atti accad. Lincei **11**, 478 (1930); L. M. Mott-Smith, Phys. Rev. **39**, 403 (1932); B. Rossi, Nature **128**, 300 (1931).
[2] G. H. Wannier, Phys. Rev. **72**, 304 (1947).
[3] W. F. G. Swann, Phys. Rev. **49**, 574 (1936).

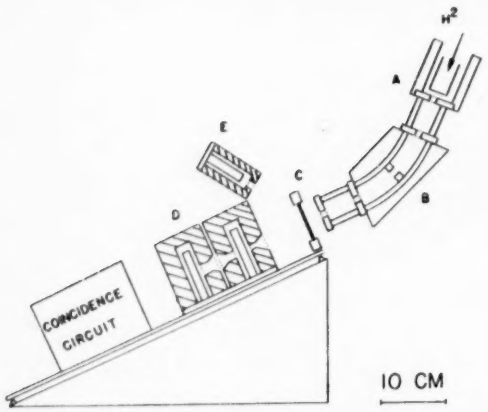

FIG. 1. Experimental setup. A=boron target; B=magnetic analyzer; C=iron scatterer; D=counter telescope; E=monitor. Shaded areas represent lead shielding.

ive field can therefore be thought of as a detection measurement of possible short-range interactions.

Successful experiments on cosmic-ray mu mesons[4] have shown the effective field to be equal to the macroscopically measured B. These experiments use calculated corrections for multiple scattering effects. A more recent experiment[5] eliminates these calculated corrections by measuring directly the change in the multiple scattering distribution of cosmic-ray mesons traversing a block of iron, due to an applied magnetic field. The results verify $b_{eff}=B$.

The only existing experiment on electron deflection was that of Alvarez,[6] the results of which are inconclusive, showing, however, that at best b_{eff} is much smaller than B. This was most probably due to the great extent multiple scattering competes with the magnetic deflection, and to the way these multiple scattering effects were corrected.[7] Calculations using Wannier's results show that, in order to be able to differentiate the magnetic deflection from Coulomb scattering, higher energies than those used by Alvarez are needed.

EXPERIMENTAL METHOD

The method of the present experiment is indicated in Fig. 1. A small Van de Graaff generator was used to produce high energy electrons from the $B^{11}(d, p)B^{12}$-$(\beta^-)C^{12}$ reaction.[8] The generator was operated at 900 kv and furnished approximately 25 microamperes of deuteron current. The electrons emerging from the boron target (a) were analyzed magnetically and collimated by the analyzer (b) which had a 17.5-cm radius of curvature. The monoenergetic beam of electrons emerging from (b) struck an iron sheet (c) perpendicular to it, which was part of a closed magnetic circuit. The electrons were multiply scattered by the 0.06-cm iron sheet and were counted by the G–M counter telescope (d). The telescope consisted of two thin wall (25 mg/cm²) G–M counters surrounded by lead cylinders with $\frac{1}{4}$-in. collimating slits. It could be rotated in steps of 3° in a plane containing the incident beam about an axis going through the iron scatterer. Counting rates were taken by a coincidence circuit having 1.6×10^{-6} sec resolving time.

In order to calibrate the energy of the incident electrons, a momentum distribution of the B^{12} beta spectrum was first measured with the telescope at 0° and with the scatterer (c) removed. This momentum distribution was then fitted to existing curves[8] and in this way an energy *vs* magnetic analyzer current calibration curve was found. This curve fitted well the one computed from magnetic field measurements and geometric considerations. An angular distribution curve without the iron scatterer was measured and the spread in the collimated beam was found to be less than 3°. Finally, the background counting rate was taken by reversing the field in the analyzer and also stopping the beam with a lead block placed in front of the collimator. It amounted to less than 20 percent of the total counting rate and was not subtracted from the final data since it did not alter the effective magnetic shift.

The actual data were obtained by taking the counting rate at different angles, with the magnetic field in the scatterer in both directions. A single thin wall G–M counter with a lead collimator (e) placed at 0° behind the scatterer and 45° above the telescope was used to monitor the electron flux. Thus, two multiple scattering curves were obtained, displaced from the symmetry position by the magnetic deflection due to the effective field. It was this displacement which was used to

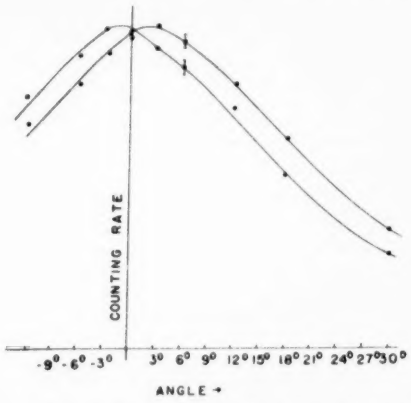

FIG. 2. Magnetically shifted multiple scattering distribution curves $f_+(\theta)$ and $f_-(\theta)$ for incident electron momentum $P_0=7.9$ Mev/c and magnetic field $B=17\,500$ gauss.

[4] F. Rasetti, Phys. Rev. **66**, 1 (1944); G. Bernardini *et al.*, Phys. Rev. **68**, 109 (1945).
[5] S. Berko, Phys. Rev. **86**, 598 (1952).
[6] L. Alvarez, Phys. Rev. **45**, 225 (1934).
[7] Professor L. Alvarez (private communication).
[8] See for example Hornyak, Dougherty, and Lauritsen, Phys. Rev. **74**, 1727 (1948).

compute b_{eff}. As a secondary effect, the displacement of the scattering curves due to hysteresis in the iron scatterer was measured. This was achieved by taking the counting rate at a given angle setting of the telescope as a function of the current in the magnetizing coil of the scatterer.

DISCUSSION OF DATA

As mentioned, it was necessary to use high-energy electrons in order to differentiate between the magnetic deflection and Coulomb multiple scattering. A complete description of the multiple scattering plus magnetic scattering phenomena would have required the solution of a generalized diffusion equation. Such an equation was set up for the case of constant magnetic field by Scott,[9] in connection with a discussion of cloud-chamber experiments. His conclusion was that for small angles the magnetic curvature is simply to be added to the scattering produced deflections. The evaluation of our results rely therefore on the fact that the magnetic deflection is, in a first approximation, independent of multiple scattering. We therefore expect, as a main effect, a total shift of the multiple scattering angular distribution curve by an amount equal to the magnetic deflection. The constancy of the shift with angle was, in first order, verified by our experimental data.

Letting $f_+(\theta)$ be the experimentally measured angular distribution function with the field in the scatterer up, and $f_-(\theta)$ the distribution with the field down, we have

$$\Delta(\theta)=f_+(\theta)-f_-(\theta).$$

In order to be able to detect such a $\Delta(\theta)$, the following conditions had to be satisfied:

(1) The ratio $\Phi/\langle\theta\rangle$, where Φ is the magnetic deflection and $\langle\theta\rangle$ the root-mean-square angle of multiple scattering, had to be as large as possible.

(2) Since we wanted to maximize the measured quantity,

$$\Delta(\theta)=f_+(\theta)-f_-(\theta)=g(\theta+\Phi)-g(\theta-\Phi), \qquad (1)$$

where $g(\theta)$ is the multiple scattering curve without field on, $dg/d\theta$ had to be large, and therefore $\langle\theta\rangle$ small.

(3) In order to have clear-cut effects, the energy of the electron beam had to be smaller than 10 Mev, so that radiation losses in iron would be small.

It has been shown[2] that for $\Phi/\langle\theta\rangle$ to be maximum, a thick target is necessary, such that

$$E\cong\tfrac{1}{4}E_0,$$

where E=energy of electrons when leaving scatterer, E_0=energy of electrons when entering scatterer. Such a scatterer would have had, for $E_0<10$ Mev, a thickness above the electron diffusion limit, and would have led to hardly detectable $\Delta(\theta)$.

In order to satisfy all conditions, a compromise value for the thickness of the scatterer and initial energy of electron beam had to be selected.

[9] W. T. Scott, Phys. Rev. **76**, 212 (1949).

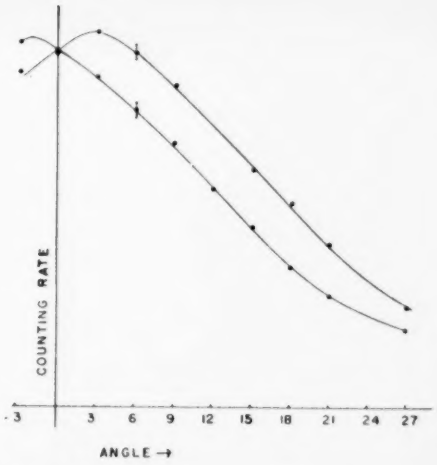

FIG. 3. Magnetically shifted multiple scattering curves $f_+(\theta)$ and $f_-(\theta)$ for incident electron momentum $P_0=8.8$ Mev/c and magnetic field $B=18\,800$ gauss. These curves were used to compute b_{eff} in text.

Figure 2 shows one set of data, used for qualitatively establishing the effect. An improvement in the experimental techniques led to Fig. 3 which is used for the quantitative discussions. The improvement consisted in an increase of the applied magnetic field, an increase in the initial electron energy, and better current normalization.

The 0.06-cm thick scatterer was a Westinghouse iron-cobalt alloy (Hyperco) capable of high magnetic saturation values.

The experimental histograms were approximated by two multiple scattering curves such as to yield the best fit for the condition:

$$f_+(\theta)-f_-(\theta)=g(\theta+\Phi)-g(\theta-\Phi).$$

The angle Φ was obtained by shifting the two scattering curves until they over-lapped, the shift being 2Φ.

Figure 3 yields $\Phi=0.040$ radian for the incident electron momentum of $P_0=8.8$ Mev/c. It was estimated that the error involved in getting Φ by curve matching was ±3 percent.

Since energy loss is not negligible it had to be corrected for, before b_{eff} could be calculated.

Given the multiple scattering formula, the expression for magnetic deflection and the range energy relation, Wannier computed the magnetic shift Φ and the multiple scattering angle $\langle\theta\rangle$ in terms of the initial and final energy of the electron beam (see formulas 36 and 37 of reference 2).

His formulas express Φ as the difference of two large terms; the precise knowledge of the energy loss in the iron is therefore imperative. As a simpler approximation to these formulas, we can assume for our case linear energy-range dependence.

Taking the known relativistic form of magnetic

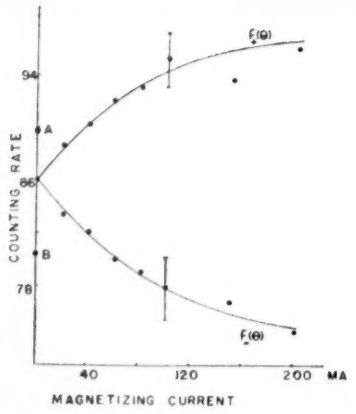

FIG. 4. Magnetization curve and hysteresis effect. $f_+(\theta)$ and $f_-(\theta)$ at $\theta=6°$ as function of magnetizing current. Points A and B are the counting rates after the current was turned off and before demagnetization, and represent the effect due to the retentivity of the iron scatterer.

deflection as

$$d\Phi/dx=300\,b_{\text{eff}}/P, \tag{2}$$

and assuming

$$dP/dx=C=\text{const}\,(\text{ev}/c\cdot\text{cm}),$$

we get for the magnetic deflection due to b_{eff},

$$\Phi=\frac{300\,b_{\text{eff}}}{C}\ln\frac{P_0}{P}. \tag{3}$$

In this expression P_0 and P are the initial and final momenta of the electron beam in ev/c, and b_{eff} is given in gauss.

As a first approximation for the multiple scattering angle one gets, for constant dP/dx and $\beta=1$,

$$\langle\theta^2\rangle=(E_s^2/PP_0)(x/X_0) \tag{4}$$

where $E_s=21\times10^6$ ev. X_0 is the radiation length for iron, P_0 and P, are the same as in Eq. (3), and x is the thickness of the iron sheet.

Instead of using the maximum range-energy relations in the above formulas, an average range-energy value was introduced,[10] yielding for iron $C=17.94$ Mev/$c\cdot$cm and $P=7.72$ Mev/c for $P_0=8.8$ Mev/c.

Introducing, then, these values in the approximate formula (3), we finally get $b_{\text{eff}}=18\,400$ gauss. The macroscopic magnetic flux density B has been measured with a ballistic galvanometer setup, calibrated with a standard mutual inductance. $B=18\,800$ gauss was found. The effective field, therefore, is within 5 percent of the macroscopic B. We expect a ±5 percent discrepancy because of the uncertain energy-range values, the error introduced in finding Φ and the intrinsic approximations involved in the formulas used. Within these approximations $b_{\text{eff}}=B$.

The approximate formula for multiple scattering [Eq. (4)] was checked only in first order; however, no better fit is to be expected, because of the background, the finite width of the incident electron beam and the large thickness of iron involved.

Figure 4 shows the results of the magnetization curve and hysteresis effect measurement. In the part of the experiment, we have plotted $f_+(\theta)$ and $f_-(\theta)$ for $\theta=6°$ as a function of the magnetizing current in the scatterer. Had $g(\theta)$ been a linear function of θ, $\Delta(\theta)$ would have been a direct measure of Φ, and therefore of b_{eff} *vs* current. This is, as a first approximation, the case for $g(6°\pm3°)$ in which region we are interested. The plot can be thought of as a magnetization curve for b_{eff} *vs* magnetizing current, with a corresponding change in ordinate. The saturation shape of the magnetization curve checks with the macroscopically measured B *vs* magnetizing current curve. Points A and B on the plot are the counting rates observed after turning the magnetizing current off and before demagnetizing the scatterer with a decreasing alternating current. They represent the effect due to the retentivity of the iron scatterer and also check quantitatively with the macroscopically measured retentivity.

An investigation with a pickup coil of the magnetic field of the magnet outside the scatterer shows negligible effects due to stray magnetic field. This was also checked by doing an experiment with a copper sheet replacing the iron scatterer in the magnet. The copper had a thickness giving about equal multiple scattering curve as the iron sheet (equal radiation lengths). No detectable shift of the scattering curves was observed by changing the direction of the magnetizing field.

CONCLUSION

Within experimental errors, and within the errors introduced by the approximations correcting for energy loss, it has been demonstrated that $b_{\text{eff}}=B$. The experiment shows, therefore, no evidence for strong short-range interaction forces between the beam electron and the spin-aligned ferromagnetic electrons. A thorough theoretical investigation of the strength of the short-range forces needed to alter the $b_{\text{eff}}=B$ result would be necessary, in order to decide, whether a similar experiment with high-energy positrons instead of electrons would show up quantitatively the existence of electron-positron annihilation forces. Such an experiment is being contemplated in the near future.

The authors would like to thank the Department of Terrestrial Magnetism of the Carnegie Institution of Washington, and in particular Dr. Norman P. Heydenburg, for the use of their Van de Graaff generator.

[10] Fowler, Lauritsen, and Lauritsen, Rev. Modern Phys. **20**, 267 (1948)

A New Approximation Method for Order-Disorder Problems*

LLOYD D. FOSDICK† AND HUBERT M. JAMES
Purdue University, West Lafayette, Indiana

(Received May 7, 1953)

This paper presents an approximation method for the treatment of Ising lattices that is essentially an extension of Bethe's method, designed to take more direct account of the short-range order in the lattice and to give a better description of this order near the Curie point. Attention is fixed on spin configurations on a small group of sites. Full account is taken of the coupling between these spins, and the effect of coupling to the rest of the lattice is described by means of one or more long-range order parameters, and a correlation parameter characteristic of the method. These parameters are determined as functions of temperature by means of a corresponding number of consistency relations. The method is among the most accurate of the approximation methods in this field, giving about the same accuracy as Kikuchi's method, for a comparable amount of labor; its main advantage over Kikuchi's method lies in the treatment of orientational correlations between relatively remote neighbors in the lattice. The method is here applied to the plane triangular, square, and hexagonal Ising lattices, and to the simple cubic lattice. Curie points are determined, and plots of long- and short-range order and the specific heat are given for all but the hexagonal lattice. Like all other approximation methods, this one indicates only a finite discontinuity in the specific heat of the plane lattices at the Curie point, instead of the logarithmic singularity given by exact solutions. Correlation functions for the orientations of up to fifth neighbors are also given for the simple cubic lattice.

I. INTRODUCTION

THE order-disorder problem for a variety of two-dimensional Ising arrays has been solved exactly by the method of Onsager[1] and Kaufman.[2] This elegant method has not been extended to the more physically interesting but much more complex three-dimensional problems. The development of more accurate approximation methods applicable to three-dimensional problems therefore continues to be of interest. This is particularly true of methods that may contribute to the understanding of the essential features of order-disorder phenomena.

In the case of two-dimensional Ising lattices the better approximation methods, such as that of Kramers and Wannier,[3] give results in good agreement with the exact solution, for temperatures not too near the Curie point. At the Curie point, however, the exact specific heat curve has a logarithmic singularity, while all approximation methods indicate only a finite discontinuity in this quantity. Since the thermal properties of the Ising model depend entirely on the short-range order in the system, it follows that existing approximation methods given an inadequate account of the very rapid changes in short-range order near the Curie point.

This paper presents a relatively simple approximation method for the treatment of Ising lattices. It is essentially an extension of Bethe's[4] method, designed to give a more accurate treatment of the short-range order in the lattice. Like Bethe, we consider in detail the weights of the different spin configurations on a small group of sites in the lattice. The coupling of these spins to the rest of array has two effects: it tends to propagate the long-range order of the system into this set of sites, and it tends to produce short-range order in the outer shell of spins. Bethe's theory takes account only of the first of these effects; direct consideration of the second effect is the characteristic feature of the present method.

Our method will here be applied to the two-dimensional triangular, square, and hexagonal Ising lattices, and to the simple cubic lattice. The Curie point, long- and short-range order, correlation functions and the specific heat will be computed. The results for the two-dimensional problems are in decidedly better agreement with the exact results than are those given by Bethe's method. All results agree closely with those found by the very different method of Kikuchi,[5] the most accurate approximation method thus far developed. In the labor of calculation our method is comparable to Kikuchi's, but it presents some advantages in the calculation of correlation functions.

II. THE TWO-DIMENSIONAL TRIANGULAR ISING LATTICE

The basic ideas of the present method are most easily presented through their application to particular problems. The simplest situation is offered by the plane triangular lattice, which will therefore be treated first.

The Ising model of a ferromagnetic system consists of an array of spins that can be oriented in just two directions, which we describe as right and left. The energy of the system will be taken to be a sum of terms

* Based on a thesis presented by L. D. Fosdick in partial fulfillment of the requirements for the Ph.D. degree at Purdue University, January, 1953.

† Now at Control Systems Laboratory, University of Illinois, Urbana, Illinois.

[1] L. Onsager, Phys. Rev. **65**, 117 (1944).

[2] B. Kaufman, Phys. Rev. **76**, 1232 (1949).

[3] H. A. Kramers and G. H. Wannier, Phys. Rev. **60**, 252, 263 (1941).

[4] H. A. Bethe, Proc. Roy. Soc. (London) **A150**, 552 (1935).

[5] R. Kikuchi, Phys. Rev. **81**, 988 (1951).

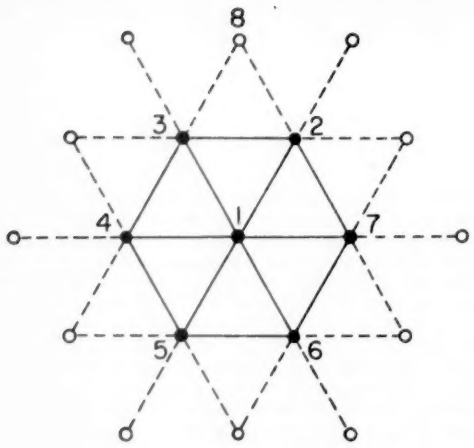

FIG. 1. Portion of triangular lattice. Site 1 is "central site"; sites 2 to 7 form "outer shell."

arising from the couplings of pairs of next neighbors in the lattice: 0 for parallel next neighbors, $v>0$ for antiparallel next neighbors. We neglect the possible presence of an external field. Long-range order in the system, if it exists, will be assumed to consist of a preponderance of right spins.

A. The Configuration Weights

Let us fix our attention on the small group of sites in the two-dimensional triangular lattice labeled 1 through 7 in Fig. 1. Site 1 will be called the central site, and sites 2 through 7 make up the outer shell. Next-neighbor bonds within the set of sites are indicated by the solid lines.

If the spins of the outer shell were not coupled to their exterior neighbors, the relative weight w for any configuration of these seven spins would be given by the Boltzmann factor $w=x^n$, where

$$x=\exp(-v/kT) \tag{1}$$

is the Boltzmann factor for a single pair of antiparallel next neighbors, and n is the number of such pairs in the given configuration. For the relative weight of this configuration in the actual system we write

$$w=x^nQ, \tag{2}$$

where Q is the additional weight factor introduced by the couplings between the outer shell of spins and their exterior neighbors.

In Bethe's theory it is assumed that interaction with the exterior lattice introduces independent weighting factors favoring right spin (that is, spin of the type favored by long-range order) on every outer shell site. If the weight for a right spin is taken to be 1, and that for a left spin $\lambda\leq 1$, the factor Q becomes simply λ^m, where m is the number of left spins in the outer shell. One then has

$$w=x^n\lambda^m. \tag{3}$$

The parameter λ will be called the long-range order parameter. According to Bethe's method, one would use this expression for the relative weights of all configurations on the seven sites to compute the probability that a right spin will be found on each individual site, as a function of x and λ. The condition that this probability be the same for sites 1 and 2, which are equivalent so far as the whole lattice is concerned, determines λ as a function of x, or of T for fixed v, and this in turn permits calculation of the order and thermal properties of the system.

Now, the orienting effects of exterior neighbors on the outer shell spins will not really be independent. For instance, the coupling of spins 2 and 3 to their common next neighbor, spin 8 in Fig. 1, will introduce a correlation in their orientations, an additional tendency for them to be parallel to each other, whether they are both left spins or both right spins. We therefore assume that Q contains an additional weight factor, $q\leq 1$, for each antiparallel pair of next-neighbor spins in the outer shell. Thus, if s is the number of such pairs in a given configuration, we take as its relative weight

$$w=x^n\lambda^m q^s. \tag{4}$$

The parameter q will be termed the correlation parameter.

It will often be convenient to express the weights in terms of the parameter

$$b=q^2x^2. \tag{5}$$

Then w will include a factor x for each antiparallel pair involving the central spin, a factor $b^{\frac{1}{2}}$ for each antiparallel pair in the outer shell, and a factor λ for each left spin in the outer shell. We shall also find it useful to introduce a dummy parameter α into the configuration weight whenever the central spin is a left spin; later we shall put $\alpha=1$.

As an example, we consider the configuration shown in Fig. 2. According to Eq. (4), this has relative weight $x^7\lambda^3q^4$, which we shall write also as $\alpha x^3\lambda^3b^2$.

The sum of the weights for all configurations on the seven sites is easily found to be

$$\begin{aligned}W=1&+\alpha x^6+\lambda^6(\alpha+x^6)+6b\{\lambda(x+\alpha x^5)+\lambda^5(x^5+\alpha x)\}\\&+(6b+9b^2)\{\lambda^2(x^2+\alpha x^4)+\lambda^4(x^4+\alpha x^2)\}\\&+(6b+12b^2+2b^3)(1+\alpha)\lambda^3x^3.\end{aligned} \tag{6}$$

B. The Consistency Conditions

From the configuration weights given by Eq. (4) one can compute the probability that a given spin will be a right spin, or a given pair of spins will be parallel, and so on, all in terms of the parameters x, λ, and q. To determine the values of the unknown parameters λ and q, as functions of x or kT/v, we shall make use of two consistency conditions.

In the infinite lattice, all sites must be equivalent as regards the probability of occurrence of right or left spins; that is, they must be equivalent as regards their contribution to the long-range order. The condition that the computed probability for finding a left spin on the central site 1 be the same as that for finding a left spin on any outer shell site (say 2) is our first consistency condition.

In the infinite lattice, all pairs of next-neighbor sites must be equivalent as regards the occurrence of parallel spins; that is, they must be equivalent as regards their contribution to the short-range order. The condition that the computed probability for occurrence of antiparallel spins on a pair of next-neighbor sites that includes the central site (say 1 and 2) shall be the same as this probability for a pair of sites in the outer shell (say 2 and 3) is our second consistency relation.

Independent consistency relations could be set up by requiring equal computed probability for given spin configurations on equivalent triples of sites, and so on. However, only two independent conditions can be satisfied by adjustment of the two parameters λ and q, and the conditions chosen above seem to be most appropriate, in view of the significance of these parameters.

When the meaning of the exponents of α, λ, x, and b in W is considered, it is easily seen that our consistency relations can be written as

$$\alpha\frac{\partial \ln W}{\partial \alpha}\bigg|_{\alpha=1}=\frac{\lambda}{6}\frac{\partial \ln W}{\partial \lambda}\bigg|_{\alpha=1}, \tag{7}$$

$$\frac{x}{6}\frac{\partial \ln W}{\partial x}\bigg|_{\alpha=1}=\frac{b}{3}\frac{\partial \ln W}{\partial b}\bigg|_{\alpha=1}. \tag{8}$$

One thus finds as the consistency conditions

$$(\lambda^2-1)\{x^6(1+\lambda^2+\lambda^4)+b[\lambda x(\lambda^2+1)(5x^4-1)+2x^2\lambda^2(2x^2-1)]+3b^2\lambda^2x^2(2x^2-1)\}=0, \tag{9}$$

and

$$x^6(1+\lambda^6)+b[(3x^5-x)(\lambda+\lambda^5)+2x^4(\lambda^2+\lambda^4)+2x^3\lambda^3]-b^2\lambda^2x^2(3+4\lambda x+3\lambda^2)-2b^3\lambda^3x^3=0. \tag{10}$$

C. Solution of the Consistency Equations for Zero Long-Range Order

The first consistency equation, Eq. (9), can be satisfied by the vanishing of either of two factors. When $\lambda=1$ the first factor vanishes, and the equation is satisfied for all values of b and x; b is then determined as a function of x by Eq. (10), with $\lambda=1$. Since $\lambda=1$ implies that the external coupling does not favor right spins over left spins, this solution must correspond to zero long-range order. It can be shown that this solution exists for all temperatures. Moreover, it is the only solution at high temperatures, since the second factor in Eq. (9) is always positive for $x>1/\sqrt{2}$.

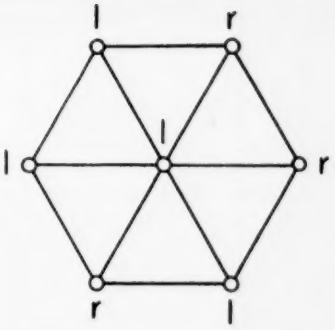

FIG. 2. Illustrative arrangement of right and left spins on the triangular lattice.

The actual solution of Eq. (10), for $\lambda=1$, was carried out numerically using Newton's method. The results of this calculation, for temperatures above the Curie point, appear in Fig. 4, in a plot of q against kT/v.

D. Location of the Curie Point

For small values of x and T, Eq. (9) can be satisfied by vanishing of the second factor, with $\lambda<1$. Such solutions of the consistency equations correspond to states of long-range order in the system. One of these solutions must be the physically significant solution for temperatures below the Curie temperature T_c, whereas the solution discussed in the previous section is the physically significant one for $T>T_c$. It is well known that in the system under consideration the long-range order goes to zero continuously as T rises to the Curie temperature T_c. Correspondingly, λ must rise continuously to the value 1 as T approaches T_c. Thus the Curie temperature corresponds to a value of x for which the second factor of Eq. (9) vanishes and Eq. (10) is satisfied, when $\lambda=1$. Elimination of b between these two equations yields the following equation for the value x_c of x at the Curie point:

$$19x_c^8+80x_c^7+88x_c^6-40x_c^5-110x_c^4-16x_c^3+40x_c^2+8x_c-5=0. \tag{11}$$

This equation has three positive roots in the range $0<x_c<1$: 0.7261, 0.6039, 0.3222. The first of these roots corresponds to a negative value of b, and thus corresponds to a solution of the consistency equations that has no physical significance. The last root corresponds to a solution with less than the maximum degree of order, more than the minimum internal energy; it does not correspond to a stable state of order of the system.[6] Thus the physically significant solution of Eq. (11) is $x_c=0.6039$, corresponding to $kT_c/v=1.983$. This is to be compared with the exact value, 1.820, found by Syozi,[7] and the approximate values 2.467, found by Bethe[4] ($z=6$), and 1.958, found by Kikuchi.[5]

[6] The significance of multiple solutions of consistency relations, and the use of the internal energy in determining which solution corresponds to a stable state of order, has been discussed by T. J. Krieger and H. M. James, J. Chem. Phys. (to be published).

[7] I. Syozi, Progr. Theoret. Phys. **5**, 341 (1950).

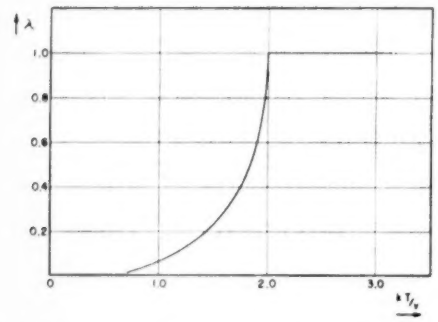

FIG. 3. Long-range order parameter λ for triangular lattice.

E. Solution of the Consistency Equations with Long-Range Order

Solution of the consistency equations for temperatures below T_c was carried out numerically by the Newton-Raphson method. The results are shown in Figs. 3 and 4. Just below T_c the long-range order parameter increases very rapidly with increasing temperature, and $d\lambda/dT$ becomes infinite as $T\rightarrow T_c$. The correlation parameter q is close to one except near T_c, where its value is 0.7737. The importance of q in the theory is measured by its deviation from 1; thus the present method offers the greatest improvement over Bethe's method in the neighborhood of the Curie point.

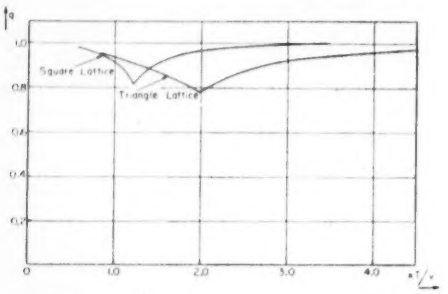

FIG. 4. Correlation parameter q for square and triangular lattice.

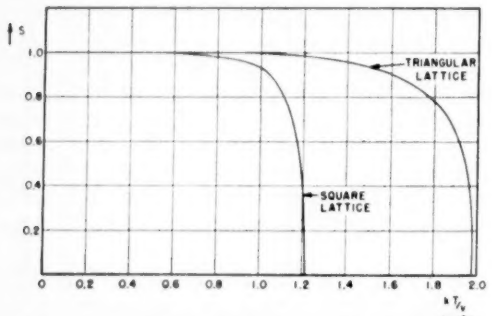

FIG. 5. Long-range order S in square and triangular lattices.

The long-range order is the probability that the spin on any site (say the central site) is a right spin, minus the probability that it is a left spin. This can be expressed in terms of W as

$$S=1-2\alpha\frac{\partial \ln W}{\partial \alpha}\bigg|_{\alpha=1}. \tag{12}$$

Similarly, the short-range order, which is the probability of parallel next-neighbors on any pair of sites (say 1 and 2) minus the probability of antiparallel next-neighbors, can be expressed as

$$\sigma=1-\frac{x}{3}\frac{\partial \ln W}{\partial x}\bigg|_{\alpha=1}. \tag{13}$$

Expressions for S and σ in terms of x, λ, and q are easily found, and need not be given here. S and σ are given as functions of kT/v in Figs. 5 and 6, respectively.

Analytic approximations for S and σ, valid near T_c, can be obtained by expanding the terms in the consistency conditions in powers of $x-x_c$, $\lambda-1$, and $q-q_c$. Note must be taken of the fact that, for $T<T_c$, $1-\lambda$ is of the order of $(T_c-T)^{\frac{1}{2}}$. One thus finds

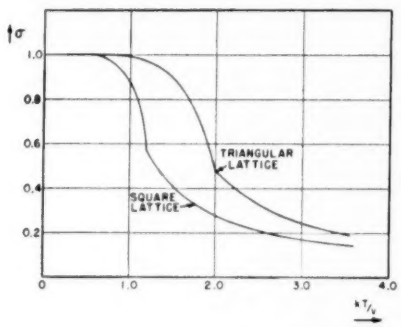

FIG. 6. Short-range order σ in square and triangular lattices.

$$S\cong 3.618(1-T/T_c)^{\frac{1}{2}}, \tag{14}$$

$$\sigma\cong 0.4779+4.093(1-T/T_c), \quad (T<T_c), \tag{15}$$

$$\sigma\cong 0.4779+0.8288(1-T/T_c), \quad (T>T_c). \tag{16}$$

The average configurational energy of an Ising array can be written

$$\bar{E}=\frac{vzN}{2}\left(\frac{1-\sigma}{2}\right), \tag{17}$$

where z is the number of next-neighbors of a site in the lattice, and N is the total number of spins. The configurational specific heat per spin is

$$c=\frac{1}{N}\frac{d\bar{E}}{dT}=-\frac{zk}{4}\left(\frac{v}{kT}\right)^2 x\frac{d\sigma}{dx}. \tag{18}$$

TABLE I. Summary of results of some order-disorder calculations.

	Triangular lattice			Square lattice			Hexagonal lattice			Cubic lattice		
	kT_c/v	$(c/k)\|_{T_{c-}}$	$(c/k)\|_{T_{c+}}$	kT_c/v	$(c/k)\|_{T_{c-}}$	$(c/k)\|_{T_{c+}}$	kT_c/v	$(c/k)\|_{T_{c-}}$	$(c/k)\|_{T_{c+}}$	kT_c/v	$(c/k)\|_{T_{c-}}$	$(c/k)\|_{T_{c+}}$
Bethe first approx.	2.467	1.90	0.119	1.44	2.14	0.214	0.9102	2.38	0.339	2.467	1.90	0.119
Bethe second approx.	...	...	...	1.31	...	...	...	...	...	2.372	2.14	0.203
New method	1.983	3.096	0.6269	1.215	3.702	0.7213	0.8017	3.375	0.8197	2.3145	2.58	0.3323
Kikuchi	1.958	3.486	0.734	1.213	3.55	0.75	...	...	...	2.3048[a]	2.902[a]	0.389[a]
Exact	1.820	∞	∞	1.135	∞	∞	0.7593	∞	∞	...	...	...

[a] Calculated with a square as the basic figure.

Since our theory predicts a finite discontinuity in $d\sigma/dT$ and $d\sigma/dx$ at $T=T_c$, it predicts a finite discontinuity in c, in contrast to the infinity in c given by the exact theory. Our theory gives as the values of c/k just below and just above the Curie point:

$$(c/k)\,|_{T_{c-}}=3.096, \quad (c/k)\,|_{T_{c+}}=0.6269.$$

Values of these quantities found by other methods are listed in Table I. Our result agrees closely with that of Kikuchi. A plot of c/k against kT/v for this lattice is shown in Fig. 7.

III. THE TWO-DIMENSIONAL SQUARE ISING LATTICE

The two-dimensional square lattice offers a slightly more complicated situation, which calls for the introduction of two long-range order parameters.

A. The Configuration Weights

We shall consider in detail the set of nine sites indicated in Fig. 8. This includes a central site labeled 1, and an outer shell of sites labeled 2 through 9. Sites 2, 4, 6, 8 will be called middle sites, and sites 3, 5, 7, 9 will be called corner sites.

As before, the relative weight for any configuration of spins on this set of sites will include a factor x for each antiparallel pair of next neighbors, and a factor Q representing the effect of coupling to the exterior spins.

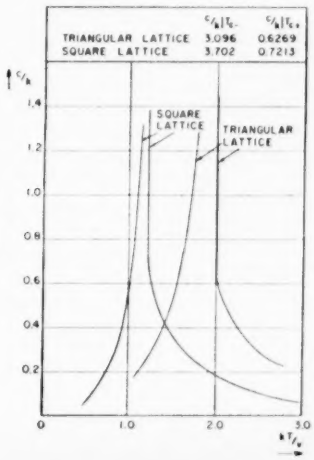

FIG. 7. Configurational specific heat per spin, c, for square and triangular lattices.

It is clear from Fig. 8 that the outer shell spins are not all equivalent in their external coupling, corner spins being coupled more strongly to the exterior spins than are middle spins. Therefore, in describing the effect of external coupling, two long-range order parameters will be used: we shall introduce into the Q for any configuration a factor $\mu\leq 1$ for each left corner spin, and a factor $\nu\leq 1$ for each left middle spin. While outer-shell spins have no common next neighbors among the exterior spins, it is clear that the existence of short-range order among the exterior spins will tend to produce short-range order in the outer shell spins. We can represent this effect by means of a single correlation parameter, $q\leq 1$, since all pairs of next neighbors in the outer shell are equivalent in their coupling to external spins. The parameter q will appear as a factor in Q once for each antiparallel pair of next-neighbor spins in the outer shell.

As before, a dummy parameter α will be included as a factor in the weight whenever the central spin is a left spin, and later set equal to 1. Again making use of the quantity b, we can then write as the weight of any configuration on the nine sites

$$w=\alpha^r\mu^s\nu^t b^u x^y, \tag{19}$$

where r is the number of left spins on the central site (0 or 1), s is the number of left corner spins, t is the

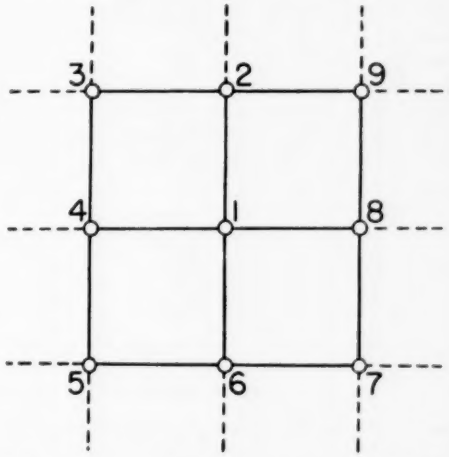

FIG. 8. Portion of square lattice. Site 1 is "central site"; sites 2, 4, 6, 8 are middle sites; sites 3, 5, 7, 9 are "corner sites."

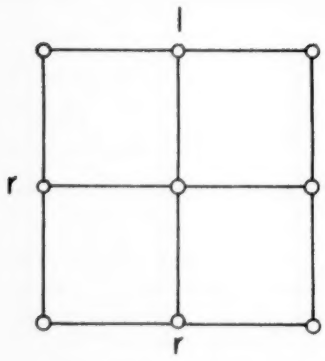

FIG. 9. Partially specified configuration in square lattice.

number of left middle spins, u is one-half the number of antiparallel next neighbors in the outer shell, and y is the number of antiparallel next-neighbor pairs that involve the central site.

The task of writing down the sum W of the weights for all possible configurations on the nine sites can be simplified by lumping together the weights of all configurations having the same assignment of spins on the middle sites.

We first consider a corner spin and its two next-neighbor middle spins. Such a set of spins will be called a corner array. The weight of any configuration can be expressed as the product of five factors. Each corner array will contribute a factor that includes a factor μ for each left corner spin, a factor $\nu^{\frac{1}{2}}$ for each left middle spin (since each middle spin is involved in two corner arrays) and a factor $b^{\frac{1}{2}}$ for each antiparallel pair of next-neighbor spins. The fifth factor, which arises from the coupling of the central spin to the middle spins, will include a factor x for each pair of antiparallel next neighbors involving the central spin, and a factor α if the central spin is a left spin.

Next let us consider the total weight of all configurations with specified spins on the middle sites. This total weight can be written as the product of five factors. Each corner array contributes a factor which is the sum of the corresponding weight factors for right corner spin and left corner spin; the fifth factor is similarly the sum of the weight factors corresponding to right and left center spins. The factor contributed by a corner array will be

$$\xi = 1+\mu b \tag{20a}$$

if the middle spins are both right,

$$\eta = \nu^{\frac{1}{2}} b^{\frac{1}{2}}(1+\mu) \tag{20b}$$

if one middle spin is right and the other left, and

$$\zeta = \nu(\mu+b) \tag{20c}$$

if both middle spins are left. The factor associated with the center spin will be

$$x^{t}+x^{4-t}\alpha, \tag{20d}$$

where, as before, t is the number of left middle spins. For example, the total weight of the configurations consistent with Fig. 9 will be $\xi\eta^2\zeta(x^2+\alpha x^2)$.

By this means, one easily finds that the total weight for all configurations on the nine sites is

$$W = \xi^4(1+\alpha x^4)+\zeta^4(\alpha+x^4)+4\xi^2\eta^2(x+\alpha x^3) + 4\eta^2\zeta^2(x^3+\alpha x)+4\xi\eta^2\zeta x^2(1+\alpha)+2\eta^4x^2(1+\alpha). \tag{21}$$

B. The Consistency Conditions

To fix the three unknown parameters μ, ν, and q, as functions of T, we require three consistency conditions. As before, there is some arbitrariness in the choice of the consistency conditions to be satisfied, but it is most natural to require the equivalence of all sites as regards long-range and short-range order. We require:

(a) the computed probability for left spin on the central site must be the same as that for left spin on any middle site;

(b) the computed probability for left spin on the central site must be the same as that for left spin on any corner site;

(c) the computed probability for antiparallel spins on next-neighbor center and middle sites must be the same as that for antiparallel spins on next-neighbor middle and corner sites.

These conditions can be expressed analytically as

$$\alpha\frac{\partial \ln W}{\partial\alpha}\bigg|_{\alpha=1} = \frac{\nu}{4}\frac{\partial \ln W}{\partial\nu}\bigg|_{\alpha=1}, \tag{22a}$$

$$\alpha\frac{\partial \ln W}{\partial\alpha}\bigg|_{\alpha=1} = \frac{\mu}{4}\frac{\partial \ln W}{\partial\mu}\bigg|_{\alpha=1}, \tag{22b}$$

$$\frac{x}{4}\frac{\partial \ln W}{\partial x}\bigg|_{\alpha=1} = \frac{b}{4}\frac{\partial \ln W}{\partial b}\bigg|_{\alpha=1}, \tag{22c}$$

respectively. On use of Eq. (21), these become

$$(\xi^2-\zeta^2)([\xi^2+\zeta^2]+\eta^2[3x^3-x])=0, \tag{23a}$$

$$b(\xi^3\mu-\nu\zeta^3)(1+x^4)+\eta^2\left(\xi^2-\zeta^2-\frac{2\xi}{1+\mu}[1-\mu^2b] - \frac{2\zeta\nu}{1+\mu}[b-\mu^2]\right)(x+x^3)+2\eta^2\left(\eta^2\left[\frac{\mu-1}{\mu+1}\right] + \frac{\zeta}{1+\mu}[\mu^2b-1]+\frac{\xi\nu}{1+\mu}[\mu^2-b]\right)x^2=0, \tag{23b}$$

$$\xi^3(\mu b-x^4)+\zeta^3\nu(b-\mu x^4)+2\eta^2b(\xi\mu+\zeta\nu)x - 2\eta^2(\xi+\zeta\mu\nu)x^3+2\eta^2\nu\mu(b^2-1)x^2=0. \tag{23c}$$

C. Solution of the Consistency Equations for Zero Long-Range Order

Equations (23a) and (23b) are satisfied identically, for all values of b and x, when $\mu=\nu=1$, or $\xi=\zeta=1+b$. Equation (23c) is not satisfied identically when $\mu=\nu=1$, and serves to determine b as a function of x. Since $\mu=\nu=1$, this solution of the consistency relations corresponds to zero long-range order. It can be shown that this solution exists for all temperatures; moreover, it is the only solution at high temperatures.[8]

Solution of Eq. (23c) with $\mu=\nu=1$, to determine $b(x)$, was carried out numerically. Figure 4 shows the corresponding variation of q with kT/v, for $T>T_c$.

D. Location of the Curie Point

The Curie temperature T_c was determined by the method used with the square lattice. For $T<T_c$, there will exist solutions with long-range order, having μ, $\nu<1$, such that the second factor of Eq. (23a) will vanish. From the known character of the second-order transition in this lattice, we conclude that μ and ν approach the value 1 continuously as T approaches T_c from below. For $T=T_c$, $\mu=\nu=1$, Eq. (23b) is satisfied for all b. If b also varies continuously around $T=T_c$, the second factor in Eq. (23a) must vanish for $T=T_c$, and Eq. (23c) must be satisfied, both for $\mu=\nu=1$. These two equations can then be solved simultaneously to give the values of b and x at the Curie point.

We find $x_c=0.4391$, corresponding to $kT_c/v=1.215$. Values determined by other methods are given in Table I. As in the case of the triangular lattice, the value of T_c found by this method agrees quite closely with that of Kikuchi and is considerably more accurate than the value given by Bethe's second approximation.

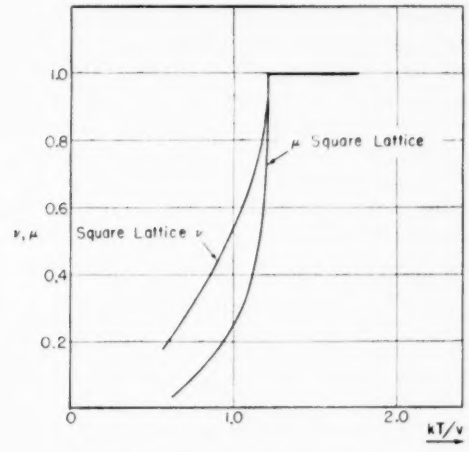

FIG. 10. Long-range order parameters μ and ν for the square lattice.

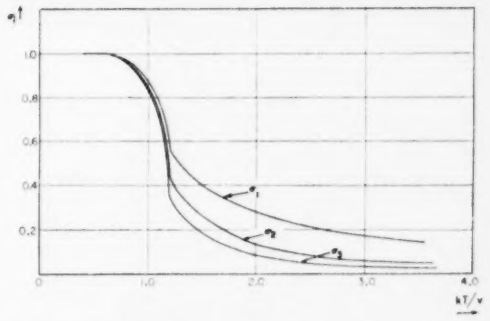

FIG. 11. Correlation functions σ_1, σ_2, σ_3 in the square lattice.

E. Solution of the Consistency Equations with Long-Range Order

Solution of the consistency equations for temperatures below the Curie point was carried out numerically by the Newton-Raphson method. Figure 4 shows the correlation parameter q for $T<T_c$, and Fig. 10 gives the values of the long-range order parameters ν and μ. Both $d\mu/dT$ and $d\nu/dT$ become infinite as $T\to T_c$. The correlation parameter is again close to 1 for all temperatures, having its greatest deviation from this value at the Curie point, where it is 0.8139.

The long-range order can again be computed by use of Eq. (12). A plot of S against kT/v appears in Fig. 5. For T just below T_c one finds

$$S\cong 4.326(1-T/T_c)^{\frac{1}{2}}. \tag{24}$$

The orientational correlation for ith neighbors in the lattice will be described by the correlation functions

$$\sigma_i=1-2\{\text{probability for antiparallel spins on } i\text{th neighbor sites}\}; \tag{25}$$

σ_1 is, of course, the short-range order, previously denoted by σ. Given the values of the parameters μ, ν, and q, one can compute σ for any pair of spins in Fig. 8, by comparing the total weight of configurations with antiparallel spins on those sites with the total weight W of all configurations. Explicit expressions for σ_1 and σ_2 can be derived easily by noting that

$$\sigma_1=1-\frac{x}{2}\frac{\partial \ln W}{\partial x}\bigg|_{\alpha=1}, \tag{26}$$

$$\sigma_2=1-\frac{\eta}{2}\frac{\partial \ln W}{\partial \eta}\bigg|_{\alpha=1}. \tag{27}$$

Plots of σ_1, σ_2, and σ_3 against kT/v are given in Fig. 11; there is a finite discontinuity in the slopes at $T=T_c$. The following approximate expressions have been ob-

[8] For $x>1/\sqrt{3}$, the second factor in Eq. (23a) is always positive; thus one must have $\xi=\zeta$. Since μ cannot exceed 1, by our definition of positive long-range order, it follows from Eqs. (20a) and (20c) that $\nu\geq\mu$. However, if $\xi=\zeta$, the quantity on the left of Eq. (23b) is negative so long as $\nu>\mu$; thus $\xi=\zeta$ demands $\mu=\nu$. It then follows from Eqs. (20a) and (20c) that $\mu=\nu=1$.

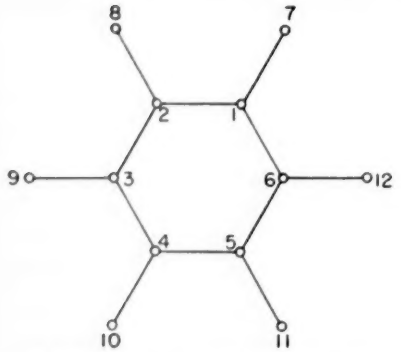

FIG. 12. Portion of hexagonal lattice. Sites 1 through 6 form "inner shell"; sites 7 through 12 make up "outer shell."

tained for σ_1:

$$\sigma_1 \cong 0.5543 + 4.498(1 - T/T_c), \tag{28}$$

for T just below T_c, and

$$\sigma_1 \cong 0.5543 + 0.8764(1 - T/T_c), \tag{29}$$

for T just above T_c.

The configurational specific heat c per spin is given by Eq. (18), with $z=4$. The specific heat is discontinuous at the Curie point, with $(c/k)\,|\,\tau_{c-}=3.702$, $(c/k)\,|\,\tau_{c+}=0.7213$. The values found by other methods are listed in Table I. A plot of c/k against kT/v is given in Fig. 7. Again, this method predicts only a finite discontinuity in the specific heat at the Curie point, rather than the logarithmic infinity given by the exact solution.

IV. THE TWO-DIMENSIONAL HEXAGONAL ISING LATTICE

The two-dimensional hexagonal Ising lattice will be considered very briefly, to illustrate another factor that may affect the choice of consistency conditions to be satisfied.

The set of sites chosen for detailed consideration is shown in Fig. 12. Sites 1 through 6 form the "inner shell" and sites 7 through 12 form the "outer shell." It is to be noted that neighboring sites in the outer shell are third neighbors, rather than first neighbors as in the previous two problems. The relative weight for any configuration of spins on these twelve sites has been expressed as $W=BQ$, where B is the Boltzmann factor corresponding to the energy of interaction of all inner-shell spins with each other and with the outer-shell spins, and Q is the weight factor arising from interaction of the outer-shell spins with their exterior neighbors.

By symmetry, all spins in the inner shell are equivalent. In our calculation, explicit account is taken of their interactions with all their neighbors. Consequently, these spins play the same role in this problem that the central spin did in the previous two problems.

All sites in the outer shell are equivalent to each other with respect to their external coupling. Therefore, one long-range order parameter, $\lambda \leq 1$, will be required to express the tendency of coupling to exterior spins to produce right spins in the outer shell: Q will contain one factor of λ for each left spin in the outer shell.

The coupling of the outer shell spins to their exterior neighbors will tend to make adjacent pairs of spins in that shell parallel to each other, even though they are only third neighbors to each other. We represent this effect by the correlation parameter $q \leq 1$, which appears once in Q for each antiparallel pair of neighbors in the outer shell.

The calculation of the configuration weights is straightforward, though more tedious than for the two lattices already considered, and will not be discussed.

The two consistency relations used to determine the parameters λ and q as functions of kT/v were the following:

(a) The computed probability for left spins on an inner shell site (say 1) shall be equal to the computed probability for left spin on an outer shell site (say 7). This condition corresponds to one used in the previous problems.

(b) The computed probability for antiparallel spins on third neighbor sites in the inner shell (say 1 and 4) shall be equal to the computed probability for antiparallel spins on third neighbor sites in the outer shell (say 7 and 8).

Condition (b) thus relates to the parallelism of third-neighbor spins, rather than to the parallelism of next neighbors, as in the preceding problems. This condition does not assure consistency with respect to next-neighbor correlations, but it seems most appropriate for the determination of the correlation parameter q.

The consistency relations have the same general structure as those previously considered, and the Curie point was determined in the same way. The value thus found, $kT_c/v=0.8017$, is compared with the results of other methods in Table I.

Since the consistency conditions did not automatically assure that the computed value of σ_1 would be the same for all pairs of next neighbors, the calculation of specific heat for the system was subject to some arbitrariness. Our calculation was based on the value of σ_1 computed for next-neighbor pairs in the inner shell, since this value is less dependent on the values of λ and q, and is thus presumably more accurate, than the slightly different values that would be computed for other pairs of next neighbors. The theory indicates a finite discontinuity in the specific heat at the Curie point, as shown in Table I.

V. THE SIMPLE CUBIC ISING LATTICE

A. The Configuration Weights

The final problem to be studied is order-disorder in the simple cubic Ising lattice. Figure 13 shows the set of sites chosen for detailed consideration. There are three types of sites in this figure: a central site, labeled 1; the six next neighbors of the central site, labeled 2–7; and the twelve second neighbors of the central site, labeled 8–19. Next neighbors of the central site will be called middle sites, and second neighbors of the central site will be called corner sites.

As in the square lattice problem, there are two types of sites in the outer shell: spins on the corner sites are coupled more strongly to the external spins than are the spins on middle sites. Therefore, two long-range order parameters, μ and ν, will be needed. The weight for any configuration of spins will include a factor $\mu \leq 1$ for each left spin in a corner site, and a factor $\nu \leq 1$ for each left spin on a middle site. Since all pairs of next-neighbor spins in the outer shell are equivalent as concerns their coupling to the external spins, only one correlation parameter is required: a factor $q \leq 1$ will appear in the configuration weight once for each antiparallel pair of next-neighbor spins in the outer shell. A dummy parameter α, later set equal to one, will be entered as a factor in the configuration weight whenever the central spin is a left spin. On introducing the quantity $b=q^2x^2$ as before, one can write the weight of any completely specified configuration as

$$w=\alpha^{\tau}\mu^{s}\nu^{t}b^{u}x^{v}. \tag{30}$$

This has the same form as Eq. (19) for the configuration weights in the square lattice, and the exponents all have the same meaning.

To simplify writing down the sum W of weights for all configurations, we again introduce weight factors ξ, η, ζ similar to but not identical with the factors ξ, η, ζ used in treating the square lattice:

$$\xi=1+\mu b, \tag{31a}$$

$$\eta=\nu^{\frac{1}{2}}b^{\frac{1}{2}}(1+\mu), \tag{31b}$$

$$\zeta=\nu^{\frac{1}{2}}(\mu+b). \tag{31c}$$

The total weight of all configurations consistent with specified orientations of the middle spins only will then contain a factor ξ for each corner array with middle spins both right, a factor η for each corner array with one right and one left middle spin, and a factor ζ for each corner array with middle spins both left. In addition, it will contain a factor $(x^t+x^{6-t}\alpha)$, where t is the total number of left middle spins. One then finds easily

$$\begin{aligned}W=&\xi^{12}(1+\alpha x^6)+\zeta^{12}(x^6+\alpha)+6\xi^8\eta^4(x+\alpha x^5)\\&+6\eta^4\zeta^8(x^5+\alpha x)+12\xi^5\eta^6\zeta(x^2+\alpha x^4)\\&+12\xi\eta^6\zeta^5(x^4+\alpha x^2)+3\xi^4\eta^8(x^2+\alpha x^4)\\&+3\eta^8\zeta^4(x^4+\alpha x^2)+12\xi^2\eta^8\zeta^2x^2(1+\alpha)\\&+8\xi^3\eta^6\zeta^3x^3(1+\alpha).\end{aligned} \tag{32}$$

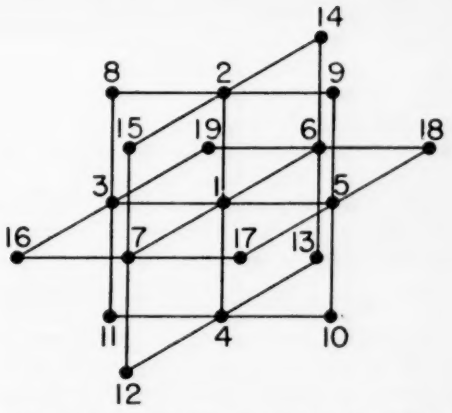

FIG. 13. Portion of simple cubic lattice. Site 1 is "central site"; sites 2 to 7 are "middle sites"; and the other numbered sites are "corner sites."

B. The Consistency Conditions

The parameters μ, ν, and q are fixed as functions of the temperature by consistency conditions equivalent to those used with the square lattice. Expressed in words, these conditions have exactly the same form as for the square lattice, but, because of the different number of middle and corner spins, they assume slightly different forms in terms of partial derivatives:

$$\alpha\frac{\partial \ln W}{\partial \alpha}\bigg|_{\alpha=1}=\frac{\nu}{6}\frac{\partial \ln W}{\partial \nu}\bigg|_{\alpha=1}, \tag{33a}$$

$$\alpha\frac{\partial \ln W}{\partial \alpha}\bigg|_{\alpha=1}=\frac{\mu}{12}\frac{\partial \ln W}{\partial \mu}\bigg|_{\alpha=1}, \tag{33b}$$

$$\frac{x}{6}\frac{\partial \ln W}{\partial x}\bigg|_{\alpha=1}=\frac{b}{12}\frac{\partial \ln W}{\partial b}\bigg|_{\alpha=1}. \tag{33c}$$

We give the explicit form only for the first of these equations:

$$\begin{aligned}(\xi^4-\zeta^4)\{&(\xi^8+\xi^4\zeta^4+\zeta^8)x^6+\eta^4(\xi^4+\zeta^4)(5x^6-x)\\&+(\eta^8+4\eta^6\xi\zeta)(2x^4-x^2)\}=0.\end{aligned} \tag{34a}$$

C. Solution of the Consistency Relations for Zero Long-Range Order

When $\mu=\nu=1$, $\xi=\zeta$, the first two consistency conditions are satisfied identically for all b and x. The third condition becomes

$$\begin{aligned}2(1+b)^8(b-x^6)+&128b^2x(1+b)^4(b-x^4)+128b^3(1+b)^2\\&\times\{(b-5)x^4+(5b-1)x^2\}+512b^4x^2(b-x^2)\\&+256b^3x^3(b-1)\{4b+(1+b)^2\}=0.\end{aligned} \tag{35}$$

This equation determines b, and thus q, as a function of kT/v. Since $\mu=\nu=1$, this is the solution of the consistency conditions that corresponds to zero long-range

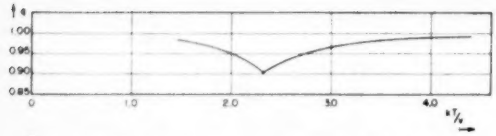

FIG. 14. Correlation parameter q for the simple cubic lattice.

order; it is the only solution for high temperatures. Numerical solution of Eq. (35) yields the values of q shown in Fig. 14, for $T>T_c$.

D. Location of the Curie Point

The procedure for locating the Curie point is exactly like that followed in the case of the square lattice. At the Curie point, $\mu=\nu=1$, and the second consistency relation is identically satisfied. Values of b and x at the Curie point are determined by simultaneous solution of Eqs. (34a) (vanishing of second factor) and Eq. (35). One finds $kT_c/v=2.3145$. As is shown in Table I, this result agrees with Kikuchi's to within 0.4 percent, and is nearly 3 percent lower than that given by Bethe's second approximation. Comparison with the results on two-dimensional problems suggests that the exact value lies lower than any of these approximations.

E. Solution of the Consistency Equations with Long-Range Order

Solution of the consistency equations for $T<T_c$ was carried out numerically using the Newton-Raphson method. Figure 14 gives the values thus obtained for the correlation parameter q, and Fig. 15 the values of the long-range order parameters μ and ν. Both $d\mu/dT$ and $d\nu/dT$ become infinite as $T\to T_c$ from below. (Figure 15 does not show this well for $d\nu/dT$, because of the abruptness with which the slope becomes infinite at $T=T_c$, and the small scale of the figure.) As usual, the parameter q has its greatest difference from 1 at the Curie point, where it is 0.9046.

An explicit formula for the long-range order S can be obtained by use of Eq. (12). A plot of S against kT/v is shown in Fig. 16, in comparison with the results of Bethe's second approximation. The agreement is good, except very near to the Curie point, where our use of the correlation parameter apparently more than compensates for the consideration of a group of spins smaller than that considered in Bethe's second approximation. We find, as an analytic expression good just below the Curie point,

$$S\cong 2.75(1-T/T_c)^{\frac{1}{2}}. \tag{36}$$

Since the set of sites considered in this method includes spins that are up to seventh neighbors, one can use the above results to compute the correlation functions σ_i for i up to 7. Figure 17 shows these functions for i up to 5. They all decrease very rapidly as T approaches T_c from below, showing the same type of behavior as the short-range order, σ_1. In general, one will expect the spin correlation functions to decrease with increasing distance between the spins. However, it will be noted that σ_3 is less than σ_4 at all T. This apparently is the case because fourth neighbors (say, spins 3 and 5 in Fig. 13), though farther apart than third neighbors (say, 3 and 15 in Fig. 13), are more directly coupled to each other through a common next neighbor (spin 1 in Fig. 13).

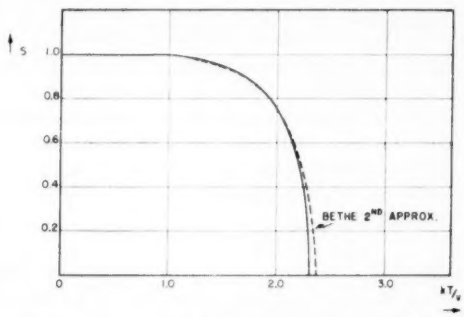

FIG. 16. Long-range order in the simple cubic lattice, by present method and Bethe's second approximation.

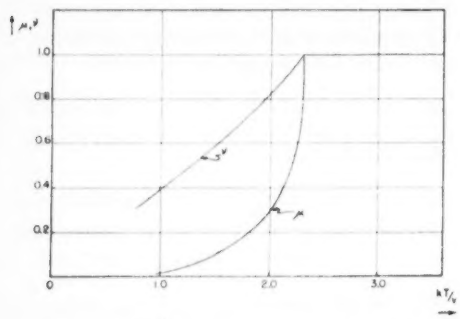

FIG. 15. Long-range order parameters μ and ν for the simple cubic lattice.

The theory yields approximate analytic expressions for σ_1 as follows: for T just below T_c,

$$\sigma_1\cong 0.2788+3.98(1-T/T_c), \tag{37}$$

and for T just above T_c

$$\sigma_1\cong 0.2788+0.5127(1-T/T_c). \tag{38}$$

Figure 18 shows plots of the configurational specific heat per spin against kT/v, computed by Bethe's second approximation, Kikuchi's method, and the present method. Agreement is close except near the Curie point. Comparison with the results on two-dimensional problems will suggest that Kikuchi's method, which gives a slightly lower value for T_c and a higher peak in c, is a little more accurate than the present method.

VI. DISCUSSION OF THE METHOD

Although Kikuchi's method and the present method yield results that are in close agreement, they represent quite different approaches to the order-disorder problem.

In the first place, these methods use quite different parameters to describe the order in the system. In Kikuchi's method, the parameters are the probabilities of the various possible spin configurations on a small set of sites in the lattice, called the basic figure. The description of correlations in the lattice is limited to spins within a single basic figure, which is ordinarily much smaller than the set of sites chosen for consideration in the present method. On the other hand, the parameters used in the present method are not themselves probabilities for spin configurations, but factors that appear in approximate expressions for such probabilities. These approximate expressions are physically natural, and take detailed account of the interactions of next neighbors in the selected group of sites, but they give an account of the effect of coupling to external spins that is clearly incomplete. Granted the

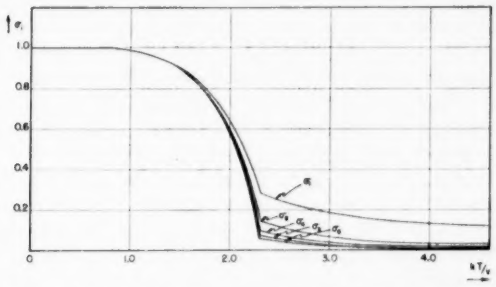

FIG. 17. Correlation functions σ_i for first to fifth neighbors in a simple cubic lattice, as functions of T.

adequacy of these expressions for the probabilities, the present method describes the correlation of orientations for spins that are relatively widely separated in the lattice.

These methods also differ strikingly in the way in which appropriate values for the parameters are determined. Kikuchi enumerates the configurations of the entire lattice that are consistent with given values of his parameters, making use of characteristic approximations. He thus obtains approximate expressions for the entropy and free energy of the lattice in terms of these parameters, and takes as the physically significant values of the parameters those which minimize the free

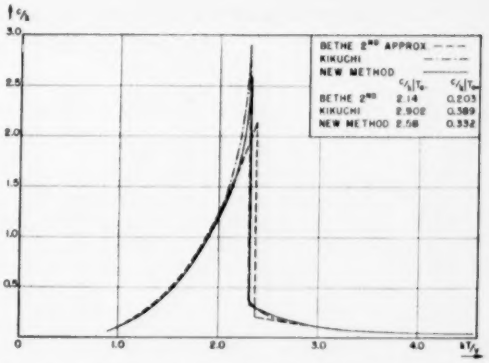

FIG. 18. Configurational specific heat per spin, ϵ, for simple cubic lattice, as given by Bethe's second approximation, Kikuchi's method, and the present method.

energy. In the present method, as in Bethe's, the free energy is not easily expressed in terms of the chosen parameters, and Kikuchi's method for determining the values of the parameters cannot be used. Instead, they are determined by means of consistency relations, which may have more than one solution. (In the case of orientational order in crystals, in the Bragg-Williams approximation, it has been shown by Krieger and James[6] that the distribution functions that satisfy such consistency relations are those which extremalize the free energy, but do not necessarily make it a minimum.) Some solutions of the consistency relations obviously have no physical significance; from the remainder one can select the physically significant one by the method of Krieger and James, which involves reference only to the internal energy or short-range order of the solutions. In the present paper, selection of the physically significant solution has also been based on the known characteristics of the system.

For given desired accuracy, the present method allows one to work with fewer parameters and fewer equations (but more complicated ones) than appear in Kikuchi's method; the labor of calculation in the two methods appears to be comparable. The main practical advantage of the present method appears to be in the calculation of the correlation functions σ_i. In treating the simple cubic lattice with the square as basic figure, Kikuchi determines only σ_1 and σ_2, whereas in the comparable treatment of the cubic lattice in this paper one can easily compute correlation functions for seventh neighbors.

Changes in the Electrical, Thermal, and Thermoelectrical Properties of Monovalent Metals by Lattice Distortions*

A. W. SÁENZ
Applied Mathematics Branch, Mechanics Division, Naval Research Laboratory, Washington, D. C.
(Received February 18, 1953)

In this paper we study theoretically the effect of static lattice distortions on the electrical resistivity, electronic thermal conductivity, and absolute thermoelectric power of monovalent metals. We base our work on a transport equation which follows from straightforward quantum-statistical arguments. Employing an iteration method, we reduce this equation to a set of integral equations in one independent variable, and solve this set explicitly for $T \gg \Theta$. We are thus able to study the three effects of interest for a distorted metallic lattice at high temperatures, and to obtain information concerning the anisotropy of a metal, containing certain types of imperfections, in a much wider temperature range. We prove the striking result that our transport equation yields the same results as the simplified one employed by Mackenzie and Sondheimer, provided that $T \gg \Theta$ and that the effect of the lattice distortions on the three properties mentioned above is small. To illustrate our general formulas, we treat in detail the case of an array of parallel edge dislocations. We express our results in terms of a quantity Q, which is proportional to the ratio of the changes in absolute thermoelectric power and electrical resistivity. For plastically deformed noble metals, the observed values of Q are appreciably larger than the corresponding theoretical values for dislocation arrays of the type mentioned above.

1. INTRODUCTION

THE purpose of this investigation is the theoretical study of the effect of static lattice distortions on the electrical resistivity, electronic thermal conductivity, and absolute thermoelectric power of monovalent metals. We shall pay particular attention to the important special case of edge dislocations, although the effect of impurities and vacancies on the three properties cited above could be dealt with equally well within the framework of this paper.

Before summarizing our results, we shall present a critical review of previous theoretical studies in this field, which will demonstrate the need for a theory based on sounder foundations.

Several authors[1-5] have calculated the tensor $\delta\boldsymbol{\varrho}$,[6] describing the change in electrical resistivity of a metal containing an array of Burgers edge dislocations.

In essence, their calculations are based on two assumptions:

(1) They suppose that it is possible to describe transport phenomena in a lattice by means of a Boltzmann equation having the simple structure

$$\begin{aligned} &[\partial f/\partial t]_{\text{fields}}+[\partial f/\partial t]_{\text{coll}}=0; \\ &[\partial f/\partial t]_{\text{coll}}\equiv-(f-f_0)/\tau+[\partial f/\partial t]_{\text{def}}; \end{aligned} \tag{1.1}$$

where f_0 is the equilibrium Fermi-Dirac distribution function for the conduction electrons; f is the corresponding perturbed function when an electric field, a thermal gradient, or both, are present; τ is the so-called relaxation time associated with the electron-phonon interaction energy H_1, and is supposed to depend only on $K\equiv|\mathbf{K}|$, where $\mathbf{K}$ is the electronic wave vector; $[\partial f/\partial t]_{\text{fields}}$ is an abbreviation for the streaming terms in Boltzmann's equation; and $[\partial f/\partial t]_{\text{def}}$ is the contribution to the collision integral $[\partial f/\partial t]_{\text{coll}}$ due to the interaction of the conduction electrons with the static deformations of the crystal, it being supposed that the latter scatter the former in an elastic, but nonisotropic, manner.[7]

(2) They calculate the matrix elements $\langle\mathbf{K}'|H_2|\mathbf{K}\rangle$ of the interaction energy H_2 between electrons and lattice defects for edge dislocations.[8] This allows them to find $[\partial f/\partial t]_{\text{coll}}$ and to evaluate $\delta\boldsymbol{\varrho}$ on the basis of the solution of Eq. (1.1) for this special case, coupled with the use of Matthiessen's rule.

Although it would superficially appear that Eq. (1.1) holds for temperatures T for which a time of relaxation τ can be defined, *viz.*, when T is much larger than the Debye temperature Θ of the lattice, this is not true. In fact, we shall prove in Sec. 2 that a set of quite general and plausible hypotheses, in conjunction with elementary principles of quantum statistics, lead us to a transport equation which is *different* from Eq. (1.1) for *all* T, if the scattering of electrons by the lattice

* This work was performed under a contract between Indiana University and the U. S. Office of Naval Reserach.

[1] J. S. Koehler, Phys. Rev. **75**, 106 (1946). A partial survey of the corresponding experimental literature is contained therein.

[2] J. K. Mackenzie and E. H. Sondheimer, Phys. Rev. **77**, 264 (1950). Their collision integral corresponding to dislocational scattering is too large by a factor of 2, as is pointed out in reference 4.

[3] R. Landauer, Phys. Rev. **82**, 520 (1951).

[4] D. L. Dexter, Phys. Rev. **86**, 770 (1952).

[5] T. Hirone and K. Adachi, Science Repts. Research Insts. Tohôku Univ. **A3**, 454 (1951).

[6] We shall employ boldface letters to designate second-rank Cartesian tensors, having indices which run from 1 to 3. Thus $\delta\boldsymbol{\varrho}$ is a tensor with components $(\delta\boldsymbol{\varrho})_{ij}$, where $i, j=1, 2, 3$.

[7] The scattering of conduction electrons is said to be isotropic when the absolute value of the matrix elements of the perturbing Hamiltonian, taken between states $\mathbf{K}'$ and $\mathbf{K}$, depends on $|\mathbf{K}'-\mathbf{K}|$ only.

[8] They employ one of two standard methods, or minor variations thereof, viz., the rigid-ion model of L. Nordheim, Ann. Physik (**5**) **9**, 607 (1931), or the deformation-potential procedure of J. Bardeen and W. Shockley, Phys. Rev. **80**, 72 (1950). For a proof of the equivalence of these methods in the limit of perfect ionic shielding, see reference 4.

defects is nonisotropic. Since the authors cited in references 1 to 5 are concerned with precisely this situation, we conclude that their use of Eq. (1.1) is unjustified. However, we shall show that our transport equation leads to the same results as Eq (1.1) under the conditions stated in the concluding paragraphs of this section.

We now turn our attention to previous investigations on the changes in electronic thermal conductivity $\delta\boldsymbol{\kappa}$ and absolute thermoelectric power $\delta\mathbf{S}$ in plastically deformed metals. No detailed theoretical work regarding $\delta\boldsymbol{\kappa}$ is available. With regard to $\delta\mathbf{S}$, we mention the early attempt of Nordheim and Gorter[9] to compute this quantity for metals with impurities and randomly oriented deformations, for which corresponding mean free paths can be defined, as well as the later papers of Kohler[10] on related topics. The only calculation of $\delta\mathbf{S}$ for the case of edge dislocations is due to Hirone and Adachi.[5] Unfortunately, they base their work on Eq. (1.1) and a rather uncritical use of free-electron theory and Matthiessen's rule. Moreover, their final formula for $\delta\mathbf{S}$ contains a serious error, which is equivalent to neglecting $\mathbf{S}^{(1)}$ with regard to $\mathbf{S}^{(0)}$ in Eq. (4.13) of the present paper, these two quantities being of the same order of magnitude for edge dislocations.

To our best knowledge, no systematic experimental work has been carried out to determine the value of $\delta\boldsymbol{\kappa}$ for cold-worked metals. We have a wealth of empirical information concerning $\delta\mathbf{S}$ for plastically deformed metals in the polycrystalline state,[11,12] but little or no data for single crystals.

We now outline the content of the succeeding sections of the present paper, in which we employ no semiempirical formulas, such as Matthiessen's rule.

In Sec. 2, we derive a transport equation for the distribution of conduction electrons in monovalent metals with static lattice distortions, employing four simple assumptions regarding H_1 and H_2. We do not use a detailed model for H_1 throughout this paper. As to H_2, we do not specialize its form until Sec. 5, and then merely to provide an illustration of the general theory.

In Sec. 3, we introduce an iteration method, which should converge rapidly for $T\gg T_0$, where T_0 is a temperature at which the eigenvalues of $\delta\boldsymbol{\rho}$, $\delta\boldsymbol{\kappa}$, and $\delta\mathbf{S}$ are of the same order of magnitude as the electrical resistivity, thermal conductivity, and absolute thermoelectric power of the corresponding undeformed metal.[13] This procedure reduces our transport equation to a set of integral equations in one independent variable, which we solve explicitly for $T\gg\Theta$. We remark that, for the cases of interest in this paper, T_0 is considerably smaller than Θ, so that the condition $T\gg T_0$ is much less restrictive than $T\gg\Theta$.[13]

In Sec. 4, we develop general expressions for $\delta\boldsymbol{\rho}$, $\delta\boldsymbol{\kappa}$, and $\delta\mathbf{S}$ for $T\gg T_0$. Employing these results and those of the previous section, we arrive at explicit formulas for the above tensors in the high-temperature range. We also consider the case when $(\boldsymbol{\tau})^{-1}=p(\epsilon)\boldsymbol{\lambda}$, where $p(\epsilon)$ is a scalar function of the electronic energy ϵ, and $\boldsymbol{\lambda}$ is a symmetric tensor of the second rank independent of ϵ and T, obtaining an interesting theorem relative to the anisotropy ratios of $\delta\boldsymbol{\rho}$, $\delta\boldsymbol{\kappa}$, $\delta\mathbf{S}$ for $T\gg T_0$.

In Sec. 5, we compute $\delta\boldsymbol{\rho}$, $\delta\boldsymbol{\kappa}$, and $\delta\mathbf{S}$ for a metal with $T\gg\Theta$ having an array of parallel positive-negative edge dislocations, by using the theory in the last section in conjunction with the formula for $|\langle\mathbf{K}'|H_2|\mathbf{K}\rangle|^2$ in reference 4. For free electrons, our result for $\delta\boldsymbol{\rho}$ coincides with that obtained in the above reference, and we shall presently see that this agreement is not fortuitous. By exploiting the theorem of Sec. 4 mentioned previously, we also succeed in showing that the anisotropy ratios of $\delta\boldsymbol{\rho}$, $\delta\boldsymbol{\kappa}$, and $\delta\mathbf{S}$ are the same and are independent of T, for $T\gg T_0$. We conclude this section by a brief comparison of our theory with experiment.

Finally, we prove the following striking result in the Appendix:

The computation of $\delta\boldsymbol{\rho}$, $\delta\boldsymbol{\kappa}$, and $\delta\mathbf{S}$ for $T\gg\Theta$ on the basis of either the simplified Eq. (1.1) or of the transport Eq. (2.9) employed in this paper yields the same results, provided only first-order terms[14] are retained in both cases.

2. TRANSPORT EQUATION FOR ELECTRONS IN DISTORTED LATTICES

In this section we shall derive a transport equation for the conduction electrons in a statically deformed monovalent metal.

We denote by $W_1(\mathbf{K}',\mathbf{K})$ and $W_2(\mathbf{K}',\mathbf{K})$ the transition probabilities per unit time for one of the two electrons with wave vector $\mathbf{K}$ to go to a state characterized by the wave vector $\mathbf{K}'$, due to the action of H_1 and H_2, respectively. We designate by $W_1(\mathbf{K},\mathbf{K}')$ and $W_2(\mathbf{K},\mathbf{K}')$ the transition probabilities for the corresponding inverse processes.

We shall base our further considerations on the four hypotheses stated below:

(*a*) the initial and final electronic energies ϵ and ϵ'

[9] L. Nordheim and C. G. Gorter, Physica **2**, 383 (1935). References to earlier work of Nordheim on this topic are contained therein.

[10] M. Kohler, Z. Physik **126**, 481 (1949). A list of previous papers by Kohler on this subject is given here.

[11] See, for example, the references in the article by G. Borelius in *Handbuch der Metall Physik* (Akademische Verlagsgesellschaft M.B.H., Leipzig, 1935), vol. 1, p. 418.

[12] C. Crussard, *Report of the 1947 Bristol Conference of the Strength of Solids* (Physical Society, London, 1948), p. 119.

[13] As is generally known, the percentage increase in resistivity is of the order of 1 percent at room temperature for heavily cold-worked metals. The paper of J. Molenaar and W. A. Aarts, Nature **166**, 690 (1950), shows that the percentage increase in resistivity is nearly 6 percent for Cu and 8 percent for Ag, for strains of 10 percent at liquid air temperatures. From these data and the rough rule that the percentage changes in the three effects considered here are of the same order of magnitude, we estimate that T_0 can be taken as 100°K for the noble metals, subjected to strains comparable to those reported by Molenaar and Aarts.

[14] The meaning of these "first-order terms" will become clear to the reader in Sec. 3 and in the Appendix.

depend solely on K and K', respectively,

$$\epsilon=\epsilon(K), \quad \epsilon'=\epsilon(K'); \tag{2.1}$$

(*b*) the total scattering potential H is thus

$$H=H_1+H_2; \tag{2.2}$$

(*c*) the scattering due to H_1 is isotropic at all T and elastic at $T\gg\Theta$,[15] and $W_1(\mathbf{K}', \mathbf{K})$ satisfies the usual stationary condition, *viz.*,

$$\begin{aligned} &W_1(\mathbf{K}, \mathbf{K}')=F(K, K'; |\mathbf{K}-\mathbf{K}'|), \textit{ all } T; \\ &W_1(\mathbf{K}, \mathbf{K}')=M(|\mathbf{K}'-\mathbf{K}|)\delta(\epsilon'-\epsilon), \ T\gg\Theta; \end{aligned} \tag{2.3a}$$

$$\begin{aligned} W_1(\mathbf{K}', \mathbf{K})f_0(\epsilon)[1-f_0(\epsilon')] \\ -W_1(\mathbf{K}, \mathbf{K}')f_0(\epsilon')[1-f_0(\epsilon)]=0; \end{aligned} \tag{2.4}$$

where

$$f_0(\epsilon)\equiv 1/(e^{(\epsilon-\zeta)/kT}+1), \tag{2.5}$$

ζ being the Fermi energy, k Boltzmann's constant, $F(K, K'; |\mathbf{K}-\mathbf{K}'|)$ a non-negative function, and $M(|\mathbf{K}'-\mathbf{K}|)$ a continuous and non-negative function of $\mathbf{K}$ and $\mathbf{K}'$.

(*d*) H_2 is independent of the coordinates of the lattice.

The detailed forms of $F(K, K', |\mathbf{K}-\mathbf{K}'|)$ and of $M(|\mathbf{K}-\mathbf{K}'|)$ are irrelevant for our present purpose. We also remark that Eqs. (2.3a) should hold satisfactorily for the monovalent metals, which are isotropic with respect to the three properties considered in this paper, when in a pure and undeformed state. These equations are satisfied exactly by the Sommerfeld-Bethe[16] deformable-ion model, and hold approximately in the case of Bardeen's[17] theory of electron-phonon interaction.

Employing the well-known selection rules for electronic transitions in a metallic lattice,[18] assumption (*d*) above, and a simple statistical argument, we conclude that

$$\begin{aligned} W(\mathbf{K}', \mathbf{K})&=W_1(\mathbf{K}', \mathbf{K})+W_2(\mathbf{K}', \mathbf{K}); \\ W(\mathbf{K}, \mathbf{K}')&=W_1(\mathbf{K}, \mathbf{K}')+W_2(\mathbf{K}, \mathbf{K}'); \end{aligned} \tag{2.6}$$

where $W(\mathbf{K}', \mathbf{K})$ is the probability per unit time for an electron to go from $\mathbf{K}$ to $\mathbf{K}'$ due to H, and $W(\mathbf{K}, \mathbf{K}')$ is the probability of the inverse process.

Hypothesis (*d*) also implies the equation

$$\begin{aligned} W_2(\mathbf{K}, \mathbf{K}')&=W_2(\mathbf{K}', \mathbf{K}) \\ &=(2\pi/h)|\langle\mathbf{K}'|H_2|\mathbf{K}\rangle|^2\delta(\epsilon'-\epsilon) \end{aligned} \tag{2.3b}$$

which states that the collisions between electrons and lattice imperfections are elastic for arbitrary T.

We shall now derive the linearized equation of transport on which the present investigation is based. We begin by writing the familiar Boltzmann equation for the conduction electrons in a distorted metal, which is subjected to an electric field $\mathbf{E}$ and to a thermal gradient $\nabla_r T$,[19]

$$\begin{aligned} &\frac{1}{\hbar}\nabla_k\epsilon\cdot\nabla_r f+\frac{e\mathbf{E}}{\hbar}\cdot\nabla_k f \\ &=\frac{\Omega}{(2\pi)^3}\int\int\int d\mathbf{K}'\{W(\mathbf{K}, \mathbf{K}')f(\mathbf{K}')[1-f(\mathbf{K})] \\ &\qquad -W(\mathbf{K}', \mathbf{K})f(\mathbf{K})[1-f(\mathbf{K}')]\}; \end{aligned} \tag{2.7}$$

where $e=-|e|$ is the electronic charge and Ω is the volume of the metal.

Following a standard procedure,[19] we introduce an auxiliary function $\Phi(\mathbf{K})$ by the equation

$$f(\mathbf{K})=f_0(\epsilon)-[\partial f_0(\epsilon)/\partial\epsilon]\Phi(\mathbf{K}). \tag{2.8}$$

Employing Eqs. (2.1), (2.3b), (2.4), (2.5), (2.6), and (2.8) and retaining only linear terms in $\Phi(\mathbf{K})$, we can reduce Eq. (2.7) to the form

$$\mathfrak{L}_0\{\Phi\}+\mathfrak{L}_1\{\Phi\}=\frac{1}{\hbar}\frac{d\epsilon}{dK}\xi\cdot\{\mathfrak{M}+\epsilon\mathfrak{N}\};$$

where

$$\xi\equiv\mathbf{K}/K,$$

$$\begin{aligned} \mathfrak{L}_0\{G\}\equiv-\frac{\Omega}{(2\pi)^3}\int\int\int d\mathbf{K}'\frac{f_0(\epsilon')}{f_0(\epsilon)}W_1(\mathbf{K}', \mathbf{K}) \\ \times\{G(\mathbf{K}')-G(\mathbf{K})\}, \end{aligned} \tag{2.9}$$

$$\begin{aligned} \mathfrak{L}_1\{G\}\equiv-\frac{\Omega}{4\pi^2\hbar}\frac{K^2}{(d\epsilon/dK)}\int\int d\omega'|\langle\mathbf{K}'|H_2|\mathbf{K}\rangle|^2 \\ \times\{G(\mathbf{K}')-G(\mathbf{K})\}, \end{aligned}$$

$$\mathfrak{M}\equiv e\mathbf{E}-T(d/dT)(\zeta/T)\nabla_r T, \quad \mathfrak{N}\equiv-(1/T)\nabla_r T;$$

where $d\omega'$ is an elementary solid angle about $\mathbf{K}'$, the corresponding integration extends over the sphere $|\mathbf{K}'|=|\mathbf{K}|$, and $G(\mathbf{K})$ is an arbitrary function of $\mathbf{K}$. We are, of course, excluding the case $(d\epsilon/dK)=0$.

3. ELIMINATION OF ANGULAR VARIABLES IN THE TRANSPORT EQUATION. EXPLICIT SOLUTION FOR $T\gg\Theta$

In order to eliminate the angular variables from (2.9), we shall require the following two properties of $\mathfrak{L}_0$.

I. Let $F(\mathbf{K})$ be a function admitting the expansion

$$F(\mathbf{K})=\sum_{L=0}^{\infty}\sum_{|M|\leq L}F_{LM}(K)Y_{LM}(\Theta, \Phi) \tag{3.1}$$

[15] See F. Seitz, *The Modern Theory of Solids* (McGraw-Hill Book Company, Inc., New York, 1940), first edition, p. 524, for a justification of this assumption of elastic scattering for metals at $T\gg\Theta$.

[16] A. Sommerfeld and H. Bethe, *Handbuch der Physik* (J. Springer, Berlin, 1933), 24_2, chap. 3.

[17] J. Bardeen, Phys. Rev. **52**, 688 (1937).

[18] See, for example, H. A. Wilson, *The Theory of Metals* (Cambridge University Press, Cambridge, 1936), p. 119, Eq. (3.08).

[19] See, for example, Nordheim, reference 8, or Kohler, Ann. Physik (5)**40**, 601 (1940), Part 1.

in terms of the complete set of spherical harmonics $Y_{LM}(\Theta,\Phi)$ normalized over the unit sphere, where Θ and Φ are the polar and azimuthal angles of $\mathbf{K}$ with respect to a Cartesian coordinate system x_1, x_2, and x_3, fixed in the crystal. Then

$$\mathfrak{L}_0\{F(\mathbf{K})\}=\sum_{L=0}^{\infty}\sum_{|M|\leq L}\Lambda_L\{F_{LM}(K)\}Y_{LM}(\Theta,\Phi), \quad (3.2)$$

where Λ_L is a linear integral operator which acts only on K, and whose structure depends solely on $\mathfrak{L}_0$ and L.

Proof. We shall carry out our proof in two steps.

First, we remark that, according to Eq. (2.3a), $W_1(\mathbf{K},\mathbf{K}')$ depends solely on K and K', and $\cos\theta$, where θ is the angle between $\mathbf{K}$ and $\mathbf{K}'$. Supposing that the angular dependence of $W_1(\mathbf{K},\mathbf{K}')$ is regular enough, we may thus write

$$W_1(\mathbf{K},\mathbf{K}')=\sum_{L=0}^{\infty}w_L(K,K')P_L(\cos\theta), \quad (3.3)$$

where we consider $P_L(\cos\theta)$ to be normalized over the surface of the unit sphere.

Second, we employ Eqs. (2.9), (3.1), (3.3), and the addition theorem for spherical harmonics. The result of this calculation is given below:

$$\mathfrak{L}_0\{F(\mathbf{K})\}=-\frac{\Omega}{4\pi^{5/2}}\sum_{L=0}^{\infty}\sum_{|M|\leq L}\int_0^{\epsilon}dK'K'^2\frac{f_0(\epsilon')}{f_0(\epsilon)}\cdot\left\{\frac{w_L(K,K')}{(2L+1)^{\frac{1}{2}}}F_{LM}(K')-w_0(K,K')F_{LM}(K)\right\}\times Y_{LM}(\Theta,\Phi); \quad (3.4)$$

where $F(\mathbf{K})$ is a function of $\mathbf{K}$ admitting the expansion Eq. (3.2).

Defining the linear integral operator Λ_L by the equation

$$\Lambda_L\{g(K)\}\equiv-\frac{\Omega}{4\pi^{5/2}}\int_0^{\epsilon}dK'K'^2\frac{f_0(\epsilon')}{f_0(\epsilon)}\cdot\left\{\frac{w_L(K,K')}{(2L+1)^{\frac{1}{2}}}g(K')-w_0(K,K')g(K)\right\}, \quad (3.5)$$

for any function $g(K)$ of K, we immediately recognize that (3.4) is equivalent to Eq. (3.2), which completes the proof.

II. Let

$$K,\ d\epsilon/dK\neq 0;\quad M(|\mathbf{K}'-\mathbf{K}|)\not\equiv 0. \quad (3.6)$$

Then

$$\Lambda_L\{g(\mathbf{K})\}=g(K)/\tau_L(\epsilon)(L\geq 1), \quad (3.7)$$

for $T\gg\Theta$, where $g(K)$ is an arbitrary function of K, and $\tau_L(\epsilon)$ depends only on ϵ and Λ_L, and satisfies the inequality

$$\tau_L(\epsilon)d\epsilon/dK>0,\quad (L\geq 1). \quad (3.8)$$

Proof. We find it convenient to introduce the notation,

$$(P(\mathbf{K}'),Q(\mathbf{K}'))\equiv\int\int d\omega' P^*(\mathbf{K}')Q(\mathbf{K}'), \quad (3.9)$$

where $P(\mathbf{K}')$ and $Q(\mathbf{K}')$ are two functions of $\mathbf{K}'$, $P^*(\mathbf{K}')$ designates the complex conjugate of $P(\mathbf{K}')$, $d\omega'$ is an element of solid angle about $\mathbf{K}'$, and the integration extends over the surface of the sphere $|\mathbf{K}'|=K$.

Taking into account the circumstance that ϵ and ϵ' depend solely on K and K', respectively, because of Eq. (2.1), and invoking Eq. (2.3a), we have

$$W_1(\mathbf{K},\mathbf{K}')=\delta(\epsilon'-\epsilon)\sum_{L=0}^{\infty}M_L(K,K')P_L(\cos\theta);\qquad M_L(K,K')\equiv(P_L(\cos\theta),M(|\mathbf{K}'-\mathbf{K}|)). \quad (3.10)$$

Comparing coefficients of $P_L(\cos\theta)$ in Eqs. (3.3) and (3.10), we find

$$w_L(K,K')=M_L(K,K')\delta(\epsilon'-\epsilon). \quad (3.11)$$

Substituting Eq. (3.11) into Eq. (3.5), and changing the variable of integration therein from K' to ϵ', we get Eq. (3.7), where $\tau_L(\epsilon)$ is given by the formula

$$\frac{1}{\tau_L(\epsilon)}=-\frac{\Omega}{4\pi^{5/2}}\frac{K^2}{(d\epsilon/dK)}\left\{\frac{M_L(K,K)}{(2L+1)^{\frac{1}{2}}}-M_0(K,K)\right\},\quad (L\geq 1). \quad (3.12)$$

The properties of $M(|\mathbf{K}-\mathbf{K}'|)$ in (*c*) and Eq. (3.6), and the elementary inequality

$$P_L(\cos\theta)\leq[(2L+1)/4\pi]^{\frac{1}{2}},$$

where the equal sign holds at a finite number of points of the interval $0\leq\theta\leq\pi$ for $L\neq 0$, imply that the quantity inside the curly brackets in Eq. (3.12) is *negative*. Combining this result with the first two inequalities, Eq. (3.6), we readily obtain Eq. (3.8).

The quantities $\tau_L(\epsilon)$ have the dimensions of time. We shall presently see that $\tau_1(\epsilon)$ is the ordinary electron-phonon time of relaxation for a monovalent metal. To conform with the current nomenclature of conductivity theory, we shall call it $\tau(\epsilon)$ from now on.

It is clear that if $\mathbf{X}^{(n)}(\mathbf{K})$ is a solution of

$$(\mathfrak{L}_0+\mathfrak{L}_1)\{\mathbf{X}^{(n)}(\mathbf{K})\}=\frac{1}{n\hbar}\frac{d}{dK}(\epsilon^n)\xi, \quad (3.13)$$

then a solution of Eq. (2.9) is given by

$$\Phi(\mathbf{K})=\mathfrak{M}\cdot\mathbf{X}^{(1)}(\mathbf{K})+\mathfrak{N}\cdot\mathbf{X}^{(2)}(\mathbf{K}), \quad (3.14)$$

because of the linearity of the operators $\mathfrak{L}_0$ and $\mathfrak{L}_1$.[20] We thus concentrate our attention on Eq. (3.13).

In what follows, we suppose that $T\gg T_0$ [see Sec. 1],

[20] Compare with reference 18, Sec. 6.5.

so that $\mathfrak{L}_1$ may be regarded as a perturbation with respect to $\mathfrak{L}_0$. This suggests that we develop $\mathbf{X}^{(n)}$ in the following manner:

$$\mathbf{X}^{(n)}=\sum_{r=0}^{\infty}\mathbf{X}^{(n,r)}, \tag{3.15}$$

where the $\mathbf{X}^{(n,r)}$'s satisfy the set of integral equations,

$$\begin{aligned}&\mathfrak{L}_0\{\mathbf{X}^{(n,0)}\}=\frac{1}{\hbar n}\frac{d}{dK}(\epsilon^n)\xi;\\ &\mathfrak{L}_0\{\mathbf{X}^{(n,r)}\}=-\mathfrak{L}_1\{\mathbf{X}^{(n,r-1)}\},\quad (r\geq 1).\end{aligned} \tag{3.16}$$

It is easy to see that the series Eq. (3.15) is a (formal) solution of Eq. (3.13), provided that the $\mathbf{X}^{(n,r)}$*'s satisfy Eq. (3.16).*

In order to solve the set Eq. (3.16), we expand $\mathbf{X}^{(n,r)}$ thus:

$$\mathbf{X}^{(n,r)}(\mathbf{K})=\sum_{L=0}^{\infty}\sum_{|M|\leq L}\mathbf{X}_{LM}{}^{(n,r)}(\epsilon)Y_{LM}(\Theta,\Phi). \tag{3.17}$$

Equations (3.2), (3.16), and (3.17) together with the orthogonality of the Y_{LM}'s, lead us to the result

$$\Lambda_L\{\mathbf{X}_{LM}{}^{(n,0)}(\epsilon)\}=\frac{1}{\hbar n}\frac{d}{dK}(\epsilon^n)(Y_{LM}(\Theta,\Phi),\xi); \tag{3.18a}$$

$$\Lambda_L\{\mathbf{X}_{LM}{}^{(n,r)}(\epsilon)\}=-(Y_{LM}(\Theta,\Phi),\mathfrak{L}_1\{\mathbf{X}^{(n,r-1)}\}),\quad (r\geq 1); \tag{3.18b}$$

where we employ the notation in Eq. (3.9) in the sense that the scalar products in Eq. (3.18) represent integrations over the unit sphere $|\xi|=1$.

Since

$$(Y_{LM}(\Theta,\Phi),\xi)=0,\quad L\neq 1,$$

Eq. (3.18a) can be satisfied by placing

$$\mathbf{X}_{LM}{}^{(n,0)}(\epsilon)=0,\quad L\neq 1,$$

which implies, according to (3.17),

$$\mathbf{X}^{(n,0)}=\sum_{|M|\leq 1}\mathbf{X}_{1M}{}^{(n,0)}Y_{1M}(\Theta,\Phi). \tag{3.19}$$

We now turn to the case of high temperatures, *viz.*, $T\gg\Theta$. Under these circumstances, we can make use of Eq. (3.7) to reduce the integral equations (3.18) to a set of algebraic equations, which express $\mathbf{X}^{(n,r)}$ in terms of $\mathbf{X}^{(n,r-1)}$, *viz.*,

$$\mathbf{X}_{LM}{}^{(n,0)}(\epsilon)=\frac{\tau_L(\epsilon)}{\hbar n}\frac{d}{dK}(\epsilon^n)(Y_{LM}(\Theta,\Phi),\xi),\quad (L\geq 1); \tag{3.20a}$$

$$\mathbf{X}_{LM}{}^{(n,r)}(\epsilon)=-\tau_L(\epsilon)(Y_{LM}(\Theta,\Phi),\mathfrak{L}_1\{\mathbf{X}^{(n,r-1)}\}),\quad (r\geq 1,\ L\geq 1). \tag{3.20b}$$

In principle, we could construct $\mathbf{X}_{LM}{}^{(n,r)}$ explicitly for *any* r of interest and $L\geq 1$ by means of (3.20). However, we shall treat only the case when the percentage changes in electrical resistivity, thermal conductivity, and absolute thermoelectric power due to lattice defects are small enough to justify the neglect of terms with $r>1$. This approximation is a good one for cold-worked monovalent metals at high temperatures.

Another fortunate circumstance arises from the fact that the only terms in Eq. (3.17) which contribute to the thermal and electrical currents, i.e., to the three effects studied in this paper, are those with $L=1$, as the reader can verify by elementary orthogonality arguments.

The explicit solution of Eq. (3.16) for $L=1$ and $r=0, 1$ can be written in an extremely compact and convenient form by means of the vectors $\boldsymbol{\varphi}_i{}^{(n,r)}$ $(i=1, 2, 3)$ defined below:

$$\begin{aligned}&\boldsymbol{\varphi}_1{}^{(n,r)}(\epsilon)\equiv(3/8\pi)^{\frac{1}{2}}[\mathbf{X}_{11}{}^{(n,r)}(\epsilon)+\mathbf{X}_{1-1}{}^{(n,r)}(\epsilon)];\\ &\boldsymbol{\varphi}_2{}^{(n,r)}(\epsilon)\equiv i(3/8\pi)^{\frac{1}{2}}[\mathbf{X}_{11}{}^{(n,r)}(\epsilon)-\mathbf{X}_{1-1}{}^{(n,r)}(\epsilon)];\\ &\boldsymbol{\varphi}_3{}^{(n,r)}(\epsilon)\equiv i(3/4\pi)^{\frac{1}{2}}\mathbf{X}_{10}{}^{(n,r)}(\epsilon).\end{aligned} \tag{3.21}$$

To find this solution, let us first calculate the jth component, $\varphi_{i,j}{}^{(n,0)}$, of $\boldsymbol{\varphi}_i{}^{(n,0)}$ with respect to the Cartesian coordinates x_1, x_2, x_3 mentioned in I, by means of Eq. (3.20a) and Eq. (3.21). We obtain

$$\varphi_{i,j}{}^{(n,0)}(\epsilon)=\frac{1}{\hbar n}\frac{d}{dK}(\epsilon^n)\tau(\epsilon)\delta_{ij}, \tag{3.22a}$$

where we have replaced $\tau_1(\epsilon)$ by $\tau(\epsilon)$.

Second, let us combine Eqs. (3.19), (3.21), and (3.22a) to express the jth component, $\chi_j{}^{(n,0)}(\mathbf{K})$, of $\mathbf{X}^{(n,0)}(\mathbf{K})$ in terms of $\varphi_{i,j}{}^{(n,0)}(\epsilon)$. Our final result is

$$\chi_j{}^{(n,0)}(\mathbf{K})=\frac{1}{\hbar n}\frac{d}{dK}(\epsilon^n)\tau(\epsilon)\xi_j. \tag{3.22b}$$

From Eqs. (3.20b), (3.21), and (3.22b), we conclude that

$$\varphi_{i,j}{}^{(n,1)}(\epsilon)=-\frac{1}{\hbar n}\frac{d}{dK}(\epsilon^n)\tau^2(\epsilon)(\boldsymbol{\tau}^{-1}(\epsilon))_{ij};$$

where

$$\boldsymbol{\tau}(\epsilon)\equiv\left\|\frac{3}{4\pi}(\xi_k,\mathfrak{L}_1\{\xi_l\})\right\|^{-1},\quad (k,l=1, 2, 3). \tag{3.22c}$$

The tensor $\boldsymbol{\tau}$ is of the dimension of time. From its definition in Eq. (3.22c) and that of $\mathfrak{L}_1$ in Eq. (2.9) we deduce: *The tensor* $\boldsymbol{\tau}$ *is symmetric and the eigenvalues of* $(d\epsilon/dK)\boldsymbol{\tau}$ *are positive, provided that* $K>0$, $d\epsilon/dK\neq 0$, *and* $\langle\mathbf{K}'|H_2|\mathbf{K}\rangle\neq 0$. These properties of $\boldsymbol{\tau}$ have important physical consequences, which we shall point out in Sec. 4. We omit their proof, which is essentially contained in the work of Kohler.[21]

[21] The reader will encounter no difficulties in supplying a proof if he employs definition (3.22c) together with Eqs. (3a), (3b) in Kohler, reference 19.

We conclude this Section by stating the equations satisfied by $\varphi_{i,j}^{(n,0)}$ and $\varphi_{i,j}^{(n,1)}$ for abitrary T, which we shall require in Secs. 4 and 5. Since this proof, which rests on Eqs. (3.18), (3.19), and (3.21), runs parallel to those of Eq. (3.22a) and (3.22c), we shall simply give the final results

$$\varphi_{i,j}^{(n,0)}(\epsilon)=\Psi^{(n)}(\epsilon)\delta_{ij}; \tag{3.23a}$$

$$\Lambda_1\{\varphi_{i,j}^{(n,1)}(\epsilon)\}=-\Psi^{(n)}(\epsilon)(\tau^{-1}(\epsilon))_{ij}; \tag{3.23b}$$

where $\Psi^{(n)}(\epsilon)$ satisfies the integral equation,

$$\Lambda_1\{\Psi^{(n)}(\epsilon)\}=\frac{1}{\hbar n}\frac{d}{dK}(\epsilon^n). \tag{3.23c}$$

For high temperatures, Eqs. (3.7) and (3.23c) imply

$$\Psi^{(n)}(\epsilon)=\frac{1}{\hbar n}\frac{d}{dK}(\epsilon^n)\tau(\epsilon),$$

from which it easily follows that Eq. (3.23a) reduces to Eq. (3.22a), and Eq. (3.23b) to (3.22c), for $T\gg\Theta$.

4. GENERAL FORMULAS FOR $\delta\varrho$, $\delta\kappa$, AND δS

In this section, we shall develop general expressions for $\delta\varrho$, $\delta\kappa$, and $\delta\mathbf{S}$, valid for a degenerate electron gas to the first nonvanishing order of the degeneracy parameter kT/ζ and for $r\leq 1$. Since our calculations follow a pattern which arises in the theory of perfect metallic lattices, we shall omit most of the intermediate steps.

We begin by introducing the tensors $\mathbf{A}^{(r)}$, $\mathbf{B}^{(r)}$, $\mathbf{C}^{(r)}$ $(r=0, 1, \cdots)$, by the following matrix schemes

$$\mathbf{A}^{(r)}\equiv\left\|-\frac{1}{3\pi^2\hbar}\int_0^\infty d\epsilon K^2\frac{\partial f_0}{\partial\epsilon}\varphi_{i,k}^{(1,r)}(\epsilon)\right\|;$$

$$\mathbf{B}^{(r)}\equiv\left\|-\frac{1}{3\pi^2\hbar}\int_0^\infty d\epsilon K^2\frac{\partial f_0}{\partial\epsilon}\varphi_{i,k}^{(2,r)}(\epsilon)\right\|; \tag{4.1}$$

$$\mathbf{C}^{(r)}\equiv\left\|-\frac{1}{3\pi^2\hbar}\int_0^\infty d\epsilon\epsilon K^2\frac{\partial f_0}{\partial\epsilon}\varphi_{i,k}^{(2,r)}(\epsilon)\right\|.$$

We shall also require the tensors

$$\mathbf{A}\equiv\sum_{r=0}^{\infty}\mathbf{A}^{(r)};\quad \mathbf{B}\equiv\sum_{r=0}^{\infty}\mathbf{B}^{(r)};\quad \mathbf{C}\equiv\sum_{r=0}^{\infty}\mathbf{C}^{(r)}; \tag{4.2}$$

which satisfy the equations[22]

$$\mathbf{A}^T=\mathbf{A};$$

$$\mathbf{B}^T=\left\|-\frac{1}{3\pi^2\hbar}\int_0^\infty d\epsilon K^2\epsilon\frac{\partial f_0}{\partial\epsilon}\varphi_{i,k}^{(1,r)}(\epsilon)\right\|; \tag{4.3}$$

$$\mathbf{C}^T=\mathbf{C};$$

[22] For a proof of Eqs. (4.3), the reader may consult reference 18, Sec. 548, or Kohler, reference 19, p. 607, Eqs. (6a), (6b).

where $\mathbf{A}^T$, $\mathbf{B}^T$, and $\mathbf{C}^T$ denote the transposes of $\mathbf{A}$, $\mathbf{B}$, and $\mathbf{C}$, respectively.

Denoting by $\boldsymbol{\sigma}^{(0)}$, $\boldsymbol{\kappa}^{(0)}$, and $\mathbf{S}^{(0)}$ the electrical conductivity, thermal conductivity, and absolute thermoelectric power of a perfect metallic lattice; and by $\boldsymbol{\sigma}$, $\boldsymbol{\kappa}$, and $\mathbf{S}$ the corresponding quantities for a distorted lattice, we may write[23]

$$\begin{aligned}&\boldsymbol{\sigma}^{(0)}\equiv e^2\mathbf{A}^{(0)};\\ &\boldsymbol{\kappa}^{(0)}\equiv T^{-1}\{\mathbf{C}^{(0)}-\mathbf{B}^{(0)}(\mathbf{A}^{(0)})^{-1}(\mathbf{B}^{(0)})^T\};\\ &\mathbf{S}^{(0)}\equiv e^{-1}T^{-1}\{(\mathbf{A}^{(0)})^{-1}(\mathbf{B}^{(0)})^T-\zeta\mathbf{1}\};\end{aligned} \tag{4.4a}$$

$$\begin{aligned}&\boldsymbol{\sigma}\equiv e^2\mathbf{A};\\ &\boldsymbol{\kappa}\equiv T^{-1}\{\mathbf{C}-\mathbf{B}\mathbf{A}^{-1}\mathbf{B}^T\};\\ &\mathbf{S}\equiv e^{-1}T^{-1}\{\mathbf{A}^{-1}\mathbf{B}^T-\zeta\mathbf{1}\};\end{aligned} \tag{4.4b}$$

where $\mathbf{1}$ is the unit tensor, with components δ_{ij}, $(\mathbf{B}^{(0)})^T$ is the transpose of $\mathbf{B}^{(0)}$, and all products are to be interpreted as matrix multiplications.

Employing Eqs. (4.1) to (4.4), together with the well-known asymptotic expansions for integrals involving $\partial f_0/\partial\epsilon$, we obtain the following formulas, valid to the first nonvanishing order in kT/ζ:

$$\begin{aligned}&\boldsymbol{\sigma}^{(0)}=\frac{e^2}{3\pi^2\hbar}\{K^2\boldsymbol{\varphi}^{(1,0)}(\epsilon)\}_{\epsilon=\zeta};\\ &\boldsymbol{\kappa}^{(0)}=\frac{k^2T}{9\hbar}\left\{\frac{d}{d\epsilon}(K^2\boldsymbol{\varphi}^{(2,0)}(\epsilon))-\epsilon\frac{d}{d\epsilon}(K^2\boldsymbol{\varphi}^{(1,0)}(\epsilon))\right\}_{\epsilon=\zeta};\\ &\mathbf{S}^{(0)}=\frac{\pi^2k^2T}{3e}\left\{(K^2\boldsymbol{\varphi}^{(1,0)}(\epsilon))^{-1}\frac{d}{d\epsilon}(K^2\boldsymbol{\varphi}^{(1,0)}(\epsilon))\right\}_{\epsilon=\zeta};\end{aligned} \tag{4.5a}$$

$$\begin{aligned}&\boldsymbol{\sigma}=\frac{e^2}{3\pi^2\hbar}\{K^2\boldsymbol{\varphi}^{(1)}\}_{\epsilon=\zeta};\\ &\boldsymbol{\kappa}=\frac{k^2T}{9\hbar}\left\{\frac{d}{d\epsilon}(K^2\boldsymbol{\varphi}^{(2)})-\epsilon\frac{d}{d\epsilon}(K^2\boldsymbol{\varphi}^{(1)})\right\}_{\epsilon=\zeta};\\ &\mathbf{S}=\frac{\pi^2k^2T}{3e}\left\{(K^2\boldsymbol{\varphi}^{(1)})^{-1}\frac{d}{d\epsilon}(K^2\boldsymbol{\varphi}^{(1)})\right\}_{\epsilon=\zeta};\end{aligned} \tag{4.5b}$$

where all products are to be interpreted as above, and where we have employed the notation

$$\boldsymbol{\varphi}^{(n,r)}(\epsilon)\equiv\|\varphi_{i,k}^{(n,r)}(\epsilon)\|;\quad \boldsymbol{\varphi}^{(n)}(\epsilon)\equiv\sum_{r=0}^{\infty}\boldsymbol{\varphi}^{(n,r)}(\epsilon), \tag{4.6}$$
$$(r=0, 1, \cdots).$$

Since $\boldsymbol{\varphi}^{(n,0)}$ is a multiple of $\mathbf{1}$, by Eq. (3.22a), we can write $\boldsymbol{\sigma}^{(0)}$, $\boldsymbol{\kappa}^{(0)}$, and $\mathbf{S}^{(0)}$ in terms of scalars $\sigma^{(0)}$, $\kappa^{(0)}$, and

[23] In terms of the definitions in Eq. (4.4) the rate dH/dt at which heat accumulates per unit volume in a distorted metal simultaneously carrying an electrical current j_i and a thermal current w_i, due to the presence of an electric field E_k and a thermal gradient $\partial T/\partial x_k$ is as follows:

$$dH/dt=(\boldsymbol{\sigma}^{-1})_{ik}j_ij_k-\partial/\partial x_k(j_i(\mathbf{S})_{ik})+\partial/\partial x_i((\boldsymbol{\kappa})_{ik}\partial T/\partial x_k),$$

where we sum from 1 to 3 over all repeated indices.

$S^{(0)}$, thus:

$$\boldsymbol{\sigma}^{(0)}=\sigma^{(0)}\mathbf{1};\quad \boldsymbol{\kappa}^{(0)}=\kappa^{(0)}\mathbf{1};\quad \mathbf{S}^{(0)}=S^{(0)}\mathbf{1};\quad (4.5c)$$

viz., our undeformed lattice is isotropic with respect to the three effects studied in this paper. This property of isotropy is a consequence of Eq. (2.3a).

Neglecting all terms of the form $\boldsymbol{\varphi}^{(n_1,r_1)}\cdots\boldsymbol{\varphi}^{(n_s,r_s)}$ with $r_1+\cdots+r_s>1$, Eqs. (4.5a) and (4.5b) yield the following formulas for the changes $\delta\boldsymbol{\sigma}$, $\delta\boldsymbol{\kappa}$, and $\delta\mathbf{S}$ of $\boldsymbol{\sigma}^{(0)}$, $\boldsymbol{\kappa}^{(0)}$, and $\mathbf{S}^{(0)}$ due to static lattice deformations:

$$\delta\boldsymbol{\sigma}=\boldsymbol{\sigma}-\boldsymbol{\sigma}^{(0)}=\frac{e^2}{3\pi^2\hbar}\{K^2\boldsymbol{\varphi}^{(1,1)}(\epsilon)\}_{\epsilon=\zeta};$$

$$\delta\boldsymbol{\kappa}=\boldsymbol{\kappa}-\boldsymbol{\kappa}^{(0)}=\frac{k^2T}{9\hbar}\left\{\frac{d}{d\epsilon}(K^2\boldsymbol{\varphi}^{(2,1)}(\epsilon))-\epsilon\frac{d}{d\epsilon}(K^2\boldsymbol{\varphi}^{(1,1)}(\epsilon))\right\}_{\epsilon=\zeta};\quad (4.7)$$

$$\delta\mathbf{S}=\mathbf{S}-\mathbf{S}^{(0)}=\frac{\pi^2k^2T}{3e}\left\{\frac{d}{d\epsilon}[(K^2\boldsymbol{\varphi}^{(1,0)}(\epsilon))^{-1}\times(K^2\boldsymbol{\varphi}^{(1,1)}(\epsilon))]\right\}_{\epsilon=\zeta}.$$

We emphasize the fact that Eqs. (4.7) hold for $T\gg T_0$.

Before discussing the case $T\gg\Theta$, we pause to derive a theorem which we shall find useful in Sec. 5.

Let T be such that the eigenvalues $(\delta\boldsymbol{\sigma})_i$, $(\delta\boldsymbol{\kappa})_j$, $(\delta\mathbf{S})_k$ $(i,j,k=1,2,3)$ of $\delta\boldsymbol{\sigma}$, $\delta\boldsymbol{\kappa}$, and $\delta\mathbf{S}$ are small compared to $\boldsymbol{\sigma}^{(0)}$, $\boldsymbol{\kappa}^{(0)}$, $\mathbf{S}^{(0)}$, respectively, *viz.*, $T\gg T_0$, and let

$$(\boldsymbol{\tau}(\epsilon))^{-1}=p(\epsilon)\boldsymbol{\lambda},\quad (4.8)$$

where $p(\epsilon)$ is a scalar function of ϵ, and $\boldsymbol{\lambda}$ is a symmetric tensor independent of ϵ and T. We then have

(1) The principal directions of $\delta\boldsymbol{\sigma}$, $\delta\boldsymbol{\kappa}$, and $\delta\mathbf{S}$ are the same as those of $\boldsymbol{\lambda}$; they do not depend on T.

(2) The eigenvalues of $\delta\boldsymbol{\sigma}$, $\delta\boldsymbol{\kappa}$, and $\delta\mathbf{S}$ are proportional to the eigenvalues λ_i of $\boldsymbol{\lambda}$,

$$(\delta\boldsymbol{\sigma})_i/(\delta\boldsymbol{\sigma})_j=(\delta\boldsymbol{\kappa})_i/(\delta\boldsymbol{\kappa})_j=(\delta\mathbf{S})_i/(\delta\mathbf{S})_j=\lambda_i/\lambda_j,\quad (4.9)$$

for $i,j=1,2,3$, i.e., the anisotropy ratios $(\delta\boldsymbol{\sigma})_i/(\delta\boldsymbol{\sigma})_j$, $(\delta\boldsymbol{\kappa})_i/(\delta\boldsymbol{\kappa})_j$, $(\delta\mathbf{S})_i/(\delta\mathbf{S})_j$ are equal and independent of T.

Proof: Eqs. (3.23b), (4.6), and (4.8) imply

$$\Lambda_1\{\boldsymbol{\varphi}^{(n,1)}(\epsilon)\}=-\Psi^{(n)}(\epsilon)p(\epsilon)\boldsymbol{\lambda}.$$

In virtue of the linearity of Λ_1, this equation shows that $\boldsymbol{\varphi}^{(n,1)}(\epsilon)$ is a scalar multiple of $\boldsymbol{\lambda}$, since the latter does not depend on ϵ by the hypotheses of our theorem. Coupling this result with the fact that $\boldsymbol{\varphi}^{(n,0)}$ is a multiple of $\mathbf{1}$, we conclude from Eq. (4.7):

$$\delta\boldsymbol{\sigma}=\alpha(T)\boldsymbol{\lambda};\quad \delta\boldsymbol{\kappa}=\beta(T)\boldsymbol{\lambda};\quad \delta\mathbf{S}=\gamma(T)\boldsymbol{\lambda};\quad (4.10)$$

where the scalars α, β, γ depend on T. Assertions (1) and (2) of our theorem are immediate consequences of Eq. (4.10) and the assumption that $\boldsymbol{\lambda}$ is independent of T, which completes the proof.

Let us now turn to the case $T\gg\Theta$. In this region, we can use Eqs. (3.22a), (3.22c), and (4.7) to prove that

$$\delta\boldsymbol{\sigma}=-\frac{e^2}{3\pi^2\hbar}\left\{K^2\frac{d\epsilon}{dK}\tau^2(\epsilon)\tau^{-1}(\epsilon)\right\}_{\epsilon=\zeta};$$

$$\delta\boldsymbol{\kappa}=\frac{\pi^2e^2T}{3e^2}\delta\boldsymbol{\sigma};\quad (4.11)$$

$$\delta\mathbf{S}=-\frac{\pi^2k^2T}{3e}\left\{\frac{d}{d\epsilon}(\tau(\epsilon)\tau^{-1}(\epsilon))\right\}_{\epsilon=\zeta}.$$

From Eq. (4.11), we see that $\delta\boldsymbol{\kappa}$ and $\delta\boldsymbol{\sigma}$ satisfy the Wiedemann-Franz law if $T\gg\Theta$.[24] This circumstance simplifies the remaining calculations in this temperature range, because it reduces our task to the computation of $\delta\boldsymbol{\sigma}$ and $\delta\mathbf{S}$.

To calculate the change in resistivity, $\delta\boldsymbol{\varrho}$, we exploit the fact that $(\delta\boldsymbol{\sigma})_i\ll\boldsymbol{\sigma}^{(0)}$ for $T\gg T_0$, which implies to first order that

$$\delta\boldsymbol{\varrho}\equiv\boldsymbol{\varrho}-\boldsymbol{\varrho}^{(0)}=-(\boldsymbol{\varrho}^{(0)})^2\delta\boldsymbol{\sigma}\quad (T\gg T_0);\quad (4.12)$$

where $\boldsymbol{\varrho}^{(0)}\equiv\rho^{(0)}\mathbf{1}$, $\rho^{(0)}\equiv1/\sigma^{(0)}$, and $\boldsymbol{\varrho}\equiv(\boldsymbol{\sigma})^{-1}$.

If $T\gg\Theta$, Eqs. (4.11) and (4.12) permit us to write, after a straightforward calculation,[25]

$$\delta\boldsymbol{\varrho}=\frac{3\pi^2\hbar^2}{e^2}\left\{K^{-2}\left(\frac{d\epsilon}{dK}\right)^{-1}\boldsymbol{\tau}^{-1}(\epsilon)\right\}_{\epsilon=\zeta};$$

$$\delta\mathbf{S}=-(\boldsymbol{\varrho}^{(0)})^{-1}\delta\boldsymbol{\varrho}\{\mathbf{S}^{(0)}+\mathbf{S}^{(1)}\};\quad (4.13)$$

where

$$\mathbf{S}^{(1)}\equiv\frac{\pi^2k^2T}{3e}\left\{\left(K^2\frac{d\epsilon}{dK}\boldsymbol{\tau}(\epsilon)\right)\frac{d}{d\epsilon}\left(K^2\frac{d\epsilon}{dK}\boldsymbol{\tau}(\epsilon)\right)^{-1}\right\}_{\epsilon=\zeta}.$$

We now make two remarks of a general nature concerning $\delta\boldsymbol{\varrho}$, $\delta\boldsymbol{\kappa}$, and $\delta\mathbf{S}$ for $T\gg\Theta$.

Provided (3.6) holds for $\epsilon=\zeta$ and that we exclude the trivial case $\langle\mathbf{K}'|H_2|\mathbf{K}\rangle\equiv0$, we may employ the inequality (3.8) and the result on the eigenvalues of $\boldsymbol{\tau}$ in Sec. 3 to conclude that

$$(\delta\boldsymbol{\varrho})_i>0,\quad T\gg\Theta.\quad (4.14)$$

This inequality provides a check of our theory in the high-temperature region, since it is well-known experimentally that the types of lattice imperfections considered here always lead to an increase of the electrical resistivity of the metal in which they are embedded.

Second, the temperature dependence of $\delta\boldsymbol{\varrho}$ for $T\gg\Theta$ can be deduced solely from Eq. (4.13) and the definition (3.22c) of $\boldsymbol{\tau}$. However, to find how $\delta\boldsymbol{\kappa}$ and $\delta\mathbf{S}$ vary

[24] This result is in agreement with a general theorem derived by Kohler. See reference 19, pp. 613–615. *Note added in proof:*— It is also in good agreement with experiment for cold-worked metals, as shown by the work of G. Tammann and W. Boehme, Ann. Physik (5) **22**, 500 (1935).

[25] Compare the second Eq. (4.13) with Eq. (9), p. 385, reference 9, which holds when the lattice imperfections scatter electrons isotropically.

with temperature in this region it is essential to know how τ depends on T. Taking $\tau \propto T^{-1}$ for $T \gg \Theta$, in accordance with the theories of Sommerfeld-Bethe,[16] Nordheim,[8] and Bardeen,[17] Eqs. (3.22c), (4.11), and (4.13) lead to the results

$$\delta\varrho,\ \delta\mathbf{S}\text{: independent of } T;\quad \delta\kappa \propto 1/T; \quad (4.15)$$

for $T \gg \Theta$.

Let us compare Eq. (4.15) with the empirical results for cold-worked metals. If $T \gg \Theta$ and T is such that no appreciable annealing takes place, the changes in electrical conductivity[26] and absolute thermoelectric power[12,27] do not vary with T, while those in thermal conductivity[24] are inversely proportional to T, in agreement with Eq. (4.15), in whose derivation we implicitly assumed that the lattice deformations were independent of T.

5. CHANGES IN THE ELECTRICAL, THERMAL, AND THERMOELECTRIC PROPERTIES OF ISOTROPIC METALS BY BURGERS DISLOCATIONS

To provide an illustration of the usefulness of the general formulas in Sec. 4, we compute $\delta\varrho$, $\delta\kappa$, and $\delta\mathbf{S}$ for the idealized situation of an elastically isotropic metal having an array of parallel positive-negative pairs of Burgers edge dislocations. The assumption of elastic isotropy is not essential; it is made solely to simplify our calculations.

In terms of a Cartesian coordinate system x_1, x_2, x_3, fixed in the crystal of interest, let us consider a positive and a negative edge dislocation, having their singular lines at $x_1=0$, $x_2=R/2$, and $x_1=0$, $x_2=-R/2$, respectively, where $R\{K\}_{\epsilon=\zeta} \gg 1$. Then it follows from the work of Dexter[4] that

$$|\langle \mathbf{K}'|H_2|\mathbf{K}\rangle|^2 = \frac{D^2 \sin^2(\bar{K}_3\Omega^{\frac{1}{3}}/2)\bar{K}_2^2}{(1+\bar{K}^2/q^2)\bar{K}_3^2\bar{K}_s^4}; \qquad D^2 \equiv \frac{128\pi^2 Z^2 e^4 \lambda^2}{\Delta^2\Omega^2 q^4}\left(\frac{1-2\nu}{1-\nu}\right); \quad (5.1)$$

where $\bar{K}_i \equiv K_i' - K_i$ $(i=1, 2, 3)$, $\bar{K}_s^2 \equiv \bar{K}_1^2 + \bar{K}_2^2$, q is a screening constant of the order of 10^8 cm^{-1}, Z is the effective nuclear charge, Δ is the atomic volume, ν is Poisson's ratio, and λ is the unit crystallographic slip distance.

From Eq. (3.22c) and Eq. (5.1) we obtain the following values for the nonvanishing components of $(\boldsymbol{\tau})^{-1}$, by direct computation:

$$(\boldsymbol{\tau}^{-1})_{11} = \frac{3}{64}\frac{\Omega^{4/3}D^2}{\hbar q(d\epsilon/dK)}a^2\left(\cot^{-1}a + \frac{a}{1+a^2}\right); \qquad (\boldsymbol{\tau}^{-1})_{22} = 3(\boldsymbol{\tau}^{-1})_{11}; \quad (5.2)$$

where $a \equiv q/2K$.

In order to avoid ambiguities, we employ $\delta\varrho^{(1)}$, $\delta\kappa^{(1)}$, and $\delta\mathbf{S}^{(1)}$ to designate the changes in electrical resistivity, thermal conductivity, and absolute thermoelectric power of a metal of volume Ω, which contains exactly one dislocation pair in its interior. If N pairs per unit area are present, we denote the corresponding changes by $\delta\varrho^{(N)}$, $\delta\kappa^{(N)}$, $\delta\mathbf{S}^{(N)}$. If we are dealing with a parallel array of positive-negative edge dislocations, such that the distances between the dislocation pairs are large enough so that no appreciable interference effects arise, we may write

$$\delta\varrho^{(N)} = \Omega^{\frac{1}{3}}N\delta\varrho^{(1)}; \quad \delta\kappa^{(N)} = \Omega^{\frac{1}{3}}N\delta\kappa^{(1)}; \quad \delta\mathbf{S}^{(N)} = \Omega^{\frac{1}{3}}N\delta\mathbf{S}^{(1)}. \quad (5.3)$$

A straightforward calculation based on Eq. (4.13), where we replace $\delta\varrho$ by $\delta\varrho^{(1)}$, Eqs. (5.2), and (5.3), leads to the result,

$$(\delta\varrho^{(N)})_{11} = \frac{36\pi^4 hZ^2e^2\lambda^2 N}{\Delta^2 q^6}\left(\frac{1-2\nu}{1-\nu}\right)^2 \cdot \left\{\frac{a^3}{K(d\epsilon/dK)^2}\left(\cot^{-1}a + \frac{a}{1+a^2}\right)\right\}_{\epsilon=\zeta}; \quad (5.4a)$$

$$(\delta\varrho^{(N)})_{22} = 3(\delta\varrho^{(N)})_{11};$$

all other components vanishing.

For the important special case of free electrons, *viz.*,

$$\epsilon = \hbar^2K^2/2m^*, \quad (5.5)$$

where m^* is the effective mass, we obtain the following explicit expression for $(\delta\varrho^{(N)})_{11}$:

$$(\delta\varrho^{(N)})_{11} = \frac{12\pi^2 Z^2e^2m^{*2}\lambda^2 N}{\hbar^3\Delta^2q^6n_0}\left(\frac{1-2\nu}{1-\nu}\right)^2 \cdot \left\{a^3\left[\cot^{-1}a + \frac{a}{1+a^2}\right]\right\}_{\epsilon=\zeta}; \quad (5.4a)'$$

where n_0 is the effective number of free electrons per unit volume at $\epsilon=\zeta$.

The second Eq. (5.4a) and Eq. (5.4a)′ coincide with the results derived by Dexter[4] from Eqs. (1.1) and (5.1). This agreement is not fortuitous, as we shall see in the Appendix.

Equations (4.11), (4.12), (4.13), (5.2), and (5.4a) lead us to the following formulas for the nonvanishing components of $\delta\kappa^{(N)}$ and $\delta\mathbf{S}^{(N)}$, by calculations similar

[26] G. Tammann and K. L. Dreyer, Ann. Physik (5) **16**, 111 (1933). It is difficult to decide whether the experiments of W. J. Rutter and J. Reekie, Phys. Rev. **78**, 70 (1950), which show that $\delta\varrho$ depends on T for severely cold-worked polycrystalline Cu and Al, contradict Eq. (4.15), which is based on the assumption that the microscopic strain field does not vary with T, or whether they can be explained in terms of a variation of the lattice strains with T. *Note added in proof:*—The work of Rutter and Reekie is in disagreement with recent experiments of C. W. Berghout, Physica **18**, 978 (1953).

[27] G. Tammann and G. Bandel, Ann. Physik (5) **16**, 120 (1933).

to those employed to derive (5.4a):

$$(\delta\boldsymbol{\kappa}^{(N)})_{11}=-\frac{\pi^2k^2}{3e^2}T(\rho^{(0)})^{-2}(\delta\boldsymbol{\varrho}^{(N)})_{11}; \tag{5.4b}$$

$$(\delta\boldsymbol{\kappa}^{(N)})_{22}=3(\delta\boldsymbol{\kappa}^{(N)})_{11};$$

$$(\delta\mathbf{S}^{(N)})_{11}=\frac{\pi^2k^2T}{3e}\left\{\frac{d}{d\epsilon}\log\left(\frac{K^2(d\epsilon/dK)}{\tau(\epsilon)}\right)-\frac{2}{K}\frac{dK}{d\epsilon}f(a)\right\}_{\epsilon=\zeta}(\boldsymbol{\varrho}^{(0)})^{-1}(\delta\boldsymbol{\varrho}^{(N)})_{11}; \tag{5.4c}$$

$$(\delta\mathbf{S}^{(N)})_{22}=3(\delta\mathbf{S})_{11};$$

where

$$f(a)\equiv\frac{a^3}{(1+a^2)^2}\left(\cot^{-1}a+\frac{a}{1+a^2}\right)^{-1}.$$

The fact that for edge dislocations $\boldsymbol{\tau}$ satisfies Eq. (4.8), coupled with Eqs. (4.12), (5.4a), (5.4b), and (5.4c), allows us to conclude for $T\gg T_0$:

(1)′ The principal directions of $\delta\boldsymbol{\varrho}^{(N)}$, $\delta\boldsymbol{\kappa}^{(N)}$, and $\delta\mathbf{S}^{(N)}$ are parallel to the x_1, x_2, and x_3 axes.

(2)′ The anisotropy ratios for the nonvanishing eigenvalues of these tensors are thus

$$(\delta\boldsymbol{\varrho})_{11}/(\delta\boldsymbol{\varrho})_{22}=(\delta\boldsymbol{\kappa})_{11}/(\delta\boldsymbol{\kappa})_{22}=(\delta\mathbf{S})_{11}/(\delta\mathbf{S})_{22}=\tfrac{1}{3}. \tag{5.5}$$

Let us now compare the results of this section with the corresponding experimental data for monovalent metals. The comparison between the observed and calculated changes in electrical resistivity due to cold work has been carried out in reference 4. We shall limit our attention to the effect of plastic deformations on the thermoelectric power of monovalent metals.

Since the majority of the experiments have been carried out with polycrystalline materials, we shall assume that the cold-working process creates N pairs of edge dislocations, whose surfaces of discontinuity (slip planes) are oriented at random. We may then write for the changes $\delta\rho$ and δS in electrical resistivity and thermoelectric power,

$$\begin{aligned}\delta\rho&=\tfrac{1}{3}\{(\delta\boldsymbol{\varrho}^{(N)})_{11}+(\delta\boldsymbol{\varrho}^{(N)})_{22}\};\\ \delta S&=\tfrac{1}{3}\{(\delta\mathbf{S}^{(N)})_{11}+(\delta\mathbf{S}^{(N)})_{22}\}.\end{aligned} \tag{5.6}$$

From now on, we shall focus our attention on the ratio

$$Q\equiv(\rho^{(0)}/T)(\delta S/\delta\rho), \tag{5.7}$$

which is independent of T and N for $T\gg\Theta$, by virtue of (4.15), (5.6), and the fact that $\rho^{(0)}\propto T$ for $T\ll\Theta$.

The only monovalent metals for which Q has been measured are the noble metals, and the results may be stated thus, for $T\gg\Theta$:[28]

$$Q\sim+10^{-8}\ \text{volt}/(^\circ\text{K})^2. \tag{5.8}$$

[28] We arrived at Eq. (5.8) by employing the data on δS in references 12 and 27, coupled with that on $(\delta\rho/\rho^{(0)})$ in reference 26.

In the present state of the theory of metals, it is not possible to predict Eq. (5.8) from first principles, because of our lack of knowledge concerning the energy dependence of τ and $d\epsilon/dK$ near $\epsilon=\zeta$. The following statements are therefore of a preliminary character.

From Eqs. (5.4c) and (5.6), we find that our theory implies for edge dislocations

$$Q=\frac{\pi^2k^2}{3e}\left\{\frac{d}{d\epsilon}\log\left(\frac{K^2(d\epsilon/dK)}{\tau(\epsilon)}\right)-\frac{2}{K}\frac{dK}{d\epsilon}f(a)\right\}_{\epsilon=\zeta}. \tag{5.9}$$

According to both the Sommerfeld-Bethe[16] and the Bardeen[17] theories of conductivity,

$$K^2(d\epsilon/dK)/\tau(\epsilon)\propto C^2, \tag{5.10}$$

where C is a *positive* number, the so-called Sommerfeld-Bethe "constant," which is proportional to the mean kinetic energy of a conduction electron in state $\mathbf{K}$.[16] It is thus plausible to suppose

$$(1/C)(dC/d\epsilon)\geq 0. \tag{5.11}$$

Since $dK/d\epsilon$ is presumably *positive* at $\epsilon=\zeta$, we see from Eq. (5.9) and Eq. (5.11) that

$$Q\leq\frac{2\pi^2k^2}{3|e|}\left\{\frac{1}{K}\frac{dK}{d\epsilon}f(a)\right\}_{\epsilon=\zeta}. \tag{5.12}$$

the equality sign corresponding to $\{dC/d\epsilon\}_{\epsilon=\zeta}=0$.

For order-of-magnitude purposes, we may write

$$\left\{\frac{2}{K}\frac{dK}{d\epsilon}\right\}_{\epsilon=\zeta}\approx\frac{1}{\zeta}, \tag{5.13}$$

so that Eq. (5.12) becomes

$$Q\lesssim(\pi^2k^2/3|e|\zeta)\{f(a)\}_{\epsilon=\zeta}. \tag{5.14}$$

Let us evaluate the right-hand side of (5.14) for the typical case of Cu, where we put $a=0.8$ for $\epsilon=\zeta$.[4] We then have

$$Q\lesssim 5\times10^{-10}\ \text{volt}/(^\circ\text{K})^2. \tag{5.15}$$

For the optimum case when $\{dC/d\epsilon\}_{\epsilon=\zeta}=0$, we see from Eq. (5.15) that Q has the correct sign but that it is considerably smaller than the corresponding experimental value in Eq. (5.8).

In spite of the many simplifications which we have introduced into our calculation, we are of the opinion that this result means that *edge dislocations do not account for the observed Q in plastically deformed monovalent metals*, contrary to the views put forward in reference 5.

It is believed that vacancies are responsible for a substantial amount of the residual electrical resistivity in plastically deformed metals.[29] We are now calculating

[29] N. F. Mott, Phil. Mag. **43**, 1167 (1952).

Q for lattice defects of this type by the methods of Sec. 4, in order to determine whether the discrepancy between our preliminary theory and experiment can be removed in this manner.

It is a pleasure to thank Professor D. L. Dexter for his stimulating discussions during the course of this work. The author also wishes to thank his colleagues, Mr. D. M. Chase, Dr. J. R. DeLaunay, Dr. E. W. Kammer, Mr. T. E. Pardue, and Dr. E. I. Salkovitz for their friendly interest in the present investigation.

APPENDIX

We shall now prove that the formulas for $\delta\boldsymbol{\sigma}$, $\delta\boldsymbol{\kappa}$, and $\delta\mathbf{S}$, derived from the simple transport Eq. (1.1) are identical to the corresponding expressions in Sec. 4, provided that $T\gg\Theta$ and that only terms of order $r\leq 1$ are retained, in the sense of Secs. 3 and 4.

We begin by introducing the notation

$$f(\mathbf{K})=f(\epsilon)-(\partial f_0/\partial\epsilon)\Phi'(\mathbf{K}), \tag{A.1}$$

where we employ the prime to avoid possible confusion with $\Phi(\mathbf{K})$ in Sec. 2.

From Eqs. (2.1), (2.3b), and (A.1) we obtain by the usual statistical argument

$$[\partial f/\partial t]_{\text{def}}=(\partial f_0/\partial\epsilon)\mathfrak{L}_1\{\Phi'\}. \tag{A.2}$$

Using Eqs. (1.1), (A.1), and (A.2), we obtain the desired form of the equation of transport,

$$\frac{1}{\tau(\epsilon)}\Phi(\mathbf{K})+\mathfrak{L}_1\{\Phi'\}=-\frac{1}{\hbar}\frac{d\epsilon}{dK}\xi\cdot\{\mathfrak{M}+\epsilon\mathfrak{N}\}. \tag{A.3}$$

Letting $\mathbf{X}'^{(n)}$ be a solution of

$$\frac{1}{\tau(\epsilon)}\mathbf{X}'^{(n)}(\mathbf{K})+\mathfrak{L}_1\{\mathbf{X}'^{(n)}(\mathbf{K})\}=\frac{1}{\hbar n}\frac{d}{dK}(\epsilon^n)\xi, \tag{A.4}$$

it is clear that

$$\Phi'=\mathfrak{M}\cdot\mathbf{X}'^{(1)}(\mathbf{K})+\mathfrak{N}\cdot\mathbf{X}'^{(2)}(\mathbf{K}), \tag{A.5}$$

is a solution of Eq. (A.3) because of the linearity of $\mathfrak{L}_1$.

Following the pattern of Sec. 3, we develop $\mathbf{X}'^{(n)}$ in a series of type (3.15), *viz.*,

$$\mathbf{X}'^{(n)}(\mathbf{K})=\sum_{r=0}^{\infty}\mathbf{X}'^{(n,r)}(\mathbf{K}), \tag{A.6}$$

where the vectors $\mathbf{X}'^{(n,r)}$ obey the set of equations,

$$\begin{aligned}\mathbf{X}'^{(n,0)}(\mathbf{K})&=\frac{1}{\hbar n}\frac{d}{dK}(\epsilon^n)\tau(\epsilon)\xi;\\ \mathbf{X}'^{(n,r)}(\mathbf{K})&=-\tau(\epsilon)\mathfrak{L}_1\{\mathbf{X}'^{(n,r-1)}(\mathbf{K})\}.\\ &\qquad(r\geq 1).\end{aligned} \tag{A.7}$$

Denoting by ${\chi'}_j^{(n,r)}$ the jth component of $\mathbf{X}'^{(n,r)}$, we can write, by a known property of complete orthonormal sets and the fact that ϵ depends on K only, by virtue of Eq. (2.1),

$${\chi'}_j^{(n,r)}(\mathbf{K})=\sum_{i=1}^{3}{\varphi'}_{i,j}^{(n,r)}(\epsilon)\xi_i+{\psi'}_j^{(n,r)}(\mathbf{K}), \tag{A.8}$$

where the coefficients ${\varphi'}_{i,j}^{(n,r)}(\epsilon)$ depend solely on ϵ, and where $({\psi'}_j^{(n,r)}(\mathbf{K}),\xi_l)=0$ for $l=1,2,3$.

From Eqs. (A.7) and (A.8) we obtain

$${\varphi'}_{i,j}^{(n,1)}=-\frac{3}{4\pi}\frac{1}{\hbar n}\frac{d}{dK}(\epsilon^n)\tau^2(\epsilon)(\xi_i,\mathfrak{L}_1\{\xi_j\}), \tag{A.9}$$

where we have employed the orthogonality of the ξ_l's.

Comparing the first Eq. (A.7) with (3.22b) and (A.9) with (3.22c), we conclude for $T\gg\Theta$ that

$${\chi'}_j^{(n,0)}(\mathbf{K})=\chi_j^{(n,0)}(\mathbf{K});\quad {\varphi'}_{j,i}^{(n,1)}(\epsilon)=\varphi_{j,i}^{(n,1)}(\epsilon). \tag{A.10}$$

Let us denote the changes in electrical resistivity, thermal conductivity, and absolute thermoelectric power computed by means of the transport equation (A.3) by $\delta\boldsymbol{\varrho}'$, $\delta\boldsymbol{\kappa}'$, and $\delta\mathbf{S}'$, respectively. Restricting ourselves to terms of order $r\leq 1$, we can prove by the methods of Sec. 4 that the tensors $\delta\boldsymbol{\varrho}'$, $\delta\boldsymbol{\kappa}'$, and $\delta\mathbf{S}'$ are functions of ${\chi'}_i^{(n,0)}$ and ${\varphi'}_{j,i}^{(n,1)}$ only, just as $\delta\boldsymbol{\varrho}$, $\delta\boldsymbol{\kappa}$, and $\delta\mathbf{S}$ are functions of $\chi_i^{(n,0)}$ and $\varphi_{j,i}^{(n,1)}$ only. Moreover, the corresponding functions in both sets are *identical*. Employing these facts in conjunction with (A.10), we conclude that

$$\delta\boldsymbol{\varrho}'=\delta\boldsymbol{\varrho},\quad \delta\boldsymbol{\kappa}'=\delta\boldsymbol{\kappa},\quad \delta\mathbf{S}'=\delta\mathbf{S}, \tag{A.11}$$

for $T\gg\Theta$, which was to be demonstrated.

The Electrical Resistance of Graphite at Low Temperatures*

J. M. Reynolds, H. W. Hemstreet, and T. E. Leinhardt
Department of Physics, Louisiana State University, Baton Rouge, Louisiana
(Received April 13, 1953)

The resistance of natural graphite and of high purity polycrystalline graphite has been measured over a range of temperature from room temperature down to 1.35°K. The resistance of large-crystal natural graphite was found to increase with increasing temperature over the entire range. For polycrystalline graphite the resistance was found to increase smoothly as the temperature was lowered to about 20°K. At this temperature the resistance begins to level off until around 5°K it is virtually independent of temperature, at a value about double the room temperature resistance. Below 5°K the resistance seems to fall slightly.

INTRODUCTION

THE electrical resistivity of large crystals of graphite is similar to that of a poor metal both in magnitude and temperature dependence.[1,2] However, by developing the band theory for graphite, Coulson[3] and Wallace[4] have shown that along its cleavage plane an infinitely large graphite crystal is a semiconductor with zero activation energy. Though Wallace has also shown that the results of measurements in natural graphite crystals are not inconsistent with the theory, such measurements are not capable of exact theoretical interpretation because of the lack of purity and the crystal imperfections of natural graphite.

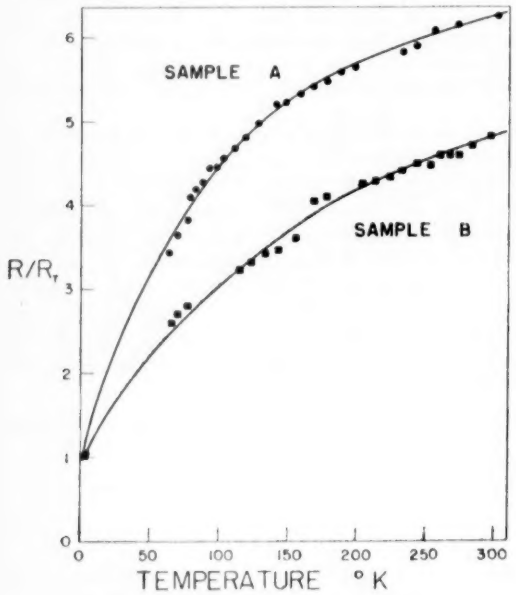

FIG. 1. Resistance of natural graphite.

Polycrystalline graphite of high purity may be produced artificially and measurements on the resistance of polycrystalline graphite have been made over a wide range of temperature.[5–7] The resistivity of polycrystalline graphite is of course always considerable larger than that of single crystals along the graphite plane, but a more striking difference exists in the temperature dependence of the resistance. While the resistance of single crystal graphite increases approximately linearly with temperature over the entire range, this is true for polycrystalline graphite only at high temperatures. The resistance-temperature curve for polycrystalline graphite shows a minimum around 1000°K, the exact value of the temperature depending strongly on the grain size of the sample.[6] At lower temperatures the resistance has an inverse temperature dependence. Several attempts have been made to extend or modify Wallace's theory to account for the observed temperature dependence of the resistance of polycrystalline graphite. Mrozowski assumes for polycrystalline graphite a nonzero activation energy, ($E \sim kT$ where T is the temperature of the minimum) and a constant number of free electrons in the conduction band in addition to those thermally activated into the conduction band. Bowen,[8] on the other hand, simply adds to Wallace's theory a temperature independent term for scattering from the crystallite boundaries. Semi-empirical equations based on either formulation may be fitted to the data within a few hundred degrees of the minimum, but both depart markedly from the data below about 150°K. By assuming that, due to impurity or surface states, the Fermi surface is displaced from the zone boundary,[7,9] the fit of Bowen's formulations may be improved somewhat at lower temperatures.

An important feature of any theory of graphite is its prediction of how the electrical resistance approaches the absolute zero temperature axis. The results reported here extend the data on the resistance of graphite down to 1.3°K.

* Supported by the National Science Foundation.
[1] H. Kamerlingh Onnes and K. Hof, Proc. Roy. Acad. Amsterdam **17**, 520 (1915).
[2] W. J. de Haas and P. M. van Alphen, Proc. Roy. Acad. Amsterdam **34**, 70 (1931).
[3] C. A. Coulson, Nature **159**, 265 (1947).
[4] P. R. Wallace, Phys. Rev. **71**, 622 (1947).
[5] A. Goetz and A. Holser, Trans. Am. Electrochem. Soc. **82**, 391 (1942).
[6] S. Mrozowski, Phys. Rev. **77**, 838 (1950); **85**, 609 (1952).
[7] W. W. Tyler and A. C. Wilson, Jr., Phys. Rev. **89**, 870 (1953)
[8] D. Bowen, Phys. Rev. **76**, 1878 (1949).
[9] G. Hennig, J. Chem. Phys. **19**, 922 (1951).

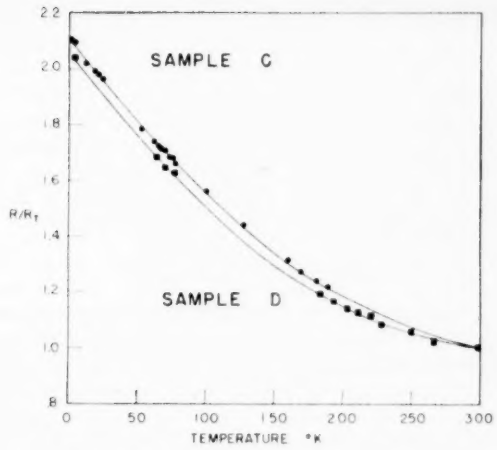

FIG. 2. Resistance of polycrystalline graphite.

PROCEDURE

The ends of the graphite sample were copper plated and current and potential leads were attached. The samples were mounted on a Lucite frame and placed in a Dewar flask in direct contact with the liquid bath. Temperatures in the ranges 1° to 4.2°K and 66° to 78°K were maintained by baths of liquid helium and liquid nitrogen, respectively. Temperatures in the liquid helium range were determined from the Mond[10] vapor pressure tables, and in the liquid nitrogen range they were determined from the *International Critical Tables*[11] vapor pressure tables.

To minimize thermal emf's the current and potential leads were brought out of the vacuum tight flask cap through an 8 inch long, thin wall, stainless steel tube, which was stuffed with cotton to prevent convection currents. The leads were soldered to the terminals of a hermetic seal at the end of the tube which was

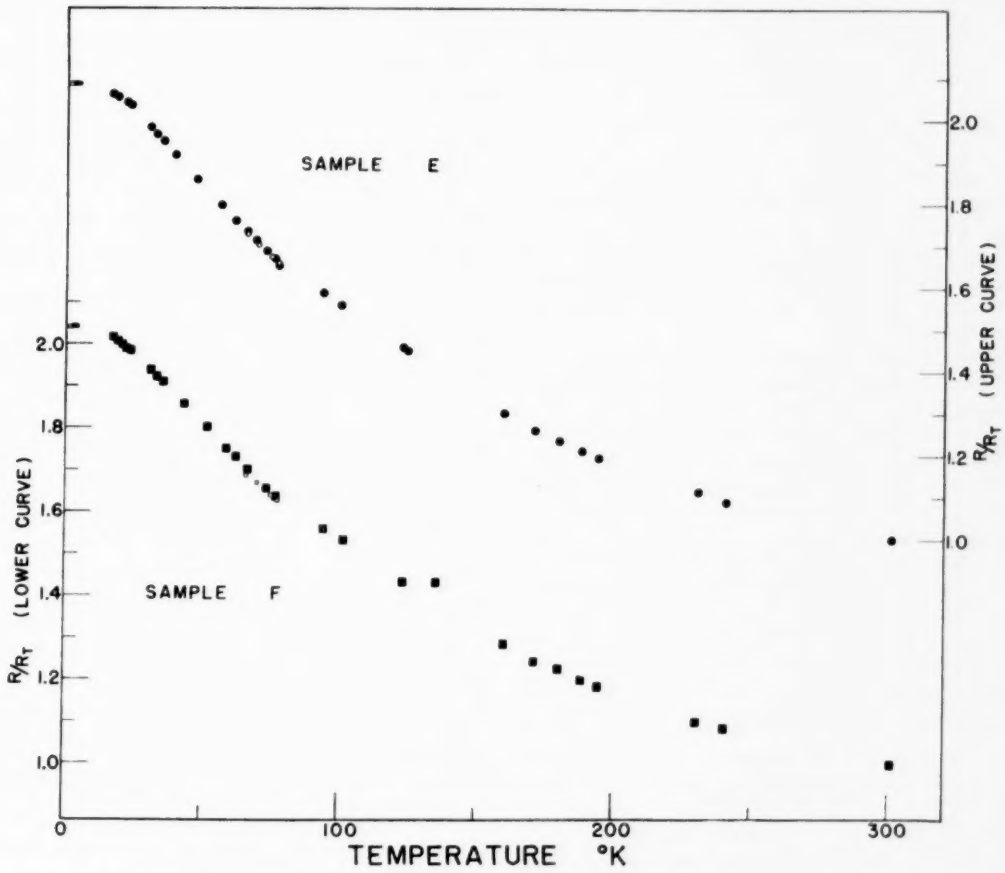

FIG. 3. Resistance of polycrystalline graphite. The solid points are taken from warmup data. The open points were taken while the samples were in liquid baths.

[10] H. van Dijk and D. Shoenberg, Nature **164**, 151 (1949).
[11] *International Critical Tables* (McGraw-Hill Book Company, Inc., New York, 1928), Vol. 3, p. 203.

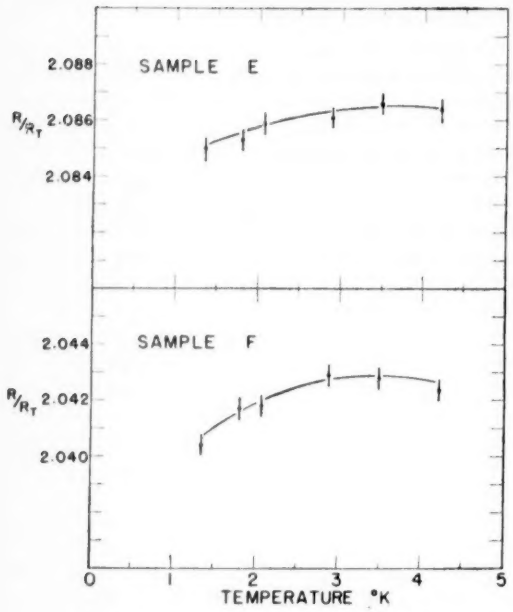

FIG. 4. The low-temperature points from Fig. 3.

effectively at room temperature. The thermal emf's were generally less than 0.5 microvolt and constant to within the sensitivity of the measuring apparatus during any set of measurements. Currents and potentials were measured on the two sides of a White double potentiometer with a dc breaker amplifier being used as the null indicator.

Points in ranges of temperature not obtainable with liquid helium or liquid nitrogen were taken from warm-up data. The warmup rate was about 12° per hour from 15° to 65° and about 8° per hour from 65° up to room temperature. During the warmup runs, temperatures were determined by means of a calibrated copper-constantin thermocouple and the emf developed across the sample, carrying a constant current, was tracked by means of a Brown recording potentiometer.

For some of the preliminary measurements reported here (Figs. 1 and 2) the breaker amplifier was not available and a rather insensitive galvanometer was used. No effort was made to eliminate thermal emf's in these measurements. These two things are responsible for the scatter of points from these measurements.

RESULTS

Natural Graphite

The samples of natural graphite were flakes, about 3 by 5 mm and 4 by 6 mm and each about 0.5 mm thick, cleaved from specimens of natural flake graphite from Ceylon. The crystallites were a millimeter or so in size. X-ray examination showed them to be very imperfect crystals with much twinning and strain. The chemical purity was not checked, though it was probably not very good. The crystals were so fragile that it was extremely difficult to get good copper plate electrical contacts to the samples. The nature of the samples did not seem to warrant refinement of measurements on them, so only preliminary measurements were taken. The results on two samples are shown in Fig. 1. The results are in qualitative agreement with other measurements[1,2] and with Wallace's theory.[4]

Polycrystalline Graphite

The polycrystalline graphite used in these measurements was high purity commercial graphite. Spectrographic analysis, performed on both the bulk material and the actual samples after the experiments, showed the purity to be greater than 99.99 percent. X-ray photography of the bulk material showed a preferred plane for the c-axis but little or no preferred direction in the plane. The grain size of the graphite was determined by the Debye-Scherrer method to be around 10^{-4} cm.

The samples were machined to square cross sections of $\frac{1}{16}$ inch by $\frac{1}{16}$ inch and were 3 to 4 inches long. Each end of each sample was copper plated. The plating covered the extreme $\frac{1}{8}$ inch of each end. To check whether or not the copper penetrated the sample, one of the samples, which had been used in a run, was broken off $\frac{3}{8}$ inch from one end and the tip burned in the spectrometer. The spectrum showed less than 0.01 percent Cu.

The results of preliminary measurements on two samples are shown in Fig. 2. The probable error of the points is about the size of the points. These measurements agree with those of Goetz and Holser[5] and Tyler and Wilson.[7] Though these measurements extend the data to the liquid helium range of temperature, they do not show how the resistance approaches the absolute zero temperature because the resistance of the graphite is so insensitive to temperature that the accuracy of the resistance values is not great enough to detect a trend over a few degrees.

Subsequent measurements on the graphite, using more refined apparatus, as described above, yielded the results seen in Fig. 3. Sample E referred to in the upper curve was cut from the bulk graphite so that the sample axis lay in the preferred plane for the c axis of the crystallites. The lower curve refers to sample F whose axis was perpendicular to this plane. The resistances are plotted as R/R_T, where R_T is the resistance of the sample at room temperature. The room

TABLE I. Room temperature data.

Sample	Dimensions (cm)	Resistance R_T(ohm)	Resistivity ρ_T(ohm-cm)
E	$0.182\times0.181\times4.77$	0.1637	11.32×10^{-4}
F	$0.182\times0.185\times5.17$	0.0851	5.55×10^{-4}

temperature data on these two samples are given in Table I.

It is interesting to note that although the resistivity of sample E is about twice that of sample F, there is no significant difference in the temperature dependence of the resistance of the two samples. The curves for R/R_T for the two samples almost coincide and were separated by arbitrary distances in Fig. 3 for clarity in presentation. At temperatures above 20°K these curves agree remarkably with those of Tyler and Wilson[7] on their sample B, where their sample B is most nearly like our polycrystalline graphite. These measurements, like those of Tyler and Wilson, do not seem to be simply interpreted by present theory.

In both curves in Fig. 3 the open symbols represent data taken while the sample was at a constant temperature in a liquid bath and the solid symbols represent values obtained from warmup data. While the sample was in liquid helium the temperature was controlled to 0.001°K, and in liquid nitrogen it was controlled to 0.1°K. The temperature values *for the warmup points* are only known to within a few degrees. However, in Fig. 3 the warmup points from 66° to 78°K match the bath points fairly well.

In Fig. 3 the resistance is seen to rise as the temperature is lowered, as previously observed, but below 10°K it levels off. Actually, below 5°K, the resistance seems to fall very slightly. The points below 5°K have limits of error which are considerably smaller than can be seen in Fig. 3. Figure 4 shows these points on a much expanded scale. One could draw a horizontal line through these points, but curves of positive slope fit somewhat better. Even so, these curves extrapolate to absolute zero temperature almost horizontally and at resistance values slightly greater than twice the resistance at room temperature.

ACKNOWLEDGMENT

We wish to express our appreciation to Dr. D. C. Ralph for many helpful suggestions. We also wish to thank Dr. Olen Nance for performing the spectrographic analysis and Dr. Paul Picar of Loyola University of the South for his aid in the x-ray studies.

PHYSICAL REVIEW VOLUME 91, NUMBER 5 SEPTEMBER 1, 1953

Photoionization Cross Section of Nitric Oxide

K. WATANABE, F. F. MARMO, AND EDWARD C. Y. INN
Geophysics Research Directorate, Air Force Cambridge Research Center, Air Research and Development Command, Cambridge, Massachusetts

(Received May 27, 1953)

The photoionization cross section of the NO molecule was measured in the spectral region 1070–1343A, at intervals of one to five angstroms, using a vacuum monochromator (band width 0.85A), an absorption cell with ion collector, and a detector calibrated against a thermocouple. The ionization continuum showed some structure which was ascribed partly to preionization of several bands in the region 1070–1150A and partly to vibrational levels of the ground state of NO^+ ion. The photoionization cross section at Lyman alpha was 1.24×10^{-18} cm², about one-half the total absorption cross section. The first ionization potential, 9.23 ± 0.02 ev, was obtained from the long wavelength limit of the ionization continuum. Application of the method to other molecules appears promising.

INTRODUCTION

"ALTHOUGH experiments on the photoionization of air and other permanent gases have been carried out intermittently ever since the photoelectric effect was first discovered, it must be admitted that the state of our knowledge regarding the ionization of these gases is extremely unsatisfactory." This statement made by Hughes and DuBridge[1] about twenty years ago seems to be still applicable. Experiments on photoionization have been conducted in the past mostly with vapors of the alkali metals, for their ionization potentials are low enough to permit measurements in a relatively accessible region of the spectrum between 2000 and 3200A. In spite of the careful measurements, particularly by Mohler and co-workers (see reference 1), a review[2] of the data suggests that even for these atoms more consistent experimental values are desirable. Recent progress, however, has been confined almost entirely to theoretical calculations of cross sections of certain neutral and ionized atoms. The methods, results, and limitation of these calculations are discussed in papers[3] by Bates and Seaton. For molecules the available information on photoionization cross sections, both experimental and theoretical, is very meager.

[1] A. L. Hughes and L. A. DuBridge, *Photoelectric Phenomena* (McGraw-Hill Book Company, Inc., New York, 1932).

[2] T. L. Page, Monthly Notices Roy. Astron. Soc. (London) **99**, 385 (1939).

[3] D. R. Bates, Monthly Notices Roy. Astron. Soc. (London) **106**, 432 (1946); D. R. Bates and M. J. Seaton, Monthly Notices Roy. Astron. Soc. (London) **109**, 698 (1949); M. J. Seaton, Proc. Roy. Soc. (London) **A208**, 408 (1951).

Very few molecules lend themselves readily to quantal methods,[4] so that progress in this direction does not appear promising. In contrast, since it has been shown[5,6] recently that energy measurements of dispersed radiation are not very difficult in the vacuum ultraviolet region, experimental determination of cross sections should be possible for many molecules. In fact, preliminary results for the direct photoionization of nitric oxide[7] and molecular oxygen[8] have already been reported.

The photoionization cross section of nitric oxide was measured in order to determine whether the formation of the *D* layer of our atmosphere might be ascribed[9,10] to the ionization of this molecule by solar radiation in the spectral region from about 1100 to 1300A. Absorption measurements[7,11] in this spectral region revealed that the total absorption cross section of NO is about fifty times greater than a previous estimate,[10] and since a number of diffuse bands were found overlying a region of continuous absorption, the question arose as to what fraction of the absorbed quanta contributed to photoionization.

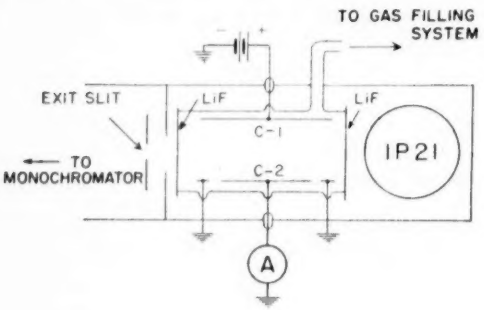

FIG. 1. Schematic diagram of photoionization cell.

EXPERIMENTAL

Most of the experimental arrangement was described in a previous paper,[6] and here the experimental conditions will be listed. Both slits of the vacuum monochromator were fixed usually at 0.05 mm, giving a band width of 0.85A, and this was sufficient to resolve lines about one angstrom apart. The discharge tube was operated at 0.4 amp dc with tank hydrogen flowing continuously into the monochromator where the pressure was held at about 10^{-4} mm Hg. The absorption cell was placed between the exit slit and the detector and connected to a gas filling system provided with a pumping system, pressure gauges, and sample bottles. The total impurity of NO was less than 0.05 percent by a mass-spectrometric analysis.

The space-charge method[12] of investigating photoionization, although very sensitive to positive ions, was not used, for it does not seem to be suitable for determining cross sections. In the present work, measurements were made with a cell shown schematically in Fig. 1, which is similar to that used by Little.[13] The cell (diameter 20 mm) and the envelope of the 1P21 tube were placed inside a vacuum tight brass box which was attached to the exit-slit mount of the monochromator. Cleaved LiF plates about 1 mm thick were used as windows of the cell. The electrodes consisted of parallel plates of platinum about 8 mm wide, placed outside of the light path. It was necessary to use rather small dimensions (lengths of *C*-1 and *C*-2 being 4.5 and 3.5 cm, respectively) so that the detector could intercept the entire beam. The two grounded electrodes served to minimize the irregularities of the electrostatic field and to confine the usable length for ion collection to *C*-2. The voltage required for saturation current was about 4 volts, and no difference in the ion current was found when 5 and 10 volts were applied between *C*-1 and *C*-2. The current was amplified with a Beckman micro-microammeter (RXG-2) and fed into a Speedomax recorder.

The 1P21 photomultiplier coated with sodium salicylate was calibrated[6] by direct comparison with a thermocouple and later checked by another observer[14] in connection with the measurements of photoelectric yields of metals. Since the quantum efficiency of sodium salicylate was nearly constant[6] in the region 850–2400A, only a single conversion factor was used for all wavelengths between 1050 and 1350A. Although the response of the detector was found to be linear[6] with intensity, it was necessary to assume that the linearity held at intensities about two orders of magnitude lower than the intensities used in the calibration.

Preliminary runs with nitric oxide and other gases showed that the method was feasible. For example, photoelectric current produced by reflected and scattered light was usually negligible (less than 10^{-13} amp) compared to the ion current. For this purpose blank runs were made with the cell evacuated and with the cell filled with strongly absorbing gases such as CO_2 as well as transparent gases. After these runs, the transmittance of the right LiF window (Fig. 1) was measured and found to vary from 22 percent at 1070A, to 56 percent (a maximum) at about 1300A, and to 52 percent at 1380A.

For the final runs the following procedure was used.

[4] Buckingham, Reid, and Spence, Monthly Notices Roy. Astron. Soc. (London) **112**, 382 (1952); A. Dalgarno, Proc. Phys. Soc. (London) **A65**, 663 (1952).
[5] D. M. Packer and C. Lock, J. Opt. Soc. Am. **41**, 699 (1951).
[6] K. Watanabe and E. C. Y. Inn, J. Opt. Soc. Am. **43**, 32 (1953).
[7] Watanabe, Marmo, and Inn, Phys. Rev. **90**, 155 (1953).
[8] N. Wainfan and W. C. Walker (to be published).
[9] M. Nicolet, Mem. Roy. Met. Inst. Belgium **19**, 1 (1945).
[10] D. R. Bates and M. J. Seaton, Proc. Phys. Soc. (London) **B63**, 129 (1950).
[11] F. Marmo, J. Opt. Soc. Am. (to be published).
[12] Mohler, Foote, and Chenault, Phys. Rev. **27**, 37 (1926); E. O. Lawrence and N. E. Edelfson, Phys. Rev. **34**, 233 (1929); R. N. Varney and L. B. Loeb, Phys. Rev. **48**, 822 (1935).
[13] E. M. Little, Phys. Rev. **30**, 109 (1927).
[14] H. E. Hinteregger and K. Watanabe, J. Opt. Soc. Am. (to be published).

The amount of light after passing through the cell (evacuated) was measured with the detector, and the number of photons entering the cell per second was obtained by applying corrections for the absorption of the LiF window. The cell was then filled with nitric oxide at pressures from 0.49 to 10.5 mm Hg and the ion current measured as a function of wavelength by scanning the spectrum at 20A per minute.

The total absorption cross section, σ in cm^2, is defined by $I=I_0\exp(-\sigma n_0 x)$, where I_0 and I are the incident and transmitted light intensities, x is the layer thickness in cm of the absorbing gas at NTP, and n_0 is the number of molecules per cm^3 at NTP. In the present case it cannot be assumed that all absorbed photons produce photoionization; some may take part in other processes such as dissociation. Hence, it is convenient to let $\sigma=\sigma_1+\sigma_2$, where σ_1 represents the photoionization cross section and σ_2 the cross section for other processes.

To determine σ_1 from the data, the number N of photons absorbed per second in that portion of the cell length corresponding to C-2 (Fig. 1) was computed using the previously determined values of σ, and the number of ions N_1 formed per second in the same path length was obtained from the ion current. The quantity, $N_1\sigma/N$, is then equal to σ_1.

RESULTS AND DISCUSSION

1. Ionization Potential

Although the determination of ionization potentials and dissociation energies by electron impact is a general method, its accuracy is usually less than that of the best spectroscopic measurements. On the other hand, the latter are frequently not possible; for example, a Rydberg series may be overshadowed by other spectral lines or bands. This is the case with nitric oxide, and its first ionization potential is known only from data[15] obtained by the electron impact method.

The present experiment exemplifies a third method of measuring ionization potentials: the determination of the long wavelength limit of the ionization continuum by observing the onset of ion current as the spectrum is scanned with a monochromator. This method was first carried out satisfactorily in the case of NO and was applied also to several other gases, so that the technique appears to be a general method capable of yielding accurate values of ionization potentials.

By this method the first ionization potential of NO was found to be 9.23 ± 0.02 ev, which appears to be more precise than the value 9.4 ± 0.2 ev obtained by Hagstrum.[15] The long wavelength limit of ionization is shown at the extreme right in Fig. 2 by the nearly vertical portion of curve B. This limit is apparently not extremely sharp because the four indicated points spread over an interval of about five angstroms, although it is possible to resolve lines about one angstrom apart. The uncertainty of the long wavelength limit and also the fact that a many-lined spectra was used as source limit the accuracy of the value given above.

The value of the first ionization potential may be helpful in the interpretation of a new emission band system recently observed by Miescher and Baer[16] and by Tanaka[17] but not definitely identified. The $v=0$ level of the upper state of the new band system is 73083.9 cm^{-1} above the $v=0$ level of the lower state (probably the ground state of the NO$^+$ ion according to Tanaka), and of the higher Rydberg series, the "γ" series,[18] of NO converges at 144717 cm^{-1}. The difference of these two wave numbers is equivalent to 9.213 ev, and it is here suggested that this value also corresponds to the first ionization potential and that the new band system represents the transition from the upper $^1\Pi$ state to the ground $^1\Sigma^+$ state of the NO$^+$ ion as suggested by Tanaka.[17] Further evidence in support of this interpretation is given in the next section.

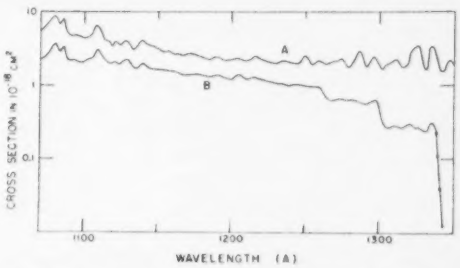

FIG. 2. Total absorption cross section (curve A) and photo ionization cross section (curve B) of nitric oxide.

2. Photoionization Cross Section

In Fig. 2, curve A represents the total absorption cross section of the NO molecule in the region 1070–1350A. This absorption curve was interpreted[11] as being made up of two or more overlapping continua and a number of diffuse bands. The diffuseness of these bands was indicated by the observation that the absorption cross section was very nearly independent of pressure; whereas, sharp bands showed a marked apparent pressure effect due to lack of resolution. The diffuseness may be ascribed to predissociation or preionization processes, both of which are possible in this spectral region.

The photoionization cross section of NO is shown by the lower curve, B, in Fig. 2. Both curves actually represent a series of about a hundred and fifty points and each point is a mean of several values corresponding to several pressures. A portion of the observed values of photoionization cross section is listed in Table I which shows that σ_1 is independent of pressure and nearly

[15] H. D. Hagstrum, Revs. Modern Phys. **23**, 185 (1951).

[16] R. Miescher and P. Baer, Nature **169**, 581 (1952).

[17] Y. Tanaka, J. Chem. Phys. **21**, 562 (1953).

[18] Y. Tanaka, Sci. Papers Inst. Phys. Chem. Research (Tokyo) **39**, 456 (1942).

TABLE I. Photoionization cross sections (in 10^{-18} cm^2) of nitric oxide in the region 1209–1235A for pressures 0.49 to 10.5 mm Hg.

λ(A) \ P(mm Hg)	0.49	0.88	1.70	4.19	10.5
1209	1.16	1.22	1.20	1.13	1.17
1211	1.14	1.22	1.20	1.13	1.19
1213	1.27	1.34	1.27	1.22	1.23
1215.5	1.37	1.16	1.21	1.22	1.25
1218.5	1.14	1.21	1.28	1.29	...
1220.5	1.11	1.22	1.17	1.25	1.17
1223.5	1.14	1.23	1.16	1.14	1.15
1226	1.23	1.19	1.06	1.04	1.02
1230	0.96	0.99	1.08	1.02	...
1234.5	1.01	1.02	1.01	0.99	1.04

constant with respect to wavelength in this region. Although the listed values are consistent, it should be noted that the absolute values may be in error by a large amount (about fifty percent) due to possible systematic errors, particularly in the detector calibration. In contrast, the estimated error for σ is only about five percent as it does not involve absolute energy measurements. From these considerations and the similarity of the two curves, particularly in the region below about 1250A, one is tempted to suggest that curve *B* is too low by about 40 percent with respect to curve *A* and that the absorption of radiation in the region below about 1250A by the NO molecule leads entirely to photoionization. This is admittedly a possibility. The diffuseness of the bands in the region from 1070 to 1150A which appear in both curves is apparently due to preionization, but the σ_1 values of these bands decreased a little with increasing pressure, whereas no pressure effect was found elsewhere. Furthermore, the ratio σ_1/σ has a broad maximum at about 1200A, so that the two curves are not entirely similar. From these data it is not possible to say that all absorption leads to photoionization.

The diffuse bands in the region above 1250A which appear in curve *A* hardly show up in curve *B*, and any indication of these bands in the latter curve is within experimental error. Thus, the bands are apparently not preionized, and their diffuseness may be ascribed to predissociation. Moreover, the continuum underlying the bands may be partly due to a dissociation continuum which starts at about 1400A and overlaps the ionization continuum in the region below 1343A.

In addition to the steep rise in curve *B* at about 1343A, there are two other places on the curve (1302A and 1263A) where there is an abrupt rise. The mean separation between the steps is about 2360 cm^{-1}. This is remarkably close to the differences (2339 and 2314 cm^{-1}) between the 0−0, 0−1, and 0−2 bands of the new band system[16,17] referred to earlier. It is suggested here that the steps in curve *B* represent the ionization of NO not only to the lowest level ($v=0$) of the $^1\Sigma^+$ state of the NO^+ ion, but also to the higher vibrational levels ($v=1, 2$) of the latter state. Thus the present data including the ionization potential supports Tanaka's proposed interpretation of the new band system. Incidentally, the contributions to the ionization cross section by the vibrational levels $v=1$ and 2 appear to be greater than that by the level $v=0$, and this may be explained by the Franck-Condon principle. Furthermore, the higher value of the ionization potential obtained by the electron impact method may be explained by the fact that the latter method tends to measure the "vertical process" and not necessarily the minimum energy for ionization.

3. Applications

As mentioned earlier, the photoionization cross section of NO was measured to provide a further clue to the formation of the *D* layer. Although the data obtained here are sufficiently accurate for this purpose, uncertainties in other parameters, such as the concentration of atmospheric NO, do not warrant a detailed calculation. A note regarding the *D* layer was, however, reported.[7]

The experiments described in this paper can be applied to other molecules, and further investigations should prove fruitful. The determination of the first ionization potential of molecules by measuring the long wavelength limit of the ionization continuum might be applied as a general method. Its application to higher ionization potentials should also be possible, since in the case of the NO molecule the method was sensitive enough to bring out what appears to be vibrational levels of the ion. There are still a number of experimental difficulties; for example, it is necessary to use windowless cells in the region below 1050A. Preliminary experiments with O_2 and other gases showed that the method is applicable even when differential pumping is used to avoid windows.

Broadening of Microwave Absorption Lines Due to Wall Collisions*

MICHAEL DANOS AND STANLEY GESCHWIND†
Radiation Laboratory, Columbia University, New York, New York
(Received May 8, 1953)

The broadening of microwave absorption lines due to wall collisions is calculated using a method introduced by Johnson and Strandberg. Two types of absorption cell are studied, i.e., infinite plane parallel plates and a circular cylinder, each in a region of uniform microwave field. The usual assumption that the half-power half-width is given by $\Delta\nu=1/2\pi\tau$, where τ is the mean time between collisions is in good agreement with the detailed calculations of the present work which show that the error in the line width as calculated by the above expression is not larger than 30 percent. Experimentally observed line widths agree with the predicted values.

ONE of the effects which limits the resolution obtainable by microwave spectroscopy is broadening of absorption lines due to collisions between absorbing gas molecules and the walls of a containing cell. Several estimates of the magnitude of this type of line broadening have been made.[1–4] Since the most recent and most detailed investigation[4] disagrees with earlier estimates and with some experimental observations, it seems worth while to discuss this question once more. It will be shown below that the earlier rough estimates[3] of line broadening due to molecular collisions with walls are actually not far from correct.

In the earlier investigations[1–3] it was tacitly assumed that this line broadening was Lorentz-shaped with a half-power half-width

$$\Delta\nu=1/2\pi\tau, \tag{1}$$

where τ is the mean time between collisions given by

$$1/\tau=(A/V)(kT/2\pi m)^{\frac{1}{2}}, \tag{2}$$

with A the total area, V the volume of the absorption cell, and m the mass of the molecules.

However, Johnson and Strandberg[4] have shown that in general the line shape will differ from that of a Lorentz line and will depend on the geometry of the absorption cell. They investigated the case of an absorption cell consisting of the space between two infinite parallel planes separated by a distance a. However, their value for the line width is several times too large and is based on an incomplete evaluation of an integral which appears below in Eq. (5).

We summarize their argument up to that point. Assume that the molecules make transitions between states with energies E_i and E_j. In an electric field described by

$$E=0 \text{ for } t<0,$$
$$E=E_0\sin(\omega t) \text{ for } t>0,$$

the increase in the probability of finding a molecule in the upper state j is given[5] by

$$|a_j(t)|^2-|a_j(0)|^2=(\Omega/\kappa)^2(|a_i(0)|^2-|a_j(0)|^2)\times\sin^2(\tfrac{1}{2}\kappa t), \tag{3}$$

where $|a_i(t)|^2$ and $|a_j(t)|^2$ are the probabilities of finding a molecule at the time t in the states i and j, respectively; $\Omega=\mu_{z_{ij}}E_0/h$, and $\mu_{z_{ij}}$ is the matrix element of the Z component of the electric dipole moment between the states i and j; $h\omega_0=E_j-E_i$; $\delta\omega=\omega_0-\omega$; $\kappa^2=(\delta\omega)^2+\Omega^2$. $|a_j(0)|^2$ is given by the Boltzmann distribution by virtue of the assumption that a collision with the wall returns the molecule to thermal equilibrium. Now let $f(t)$ be a distribution function such that, if there are N molecules, then

$$dn=Nf(t)dt$$

is the number which had their last collision between the times t and $t+dt$ in the past. The power attenuation constant is then given by

$$\alpha=\frac{h\omega\rho}{\langle S\rangle}\int_0^\infty dtf(t)\frac{d}{dt}(|a_j(t)|^2-|a_j(0)|^2), \tag{4}$$

where ρ is the density of molecules and $\langle S\rangle$ is the time average of the Poynting vector.

In the case of plane parallel plates separated by the distance a, $f(t)$ is such that Eq. (4) becomes

$$\alpha=(B/\epsilon)\int_0^\infty[1-\exp(-1/\zeta^2)]\sin(\epsilon\zeta)d\zeta, \tag{5}$$

where $\epsilon=\kappa\beta$, $\beta=a(m/2kT)^{\frac{1}{2}}$ and

$$B=16\pi^{5/2}(\nu^2\rho\beta|\mu_{z_{ij}}|^2/ckT)(e^{-E_i/kT}/\textstyle\sum_j e^{-E_j/kT}).$$

The integral appearing in (5) can be evaluated approximately in closed form[6] if $1-\exp(-1/\zeta^2)$ is

* Work supported jointly by the Signal Corps and the U. S. Office of Naval Research.
† Now at Bell Telephone Laboratories, Murray Hill, New Jersey.
[1] W. Gordy, Revs. Modern Phys. **20**, 668 (1948).
[2] B. Bleaney and R. P. Penrose, Proc. Phys. Soc. (London) **60**, 83 (1948).
[3] C. H. Townes, J. Appl. Phys. **22**, 1365 (1951).
[4] R. H. Johnson and M. W. P. Strandberg, Phys. Rev. **86**, 811 (1952).
[5] I. I. Rabi, Phys. Rev. **51**, 652 (1937).
[6] W. Magnus and F. Oberhettinger, *Formeln und Sätze fur die speziellen Funktionen der mathematischen Physik* (J. Springer, Berlin, 1943).

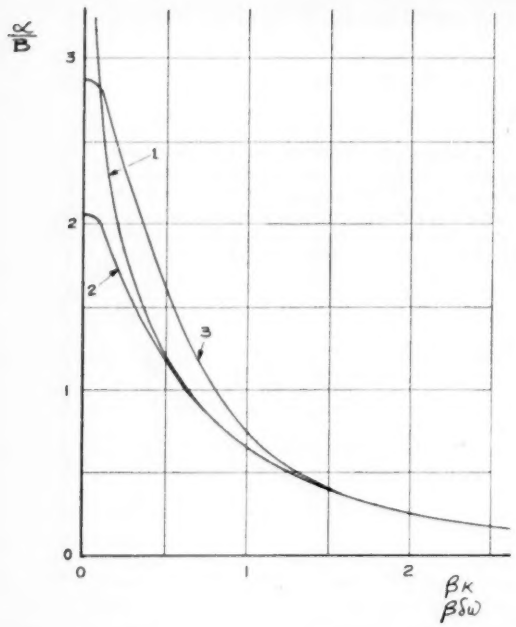

FIG. 1. Line shapes due to wall broadening; infinite parallel planes. Curve 1: α/B as function of $\kappa\beta$; curve 2: α/B as function of $\beta\delta\omega$ at a power level where $\beta\Omega=0.2$; curve 3: Lorentz-line with $2\pi\beta\Delta\nu=0.6$ as function of $\kappa\beta$.

replaced by $1/(1+\xi^2)$. The result so obtained is exact both for $\epsilon\to 0$ and $\epsilon\to\infty$ and has its maximum error around $\epsilon\approx 0.5$. The maximum error is less than 30 percent. With this approximation the power attenuation constant is

$$\alpha=(B/2\epsilon)[e^{-\epsilon}\,\mathrm{Ei}(\epsilon)-e^{\epsilon}\,\mathrm{Ei}(-\epsilon)], \tag{6}$$

where $\mathrm{Ei}(\epsilon)$ is the exponential integral.[6]†

α varies as $1/\epsilon^2$ down to $\epsilon\approx 1.5$. [As a matter of fact any nonadiabatic collision process will yield a line shape which varies asymptotically as $1/(\delta\omega)^2$.] For $\epsilon\to 0$, the attenuation constant goes logarithmically to infinity (see curve 1, Fig. 1). This last feature makes the definition of a line width ambiguous for vanishingly small power. However, in the presence of a finite amount of power the singularity is removed because $\epsilon\geq\beta\Omega$. Under this condition the line width is well defined by Eq. (6) (plotted as curve 2 in Fig. 1 for $\beta\Omega=0.2$) and a measure of the contribution of wall collisions to this line width can be obtained in the following manner. We define a quantity η such that

$$2\pi\beta\Delta\nu=(\beta^2\Omega^2+\eta^2)^{\frac{1}{2}},$$

where $\Delta\nu$ is the half-power half-width. We find that for $\beta\Omega\geq 0.2$, η is essentially constant and has the value $\eta\approx 0.6$. This term η appearing in addition to the power term $\beta\Omega$ is properly identified as arising from wall collisions, giving

$$\Delta\nu(\text{wall collisions})=\eta/2\pi\beta\approx 0.1(1/a)(2kT/m)^{\frac{1}{2}}. \tag{7}$$

A Lorentz line given by $1/(\epsilon^2+\eta^2)$ (curve 3, Fig. 1) with $\eta=0.6$ gives the same line width as Eq. (6) down to a power level $\beta\Omega=0.2$. This, for example, corresponds to a power level of roughly 10^{-7} watt/cm^2 for OCS at room temperature and for a plate separation equal to one cm. With decreasing power level, i.e., $\beta\Omega\to 0$, $\eta\to 0$.

The error introduced by the approximation used in going from Eq. (5) to Eq. (6) is such that the actual line width is no more than 30 percent larger than the line width given by Eq. (7).

Returning now to Eqs. (1) and (2) and specializing to the present geometry, we have

$$\Delta\nu=\frac{1}{2\pi^{\frac{1}{2}}}\left(\frac{1}{a}\right)\left(\frac{2kT}{m}\right)^{\frac{1}{2}}=0.09\left(\frac{1}{a}\right)\left(\frac{2kT}{m}\right)^{\frac{1}{2}}, \tag{8}$$

a result only 10 percent smaller than the value given by Eq. (7).

As can be seen from Eq. (3), the absorption of energy by a molecule at resonance and for vanishing power level increases proportionally to the time. This, together with the fact that there are too many molecules with infinitely long times of flight, gives rise to the singularity of α at the origin. As this singularity is only logarithmic, one is led to expect that any reduction in the long times of flight would remove it. Such a reduction can be achieved for example, by the addition of side walls somewhere at a finite distance. We shall therefore investigate the simplest case of this kind, which is that of a circular cylindrical absorption cell located in a region of a wave guide where the electric field is essentially uniform.

For this calculation it is easier to use directly the expression, Eq. (3), which after multiplication with $\hbar\omega$ gives the energy $W(t)$ a molecule has absorbed between two collisions, if one specifies t as the time of flight between collisions.

If N is the number of molecules colliding with the wall per unit length of the cell per second, and $F(t)$ the distribution function of the times of flight from their last collisions of those molecules which at the present time are colliding with the wall, then the power absorbed per unit length of cell is

$$\Delta P=\int_0^\infty NF(t)W(t)dt.$$

The power absorption coefficient α is therefore

$$\alpha=\frac{\hbar\omega N}{\pi R^2\langle S\rangle}\int_0^\infty(|a_j(t)|^2-|a_j(0)|^2)F(t)dt, \tag{9}$$

where R is the radius of the cell.[7]

† *Note added in proof.*—A similar result has been obtained by G. S. Newell, thesis, Princeton University, 1952 (unpublished).

[7] The connection of $F(t)$ in Eq. (9) with $f(t)$ of Eq. (4) can be established by integrating Eq. (4) by parts.

The function $F(t)$ depends on the geometry of the absorption cell and in our case can be found as follows. Since the length of the cell in the x direction is assumed infinite only components of the velocity of the molecules in the y and z direction contribute to a motion approaching the walls. Let θ be the projection on the y–z plane of the angle between the normal to the wall and the direction of motion of a molecule colliding with the wall. If v is the projection of the velocity on the y–z plane then the probability for such a collision, dw is

$$dw \sim dA \cos\theta v \exp(-mv^2/2kT)d\theta v dv,$$

where dA is the surface element. The time of flight for the considered molecule is given by

$$t = 2R\cos\theta/v.$$

Expressing v in terms of t and inserting (3) in (9) we find that the integral in Eq. (9) is proportional to

$$I = \int_0^\infty dt \int_0^{\pi/2} d\theta \cos^4\theta \sin^2(\kappa t/2) t^{-4} \exp(-\sigma^2 \cos^2\theta/t^2), \tag{10}$$

TABLE I. Comparison of line width parameters Q [see Eq. (14)] of microwave absorption lines broadened by wall collisions.

	L	Q Elementary theory	Q Present work
Parallel planes	a	0.09	0.10
Circular cylinder	$2R$	0.18	0.20

where $\sigma^2 = (2R)^2 m/2kT$. By substituting

$$\xi = t/(\sigma\cos\theta), \quad \lambda = \kappa\sigma,$$

we obtain

$$I = \frac{1}{2\sigma^3}\int_0^\infty d\xi \exp(-1/\xi^2)\xi^{-4}\int_0^{\pi/2} d\theta[1-\cos(\xi\lambda\cos\theta)]$$

$$= (\pi/4\sigma^3)\int_0^\infty d\xi \exp(-1/\xi^2)\xi^{-4}H_1(\xi\lambda), \tag{11}$$

where $H_1(x)$ is the Struve-function of the first order.[6] Using the expansion,

$$H_1(x) = \frac{2}{\pi}\left[\frac{x^2}{3} - \frac{x^4}{45} + \cdots\right],$$

one finds for the peak absorption

$$\alpha(0) = (64/3)\pi^{5/2}(\nu^2\rho\sigma|\mu_{ij}|^2/ckT) \times (e^{-E_i/kT}/\textstyle\sum_j e^{-E_j/kT}). \tag{12}$$

The shape of the line has been found by numerical integration (plotted as curve 1 in Fig. 2), yielding a

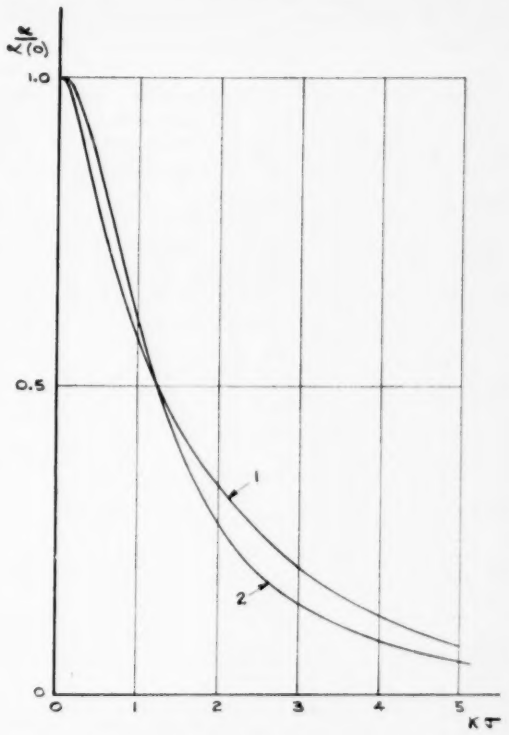

FIG. 2. Line shapes due to wall broadening in a circular absorption cell; curve 1: $\alpha/\alpha(0)$ as a function of $\kappa\sigma$; curve 2: Lorentz line with the same peak absorption and half-width as a function of $\kappa\sigma$.

half-power half-width due to wall collisions, of

$$\Delta\nu = \frac{1.25}{2\pi}\frac{1}{2R}\left(\frac{2kT}{m}\right)^{\frac{1}{2}}. \tag{13}$$

For purposes of comparison, a Lorentz line having the same peak absorption and the same half-width is plotted as curve 2 in Fig. 2.

The results may be summarized in the following way. Let us express the half-width of the line broadening due to wall collisions by

$$\Delta\nu = \frac{Q}{L}\left(\frac{2kT}{m}\right)^{\frac{1}{2}}, \tag{14}$$

where Q is a numerical factor and L is a length characteristic of the absorption cell. Specifying L, then Q as calculated both by the elementary theory [Eqs. (1) and (2)] and by the present work, are listed in Table I.

As seen from the table, the agreement between the elementary and the more exact calculation is sufficiently good to justify the use of the elementary theory is calculating line width due to wall collisions. The values of the line widths calculated this way can be expected to have an error of at most 30 percent.

Line widths regularly observed on a high resolution

microwave spectrometer at the Columbia Radiation Laboratory have been in general agreement with the above calculations. As an example, we cite the recent experimental work of Gunther-Mohr and White on an additional fine structure in the ammonia quadrupole spectrum,[8] where the measured total width at half-maximum for NH_3 at dry ice temperature in X-band Stark guide was found to be 68 ± 5 kc/sec. The calculated Doppler broadening and collision broadening for NH_3 under these conditions are, respectively, $2\Delta\nu_{\text{Doppler}}=60$ kc/sec and $2\Delta\nu_{\text{coll}}=25$ kc/sec. Born has tabulated the resultant shape for a Lorentz line broadened by Doppler effect.[9] His tabulated results show that the total line width is given to a good approximation by

$$\Delta\nu\simeq[(\Delta\nu_{\text{Doppler}})^2+(\Delta\nu_{\text{coll}})^2]^{\frac{1}{2}}. \quad (15)$$

Extrapolating from the results of the present paper, one is led to expect that in practice, quite generally (and at least for a rectangular wave guide) the line shape of broadening due to collisions with the wall will be sufficiently close to that of a Lorentz line so that expression (15) can be used. Thus the combined theoretical line width is $2\Delta\nu=(60^2+25^2)^{\frac{1}{2}}=65$ kc/sec in agreement with the observed value.

We wish to thank Professor Townes for his active aid. We also wish to thank Professor Strandberg for an interesting discussion. The help of Mr. George Dousmanis who performed the numerical calculations is gratefully acknowledged.

[8] G. R. Gunther-Mohr and R. White (to be published).
[9] M. Born, *Optik* (J. Springer, Berlin, 1933), Table 38, p. 486, and p. 431 and the following.

PHYSICAL REVIEW VOLUME 91, NUMBER 5 SEPTEMBER 1, 1953

Polarizability of the Deuteron*

N. F. RAMSEY, B. J. MALENKA, AND U. E. KRUSE
Harvard University, Cambridge, Massachusetts

(Received May 25, 1953)

The theory of the polarizability of the deuteron in a uniform electric field is developed. Using the properties of the deuteron Green's function, we obtain an expression for polarizability of the deuteron which exhibits its dependence upon the spin orientation of the deuteron. This dependence arises from the inclusion of a tensor force in the neutron-proton interaction. In terms of the magnetic quantum number m, with respect to the direction of the electric field, the polarizability α is $\alpha_{SS}+(3m^2-2)\alpha_{SD}+(3m^2-2)^2\alpha_{DD}$. When Hulthén wave functions are used for the deuteron, α_{SS} is found to be approximately 0.56×10^{-39} cm^3 and α_{SD} 0.027×10^{-39} cm^3. The applicability of the theory to intramolecular interaction measurements and deuteron scattering experiments is discussed.

I. INTRODUCTION

THE particles which constitute the deuteron do not all have the same ratio of charge to mass so that, because of reorientation and stretching, the deuteron will exhibit a polarizability with respect to an external electric field.

It has been pointed out earlier by Ramsey[1] that this polarizability of the deuteron should give rise to a measurable departure from Rutherford scattering in certain cases where deuterons are scattered by heavy nuclei. In addition, the dependence of the deuteron polarizability upon its spin orientation should also give rise to a small change in the deuteron quadrupole interaction in D_2 and HD as a result of the difference is amplitude of zero-point vibration in the two molecules and consequently of the oscillating electric field at the deuteron.

In this paper, we calculate the polarizability of the deuteron in an adiabatically applied uniform external electric field. The electric scattering of the deuteron will be examined in a subsequent paper.

The polarizability of a nucleus is related to its polarization energy W_p, in an adiabatically applied, uniform electric field $\mathcal{E}$, by the equation[2]

$$\alpha=-2W_p/\mathcal{E}^2. \quad (1)$$

The W_p is the energy of the second-order Stark effect arising from the perturbation

$$V=-\tfrac{1}{2}ez\mathcal{E}, \quad (2)$$

where z is the component along the direction of the electric field $\mathcal{E}$ of the relative distance $\mathbf{r}=\mathbf{r}_p-\mathbf{r}_n$ of the proton from the neutron. The factor $\frac{1}{2}$ enters because we are concerned with the displacement of the proton with respect to the center of mass of the deuteron. The polarization energy is then

$$W_p=-\tfrac{1}{4}e^2\mathcal{E}^2\sum_{n\neq0}{}'(0|z|n)(n|z|0)/(E_n-E_0), \quad (3)$$

where $\sum'_{n\neq0}$ represents the sum over all the discrete and continuum intermediate states except the ground

* This work was partially supported by the joint program of the U. S. Office of Naval Research and the U. S. Atomic Energy Commission.
[1] N. F. Ramsey, Phys. Rev. **83**, 659 (1951).
[2] D. Bohm, *Quantum Theory* (Prentice Hall, Inc., New York, 1951) p. 461.

state, $n=0$, so that

$$\alpha=\tfrac{1}{2}e^2(2\mu/\hbar^2)\sum_{n\neq 0}'(0|z|n)(n|z|0)/(k_n^2+\gamma^2), \quad (4)$$

where $k_n^2=(2\mu/\hbar^2)E_n$ and $\gamma^2=(2\mu/\hbar^2)\epsilon$. As usual, $\epsilon=-E_0$ denotes the binding energy and μ the reduced mass of the deuteron.

In this paper, we will take the ground state of the deuteron to be the usual admixture of ${}^3S_1$ and approximately 4 percent of ${}^3D_1$ states. We note that for the deuteron, as described in terms of the customary central and tensor interactions, parity is a good quantum number. The ground state then being of a definite (even) parity, we have $(0|z|0)=0$. If we now consider ϵ to be slightly different from the binding energy, we can then extend the summation in Eq. (4) over the complete set of deuteron wave functions. Then writing the wave function explicitly,[3] we can express (4) in the form

$$\alpha=\tfrac{1}{2}e^2(2\mu/\hbar^2)\int\int\Psi_0^*(\mathbf{r})zG_d(\mathbf{r},\mathbf{r}')z'\Psi_0(\mathbf{r}')(d\tau)(d\tau'), \quad (5)$$

where

$$G_d(\mathbf{r},\mathbf{r}')=\sum_n'\frac{\Psi_n(\mathbf{r})\Psi_n^*(\mathbf{r}')}{k_n^2+\gamma^2}. \quad (6)$$

This sum of the bilinear product over the complete set of deuteron wave functions will be recognized to be the Green's function satisfying the Schrödinger equation for the deuteron,

$$[-\nabla^2+\gamma^2+(2\mu/\hbar^2)V_d(\mathbf{r})]G_d(\mathbf{r},\mathbf{r}')=\delta(\mathbf{r}-\mathbf{r}'). \quad (7)$$

Here $V_d(\mathbf{r})$ is the relative proton-neutron potential in the deuteron.

To simplify the evaluation of α in Eq. (5), we note that G_d is related to the free particle Green's function G by the equation

$$G_d(\mathbf{r},\mathbf{r}')=G(\mathbf{r},\mathbf{r}')-(2\mu/\hbar^2)\int G(\mathbf{r},\mathbf{r}'')V_d(\mathbf{r}'')G_d(\mathbf{r}'',\mathbf{r}')(d\tau''). \quad (8)$$

This relation can be easily verified by operating on both sides with $-\nabla^2+\gamma^2$. If we put this expression for G_d into Eq. (5), we observe that the contribution of the second term in the right-hand side of Eq. (8) to α must be small since the short-range potential $V_d(\mathbf{r})$ contributes mainly for S states but the z matrices vanish for states of even parity and hence annul any such contribution. We can then make the approximation

$$\alpha\approx\tfrac{1}{2}e^2(2\mu/\hbar^2)\int\int\Psi_0^*(\mathbf{r})zG(\mathbf{r},\mathbf{r}')z'\times\Psi_0(\mathbf{r}')(d\tau)(d\tau'). \quad (9)$$

Explicitly including the effect of spin, the wave function with magnetic quantum number m for the ground state of the deuteron can be written as[4]

$$\Psi_0(\mathbf{r})\rightarrow\psi_{1,m}(\mathbf{r},\sigma)=(4\pi)^{-\frac{1}{2}}[u(r)/r+2^{-\frac{1}{2}}S_{12}w(r)/r]\chi_{1,m}(\sigma), \quad (10)$$

where $S_{12}=[3(\boldsymbol{\sigma}_1\cdot\mathbf{r})(\boldsymbol{\sigma}_2\cdot\mathbf{r})/r^2]-\boldsymbol{\sigma}_1\cdot\boldsymbol{\sigma}_2$ and $\chi_{1,m}(\sigma)$ is the spin wave function. The free particle Green's function is

$$G(r,r')\rightarrow G_{\sigma,\sigma'}(\mathbf{r},\mathbf{r}')=(2\pi)^{-3}\int(k^2+\gamma^2)^{-1}e^{i\mathbf{k}\cdot(\mathbf{r}-\mathbf{r}')}(d\mathbf{k})\times\sum_{m'}\chi_{1,m'}(\sigma)\chi_{1,m'}^*(\sigma'), \quad (11)$$

where the usual form[5] of G is somewhat modified by the inclusion of the spin wave functions.

We then evaluate Eq. (9), making use of the relations

$$\sum_\sigma\chi_{1,m}^*(\sigma)\chi_{1,m'}(\sigma)=\delta_{m,m'},$$

$$\sum_\sigma S_{12}^*\chi_{1,m}^*(\sigma)\chi_{1,m'}(\sigma)=\sum_\sigma\chi_{1,m}^*(\sigma)S_{12}\chi_{1,m}(\sigma)\delta_{m,m'}=(3m^2-2)(3\cos^2\theta-1)\delta_{m,m'}, \quad (12)$$

where θ is the angle between $\mathbf{r}$ and this z axis. We find

$$\alpha=\alpha_{SS}+(3m^2-2)\alpha_{SD}+(3m^2-2)^2\alpha_{DD}, \quad (13)$$

where

$$\alpha_{SS}=(e^2/64\pi^4)(2\mu/\hbar^2)\int(k^2+\gamma^2)^{-1}\times\left|\int u(r)\cos\theta e^{i\mathbf{k}\cdot\mathbf{r}}(d\tau)\right|^2(d\mathbf{k}), \quad (14)$$

$$\alpha_{SD}=(e^2/64\pi^4\sqrt{2})(2\mu/\hbar^2)\int(k^2+\gamma^2)^{-1}\times\left[\int u(r)\cos\theta e^{i\mathbf{k}\cdot\mathbf{r}}(d\tau)\int w(r')\cos\theta'\times(3\cos^2\theta'-1)e^{-i\mathbf{k}\cdot\mathbf{r}'}(d\tau')\right](d\mathbf{k}), \quad (15)$$

$$\alpha_{DD}=(e^2/512\pi^4)(2\mu/\hbar^2)\int(k^2+\gamma^2)^{-1}\times\left|\int w(r)\cos\theta(3\cos^2\theta-1)e^{i\mathbf{k}\cdot\mathbf{r}}(d\tau)\right|^2(d\mathbf{k}). \quad (16)$$

Since we are assuming the admixture of the deuteron ground state to be approximately 96 percent triplet S state, most of the contribution to α comes from the α_{SS} term.

To evaluate the α's we take $u(r)$ to the Hulthén[4] wave function,

$$u(r)=Ne^{-\gamma r}(1-e^{-r/R})=N(e^{-\gamma r}-e^{-\Gamma r}), \quad (17)$$

where R is the Hulthén range of the nuclear force and $\Gamma=\gamma+1/R$.

For $w(r)$, we use the form that is appropriate outside the range nuclear forces,

$$w(r)\approx N'e^{-\gamma r}[3(\gamma r)^{-2}+3(\gamma r)^{-1}+1], \quad (18)$$

which although incorrect for small r, will only slightly alter the value of the already small α_{SD} and still smaller α_{DD} terms since the r and r' integrals contain factors of

[3] The appropriate spin indices and summations are understood.
[4] H. Feshback and J. Schwinger, Phys. Rev. **84**, 194 (1951).
[5] L. I. Schiff, *Quantum Mechanics* (McGraw-Hill Book Company, Inc., New York, 1949), pp. 160–161.

r^2 and r'^2, respectively. The N and N' are normalization factors. In carrying out the indicated integration, it is convenient to do the angular and radial integrals first. The final k integration can then be evaluated by the method of residues.

Neglecting the small α_{DD} term, we find

$$\alpha_{SS}=A\gamma^{-3}(1+3\gamma R+2(\gamma R)^2)\{1-[1+(\Gamma/\gamma)]^{-4} \times(32-(8/3)(\Gamma/\gamma)^{-3}[1+4(\Gamma/\gamma)+(\Gamma/\gamma)^2])\}, \quad (19)$$

where $A=(32)^{-1}(1-P_D)(e^2/hc)(2\mu c/h)\gamma^{-1}$ and P_D is the ${}^3D_1$ state probability. Similarly we find

$$\alpha_{SD}=NN'2^{-9/2}(e^2/hc)(2\mu c/h)\gamma^{-5} \times\{1-(2^4/5)[1+(\Gamma/\gamma)]^{-4}[3+2(\Gamma/\gamma)]\} \approx 2^{-3}Q\gamma^{-2}(e^2/hc)(2\mu c/h)[1+(6/5)\gamma R], \quad (20)$$

to first order in γR, where Q is the deuteron quadrupole moment.[6] Taking $\Gamma/\gamma\approx 7$, and hence $\gamma R\approx 0.17$,[7] we find

$$\alpha_{SS}\approx 0.56\times 10^{-39}\ \text{cm}^3, \quad (21)$$

$$\alpha_{SD}\approx 0.027\times 10^{-39}\ \text{cm}^3. \quad (22)$$

We see that, as expected, the α_{SD} term is considerably smaller than the α_{SS} term; also, making a rough calculation, we find that neglecting the second term in Eq. (8) for the Green's function, apparently alters the value of α_{SS} by only about 2 percent so that the free particle Green's function approximation is apparently valid for this calculation.

III. APPLICATIONS TO DEUTERON QUADRUPOLE MEASUREMENTS AND TO ELECTRIC SCATTERING EXPERIMENTS

A possible manifestation of the deuteron polarizability might be the molecular beam experiments which measure the deuteron electric quadrupole moment.[8,9] When the deuteron is in a molecule, such as D_2, it is subject to zero-point oscillations and consequently is acted upon by an electric field which has a nonvanishing expectation value for $\langle\mathcal{E}^2\rangle$ even though $\langle\mathcal{E}\rangle$ vanishes. As a result and by Eq. (1), the deuteron will possess a polarization energy. Since, by Eq. (13), the polarizability depends upon the orientation of the deuteron spin, the polarizability energy will vary with the orientation. Furthermore, the polarizability relations in Eq. (13) depends upon m^2 and not upon m and in this respect is similar to the deuteron electric quadrupole interactions. Consequently, the deuteron polarizability will give rise to a change in the apparent magnitude of the deuteron quadrupole moment.

At first sight, it might be thought that this polarizability effect could not be distinguished from the deuteron quadrupole moment. However, the apparent deuteron quadrupole moment can be measured both in HD and D_2. Since the amplitudes of zero-point vibration in these two molecules are different, the values of $\langle\mathcal{E}^2\rangle$ and of polarization energy will differ. Consequently, the anisotropy of the deuteron polarizability can, at least in principle, be measured by the variation in the apparent deuteron quadrupole moment when measured in D_2 and HD.

The above analysis can be made quantitative, as follows. From Eqs. (1) and (13), if $W_{p,m}$ is the polarization energy in nuclear orientation state m,

$$W_{p,1}-W_{p,0}=-\tfrac{1}{2}(3\alpha_{SD}-3\alpha_{DD})\langle\mathcal{E}^2\rangle. \quad (23)$$

On the other hand, as discussed in the literature,[10] one can easily show that the energy difference for the same transition for an effective nuclear electric quadrupole moment Q' is

$$W_{q,1}-W_{q,0}=\tfrac{3}{4}eQ'(\partial^2V^e/\partial z_0^2). \quad (24)$$

Consequently, from Eqs. (23) and (24), the apparent quadrupole interaction caused by the nuclear polarizability becomes

$$h^{-1}eQ'(\partial^2V^e/\partial z_0^2) =h^{-1}\langle\mathcal{E}^2\rangle[-2\alpha_{SD}+2\alpha_{DD}] =(hc/e^2)^38\pi^3(\mu/m)^2\omega_e^4c(R_e/a_0)^2Z^{-2} \times[(B_e/\omega_e)+(B_e/\omega_e)^2(aR_e)^2][-2\alpha_{SD}+2\alpha_{DD}], \quad (25)$$

where the value for $\langle\mathcal{E}^2\rangle$ which can be calculated by normal procedures[11] from the zero-point vibration of the molecules has been substituted in the last form of the equation, and where the symbols used have their conventional meaning.[11] If numerical values are substituted in Eq. (25), the apparent quadrupole interaction arising from the deuteron polarizability becomes 0.0075 cps for HD and 2.0060 cps for D_2, which is unfortunately much too small to be detected with the present experimental accuracy.

Another and more favorable way in which the deuteron polarizability should be observable is in the electric scattering of deuterons by highly charged nuclei. If the deuteron is polarized by the electric field of the scattering nucleus, it will be less deflected than if the deuteron were not polarizable. It can be shown that 8-Mev deuterons with the above calculated polarizability, when scattered by Bi, should have their scattering cross section in the backward direction reduced below the Rutherford scattering by 3 percent as a result of the deuteron polarizability. At such energies and with such a highly charged a nucleus, the effects of nuclear interaction, deuteron disintegration, etc., should be small compared to the 3 percent polarizability effect on the scattering. A detailed discussion of this application will be given in an accompanying paper.[12]

[6] J. M. Blatt and V. F. Weisskopf, *Theoretical Nuclear Physics* (John Wiley and Sons, Inc., New York, 1952), p. 105.
[7] J. B. French and M. L. Goldberger, Phys. Rev. **87**, 899 (1952). This is also the approximate value of Γ/γ used in reference 4.
[8] Kellogg, Rabi, Ramsey, and Zacharias, Phys. Rev. **57**, 677 (1940).
[9] Kolsky, Phipps, Ramsey, and Silsbee, Phys. Rev. **87**, 395 (1952).
[10] N. F. Ramsey, *Nuclear Moments* (John Wiley and Sons, Inc., New York, 1953).
[11] N. F. Ramsey, Phys. Rev. **87**, 1075 (1952); **90**, 232 (1953).
[12] Malenka, Kruse, and Ramsey, Phys. Rev. **91**, 1165 (1953).

The Electric Scattering of the Polarizable Deuteron*

B. J. MALENKA, U. E. KRUSE, AND N. F. RAMSEY
Harvard University, Cambridge, Massachusetts

(Received May 25, 1953)

The effect of the electric polarizability of the deuteron upon its electric scattering is discussed for cases in which $Ze^2/\hbar v \gg 1$ and the classical closest distance of approach is so large that the effects of direct nuclear interaction are negligible. Under such circumstances, the chief departure from the Rutherford scattering law is due to the polarizability of the deuteron. The magnitude of the departure is calculated, and in particular, the polarizability contribution to backward scattering is estimated to be respectively about 3 percent and 4 percent for 8-Mev and 10-Mev deuterons scattered by bismuth and uranium.

I. INTRODUCTION

As has been shown in the previous paper,[1] the structure of the deuteron is such that it exhibits a polarizability when placed in an electric field. This phenomenon leads us to expect that the Rutherford cross section for electric scattering of a nucleus of charge Z will be somewhat modified.[2] Under ordinary circumstances this effect is likely to be obscured by nuclear interactions. Consequently, in this paper, we will confine our considerations to the energy regions where the nuclear effects are negligible, that is, the energy regions where the penetration of any part of the deuteron through the Coulomb barrier to the scattering nucleus is negligibly small. The approximate conditions for this are that the classical distance of closest approach be considerably larger than the nuclear radius and that the penetrability much beyond the classical distance of closest approach be small, which occurs when $Ze^2/\hbar v \gg 1$.

The condition $Ze^2/\hbar v \gg 1$ is also the condition in Coulomb scattering that the classical approximation be valid. This approximation can be successfully used in obtaining numerical results as is done below in Sec. III. This section, in conjunction with the preceding paper,[1] provides a complete procedure for calculating the polarizability anomaly of the deuteron. Section II has been included in order to exhibit the relation of this paper to the recent work of French and Goldberger,[3] and it is not essential for an understanding of Sec. III.

II. DEUTERON STRUCTURE AND POLARIZABILITY SCATTERING

In order to compare this calculation of the deuteron polarizability scattering with the French and Goldberger[3] treatment of the effects of the finite deuteron size, we can start with their wave equation[3] for a deuteron of incident momentum $\hbar\mathbf{k}$ which is electrically scattered by a nucleus of charge Z. We then have

$$[\tfrac{1}{2}(\hbar^2/m)(\nabla_R^2+k^2)-Ze^2R^{-1} +\tfrac{1}{2}(\hbar^2/\mu)\nabla_r^2-V(\mathbf{r})-\epsilon]\Psi(\mathbf{R},\mathbf{r}) =Ze^2[|\mathbf{R}+\tfrac{1}{2}\mathbf{r}|^{-1}-R^{-1}]\Psi(\mathbf{R},\mathbf{r}), \quad (1)$$

where $\mathbf{R}=\frac{1}{2}(\mathbf{r}_p+\mathbf{r}_n)$, $\mathbf{r}=\mathbf{r}_p-\mathbf{r}_n$, m = deuteron mass, μ = deuteron reduced mass, $V(\mathbf{r})$ = neutron-proton potential, and ϵ = deuteron binding energy. If we expand $\Psi(\mathbf{R},\mathbf{r})$ in terms of the complete set of normalized neutron-proton wave functions $\chi_n(\mathbf{r})$ so that $\Psi(\mathbf{R},\mathbf{r})=\sum_n \chi_n(\mathbf{r})\Omega_n(\mathbf{R})$, then multiply from the left by $\chi_0^*(\mathbf{r})$, and finally integrate over $\mathbf{r}$ space, Eq. (1) becomes

$$\left[\frac{\hbar^2}{2m}(\nabla_R^2+k^2)-\frac{Ze^2}{R}\right]\Omega_0(\mathbf{R}) =Ze^2\int\chi_0^*(\mathbf{r})\left[\frac{1}{|\mathbf{R}+\frac{1}{2}\mathbf{r}|}-\frac{1}{R}\right]\Psi(\mathbf{R},\mathbf{r})(d\mathbf{r}), \quad (2)$$

where $\Omega_0(\mathbf{R})$ is the wave function for elastic scattering. Treating the right-hand side as a perturbation, we make the approximation $\Psi(\mathbf{R},\mathbf{r})=\chi_0'(\mathbf{r})\psi(\mathbf{R})$ where $\chi_0'(\mathbf{r})$ is the ground-state wave function of the deuteron as distorted by the electric field of the nucleus, so that approximately

$$\chi_0'(\mathbf{r})=\chi_0(\mathbf{r})-\sum_{n\neq 0}'[E_n+\epsilon]^{-1} \times\left(n\left|\frac{1}{|\mathbf{R}+\frac{1}{2}\mathbf{r}|}-\frac{1}{R}\right|0\right)\chi_n(\mathbf{r}), \quad (3)$$

where the summation is over both discrete and continuum states. We then have

$$\left[\frac{\hbar^2}{2m}(\nabla_R^2+k^2)-\frac{Ze^2}{R}\right]\Omega_0(\mathbf{R}) \approx Ze^2\left(0\left|\frac{1}{|\mathbf{R}+\frac{1}{2}\mathbf{r}|}-\frac{1}{R}\right|0\right)\psi(\mathbf{R}) -\sum_{n\neq 0}'[E_n+\epsilon]^{-1}\left|\left(n\left|\frac{1}{|\mathbf{R}+\frac{1}{2}\mathbf{r}|}-\frac{1}{R}\right|0\right)\right|^2\psi(\mathbf{R}). \quad (4)$$

In the French and Goldberger[3] treatment, just the first

* This work was partially supported by the joint program of the U. S. Office of Naval Research and the U. S. Atomic Energy Commission.

[1] Ramsey, Malenka, and Kruse, preceding paper [Phys. Rev. **91**, 1162 (1953)].

[2] N. F. Ramsey, Phys. Rev. **83**, 659 (1951); Breit, Hull, and Gluckstern, Phys. Rev. **87**, 74 (1952).

[3] J. B. French and M. L. Goldberger, Phys. Rev. **87**, 899 (1952).

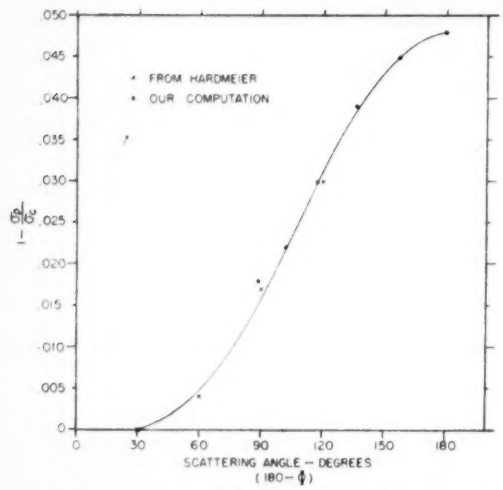

FIG. 1. The negative of the ratio of the polarizability to the Coulomb differential cross section plotted as a function of scattering angle for $\beta=0.2$.

term is obtained, since they introduce only the unperturbed deuteron wave function. In this paper, we are confining ourselves to the region where $Z\gg1$ and $Ze^2/\hbar v\gg1$; hence $\psi(\mathbf{R})$ is small for R less than the nuclear radius. On the other hand, the main contribution to the matrix elements on the right-hand side of Eq. (4) comes from the small values r since the wave function $\chi_0(r)$ vanishes exponentially for r greater than the deuteron radius. It is therefore a reasonable approximation to make a multipole expansion of the matrix arguments in terms of $R^{-1}(r/R)^l P_l(\cos\theta)$. From the angular integration, it then follows that the first term vanishes in agreement with the statement of French and Goldberger[3] for $R>\frac{1}{2}r$. If, in the second term, we keep only the lowest order term in r/R, Eq. (4) becomes approximately

$$[\tfrac{1}{2}(\hbar^2/m)(\nabla_R^2+k^2)-Ze^2R^{-1}]\Omega_0(\mathbf{R}) \approx -\tfrac{1}{2}\alpha(ZeR^{-2})^2\psi(\mathbf{R}), \quad (5)$$

where

$$\alpha=\tfrac{1}{2}e^2\sum_{n\neq0}{}'[E_n+\epsilon]^{-1}|(n|r\cos\theta|0)|^2. \quad (6)$$

From our previous paper,[1] we identify the α of Eq. (6) as the deuteron polarizability, where $\frac{1}{2}\alpha\mathcal{E}^2=\frac{1}{2}\alpha(ZeR^{-2})^2$ is the polarization energy, so that for $Z\gg1$ and $Ze^2/(\hbar v)\gg1$ we can speak of the polarizability of the deuteron as causing the principal departure from Rutherford scattering.[4]

III. CLASSICAL SCATTERING

In a more approximate treatment of the scattering problem, the difficulties of solving Eq. (4) or (5) can be avoided by noting that the condition $zZe^2/(\hbar v)\gg1$ is the criterion[5] for the validity of the classical Coulomb scattering. To be somewhat more general, in this section, we assume that the scattered particle has a charge z. We can then replace Eq. (5) with its classical counterpart,

$$E=\tfrac{1}{2}m\dot{R}^2+\tfrac{1}{2}mR^2\dot{\varphi}^2+zZe^2R^{-1}-\tfrac{1}{2}\alpha(ZeR^{-2})^2. \quad (7)$$

Let Φ be the supplement of the scattering angle, then

$$\Phi=2\int_0^{u_1}\frac{sdu}{[1-zZe^2E^{-2}u+\frac{1}{2}\alpha(Ze)^2E^{-2}u^4-s^2u^2]^{\frac{1}{2}}}, \quad (8)$$

where $u=R^{-1}$, $u_1=$ inverse distance of closest approach, and s is the impact parameter using the results of classical scattering theory.[6] The differential cross section is

$$\sigma(\Phi)=\frac{sds}{\sin\Phi d\Phi}, \quad (9)$$

and for pure Coulomb scattering

$$s_0=\tfrac{1}{2}(zZe^2/E)\tan(\tfrac{1}{2}\Phi_0). \quad (10)$$

Following the approach used by Hardmeier,[7] we say that for a given impact parameter s_0, the presence of the polarizability term produces a small decrease δ in the scattering angle, so that the supplement of the scattering angle can be written as

$$\Phi=\Phi_0+\delta. \quad (11)$$

The pure Coulomb impact parameter required for the deuteron to arrive at this angle is

$$s_1=\tfrac{1}{2}(zZe^2/E)\tan(\tfrac{1}{2}(\Phi_0+\delta))=\tfrac{1}{2}(zZe^2/E)\tan(\tfrac{1}{2}\Phi). \quad (12)$$

Then, it follows that the ratio of the Coulomb plus polarizability to the pure Coulomb differential cross section at $\Phi=\Phi_0+\delta$ is

$$\frac{\sigma_p}{\sigma_c}(\Phi)=\left(\frac{s_0ds_0}{\sin\Phi d\Phi}\right)\Big/\left(\frac{s_1ds_1}{\sin\Phi d\Phi}\right)=\left(\frac{ds_0^2}{d\Phi}\right)\Big/\left(\frac{ds_1^2}{d\Phi}\right)$$
$$=\frac{\tan(\frac{1}{2}\Phi_0)\sec^2(\frac{1}{2}\Phi_0)(d\Phi_0/d\Phi)}{\tan(\frac{1}{2}\Phi)\sec^2(\frac{1}{2}\Phi)}$$
$$=\frac{\sin(\frac{1}{2}\Phi_0)\cos^3\frac{1}{2}(\Phi_0+\delta)}{\sin(\frac{1}{2}(\Phi_0+\delta))\cos^3(\frac{1}{2}\Phi_0)}\left[1+\frac{d\delta}{d\Phi_0}\right]^{-1}. \quad (13)$$

From Eqs. (8) and (11) we can write δ as

$$\delta=2\int_0^{r_1}\frac{tdr}{[1-2r-f^2r^2+\beta r^4]^{\frac{1}{2}}} -2\int_0^{r_0}\frac{tdr}{[1-2r-f^2r^2]^{\frac{1}{2}}}, \quad (14)$$

[4] It should be noted, however, that in the neighborhood of the origin Eq. (5) breaks down, because although $\psi(\mathbf{R})$ becomes small as R goes to zero, it does remain finite.

[5] N. F. Mott and H. S. W. Massey, *The Theory of Atomic Collisions* (Oxford University Press, London, 1949), p. 124.

[6] H. Goldstein, *Classical Mechanics* (Addison-Wesley Press, Inc., Cambridge, 1950), p. 82.

[7] W. Hardmeier, Physik. Z. **28**, 181 (1925).

where we have made the substitution $v=\frac{1}{2}(zZe^2/E)u$ and are using the dimensionless constants

$$t=[2E/(zZe^2)]s=\tan(\tfrac{1}{2}\Phi_0), \tag{15}$$

$$\beta=\alpha 8(hc/e^2)z^{-4}Z^{-2}(E/hc)^3 \approx 2.68\times 10^{39}\alpha z^{-4}Z^{-2}E_{\text{Mev}}^3, \tag{16}$$

where α is in cm^3.

Hardmeier[7] has given a formula for δ at small scattering angles and has evaluated it explicitly for large scattering angles for $\beta=1, 2, 4, 6$. We have evaluated δ at large scattering angles for $\beta=0.2$ by numerically integrating the difference of the integrals appearing in Eq. (4) except near the ends of the region of integration. At the ends, the difference was approximated by expressions that could be integrated directly. $d\delta/d\Phi_0$ was then obtained by numerical differentiation. The results for σ_p/σ_c are given in Fig. 1 using also Hardmeier's[7] results for small scattering angles.

In the case of head on collisions, σ_p/σ_c reduces to $[1+(d\delta/d\Phi_0)]^{-2}$; also, as $t\to 0$, we have

$$\lim_{t\to 0}\frac{d\delta}{d\Phi_0}=\lim_{t\to 0}\frac{\delta}{\Phi_0}=\lim_{t\to 0}\frac{\delta}{2t}=\int_0^{v_1}\frac{dv}{[1-2v+\beta v^4]^{\frac{1}{2}}}-\int_0^{v_0}\frac{dv}{[1-2v]^{\frac{1}{2}}}. \tag{17}$$

If we evaluate this as a power series in β, we obtain for backward scattering

$$\frac{\sigma_p}{\sigma_c}(0)=1-0.229\beta-0.0354\beta^2. \tag{18}$$

For $\beta=0.2$, this gives us a 4.7 percent deviation from pure Coulomb scattering in the backward direction. For the deuteron $z=1$ and from reference 1, we have[8] $\alpha=0.56\times 10^{-39}$ cm^3. Then, applying Eqs. (16) and (18) to some examples where the nuclear effects should be comparatively small[2,9] and hence our treatment be valid, we find for 8-Mev deuterons scattered by $_{83}$Bi where $\beta=0.112$ a deviation of 2.7 percent in the backward direction, and for 10-Mev deuterons scattered by $_{92}$U where $\beta=0.177$ a deviation of 4.2 percent in the backward direction.

[8] The value of α is taken from Eqs. (13) and (21) of reference 1 by noting that for the scattering problem, we must average over the magnetic quantum number so that $\langle\alpha\rangle_{Av}=\alpha_{SS}+2\alpha_{DD}\approx\alpha_{SS}=0.56\times 10^{-39}$ cm^3.

[9] D. C. Peaslee, Phys. Rev. **74**, 1001 (1948); C. J. Mullin and E. Guth, Phys. Rev. **82**, 141 (1951).

PHYSICAL REVIEW VOLUME 91, NUMBER 5 SEPTEMBER 1, 1953

Exchange Scattering of an Electron by the Hydrogen Atom*

SAUL ALTSHULER
Department of Physics, Iowa State College, Ames, Iowa
(Received April 17, 1953)

The theory of scattering of electrons by hydrogen has been re-examined with the objective of identifying the matrix element for the exchange scattered amplitude from the same integral equation which provides direct scattered amplitudes. The theory of Mott and Massey is verified, but it is demonstrated that their result contains contributions from the incident wave which must be removed before computing exchange amplitudes. The result is a theoretical justification for the Oppenheimer (prior) matrix element.

THE analysis of exchange scattering was originally made by Oppenheimer,[1] and an entirely different treatment of this problem which has become standard was given by Mott and Massey.[2] The reason for the superiority of the latter method is that the general matrix element for the exchange scattered amplitude is identified, while Oppenheimer's solution is an approximate one from the outset so that the possibility for improved estimates is automatically ruled out. However, the method of Mott and Massey involves the assumption that the usual stationary state solution from which the direct scattered amplitude is derived has the asymptotic form

$$\operatorname{Lim}_{r_2\to\infty}\psi(\mathbf{r}_1,\mathbf{r}_2)=\sum_\alpha\frac{e^{ik_\alpha r_2}}{r_2}\cdot g_\alpha\cdot\varphi_\alpha(\mathbf{r}_1), \tag{1}$$

where $\mathbf{r}_1$ and $\mathbf{r}_2$ refer to the primary and hydrogenic electrons, respectively. (This labeling will prevail throughout the present paper.) The φ's are Coulomb functions; the sum includes integration over continuum states. Mott and Massey point out that no proof of this assumption has been given but that one should be possible. It is the purpose of this paper to provide such

* The research reported in this paper has been sponsored by the Geophysical Research Directorate of the Air Force Cambridge Research Center, Air Research and Development Command.

[1] J. R. Oppenheimer, Phys. Rev. **32**, 361 (1928).

[2] N. F. Mott and H. S. W. Massey, *Theory of Atomic Collisions* (Oxford University Press, New York, 1949), second edition.

a proof[3] and to discuss other consequences arising from the analysis. Unless the validity of Eq. (1) is demonstrated, it is impossible to guarantee that the usual solution, which is conveniently outgoing in the coordinate of the primary particle, is indeed capable of describing a bound hydrogenic state in the coordinate of the primary electron together with a free wave in the coordinate of the target electron.

We begin with the Schrödinger equation,

$$(-\nabla_1^2-\nabla_2^2+v(r_1)+v(r_2)+V(|\mathbf{r}_1-\mathbf{r}_2|))\psi(\mathbf{r}_1,\mathbf{r}_2) = E\psi(\mathbf{r}_1,\mathbf{r}_2), \quad (2)$$

where the v's are the potentials between the particles, and the nucleus is presumed at rest. The Hamiltonian is split into two unsymmetrical terms so that the unperturbed states describe a freely moving primary electron in the presence of the hydrogen atom. That is,

$$\begin{aligned} H&=H_0(\mathbf{r}_1,\mathbf{r}_2)+V(\mathbf{r}_1,\mathbf{r}_2),\\ H_0&=-\nabla_1^2-\nabla_2^2+v(r_2),\\ V(\mathbf{r}_1,\mathbf{r}_2)&=v(r_1)+V(|\mathbf{r}_1-\mathbf{r}_2|). \end{aligned} \quad (3)$$

In order to incorporate the boundary conditions required in a collision problem, that of an incident wave in the coordinate $\mathbf{r}_1$ with the hydrogen atom in, say, the ground state together with outgoing waves in either coordinate, we introduce the Green's function for the operator $(E-H_0(\mathbf{r}_1,\mathbf{r}_2))$ which satisfies the equation

$$(E-H_0(\mathbf{r}_1,\mathbf{r}_2))(r_1r_2|G|r_1'r_2')=\delta(\mathbf{r}_1-\mathbf{r}_1')\delta(\mathbf{r}_2-\mathbf{r}_2'). \quad (4)$$

Here

$$(r_1r_2|G|r_1'r_2')=\operatorname{Lim}_{\epsilon\to 0}\sum_\alpha\int\frac{d\mathbf{k}e^{i\mathbf{k}\cdot(\mathbf{r}_1-\mathbf{r}_1')}}{(2\pi)^3(E-\epsilon_\alpha-k^2+\epsilon i)} \times\varphi_\alpha(\mathbf{r}_2)\varphi_\alpha^*(\mathbf{r}_2'), \quad (5)$$

with $\epsilon>0$. The positive imaginary addition to the energy establishes the appropriate boundary conditions upon the scattered wave. If the integral over $\mathbf{k}$ is performed, then (5) becomes

$$(r_1r_2|G|r_1'r_2')=\sum_\alpha\frac{e^{ik_\alpha|\mathbf{r}_1-\mathbf{r}_1'|}}{-4\pi|\mathbf{r}_1-\mathbf{r}_1'|}\varphi_\alpha(\mathbf{r}_2)\varphi_\alpha^*(\mathbf{r}_2'), \quad (6)$$

$$k_\alpha=(E-\epsilon_\alpha)^{\frac{1}{2}}.$$

We now replace (2) by the following integral equation:

$$\psi(\mathbf{r}_1,\mathbf{r}_2)=e^{i\mathbf{k}_0\cdot r_1}\varphi_0(\mathbf{r}_2) +\int\int(r_1r_2|G|r_1'r_2')V(\mathbf{r}_1',\mathbf{r}_2')\psi(\mathbf{r}_1',\mathbf{r}_2')d\mathbf{r}_1'd\mathbf{r}_2. \quad (7)$$

[3] Private communication with H. E. Moses reveals that he has substantially verified the Mott-Massey conjecture using the Schwartz distribution analysis. This work appears in Research Report No. CX-5 and is issued by New York University, Washington Square College of Arts and Science Mathematics Research Group.

It is an elementary calculation to show that the asymptotic behavior of (7) as $r_1\to\infty$ is given by

$$\operatorname{Lim}_{r_1\to\infty}\psi(\mathbf{r}_1,\mathbf{r}_2) =e^{i\mathbf{k}_0\cdot r_1}\varphi_0(\mathbf{r}_2)+\sum_\alpha\frac{e^{ik_\alpha r_1}}{r_1}f_\alpha(\mathbf{k}_\alpha)\varphi_\alpha(\mathbf{r}_2). \quad (8)$$

The coefficient $f_n(\mathbf{k}_n)$ is then the direct scattered amplitude corresponding to excitation of the hydrogen atom into it's nth state.

Since (7) contains a complete statement of the boundary conditions, it is desirable to isolate the functional for the exchange scattered amplitude from this same integral equation. It is, however, inconvenient, if at all possible, to attack this problem directly by performing the sum on α involving the Coulomb functions in (5) in order, subsequently, to find the asymptotic behavior in the coordinate $\mathbf{r}_2$. Such a procedure is the analog to that carried out conveniently in the derivation of (6). Consequently, we proceed by rewriting (7) as follows:

$$\psi(\mathbf{r}_1,\mathbf{r}_2)=e^{i\mathbf{k}_0\cdot r_1}\varphi_0(\mathbf{r}_2) +\int\int\int\int d\mathbf{r}_1'd\mathbf{r}_2'd\mathbf{r}_1''d\mathbf{r}_2''\delta(\mathbf{r}_1-\mathbf{r}_1') \times\delta(\mathbf{r}_2-\mathbf{r}_2')(r_1'r_2'|G|r_1''r_2'') \times V(\mathbf{r}_1'',\mathbf{r}_2'')\psi(\mathbf{r}_1'',\mathbf{r}_2''). \quad (9)$$

We now interchange primed and unprimed coordinates separately in (4), and obtain

$$(E-H_0(\mathbf{r}_2,\mathbf{r}_1))(r_2r_1|G|r_2'r_1')=\delta(\mathbf{r}_1-\mathbf{r}_1')\delta(\mathbf{r}_2-\mathbf{r}_2'), \quad (10)$$

which is the same as

$$(E-H_0(\mathbf{r}_2',\mathbf{r}_1'))(r_2r_1|G|r_2'r_1') =\delta(\mathbf{r}_1-\mathbf{r}_1')\delta(\mathbf{r}_2-\mathbf{r}_2'), \quad (11)$$

since the Green's function is a symmetric operator with respect to an interchange of primed with unprimed coordinates. Upon substituting into (9), we have

$$\psi(\mathbf{r}_1,\mathbf{r}_2)=e^{i\mathbf{k}_0\cdot r_1}\varphi_0(\mathbf{r}_2) +\int\int\int\int d\mathbf{r}_1'd\mathbf{r}_2'd\mathbf{r}_1''d\mathbf{r}_2'' \times[(E-H_0(\mathbf{r}_2',\mathbf{r}_1'))(r_2r_1|G|r_2'r_1')] \times(r_1'r_2'|G|r_1''r_2'')V(\mathbf{r}_1'',\mathbf{r}_2'')\psi(\mathbf{r}_1'',\mathbf{r}_2''). \quad (12)$$

It is demonstrated in Appendix I that $H_0(\mathbf{r}_2',\mathbf{r}_1')$ is Hermitian with respect to the functions $(r_2r_1|G|r_2'r_1')$ and $(r_1'r_2'|G|r_1''r_2'')$. Therefore, (12) may be written

$$\psi(\mathbf{r}_1,\mathbf{r}_2)=e^{i\mathbf{k}_0\cdot r_1}\varphi_0(\mathbf{r}_2) +\int\int\int\int d\mathbf{r}_1'd\mathbf{r}_2'd\mathbf{r}_1''d\mathbf{r}_2''(r_2r_1|G|r_2'r_1') \times\{[E-H_0(\mathbf{r}_2',\mathbf{r}_1')](r_1'r_2'|G|r_1''r_2'')\} \times V(\mathbf{r}_1'',\mathbf{r}_2'')\psi(\mathbf{r}_1'',\mathbf{r}_2''). \quad (13)$$

We now make use of the identity,

$$H_0(\mathbf{r}_2, \mathbf{r}_1)=H_0(\mathbf{r}_1, \mathbf{r}_2)+v(r_1)-v(r_2),$$

and Eq. (4), in order to rewrite Eq. (13) as follows:

$$\psi(\mathbf{r}_1, \mathbf{r}_2)=e^{i\mathbf{k}_0\cdot\mathbf{r}_1}\varphi_0(\mathbf{r}_2)$$
$$+\int\int\int\int d\mathbf{r}_1'd\mathbf{r}_2'd\mathbf{r}_1''d\mathbf{r}_2''(r_2r_1|G|r_2'r_1')$$
$$\times\{\delta(\mathbf{r}_1'-\mathbf{r}_1'')\delta(\mathbf{r}_2'-\mathbf{r}_2'')V(\mathbf{r}_1'', \mathbf{r}_2'')\psi(\mathbf{r}_1'', \mathbf{r}_2'')$$
$$+[v(r_2')-v(r_1')](r_1'r_2'|G|r_1''r_2'')$$
$$\times V(\mathbf{r}_1'', \mathbf{r}_2'')\psi(\mathbf{r}_1'', \mathbf{r}_2'')\}, \quad (14)$$

and after employment of the original integral, Eq. (7), Eq. (14) becomes

$$\psi(\mathbf{r}_1, \mathbf{r}_2)=e^{i\mathbf{k}_0\cdot\mathbf{r}_1}\varphi_0(\mathbf{r}_2)$$
$$+\int\int d\mathbf{r}_1'd\mathbf{r}_2'(r_2r_1|G|r_2'r_1')\cdot V(\mathbf{r}_1', \mathbf{r}_2')\psi(\mathbf{r}_1', \mathbf{r}_2')$$
$$+\int\int d\mathbf{r}_1'd\mathbf{r}_2'(r_2r_1|G|r_2'r_1')[v(r_2')-v(r_1')]$$
$$\times[\psi(\mathbf{r}_1', \mathbf{r}_2')-e^{i\mathbf{k}_0\cdot\mathbf{r}_1'}\varphi_0(\mathbf{r}_2')]. \quad (15)$$

It is shown in Appendix II that the following identity holds:

$$\int\int(r_2r_1|G|r_2'r_1')(v(r_2')-v(r_1'))e^{i\mathbf{k}_0\cdot\mathbf{r}_1'}$$
$$\times\varphi_0(\mathbf{r}_2')d\mathbf{r}_1'd\mathbf{r}_2'=e^{i\mathbf{k}_0\cdot\mathbf{r}_1}\varphi_0(\mathbf{r}_2). \quad (16)$$

On using this relation, (15) reduces to

$$\psi(\mathbf{r}_1, \mathbf{r}_2)=\int\int d\mathbf{r}_1'd\mathbf{r}_2'(r_2r_1|G|r_2'r_1')$$
$$\times[V(\mathbf{r}_1', \mathbf{r}_2')+v(r_2')-v(r_1')]\psi(\mathbf{r}_1', \mathbf{r}_2') \quad (17)$$

or

$$\psi(\mathbf{r}_1, \mathbf{r}_2)=\int\int d\mathbf{r}_1'd\mathbf{r}_2'(r_2r_1|G|r_2'r_1')$$
$$\times V(\mathbf{r}_2', \mathbf{r}_1')\psi(\mathbf{r}_1', \mathbf{r}_2'). \quad (18)$$

On evaluating the asymptotic behavior in the coordinate $\mathbf{r}_2$, we find precisely the form in (1). Therefore, we have succeeded in demonstrating that the same wave function satisfying the condition (8) behaves according to the assumption of Mott and Massey.

DISCUSSION

It is now possible to understand how the homogeneous integral Eq. (18) can satisfy the boundary conditions which characterize scattering problems. For example, if we replace $\psi(\mathbf{r}_1', \mathbf{r}_2')$ by the undisturbed wave, $e^{i\mathbf{k}_0\cdot\mathbf{r}_1'}\varphi_0(\mathbf{r}_2')$, under the integral in (17), and utilize (16), the result is

$$\psi(\mathbf{r}_1, \mathbf{r}_2)=e^{i\mathbf{k}_0\cdot\mathbf{r}_1}\varphi_0(\mathbf{r}_2)$$
$$+\int\int d\mathbf{r}_1'd\mathbf{r}_2'(r_2r_1|G|r_2'r_1')V(\mathbf{r}_1', \mathbf{r}_2')$$
$$\times e^{i\mathbf{k}_0\cdot\mathbf{r}_1'}\varphi_0(\mathbf{r}_2'); \quad (19)$$

or more generally, if any approximation to the scattered wave, $\psi(\mathbf{r}_1', \mathbf{r}_2')-e^{i\mathbf{k}_0\cdot\mathbf{r}_1'}\varphi_0(\mathbf{r}_2')$, is inserted into the second integral in (15), it is clear that the incident as well as the scattered wave is present. In other words, Eq. (18) can be considered as an integral equation for $\psi(\mathbf{r}_1, \mathbf{r}_2)$ with the proviso that the form $\psi=e^{i\mathbf{k}_0\cdot\mathbf{r}_1}\varphi_0(\mathbf{r}_2)+\psi_{\text{scatt}}$ obtains.

That Oppenheimer's and Mott-Massey's exchange amplitudes in Born approximation are in fact identical follows by comparing (19), which yields Oppenheimers' result, with (18) after replacing $\psi(\mathbf{r}_1', \mathbf{r}_2')$ by $e^{i\mathbf{k}_0\cdot\mathbf{r}_1'}\varphi_0(\mathbf{r}_2')$ in the integral, with the result

$$\psi(\mathbf{r}_1, \mathbf{r}_2)=\int\int d\mathbf{r}_1'd\mathbf{r}'(r_2r_1|G|r_2'r_1')V(\mathbf{r}_2', \mathbf{r}_1')$$
$$\times e^{i\mathbf{k}_0\cdot\mathbf{r}_1'}\varphi_0(\mathbf{r}_2'). \quad (20)$$

This equivalence is apparent from the vanishing as $r_2\rightarrow\infty$ of the quantity appearing on the left side of (16). A difference does exist, however, if inexact target wave functions are employed. This is necessarily the case in scattering from atoms other than the hydrogen atom, and the consequent ambiguity has been labeled "post-prior discrepancy."[4] But, since the scattering events derive from the scattered part of the wave function, it is evidenced in (19) that the Oppenheimer amplitudes are, in principle, the correct ones. These are the quantities referred[4] to as "prior" matrix elements. Furthermore, as Borowitz and Friedman[5] have discovered, the Born exchange amplitude for excitation to a continuum state fails to converge when calculated from (20). Verification is to be found in connection with the proof of (16), which appears in Appendix II. To be more specific, let us write the asymptotic form of the left side of (16), namely,

$$\sum_\alpha\frac{e^{ik_\alpha r_2}}{r_2}\varphi_\alpha(\mathbf{r}_1)\int\int\varphi_\alpha^*(\mathbf{r}_1')e^{-i\mathbf{k}_\alpha\cdot\mathbf{r}_2'}[v(r_2')-v(r_1')]$$
$$\times e^{i\mathbf{k}_0\cdot\mathbf{r}_1'}\varphi_0(\mathbf{r}_2')d\mathbf{r}_1'd\mathbf{r}_2'.$$

Although the integral in this expression does not converge for a particular continuum state α, the sum over the continuum values converges to zero. That this lack of convergence raises no difficulty is clear from what has already been said concerning the necessity of computing all scattering amplitudes from the scattered part of the wave in (19) which does provide continuum

[4] Bates, Fundaminsky, Leech, and Massey, Trans. Roy. Soc. (London) **A243**, 117 (1950).

[5] S. Borowitz and B. Friedman, Phys. Rev. **89**, 441 (1953).

exchange amplitudes in Born approximation that converge.

CONCLUDING REMARKS

The theory of exchange scattering has been examined without developing two solutions based upon the separate expansions $\psi=\sum_\alpha F_\alpha(\mathbf{r}_1)\varphi_\alpha(\mathbf{r}_2)$ and $\psi'=\sum_\alpha G_\alpha(\mathbf{r}_2)d_\alpha(\mathbf{r}_1)$ which require the imposition of separate sets of boundary conditions on $F_n(\mathbf{r}_1)$ and $G_n(\mathbf{r}_2)$. This lack of symmetry for the enforcement of the boundary conditions is objectionable since there is no assurance that the two solutions are the same. To assume this equivalence is precisely the assumption in (1), the validity of which is now confirmed. Such a difficulty does not arise if the perturbation is taken to be the symmetrical one, $V(|\mathbf{r}_1-\mathbf{r}_2|)$, for the Green's function for the problem becomes correspondingly symmetric in $\mathbf{r}_1$ and $\mathbf{r}_2$. However, this procedure possesses the disadvantage of mathematical intractibility since the Green's function is now constructed of Coulomb functions in the coordinates of both particles.

Finally, it must be pointed out that the present analysis may be extended to scattering from arbitrary atomic targets with the result that the "prior" matrix element is in principle the correct one for Born exchange scattered amplitudes.

ACKNOWLEDGMENTS

The author is indebted to Dr. J. F. Carlson for many valuable discussions, and has also profited from correspondence and discussion with Dr. E. Gerjuoy.

APPENDIX I

We consider the expression

$$\int\int d\mathbf{r}_1'd\mathbf{r}_2'\{[E-H_0(\mathbf{r}_2',\mathbf{r}_1')](\mathbf{r}_2\mathbf{r}_1|G|\mathbf{r}_2'\mathbf{r}_1')\}\times(\mathbf{r}_1'\mathbf{r}_2'|G|\mathbf{r}_1''\mathbf{r}_2'')\equiv\int\int d\mathbf{r}_1'd\mathbf{r}_2'\{[E+\nabla_1'^2+\nabla_2'^2-v(\mathbf{r}_1')](\mathbf{r}_2\mathbf{r}_1|G|\mathbf{r}_2'\mathbf{r}_1')\}(\mathbf{r}_1'\mathbf{r}_2'|G|\mathbf{r}_1''\mathbf{r}_2''). \quad (1)$$

The theorem to be proved is that the Laplacians are Hermitian with respect to the functions $(\mathbf{r}_2\mathbf{r}_1|G|\mathbf{r}_2'\mathbf{r}_1')$ and $(\mathbf{r}_1'\mathbf{r}_2'|G|\mathbf{r}_1''\mathbf{r}_2'')$. Therefore, treating the term in $\nabla_1'^2$ alone, we apply Green's theorem and prove that the resulting surface integral vanishes. The proof for the operator $\nabla_2'^2$ is identical. The surface integral† in question is

$$\operatorname*{Lim}_{r_1'\to\infty}\int_{S_1'}dS_1'\left\{(\mathbf{r}_1'\mathbf{r}_2'|G|\mathbf{r}_1''\mathbf{r}_2'')\frac{\partial}{\partial\mathbf{r}_1'}(\mathbf{r}_2\mathbf{r}_1|G|\mathbf{r}_2'\mathbf{r}_1')-(\mathbf{r}_2\mathbf{r}_1|G|\mathbf{r}_2'\mathbf{r}_1')\frac{\partial}{\partial\mathbf{r}_1'}(\mathbf{r}_1'\mathbf{r}_2'|G|\mathbf{r}_1''\mathbf{r}_2'')\right\}. \quad (2)$$

† Contributions of the pole in $(\mathbf{r}_2\mathbf{r}_1|G|\mathbf{r}_2'\mathbf{r}_1')$ are automatically accounted for by the use of delta functions.

Upon inserting specific expressions for the Green's functions, we obtain

$$\operatorname*{Lim}_{r_1'\to\infty}\sum_{\alpha,\gamma}\frac{\varphi_\alpha(\mathbf{r}_2')\varphi_\alpha^*(\mathbf{r}_2'')}{-4\pi|\mathbf{r}_2-\mathbf{r}_2'|}\int_{S_1'}e^{ik_\gamma|r_2-r_2'|}\varphi_\gamma(\mathbf{r}_1)\times\left\{\frac{e^{ik_\alpha|r_1'-r_1''|}}{-4\pi|\mathbf{r}_1'-\mathbf{r}_1''|}\frac{\partial}{\partial r_1'}\varphi_\gamma^*(\mathbf{r}_1')-\varphi_\gamma^*(\mathbf{r}_1')\frac{\partial}{\partial r_1'}\frac{e^{ik_\alpha|r_1'-r_1''|}}{-4\pi|\mathbf{r}_1'-\mathbf{r}_1''|}\right\}ds_1'. \quad (3)$$

This quantity vanishes at once for the discrete γ's, or for the states for which k_α is imaginary. For the remaining case involving real k_α and the continuum γ, we rewrite (3) after introducing asymptotic forms given by

$$\operatorname*{Lim}_{r_1'\to\infty}\frac{e^{ik_\alpha|r_1'-r_1''|}}{|\mathbf{r}_1-\mathbf{r}_1''|}=\frac{e^{ik_\alpha r_1'}}{r_1'}e^{-ik_\alpha\mathbf{r}_0\cdot\mathbf{r}_1''}, \quad (4)$$

where $\mathbf{r}_0$ is a unit vector in the direction of $\mathbf{r}_1'$, and

$$\operatorname*{Lim}_{r_1'\to\infty}\varphi_\gamma^*(\mathbf{r}_1')=(2/\pi k)^{\frac{1}{2}}\frac{\sin(kr_1'+\delta_l)}{r_1'}Y_l^{m*}(\theta_1',\varphi_1'),\qquad \delta_l=\ln(2kr)/k-\arg\Gamma(l+1+i/k). \quad (5)$$

Here the Coulomb function is normalized on the energy scale, $\epsilon=k^2$. We now consider the first of the two terms in the surface integral. After incorporating (4) and (5), the following result is obtained:

$$\operatorname*{Lim}_{r_1'\to\infty}\int_{S_1'}\sum_{l,m}\int_0^\infty d\epsilon\exp[i(E-k^2)^{\frac{1}{2}}|\mathbf{r}_2-\mathbf{r}_2'|]\times Y_l^m(\theta_1,\varphi_1)R_{k,l}(r_1)\left\{\frac{e^{ik_\alpha r_1'}}{r_1'\sqrt{k}}e^{-ik_\alpha\mathbf{r}_0\cdot\mathbf{r}_1''}\times\frac{k\cos(kr_1'+\delta_l)}{r_1'}Y_l^{m*}(\theta_1',\varphi_1')\right\}r_1'^2\sin\theta_1'd\theta_1'd\varphi_1'. \quad (6)$$

Here, we have dropped the term in $1/r_1'^2$ which arises from differentiating with respect to r_1'. Clearly the angular integration does not affect the k or r_1' dependence. Consequently, the integration over the energy may be examined directly. This integral is

$$\operatorname*{Lim}_{r_1'\to\infty}\int_0^\infty k^{\frac{1}{2}}dk\exp[i(E-k^2)^{\frac{1}{2}}|\mathbf{r}_2-\mathbf{r}_2'|]R_{k,l}(r_1)\times\cos(kr_1'+\delta_l),$$

apart from irrelevant factors. It is not difficult to show the convergence of this integral. Consequently, the entire quantity vanishes in the limit $r_1'\to\infty$. The second term in (3) may be handled in the same way. Thus the vanishing of (3) completes the proof.

APPENDIX II

By using the Schrödinger equation defining the ground state of the hydrogen atom we can rewrite the expression on the left in (16) as

$$\int\int (r_2 r_1|G|r_2' r_1')[\nabla_2'^2+\epsilon_0-v(r_1')] \times e^{ik_0\cdot r_1'}\varphi_0(\mathbf{r}_2')d\mathbf{r}_1'd\mathbf{r}_2'. \quad (1)$$

On adding and subtracting k_0^2, the energy of the incident electron, (1) becomes

$$\int\int (r_2 r_1|G|r_2' r_1')[E+\nabla_2'^2+\nabla_1'^2-v(r_1')] \times e^{ik_0\cdot r_1'}\varphi_0(\mathbf{r}_2')d\mathbf{r}_1'd\mathbf{r}_2'. \quad (2)$$

Here $E=k_0^2+\epsilon_0$, the total energy of the system, and $-k_0^2$ has been replaced by $\nabla_1'^2$. On using (2), we observe that the difference,

$$e^{ik_0\cdot r_1}\varphi_0(\mathbf{r}_2)-\int\int (r_2 r_1|G|r_2' r_1')[E-H_0(\mathbf{r}_2',\mathbf{r}_1')] \times e^{ik_0\cdot r_1'}\varphi_0(\mathbf{r}_2'), \quad (3)$$

is an eigenfunction of the operator $H_0(\mathbf{r}_2,\mathbf{r}_1)$. Verification is immediate by operating from the left with $[E-H_0(\mathbf{r}_2,\mathbf{r}_1)]$. This result is the physical basis for the vanishing of (3), for $H_0(\mathbf{r}_2,\mathbf{r}_1)$ contains no coupling between electronic coordinates and thus cannot represent an incident and scattered wave as (3) appears to suggest; nor can (3) describe a bound state in $\mathbf{r}_2$. To proceed with the demonstration that (3) vanishes, we first observe that $\nabla_2'^2$ behaves as a Hermitian operator in the presence of the ground state $\varphi_0(\mathbf{r}_2')$. Therefore, we rewrite the second term in (3) as

$$\int\int [E-H_0(\mathbf{r}_2',\mathbf{r}_1')](r_2 r_1|G|r_2' r_1') \times e^{ik_0\cdot r_1'}\varphi_0(\mathbf{r}_2')d\mathbf{r}_1'd\mathbf{r}_2' + \lim_{r_1'\to\infty}\int d\mathbf{r}_2'\int_{S_1'}\varphi_0(\mathbf{r}_2')\left\{(r_2 r_1|G|r_2' r_1')\frac{\partial}{\partial \mathbf{r}_1'} \times e^{ik_0\cdot r_1'}-e^{ik_0\cdot r_1'}\cdot\frac{\partial}{\partial \mathbf{r}_1'}\partial r_1'(r_2 r_1|G|r_2' r_1')\right\}ds_1', \quad (4)$$

after applying Green's theorem with respect to $\nabla_1'^2$. On referring to (11), we observe that the term on the left in (4) is just the incident wave, $e^{ik_0\cdot r_1}\varphi_0(\mathbf{r}_2)$. We now show that the surface integral vanishes when S_1' is allowed to recede to infinity. Let us rewrite this expression in detail. We have, after some minor rearrangement,

$$\int\frac{d\mathbf{r}_2'\varphi_0(\mathbf{r}_2')}{-4\pi|\mathbf{r}_2-\mathbf{r}_2'|}\lim_{r_1'\to\infty}\sum_\alpha e^{ik_\alpha|r_2-r_2'|}\varphi_\alpha(\mathbf{r}_1) \times\int_{S_1'}\left\{\varphi_\alpha^*(\mathbf{r}_1')\frac{\partial}{\partial r_1'}e^{ik_0\cdot r_1'}-e^{ik_0\cdot r_1'}\frac{\partial}{\partial r_1'}\varphi_\alpha^*(\mathbf{r}_1')\right\}ds_1'. \quad (5)$$

It is obvious that only the contribution arising from the continuum α need be investigated. It is sufficient for our purpose to examine the expression to the right of the limit symbol which is written as

$$\lim_{r_1'\to\infty}\sum_{m,l}Y_l^m(\theta_1,\varphi_1) \times\int_0^\infty kdk\exp[i(E-k^2)^{\frac{1}{2}}|r_2-r_2'|]R_{k,l}(r_1) \times\int_{S_1'}Y_l^{m*}(\theta_1',\varphi_1')\left\{\frac{\sin(kr_1'+\delta_l)}{\sqrt{k}\cdot r_1'}\frac{\partial}{\partial r_1'}e^{ik_0\cdot r_1'} -\frac{e^{ik_0\cdot r_1'}\cdot k}{\sqrt{k}r_1'}\cos(kr_1'+\delta_l)\right\}r_1'^2\sin\theta_1'd\theta_1'd\varphi_1'. \quad (6)$$

Here we have employed (4) and (5) in Appendix I. On choosing the direction of $\mathbf{k}_0$ as polar axis, the angular integrations for the first term in the curly bracket is carried out as follows:

$$\int_{S_1'}Y_l^{m*}(\theta_1',\varphi_1')ik_0\cos\theta_1'e^{ik_0r_1'\cos\theta_1'}r_1'\sin\theta_1'd\theta_1'd\varphi_1' =2\pi ik_0r_1'\int_{-1}^{1}dx\cdot xP_l(x)e^{ik_0r_1'x} =2\pi[P_l(x)\cdot x\,e^{ik_0r_1'x}]_{-1}^{1}=2\pi(e^{ik_0r_1'}+(-1)^le^{-ik_0r_1'}). \quad (7)$$

In the third step we have performed partial integration and retained only the leading term in $1/r_1'$. with this result the integral in (6) becomes

$$\lim_{r_1'\to\infty}\int_0^\infty k^{\frac{1}{2}}dk\cdot\exp[i(E-k^2)^{\frac{1}{2}}|\mathbf{r}_2-\mathbf{r}_2'|]R_{k,l}(r_1) \times(e^{ik_0r_1'}+(-1)^le^{-ik_0r_1'})\sin(kr_1'+\delta_l). \quad (8)$$

As in Appendix I, the integral is convergent so that (8) vanishes in the limit $r_1'\to\infty$. By an exactly analogous argument, the contribution of the second term in curly brackets vanishes. Thus, the surface term in (4) vanishes and the proof of the equality in (16) is concluded.

Shift of the 1^1S State of Helium

S. CHANDRASEKHAR AND DONNA ELBERT, *Yerkes Observatory, University of Chicago, Williams Bay, Wisconsin*

AND

G. HERZBERG, *Physics Division, National Research Council, Ottawa, Canada*

(Received May 22, 1953)

In this paper the shift of the 1^1S state of helium is reconsidered and it is shown that recent discussions of the problem are subject to considerable doubt. The doubt arises from the unreliability (to the required precision) of the current theoretical determinations of the energy of the ground state. The result of an improved calculation for the latter is presented; and if this is accepted as a sufficient approximation, an unexplained shift of 21.5 cm^{-1} (opposite in direction to that previously suggested) would result for He. Similar unexplained shifts (but in the same direction as those suggested earlier) are also predicted for the other He-like ions.

A NUMBER of investigators[1] have recently tried to determine the electromagnetic shift (Lamb shift) of the ground state of He and He-like ions. Unfortunately, the experimental value for the ionization potential of He is known[2] only to ± 15 cm^{-1}, or perhaps ± 5 cm^{-1}, which is of the order of the expected shift. In preparation for a new and more precise spectroscopic determination of the ionization potential of He at Ottawa, it appeared of interest to inquire how reliable the presently accepted theoretical value of $I(\mathrm{He})$ is and whether its accuracy can be improved. It is generally assumed that the energy of the ground state of helium is known from theory with an accuracy (± 2 cm^{-1}) appreciably better than from experiment. But an examination of the calculations in the literature shows that the situation is by no means so favorable.

As is well known, Hylleraas[3] made the first successful attempt to reach a high degree of accuracy in the theoretical prediction of the ground state of two-electron systems, including helium and the negative hydrogen ion. His calculations were based on the variational principle; and in minimizing the energy given by wave functions of chosen forms, Hylleraas assumed that

$$\psi = e^{-\frac{1}{2}ks} \sum c_{lmn} (k)^{l+m+n} s^l t^m u^n, \tag{1}$$

where s, t, and u are related to the distances r_1, r_2, and r_{12} (measured in atomic units) of the two electrons from the nucleus and each other, respectively, by

$$s = r_1 + r_2, \quad t = r_2 - r_1, \quad \text{and} \quad u = r_{12}. \tag{2}$$

Further in Eq. (1), k and the c_{lmn}'s are constants with respect to which the energy is minimized. By choosing a wave function of the form

$$\psi = e^{-\frac{1}{2}ks}(1 + \beta u + \gamma t^2 + \delta s + \epsilon s^2 + \zeta u^2), \tag{3}$$

with six parameters, Hylleraas[4] found for E the value

$$E(\mathrm{helium}) = -2.90324 \text{ atomic units.} \tag{4}$$

Also it has generally been stated that "an eighth approximation" gives the improved value[5,6]

$$E(\mathrm{helium}) = -2.903745 \text{ atomic units.} \tag{5}$$

Though this value has been widely quoted and used, it must be pointed out that it was not found by a strict application of the variational principle. The value (5) was derived by a semiempirical procedure based on an alternative method in which the energy of the ground state of a two-electron system is expressed as a series in the reciprocal of the nuclear charge Z. But this latter method cannot be relied upon to the same extent as the variational principle in that we cannot even be certain whether the calculated value is greater or less than the true value. That the value (5) should be suspect is apparent when we note that using the same method Hylleraas derived for the ground state of the negative hydrogen ion the value

$$E(\mathrm{H}^-) = -0.52642 \text{ atomic unit,} \tag{6}$$

whereas Henrich[7] has derived the value

$$E(\mathrm{H}^-) = -0.52756 \text{ atomic unit} \tag{7}$$

by a variational method using a wave function of the form (1) with eleven parameters.

For the reasons stated earlier, we have attempted an improved calculation of the energy of the ground state of helium by applying the variational principle to a wave function of the form

$$\psi = e^{-\frac{1}{2}ks}(1 + \beta u + \gamma t^2 + \delta s + \epsilon s^2 + \zeta u^2 + \chi_6 su + \chi_7 t^2 u + \chi_8 u^3 + \chi_9 t^2 u^2) \tag{8}$$

[1] H. A. S. Eriksson, Nature **161**, 393 (1948); M. Günther, Physica **15**, 675 (1949); H. E. V. Håkansson, Arkiv. Fysik **1**, 555 (1950); B. Edlén, Arkiv. Fysik **4**, 441 (1951).

[2] C. E. Moore [*Atomic Energy Levels*, National Bureau of Standards Circular No. 467 (Government Printing Office, Washington, D. C. 1952)] gives the old Paschen value 198305 ± 15 cm^{-1}, while J. J. Hopfield [Astrophys. J. **72**, 133 (1930)] and B. Edlén (reference 1) gives values of 198314 and 198312 ± 5 cm^{-1}, respectively. *Note added in proof:*—Recent measurements by R. Zbinden and one of us (G. H.) at Ottawa confirm that the last-mentioned limit of error is a very conservative one.

[3] An account of Hylleraas's investigations will be found in H. Bethe, *Handbuch der Physik* (J. Springer, Berlin, 1933), Vol. 24, No. 1, pp. 353–363, see particularly pp. 358, 362, and 363.

[4] E. A. Hylleraas, Z. Physik **54**, 347 (1929), particularly p. 358.

[5] For example, Bethe (reference 3) states that "und nach einer noch genaueren Rechnung von Hylleraas wird schliesslich in achter Näherung."

[6] E. A. Hylleraas, Z. Physik **65**, 209 (1930).

[7] L. R. Henrich, Astrophys. J. **99**, 59 (1944).

with ten parameters. [It may be noted here that the terms in u, l^2, s, s^2, u^2, su, l^2u, and u^3 are the same ones which Hylleraas used in his calculations for determining the value (5).] The results of the calculations are summarized in Table I. This table gives the coefficients β, γ, etc., for three wave functions in the range in which E takes the minimum value. The energy of the ground state given by the calculations is therefore

$$E(\text{helium}) = -2.903603 \text{ atomic units.} \quad (9)$$

We conclude that there is no basis for supposing that the ground state of helium is given by the often quoted value (5).

The value (9), like Hylleraas's values (4) and (5), represents the total energy of He assuming infinite mass of the nucleus and is based on the nonrelativistic wave equation. Hylleraas and Bethe have shown that most of the effect of the motion of the nucleus can be taken into account by using the Rydberg constant R_{He} for He rather than that for infinite mass R_∞ in converting the atomic units to cm^{-1}. A small residual correction, called mass polarization by Bethe, amounts to only 5.2 cm^{-1}.

TABLE I. The constants of a ten-parameter wave function for the ground state of helium: $\psi = \mathfrak{N} e^{-ks}(1+\beta u+\gamma l^2+\delta s+\epsilon s^2+\zeta u^2+\chi_6 su+\chi_7 l^2 u+\chi_8 u^3+\chi_9 l^2 u^2)$ ($\mathfrak{N}$ is the normalization factor).

k	3.5100255	3.5299360	3.5498639
β	+0.350563	+0.352547	+0.353024
γ	+0.157394	+0.157622	+0.160254
δ	−0.129341	−0.120909	−0.112542
ϵ	+0.0130191	+0.0126717	+0.0124213
ζ	−0.0681335	−0.0708333	−0.0722356
χ_6	+0.0192383	+0.0231770	+0.0272757
χ_7	−0.0338436	−0.0322601	−0.0333144
χ_8	+0.0055753	+0.0057980	+0.0056875
χ_9	+0.0053420	+0.0051526	+0.0056020
E	−2.9036027	−2.9036022	−2.9036014
$\mathfrak{N}$	0.37984145	0.37356893	0.36764807

The relativity correction has been subject to considerable change depending on the approximation used. According to a first approximation worked out by Bethe,[3] it was estimated to be -27 cm^{-1} with Hartree functions and -10 cm^{-1} using a still simpler eigenfunction. Eriksson,[8] on the basis of higher approximations, obtains $+2$ cm^{-1}. These numbers are to be understood as net corrections for the energy difference between the ground states of He and He^+. Including the mass and relativity corrections, one finds from (9) for the ionization potential of He, the value

$$I_{\text{calc}}(\text{He}) = 198287.7 \text{ cm}^{-1}, \quad (10)$$

while the observed value[2] is

$$I_{\text{obs}}(\text{He}) = 198313 \pm 5 \text{ cm}^{-1}. \quad (11)$$

In computing (10) from (9), the Lamb shift of the ground state of He^+ has been neglected. If it is assumed that this shift of He^+ is correctly given by the Bethe-Schwinger theory, i.e., is 3.8 cm^{-1}, one obtains

$$I_{\text{calc}}(\text{He}) = 198291.5 \text{ cm}^{-1}. \quad (12)$$

[8] H. A. S. Eriksson, Z. Physik **109**, 762 (1938).

TABLE II. Observed and calculated values of the ionization potentials of He-like ions.

Z	Ion	I.P.$_{\text{obs}}$, cm^{-1}	I.P.$_{\text{calc}}$, cm^{-1}	I.P.$_{\text{obs}}$ − I.P.$_{\text{calc}}$, cm^{-1}
2	He I	198313	198291.5	+21.5
3	Li II	610079	610049	+30
4	Be III	1241225	1241309	−84
5	B IV	2091960	2092240	−280
6	C V	3162450	3163009	−559
7	N VI	4452800	4453848	−1048
8	O VII	5963000	5964970	−1970

The difference between observed and calculated values is much greater than the estimated limit of error of the observed value. The question whether the difference (21.5 cm^{-1}) is due to an electromagnetic shift (opposite in direction to the Lamb shift), or to incorrect mass or relativistic corrections, or to a failure of the tenth-order approximation in approaching the correct value, must be left to future investigations. With regard to this last point, we are at the present time working on a wave function with 14 parameters.

Similar large discrepancies between observed and calculated values arise for the He-like ions. Hylleraas has derived a widely quoted general interpolation formula for the ionization potentials of these ions from the values for H^-, He, and a hypothetical ion with $Z=\infty$. Using the revised values for H^- and He and Hylleraas's value for $Z=\infty$, one finds the following modified formula

$$\text{I.P.} = R_Z\left(Z^2 - \frac{5}{4}Z + 0.31488 - \frac{0.020896}{Z} + \frac{0.011096}{Z^2}\right).$$

The values calculated from this formula, and corrected for relativity and mass polarization effects according to Eriksson[8] as well as for the Lamb shifts of the H-like ions, are compared with the observed values as given by Edlén[1] in Table II. The observed values are larger than the calculated ones for He and Li^+, but smaller for the other He-like ions and increasingly so with increasing Z. The difference (last column of Table II) represents a shift of the $1s^2\ ^1S$ ground state referred to the state of the bare nucleus and the two electrons at infinite distance. For Li^+, as for He, this shift is opposite in direction to, and appreciably larger than, the "ordinary" Lamb shift, while for the other elements it is in the same direction and about twice as large as the Lamb shift for the corresponding one-electron systems. In agreement with expectation, the shift for $Z \geq 4$ is roughly proportional to Z^4 as was already found by Edlén on the basis of the Hylleraas formula. Edlén's shifts are approximately half those of Table II, since he referred the ionization potential to the unshifted ground state of the corresponding H-like ions. It must be emphasized that for the higher He-like ions the probable error of the observed ionization potentials is a considerable fraction (about one-third) of the shift.

The Excitation of Molecular Rotations and Vibrations in Inelastic Scattering Processes*

EDWARD H. KERNER
Department of Physics, Iowa State College, Ames, Iowa
(Received April 23, 1953)

A discussion is first given of the collisions of composite systems in general, where it is shown how the scattering amplitude may be written as a superposition of little amplitudes for the scattering of each particle in one system by each particle in the other. This is followed by the calculation of scattering cross sections for single charges by nitrogen molecules with excitation of rotational and vibrational states of motion; the collision of molecules with molecules, including the case that they are identical, is also discussed and applied to N_2-N_2 scattering. The smallness of internal rotational and vibrational velocities is exploited in the use of the Born approximation. Detailed numerical results are given.

INTRODUCTION

THE question of the exchange of energy between translational motion and molecular vibration and rotation has been discussed heretofore on a highly simplified basis involving usually a one- or two-dimensional model for the molecule,[1] and with some attempt to calculate inelastic cross sections by the method of distorted waves;[2] only meager quantitative results have been obtained. In this report we re-examine the question and capitalize on the smallness of internal rotational and vibrational velocities in the use of the Born approximation to obtain detailed results for the scattering of single charged particles and of molecules by molecules. In a preliminary discussion we make a few general observations on the scattering of composite systems which will be of perhaps wider application than in just molecular collisions.

REMARKS ON COLLISIONS OF COMPOSITE SYSTEMS

Consider the collision of a system of particles with internal coordinates $\boldsymbol{\varrho}_i$ (referred to the system's own center of mass) and a second system with internal coordinates $\mathbf{r}_j$, the two systems being separated by the distance $\mathbf{R}$ (Fig. 1).

For the present we ignore the possibility that the systems may be identical and that a rearrangement collision can take place. We write the Hamiltonian for the total system in the coordinate frame in which the center of mass of the complete system is at rest as

$$H=-(\hbar^2/2\mu)\nabla_R^2+H_r(\mathbf{r}_j)+H_\rho(\boldsymbol{\varrho}_i)+V(\boldsymbol{\varrho}_i,\mathbf{r}_j,\mathbf{R}), \quad (1)$$

μ being the reduced mass $M_\rho M_r/(M_\rho+M_r)$, H_r and H_ρ the internal Hamiltonians of the individual systems referred to their mass centers, and V their interaction energy. Expanding Ψ, which satisfies $H\Psi=E\Psi$ with suitable boundary conditions, in eigenstates $f_\alpha(\mathbf{r})\varphi_\beta(\boldsymbol{\varrho})$ of H_r+H_ρ as $\sum_{\alpha,\beta}F_{\alpha\beta}(\mathbf{R})f_\alpha(\mathbf{r})\varphi_\beta(\boldsymbol{\varrho})$ gives

$$(\nabla_R^2+k_{st}^2)F_{st}(\mathbf{R})=\frac{2\mu}{\hbar^2}\int\int f_s^*(\mathbf{r})\varphi_t^*(\boldsymbol{\varrho})V\Psi d\mathbf{r}d\boldsymbol{\varrho}, \quad (2)$$

$$k_{st}^2=\frac{2\mu}{\hbar^2}(E-E_s-E_t),$$

whence, introducing the Green's function for the left-hand side and taking the limit as $R\to\infty$,

$$F_{st}(\mathbf{R})\to-\frac{1}{4\pi}\frac{2\mu}{\hbar^2}\frac{e^{ik_{st}R}}{R}\int\int\int e^{-i\mathbf{k}_{st}\cdot\mathbf{R}}f_s^*\varphi_t^*V\Psi d\mathbf{r}d\boldsymbol{\varrho}d\mathbf{R}$$

$$+e^{ik_{ab}Z}\delta_{sa}\delta_{tb}\to\frac{e^{ik_{st}R}}{R}f_{st}(\theta,\varphi)+e^{ik_{ab}Z}\delta_{sa}\delta_{tb}. \quad (3)$$

In Born approximation we replace Ψ by $e^{i\mathbf{k}_{ab}\cdot\mathbf{R}}f_a(\mathbf{r})\varphi_b(\boldsymbol{\varrho})$ and obtain for the amplitude for scattering from the initial state $f_a(\mathbf{r})\varphi_b(\boldsymbol{\varrho})$ to the final state $f_s(\mathbf{r})\varphi_t(\boldsymbol{\varrho})$,

$$f_{st}^{ab}=-\frac{1}{4\pi}\frac{2\mu}{\hbar^2}\int\int\int e^{i\mathbf{K}\cdot\mathbf{R}}f_s^*\varphi_t^*Vf_a\varphi_b d\mathbf{r}d\boldsymbol{\varrho}d\mathbf{R} \quad (4)$$

$$\mathbf{K}=\mathbf{k}_{ab}-\mathbf{k}_{st}.$$

For a large class of problems

$$V=\sum_{i=1,\,j=1}^{\nu,\,n}v_{ij}(\mathbf{R}_{ij})$$

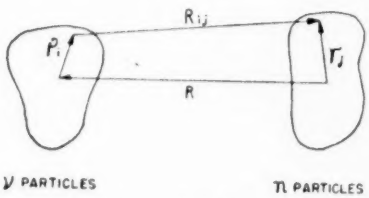

FIG. 1. Schematic representation of two colliding composite systems, showing labels of coordinates.

* The research reported in this paper has been sponsored by the Geophysical Research Directorate of the Air Force Cambridge Research Center, Air Research and Development Command under Contract AF 19(122)-469.

[1] N. F. Mott and H. S. W. Massey, *Theory of Atomic Collisions* (Clarendon Press, Oxford, 1949), Chap. XII, Sec. 3.5, where further references are given. After preparation of this paper, an article by P. M. Morse appeared in Phys. Rev. **90**, 51 (1953) which contains a similar treatment; the overlap in results with the present paper, however, is small.

[2] Reference 1, Chap. VII, Sec. 5.

or, for central forces, $\sum v_{ij}(|\mathbf{R}_{ij}|)$, where $\mathbf{R}_{ij}\equiv\mathbf{r}_j-\mathbf{R}-\boldsymbol{\rho}_i$, from Fig. 1. Hence Eq. (4) may be written

$$f_{st}^{ab}=-\frac{1}{4\pi}\frac{2\mu}{\hbar^2}\sum_{i,j}\int\int\int \exp[i\mathbf{K}\cdot(\mathbf{r}_j-\boldsymbol{\rho}_i+\mathbf{R}_{ji})]\times v_{ji}(\mathbf{R}_{ji})f_s^*\varphi_t^*f_a\varphi_b d\boldsymbol{\tau}d\boldsymbol{\rho}d\mathbf{R}$$

$$=-\frac{1}{4\pi}\frac{2\mu}{\hbar^2}\sum_{i,j}\int \exp[i\mathbf{K}\cdot\mathbf{r}_j]f_s^*f_a d\boldsymbol{\tau}\times\int\exp[-i\mathbf{K}\cdot\boldsymbol{\rho}_i]\varphi_t^*\varphi_b d\boldsymbol{\rho}\times\int\exp[i\mathbf{K}\cdot\mathbf{R}_{ji}]v_{ji}(\mathbf{R}_{ji})d\mathbf{R}$$

$$=-\frac{1}{4\pi}\frac{2\mu}{\hbar^2}\sum_{i,j}F_j(K)\phi_i(K)h_{ij}(K). \tag{5}$$

The factor

$$h_{ij}(K)=\int\exp[i\mathbf{K}\cdot\mathbf{R}_{ji}]v_{ji}(\mathbf{R}_{ji})d\mathbf{R}=\int\exp[i\mathbf{K}\cdot\mathbf{S}]v_{ji}(\mathbf{S})d\mathbf{S}$$

($\mathbf{S}$ being just a dummy variable of integration), is just the Born amplitude for the elastic scattering of the ith particle in the ρ system by the jth particle in the r system with momentum change $\mathbf{K}$, provided that the collision of the two systems is itself elastic ($a=s$ and $b=t$). In this case the result (5) states that the elastic Born amplitude $f_{ab}{}^{ab}$ is a superposition of little elastic Born amplitudes for the scattering of each particle in one system by each in the other. One can, as was first done by Massey and Bullard for electron-nitrogen molecule scattering,[3] replace the little Born amplitudes by the *exact* amplitudes at this point, and thereby effect a considerable improvement in $f_{ab}{}^{ab}$. This is difficult to justify theoretically but in practice proves to be very valuable (see reference 3); it is as if the general result of superposition of individual amplitudes has a validity considerably exceeding the range of validity of these amplitudes as found in Born approximation. Even for the inelastic scattering of the two systems ($|\mathbf{k}_{ab}|\neq|\mathbf{k}_{st}|$), one still identifies $h_{ij}(K)$ as a Born amplitude for elastic scattering with momentum change $\mathbf{K}$, and can replace this with the exact amplitude for the same momentum change; then $f_{st}{}^{ab}$ is a superposition of some sort of "quasi-elastic" amplitudes.[4]

[3] H. S. W. Massey and E. C. Bullard, Proc. Cambridge Phil. Soc. **29**, 511 (1933).

[4] The idea of superposing improved amplitudes in otherwise used in a different sense in nuclear scattering problems. See G. F. Chew, Phys. Rev. **80**, 196 (1950); G. F. Chew and G. C. Wick, Phys. Rev. **85**, 636 (1952); also R. L. Gluckstern and H. A. Bethe, Phys. Rev. **81**, 761 (1951). The latter, for *n-d* scattering, replace Born cross sections for individual nucleon-nucleon collisions in the final result by experimental cross sections; our approximation is distinct from Chew's impulse approximation. The replacement of $h_{ij}(K)$ by a quasi-elastic two-particle amplitude is the replacement $h_{ij}=\int\exp(-i\mathbf{k}_{st}\cdot\mathbf{S})v_{ji}(S)\mathbf{X}_{ji}(\mathbf{S})d\mathbf{S}$, where $\mathbf{X}_{ji}$ satisfies $[-(\hbar^2/2\mu)\nabla_S^2+v_{ji}(S)]\mathbf{X}_{ji}=(E-E_s-E_t)\mathbf{X}_{ji}$ such that $\mathbf{X}_{ji}\rightarrow\exp(i\mathbf{k}_{st}'\cdot\mathbf{S})+\exp(ik_{st}'S)/Sf^{ij}(K)$ with $|\mathbf{k}_{st}'|=|\mathbf{k}_{st}|$ and $|\mathbf{K}|=|\mathbf{k}_{st}'-\mathbf{k}_{st}|=|\mathbf{k}_{ab}-\mathbf{k}_{st}|$. This result can be made to follow formally from (3) when Ψ is approximated as $\Sigma_{i,j}(v_{ij}/V)\mathbf{X}_{ij}\exp[i\mathbf{K}\cdot(\mathbf{r}_j-\boldsymbol{\rho}_i)]f_a\varphi_b$, being a superposition of two-particle scattering wave functions weighted by the relative weights of the strengths of their interactions compared to the total interaction energy. As has been noted, the quasi-elastic amplitude is a true elastic amplitude when the scattering is itself elastic.

It may be noted in passing that when the eigenfunctions $f_a(\mathbf{r})$ and $\varphi_\beta(\boldsymbol{\rho})$ of $H_r(r)$ and $H_\rho(\rho)$ are represented as products $f_{\alpha1}(\mathbf{r}_1)f_{\alpha2}(\mathbf{r}_2)\cdots f_{\alpha n}(\mathbf{r}_n)$ and $\varphi_{\beta1}(\boldsymbol{\rho}_1)\varphi_{\beta2}(\boldsymbol{\rho}_2)\cdots\varphi_{\beta\nu}(\boldsymbol{\rho}_\nu)$ of one particle eigenfunctions in a self-consistent field (Hartree) type of approximation, one has

$$F_j(K)=\int\exp[i\mathbf{K}\cdot\mathbf{r}_j]f_{sj}^*(\mathbf{r}_j)f_{aj}(\mathbf{r}_j)d\mathbf{r}_j\cdot\prod_{l\neq j}\int f_{sl}^*(\mathbf{r}_l)f_{al}(\mathbf{r}_l)d\mathbf{r}_l,$$

$$\phi_i(K)=\int\exp[-i\mathbf{K}\cdot\boldsymbol{\rho}_i]\varphi_{ti}^*(\boldsymbol{\rho}_i)\varphi_{bi}(\boldsymbol{\rho}_i)d\boldsymbol{\rho}_i\cdot\prod_{k\neq i}\int\varphi_{tk}^*(\boldsymbol{\rho}_k)\varphi_{bk}(\boldsymbol{\rho}_k)d\boldsymbol{\rho}_k.$$

To an approximation sufficient for many purposes, the self-consistent fields for the states a and s (or b and t) may be taken as the same (or indeed one can often build the one-particle eigenfunctions for a system from a single average field, the same for each particle). Then the orthogonality of the f_{sl}, f_{al} is assured and the $\prod_{l\neq j}$ is one or zero according as the states a and s are the same except for their $\mathbf{r}_j$ eigenfunctions or are different in any $\mathbf{r}_l$ eigenfunctions; and similarly for the $\prod_{k\neq i}$. The scattering amplitude for the process in which the pth particle in the r system goes from state a to state s and the qth particle in the ρ system goes from state b to state t is in this picture just

$f_{st}{}^{ab}$ (simple Hartree approx) =

$$-\frac{1}{4\pi}\frac{2\mu}{\hbar}\int\exp[i\mathbf{K}\cdot\mathbf{r}_p]f_{sp}^*f_{ap}d\mathbf{r}_p\times\int\exp[-\mathbf{K}\cdot\boldsymbol{\rho}_q]\varphi_{tq}^*\varphi_{bq}\int\exp[i\mathbf{K}\cdot\mathbf{S}]v_{pq}(S)d\mathbf{S}$$

while the amplitude for excitation of more than one particle in either system is zero (i.e., small in the general case).

EXCITATION OF MOLECULAR ROTATION

We send a single charged particle against a homonuclear diatomic molecule, which we treat as a rigid dumbbell, and ask for the amplitude for excitation of

rotational levels in a process in which the incident particle is scattered through a given angle. So long as the energy, or velocity, or relative motion far exceeds the energy, or velocity, of internal rotational motion, we expect the Born approximation to give an adequate picture of the inelastic scattering. For a nitrogen molecule, for example, one has internal energies $E_l \simeq 2.5\times10^{-4} l(l+1)$ ev and velocities $v_l \simeq 1.9\times10^{-5}\times[l(l+1)]^{\frac{1}{2}}$ atomic units, so that the Born approximation should suffice down to even very small incident energies.

For the interaction between the incident charge (proton, electron, or alpha particle for example) and the molecule we use the static Fermi-Thomas field of the molecule. This has been shown by Hund[5] to be well represented by a function of the form $v(r_1)+v(r_2)$, r_1 and r_2 being radial distances measured from the two nuclei. Though distortion of this field due to polarization of the electron swarm is neglected, this will have no serious effect on the qualitative character of the results (barring only a gross alteration of the molecular bond, an effect that we do not consider at all), and we use the Hund field merely as the best one available, with due reservation as to its detailed quantitative significance.

Following the discussion above on composite collisions, we write $\mathbf{R}=\mathbf{r}_1+\frac{1}{2}\boldsymbol{\varrho}=\mathbf{r}_2-\frac{1}{2}\boldsymbol{\varrho}$, $\boldsymbol{\varrho}$ being the nuclear separation, and $V=v(r_1)+v(r_2)$. The amplitude for scattering and exciting from state b to l is then, after straightforward reductions,

$$f_l{}^b=-\frac{1}{4\pi}\frac{2\mu}{h^2}2\int\exp(i\mathbf{K}\cdot\mathbf{S})v(S)d\mathbf{S}\int\cos\tfrac{1}{2}\mathbf{K}\cdot\boldsymbol{\varrho}\,\varphi_l{}^*\varphi_b d\boldsymbol{\varrho},$$

which we write as

$$f_l{}^b=-2\frac{\mu}{m}\underbrace{\frac{2\pi m}{h^2}\int\exp(i\mathbf{K}\cdot\mathbf{S})v(S)d\mathbf{S}}_{h(K)}\times\underbrace{\int\cos\tfrac{1}{2}\mathbf{K}\cdot\boldsymbol{\varrho}\,\varphi_l{}^*\varphi_b d\boldsymbol{\varrho}}_{J_{lb}},\quad(6)$$

in order to make use of Massey and Bullard's[3] evaluation of the factor $h(K)$ for N_2. Here m is the electron mass, μ the reduced mass of target and incident particle; the φ's in J_{lb} are just spherical harmonics; and $K^2=k_b^2+k_l^2-2k_bk_l\cos\theta$, where θ is the angle of scattering of the incident particle in the center-of-mass system, and $k_b^2=(2\mu/h^2)(E-E_b)$, $E=E_b+\frac{1}{2}\mu v^2$, $v=\dot{R}$.

The factor J_{lb} is explicitly

$$J_{lj}=N_lN_j\,\mathrm{Re}\int\int P_l{}^{m_l}(\cos\theta)P_j{}^{m_j}(\cos\theta)\times e^{i\frac{1}{2}K\rho\cos\theta}e^{-im_l\varphi}e^{im_j\varphi}\sin\theta d\theta d\varphi,$$

so m_l must be the same as m_j. The θ integration tells that l and j must be of the same parity. A simple case of the general integral[6] is J_{l0}, for the excitation of the lth rotational state from the ground state. Expanding $e^{i\frac{1}{2}K\rho\cos\theta}$ in Legendre polynomials gives at once

$$J_{l0}=(2l+1)^{\frac{1}{2}}(-1)^{l/2}(\pi/K\rho)^{\frac{1}{2}}J_{l+\frac{1}{2}}(\tfrac{1}{2}K\rho)=(2l+1)^{\frac{1}{2}}(-1)^{l/2}j_l(\tfrac{1}{2}K\rho).\quad(7)$$

Hence the differential cross section is

$$d\sigma/d\omega=(k_l/k_0)4(\mu/m)^2h^2(K)(2l+1)j_l{}^2(\tfrac{1}{2}K\rho),$$

and the total cross section

$$\sigma(k_0)=4\left(\frac{\mu}{m}\right)^2\frac{2\pi}{k_0{}^2}\int_{k_0-k_l}^{k_0+k_l}h^2J_{l0}{}^2KdK.$$

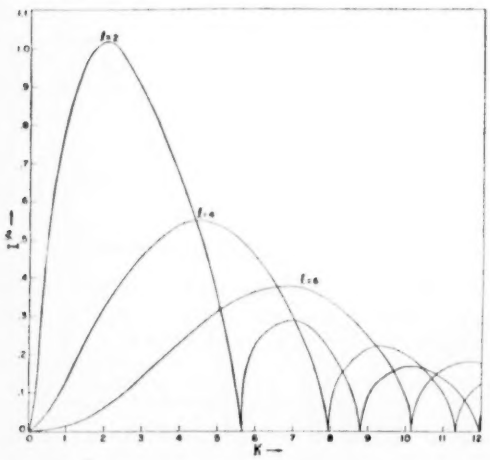

FIG. 2. Plot of the fourth root of $I=(d\sigma/d\omega)/(\mu/m)^2$, giving the differential cross section in units $\pi a_0{}^2$, as a function of the momentum change K in atomic units, for the scattering of charged particles by N_2 with excitation of the rotational states $l=2$, 4, and 6.

In Fig. 2 we illustrate the behavior of the cross section for $l=2$, 4, and 6 by plotting $[(d\sigma/d\omega)/(\mu/m)^2]^{\frac{1}{4}}$ as a function of K.[7] in Fig. 3 we give actual angular distributions for $l=2$, 4, and 6 and for several different k_0. Figure 4 shows total cross sections for excitation of $l=2$, 4, and 6 as functions of k_0, when protons are the incident particles. These results all refer to scattering by nitrogen molecules.

Several interesting points are at once evident. First, the general order of magnitude of the cross section decreases rapidly with increasing excitation of the target, roughly by a factor of 10 for each successive stage of excitation. Second, in the diffraction-like maxima in the angular distributions (that arise physically from the scattering from two centers of force which

[5] F. Hund, Z. Physik **77**, 12 (1932).

[6] H. S. W. Massey and C. B. O. Mohr, Proc. Roy. Soc. (London) **132**, 615 (1931) discuss the general integral.

[7] Atomic units are to be understood throughout, except where otherwise stated.

in effect constitute a sort of little grating), the small-angle maximum is indeed very prominent and peaked above all others; this is especially evident in the $l=2$ excitation where the chief maximum should be easily discernible experimentally. Third, the total cross-section data substantiates the usefulness of the Born approximation even down to small absolute incident energies so long as these are still well above the internal energies that are excited in the target; for, the bulk of past experience shows the validity of Born results for incident energies above, roughly, an energy as far beyond that corresponding to the maximum in the total cross section as this maximum is above the threshold energy. In Fig. 3, for instance, the angular distributions

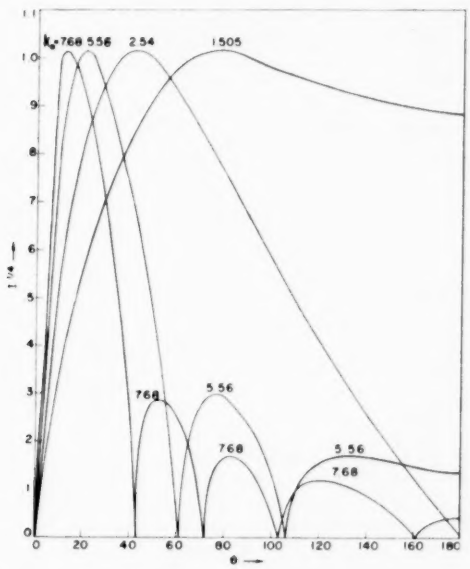

FIG. 3. Angular distribution of single charged particles scattered from N_2 with excitation of the rotational state $l=2$ for various incident initial momenta k_0 in atomic units; θ is the scattering angle in the center-of-mass system. The graph gives the fourth root of $I=(d\sigma/d\omega)/(\mu/m)^2$, $d\sigma$ being in units of πa_0^2, *versus* θ.

for $k_0=1.505$, 2.54, 5.56, 7.68 correspond to electron energies of 30.7, 87.4, 419, 799 ev (electron velocities of 1.505, 2.54, 5.56, 7.68 atomic units), and proton energies of 0.0173, 0.0493, 0.236, 0.451 ev (proton velocities of 8.49×10^{-4}, 1.43×10^{-3}, 3.14×10^{-3}, 4.33×10^{-3} atomic unit), while the internal motion of the excited state is of energy 1.53×10^{-3} ev and velocity 4.70×10^{-5} atomic unit; at the same time a glance of Fig. 4 shows that for $k_0=1.5$ one is already past the maximum of the total cross section and coming into the region of Born validity.

In the case that the incident particle is an atom instead of a charge, one usually represents the interaction potential $V=v(r_1)+v(r_2)$ through a choice of

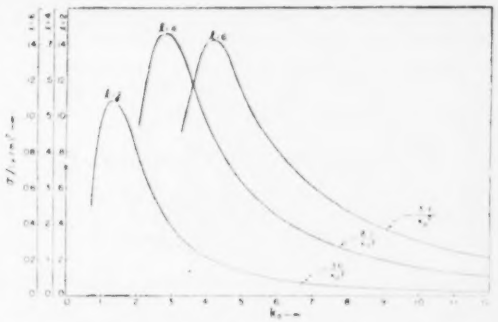

FIG. 4. Total cross sections for excitation of rotational states $l=2$, 4, and 6 of N_2 by incident protons. Curves give $\sigma/(\mu/m)^2$ in units πa_0^2 as a function of incident initial momentum k_0 in atomic units.

$v(r)=ce^{-\alpha r}$, or perhaps $Ce^{-\alpha r}/r$. This has only the qualitative significance of assigning an effective range and strength to the interaction between incident atom and molecular atom. The amplitude $h(K)$ in (6) is then

$$\frac{16\pi^2 m}{h^2}\frac{\alpha c}{(\alpha^2+K^2)^2} \quad \text{or} \quad \frac{8\pi^2 m}{h^2}\frac{c}{\alpha^2+K^2}, \tag{8}$$

which are roughly similar in shape to the h based on Hund's $v(r)$.

EXCITATION OF MOLECULAR VIBRATION

This is altogether similar to the rotator calculation except that $v(s)$ in $h(K)$ of Eq. (6) has, according to the Hund-Fermi-Thomas model that has been assumed, an explicit dependence on the now variable nuclear separation ρ; this dependence will be quite weak,[8] however, (except for vibrations of large amplitude) so that no serious error is made by taking, as for the rotator, that $v(S)$ corresponding to the equilibrium nuclear separation. What is thus ignored is a slight pulsation of the range and shape of v as the molecule vibrates.

We need only evaluate the factor J_{ib} in (6) for suitably chosen vibrator functions $\varphi_i(\rho)$ and $\varphi_b(\rho)$; we assume for simplicity that the molecule stays in the rotational ground state. An adequate model for the vibrator when the vibrational quantum number is not too large is an old one due to Fues[9] in which the internuclear interaction potential is

$$U(\rho)=-D+4\pi^2\nu_0^2\rho_0^2M(\tfrac{1}{2}-\rho_0/\rho+\tfrac{1}{2}\rho_0^2/\rho^2),$$

D, ν_0, ρ_0, and M being the depth of the potential curve, frequency of small oscillations about equilibrium, equilibrium nuclear separation, and reduced molecular mass, respectively. This function with parameters

[8] See Fig. 3 in reference 3.

[9] E. Fues, Ann. Physik **80**, 367 (1926); an account of Fues's vibrator will be found in E. U. Condon and P. M. Morse, *Quantum Mechanics* (McGraw-Hill Book Company, Inc., New York, 1929), Chaps. II and V.

appropriate to the N_2 molecule[10] is illustrated in Fig. 5 together with harmonic oscillator and Morse functions for comparison (the latter is chosen to give the correct D and ν_0 but not the correct "$w_e x_e$"; the former gives the correct ν_0). The eigenfunctions $\varphi_\beta(\rho)$ are

$$\varphi_n(\rho)=(4\pi)^{-\frac{1}{2}}N_n e^{-\frac{1}{2}\alpha_n\rho}\rho^\lambda F(-n,\,2\lambda+2,\,\alpha_n\rho),$$
$$N_n=\frac{\alpha_n^{\lambda+\frac{1}{2}}}{(2\lambda+1)!}\left\{\frac{(n+2\lambda+1)!}{n!(2\lambda+2n+2)}\right\}^{\frac{1}{2}}, \tag{9}$$

belonging to the vibrator levels $W_n\simeq -D+h\nu_0(n+\frac{1}{2})$, where $\lambda=-\frac{1}{2}+\frac{1}{2}(1+4b)^{\frac{1}{2}}$, $\alpha_n=(\lambda+n+1)^{-1}(\rho_0/2b)^{-1}$, and $b=4\pi^2\nu_0^2M^2\rho_0^4/h^2=$ dimensionless constant; F is the confluent hypergeometric function, here a polynomial of degree n.

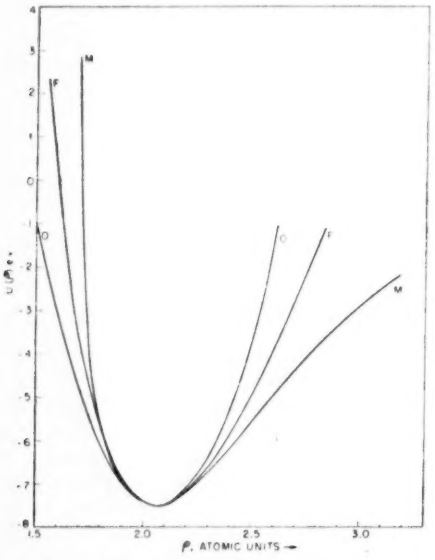

FIG. 5. Comparison of the Fues potential curve F, used to give vibrator eigenfunctions for N_2, with Morse, M, and harmonic oscillator, O, curves.

The integral to be evaluated for the transition $\nu\to n$, say, is

$$J_{n\nu}=\frac{N_nN_\nu}{4\pi}\int_0^\infty \rho^{2\lambda}\exp[-\tfrac{1}{2}(\alpha_n+\alpha_\nu)\rho]\times F(-n,\,2\lambda+2,\,\alpha_n\rho)F(-\nu,\,2\lambda+2,\,\alpha_\nu\rho)\rho^2d\rho\times\int_{-1}^{1}\cos\tfrac{1}{2}K\rho x\,2\pi dx$$
$$=\frac{2N_nN_\nu}{K}\operatorname{Im}\int_0^\infty \rho^{2\lambda+1}\exp[-\tfrac{1}{2}(\alpha_n+\alpha_\nu+\tau)\rho]\times F(-n,\,2\lambda+2,\,\alpha_n\rho)F(-\nu,\,2\lambda+2,\,\alpha_\nu\rho)d\rho, \tag{10}$$

where $\tau=-iK$. This is similar to the matrix element for optical transition probabilities in hydrogen, and may be evaluated by a generalization of the well-known Gordon[11] integral giving these probabilities, as follows. Calling the integral in (10) $j_{\mu\nu}$ we write

$$j_{n\nu}=A\oint_z\int_\rho \frac{z^{-n-1}}{(1+z)^{2\lambda+2}}\exp\left[-\rho\left(\frac{\alpha_n+\alpha_\nu+\tau}{2}-\frac{\alpha_nz}{1+z}\right)\right]\times\rho^{2\lambda+1}\sum_j\binom{\nu}{j}\frac{(-\alpha_\nu\rho)^j}{(2\lambda+2)_j}d\rho dz$$
$$=A\sum_j\oint\int\frac{z^{-n-1}}{(1+z)^{2\lambda+2}}\exp\left[-\rho\left(\frac{1+zu}{v(1+z)}\right)\right]\times\binom{\nu}{j}\frac{(-\alpha_\nu)^j}{(2\lambda+2)_j}\rho^{j+2\lambda+1}d\rho dz$$
$$=A(2\lambda+1)!\oint z^{-n-1}\frac{v^{2\lambda+2}}{(1+zu)^{2\lambda+2}}\times\sum_j\binom{\nu}{j}\left[-\frac{\alpha_\nu v(1+z)}{1+zu}\right]^jdz$$
$$=A(2\lambda+1)!v^{2\lambda+2}\oint\frac{z^{-n-1}}{(1+zu)^{2\lambda+2}}\times\left(1-\frac{\alpha_\nu v(1+z)}{1+zu}\right)^\nu dz$$
$$=A(2\lambda+1)!v^{2\lambda+2}\oint\frac{z^{-n-1}}{(1+zu)^{2\lambda+2}}\times\left(\frac{\tau v-u+(\tau v-1)z}{1+zu}\right)^\nu dz$$
$$=A(2\lambda+1)!v^{2\lambda+2}(\tau v-u)^\nu\times\oint\frac{z^{-n-1}}{(1+zu)^{2\lambda+2+\nu}}\left(1-z\frac{\tau v-1}{\tau v-u}\right)^\nu dz$$
$$=(2\lambda+1)!v^{2\lambda+2}(\tau v-u)^\nu\times u^nF\left(-n,\,-\nu,\,2\lambda+2,\,1-\frac{\tau v-1}{u(\tau v-u)}\right). \tag{11}$$

In the first line, the first F function has been replaced by an equivalent contour integral on z, where

$$A=e^{-\pi in}n!(2\lambda+1)!/(2\pi i)(2\lambda+n+1)!$$

and the contour is a closed circuit around the origin; the second F function has been replaced by its series expansion, $(2\lambda+2)_j$ standing for $(2\lambda+2)(2\lambda+3)\cdots$

[10] G. Herzberg, *Spectra of Diatomic Molecules* (D. Van Nostrand Company, Inc., New York, 1950), Appendix, Table 39; see also E. A. Hylleraas, Z. Physik **96**, 661 (1935).

[11] W. Gordon, Ann. Physik **2**, 1031 (1929), especially Sec. 1 and Sec. 4.

$\times(2\lambda+1+j)$ [but $(2\lambda+2)_0=1$]. In the second line the abbreviations

$$u=(\alpha_\nu+\tau-\alpha_n)/(\alpha_\nu+\tau+\alpha_n) \quad \text{and} \quad v=2/(\alpha_\nu+\tau+\alpha_n).$$

or $\alpha_n=(1-u)/v$ and $\alpha_\nu+\tau=(1+u)/v$, are introduced. In the third line the ρ integration is performed and then the summation over j is performed. In the fifth line $\alpha_\nu v$ is replaced by $1+u-\tau v$, and in the sixth line the remaining contour integral is that for the hypergeometric function in the last line.

For the transition $0-n$, the results (10) and (11) give

$$J_{n0}{}^2=\frac{4}{K^2}\frac{\alpha_n\alpha_0}{n!(2\lambda+2n+2)}\frac{(2\lambda+n+1)!}{(2\lambda+2)!}\times\left[\frac{(\alpha_0{}^2-\alpha_n{}^2+K^2)^2+4\alpha_n{}^2K^2}{((\alpha_0+\alpha_n)^2+K^2)^2}\right]^n\times\left[\frac{4\alpha_n\alpha_0}{(\alpha_0+\alpha_n)^2+K^2}\right]^{2\lambda+2}\sin^2[(2\lambda+2)\theta_\lambda-n\theta_n], \quad (12)$$

$$\theta_\lambda=\tan^{-1}\frac{K}{\alpha_0+\alpha_n}, \quad \theta_n=\tan^{-1}\frac{2\alpha_nK}{\alpha_0{}^2-\alpha_n{}^2+K^2},$$

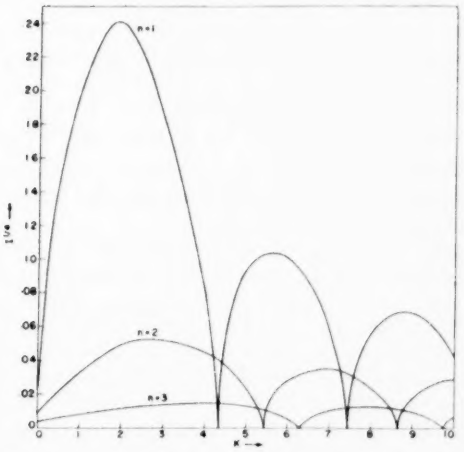

FIG. 6. Plot of the fourth root of $I=(d\sigma/d\omega)/(\mu/m)^2$, giving the differential cross section in units $\pi a_0{}^2$, as a function of the momentum change K in atomic units, for the scattering of charged particles by N_2 with excitation of the vibrational states $n=1$, 2, and 3.

from which the differential and total cross sections are readily found.

Illustrative results are given in Figs. 6 and 7 where differential cross sections for $n=1$, 2, and 3, and total cross sections for $n=1$ and 2 for incident protons are plotted, the target molecule being N_2. The scattering is qualitatively like that for the rotator, but smaller all over by a factor of some 10^4 or 10^5.

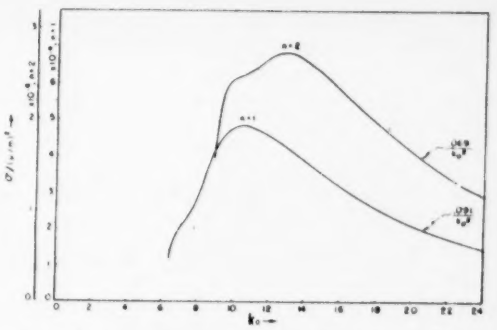

FIG. 7. Total cross sections for excitation of vibrational states $n=1$, and 2 of N_2 by incident protons. Curves give $\sigma/(\mu/m)^2$ in units $\pi a_0{}^2$ as a function of incident initial momentum k_0 in atomic units.

For a scattering process in which both the rotational and vibrational states of the molecule are altered, one has for the factor J_{lb} in (6), apart from normalization constants,

$$J_{nl,\nu j}=2\pi\int_0^\infty\int_{-1}^1\cos(\tfrac{1}{2}K\rho x)\varphi_{nl}{}^*(\rho)\varphi_{\nu j}(\rho)\times P_l{}^m(x)P_j{}^m(x)P^2d\rho dx,$$

where φ_{nl} is a slight generalization of φ_n of Eq. (9), namely, λ is replaced by $-\frac{1}{2}+\frac{1}{2}[1+4(b+l(l+1))]^{\frac{1}{2}}$. The calculation of $J_{nl,00}$ is particularly straightforward, since the angular integration yields a spherical Bessel function as before. In the remaining ρ integration the l and j dependence of the φ's can usually be ignored because of the largeness of b bompared with $l(l+1)$, $j(j+1)$; then when the Bessel factor is written in any particular case in terms of trigonometric functions and polynomials in ρ^{-1} the integration may be performed directly.

MOLECULE-MOLECULE COLLISIONS

In the general case of the collision of two diatomic molecules when all of the atoms are different one can investigate the scattering by making a simple but reasonable model in which the intermolecular forces are given by central interaction potentials between each atom in one molecule and each in the other. These can be taken to be roughly of the forms $Ce^{-\alpha r}$ or $Ce^{-\alpha r}/r$ previously mentioned; attractive interactions can be introduced where warranted. Upon specifying a model for the intramolecular binding forces, one can then calculate a scattering amplitude of interest by Eq. (5). These remarks indeed are not confined to diatomic molecules, but in the subsequent discussion we so limit ourselves.

An interesting special case of the general type of collision is that in which the colliding molecules are homonuclear but distinct. When they are also identical, special considerations are needed and these are taken

up in the next section. The simplifying feature here is that the four interaction potentials between the atoms in different molecules are the same, say v. Hence, harking back to Eq. (5), we find the scattering amplitude to be just

$$f_{st}^{ab}=-\frac{1}{4\pi}\frac{2\mu}{\hbar^2}\int \exp(i\mathbf{K}\cdot\mathbf{S})v(S)d\mathbf{S}\int f_s^*\varphi_t^* f_a\varphi_b \times\{\exp[i\mathbf{K}\cdot\tfrac{1}{2}(\mathbf{r}-\boldsymbol{\varrho})]+\exp[-i\mathbf{K}\cdot\tfrac{1}{2}(\mathbf{r}-\boldsymbol{\varrho})] +\exp[i\mathbf{K}\cdot\tfrac{1}{2}(\mathbf{r}+\boldsymbol{\varrho})]+\exp[-i\mathbf{K}\cdot\tfrac{1}{2}(\mathbf{r}+\boldsymbol{\varrho})]\}d\mathbf{r}d\boldsymbol{\varrho}$$

$$=-\frac{1}{4\pi}\frac{2\mu}{\hbar^2}4\int \exp(i\mathbf{K}\cdot\mathbf{S})v(S)d\mathbf{S} \times\int f_s^*\cos(\tfrac{1}{2}\mathbf{K}\cdot\mathbf{r})f_a d\mathbf{r}\int\varphi_t^*\cos(\tfrac{1}{2}\mathbf{K}\cdot\boldsymbol{\varrho})\varphi_b d\boldsymbol{\varrho}, \quad (13)$$

$\mathbf{r}$ and $\boldsymbol{\varrho}$ being the nuclear separations in the two molecules. The use of Eqs. (7), (8), and (12) now gives explicitly the amplitude for scattering from the ground states of both molecules to excited rotational or vibrational states in either or both. We postpone numerical results until the effect of identity has been discussed.

SCATTERING OF IDENTICAL HOMONUCLEAR MOLECULES

We now examine the effect of the symmetry of the Hamiltonian (1) when the homonuclear molecules are identical. Because our model assumes the forces between identical atoms in separate molecules to be generally different from the forces between the identical atoms in the same molecule (in effect an assumption of many-body forces between identical "particles" that we call atoms), the Hamiltonian is symmetric with respect to an interchange of coordinates of all particles in the two molecules (i.e., an interchange of the entire molecules themselves), but not necessarily with respect to an interchange of coordinates of but one particle in each of the separate molecules. Under the complete interchange of coordinates (including nuclear spin coordinates) we must require the total wave function to be symmetric since the total number of particles in each system is necessarily even. In the case of identical but not homonuclear molecules the total wave function could be either symmetric or antisymmetric, depending on the molecule.

Writing the spatial part of the wave function now as $\Psi(\mathbf{R},\mathbf{r},\boldsymbol{\varrho})=\sum_{\alpha,\beta}F_{\alpha\beta}(\mathbf{R})\varphi_\alpha(\mathbf{r})\varphi_\beta(\boldsymbol{\varrho})$, we have that, for large R,

$$\Psi(\mathbf{R},\mathbf{r},\boldsymbol{\varrho})\rightarrow\sum_{\alpha,\beta}\frac{e^{ik_{ab}R}}{R}f_{\alpha\beta}(\theta,\varphi)\varphi_\alpha(\mathbf{r})\varphi_\beta(\boldsymbol{\varrho}) +e^{ik_{ab}Z}\varphi_a(\mathbf{r})\varphi_b(\boldsymbol{\varrho}).$$

Under interchange of coordinates of all particles, $\boldsymbol{\varrho}\rightarrow\mathbf{r}$, $\mathbf{r}\rightarrow\boldsymbol{\varrho}$, and $\mathbf{R}\rightarrow-\mathbf{R}$; hence

$$\Psi(-\mathbf{R},\boldsymbol{\varrho},\mathbf{r})\rightarrow\sum_{\alpha,\beta}\frac{e^{ik_{\alpha\beta}R}}{R}f_{\alpha\beta}(\pi-\theta,\pi+\varphi)\varphi_\alpha(\boldsymbol{\varrho})\varphi_\beta(\mathbf{r}) +e^{-ik_{ab}Z}\varphi_a(\boldsymbol{\varrho})\varphi_b(\mathbf{r});$$

or, using $k_{\alpha\beta}=k_{\beta\alpha}$ and relabeling the dummy indices α and β,

$$\Psi(-\mathbf{R},\boldsymbol{\varrho},\mathbf{r})\rightarrow\sum_{\alpha,\beta}\frac{e^{ik_{\alpha\beta}R}}{R}f_{\beta\alpha}(\pi-\theta,\pi+\varphi)\varphi_\alpha(\mathbf{r})\varphi_\beta(\boldsymbol{\varrho}) +e^{-ik_{ab}Z}\varphi_a(\boldsymbol{\varrho})\varphi_b(\mathbf{r}).$$

Therefore, the symmetrical and antisymmetrical spatial wave functions are

$$\overset{S}{\Psi}{}^{A}=\Psi(\mathbf{R},\mathbf{r},\boldsymbol{\varrho})\pm\Psi(-\mathbf{R},\boldsymbol{\varrho},\mathbf{r}) \rightarrow\sum_{\alpha,\beta}\frac{e^{ik_{\alpha\beta}R}}{R}[f_{\alpha\beta}(\theta,\varphi)\pm f_{\beta\alpha}(\pi-\theta,\pi+\varphi)] \times\varphi_\alpha(\mathbf{r})\varphi_\beta(\boldsymbol{\varrho})+e^{ik_{ab}Z}\varphi_a(\mathbf{r})\varphi_b(\boldsymbol{\varrho}) \pm e^{-ik_{ab}Z}\varphi_a(\boldsymbol{\varrho})\varphi_b(\mathbf{r}). \quad (14)$$

Whether we symmetrize before or after taking the asymptotic form of Ψ makes no difference in this result. The scalar product $(\varphi_s(\mathbf{r})\varphi_t(\boldsymbol{\varrho}),\overset{S}{\Psi}{}^{A})$ isolates the amplitudes $\overset{S}{f}{}^{A}=f_{st}(\theta,\varphi)\pm f_{ts}(\pi-\theta,\pi+\varphi)$ for arrival of one of the identical molecules in state s at θ, φ and the other in the state t at $\pi-\theta$, $\pi+\varphi$; these amplitudes are in general distinct from $f_{ts}(\theta,\varphi)\pm f_{st}(\pi-\theta,\pi+\varphi)$, the amplitudes for finding t at θ, φ and s at $\pi-\theta$, $\pi+\varphi$.

We must now weight the amplitudes $\overset{S}{f}{}^{A}$ properly in constructing the differential cross section. It will be assumed that the electronic states in the molecules remain as ground states and that, as they usually are, are symmetric states, and so play no role other than the one that has been already assigned to them, i.e., that they produce fixed kinds of interactions between the atomic centers within one molecule and between the centers in separate molecules, and in addition make the symmetry character of the molecular wave function dependent solely on its rotational part. For a nuclear spin I of each of the nuclei, we have that each molecule possesses $\omega=(2I+1)^2$ nuclear spin states and that the system of two molecules, call them 1 and 2, has ω^2 spin states. Of these latter, there are ω which are symmetrical of the form $\mathbf{X}_1(s)\mathbf{X}_2(s)$, s assuming ω values; and $\frac{1}{2}(\omega^2-\omega)$ other symmetrical and the same number of antisymmetrical states of the form $\mathbf{X}_1(s)\mathbf{X}_2(s')\pm\mathbf{X}_1(s')\mathbf{X}_2(s)$. The weights $\overset{S}{W}{}^{A}$ of symmetrical and antisymmetrical states are therefore $\frac{1}{2}(\omega\pm1)/\omega$. The differential cross section for a molecule in state s to be scattered at θ, φ and the other in state t to be scattered at $\pi-\theta$, $\pi+\varphi$ is now

$$d\sigma/d\omega=(k_{st}/k_{ab})(W^S|f^S|^2+W^A|f^A|^2). \quad (15)$$

If, however, we know that there are selection rules which prevent the excitation of certain states, an alteration of ω from its value $(2I+1)^2$ may be necessary. For example, suppose the two colliding molecules are initially in the ground state; then according to the discussion of rotational excitations given before, only even rotational states can be excited; hence of the $(2I+1)^2$ possible nuclear spin states per molecule only either the $I(2I+1)$ antisymmetrical ones or the $(I+1)(2I+1)$ symmetrical ones, depending on whether the nucleus has an odd or even number of nucleons, can enter into consideration, and ω must be reckoned as either $I(2I+1)$ or $(I+1)(2I+1)$.

Making use of Eqs. (7), (12), (13), (15), and the first alternative in (8), we construct some illustrative results for N_2-N_2 scattering, for which $I=1$,

$$\omega=(I+1)(2I+1)=6,$$

and the molecules are initially in their ground states. We write the differential cross section for scattering of one molecule in state s at angle θ and the other in state t at angle $\pi-\theta$ as

$$\left.\frac{d\sigma}{d\omega}\right|_s^t=\frac{k_{st}}{k_{00}}\frac{256}{\pi}\left(\frac{\mu}{m}\right)^5C^2\left\{\frac{7}{12}|A_s{}^t+B_s{}^t|^2+\frac{5}{12}|A_s{}^t-B_s{}^t|^2A\right\}$$

in units πa_0^2, where $h(K)$ of Eq. (8) has been written

$$h(K)=\frac{1}{\sqrt{\pi}}\frac{4C\alpha}{(\alpha^2+K^2)^2}=\frac{4C}{\sqrt{\pi}}g(K)$$

in units $a_0\sqrt{2\pi}$ when C, α, K are in atomic units; a reasonable value for α is $\alpha=2$. For s and t both rotational or both vibrational states, we have, for example

$$A_l{}^{l'}(K)=g(K)J_{l0}(K)J_{l'0}(K),\quad B_l{}^{l'}=A_l{}^{l'}(K'),$$
$$A_n{}^{n'}(K)=g(K)J_{n0}(K)J_{n'0}(K),\quad B_n{}^{n'}=A_n{}^{n'}(K'),$$

respectively, where

$$K=(k_{00}{}^2+k_{st}{}^2-2k_{00}k_{st}\cos\theta)^{\frac{1}{2}}\simeq 2k_{00}\sin(\tfrac{1}{2}\theta)$$

and

$$K'=(k_{00}{}^2+k_{st}{}^2+2k_{00}k_{st}\cos\theta)^{\frac{1}{2}}=[2(k_{00}{}^2+k_{st}{}^2)-K^2]^{\frac{1}{2}}.$$

In Fig. 8 we plot $[(d\sigma/d\omega)/(\mu/m)^2C^2]^{\frac{1}{4}}$ as a function of θ for $s=l=2$, $t=l'=0$; $s=l=2$, $t=l'=2$; $=ns=1$, $t=n'=0$; and $s=n=1$, $t=n'=1$ for the excitation of the lowest rotational states in one and both molecules, and

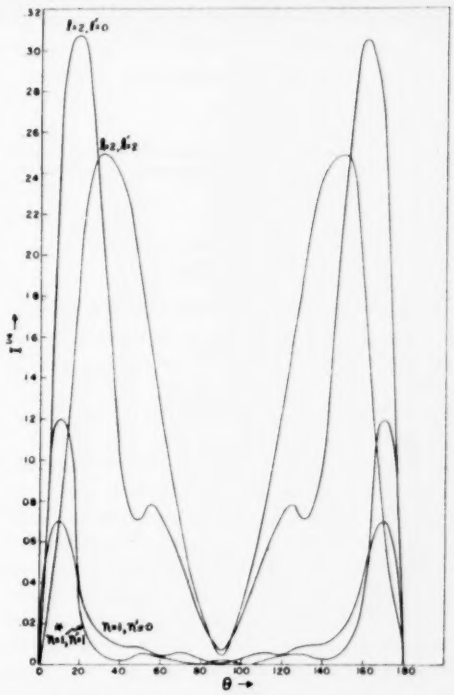

FIG. 8. Angular distribution of N_2 molecules scattered by N_2 molecules with excitation of rotational state $l=2$ in one and both molecules (for $k_0=4$) and of vibrational state $n=1$ in one and both (for $k_0=15$). The ordinate is the fourth root of $I=(d\sigma/d\omega)/(\mu/m)^2C^2$, giving $d\sigma$ in units $\pi a_0{}^2$ when C, the strength of the interatomic interaction potential between atoms in different molecules, is in atomic units; θ is the scattering angle in the center-of-mass system. The scale of ordinates for the $n=1$, $n'=1$ curve is 10^{-1} that of the scale shown.

of the lowest vibrational states in one and both molecules, respectively, for $k_{00}=4$ for the rotational excitations and $k_{00}=15$ for the vibrational excitations. It is not very much harder for both molecules to be rotationally excited than for one to be, but it *is* considerably more difficult to vibrationally excite both rather than one. The excitation of rotation is of course, as in the scattering of single charges, generally much more probable than for vibrational excitation; and again the principal maxima in the excitation of rotation should be visible experimentally.

The author is indebted to Mrs. Ernestine Goodman for assistance in the numerical computations.

Complex Amplitudes for Electron Scattering by Atoms*

JEAN A. HOERNI AND JAMES A. IBERS†
Gates and Crellin Laboratories of Chemistry, California Institute of Technology,‡ Pasadena, California
(Received May 26, 1953)

The partial waves scattering theory has been applied to electron scattering by U and F atoms at 40 and 11 kev. The electron scattering by the UF_6 molecule, predicted from these results, is in good agreement with experiment.

I. INTRODUCTION

RECENTLY, Schomaker and Glauber[1] have pointed out that anomalies, e.g., apparent asymmetry, in the structures of molecules containing both heavy and light atoms as determined by electron diffraction can be removed by using complex atomic scattering amplitudes $f(\theta)$ and hence by rejecting the first Born approximation which gives only real amplitudes. This approximation, although theoretically justified only for $-\alpha=Ze^2/(h\nu)$ small, has nevertheless been universally employed in investigations of the molecular structure of gases by electron diffraction. Using the second Born approximation, Glauber and Schomaker[2] evaluated the phase of the complex amplitude, $\eta(\theta)=\arg f(\theta)$, for the exponentially screened Coulomb potential $-Ze^2e^{-r/a}/r$; agreement was obtained for a large group of molecules at 40 kev. However, good agreement is not obtained for the UF_6 pattern at 11 kev,[3] and, in any case, the second Born approximation and the assumption of the screened Coulomb field are both uncertain, so that a more adequate calculation is desired. We describe below an application of the partial waves scattering theory to the problem of the scattering of electrons by atoms (U and F). The energies considered (11 and 40 kev) are sufficiently high so that electron exchange and polarization effects can be neglected.

II. THEORY[4]

The solution to the problem of the elastic scattering of a beam of particles by a central potential $V(r)$ is given by

$$f(\theta)=(2ik)^{-1}\sum_{l=0}^{\infty}(2l+1)(e^{2i\delta_l}-1)P_l(\cos\theta), \quad (1)$$

where θ is the scattering angle, k is $2\pi/\lambda$, and the phases δ_l may be interpreted as the phase differences between the perturbed and unperturbed radial functions at large distances from the nucleus. The δ_l's can be evaluated in several ways for electron scattering. When $\delta_l\ll 1$, (1) can be rewritten as

$$f(\theta)=k^{-1}\sum_{l=0}^{\infty}(2l+1)\delta_l P_l(\cos\theta), \quad (2)$$

and the δ_l's are given by

$$\delta_l{}^0=\frac{k\alpha\pi}{Ze^2}\int_0^{\infty}V(r)J_{l+\frac{1}{2}}{}^2(kr)rdr. \quad (3)$$

Substitution of (3) into (2) yields the first Born approximation for the scattering amplitudes, namely,

$$f^B(\theta)=\frac{2k\alpha}{Ze^2}\int_0^{\infty}V(r)\frac{\sin(sr)}{sr}r^2dr, \quad (4)$$

where $s=2k\sin(\theta/2)$. When the δ_l's are not small, they may be evaluated conveniently by the WKB method. Starting with the relativistic Schrödinger equation,

$$\nabla^2\psi+\kappa^2(r)\psi=0, \quad (5)$$

where

$$\kappa^2(r)=\frac{[E-V(r)]^2-m^2c^4}{h^2c^2}=k^2+\frac{V^2(r)-2EV(r)}{h^2c^2},$$

we obtain

$$\delta_l=\int_{r_1}^{\infty}G(r)dr-\int_{r_2}^{\infty}G_0(r)dr, \quad (6)$$

with

$$G(r)=\{\kappa^2(r)-[(l+\tfrac{1}{2})/r]^2\}^{\frac{1}{2}},\quad G_0(r)=\{k^2-[(l+\tfrac{1}{2})/r]^2\}^{\frac{1}{2}}.$$

Here, the energy E includes the rest energy, and $r_1, r_2>0$ are the zeros of the respective integrands. In accordance with the work of Langer,[5] we have replaced $l(l+1)$ by $(l+\frac{1}{2})^2$. The δ_l's may also be evaluated exactly. This has been done by Bartlett and Welton[6] with a differential analyzer for Hg at 100 and 230 kev starting with Gordon's solutions of the Dirac equation. Although the δ_l's from the WKB method are generally supposed to be reliable only when large, and hence only when l is small, Bartlett and Welton found these values to be in excellent agreement with the exact values over the entire range of l; they found the $\delta_l{}^0$'s to be reliable at large l.

* This work was supported in part by the U. S. Office of Naval Research.
† National Science Foundation Predoctoral Fellow, 1952–1953.
‡ Contribution No. 1812.
[1] V. Schomaker and R. Glauber, Nature **170**, 290 (1952).
[2] R. Glauber and V. Schomaker, Phys. Rev. **89**, 667 (1953).
[3] Preliminary results by G. Felsenfeld and J. Ibers.
[4] As a general reference, we give N. F. Mott and H. S. W. Massey, *The Theory of Atomic Collisions* (Oxford University Press, London, 1949), second edition, particularly Chapter VII.
[5] R. E. Langer, Bull. Am. Math. Soc. **40**, 574 (1934); Phys. Rev. **51**, 669 (1937).
[6] J. H. Bartlett, Jr., and T. A. Welton, Phys. Rev. **59**, 281 (1941).

III. PROCEDURE AND RESULTS

We first compute the complex atomic scattering amplitudes for U and F at 40 and 11 kev and then apply these to the scattering by the UF_6 molecule. UF_6 was selected because it offers the most severe test (the molecule exhibits the largest apparent asymmetry[1]) and because only for it do we have electron diffraction photographs prepared at 11 kev as well as at the usual 40 kev.

For U we adopted the Thomas-Fermi potential, using the approximate form[7]

$$V(r)=-\frac{Ze^2}{r}\sum_{i=1}^{3}a_i e^{-b_i r/a}, \tag{7}$$

where $a_1=0.10$, $a_2=0.55$, $a_3=0.35$, $b_1=6.0$, $b_2=1.2$, $b_3=0.3$, and a, the screening radius, is $0.4685/Z^{\frac{1}{3}}$. For F we used the Hartree potential[8] in the approximate form

$$V(r)=-(Ze^2/r)(e^{-\beta_1 r}+cre^{-\beta_2 r}), \tag{8}$$

where $\beta_1=3.94$, $\beta_2=17.0$, and $c=-2.67$. Preliminary calculations indicated that the effect of electron spin would be important only for $l\leqslant 2$,[9] and since in the final summation (1) these terms are reduced in importance by the factor $2l+1$, we felt justified in adopting the relativistic Schrödinger equation (5). For small l, the δ_l's were calculated for 40 and 11 kev from the WKB expression (6); for large l ($\gtrsim 25$), it was found that the δ_l^0's (3) and δ_l's (6) were in excellent agreement, as anticipated from the work of Bartlett and Welton.[6] With the δ_l's obtained in this way (Table I), we have evaluated the magnitudes $|f(\theta)|$ and the arguments $\eta(\theta)$ of the complex scattering amplitudes (Table II). The δ_l's for U can also be computed over the entire l range from the asymptotic expression (15) below. In this case, although the δ_l's differ from the above by as much as 8 percent at 40 kev and 15 percent at 11 kev, the resultant magnitudes and arguments in no case differ by more than 3 percent from those in Table II, the relative error increasing with increasing θ.

In the application of these results to the molecule UF_6, the assumption is made that multiple scattering and valence distortion are negligible. Then for visual data the following expression for the intensity function (specialized for the case of UF_6) is suitable:

$$\begin{aligned}I(s)K(s)=&(6/r_{U\text{-}F})\cos[\eta_U(\theta)-\eta_F(\theta)]\sin(r_{U\text{-}F}s)\\&+(|f_F(\theta)|/|f_U(\theta)|)\\&\times\{(12/r_{F\text{-}F})\{\exp[-(a_{F\text{-}F}-a_{U\text{-}F})s^2]\}\sin(r_{F\text{-}F}s)\\&+(3/r_{F\text{-}F})\{\exp[-(a_{F\text{-}F}-a_{U\text{-}F})s^2]\}\sin(r_{F\text{-}F}s)\},\end{aligned} \tag{9}$$

where $I(s)$ is the modified scattering intensity, $K(s)$ is is a smoothly decreasing function of s, and $\exp(-a_{i,j}s^2)$ is the temperature factor for the distance $r_{i,j}$ between atoms i and j.[1,10] Using our complex amplitudes and a symmetric UF_6 model,[11] we have evaluated the function $I(s)K(s)$ at 11 and 40 kev. Figure 1 compares the calculated and the visually estimated versions of this function. When one considers that the visual curves are significant only for comparisons of intensity over a small range of s (e.g., that one usually can compare the height of maximum n only with the average of the heights of maximum $n+1$ and maximum $n-1$), the agreement is excellent. For the present purpose, the most significant parts of the patterns are the very sensitive regions where $\eta_U(\theta)-\eta_F(\theta)=\pi/2$, and these are reproduced satisfactorily (Table III).

TABLE I. Selected values of δ_l.[a]

l	Uranium 40 kev	Uranium 11 kev	Fluorine 40 kev	Fluorine 11 kev
0	6.11	7.20	0.571	1.05
2	3.49	4.67	0.414	0.555
4	2.47	2.96	0.317	0.391
6	1.87	2.06	0.258	0.297
8	1.53	1.52	0.218	0.234
10	1.26	1.16	0.189	0.188
15	0.847	0.679	0.135	0.113
20	0.602	0.441	0.101	0.071
25	0.452	0.302	0.077	0.046
30	0.353	0.212	0.059	0.029
35	0.282	0.152	0.046	0.019
40	0.228	0.110	0.036	
50	0.155	0.059	0.022	
70	0.076	0.018		
100	0.028			

[a] The actual values used were 39.470 and 11.380 kev.

Table II also provides a comparison with the magnitudes $f^B(\theta)$ calculated by the first Born approximation[12] [using (18) and (19)] and the phase angles $\eta^B(\theta)$ for U calculated by the second Born approximation. For the latter it was necessary to extend the calculations of Glauber and Schomaker[2] to the potential for U used here. Their formula is

$$\eta^B(\theta)=\eta^B(\mathbf{k}',\mathbf{k})=\frac{k}{4\pi f^B(\theta)}\times\int f^B(\mathbf{k}'\mathbf{k}'')f^B(\mathbf{k}'',\mathbf{k})d\Omega_{\mathbf{k}''}, \tag{10}$$

[7] G. Molière, Z. Naturforsch. **2a**, 142 (1947).
[8] F. W. Brown, Phys. Rev. **44**, 214 (1933).
[9] See reference 4, Chap. IV, Eq. (23).

[10] Shaffer, Schomaker, and Pauling, J. Chem. Phys. **14**, 659 (1946).
[11] $r_{U\text{-}F}=2.00$A, $r_{F\text{-}F}=2.83$A, $r_{F\text{-}F}=4.00$A, $a_{F\text{-}F}-a_{U\text{-}F}=2.2\times10^{-3}A^2$, $a_{F\text{-}F}-a_{U\text{-}F}=0.75\times10^{-3}A^2$.
[12] It should be noted that $f^B(\theta)$ is related to $F(\theta)$, the x-ray form factor, by the relation

$$f^B(\theta)=(-2k\alpha/s^2)[1-(F(\theta))/Z].$$

The $F(\theta)$ for U obtained from the corresponding $f^B(\theta)$ given in Table II agree to within 1½ percent with the Thomas-Fermi values given in *Internationale Tabellen zur Bestimmung von Kristallstrukturen* (Gebrüder Borntraeger, Berlin, 1935), Vol 2, p. 573. The $F(\theta)$ for F agree to within 10 percent with those of R. W. James and G. W. Brindley [Phil. Mag. **12**, 81 (1931)], and to within 6 percent with the f of R. McWeeny [Acta Cryst. **4**, 513 (1951)]; our values being in general lower than those of McWeeny and higher than those of James and Brindley. We suspect these differences arise from differences in the models used.

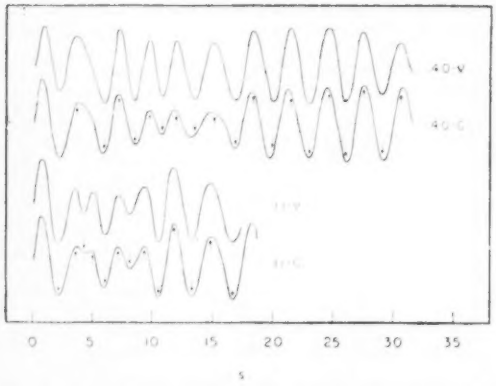

FIG. 1. Intensity curves for UF_6. "V" visual, "C" calculated for "40" or "11" kev. Further photographs will be made both at 40 and 11 kev, and the visual curves (40 V is due to Dr. Otto Bastiansen and 11 V to Felsenfeld and Ibers (reference 3)) are not to be regarded as final.

where $\mathbf{k}$ and $\mathbf{k}'$ refer to the directions of incidence and scattering, respectively, and $\mathbf{k}''$ is integrated over the sphere $|\mathbf{k}''|=k$. When the potential (7) for U was inserted and the integration performed there resulted

$$\eta^B(\theta)=\frac{\alpha^2}{2kf^B(\theta)\cos(\theta/2)}\sum_{i,j=1}^{3}\frac{a_ia_j}{\mu_{ij}}\times\tanh^{-1}\frac{2\mu_{ij}\cos(\theta/2)}{g_{ii}g_{jj}-\cos\theta}, \quad (11)$$

$$g_{ij}=1+(b_i^2+b_j^2)/(4k^2a^2),$$

$$\mu_{ij}=\{[(b_i^2-b_j^2)/(4k^2a^2)]^2+[g_{ij}^2-\cos^2(\theta/2)]\tan^2(\theta/2)\}^{\frac{1}{2}},$$

which is in serious disagreement with the partial waves values and with experiment, as may be seen from Tables II and III. The good agreement with experiment obtained previously[2] must be due to a fortuitous cancellation of errors: For heavy atoms the exponentially screened Coulomb field is quite unsatisfactory and (10), even at 40 kev, is inadequate.

It is planned to extend the calculations for 40-kev electrons to other atoms with the hope of achieving a sufficiently general theoretical basis for electron diffraction studies of the molecular structures of gases.

We thank Professor Verner Schomaker for reading this paper and for making many helpful suggestions.

IV. APPENDIX—MATHEMATICAL DETAILS

The Phases δ_l and δ_l^0

When computing δ_l it is convenient to split up (6) as follows:

$$\delta_l=\int_{r_1}^{r_3}G(r)dr-\int_{r_2}^{r_3}G_0(r)dr+\int_{r_3}^{\infty}[G(r)-G_0(r)]dr$$

$$=I_1-I_2+I_3. \quad (12)$$

Here, r_3 is sufficiently large so that for $r>r_3$, $G(r)$ and $G_0(r)$ do not differ by more than 10 percent. Then I_3 reduces to

$$I_3=\frac{k\alpha}{Ze^2}\int_{r_3}^{\infty}[V(r)]/[G_0(r)]dr. \quad (13)$$

r_1 was evaluated graphically and I_1 was integrated numerically using Simpson's rule; I_2 can be integrated analytically. I_3(13) can be expressed in terms of various power expansions and when $V(r)$ is given by (7), the following expression is convenient:

$$I_3=-\alpha\sum_{i=1}^{3}a_i\int_{r_3}^{\infty}[e^{-b_ir/a}]/[r^2-((l+\tfrac{1}{2})/k)^2]^{\frac{1}{2}}dr,$$

$$=-\alpha\sum_{i=1}^{3}a_i\left\{K_0(u_i)-e^{-u_i}\left[m-u_i\frac{m^3}{3!}+(3u_i^2-u_i)\frac{m^5}{5!}-(15u_i^3+u_i-15u_i^2)\frac{m^7}{7!}+\cdots\right]\right\}, \quad (14)$$

$$u_i=b_i(l+\tfrac{1}{2})/(ka), \quad m=\cosh^{-1}[(r_3k)/(l+\tfrac{1}{2})].$$

For large values of l ($\gtrsim 25$), it was found that $r_1\approx r_2\approx r_3$,

TABLE II. Magnitudes and arguments of the scattering amplitudes.

	Uranium								Fluorine					
	40 kev				11 kev				40 kev			11 kev		
θ	$\lvert f(\theta)\rvert$	$\eta(\theta)$	$f^B(\theta)$	$\eta^B(\theta)$	$\lvert f(\theta)\rvert$	$\eta(\theta)$	$f^B(\theta)$	$\eta^B(\theta)$	$\lvert f(\theta)\rvert$	$\eta(\theta)$	$f^B(\theta)$	$\lvert f(\theta)\rvert$	$\eta(\theta)$	$f^B(\theta)$
0	14.51	0.317	17.24	0.50	12.01	0.414	16.36	0.90	2.31	0.079	2.32	2.15	0.141	2.20
1	10.30	0.424	12.78		10.64	0.456	14.88		1.90	0.093	1.91	2.03	0.148	2.08
2	5.54	0.687	7.52		7.85	0.579	11.78		1.24	0.128	1.24	1.73	0.169	1.77
3	3.21	1.00	4.74	1.39	5.37	0.772	8.86	1.51	0.776	0.179	0.781	1.39	0.201	1.43
4	2.08	1.31	3.27		3.67	1.01	6.72		0.507	0.231	0.511	1.08	0.243	1.12
5	1.46	1.60	2.42		2.61	1.28	5.23		0.349	0.281	0.352	0.841	0.290	0.871
6	1.08	1.88	1.87	2.41	1.94	1.57	4.18	2.63	0.252	0.329	0.254	0.660	0.341	0.685
7	0.837	2.16	1.49		1.52	1.85	3.44		0.190	0.376	0.192	0.525	0.396	0.546
8	0.683	2.42	1.21		1.24	2.13	2.88		0.148	0.420	0.149	0.424	0.447	0.442
10	0.500	2.89	0.848	3.44	0.930	2.64	2.12	3.96	0.096	0.487	0.098	0.291	0.552	0.302
12	0.403	3.26	0.624		0.756	3.03	1.63		0.068	0.551	0.070	0.211	0.651	0.218
14	0.327	3.61	0.478		0.623	3.34	1.30		0.051	0.623	0.052	0.162	0.748	0.164
16	0.263	3.95	0.378	4.64	0.520	3.60	1.06	5.60	0.040	0.676	0.041	0.128	0.830	0.128

so that (12) reduces to

$$\delta_l = -\alpha \sum_{i=1}^{3} a_i K_0(u_i). \tag{15}$$

For the same potential, (3) becomes

$$\delta_l^0 = -\alpha \sum_{i=1}^{3} a_i Q_l\left[1+\frac{1}{2}\left(\frac{b_i}{ka}\right)^2\right]. \tag{16}$$

The Q_l's were computed for $0 \leqslant l \leqslant 10$, using the polynomial expansions,[13] for $l \geqslant 10$ they were evaluated using Watson's relation[14]

$$Q_l(\cosh\xi) \sim (\exp[-(l+\tfrac{1}{2})(\xi-\tanh\xi)])(\operatorname{sech}^{\frac{1}{2}}\xi) \times (K_0[(l+\tfrac{1}{2})\tanh\xi]) + O(e^{-l\xi}/l). \tag{17}$$

At $l=10$, (17) gave values in excellent agreement with the exact values and therefore its use was justified for higher l. When computing the phases for large l ($\geqslant 25$), only the term for $i=3$ is of importance in (7). Since the corresponding ξ is much less than unity, (17) reduces very nearly to

$$K_0[(l+\tfrac{1}{2})\xi] = K_0[(l+\tfrac{1}{2})(b_3/(ka))],$$

so that the δ_l's and δ_l^0's are in close agreement.

Corresponding quantities for the F potential (8) can be readily obtained: Integrals involving a term of the form $cre^{-\beta r}$ are obtained by differentiating with respect to β the integrals already obtained for terms of the form $ce^{-\beta r}$ (the U potential).

The Scattering Amplitudes

In summing (1), the convergence of the real part is improved by subtracting $f^B(\theta)$ as given by its series expansion (2) and adding it as obtained by the integration of (4). The integrated expressions are respectively, for U and F,

$$f^B(\theta) = -2k\alpha a^2 \sum_{i=1}^{3} a_i (b_i^2 + a^2 s^2)^{-1}, \tag{18}$$

and

$$f^B(\theta) = -2k\alpha[(\beta_1^2+s^2)^{-1} + (2c\beta_2)(\beta_2^2+s^2)^{-2}]. \tag{19}$$

By substituting the following asymptotic expressions:[15]

$$K_0(x) \sim (\tfrac{1}{2}\pi/x)^{\frac{1}{2}} e^{-x}, \tag{20}$$

and

$$P_l(\cos\theta) \sim \sqrt{2}(\pi l \sin\theta)^{-\frac{1}{2}} \sin[(l+\tfrac{1}{2})\theta + \pi/4] \leqslant \sqrt{2}(\pi l \sin\theta)^{-\frac{1}{2}}, \tag{21}$$

into the respective expressions for the real and the imaginary parts of $f(\theta)$, it was shown that negligible errors would arise from termination of the summation at $l=70$ for the real part and at $l=100$ for the imaginary part, for $\theta \geqslant 1°$. For $\theta = 0°$, $P_l(\cos\theta) = 1$ and an exact termination correction can be made.

The $P_l(\cos\theta)$ were obtained from the available tables up to $l=10$ and for $10 \leqslant l \leqslant 100$, $1° \leqslant \theta \leqslant 16°$ they were computed from the relation

$$P_l(\cos\theta) \sim (\theta/\sin\theta)^{\frac{1}{2}} J_0[(l+\tfrac{1}{2})\theta] \tag{22}$$

which may be derived from the corresponding asymptotic expressions.[16] Equation (22) was satisfactory for l as low as 5 over the whole range of θ indicated in Table II.

TABLE III. Values of s where $\eta_U(\theta) - \eta_F(\theta) = \pi/2$.

Voltage, kev	$s_0$observed	$s$partial waves	s2nd Born
40	10.7±0.6	10.9	7.7
11	6.6±0.6	7.1	3.8

[13] A. Cayley, Messenger Math. **17**, 21 (1887). The same polynomials with decimal coefficients are given by N. Rosen, Phys. Rev. **38**, 255 (1931).

[14] G. N. Watson, Messenger Math. **47**, 151 (1918).

[15] See, for example, E. Jahnke and F. Emde, *Funktionentafeln* (Dover Publications, New York, 1945), fourth edition, p. 138, noting that $K_0(x) = (\pi/2)iH_0^{(1)}(ix)$, and p. 117.

[16] Reference 15, pp. 117, 138; see also reference 7, p. 144.

Ionization Energy Losses of Relativistic μ Mesons in Gases*†

J. E. KUPPERIAN, JR.,‡ AND E. D. PALMATIER
Department of Physics, University of North Carolina, Chapel Hill, North Carolina

(Received May 8, 1953)

By means of proportional counters the ionization energy losses in gases of μ mesons of several high-energy groups have been compared with the loss for mesons at minimum ionization. It is shown that in a normal proportional counter and Geiger counter telescope arrangement as was used in this work, the effects of locally generated showers and counter-wall-generated secondary electrons tend to mask the increase in ionization loss accompanying increasing μ-meson energy. When such effects are considered, the theoretical rise as predicted by the Bethe-Bloch-Williams theory is confirmed.

I. INTRODUCTION

ALTHOUGH the relativistic rise of the energy loss of fast charged particles traversing gases[1–5] was confirmed rather early for electrons[6–9] by means of cloud chambers and low efficiency Geiger counters, the initial observations on mesons with cloud chambers and with proportional counters did not yield the expected rise.[7, 8, 10–12] This measurement was undertaken not only with the objective of determining the extent of a possible rise for μ mesons but also to study some of the errors associated with the use of a proportional counter in such an investigation. Our results confirming the existance of the relativistic rise for μ mesons which have been published in preliminary form[13] are in excellent agreement with other recent studies in which proportional counters, low efficiency Geiger counters, high-pressure ionization chambers, and cloud chambers were used.[14–18]

II. EXPERIMENTAL METHOD

In Fig. 1 the arrangement of the apparatus is shown. It consisted essentially of eight Geiger counter telescopes, providing eight well-collimated vertical beams of cosmic-ray particles, two proportional counters in which the ionization losses were observed, lead absorbers and Geiger counter trays with associated neon lights for range measurements, and the required recording apparatus.

The eight telescopes were each composed of five Geiger counters as follows: A_1, A_2, C one from Tray B_1, plus the Geiger counter from Tray B_2 located directly below that from B_1. All Geiger counter axes lay in the horizontal plane and the axes of Counters A_1 and A_2 were oriented at right angles to the axes of the counters in the Trays B_1 and B_2. With this geometry no path length in the proportional counters, of a particle traversing the telescope, could differ from the mean path length through the proportional counters by more than one and one-half percent. For most of the particles the deviation was less than this. Ten centimeters of lead absorber located within the telescope just above Counter C served to eliminate the soft component.

The proportional counters were 15.5 inches in length and were constructed from seamless brass tubing of 3.75-inch inner diameter and 0.125-inch wall thickness. The center wire was of 4-mil tungsten supported at both ends by Stupakoff 96.0022 seals to allow flashing. Since the distance between the support tubes of the seals was 14 inches while only the center 8 inches of the proportional counters lay within the telescope, a reduction of less than 3 percent in gas gain is expected at the edge of the beam defined by the counter telescope.[19, 20] Thus field tubes were not added.

The major components of the gas system were a calcium purifier[19] and the two proportional counters which were all connected in series to form a closed loop. The gains of the two proportional counters were nearly identical under a wide variety of gas pressures and voltages and no electrical interaction between the two counter channels was ever detected during a series of tests devised for this purpose. The counters were operated well within the proportional region throughout the experiment.

The arrangement of the lead absorber and the range Trays D, E, and F as shown in Fig. 1 allowed the

* Based, in part, on a dissertation submitted by one of the authors (J. E. K.) to the Graduate School of the University of North Carolina in partial fulfillment of the requirements for the degree of Doctor of Philosophy.

† Supported by the U. S. Atomic Energy Commission.

‡ Now on active duty with the U. S. Navy.

[1] N. Bohr, Kgl. Danske Videnskab. Selskab, Mat.-fys. Medd. **18**, 8 (1948).
[2] H. A. Bethe, Z. Physik **76**, 293 (1932).
[3] F. Bloch, Z. Physik **81**, 363 (1933).
[4] E. J. Williams, Proc. Roy. Soc. (London) **A139**, 163 (1933).
[5] B. Rossi and K. I. Greisen, Revs. Modern Phys. **13**, 240 (1941).
[6] D. R. Corson and R. B. Brode, Phys. Rev. **53**, 773 (1938).
[7] D. R. Sen Gupta, Nature **146**, 65 (1940).
[8] W. E. Hazen, Phys. Rev. **67**, 269 (1945).
[9] F. L. Hereford, Phys. Rev. **74**, 574 (1948).
[10] W. E. Hazen, Phys. Rev. **65**, 259 (1944).
[11] E. Hayward, Phys. Rev. **72**, 937 (1948).
[12] Goodman, Nicholson, and Rathgeber, Proc. Phys. Soc. (London) **A64**, 96 (1951).
[13] J. E. Kupperian, Jr., and E. D. Plamatier, Phys. Rev. **85**, 1043 (1952).
[14] Becker, Chanson, Nageotte, Treille, Price, and Rothwell, Proc. Phys. Soc. (London) **A65**, 437 (1952).
[15] M. H. Shamos and I. Hudes, Phys. Rev. **84**, 1056 (1951).
[16] G. W. McClure, Phys. Rev. **87**, 680 (1952).
[17] Ghosh, Jones, and Wilson, Proc. Phys. Soc. (London) **A65**, 68 (1952).
[18] R. S. Carter and W. L. Whittemore, Phys. Rev. **87**, 494 (1952).
[19] B. Rossi and H. Staub, *Ionization Chambers and Counters* (McGraw-Hill Book Company, Inc., New York, 1949).
[20] A. L. Cockroft and S. C. Curran, Rev. Sci. Instr. **22**, 37 (1951).

grouping of mesons into four energy bands:

(a) 160 to 400 Mev (c) 810 to 1800 Mev
(b) 400 to 810 Mev (d) over 1800 Mev.

The first group provided a reference point at minimum ionization.

The recording of the amplitude of the voltage pulses produced by the proportional counters was accomplished in two similar channels each consisting of a preamplifier, amplifier,[21] gate, pulse lengthener,[22] and vacuum tube voltmeter. A master pulse originating from a fivefold coincidence in any one of the eight telescopes gated the pulse lengtheners to accept proportional counter signals associated with the passage of the particle. The outputs of the pulse lengtheners fed two vacuum tube voltmeters. These, in turn, were photographed along with the range lights. The photographic record of the meter readings was read to the nearest scale division, namely, one percent of full scale. The linearity and null reading of each channel were checked to within the limit of accuracy of the reading of the meter by comparing the responses of the two channels to a common input signal when the operating conditions of one channel were varied widely while those of the other were maintained

TABLE I. Operating conditions for Experiment A.

Condition	Run I	Run II
Gas pressure	1.65 atmos.	1.60 atmos
Proportional counter voltage[a]	2700 volts	2610 volts
Duration of run	44.8 hr	83 hr
Counting rate (total for eight telescopes)	10.8 ± 0.5 hr^{-1}	10.8 ± 0.4 hr^{-1}
Amplifier gain	2×10^3	6×10^4
Amplifier rise time	4.0×10^{-6} sec	0.7×10^{-6} sec
Amplifier clipping time	32×10^{-6} sec	8.0×10^{-6} sec

[a] Supplied by battery packs.

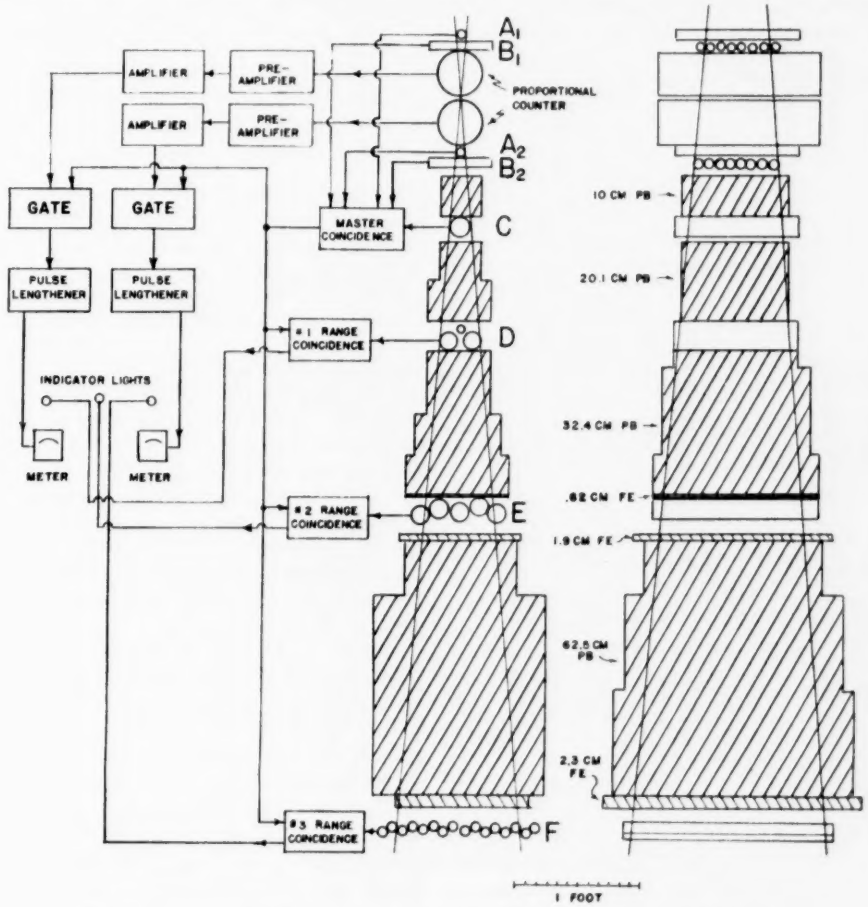

FIG. 1. Arrangement of the apparatus used for the determination of the relativistic rise of the ionization energy losses of μ mesons.

[21] W. H. Jordan and P. R. Bell, Rev. Sci. Instr. **18**, 703 (1947).
[22] J. T. Dewan and W. K. Allen, Rev. Sci. Instr. **21**, 823 (1950).

constant and vice versa. It was found that no corrections were warranted over the range of pulse height within which our observations were made (ratio of maximum to minimum observed pulse height of less than five to one).

III. OBSERVATIONS AND INTERPRETATION OF DATA

Several different sets of operating conditions and gases were used as described below. An auxiliary experiment was also performed with guard counters to aid in the interpretation of the experiments.

Experiment A. Ionization Losses in a Mixture of 97 Percent Argon and 3 Percent CO_2

Two separate runs were made in this experiment. The operating conditions are given in Table I. During the latter part of the first run, a tube failure in the E tray circuit made an assignment of readings between the second and third range groups impossible; hence these readings have been combined for this run. The on-scale readings for both proportional counters in the two runs are plotted in histogram form in Figs. 2 to 5.

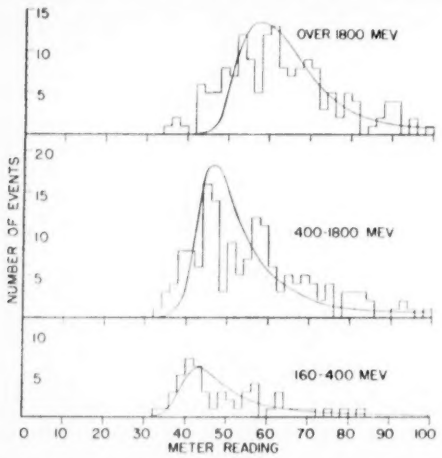

FIG. 2. Histogram of the meter readings for the upper proportional counter of Run I, Experiment A. The curve is the distribution calculated from Landau's theory.

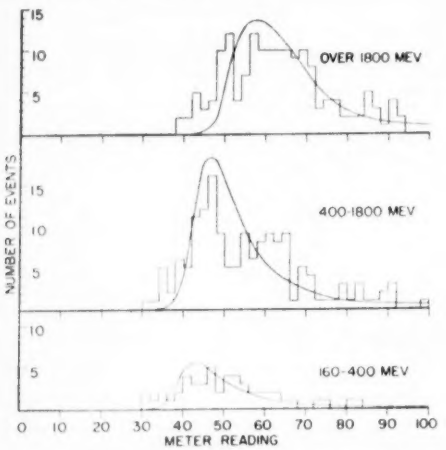

FIG. 3. Histogram of the meter readings for the lower proportional counter of Run I, Experiment A. The curve is the distribution calculated from Landau's theory.

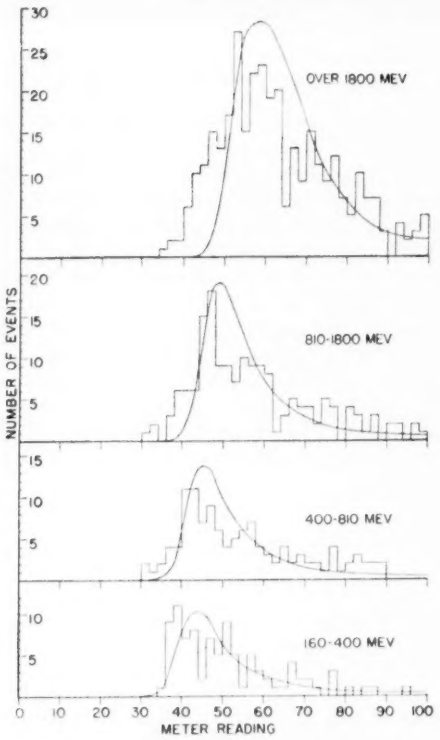

FIG. 4. Histogram of the meter readings for the upper proportional counter of Run II, Experiment A. The curve is the distribution calculated from Landau's theory.

A considerable portion (30 percent) of the photographs showed either one or both of the meters to possess off-scale readings; a breakdown of the results into on-scale and single or double off-scale readings is given in Tables II and III.

While a comparison of these results with theory will be reserved for a later section, several observations concerning these data can appropriately be made here.

(a) Considering the on-scale readings only, in each case a definite increase of mean pulse height with increasing particle range is readily observable in the histograms. Furthermore, as first shown by Landau[23] and later more generally by Symon[24] for each group of mesons in a given range, the distribution in pulse height possesses a pronounced tail in the direction of higher energy losses.

[23] L. Landau, J. Phys. (U.S.S.R.) **8**, 201 (1944).
[24] B. Rossi, *High Energy Particles* (Prentice-Hall Publishing Company, New York, 1952).

TABLE II. On and off-scale grouping of observations for Run I of Experiment A.

Proportional counter	Energy group (Mev)	Number of events: On-scale	Single Off-scale	Double Off-scale	Total
Upper	160–400	51	5	19	75
Upper	400–1800	154	26	21	201
Upper	Over 1800	159	29	20	208
Lower	160–400	48	8	19	75
Lower	400–1800	155	25	21	201
Lower	Over 1800	160	28	20	208

TABLE III. On and off-scale grouping of observations for Run II of Experiment A.

Proportional counter	Energy group (Mev)	Number of events: On-scale	Single Off-scale	Double Off-scale	Total
Upper	160–400	92	6	25	123
Upper	400–810	117	12	23	152
Upper	810–1800	163	22	21	206
Upper	Over 1800	334	48	36	418
Lower	160–400	88	10	25	123
Lower	400–810	117	12	23	152
Lower	810–1800	160	25	21	206
Lower	Over 1800	316	66	36	418

(b) The proportion of single off-scale events is a slowly increasing function of the energy while the proportion of double off-scale readings decreases strongly with increasing energy (Tables II and III). Now the probability that a meson in traversing a proportional counter will give rise to a wall-generated secondary electron which results in an off-scale reading, is readily calculated[25] as 4.5 percent for our counters. When this correction has been applied to the single-off-scale events, the residue (shown in column 3 of Table IV) is interpreted as arising from high energy losses occurring within the gas of the proportional counter. The behavior of this single off-scale group is just what one would expect on the basis of the observations made in (a) above. Thus, as the meson energy increases, the observed shift of the mean energy loss leads us to expect an increase in the fraction of off-scale readings. The fraction of off-scale readings, predicted by the Landau theory for our experimental arrangement, has been computed as will be discussed later. The results of this computation which are in good agreement with the observations are given in column 4 of Table IV.

A small portion (12 percent) of the double off-scale readings arise from the chance occurrence of two independent knock-on secondaries of the same meson, one in each counter. The major portion of these events, however, we consider to originate from showers, arising locally, just above the apparatus. That this interpretation is reasonable is borne out by the following guard counter studies.

[25] Brown, McKay, and Palmatier, Phys. Rev. **76**, 506 (1949).

Experiment B. Guard Counter Studies of Off-Scale Events

Several short runs were made with two horizontal trays of guard counters, each of 380 cm² effective area, located one on either side of the telescope. In the first run the guard trays were located slightly above the level of the A_1 counter (upper position) and in the second run were lowered to a position midway between the two proportional counters (lower position). A summary of the off-scale readings for these two positions is given in Table V where the results of Experiment A, performed with no guard counters, have been included for comparison. Although the number of events observed in this auxiliary experiment is not large, it is readily apparent that (a) double off-scale events are predominantly associated with a high probability of discharge of the guard trays (85 percent), while single off-scale events are characterized by a very small probability of discharge of the guard trays (10 percent). (b) the probability of occurrence of a double off-scale event is about ten percent provided that the guard tray is in the lower position or is absent; this chance is increased, however, by a factor of three when the guard tray is placed in the upper position.

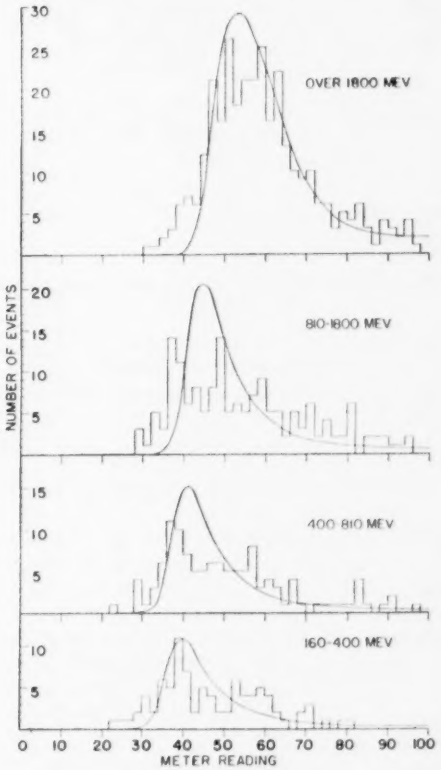

FIG. 5. Histogram of the meter readings for the lower proportional counter of Run II, Experiment A. The curve is the distribution calculated from Landau's theory.

TABLE IV. Percentage of single off-scale events in Experiment A which originates from processes occurring in the gas of the proportional counter.

Energy group	Observed (uncorrected)	Observed (corrected)	Calculated (from Landau distribution)
	Run I[a]		
160–400 Mev	12 ±3	7.5±3	6 ±0.5
400–1800 Mev	14 ±2	9.5±2	6 ±0.5
Over 1800 Mev	16 ±2	11.5±2	9 ±0.5
	Run II[a]		
160–400 Mev	9.5±2	5 ±2	5.5±0.5
400–810 Mev	9.5±2	5 ±2	5.5±0.5
810–1800 Mev	13 ±2	8.5±2	6 ±0.5
Over 1800 Mev	15 ±1.5	10.5±2	8 ±0.5

[a] The results for both proportional counters have been grouped together for each run, as no significant difference was observed between the results for the two counters.

We conclude that these results confirm the previous division of off-scale events into two classes: low-energy wall-generated secondaries which for the most part only appear in one proportional counter during a given meson traversal, and multiple-particle locally generated showers which originate above the apparatus and give rise to large pulses in both counters.

Experiment C. Ionization Losses in a Mixture of 94 Percent Argon and 6 Percent Ethylene at 1.6 Atmosphere Pressure

The procedure of Experiment A was repeated using the gas mixture for which it had previously been reported that no significant rise in energy loss was obtained.[12] This run was continued only long enough to indicate that the trend of the results was similar to that of Experiment A.

IV. TREATMENT OF THE DATA AND COMPARISON WITH THEORY

Owing to the width of our distributions and the number of events observed, the determination of the mean pulse height is much simpler and more accurate than a determination of the most probable pulse height and we shall work with the former quantity. This, of course, requires that we reject multiple-particle events which appear mainly as large pulses. With our method of accomplishing this rejection we thus lose a small fraction of the desired events, and this must be considered in any comparison of theory and experiment. We also note that in this study we have not obtained an absolute measurement of the energy loss but rather a comparison of energy loss of high-energy mesons with that for mesons of lower energy. Both of these factors enter into the following comparison of the theory and experiment, which amounts essentially to a calibration of the maximum observed energy loss in the apparatus by fitting the theory and experimental results for the minimum ionizing energy groups only.

The Landau energy loss distribution was calculated for each group of mesons of lowest range by first splitting each group into two approximately equal subgroups,[26] computing the distribution at the mean momentum of each subgroup, and then combining the two curves thus obtained, weighted according to the number of mesons in each subgroup. In view of the observed linear relationship[27, 28] between the energy loss and pulse height in proportional counters and the observed linear behavior of our apparatus, we may fit the Landau curve to the data by terminating the former at an energy loss such that the following relationship is satisfied:

$$\frac{\text{Mean energy loss for the terminated Landau distribution}}{\text{Terminating energy loss}} = \frac{\text{Mean meter reading}}{\text{Full scale meter reading}}.$$

The terminating energy loss which fulfills this condition for a given run is, of course, the maximum energy loss observable in the apparatus during that run. The values obtained ranged from 55 to 60 kev for the four sets of data of Experiment A.

When the terminating energy loss for a minimum range group has been obtained, the theoretical Landau curves to be assigned to the other range groups of the run are determined and may readily be computed. We note here that the intermediate range groups were all divided into two subgroups, similarly to the minimum range groups, while the greatest range groups were

TABLE V. Off-scale readings for various guard tray positions.

Location of guard tray	Total No. of events	Double off-scale: Shower	Double off-scale: No shower	Upper only off-scale: Shower	Upper only off-scale: No Shower	Lower only off-scale: Shower	Lower only off-scale: No shower
Upper position	240	61	8	4	26	3	23
Lower position	128	9	2	1	9	1	24
None	1383	165		148		174	

TABLE VI. Final results for Experiment C.

Energy of group	No. of on-scale[a] events observed	Ratio of the mean pulse height of a group to the mean pulse height of the minimum range group: Observed	Theoretical
160–400 Mev	35	1.00	1.00
400–810 Mev	74	0.98±0.07	1.05
810–1800 Mev	82	1.15±0.07	1.08
Over 1800 Mev	131	1.28±0.07	1.25

[a] Data for both counters have been combined.

[26] B. Rossi, Revs. Modern Phys. **20**, 537 (1948).
[27] L. H. Gray, Proc. Cambridge Phil. Soc. **40**, 95 (1944).
[28] Jesse, Forstat, and Sadauskis, Phys. Rev. **77**, 782 (1950).

divided into four range subgroups. Only in the latter case did the Landau curves differ in any appreciable way from the curves obtained by not splitting a group but by considering the mesons to possess the mean momentum of the group. The distributions so obtained are plotted on the appropriate histograms Figs. 2–5. The theoretical contributions to the off-scale reading given in column 4 of Table IV have been determined from the calculations as the number of events lying beyond the terminating energy.

The means of the observed histograms of the on-scale readings and the means of the terminated distributions for all the runs of Experiment A are given in Fig. 6, where these means are plotted as a function of the mean momentum of the appropriate group. The agreement is seen to be quite good. The same results for Experiment C are presented in Table VI along with the data on the number of events observed in each meson group. Although the statistics are poor, the agreement between theory and experiment is well within the limits of error and certainly indicates that the relativistic rise exists here also.

However, when the off-scale readings are included in the determination of the mean pulse height (amounting to a failure to correct for the effects of wall-generated secondaries and local showers) the relativistic rise in pulse height is masked. We may see this as follows:

Owing to the manner in which our data were obtained, the average pulse heights to be associated with the various groups of off-scale readings are not known. However, a lower limit is obviously set by full-scale meter deflection while an upper limit of twice full-scale deflection (associated with an average traversal of four particles) does not seem unreasonable. On the basis of these limiting average pulse heights to be assigned to the off-scale readings, we may recalculate the means of the observed pulse heights for all the groups when none of the data are rejected. The results are given in Fig. 7, all minimum range runs being normalized to the same point. The masking of the rise, which results from the greater fraction of off-scale events in the lower range groups, is quite apparent.

As a final observation, we note that although there is a good agreement in the behavior of the means of the observed and the Landau distributions, the theoretical curves in all cases are slightly narrower than the histograms. Owing to the absence of an absolute calibration in our work and the possible presence of a slow drift in amplifier characteristics, we have not made any analysis of this result. A small drift would only widen the observed distributions and would not affect the shift of the mean pulse heights of the various range groups since in any given run all ranges were observed simultaneously. Such an effect, however, has definitely been noted previously[14,29] with both electrons and

[29] P. Rothwell, Proc. Phys. Soc. (London) **B64**, 911 (1951).

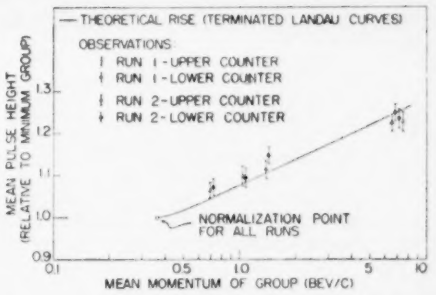

FIG. 6. Comparison of the theoretical rise in mean ionization loss with the rise in the mean pulse height for the corrected data of Experiment A.

mesons in proportional counters when the instruments have been calibrated.

V. CONCLUSIONS

Our results, in conjunction with the latest findings of other workers,[14–18] all confirm the predicted rise in the ionization energy loss of relativistic μ mesons in gases, near atmospheric pressures. The general shape of the Landau distribution in energy loss is also confirmed, although there is an indication that the observed distributions are wider than the theoretical distributions, this tendency being especially evident on the low-energy side of the curve.

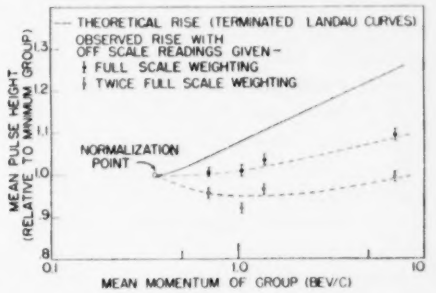
THEORETICAL RISE (TERMINATED LANDAU CURVES)
OBSERVED RISE WITH OFF SCALE READINGS GIVEN-
FULL SCALE WEIGHTING
TWICE FULL SCALE WEIGHTING
NORMALIZATION POINT
MEAN PULSE HEIGHT (RELATIVE TO MINIMUM GROUP)
MEAN MOMENTUM OF GROUP (BEV/C)

FIG. 7. Illustration of the masking of the relativistic rise in ionization energy loss when multiple-particle events are not eliminated.

From the experimental viewpoint we have shown that a failure to exclude the multiple-particle events in a standard experimental arrangement will introduce serious errors which will tend to mask the rise. Such errors may readily be eliminated by the use of a cloud chamber along with the proportional counter.[14] However, since the most serious error arises from the showers generated locally but above and external to the telescope, the use of a suitable anticoincidence tray should simply and effectively eliminate the multiple-particle events; the wall-generated secondaries are small in number and occur to the same extent in all groups.

We are grateful to Dr. W. A. Bowers for helpful advice and criticism in the analysis of this experiment.

Gamma-Ray Spectrum of As^{77}†

F. Rasetti and E. C. Booth
The Johns Hopkins University, Baltimore, Maryland
(Received May 18, 1953)

The gamma-ray spectrum following the beta decay of As^{77} was investigated by means of a scintillation spectrometer. The following gamma-ray energies (in kev) and intensities (quanta per disintegration) were observed: 88(0.003); 155(~0.002); 243(0.023); 528(0.007). Coincidence experiments show that the 88- and 155-kev lines are emitted in cascade, while the other two lines do not coincide with any other. A level diagram for the product nucleus Se^{77} is suggested.

I. INTRODUCTION AND EXPERIMENTAL ARRANGEMENT

THE isotope As^{77} is known to decay by beta emission with a half-life between 38 and 40 hours and a maximum beta energy near 0.7 Mev.[1,2] Analysis of the electron spectrum failed to show conversion lines.[1,2] Hence it was concluded that, if a gamma radiation is present, it must be very weak. Mandeville *et al.*[3] reported no gamma rays.

A source of As^{77} resulting from the decay of 12-hour Ge^{77} was prepared by a method similar to the one employed by Arnold and Sugarman.[4] The authors are greatly indebted to Dr. G. Friedlander and Dr. W. S. Koski for performing the chemical separation. The arsenic solution, containing a few milligrams of carrier, was finally evaporated on a disk of thin tissue paper 1.5 cm in diameter.

The gamma-ray spectrum was analyzed by means of two scintillation spectrometers which could be used in coincidence. A description of the experimental arrangement was given in connection with a similar investigation.[5] For energy measurements, the 87.5-kev line of Cd^{109}, the 238.6-kev line of ThB, and the annihilation radiation were used as standards. In order to determine absolute intensities of the gamma-ray lines, integral counts of the photoelectric peaks were determined; from the knowledge of the efficiency of the crystal (thickness 1.1 cm), percentage of pulses in the photoelectric peak, and effective solid angle, it is possible to evaluate the number of quanta emitted by the source. To determine its absolute strength, the source on a thin support was suspended in front of a thin-window (2 mg/cm^2) Geiger counter, covered with a diaphragm of known diameter, and counts were taken at different distances. When corrected for absorption in air and the mica window (an absorption coefficient of the beta rays of 22 cm^2/g was assumed), these data showed good proportionality to $1/r^2$ and yielded an absolute strength of 5×10^6 betas per minute at the time when the measurement was performed.

II. ENERGY AND INTENSITY MEASUREMENTS

Preliminary inspection of the pulse-size spectrum on an oscilloscope screen indicated the presence of three well-marked photoelectric peaks and possibly a fourth. Accurate curves were taken by means of a single-channel pulse analyzer. One such curve is shown in Fig. 1, showing photoelectric peaks corresponding to four gamma-ray lines.

It was important to ascertain that these lines were not due to impurities. For this purpose, the decay of each separate line was followed for 3 or 4 half-lives by setting the channel of a scintillation spectrometer to cover the photoelectric peak of the line. All lines decayed with the same period, the average of our determinations being 39 hours, in good agreement with the accepted value. This fact absolutely excludes that any of the reported lines may belong to the parent nucleus, the 12-hour Ge^{77}.

The intensity measurements are satisfactory for the lines at 243 and 528 kev, much less so for the line at 88 kev, and especially for the one at 155 kev, for which neither energy nor intensity could be measured with any accuracy, as it falls between the wings of the

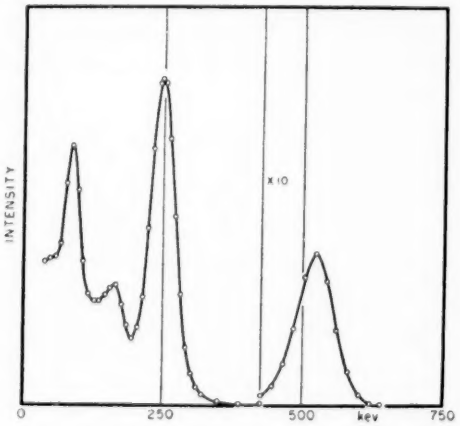

FIG. 1. Pulse-height spectrum from As^{77} showing photoelectric peaks at 88, 155, 243, and 528 kev.

† Work supported by the U. S. Atomic Energy Commission.
[1] Jensen, Nichols, and Clement, Phys. Rev. **81**, 143 (1951).
[2] R. Canada and A. C. G. Mitchell, Phys. Rev. **81**, 485 (1951).
[3] Mandeville, Woo, Scherb, Keighton, and Shapiro, Phys. Rev. **75**, 1528 (1949).
[4] J. R. Arnold and N. Sugarman, J. Chem. Phys. **15**, 703 (1947).
[5] F. Rasetti and E. C. Booth, Phys. Rev. **91**, 315 (1953).

stronger photoelectric peaks of the 88- and 243-kev lines, and is superimposed on the Compton pulses due to the latter. The intensity of the line at 88 kev could not be measured accurately owing to a strong continuum in this region, due to the Compton pulses of the 243-kev line, backscattering of the same by the materials surrounding the source and the detector, and possibly also to brensstrahlung produced in stopping the electrons from the source in a Lucite plate interposed between source and crystal. The energy of the 155-kev line as given does not result from the inaccurate direct measurement, but is deduced as a combination of the 88- and 243-kev lines on account of the coincidence experiments reported later.

The results concerning the energies and intensities of the four lines are summarized in Table I.

III. COINCIDENCE EXPERIMENTS

Possible coincidences between pairs of gamma rays were investigated using two crystal spectrometers connected to pulse-height analyzers. The source was placed between the two scintillating crystals, which subtended large solid angles (of the order of $\frac{1}{5}$ of the total). Other details of the arrangement were previously described.[5] The background coincidence rate, due to cosmic rays plus accidentals, was of the order of a few percent of the rates expected for two coincident gamma rays. No coincidences were observed for the pairs (528, 243), (528, 155), (528, 88), (243, 155), and (243, 88). On the contrary, a high coincidence rate appeared when the two channels recorded the 155-kev and 88-kev lines, respectively. To better establish that these two gamma rays are in cascade, one channel was set to record the 88-kev line, while the spectrum was scanned with the relatively narrow channel. The second spectrometer then recorded a sharp peak in the region of 150 kev, much better defined than in the single-pulse spectrum. Conversely, with one channel set at 150 kev, the other gave a sharp peak near 90 kev.

TABLE I. Energies and intensities of the As^{77} gamma-ray lines.

Energy kev	Pulses in photopeak per minute	Fraction of total solid angle	Efficiency of crystal	Percentage of pulses in photo-peak	Quanta per minute	Quanta per decay
88±2	1140	0.080	1.00	100	14 200	0.0028
155±5	~600	0.067	0.90	100	~10 000	~0.002
243±3	2900	0.060	0.52	80	116 000	0.023
528±5	187	0.060	0.25	36	34 600	0.007

IV. CONCLUSIONS AND DISCUSSION

From the coincidence experiments it is clear that the 88-kev line and the one near 150 kev are in cascade. Since there is a line at 243 kev, whose energy within the accuracy of the measurements is the sum of the two, we assume that the latter represents the cross-over transition and hence assign to the less well-determined line an energy of 243−88=155 kev. The 528-kev line almost certainly represents an independent transition to the ground state, since it shows no coincidences with any other line; furthermore, it could not lead to a high-excited state, as it involves most of the energy (0.7 Mev) available in the decay.

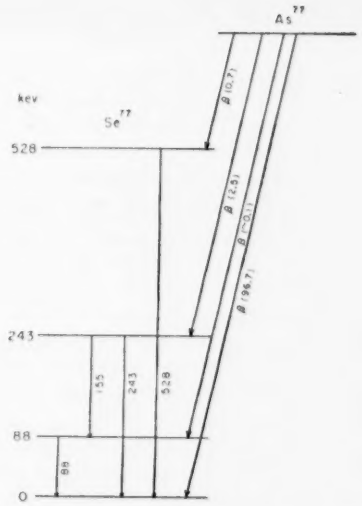

FIG. 2. Decay scheme of As^{77}. Percentage of decay to various levels of Se^{77} is indicated.

On the basis of the reported experimental data, it is possible to construct a complete decay scheme, except for one detail. It is not certain which of the 88-kev and 155-kev transitions precedes the other. If the intensities could be measured more accurately and were found different, the question would be settled, since the second transitions cannot be weaker than the first (the argument applies to the total number of transitions, resulting either in gamma emission or internal conversion; in the present case, the conversion coefficients are probably small, since no conversion lines were observed in the beta-ray spectrum[1,2]). The intensities of the two above-mentioned lines are of the same order of magnitude, and although in the data of Table I the 155-kev line is reported somewhat weaker, this result is by no means certain. Tentatively assuming a greater intensity for the 88-kev line, in the decay scheme of Fig. 2 this line is represented as a transition to the ground state. Approximate numbers of beta rays leading to the various levels of Se^{77} are also indicated. The fact that all these gamma-ray lines are weak explains the fact that As^{77} was previously reported as a pure beta emitter. Transitions to excited levels are also too weak to produce an appreciable distortion of the beta-ray spectrum.

The Photoionization of Molecules in the Vacuum Ultraviolet

EDWARD C. Y. INN
Atmospheric Physics Laboratory, Geophysics Research Directorate, Air Force Cambridge Research Center, Air Research and Development Command, Cambridge, Massachusetts

(Received May 13, 1953)

A method of measuring thresholds for photoionization of molecules, corresponding to the first ionization potential, is described. The method is applied to several different molecules (O_2, NO, NH_3, SO_2, C_2H_4, CH_3I, CH_3OH, C_2H_5Br). The first ionization potentials obtained are compared with those measured by other methods, e.g., electron impact and spectroscopic. The photoionization method gives greater precision than the electron impact method and is applicable to cases where the spectroscopic method fails.

THE usual methods of determining ionization potentials of molecules are by electron impact and spectroscopically by the convergence limit of Rydberg series. We report here a somewhat different, and perhaps more direct, method for measuring the first ionization potential of molecules by determining the threshold for photoionization. Since the ionization potentials of many molecules are greater than 6 ev, the photoionization measurements must be made in the vacuum ultraviolet.

The apparatus used for these measurements has been described elsewhere.[1,2] Briefly, monochromatic radiation (0.85A band width) from a Baird 1-meter vacuum monochromator was allowed to pass through a photoionization cell located behind the exit slit (0.05 mm wide) of the monochromator. Parallel plate (Pt) electrodes in the cell were used to collect the ions produced by photoionization. To insure collection of all ions, the voltage applied (about 10 volts) to the electrodes was set a few volts above saturation, end plates used, and the monochromatic beam centrally located in the volume element defined by the electrodes. The ion current was measured with a Beckman micro-microammeter ($10^{-8}-10^{-14}$ amp) and recorded on a Speedomax recorder. The cell was in communication with a gas filling system, thus allowing the cell to be readily filled with the purified gas or vapor at any desired pressure. By scanning (20A per minute) the spectral region near the threshold, the ion current is recorded and the wavelength at which the first ions appear, followed by a sharp increase in ion current, is determined with considerable accuracy. Photoelectric effects due to scat-

TABLE I. Observed ionization potentials compared with those obtained by other methods.

Molecule	Threshold (A)	Ionization potential ev: Our values	Previously reported values	Method
O_2	1029	12.04 ±0.01	12.2 ±0.1	cycle[b]
			12.1 ±0.2	electron impact[c]
NO	1343	9.23 ±0.02[a]	9.4 ±0.2	electron impact[c]
NH_3	1223	10.13 ±0.02	10.5 ±0.1	electron impact[d]
SO_2	998	12.42 ±0.06	12.05 ±0.05	rough extrapolation of Rydberg series[e]
			13.3 ±0.3	electron impact[f]
C_2H_4	1184	10.47 ±0.02	10.45 ±0.03	Rydberg series[g]
			10.80 ±0.05	electron impact[h]
			10.62	electron impact[i]
CH_3I	1305	9.497±0.007	9.490±0.002	Rydberg series[j]
			9.1 ±0.25	electron impact[k]
	1349	9.19 ±0.02		
CH_3OH	1178	10.52 ±0.03	10.8	electron impact[l] (quoted by Price)
C_2H_5Br	1211	10.24 ±0.02	10.24 ±0.02	by comparison with CH_3Br Rydberg series[m]
			10.0 ±0.25	electron impact[k]
	1255	9.88 ±0.03		

[a] See reference 2.
[b] R. S. Mulliken and D. S. Stevens, Phys. Rev. **44**, 720 (1933).
[c] H. D. Hagstrum, Revs. Modern Phys. **23**, 185 (1951).
[d] Mann, Hustrulid, and Tate, Phys. Rev. **58**, 340 (1940).
[e] W. C. Price and D. M. Simpson, Proc. Roy. Soc. (London) **A165**, 272 (1938).
[f] H. D. Smyth and D. W. Mueller, Phys. Rev. **43**, 121 (1933).
[g] W. C. Price and W. T. Tutte, Proc. Roy. Soc. (London) **A174**, 207 (1940).
[h] Kusch, Hustrulid, and Tate, Phys. Rev. **52**, 843 (1937).
[i] R. E. Honig, J. Chem. Phys. **16**, 105 (1948).
[j] W. C. Price, J. Chem. Phys. **4**, 539 (1936).
[k] T. N. Jewitt, Phys. Rev. **46**, 616 (1934).
[l] W. C. Price, Chem. Revs. **41**, 257 (1947).
[m] W. C. Price, J. Chem. Phys. **4**, 547 (1936).

[1] Watanabe, Inn, and Zelikoff, J. Chem. Phys. (to be published).
[2] Watanabe, Marmo, and Inn, Phys. Rev. **90**, 155 (1953).

tered and multiply-reflected radiation at the electrodes were exceedingly small compared to the ion currents measured.

In order to compare this method of determining ionization potentials with those mentioned above, a number of molecules were studied and the results are shown in Table I. The accuracy of the values obtained is indicated in the third column, which represents the degree of uncertainty in determining the exact wavelength at which the first ions appear in the measurement of the photoionization current. It is seen that, in general, there is good agreement with those reported by other investigators, exceptionally so with those determined by Rydberg series methods. Since election impact values essentially correspond to vertical processes, it is not surprising that our values are lower and agree better with the more correct spectroscopic values corresponding to adiabatic processes.

An unusual effect was noted in the case of CH_3I and C_2H_5Br. There appeared to be a second threshold at longer wavelengths, although the cutoff was much less pronounced and sharp as compared to the shorter wave length threshold. The ion current was also much smaller than that produced at the shorter wavelength threshold. Two possible explanations for this effect may be given: (1) photoionization of dissociation products which may have lower ionization potentials; or (2) ionization due to transitions $v''>0$ of the ground state of the normal molecule to the $v'=0$ of the ground state of the ionized molecule.

In the case of O_2, NO, NH_3, and CH_3OH, in which no Rydberg series has been observed with any degree of success, it can be seen that the present method is particularly adapted for obtaining accurate measurements of the ionization potential. In fact, this method should be generally applicable for determining first ionization potentials of a wide variety of molecules and in addition for determining molecular ionization cross sections.[2]

PHYSICAL REVIEW VOLUME 91, NUMBER 5 SEPTEMBER 1, 1953

Accurate Determinations of Nuclear Reaction Energies*

K. F. Famularo † and G. C. Phillips
Rice Institute, Houston, Texas

(Received May 29, 1953)

A precise magnetic spectrometer of the annular type is described; the focusing properties and line shapes are analyzed. The use of the instrument to measure absolute particle momenta in terms of the proton magnetic moment precessional frequency and a standard length is presented for three nuclear transmutations and for the determination of the energy necessary to excite a state in Ne^{20}. The Q values obtained are: $C^{12}(d,p)C^{13}$, $Q=2.722\pm0.004$ Mev; $O^{16}(d,\alpha)N^{14}$, $Q=3.119\pm0.005$ Mev; and $Li^7(p,\alpha)He^4$, $Q=17.344\pm0.013$ Mev. The energy at a resonance in the reaction $F^{19}(p,\alpha\gamma)O^{16}$ was determined to be 872.5 ± 1.8 kev.

I. INTRODUCTION

ACCURATE determinations of the energies of evolution of nuclear transmutations yielding heavy particles have been performed in a number of laboratories in recent years; modern techniques have allowed the construction of very precise magnetic and electrostatic spectrometers,[1] and one result of the measurements performed with these instruments has been the preparation of accurate tables of atomic masses for the light elements.[2] A precise knowledge of these masses is desirable so that theories of binding energies of nuclei may be constructed, and to allow the prediction of particle energies and the energies of excitation of nuclei. Atomic masses are also determined with great accuracy by the methods of mass spectrometry; however, it has been pointed out that the nuclear and mass spectroscopic methods have not always yielded mass values that agreed within the assigned errors for the measurements.[2] Since either or both methods could have small errors that might account for this disagreement, it seemed desirable to attempt an accurate, absolute, and independent redetermination of the nuclear data. This paper will describe the techniques developed to accomplish the determinations and will present some of the results.

In reviewing the possibilities of obtaining nuclear disintegration data of greater absolute accuracy than in earlier determinations, five possible sources of error in the previous determinations were noted and an attempt has been made to diminish the magnitude of these possible errors. (1) Most measurements of nuclear transmutation energies have been performed on particles emitted in directions θ that were not optimum with respect to the direction of bombardment. The classical expression for the energy of evolution, Q, of a nuclear

* Supported by the U. S. Atomic Energy Commission.
† Now at the University of Minnesota, Minneapolis, Minnesota.
[1] Buechner, Strait, Stergiopoulos, and Sperduto, Phys. Rev. **74**, 1569 (1948); Snyder, Ruben, Fowler, and Lauritsen, Rev. Sci. Instr. **21**, 852 (1950); Brown, Craig, and Williamson, Rev. Sci. Instr. **22**, 952 (1951).
[2] Li, Whaling, Fowler, and Lauritsen, Phys. Rev. **83**, 512 (1951).

reaction is[3]

$$Q=(M_2+M_3)E_2/M_3-(M_3-M_1)E_1/M_3 -2(M_1M_2E_1E_2)^{\frac{1}{2}}\cos\theta/M_3, \quad (1)$$

where the subscripts 0, 1, 2, 3 refer to the target nucleus, incident particle, produced particle, and the residual nucleus, respectively. Equation (1) may be solved to give

$$E_2^{\frac{1}{2}}=(M_1M_2E_1)^{\frac{1}{2}}\cos\theta/(M_2+M_3) \pm\{M_1M_2E_1\cos^2\theta/(M_2+M_3)^2 +(M_3-M_1)E_1/(M_2+M_3) +M_3Q/(M_2+M_3)\}^{\frac{1}{2}}. \quad (2)$$

Equation (2) shows that $\partial E_2/\partial\theta$ is zero for $\theta=0, \pi$. In the experiments to be described $\theta=\pi$ and the deviation from $\theta=180°$ is $\pm 2°$.

(2) Most previous determinations of nuclear transmutation energies have been measurements relative with respect to the older determinations of the natural alpha-particle energies.[4] Although the indications are that the alpha-particle energies are very well known, it seemed desirable to use a more fundamental and independent scale of energies. The scale of energies employed with the Rice spectrometer is derived from the Larmor precessional frequency of the proton magnetic moment in the same magnetic field where the magnetic analysis is performed, and from the radius of curvature as established with a standard meter bar.

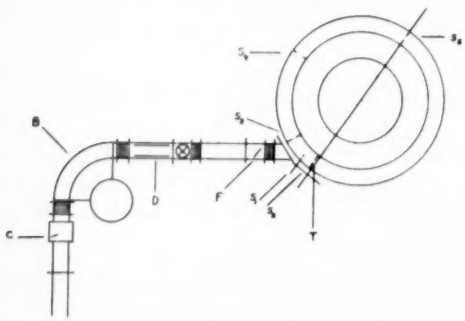

FIG. 1. Experimental arrangement. The accelerated beam is deflected through 90° by the beam analyzing magnet, passes through an auxiliary deflector, and enters the gap of the spectrometer magnet so that its direction is tangent to the mean circle of the spectrometer at the target.

(3) Since a particle spectrometer yields a plot of the number of particles *versus* the momentum (or energy), it seemed necessary to develop an objective and fundamental method of assigning a momentum to each group. In the Appendix a simple analysis of the line shapes to be expected from a spectrometer is presented. This knowledge of line shapes has allowed the use of two objective and fundamental methods of assigning momentum.

(4) Because the energy E_2 of the disintegration particles is a function of the bombarding energy E_1, it seemed desirable to use a bombarding energy that could be easily and precisely established, maintained for long periods of time, and monitored frequently. In the experiments to be described the use of a narrow resonance in the $F^{19}(p,\alpha\gamma)O^{16}$ reaction has allowed the bombarding energy to be quickly established.[5] Another proton moment magnetometer in the field of the beam analyzing magnet served to stabilize the magnetic field in the beam analyzer and thus stabilized the energy of the electrostatic generator.

(5) The accumulation of thin surface deposits of contaminants on targets under the conditions of bombardment decreases the energy of the disintegration particles. This difficulty does not meet with any easy, universal solution. Fresh targets, small beam currents, liquid air trapping, and a clean vacuum system have reduced this undesirable effect. Attempts have been made to estimate the thickness of the surface layer by secondary means.

II. APPARATUS

The magnet used for the measurements and the proton moment magnetometer for field stabilization have been described previously.[5] The magnet, of the annular type, has a mean radius of curvature of 35 centimeters, and an annular width of 5 centimeters, although only the central half of the annular region is used. The incident beam from the accelerator is analyzed and then enters the gap of the magnet so that its direction is tangent to the mean circle of the annulus at the target. As shown in Fig. 1, the particles to be analyzed are deflected through 180° of arc and are counted by a detector located diametrically opposite the target.

Magnetic field measurements are made in terms of the Larmor precessional frequency of the magnetic moment of the proton. The stability of the system was such that the field could be held constant to one gauss. The vacuum chamber could be removed from and replaced in the gap of the magnet without disturbing the magnet. This allowed the use of an additional magnetometer to probe the field in the region used to analyze the reaction particles. Nonmagnetic materials were used in constructing the vacuum chamber. A discussion of the method used to correct for small variations of the magnetic field with trajectory arc angle ϕ is given in Appendix A.

The vacuum chamber consists of a two-inch copper tube bent into a semicircle and then flattened. Openings were cut into the chamber, and brass face plates were soldered on to permit the attachment of the beam

[3] M. S. Livingston and H. A. Bethe, Revs. Modern Phys. **9**, 245 (1937). Brown, Snyder, Fowler, and Lauritsen, Phys. Rev. **82**, 159 (1951).

[4] W. B. Lewis and B. V. Bowden, Proc. Roy. Soc. (London) **A145**, 235 (1934); S. Rosenblum and G. Dupouy, Compt. rend. **194**, 1919 (1932).

[5] E. D. Klema and G. C. Phillips, Phys. Rev. **86**, 951 (1952).

entrance port and the insertion of the target assembly at one end and the insertion of the proportional counter detector at the other end.

Comparison of particle group locations before and after removal, disassembly, and replacement of the chamber assured the rigidity and geometrical reproducibility of the system.

The over-all arrangement is shown in Fig. 1. There are five slits in the 180° magnetic analyzer. The beam from the accelerator, after being analyzed by the magnet B (see Fig. 1) and positioned by the electrostatic deflector D, passes through S_1, which is driven by a micrometer screw, then through S_2, and onto the target T. The position of S_1 with respect to S_2 determines the angle at which the beam strikes the target. The slit S_3 prevents particles scattered from S_1 from arriving at the detector. S_4 confines the observed particles to the desired portion of the field. S_5 is in front of the detector and is diametrically opposite to and coplanar with the target.

The width W_c of the detector slit S_5 was about 0.9 mm for most of the measurements while the width W_s of the source was usually determined by the width of S_1 and the geometry of the beam trajectory. Values of W_s ranged from 0.4 mm to 1.4 mm. The incident ion beam was positioned so that when the micrometer position of S_1 was properly placed the beam just grazed the inner edge of S_2. This procedure maintained a constant value $2r_0$ for the distance between the inner edges or source and detector.

The source of proton and deuteron beams for the bombardments was the Rice Institute pressurized Van de Graaff generator.[6] The beam analyzing magnet was monitored with a proton moment apparatus similar to that used with the annular magnet. The stability of the system was such that the spread in bombarding energy due to magnetic field fluctuations and due to the analyzer slit width was no more than ±0.9 kev.

The bombarding energy was determined by means of the resonance at 873.5 kev in the $F^{19}(p,\alpha\gamma)O^{16}$ reaction;[7] thin targets of CaF_2 or ZnF_2, located at C and F in Fig. 1, were used for the calibrations. They were mounted so that they could intercept the beam, or could be rotated aside to let the beam pass. For proton calibration the target at F was used. For deuteron calibration the target at C was positioned to intercept the proton beam from the accelerator, while the molecular hydrogen beam passed through the beam analyzing magnet to give the signal to the electron gun that regulates the generator voltage. This procedure necessitated a correction of +0.7 kev for the difference of mass of H_2^+ and D^+ ions.

Since the beam analyzing magnet and the annular magnet were separated by a distance of about one meter, their fields interacted slightly. Hence, the energy calibration of the generator was always performed with the field of the annular magnet held at the field that was to be used for the bombardment.

[6] Bennett, Bonner, Mandeville, and Watt, Phys. Rev. **70**, 882 (1946); S. J. Bame, Jr., and L. M. Baggett, Rev. Sci. Instr. **20**, 839 (1949); B. E. Watt, Rev. Sci. Instr. **17**, 334 (1946).

[7] Herb, Snowdon, and Sala, Phys. Rev. **75**, 246 (1949).

TABLE I. Scattering of 873.5-kev protons from a 34 μg/cm² Au target for various widths and positions of openings of the slit $S4$ located at 90° of trajectory arc.

Width of slit S_4 (inches)	Displacement (inches) of the center of the opening at S_4 relative to the mean circle of the annulus. (+out, −in)	Intercept of tangent Mc/sec	Width at half-maximum Mc/sec
$\frac{1}{4}$	$-\frac{3}{8}$	16.290	0.047
$\frac{1}{4}$	$-\frac{1}{8}$	16.303	0.049
$\frac{1}{4}$	$+\frac{1}{8}$	16.332	0.046
$\frac{1}{4}$	$+\frac{3}{8}$	16.302	0.047
$\frac{1}{4}$	$-\frac{3}{8}$	16.300	0.047
$\frac{1}{4}$	$-\frac{1}{8}$	16.306	0.043
$\frac{1}{4}$	$+\frac{1}{8}$	16.291	0.043
$\frac{1}{4}$	$+\frac{3}{8}$	16.295	0.050
1	0	16.294	0.050
$1\frac{1}{2}$	0	16.294	0.052
2	0	16.306	0.055

III. THE ASSIGNMENT OF MOMENTUM TO PARTICLE GROUPS

Since the particle momenta were to be assigned from a knowledge of the radius of curvature in the magnetic

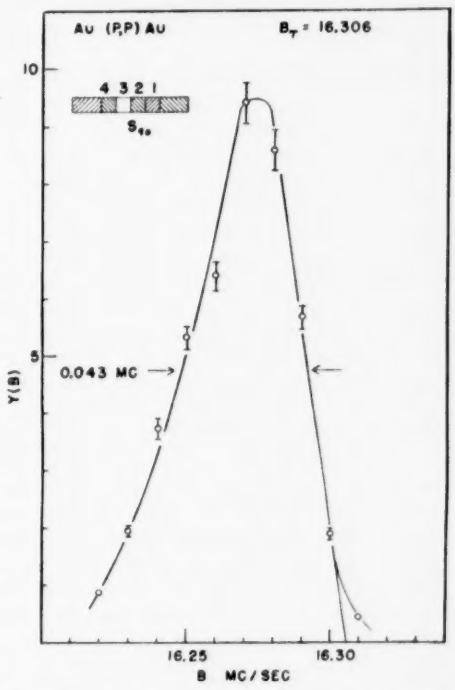

FIG. 2. Proton counting rate *versus* magnetic field for protons elastically scattered by a 34 μg/cm² evaporated Au layer. The energy of the scattered protons is about 855 kev.

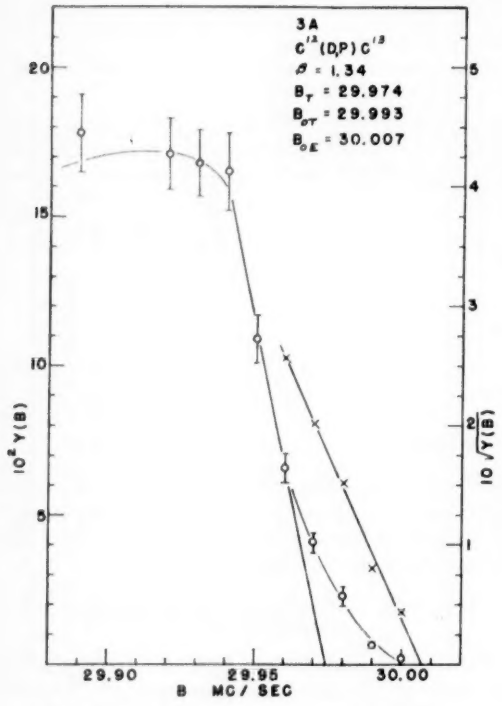

FIG. 3. Proton counting rate *versus* magnetic field for protons from $C^{13}(d, p)C^{13}$ (thick target).

field, it was necessary to develop criteria for this assignment and to understand the focusing properties of the spectrometer. The focusing characteristics of the field were investigated by the scattering of protons, whose energy was standardized with the 873-kev resonance of the $F^{19}(p, \alpha\gamma)O^{16}$ reaction. The target was a thin layer (34 μg/cm^2) of gold evaporated onto an aluminum foil. A typical counting rate *versus* magnetic field curve is shown in Fig. 2. Between successive bombardments the slit S_4 at the trajectory arc angle $\phi = 90°$ was changed in position and width, so that the focusing properties of each part of the field could be observed. In Table I are recorded the widths at half-maxiumm of the peaks, and the intercept, B_T, of the tangent to the peak on the high momentum side. When more than the central one-half of the annulus was open at $\phi = 90°$, it was observed that the peaks developed tails on both sides, and that the peak counting rates did not increase proportional to the solid angle. For this reason the slit S_4 was permanently set so that just the central half of the annulus was open. The intercept, B_T, obtained from the data using different one-quarter inch fractional apertures of the central one inch of the annulus were as consistent as it was possible to reset and maintain the incident proton energy. The spread of ± 0.008 Mc/sec (excluding one bombardment) corresponds to a variation of the generator voltage of ± 0.9 kev. The widths of the peaks agreed with that expected from the thickness of the target, and source size and detector slit width.

Thus, it was concluded that the extrapolated end point was a reliable measure of the particle momenta, and further that this end point did not vary over the particle trajectories in the usable region of the annulus. The observations implied that, to the limits of our ability to discern, the spectrometer acted as an ideally focusing instrument; a line should be focused to a line. Hence, it seemed reasonable to assign as the radius of curvature, r_0, one-half the distance between the inner edges of the slits S_2 and S_5. This distance is the natural one that arises in the analysis of line shapes for an ideally focusing instrument and is the radius of curvature of the first particles to be detected when the magnetic field, initially too large, is lowered to allow the group to enter the detector. The Appendix B discusses the analysis of line shapes.

The shape of lines to be expected from thick targets indicated that the lower part of the high momentum edge is parabolic and that, if the square root of each datum point in this region is plotted, the intercept, B_{0E}, of the resulting straight line is the magnetic field corresponding to r_0. The analysis also indicated that the tangent at half-maximum to the group on the high-momentum side possesses an intercept, B_T, that when appropriately corrected upwards corresponds to r_0 also.

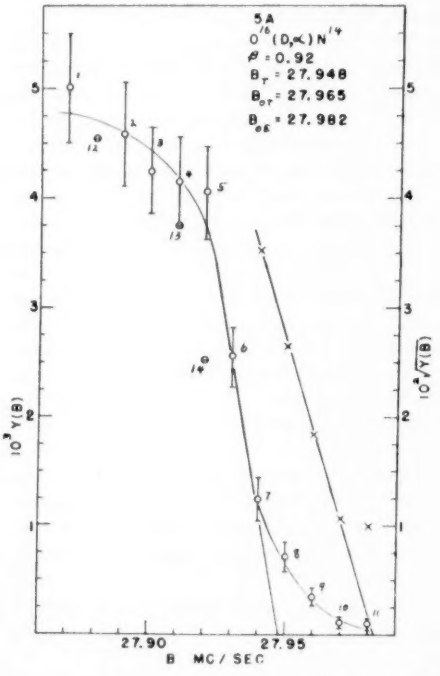

FIG. 4. Alpha counting rate *versus* magnetic field for alpha particles from $O^{16}(d, \alpha)N^{14}$. Points plotted as θ's were taken last and show the shift due to formation of carbon contamination.

Both of these methods were used for the $C^{12}(d, p)C^{13}$ reaction and gave satisfactory agreement. When thin targets were used, the tangent to the linear part of the high momentum edge of the peak was extended to zero counting rate, and the intercept, B_T, corrected upwards to obtain the true magnetic field, B_{0T}.

IV. RESULTS

The measurements of the Q values for three nuclear reactions are discussed below, along with a description of an absolute determination of the resonant energy of a level in Ne^{20} excited by the $F^{19}(p, \alpha\gamma)O^{16}$ reaction.

$C^{12}(d, p)C^{13}$

Altogether, eight determinations were made on the particles from this reaction. The corrected extrapolated end points appeared to be independent of the source width and the thickness of the target and thus lent credence to the line shape analysis. In order to test the validity of corrections to the field necessitated by small field variations along the trajectory arc angle ϕ, the magnet was reshimmed so that the correction changed in magnitude and sign. The corrected end points before and after shimming showed satisfactory agreement. This reaction also served to monitor the rigidity of the system, by determining the location of the proton group before and after the determination of the other reactions. Since the maximum yield from a thick target of carbon bombarded by deuterons was well established by these measurements, it was then possible to determine quickly the amount of carbon that had accumulated on other targets by observing the $C^{12}(d, p)C^{13}$ maximum yield. This procedure only required a few minutes of bombardment.

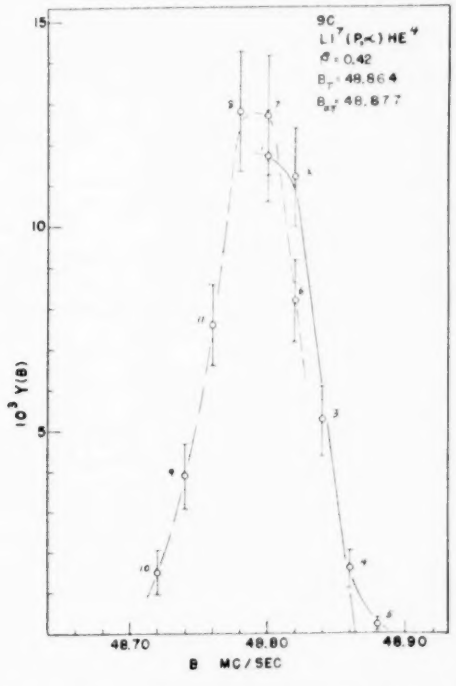

FIG. 5. Alpha counting rate *versus* magnetic field for alpha particles from $Li^7(p, \alpha)He^4$. The high momentum edge was first obtained. The remainder of the curve (dashed) shows effect of carbon contamination layer.

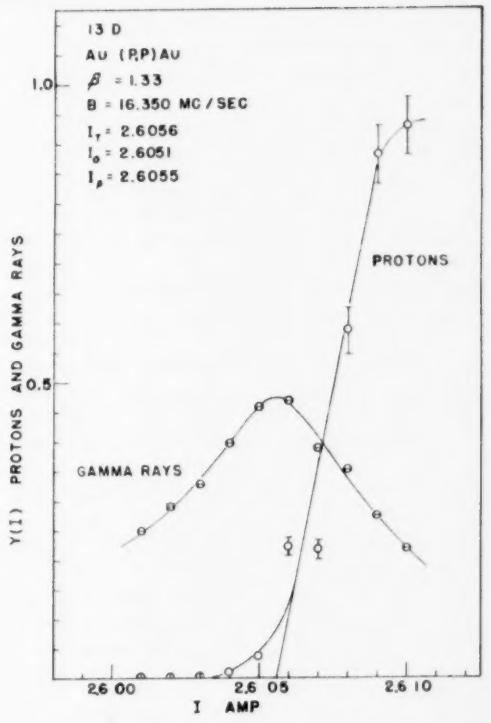

FIG. 6. Determination of the 873.5-kev gamma-ray resonance in $F^{19}(p, \alpha\gamma)O^{16}$. The spectrometer field was held constant and the bombarding energy varied. Circles are the scattered protons; the points, θ, are the gamma rays.

Typical thick target data, with the square root of the parabolic tail plotted, and with the tangent at half-maximum constructed, is shown in Fig. 3.

$O^{16}(d, \alpha)N^{14}$

Thick targets of copper oxide were used, and the data for one measurement are shown in Fig. 4. The corrections for carbon contamination, as discussed above, applied to E_1 and E_2 were -1.8 kev and $+5.0$ kev, respectively. The yield from this reaction is relatively weak and necessitated long bombardments and the consequent accumulation of the carbon layer. The data points plotted as θ show the downward shift that the particles momenta suffered due to the surface layer.

$Li^7(p, \alpha)He^4$

The targets for these experiments consisted of 60 $\mu g/cm^2$ of LiF evaporated onto 0.2 mg/cm^2 aluminum foils. The data of one bombardment are shown in Fig. 5. The carbon contamination corrections applied to E_1 and E_2 were -1.2 kev and $+2.6$ kev, respectively.

$Au(p, p)Au$

A redetermination of the position of the 873.5-kev resonance in $F^{19}(p, \alpha\gamma)O^{16}$ was made by the scattering of protons from a 5 $\mu g/cm^2$ gold layer evaporated on an aluminum foil. One determination was obtained by setting the energy of the proton beam at the peak of the gamma-ray resonance and then varying the field of the spectrometer to obtain the momentum of the scattered proton group. The second method consisted of varying the energy of the incident protons while the field in the spectrometer was held constant. At each energy the proton beam was first intercepted by a thin CaF_2 target and the gamma-ray yield from the target recorded, and then the beam was passed into the spectrometer and the yield of scattered protons recorded. These data are shown in Fig. 6. Corrections for the thickness of the CaF_2 target were determined by comaprison with a very thin target. No carbon contamination correction was applied to the data, but an error of 1 kev was assigned for this possibility.

A summary of these measurements and their assigned errors is presented in Table II. The Q values, calculated as is indicated in Appendix C, are also tabulated for the three transmutations, while for the gold scattering the Q value must be zero and so the bombarding energy at resonance can be calculated.

CONCLUSIONS

The energy values determined from these measurements are compared with other recent precise determinations in Table III. It is seen that in all of the cases the agreement is rather close.

In the case of the $C^{12}(d, p)C^{13}$ reaction the Q value of this report falls about at the mean of the two previous determinations,[5,8] which had shown a realtively large dispersion.

For the $Li^7(p, \alpha)He^4$ and the $O^{16}(d, \alpha)N^{14}$ reactions the Q values of this experiment overlap in probable errors with the previous accurate measurements,[8–10] while the redetermination of the resonance enregy of the 873-kev for the $F^{19}(p, \alpha\gamma)O^{16}$ reaction agrees reasonably well with the earlier standard.[7]

Thus, it can be concluded that the results of these experiments have not revealed any errors in the natural alpha-particle energy scale,[4] nor in the electrostatic energy scales.[7,9]

As an example of the disagreement that remains between nuclear and mass-spectroscopic mass values, we

TABLE II. A summary of the measurements of the three nuclear reactions and the resonant energy determination experiment.

Experiment No.	Reaction	Extrapolated end point Mc/sec: From square root plot	Extrapolated end point Mc/sec: From correction of intercept of tangent	Extrapolated end point Mc/sec: Mean	Field correction Mc/sec	Final end point Mc/sec	Bombarding energy before contamination correction Mev
1	$C^{13}(d, p)C^{13}$		29.995	29.995	+0.065	30.060	0.8755
2			29.990	29.990	+0.065	30.055	0.8747
3		30.007	29.993	30.000	+0.065	30.065	0.8760
4			29.995	29.995	+0.065	30.060	0.8769
6			29.996	29.996	+0.065	30.061	0.8778
7		29.995	29.998	29.996	+0.065	30.061	0.8782
11		30.081	30.080	30.080	−0.019	30.061	0.8767
						30.060	0.8765
						±0.005	±0.0023
						Mean	Mean
5	$O^{16}(d, \alpha)N^{14}$	27.982	27.965	27.973	+0.061	28.034	0.879
						±0.008	±0.002
9	$Li^7(p, \alpha)He^4$		48.887	48.877	−0.005	48.872	0.8758
10			48.881	48.881	−0.005	48.876	0.8758
						48.874	0.8758
						±0.005	±0.0014
						Mean	Mean
12	$Au(p, p)Au$		16.357	16.357	−0.013	16.344	
13			16.352	16.352	−0.013	16.339	
						16.341	
						±0.005	
						Mean	

[8] Strait, Van Patter, Buechner, and Sperduto, Phys. Rev. **81**, 747 (1951).
[9] Craig, Donahue, and Jones, Phys. Rev. **88**, 808 (1952).
[10] Collins, McKenzie, and Ramm, Proc. Roy. Soc. **A216**, 242 (1953).

have calculated the mass of N^{14}. To do this one must assume masses for the deuteron and alpha particle. The values given by Li, Whaling, Fowler, and Lauritsen[2] have been used. The mass obtained for N^{14} is 14.07512 ($\pm$11) amu, while Nier[11] gives 14.007564 ($\pm$7) amu. These masses differ by 46 kev, which is considerably outside the errors assigned to the two determinations.

The redeterminations of the Q values with the Rice spectrometer are being continued.

The authors wish to thank Professor T. W. Bonner for his continued encouragement and advice. We wish to thank Mr. J. F. Vander Henst and Mr. Earl J. Harmening for construction of the vacuum tube, and Mr. C. R. Gossett for aid in operation of the accelerator and spectrometer.

APPENDIX A. MAGNETIC FIELD CORRECTIONS

At the conclusion of the measurements determining the magnetic rigidity of a particle group, the variation of the magnetic field with the trajectory arc angle ϕ was investigated. The vacuum tube was removed from the annular gap of the magnet and a proton moment magnetometer was used to measure these variations with respect to the magnetometer that regulated the magnetic field. The measurements were carried out with both the 180° magnetic spectrometer and the beam analyzing magnet at the field strengths used in the preceding experiments. A typical result of such a measurement is shown in Fig. 7.

TABLE III. Q values reported in this work compared with other determinations.

	This report Mev	Previous determinations Mev
$C^{12}(d, p)C^{13}$	2.722±0.004	2.716±0.005[8] 2.732±0.006[5]
$O^{16}(d, \alpha)N^{14}$	3.119±0.005	3.112±0.006[8] 3.119±0.005[2] 3.113±0.003[9]
$Li^{7}(p, \alpha)He^{4}$	17.344±0.013	17.340±0.014[8] 17.338±0.011[2] 17.352±0.009[10]
$F^{19}(p, \alpha\gamma)O^{16}$ resonance	0.8725±0.0018	0.8735±0.0009[7]

The correction δB, to the observed field, $B(0)$, at the source, necessary to give the effective field was that given by Hartree:[12]

$$\delta B = \tfrac{1}{2}\int_0^{\pi} \Delta B(\phi)\, \sin\phi d\phi,$$

where $\Delta B(\phi) = B(\phi) - B(0)$.

[11] A. O. Nier, Phys. Rev. **81**, 624 (1951).
[12] D. R. Hartree, Proc. Cambridge Phil. Soc. **21**, 746 (1923).

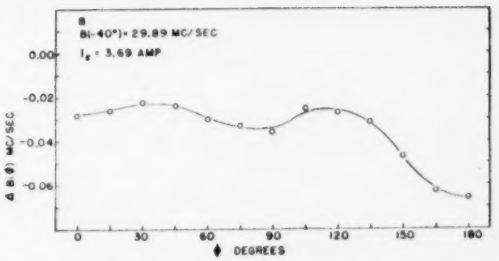

FIG. 7. The deviation of magnetic field strength, expressed in Mc/sec, *versus* the trajectory arc angle ϕ, measured from the target position.

APPENDIX B. LINE SHAPE ANALYSIS

The results of the scattering of protons from gold as performed in the Rice spectrometer indicated that: (1) the central one-half of the available solid angle produces a group whose extrapolated end point was a reproducible relative measure of the particle momentum (2) the line width was entirely explicable as due to the source and detector slit widths. The facts presented in Sec. III indicated that to a good approximation the spectrometer acted as a perfect focusing one; it acted as though it focused a line source of monoenergetic particles to a line. If this is assumed and if it is also assumed that the source emits equal numbers of particles per unit momentum interval, and that the momentum loss of particles produced in a thick target is proportional to the depth in the target, then one may derive a simple theory of the line shape to be expected.

The symbols are defined as:

W_s, W_c are the widths of the source and detector slits, respectively.
h is the height of the slits.
σ is the cross section for the reaction $\times N$, the number of atoms/cm^3, $\times 1/e$, where e is the electronic charge in μ coulombs.
Ω is the acceptance solid angle of the spectrometer.
P_0 is the momentum of particles originating at the surface of the target.
k_1 and k_2 are the stopping cross sections for the incident and observed particles in the target material.
ρ_0 is the radius of curvature of particles with momentum P_0 in a magnetic field B.
a is defined by $P_0 = aB\rho_0$, so that $a = Ze/\gamma$.
$p(\eta)$ is the observed momentum of particles originating at a depth η in the target is $P_0 - p(\eta)$, where $p(\eta) = (NP_0/2E_2)\times(k_1\partial E_2/\partial E_1 + k_2)\eta$ and C is a constant defined by the equation $p(\eta) = C\eta$.
x is the coordinate of a point in the focal plane.
r_0 is one-half the distance from the inner edges of the source and detector slits.

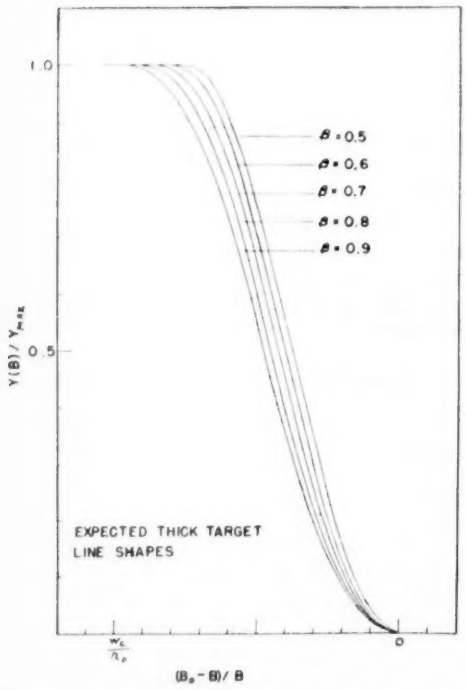

FIG. 8. Expected thick target line shapes. The ratio, $Y(B)/Y_{max}$, of yield to maximum yield is plotted *versus* the normalized magnetic field strength $(B_0-B)/B$, where B is the magnetic field and (B_0-B) is the deviation from the end-point field B_0. Curves for various values of the ratio, $\beta=W_s/W_c$, of the source to list widths are presented.

The particles originating in a volume element $d\tau=hW_s d\eta$ in the target are focused into a rectangular intensity distribution $n(x,\rho_0)d\eta$ in the focal plane, where

$$n(x,\rho_0)=(\Omega\sigma/W_s)$$

for

$$2\rho_0(1-p(\eta)/P_0)-W_s\leqslant x\leqslant 2\rho_0(1-p(\eta)/P_0)$$

and $n(x,\rho_0)=0$ otherwise.

The number arriving at x in dx is

$$N(x,\rho_0)=\int_{\eta_1}^{\eta_2} n(x,\rho_0)d\eta.$$

Then for $W_s\geqslant 2\rho_0-x$, $\eta_1=0$ and $\eta_2=(P_0/2C\rho_0)(2\rho_0-x)$, while for $W_s\leqslant 2\rho_0-x$, $\eta_2-\eta_1=P_0W_s/2C\rho_0$. Thus

$$N(x,\rho_0)=(\Omega\sigma aB/2CW_s)(2\rho_0-x) \quad \text{for} \quad 0\leqslant 2\rho_0-x\leqslant W_s;$$

$$N(x,\rho_0)=(\Omega\sigma aB/2C) \quad \text{for} \quad 2\rho_0-x\geqslant W_s.$$

The number of particles that enter the detector slit is then given by:

$$Y(B)=(ABr_0^2/W_s)[(B_0-B)/B]^2 \quad \text{for } 0\leqslant(B_0-B)/B\leqslant W_s/2r_0;$$

$$Y(B)=ABr_0[(B_0-B)/B-W_s/4r_0] \quad \text{for } W_s/2r_0\leqslant(B_0-B)/B\leqslant W_c/2r_0;$$

$$Y(B)=(ABr_0^2/W_s)\{W_sW_c/2r_0^2-[(B-B_0)/B-(W_s+W_c)/2r_0]^2\} \quad \text{for } W_c/2r_0\leqslant(B_0-B)/B\leqslant(W_s+W_c)/2r_0;$$

$$Y(B)=ABW_c/2 \quad \text{for} \quad (W_s+W_c)/2r_0\leqslant(B_0-B)/B;$$

where $A=\Omega\sigma a/C$ and $W_s<W_c$. Similar expression may be obtained for $W_s>W_c$. Typical thick target line shapes are shown in Fig. 8 for $W_s<W_c$.

Two facts are to be noted from this analysis: (1) the high momentum edge of the line is parabolic, and if the square root of the experimental $Y(B)$ is plotted in this region, then the true end point B_0 is the intercept of the resulting straight line with the abscissa. (2) The line at half-maximum is linear and an extrapolation of this line to the abscissa, corrected upwards by the factor $(1+W_s/4r_0)$ for $W_s<W_c$ and $(1+W_c/4r_0)$ for $W_s>W_c$, will yield the same true end point B_0.

Thin target curves may be easily obtained by subtracting two thick target curves where one curve is displaced by a distance in the focal plane given by

$$\delta=(r_0\Delta E_1/E_2)(\partial E_2/\partial E_1+k_2/k_1).$$

The resultant distributions are triangular or trapezoidal, and when integrated over the finite detector slit width, various types of line shapes are obtained. One can easily see, however, that there will again be a linear portion to the high momentum edge of the line and the intercept of this may be corrected, upwards to give the true end point. The correction factors are $(1+\delta/4r_0)$ for $\delta<W_s$, $W_s<W_c$, and $(1+W_s/4r_0)$ for $W_s<\delta$, $W_s<W_c$.

APPENDIX C. CALCULATION OF Q VALUES

The equations used for computing the Q values were[3]

$$Q=E_2+E_3-E_1,$$

and since the observation angle $\theta=\pi$ the momenta obey the scalar relations

$$P_3=P_1+P_2.$$

The spectrometer measures the nonrelativistic energy $P_2^2/2M_2$, where

$$(2\pi^2Z_2^2/10^{14}\gamma_p^2)(M_p/M_2)(e/M_p)B_0^2r_0^2=P_2^2/M_2,$$

and this energy is related to the relativistic energy by

$$E=P^2/2M-E^2/2MC^2.$$

We have used $\gamma_p=(2.67523\pm0.00006)\times10^4$ sec^{-1} gauss^{-1}, and $e/M_p=(9579.4\pm0.3)$ emu/g.[13,14]

In the above formula P_2, M_2, and Z_2 are the momentum, mass, and charge number of the analyzed particles, while r_0 is one-half the distance in centimeters between the inside edge of the source and the inside edge of the detector slit. B_0 is the corrected end point of the line expressed in mc/sec. Nuclear masses were used in the calculations.[2]

[13] Summer, Thomas, and Hipple, Phys. Rev. **82**, 697 (1951).
[14] J. W. M. DuMond and E. R. Cohen, Phys. Rev. **82**, 555 (1951).

Radiations from Zr^{89}*†

F. J. Shore,‡ W. L. Bendel,§ H. N. Brown,|| and R. A. Becker
Department of Physics, University of Illinois, Urbana, Illinois

(Received April 1, 1953)

A betatron-induced γ, n reaction on Zr^{90} has been found to produce a third branch in the decay of the 4.4-minute state of Zr^{89}. The new branch includes a 1.53-Mev gamma ray (8 percent as intense as the 588-kev gamma ray) coincident with positrons of approximately 850-kev maximum energy. These particles (log ft = 4.2±0.1) are in competition with the 2.4-Mev positron group (log ft = 6.9±0.3) emitted in the decay, to the ground state of Y^{89}, of the 4.4-minute Zr^{89m}. Anomalous behavior of the comparative half-lives is indicated, since both the 2.4-Mev and the 901-kev, 79-hour positron transitions are thought to be allowed. $K/(L+M)$ conversion ratios for the 4.4-minute, 588-kev and the 79 hour, 913-kev gamma radiations are, respectively, 5.4±0.7 and 7±2. A ten-channel scintillation spectrometer, based on a cathode-ray tube, light pipes, and photomultiplier tubes, to effect pulse-height selection, is also described.

I. INTRODUCTION

RECENT experiments by Shure and Deutsch,[1] and Goldhaber *et al.*[2] have shown that the 79-hour activity in Zr^{89} decays mainly with the emission of a positron of about 900-kev maximum energy, followed by a 14-second gamma ray of similar energy. As a result of considerations of lifetime, energy, and total conversion coefficient for the gamma ray, the multipolarity of the radiation was set by them as magnetic 2^4-pole ($M4$). Preliminary findings concerning the associated 4.4-minute decay process in Zr^{89} have been reported[3] by this laboratory. In this work it was found that the 4.4-minute state of zirconium (interpreted as an isomer of Zr^{89}, and designated as Zr^{89m}) decayed, principally by the emission of partially-converted, 588-kev gamma radiation to the ground state of Zr^{89}, and somewhat by the emission of a high-energy positron of about 2.4-Mev maximum energy. In the course of that work some of the salient features of the 79-hour activity were confirmed.

Subsequent measurements in this laboratory, of the 4.4-minute activity, have revealed the presence of an additional gamma ray of 1530-kev energy, apparently following a positron group of about 850-kev maximum energy. The intensity of the 850-kev transition is deduced to be over ten times that of the 2.4-Mev transition to the ground state of Y^{89}. Consequently an abnormally low log ft value results if the low-energy group is indeed concerned with Zr^{89}, and not with another isotope or an impurity. Since the association of the low-energy group with Zr^{89m} has such disturbing consequences, it was necessary to investigate in detail whether or not the transition is concerned with Zr^{89m}. A number of experiments, performed in order to accomplish this end, are described below.

A ten-channel scintillation spectrometer, employing a cathode-ray tube, together with associated light pipes and phototubes as a discriminator, found extensive use in the present experiments. A discussion of the design and properties of this instrument comprises most of Sec. II.

II. APPARATUS

In the course of this work use was made of two magnetic beta-ray spectrometers, a 180° type previously described,[4] and a 255° double-focusing type with a 15-cm mean-radius of curvature. Coincidence measurements were made with scintillation detectors employed in conjunction with either of two coincidence circuits. The faster of these had a resolving time of 2×10^{-8} second. Coincident pulses were selected in a Rossi type mixer using crystal diodes. The second circuit, with a resolving time of approximately a microsecond, employed blocking oscillators for pulse shaping, and a *6AS6* tube to select coincident pulses.

Extensive use was made of a 10-channel scintillation spectrometer in which pulse-height selection was effected by means of a gated-beam cathode-ray tube (C.R.T.) on the screen of which were disposed 10 light pipes, and associated photomultiplier tubes and circuits. In Fig. 1(a) there is presented a block diagram which indicates the arrangement of the parts of the pulse-height discriminator. In Fig. 1(b) is shown the time sequence and flat-topped shape[5] of pulses which occur on the vertical deflecting plates and intensifier grid of the C.R.T. for two input pulses of different amplitude. Corresponding to two input pulses of Fig. 1(b), there are observed on the screen of the C.R.T., two stationary light spots. These differ in vertical

* Aided by the joint program of the U. S. Office of Naval Research and the U. S. Atomic Energy Commission. The AEC is also to be thanked for the radioisotopes Na^{22}, Cs^{137}, Hg^{203}, and the separated zirconium isotopes employed in this work.

† This work was taken from the Ph.D. dissertation of F. J. Shore, Jr.

‡ Now at Brookhaven National Laboratory, Upton, Long Island, New York.

§ U. S. Atomic Energy Commission Predoctoral Fellow. Now in the Nucleonics Division, U. S. Naval Research Laboratory, Washington 20, D. C.

|| National Science Foundation Predoctoral Fellow.

[1] K. Shure and M. Deutsch, Phys. Rev. **82**, 122 (1951).

[2] Goldhaber, der Mateosian, Scharff-Goldhaber, Sunyar, Deutsch, and Wall, Phys. Rev. **83**, 661 (1951).

[3] Shore, Bendel, and Becker, Phys. Rev. **83**, 688 (1951).

[4] Brown, Bendel, Shore, and Becker, Phys. Rev. **84**, 292 (1951).

[5] The pulse shaping circuit is that of D. A. Watkins, Rev. Sci. Instr. **20**, 195 (1949).

displacement and temporal occurrence, but are the same in duration and brightness. These light pulses are conducted through different light pipes to separate photomultiplier tubes (Type 931-A). The light pulses are than transformed into electrical signals which actuate scales-of-10 and mechanical registers.

A channel acceptance window is determined mainly by the relative sizes of the light spot and of the defining aperatures for the light pipe. When the light spot is only partially within the acceptance window of the light pipe, an uncertainty arises in the triggering of the scalers. This uncertainty may be large if the spot size is comparable to that of the light pipe. It was found that with a channel acceptance window having approximately 6 times the diameter of the spot, and with channel-center separations of 8 spot diameters, a pulse-height discriminator resulted for which effective widths of single channels varied by as much as 1 percent per hour. This permitted energy and intensity measurements to be made over periods of a few hours, after which it was advisable to check the channel widths.

A type 5CP5A C.R.T. was employed with the cathode at -1800 v and the post-accelerating electrode at $+1800$ v. The positive intensification pulses which were applied to the C.R.T. control grid were flat-topped with an amplitude of 35 v and a duration of 1.5 microseconds.

In order to test the performance of the discriminator, a pulse generator was employed. This gave flat-topped pulses of variable amplitude and 1-microsecond duration at a repetition rate of 60 per second. Shown in Fig. 2 is a typical channel profile. The shape is essentially that of a rectangle with narrow triangular wings, the latter comprising about 3.5 percent of the total area under the profile curve.

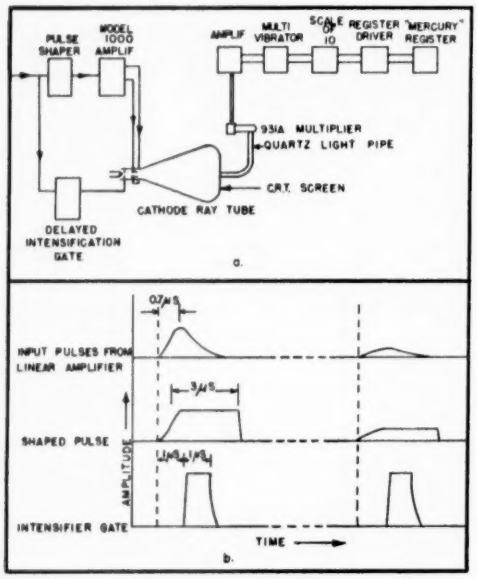

FIG. 1(a). Block diagram of the differential pulse-height discriminator. One channel is shown in the diagram; (b) Sequence of input, shaped, and intensifier pulses. Two different pulse heights are shown. [Note that the final shaped pulse arriving at the intensifier gate (bottom curves) is the same in both cases.]

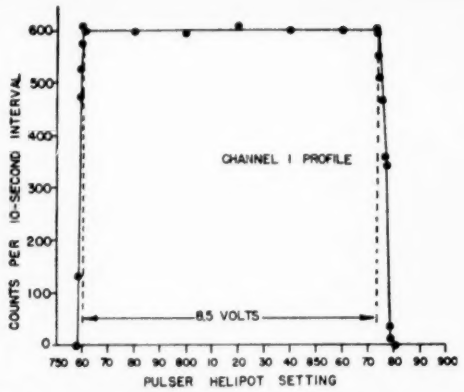

FIG. 2. Typical channel profile. For a given point, counts are recorded for 10 seconds with input pulses of fixed amplitude. The amplitude then is varied to obtain the remaining points.

The linearity of the positions of the channel centers was investigated by employing a constant amplitude input pulse and varying the position of the spot for zero pulse amplitude. It was found that the deviation of the separation of adjacent channels from the average separation did not exceed 2 percent. Keeping the sensitivity constant and varying the position of the spot for zero pulse amplitude, the instrument could be made to examine spectra comprising 28 channel-center separations with a linearity of better than 2 percent.

The scintillation detectors usually were NaI(Tl) crystals. These were mounted inside of air-tight, diffusely-reflecting units placed on top of 5819 photomultiplier tubes. The reflectors were thin Al hemispheres smoked on the inside with magnesium oxide. Both the crystal (cleaved in a dry box into parallelepipeds) and reflector were cemented to 1-mm thick glass disks by means of Gelva.[6] The power supply for the 5819 photomultiplier tube was stabilized to such an extent that over a period of 5 days the drift in output voltage was less than 0.05 percent. An Atomic Instrument Company, 204-C linear amplifier was employed to amplify the signals. It was modified by including crystal-diode limiters between certain stages in order to allow detection of small pulses in the presence of large ones.

III. DATA

Both the long and the short-period activities were produced in the 22-Mev betatron by means of the probe

[6] Made by Shawinigan Products Corporation, 350 Fifth Avenue, New York. The technique of J. S. Moenich and R. Swank of Argonne Laboratory, described by W. L. Buck in a private communication, was employed.

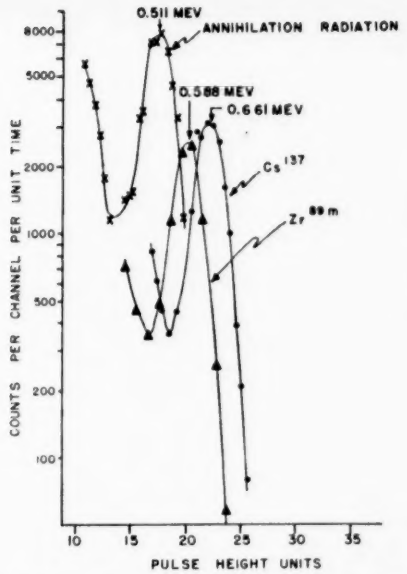

FIG. 3. Scintillation-spectrometer determination of the 588-kev gamma ray in Zr^{89m}. Comparison is made with annihilation radiation from Ag^{106} and with the 661-kev gamma ray following the decay of Cs^{137}.

technique[7] previously described. The sources usually were metallic foils (0.5 mil and 1.0 mil in thickness) of zirconium. For some of the irradiations, in order to check for the effect of impurities, chemically pure ZrO_2 was activated, due account being taken of the 126-second oxygen activity which was also produced. Finally, separated Zr^{90} was irradiated in order to eliminate the possibility of some of the radiations being associated with isotopes of zirconium other than Zr^{89}.

4. 4-Minute Radiations

1. Energy and Lifetime Measurements of the Gamma Radiation

The energies of the gamma radiation associated with the 4.4-minute activity were measured with the scintillation spectrometer mentioned above. The detector was a 1.2-cm cube of NaI(Tl). The instrument was calibrated by means of the 661-kev gamma ray of Ba^{137}, annihilation radiation, and the 1277-kev radiation from Ne^{22}. The results for the lower-energy range are displayed in Fig. 3. The peaks shown are produced by photoelectric absorption in the iodine of the crystal. Energywise they represent the total energy of the primary gamma ray, since most of the low-energy secondaries would be reabsorbed in the crystal. The center peak is due to 4.4-minute Zr^{89m}. Here a 1-mil zirconium foil was irradiated in the 22-Mev betatron. A mean of five determinations yielded a value of 588±3 kev. A measurement, described next, of the associated internal conversion line, with the 255° spectrometer yielded a value of 586±3 kev. Both figures agree with the previously reported value.[8]

Figure 3 furnishes a good picture of the resolution attainable with the scintillation spectrometer. The full width at half-maximum for the Ba^{137m} line is 12 percent, with a peak-to-valley ratio of 8.5. The upward trend of the points below the peaks is attributed to Compton absorption of the primary radiation. The peak counting rate of the 588-kev line in Fig. 3 was found to decay with a half-life of 4.5±0.5 minutes. This is in good agreement with the value 4.40±0.04 minutes found as a mean of four determinations of the half-life (primarily of the internal conversion electrons) employing a Geiger counter having a mica window of thickness 3.5 mg/cm².

The scintillation detector also revealed a photo peak corresponding to a high-energy gamma-ray line (not shown in Fig. 3). A mean of six determinations of the energy (including the use of separated zirconium isotopes, to be described below) yielded a value of 1.53±0.03 Mev. A mean of four determinations of the half-life of the high-energy radiation gave a value of 4.4±0.3-minutes, in good agreement with the half-life of the particles and of the 588-kev line. This suggests that the 1530-kev gamma ray is also associated with Zr^{89}.

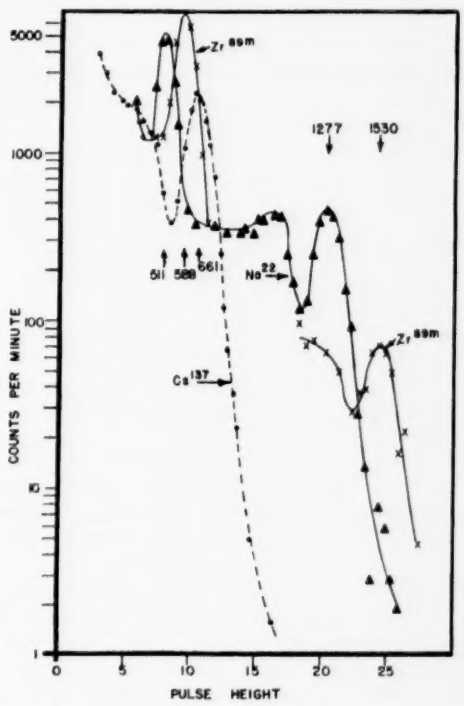

FIG. 4. Scintillation-spectrometer comparison of the gamma rays following the decay of Na^{22}, Cs^{137} with those of Zr^{89} produced from enriched $Zr^{90}O_2$.

[7] R. A. Becker, Rev. Sci. Instr. **22**, 773 (1951).

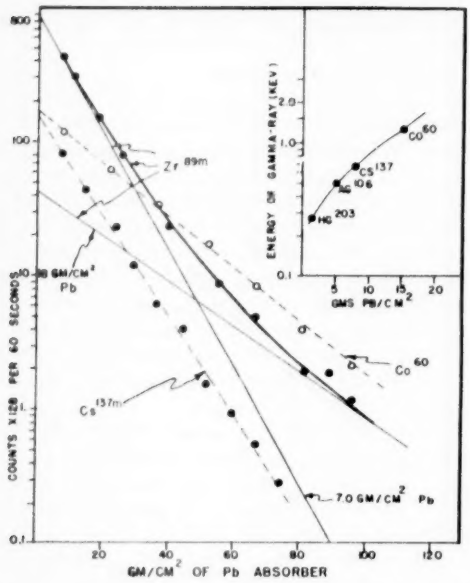

FIG. 5. Absorption in lead of the gamma radiation from Zr^{89m}. Shown for comparison are curves for Cs^{137} and Co^{60}. The inset shows the energy as a function of absorber half-thickness. The Zr^{89m} curve is decomposed into two straight lines corresponding to energies of 588 and 1530 kev.

2. Confirmation of the 1530-kev Radiation

It will be pointed out in Sec. IV, that the presence of the 1530-kev gamma ray, with an intensity as high as is here observed, introduces difficulty into the disintegration scheme. Consequently it was necessary to check carefully whether the 1530-kev radiation was real and associated with the decay of Zr^{89m}. That the radiation in question concerns the Zr^{90} isotope is supported by the fact that a source produced from enriched Zr^{90} ($Zr^{90}O_2$) yielded the same relative intensity for the 588 and 1530-kev radiation as did a source produced from commercial zirconium foil.

Data obtained from such an enriched source are presented in Fig. 4. The bump on the sodium calibration curve near 17 on the horizontal scale is interpreted as arising from Compton absorption of the 1277-kev radiation. Such "Compton peaks" accompany the photo lines in this type of instrument.[8] The effect of source decay was taken into account, and the relative peak heights at 588 and 1530 kev represent the apparent relative intensity of the two radiations, uncorrected for the relative efficiency of the detector.

Attention was also paid to such considerations as the adding together, or "pileup," of several pulses which occur close together in time, in such a way that the amplitude recorded for any one of them is increased by the presence of the others. Simultaneous detection of two quanta by the crystal may occur either if both are randomly distributed in time, or if they are "truly coincident" (such as being in cascade). The pulse amplitude which results in this case should be the sum of those for the component radiations. Evidence that this new gamma ray is not caused by such "pileup" in the crystal is furnished by the fact that the high-energy edge of the Ba^{137m} gamma ray is roughly a straight line over nearly three cycles of intensity in the semilog plot. In contrast it was found that the upper edge of the 588-kev curve from zirconium became nonlinear at 3 percent of the peak counting rate.

Additional verification that the 1530-kev gamma ray is real is obtained by noting that the decay rate and relative intensity of the two zirconium radiations are unchanged when the solid angle subtended by the detector at the source is varied.

The presence of radiation of energy greater than 588 kev is further confirmed by the Pb absorption curves, employing a scintillation detector, shown in Fig. 5. The source was 5 inches above the detector, which in turn was 15 inches above the top of a table. A Bakelite-lined Pb shield $\frac{5}{8}$ in. to $1\frac{1}{4}$ in. thick surrounded the detector in order to minimize scattering. The system was calibrated by means of data obtained with Hg^{203}, Cs^{137}, Ag^{106}, and Co^{60} sources in the decay of which are involved gamma rays, respectively, of energy 0.28, 0.66, 0.51,[9] and approximately 1.25 Mev. It is seen that the absorption curves for the Ni^{60} and Ba^{137m} radiations are linear over the ranges of absorber used, whereas that of the zirconium radiation is not, supporting the existence of radiation of energy higher than 588 kev. Making the assumption that the higher-energy radiation is indeed 1530 kev (18 g/cm²), results are obtained which are consistent with an energy of about 600 kev for the soft radiation.

3. Relative Intensity of the Gamma Rays

From the ratio of the extrapolated intercepts at zero absorber thickness, the relative intensity of the gamma rays was derived. A correction was made for the total absorption in the NaI of the two different energies. The result was $I_{588}/I_{1530}=12\pm3$.

The relative intensity was also determined with the scintillation spectrometer by means of a comparison of the zirconium radiation with the 1277-kev and annihilation quanta from Na^{22}. The ratio of the peak counting rates of the two 4.4-minute gamma rays, corrected for background and absorption in NaI, was compared to the two photopeaks obtained from Na^{22}. The ratio I_{511}/I_{1277} for Na^{22} was taken as $1.80_{-0.05}{}^{+0.25}$, since the gamma-ray transition in Ne^{22} follows positron emission from Na^{22} (10 percent K-capture assumed, although there is some experimental evidence[10]

[8] R. Hofstadter and J. A. McIntyre, Phys. Rev. **79**, 390 (1950); **80**, 631 (1950).

[9] Way, Fano, Scott, and Thew, *Nuclear Data*, Natl. Bur. Standards Circ. 499 (Government Prinitng Office, Washington, D. C., 1950).

[10] Good, Peaslee, and Deutsch, Phys. Rev. **69**, 313 (1946).

that there is no K-capture). By comparing the two ratios of corrected photopeak counting rates, the effect of counts appearing under the photopeaks via absorption of the secondary Compton photons in the NaI crystal can be largely canceled out. A small correction was applied in comparing the two ratios, to account for the variation with energy of the photoelectric absorption of Compton secondary photons. Employing a $(1.2\text{-cm})^3$ crystal, the peak counting rates for the zirconium radiation were estimated to correspond to an intensity ratio of $I_{588}/I_{1530}=14_{-4}^{+5}$. An average of this value with that of the Pb absorption result gave a figure of 13 ± 3 for the relative intensity.

The effect of betatron energy on the relative intensity of the gamma rays was also considered. Irradiation with x-rays of maximum energy 23.5, 22, 21, 17.5, and 14 Mev gave no appreciable change in the relative intensity of the gamma rays. Thus the ratio remains essentially constant even close to the experimental threshold of about 12.5 Mev for the Zr^{89} activity. Accordingly, detailed considerations involving experimental thresholds, calculated thresholds using the tables of Metropolis and Reitwiesner,[11] and estimated Coulomb barrier heights show that the 1530-kev gamma radiation cannot arise from a $(\gamma, 2n)$, (γ, d), (γ, t), (γ, p), or (γ, α) photoreaction. (The γ, p threshold also can be deduced empirically from the present work. See Fig. 9 below.)

Evidence tending to disprove that the 1530-kev radiation arises from an n-capture reaction is afforded by varying the probe material and/or probe geometry in the betatron irradiations. Since the bremsstrahlung are confined to a narrow cone in the forward direction, and since the neutron flux is approximately spherically symmetric, it is to be expected that variations in the position[7] of the material being activated behind the probe will produce large variations in the relative intensity of photo to n-capture processes. Such variations were not found for the 588- and 1530-kev radiations. Actually when the target was moved $\frac{1}{2}$ in. back from the probe tip no appreciable activity was observed at all. Further evidence that an n-capture process is not involved is given by changing the converter material at the probe tip from lead to copper. Again no variation in the relative intensity of the 1530- and 588-kev radiation was observed. Evidence disproving the existence of an n-capture-produced activity of half-life less than 5 minutes in separated zirconium isotopes is also given elsewhere.[9]

4. *High-Energy Positrons*

Indications have been cited previously[3] for the existence of a weak positron group at about 2.5-Mev maximum energy. The existence of 4.4-minute positrons has been confirmed in the present work by the detection of 180° coincidences which were ascribed to pairs of annihilation quanta. Two anthracene crystals were situated $4\frac{1}{2}$ inches apart and a Zr source was situated midway between the crystals in a small hole in a lead sheet. The sheet was normal to the line joining the crystals and was covered with a thick enough sheet of aluminum to stop 2.5-Mev positrons. The lead sheet was of sufficient thickness to attenuate backscattered Compton radiation by a factor of 10^3. The coincidence and the single-counting rates both decayed with a half-life of 4.4 minutes. (A small isotropic coincidence rate was also observed when the source was slightly displaced laterally from the position in line with the crystals. This is confirmed below by the measurement of particle-gamma coincidences.)

In order to fix the energy of the 4.4-minute particles, two anthracene crystals (1 in.$\times$1 in.$\times\frac{1}{2}$ in.), separated by about $\frac{1}{16}$ in. were attached to the end of a 5819. With sources placed between the crystals, particles which were backscattered out of one crystal were detected in the other. In this way the pulse heights for the positrons from Ag^{106}, Cu^{62}, and Zn^{63} were compared with those from Zr^{89m}. Figure 6 presents Kurie plots, uncorrected for resolution, of the spectra. The three runs, shown for Zr^{89m}, were taken with the same source at different times. The inset shows ϵ_0 (maximum total energy) for the three known end points. From this the end point for Zr^{89m} is deduced to be 2.43 ± 0.06 Mev. The apparent nonlinearity of the derived curve for ϵ_0 may be a property of the two-crystal geometry.

In addition, the maximum energy and the sign of

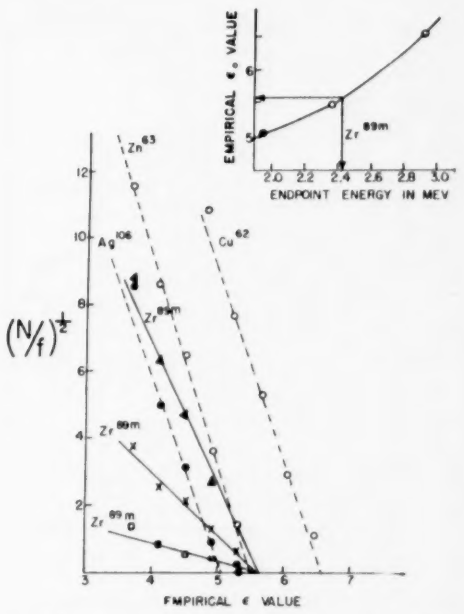

FIG. 6. Kurie plots comparing positrons from Cu^{62}, Zn^{63}, and Ag^{106} with Zr^{89m} in the split-crystal spectrometer.

[11] N. Metropolis and G. Reitwiesner, U. S. Atomic Energy Commission Report NP-1980 (unpublished).

the charge of the Zr^{89m} particles was confirmed by means of a Feather-absorption comparison with Cu^{62}, Zn^{63}, and Ag^{106} in the presence of a magnetic field.

5. Particle-Gamma Coincidences

For these measurements a resolving time of one microsecond was employed. Both the gamma and particle detectors were NaI(Tl) crystals, the former being 1.75 cm, and the latter 0.2-cm thick. A 6-g/cm² Pb absorber, interposed between the source and the gamma detector, attenuated the backscattered Compton photons. The source was a small piece of 1-mil zirconium foil. Aluminum absorbers were used to estimate the energy of the coincident particles. A study of the system was made with Co^{60}, Cs^{137}, Ag^{106}, and Hg^{203} to determine the counting rate *versus* amplifier gain characteristic of the gamma detector. The gain was so adjusted that the counting rate for 511-kev radiation was down by a factor of 2000 when the corresponding rate for the Co^{60} radiation was down by a factor of 5. In this way particle-annihilation-quanta coincidences were discriminated against.

Figure 7 shows the decay of the coincidences, for Al absorber thicknesses, on the particle side, of 0, 66, and 138 mg/cm². A half-life between 4 and 5 minutes is evident for each case. The data obtained with the singles rates (not shown), for both particles and gamma rays, confirmed the 4.4-minute half-life. The points plotted in the inset correspond to coincidence rates at zero time. A value of 59±6 mg/cm² of aluminum absorber was estimated as the half-thickness for the particles.

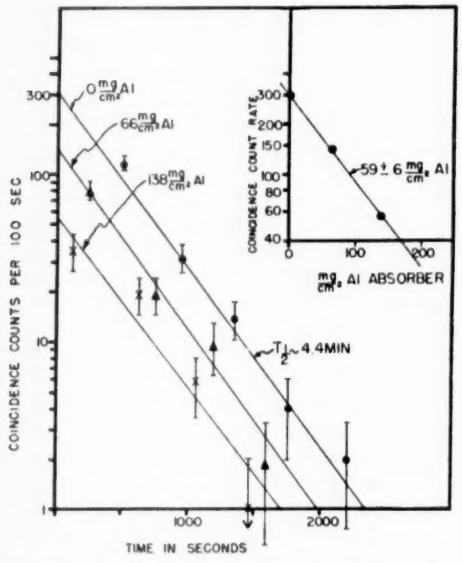

FIG. 7. Decay with time of coincidence counts for Zr^{89m} as a function of Al absorber placed in front of the particle counter. The gamma-ray counts are strongly biased against annihilation radiation. The inset shows the absorption curve of the particles.

Employing the same geometry, half-thicknesses were obtained (data not shown) for the positrons associated with Hg^{203}, and with 79-hour Zr^{89}. The measured half-thicknesses for these furnished the basis for an estimate of 850 kev as the end-point energy of the 4.4-minute particles. Similar results were obtained with the gamma counter biased still more strongly (annihilation radiation down by about 10^5). However, with the smaller coincidence rates the statistical uncertainties were larger.

Since the gamma spectrum in the scintillation spectrometer shows the presence of 588- and 1530-kev gamma rays only, the 1530-kev gamma ray must be involved in the coincidences with the 850-kev particle group since, in the present experiment, the 588-kev gamma rays would not be detected. As will be seen below, when the decay scheme is considered, this end-point energy is consistent with interpreting this group of particles as positrons. Additional support for this is obtained from the consideration of the relative intensities of the 4.4-minute x-rays from zirconium and yttrium.

6. Relative Intensities of the Particles as Determined by Absorption

The intensity of the 2.4-Mev positrons relative to the other 4.4-minute particles was derived from Al absorption measurements made with an end-window Geiger counter. In addition to penetrating radiation, there were two soft radiations which had half-thicknesses corresponding to beta energies of 2.9±0.6 Mev and 0.9±0.2 Mev. The latter group is thought to be comprised of both the 850-kev positrons and the conversion electrons from the 588-kev radiation, whereas the higher energy group is identified with the 2.4-Mev positrons. From the extrapolated counting rates at zero thickness, the relative numbers of 2.4-Mev to 850- and 570-kev particles is $0.06_{-0.02}^{+0.04}$.

7. Critical Absorption of X-Rays and x/γ Intensity Ratio

Since the decay of Zr^{89m} involves positron emission, K-capture, gamma radiation, and internal conversion, a knowledge of the relative intensity of x-rays to other radiations is desirable. The scintillation spectrometer revealed 4.4-minute x-rays of approximately 15 kev but, owing to the poor resolution, it was not possible, from the pulse-height distribution, to determine whether the radiation was characteristic of zirconium or yttrium. Critical absorption measurements, employing NaBr and RbCl, showed the presence of both Y and Zr x-radiation. The detector was a 0.1-cm thick NaI crystal on a 5819. The absorbers were placed close to the source to reduce detection of fluorescent x-rays characteristic of the absorber. An analysis of the results showed that the ratio of the intensities of the Y to the Zr x-rays is 1.4±0.5. The large uncertainty resulted mainly from

the difficulty in estimating how much background to subtract because of Compton events in the crystal.

An estimate was made of the intensity of the 4.4-minute x-rays relative to the 588-kev gamma rays in terms of the x-rays and 79-hour, 913-kev gamma rays. The method was to use two NaI scintillation detectors, one detector for x-rays (0.2 cm thick) and one for gamma rays (1.75 cm thick). The photomultipliers were so arranged that x and gamma radiation from the source alternately could be studied with the pulse-height discriminator. The data obtained were corrected for the instrumental variation, with energy, of the photopeak heights. This arose because of different primary absorption, in the crystal, of the two gamma rays via the photoelectric effect, and for the counts which appear under the photopeak via photoelectric absorption of the Compton secondary photons. The ratio of the two gamma-ray to x-ray ratios, $(N_g/N_x)_1$ and $(N_g/N_x)_2$, which were observed, respectively, for the 4.4-minute and 79-hour radiations, after the corrections were applied, was found to be 6.3 ± 2.

8. Relative Intensity of Positrons and Gamma-Rays

This was determined from 180° coincidence data following the method of Griffiths.[12] The anthracene crystals (1 in.×1 in.×½ in.) were 13 inches apart.

The relative efficiency of the detectors was determined from a knowledge of the singles and 180°-coincidence-counting rates when 24-minute Ag^{106} was studied with the same geometry. For this source, there is a 0.51-Mev gamma ray about 13 percent as abundant as the annihilation radiation which is present.[13] The relative efficiencies for the annihilation radiation, 588-kev, and 1530-kev gamma rays was estimated from the absorption data of Gillette[14] for anthracene.

The ratio of the positrons to 588-kev quanta was determined to be 0.019 ± 0.002. This included a correction for the presence of 1530-kev quanta to the extent of 8 percent of the 588-kev line.

9. $K/(L+M)$ Ratio for the 588-kev Radiation

Conversion electron spectra [see Fig. 8(a)] were studied with the 255° spectrometer using ½-mil metal foils (8m/cm²). The solid curve represents the contributions from all shells. The dashed curves represent the derived K and $L+M+\cdots$ electron lines. The ratio was found to be $K/(L+M)=5.4\pm0.7$. This is less than the previously reported value of 7 ± 2 obtained with the 180° spectrometer.[3]

10. Total Conversion Coefficient for the 588-kev Gamma Ray

The total conversion coefficient for the 588-kev gamma ray was estimated by using two detectors.

[12] G. M. Griffiths, Phys. Rev. **83**, 852 (1951).
[13] W. L. Bendel (private communication).
[14] R. Gillette, Rev. Sci. Instr. **21**, 294 (1950).

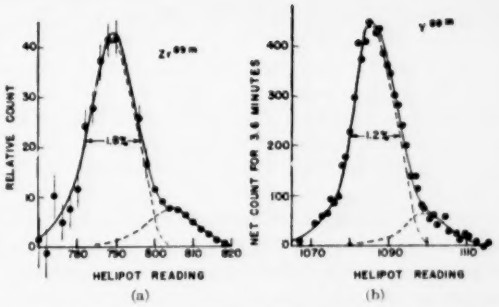

FIG. 8(a). Internal conversion electrons associated with the 4.4-minute, 588-kev transition; (b) Internal conversion electrons associated with the 913-kev transition following the 79-hour decay of Zr^{89}.

The intensity of the Zr^{89m} conversion electrons measured with one detector (less than 1-mm thick NaI) was compared to the intensity of the gamma rays measured in the other detector (1.2 cm-thick NaI). Employing the same geometry, a similar comparison was made for the Ba^{137m} 661-kev gamma ray. The particle line-spectra were superimposed on weak continua, and, for the Cs^{137} case, 5 percent of the area under the peak was subtracted to account for the 1.18-Mev particle continuum. For the Zr^{89m} case, a 10-percent contribution to the area under the electron peak, ascribed to the 850-kev positron group, was subtracted. The total conversion coefficient for Zr, computed with the aid of the results of Waggoner[15] and Bendel,[13] was $\alpha=0.076\pm0.014$.

79-Hour Radiations

1. Positrons and Conversion Electrons

The particle spectrum of the 79-hour activity was measured with the 180° magnetic spectrometer. The source was a 2-mm-wide strip of 1-mil ($\sim$16 mg/cm²) zirconium. The positron group reported previously[1,3] was confirmed, and found to have an end-point energy of 901 ± 10 kev, the difference between this value and the previous one[3] arising as a result of a better energy calibration of the spectrometer. The half-life for the particles was in agreement with the value of Shure and Deutsch.[1]

The 79-hour conversion line at 896 kev (913 ± 5 kev, upon adding the K binding energy of yttrium) has already been reported.

2. Gamma Radiation

The gamma radiation associated with the 79-hour activity was also investigated with the scintillation spectrometer, employing the 661-kev radiation of Ba^{137m} as a calibration. The measured value is 0.92 ±0.01 Mev, in good agreement with the more accurate measurement of the magnetic spectrometer.

[15] M. A. Waggoner, Phys. Rev. **82**, 906 (1951).

A careful search was made for gamma radiation of energy in the range 0.95 to 2.0 Mev, employing a separated Zr^{90} sample. None was found to be present. In particular, the gamma ray reported by Hyde and O'Kelley,[16] at 1256 kev, was not detected. The present measurements indicate that its intensity, if present, cannot be greater than one percent of the 913-kev gamma ray.

The relative intensity of the 913-kev and annihilation radiation was estimated in the same manner as that employed above for the 4.4-minute gamma radiation. The value for the ratio of 913-kev gamma rays to positrons was found to be 5 ± 1. This compares favorably with the value of Goldhaber *et al.*[2]

The decay with time of the 913-kev radiation was followed for several days with the scintillation spectrometer. By comparing the peak counting rates obtained with the zirconium to that with a Na^{22} source, a value of 79 ± 2 hours was obtained for the half-life. This is in good agreement with the more accurate value given by Shure and Deutsch.[1]

3. $K/(L+M)$ Ratio for the 913-kev Radiation

Figure 8(b) shows the conversion electron spectrum as obtained with the 255° spectrometer, employing an 8-mg/cm² source. The presence of the $(L+M)$ peak is derived by comparing, for comparable conditions, with the conversion lines associated with Cs^{137}. On the basis of relative peak heights the ratio is found to be 7 ± 2.

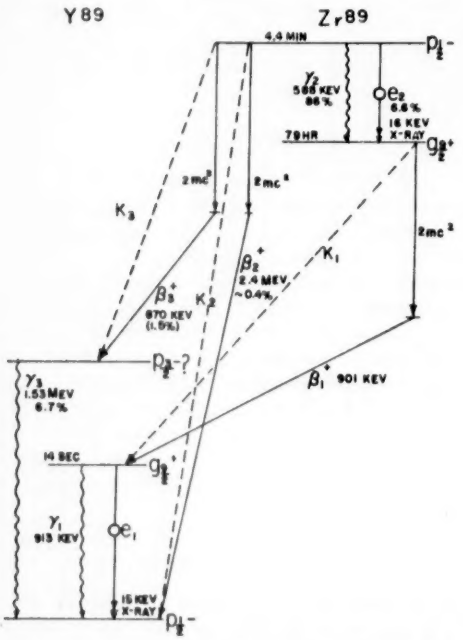

FIG. 9. Suggested decay scheme for the two zirconium activities. The intensities indicated are percentages of the total modes of decay of the 4.4-minute state of Zr^{89}.

IV. DISCUSSION

Figure 9 shows a tentative level scheme embodying the results of the present work and of the work previously reported.[1-3] The spin assignments and parities of the ground states and of the first excited states are as given before.[3] For the 588 and 913-kev gamma rays the conversion ratios determined in the present experiment provide additional confirmation that the two transitions are of the $M4$ type. The 1530-kev gamma ray and the 850-kev particles are indicated in the figure as a new branch of decay for 4.4-minute Zr^{89m}. The maximum energy of the particles is given in the diagram as 870 kev in order to yield consistent results for the energy difference between Zr^{89m} and Y^{89}, as determined from the remaining two branches of decay. It is to be recalled that the measured value, 850 kev, was subject to an uncertainty of 50 kev.

A compelling reason for placing the 4.4-minute state of Zr^{89} above the 79-hour state is the existence of several 4.4-minute branches, all of which have energetics consist with such a level scheme. Energy considerations also confirm that the 870-kev particles are positrons since the Nb^{89} ground state lies about 2.9 Mev above the Zr^{89} ground state (calculated from the tables of Metropolis and Reitwiesner[11]). Intensities are given for the radiation proceeding from the 4.4-minute state, each number representing a percentage of the total modes of decay of Zr^{89m}.

Much of the data employed in determining the relative intensities suffers because of limited counting rates and the short half-life involved. The gamma-ray coincidences at 180° gave, for the 4.4 minute radiations, $(\beta_2+\beta_3)/\gamma_2=0.019\pm0.002$ positron per 588-kev quantum. The absorption experiment yielded $\beta_2/(e_2+\beta_3)=0.06_{-0.02}{}^{+0.04}$. This, combined with the total conversion coefficient, $e_2/\gamma_2=0.076\pm0.014$, gave $\beta_2/\gamma_2=0.0054_{-0.0025}{}^{+0.0048}$. The experimental ratio, $\gamma_2/\gamma_3=13\pm3$, when combined with the theoretical[17] ratio of K-capture to positron emission, yields $\beta_3/\gamma_2=0.017\pm0.005$. Combining these, the relative intensities of the various 4.4-minute radiations are estimated to be $\gamma_2=0.86\pm0.03$, $\beta_2=0.0035_{-0.0015}{}^{+0.0024}$, $e_2=0.066\pm0.012$, $\gamma_3=0.067\pm0.012$, and $\beta_3=0.015\pm0.005$. These determine the comparative half-lives to be log $ft=6.9\pm0.3$ for β_2, and log $ft=4.2\pm0.1$ for (β_3+K_3).

The general features of the decay scheme are consistent with the measured x-ray intensities. The critical absorption experiment indicated that 4.4-minute x-rays of yttrium are 1.4 ± 0.5 times as numerous as are those of zirconium. An examination of the decay scheme reveals that only a negligible amount of the x-radiation

[16] E. K. Hyde and G. O'Kelley, Phys. Rev. **82**, 944 (1951); University of California Radiation Laboratory Report UCRL-1064, 1950 (unpublished).

[17] E. Feenberg and G. L. Trigg, Revs. Modern Phys. **22**, 399 (1950).

arises in transitions other than K_3 and e_2. Hence, as the fluorescent yields[18] for zirconium and yttrium are nearly equal, this gives $K_3/e_2=1.4\pm0.5$. Employing the theoretical β_3/K_3 ratio,[17] we have $\gamma_3/e_2=1.8\pm0.6$. Both L-capture and L-conversion have been neglected here. The branching ratios previously assigned indicate $\gamma_3/e_2=1.0\pm0.4$, which agrees roughly with the x-ray estimate.

When one examines the ft values for the three positron groups, anomalous behavior is apparent. Both the 901-kev group, log $ft=6.1$, and the 2.4-Mev group, log $ft=6.9$, are involved in allowed transitions, with no angular momentum or parity changes. It is evident that the comparative half-life in the second case is substantially larger than that for the first.

Even more unusual is the case of the comparative half-life for the transition to the 1.53-Mev Y^{89} state. In this instance log $ft=4.2$, and evidently we are concerned with a highly allowed transition. Hence $\Delta I=0, 1$ and, from Gamow-Teller rules, no parity change is expected. Thus the 1.53-Mev state must be either $p_{\frac{1}{2}}$ or $p_{\frac{3}{2}}$. The choice of $p_{\frac{1}{2}}$ would be consistent with Mayer's shell model, since the ground state has already been designated as a $p_{\frac{1}{2}}$ state. However, the comparative half-life is 600 times smaller than that for the $p_{\frac{3}{2}}$ to $p_{\frac{1}{2}}$ transition to the ground state, for which $\Delta I=0$.

If, following Mayer's shell model, we examine the nuclear configurations corresponding to the various states of zirconium and yttrium involved in these transitions, it becomes difficult to explain all three of the comparative lifetimes solely on the basis of single-nucleon transformations.

The anomalous behavior noted for the present Zr^{89} transitions is similar to that in two other apparent exceptions, recently found, to the usual rules of beta decay. The other cases are Y^{87} to Sr^{87}, studied by Mann and Axel,[19] and Kr^{85} (and Sr^{85}) to Rb^{85}, studied by Sunyar, Mihelich, Scharff-Goldhaber, and Goldhaber.[20] The latter authors have suggested that the large ft values, found in these three cases for transitions which presumably are allowed, and in which all of the nuclei are in the region of near-closed shells, each can be interpreted as being due to a rearrangement of nucleons in the even-even core of an odd-A nucleus.

[18] Steffen, Huber, and Humbel, Helv. Phys. Acta **22**, 167 (1949).

[19] L. G. Mann and P. Axel, Phys. Rev. **84**, 221 (1951).

[20] Sunyar, Mihelich, Scharff-Goldhaber, and Goldhaber, Phys. Rev. **86**, 1023 (1952).

Decay of K^{42}†

BERND KAHN AND W. S. LYON
Health Physics and Analytical Chemistry Divisions, Oak Ridge National Laboratory, Oak Ridge, Tennessee
(Received May 8, 1953)

The gamma spectrum of 12.44-hour K^{42} has been examined using a NaI(Tl) gamma-ray spectrometer. One gamma ray of energy 1.5 Mev has been found; the fraction of the decay proceeding through this transition is 0.200 ± 0.010.

THE nuclide K^{42} has recently been investigated using NaI(Tl) gamma-ray spectroscopy, 4π and 4π coincidence counting, absolute beta counting, beta-gamma coincidence counting, and high pressure ion chamber measurements. K^{42} was prepared by irradiating cp K_2CO_3 in the ORNL graphite reactor for periods varying from 16 to 62 hours. The K_2CO_3 upon removal was dissolved in water, made 0.1N in HCl and passed through an ion exchange column containing IR-100 resin.[1] No active fractions other than that containing K^{42} were found, indicating the K_2CO_3 to be quite free of other alkali metals. Half-life measurements using a high-pressure ion chamber were made on both purified and unpurified material. The value obtained over 7 half-lives was 12.44 ± 0.08 hours.

Measured aliquots of the K^{42} activity were examined on a NaI(Tl) gamma-ray spectrometer. Figure 1 is a plot of the γ-ray spectrum so obtained. Only one gamma ray was found; its energy is 1.51 Mev. The gamma-ray energy and the observed half-life are in agreement with data reported by Siegbahn.[2,3] The number of disintegrations going through the γ transition was obtained by multiplying the integrated area beneath the γ photopeak by an efficiency factor obtained from an experimentally determined plot of counter efficiency *vs* γ energy. In addition, the number of γ quanta was obtained with a calibrated high-pressure gamma ionization chamber measurement. The branching ratio was then determined by dividing this number by the number of absolute β disintegrations. This absolute disintegration rate was determined by 4π, 4π-coincidence counting and absolute β counting. For 4π counting a small aliquot of active material was evaporated on a thin $\sim$10-μg/cm^2 polystyrene film coated with $\sim$25-μg/cm^2 Al to render it conducting. The 4π counters were filled to $\frac{1}{2}$ atmosphere with methane and gave plateaus of over 200 volts. The gamma detector was a NaI crystal counter. The agreement between the 4π count and the 4π-coincidence count was within 0.5 percent. The absolute β count was made using a source mounted on 1 mg/cm^2 polystyrene film and a Tracerlab helium filled TG 1 GM counter as detector. The absolute disintegration rate of the K^{42} so obtained agreed with the 4π, and 4π-coincidence values. The fraction of the disintegrations occurring through the γ transition was found to be 0.200 ± 0.010.

Sources of K^{42} were also coincidence-counted using a beta-proportional thin end window tube as a β detector and the NaI crystal counter as a gamma detector. A large amount of weak continuous electromagnetic radiation is observed in the γ spectrum of K^{42} (Fig. 1), and therefore, at the suggestion of F. K. McGowan, the γ detector was biased to accept only radiation with energy greater than 0.3 Mev. Data so obtained agreed closely with the values obtained by the 4π method. The ratio of the beta counts to $\beta\gamma$ coincidence counts as a

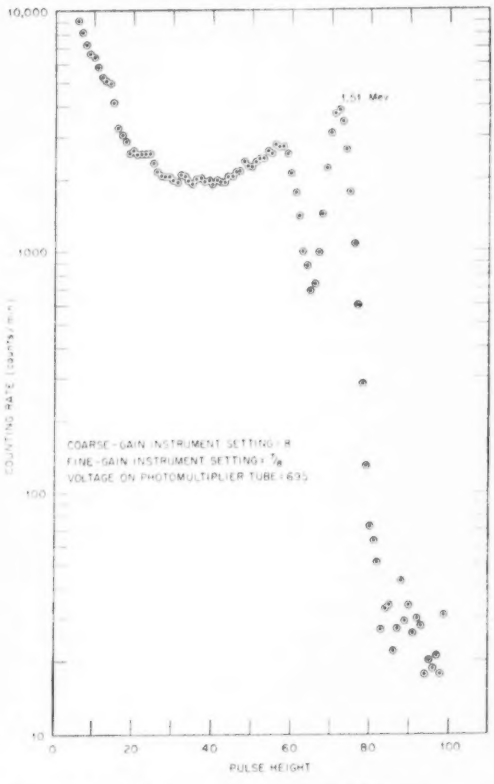

FIG. 1. Gamma-ray spectrum of K^{42} on NaI(Tl) spectrometer (resolution 10 percent).

† Work performed under contract with the U. S. Atomic Energy Commission.

[1] Thanks are due J. H. Oliver and W. A. Brooksbank for their advice and assistance in performing these separations.

[2] K. Siegbahn and A. Johansson, Arkiv Mat. Astron. Fysik **34A**, No. 10 (1947).

[3] K. Siegbahn, Arkiv Mat. Astron. Fysik **34B**, No. 4 (1947).

TABLE I. K^{42} decay data.

Half-life—12.44±0.08 hr
γ energy—1.51 Mev
Fraction accompanied by γ—0.200±0.010

function of Al absorber before the beta side, increased only slowly. When the γ detector was set to discriminate at a lower energy, the observed disintegration rate was ~50 percent higher.

Schull and Feenberg,[4] using the data of Siegbahn,[2,3] have made spin and parity assignments. Beyster and Wiedenbeck[5] and Stevenson and Deutsch[6] have reported angular correlation in K^{42}.

Table I is a summation of the data obtained on the decay of K^{42}.

[4] F. B. Schull and E. Feenberg, Phys. Rev. **75**, 1768 (1949).
[5] J. R. Beyster and M. L. Wiedenbeck, Phys. Rev. **79**, 728 (1950).
[6] D. T. Stevenson and M. Deutsch, Phys. Rev. **84**, 1071 (1951).

PHYSICAL REVIEW VOLUME 91, NUMBER 5 SEPTEMBER 1, 1953

Complementarity in Angular-Momentum States

B. A. LIPPMANN
Technical Research Group, New York, New York
(Received May 15, 1953)

By introducing operator representations for angular-momentum states referred to arbitrary axes of quantization, two independent angular momenta, each referred to its own axis of quantization, may be combined quantum-mechanically. An interpretation in terms of complementarity shows that this method of adding angular momenta corresponds to a "causal" description, while the usual method (using only one axis of quantization) is a "geometric" or spacetime description. "Causal" angular-momentum states automatically avoid the sums over magnetic quantum numbers in cascade processes.

ALTHOUGH the addition of two independent angular momenta is straightforward in quantum mechanics, the conventional procedure assumes that all operators and eigenvectors are referred to a common axis of quantization.

In contrast to this, many processes are most naturally described by referring the quantities belonging to each partial system to individual axes of quantization. For example, when two systems—initially isolated from one another and each in a definite state—are permitted to interact, since each system is prepared independently, the axes of quantization need bear no relation to one another.

This is ignored in the usual treatment of angular momentum; one of the systems, say 1, is selected, and the states of both systems are expressed relative to the axis of quantization natural to 1. The addition of the two angular momenta may then be carried through, but what may have been a single state of the other system, say 2, relative to its own axis of quantization, becomes, in general, a superposition of states, and the specification of 2 loses its simplicity.

In the following, we wish to discuss the quantum-mechanical addition of two independent angular momenta, each referred to its own axis of quantization. We shall show that: (A) By introducing operator representations for angular momentum states referred to arbitrary axes of quantization, the customary formalism may be applied, unchanged, to this more general case, and, (B) The resultant "causal" angular momentum states so constructed may be given a simple physical interpretation in terms of complementarity.

We believe that A provides an analytical tool that may be used to simplify the calculation of angular distributions in nuclear reactions, while B, by extending Bohr's discussion of complementarity to angular momentum, will be helpful in the physical interpretation.

"CAUSAL" ANGULAR-MOMENTUM STATES[1]

Suppose that system 1, in the state j_1, m_1, absorbs system 2, in the state j_2, m_2, to form the compound system i, of total angular momentum j_i. In the simplest case, all states are specified in the same reference system, say r_1, the z axis of which is taken as the axis of quantization. The system i must then be in the state j_i, m_i, where

$$m_i = m_1 + m_2. \tag{1}$$

This case, however, is too special. Ordinarily, if systems 1 and 2 are in definite angular momentum states, as above, their axes of quantization will not be the same. For, while the axis of quantization of 2 is usually determined by the direction from which absorption takes place,[2] this direction is not particularly meaningful for 1: clearly, the axis of quantization of 1 depends only on the previous history of 1.

[1] Here we prove A directly from abstract principles; an explicit analytical discussion is given in the Appendix.
[2] The spins of Dirac electrons and light quanta, for example, are constants of the motion only along the directions of their linear momenta.

Recognizing this, we now assume that 1 and 2 have the same quantum numbers as above, but now 1 is described relative to the reference axes r_1, while 2 is specified relative to the axes r_2. The z components, m_1 and m_2, now are associated not only with different systems, but also with different axes of quantization. While it is true that the initial state is still described completely by giving j_1, m_1 and j_2, m_2 (as well as r_1 and r_2), m_1 and m_2 now are constants of the motion only when each of the systems 1 and 2 is described relative to its own set of coordinate axes.

Comparing this more general initial state with the previous one, we see that the only difference is that the reference frame of system 2 has been rotated from coincidence with r_1 to the position of r_2. The new eigenvectors of system 2, described in r_2, therefore are obtained by applying a (unitary) rotation operator to the corresponding eigenvectors taken relative to r_1.

Thus, the present case differs by a canonical transformation from the special case previously considered. Since such transformations leave the equations used in the discussion of angular momenta unchanged, it follows that two angular momenta may also be combined when each is defined relative to a different set of coordinate axes. There are no formal difficulties; indeed, because a canonical transformation leaves algebraic relations unaffected, the analysis is formally identical in both cases.[3]

In particular, (1) is unaffected: only one state is allowed for the system i if its angular momentum operator is defined as the sum of the operators of systems 1 and 2—even when the latter operators are referred each to its own coordinate axes.

Suppose, now, that the process of 1 absorbing 2 to form i were followed by another process. The probability of the double process would be just the product of the probabilities of each of the two stages taken alone, since only one state of i is involved. The classical law of compounding independent probabilities would hold, and the interference of probabilities characteristic of quantum mechanics would be absent. For this reason, when combining definite states of two independent systems leads to only one state for the resultant, we shall call the states of the resultant "causal" angular-momentum states.

As an alternative to the procedure used above, we could expand the single state of 2 relative to r_2 in terms of states relative to r_1, according to the conventional prescription. The system i then becomes a superposition of states simultaneously present; its deterministic character disappears, and interference phenomena emerge if a second transition follows. States formed in this way we shall call "geometric" angular momentum states.

COMPLEMENTARITY INTERPRETATION

The system i, constructed according to the "causal" prescription, has rather curious properties. Ordinarily, when the $2j+1$ dimensional angular-momentum space of a system of angular momentum j is rotated, this can be correlated with a single rotation of the system in real, physical space. But now the part of i that came from 1 has the angular information inherent in r_1 embodied in it, while the part that came from 2 is still referred to the axes r_2. When the $2j_i+1$ dimensional space of system i is rotated, if we look for the associated rotation in physical space, we find that the part of i that came from 1 rotates relative to the coordinate system r_1, and the part from 2 undergoes the corresponding rotation relative to the axes r_2. There are *two* axes of rotation in real space to be correlated to every rotation in the angular momentum space of i.

This is consistent with complementarity. By deliberately choosing a method of addition that led to a single state for i, we have imposed a causal description. In exchange for this, we lose the possibility of a geometric description. For, according to complementarity, choosing a causal description destroys the basis of a description in terms of space and time and conversely.[4]

Alternatively, if we use the "geometric" method of composition, 1 and 2 rotate about the same axis in real space when the angular-momentum space of i is rotated; but then we find more than one state of i simultaneously present, and we lose the possibility of a causal description.

We therefore have a choice between an operator formalism, yielding a "causal" method of combining angular momenta that cannot be visualized geometrically, or a "geometric" method that permits a description in space-time but is void of causality. We can change at will from one to the other by the use of transformation theory.

An operator formalism, because of its conciseness, is usually preferable for the intermediate stages of a calculation. Only at the end, when results are to be interpreted in terms of a space-time description, need we transform to a particular geometric representation.

We feel that the formalism employed in calculating the angular distributions of nuclear reactions can be understood and simplified in the light of the point of view presented here. For example, the "causal" angular-momentum states, defined by the operator formalism considered here, always obey (1). Their use therefore eliminates the need to sum over magnetic quantum numbers[5] in cascade processes and explicitly exhibits the "geometrical" nature of such sums.

[3] One feature should be noticed, however. When both angular momenta are defined relative to the same set of coordinate axes, the resultant angular momentum also refers to this set of axes. In the more general case, when we combine two independent angular momenta referred to different axes, the resultant refers to *both* axes, in a complex manner that will be discussed in the next section.

[4] W. Heisenberg, *The Physical Principles of the Quantum Theory* (Dover Publications, New York, 1930), p. 65.

[5] The "causal" states introduced here are the same as those in O. Halpern and B. A. Lippmann, Phys. Rev. **87**, 1128 (1952).

The detailed application to these problems is in preparation.

APPENDIX

The analytical discussion of A is facilitated by a simple extension of Dirac notation. We propose, in what follows, to label all operators and eigenvectors so that the coordinate system to which they are referred is explicitly indicated.

Thus, in the reference frame a, the angular-momentum operator is $\mathbf{J}^{(a)}$; taking $\hbar=1$, the vector $|jma\rangle$ represents the state for which $(\mathbf{J}^{(a)})^2=j(j+1)$ and $J_z^{(a)}=m$. If $R(b, a)$ is the (unitary) operator that rotates the reference axes a into the set b, then[6]

$$\mathbf{J}^{(b)}=R(b, a)\mathbf{J}^{(a)}R^{-1}(b, a), \tag{A-1}$$

$$|jmb\rangle=R(b, a)|jma\rangle. \tag{A-2}$$

These equations express the physical requirement that the specification of a state must be independent of the coordinate system: when a sees the state j, m for his operator, $\mathbf{J}^{(a)}$, b sees the same state for *his* operator, $\mathbf{J}^{(b)}$.

Suppose we use only one set of axes, say a. This is the customary method, called the "geometric" method in the text.

The addition of independent angular momenta is expressed, in this case, by the operator equation,

$$\mathbf{J}_i^{(a)}=\mathbf{J}_1^{(a)}+\mathbf{J}_2^{(a)}, \tag{A-3}$$

or the equivalent eigenvector relation,

$$|j_i m_i a\rangle=\sum_{m_1, m_2}|j_1 m_1 a\rangle|j_2 m_2 a\rangle\langle m_1 m_2|j_i m_i\rangle. \tag{A-4}$$

Since the Wigner coefficient $\langle m_1 m_2|j_i m_i\rangle$ is an invariant, the explicit reference to the coordinate system is omitted. The Wigner coefficient is different from zero only if

$$m_i=m_1+m_2. \tag{A-5}$$

This condition, which restricts the summations in (A-4), follows by taking the z component of (A-3):

$$J_{iz}^{(a)}=J_{1z}^{(a)}+J_{2z}^{(a)}. \tag{A-6}$$

Now suppose 1 is referred to the axes a and 2 to the axes b, and let $R_2(b, a)$ be the operator that rotates the space of 2 alone. Then,

$$\mathbf{J}_2^{(b)}=R_2(b, a)\mathbf{J}_2^{(a)}R_2^{-1}(b, a), \tag{A-7}$$

$$|j_2 m_2 b\rangle=R_2(b, a)|j_2 m_2 a\rangle, \tag{A-8}$$

are, respectively, the angular-momentum operator and the state vector of 2 referred to the coordinate system b. We now find, from (A-3) and (A-4), with $\mathbf{J}_i^{(c)}$, $J_{iz}^{(c)}$ defined as below,

$$\mathbf{J}_i^{(c)}=R_2(b, a)\mathbf{J}_i^{(a)}R_2^{-1}(b, a)=\mathbf{J}_1^{(a)}+\mathbf{J}_2^{(b)}, \tag{A-9}$$

$$|j_i m_i c\rangle=R_2(b, a)|j_i m_i a\rangle$$
$$=\sum_{m_1, m_2}|j_1 m_1 a\rangle|j_2 m_2 b\rangle\langle m_1 m_2|j_i m_i\rangle; \tag{A-10}$$

while from (A-6),

$$J_{iz}^{(c)}=R_2(b, a)J_{iz}^{(a)}R_2^{-1}(b, a)=J_{1z}^{(a)}+J_{2z}^{(b)}. \tag{A-11}$$

These equations show that the "causal" method of adding two angular momenta referred to different axes of quantization is formally identical with the "geometric" method. (A-11) shows that (A-5) holds for (A-10) just as it does for (A-4). This latter fact also follows from the presence of the same Wigner coefficient in both equations.

The fact that a rotation in the space of j_i causes the corresponding rotations in the spaces of j_1 and j_2 to be correlated with different axes of rotations in real space follows from (A-9).

Now consider the example in the text, where 1 absorbs 2 to form i. Suppose the axis of quantization of 1 is along the z axis of a. If 2 is in the state described by $|j_2 m_2 a\rangle$, this corresponds to the absorption of 2 from the z direction in a. (A-3), (A-4), (A-5), and (A-6) now apply. In particular, because of (A-5), only one state of i results.

The eigenvector $|j_2 m_2 b\rangle$ corresponds to the absorption of 2 from the z direction in b. This eigenvector can be expanded in terms of states of 2 relative to the axes a, but then (A-5) no longer insures that only one state of i occurs since many values of m_2 appear. This is the "geometric" method of the text.

An alternative is to use the operator representation of the state of 2 given by (A-8). (A-9)–(A-11) then follow, and the analysis is formally no different from the case of absorption from the direction of the z axis of a. This is the "causal" method.

It was shown in this reference that in the most general cascade process it is always possible to choose a set of intermediate states such that the system passes through only one state at each step of the process. The proper choice of intermediate states to accomplish this is given by the "causal" states constructed here.

[6] If successive rotations through the Euler angles α, β, γ effect the transition from a to b,

$$R(b, a)=\exp(-iJ_z^{(a)}\alpha)\exp(-iJ_y^{(a)}\beta)\exp(-iJ_z^{(a)}\gamma).$$

Radiations from Arsenic 77 and Germanium 71*†

B. L. SARAF,‡ J. VARMA,§ AND C. E. MANDEVILLE
Bartol Research Foundation of the Franklin Institute, Swarthmore, Pennsylvania
(Received May 21, 1953)

The radionuclide As^{77} has been shown by scintillation spectrometry to emit gamma rays of energies 32, 87, 160, 247, 270, and 520 kev. It is estimated that these quanta are associated with beta-ray branches totaling about 2.5 percent of the total beta radiation. The continuous gamma-ray spectrum accompanying orbital electron capture in Ge^{71} has been shown to have an end point at 225±12 kev. Log *ft* is calculated to be 4.4(ΔI=0, 1; no), consistent with an assignment of spin ½ to the ground state of Ge^{71} in accord with the theory of the shell model.

Some data relative to gamma rays from Os^{193} and Ge^{77} are included.

INTRODUCTION

WITH the advent of scintillation counting, sensitivities of detection have become available for nuclear investigations which make possible the detection of gamma rays of intensity several orders of magnitude less than that previously observable by the earlier methods. Accordingly, it has been decided to reexamine "pure" beta-ray emitters in search of faint gamma radiation. The results of some researches in this direction are presented in connection with the decay of the 40-hr As^{77} along with some measurements relating to the continuous gamma-ray spectrum of the 11-day Ge^{71}.

ARSENIC 77

The beta rays of As^{77} have been shown to have a maximum energy of 0.700±0.007 Mev.[1] Very early measurements[2,3] gave evidence of no detectable gamma radiation. The residual nucleus is Se^{77}, which is also produced[4] by orbital electron capture in Br^{77}. Gamma rays having quantum energies of 160, 237, 284, 298, 520, 641, and 813 kev have been observed[4] to follow *K* capture in Br^{77}, indicating energy levels in Se^{77} as shown in Fig. 1.

For the purposes of the present investigation, As^{77} was grown from its 12-hr parent, Ge^{77}, when GeO_2 was irradiated by slow neutrons in the Oak Ridge pile. The energy spectrum of the gamma rays of As^{77} as determined from the pulse height distribution resulting from gamma rays on NaI(Tl) is shown in Fig. 2. This distribution was observed on twelve occasions over a time of four half-periods, and the ordinates of the spectrum were found to decay at all points with a half-period of 40 hr, that of As^{77}. Measurements were not commenced until sufficient time had elapsed to make negligible the 12-hr Ge^{77}. Moreover, the measurements on As^{77} were always preceded by a chemical separation of arsenic from germanium. The energies, with an estimated accuracy of five percent, are 87, 160, 247, and 520 kev, with approximate relative intensities of 3, 1, 20, and 6, respectively.

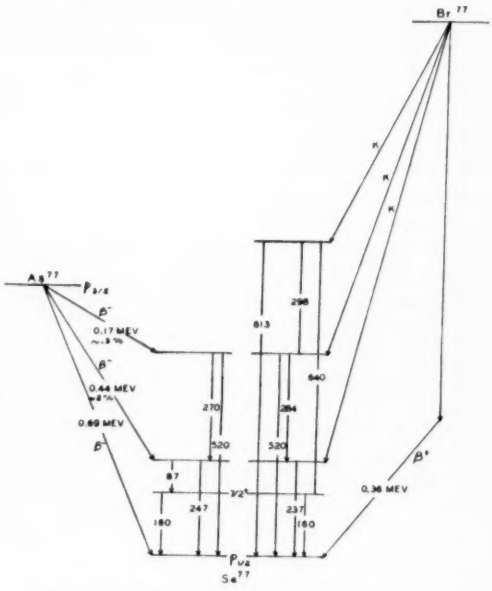

FIG. 1. Disintegration scheme for As^{77} and Br^{77}.

* Assisted by the joint program of the U. S. Office of Naval Research and the U. S. Atomic Energy Commission.

† A preliminary account of these results was presented at the Conference on Nuclear Spectroscopy and the Shell Model of the Nucleus, Indiana University, May 14–16, 1953, and also in Bull. Am. Phys. Soc. **28**, No. 4, 12 (1953).

‡ On leave of absence from Agra College, Agra, India.

§ Permanent address, Morena (M.B.), India.

[1] R. Canada and A. C. G. Mitchell, Phys. Rev. **81**, 485 (1951).

[2] U. S. Atomic Energy Commission Catalog and Price List No. 3, March 1, 1947, September 1, 1947, and No. 3, July, 1949, describe the number of gamma rays emitted by As^{77} as "none." This description may be based upon the measurements of E. P. Steinberg and D. W. Engelkemir, *Radiochemical Studies: The Fission Products* (McGraw-Hill Book Company, New York, 1950), Paper No. 54, National Nuclear Energy Series, Plutonium Project Record, Vol. 9, Div. IV, who mention no detectable gamma rays from As^{77}.

[3] Mandeville, Woo, Scherb, Keighton, and Shapiro, Phys. Rev. **75**, 1528 (1949), stated in the introduction of their paper that As^{77} emits no gamma rays. This remark was a citation of the comments of reference 2. There are no published data in the paper by Mandeville *et al.* relating to the gamma rays of As^{77}. However, an unpublished beta-ray absorption curve was obtained by Mandeville *et al.* to find the absorption limit, and no gamma-rays were detected in a Geiger counter beyond the beta-ray end point. The present writers could detect several hundred counts per minute, gamma rays from As^{77}, in a Geiger counter shielded from the beta rays in the presence of a relatively intense pile-produced source.

[4] R. Canada and A. C. G. Mitchell, Phys. Rev. **83**, 955 (1951).

Gamma-gamma coincidences were measured in two scintillation counters in coincidence. The coincidence rate was noted for various settings of integral pulse-height discriminators in either channel. From the data, it was found that the coincidence rate decreased as the discriminator setting in one channel was increased, until when the discrimination level was greater than the height of pulses in the photoelectric peak of a 270-kev gamma ray, all genuine gamma-gamma coincidences ceased. With both integral pulse-height discriminators set to pass pulses only of height corresponding to 247 kev or more, a considerable number of genuine gamma-gamma coincidences remained, suggesting that the intense 247-kev line is complex. To locate accurately the photoelectric peak of the radiation in cascade with the 247-kev gamma ray, the pulses from either phototube were passed through single channel differential pulse-height discriminators, one set at the photopeak of the 247-kev line. As the base line of the coincident

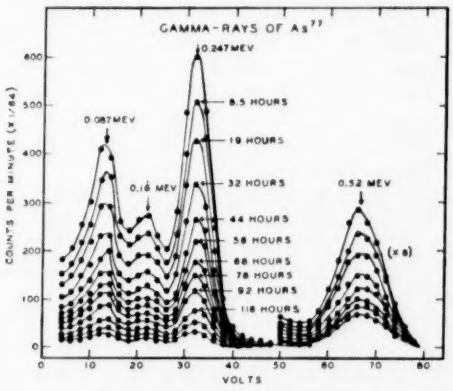

FIG. 2. Pulse-height distribution of gamma rays from As^{77} on NaI-Tl.

differential pulse-height discriminator was raised above 247 kev, the gamma-gamma coincidence rate was found to have a maximum at 270 kev, giving the location in energy of the photopeak of the gamma ray in cascade with the 247-kev line. From the single counting rates in either channel and the gamma-gamma coincidence rate, the intensity of the 270-kev gamma ray relative to that of the 247-kev line was estimated to be two percent. In subsequent measurements, a gamma ray at 32 kev, not shown in Fig. 2, was detected. The gamma ray at 520 kev was found to be noncoincident with the other quantum radiations. The cascade relation between the various gamma rays as indicated by the coincidence experiments is shown in Fig. 1.

The absolute intensity of the beta rays of As^{77} was measured in a thin-walled Geiger counter (window thickness 3 mg/cm^2), and the intensities of the gamma rays were estimated from the areas under the photoelectric peaks and the calculated efficiency of the sodium iodide crystal. From the energies and relative

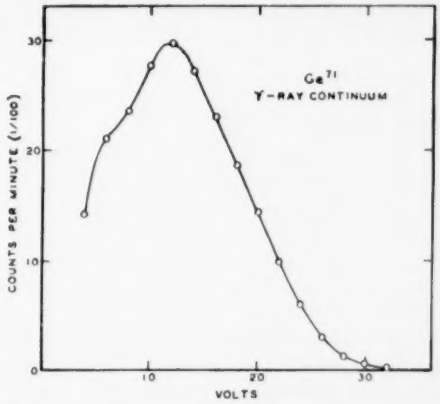

FIG. 3. Pulse-height distribution arising from the gamma-ray continuum of $Ge^{71}+e^- \rightarrow Ga^{71}+\eta+\gamma$.

intensities of the gamma rays, the values of log ft for the associated beta-ray spectra were calculated in the order of ascending energy to be 6.6, 7.2, and 5.7, the latter value referring to the beta spectrum leading to the ground state of Se^{77}. Thus, the ground-state transition is allowed, and the remaining two spectra are first forbidden. Beta-gamma coincidences were measurable between the inner spectrum at 0.44 Mev and the 247-kev gamma ray.

As previously indicated, the gamma-ray energy measurements and coincidence data have been combined with those of Canada and Mitchell[4] to give the decay scheme of Fig. 1. As^{75} is known to have a spin of $\frac{3}{2}$. Since As^{77} differs from As^{75} by two neutrons, its ground state orbital is assumed to be $p_{\frac{3}{2}}$ in agreement with the prediction of the nuclear shell model. The spin of Se^{77} has been shown[5] to be $\frac{1}{2}$. Therefore, the beta spectrum at 0.700±0.007 Mev (noncoincident with gamma rays, log $ft=5.7$) is properly characterized by[6] $p_{\frac{3}{2}} \rightarrow p_{\frac{1}{2}}(\Delta I=1$, no). The 160-kev metastable state has been classified[7] as being the initial state of an $E3$ transition with spin $7/2^+$. The values of log ft for the two inner beta spectra correspond to ($\Delta I=0, 1$; yes,) ruling out the possibility that either of them terminate at a level in Se^{77} of spin 9/2. Assignment of spins to the remaining excited levels of Se^{77} shown in Fig. 1 is made difficult, because of the great number of configuration levels which can result from $(g_{9/2})^3$.

GERMANIUM 71

The radiations of Ge^{71} have been shown to include no charged particles or monoenergic nuclear gamma rays.[8,9,3] This activity decays solely by orbital electron

[5] S. P. Davis and F. A. Jenkins, Phys. Rev. **83**, 1269 (1941).
[6] Mayer, Moszkowski and Nordheim, Revs. Modern Phys. **23**, 315 (1951).
[7] M. Goldhaber and A. W. Sunyar, Phys. Rev. **83**, 906 (1951).
[8] Seren, Friedlander, and Turkel, Phys. Rev. **72**, 888 (1947).
[9] McCown, Woodward, and Pool, Phys. Rev. **74**, 1311 (1948).

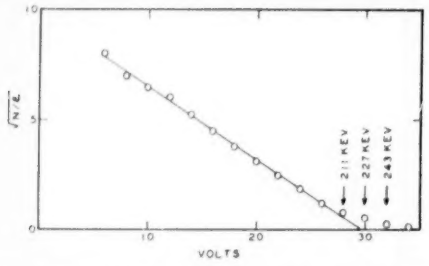

FIG. 4. Fermi plot of the gamma-ray spectrum of Ge^{71}.

capture. It has been shown theoretically[10] that a small fraction of K-capture disintegrations are accompanied by emission of a continuum of quanta and corresponding continuum of neutrinos rather than the usual monoenergic neutrino. Examples of this mode of decay have been found[11,12] in Fe^{55} and in argon 37.[13] Since Ge^{71} decays only by K capture and always to the ground state of Ga^{71}, it was thought to offer an excellent opportunity for the detection of its related gamma-ray continuum. Accordingly, Ge^{71} produced by slow neutron capture in the Oak Ridge pile was studied.

The pulse-height distribution of the continuous gamma-ray spectrum of Ge^{71} is shown in Fig. 3. The Fermi plot of the data of Fig. 3, given in Fig. 4, yields an end point of 225 ± 12 kev. Because of the low specific gamma-ray activity of the source of Ge^{71}, it was necessary to employ a relatively thick, broad, source of irradiated GeO_2. Consequently, the points of Fig. 3 were not corrected for absorption, instrumental resolution, or detection efficiency as a function of gamma-ray energy. The energy of disintegration of Ge^{71} to Ga^{71} by K capture is, of course, equal to the end point of the continuum.

The spin of the ground state of Ga^{71} has been measured[14] and found to be $\frac{3}{2}$. The spin of Ge^{71} is predicted by the shell model[15] to be $p_{\frac{1}{2}}$. From the end point of Fig. 4, log ft is 4.4, and the transition is allowed ($\Delta I=0$, ±1; no), consistent with the shell model prediction. These interpretations and data are summarized in the decay scheme of Fig. 5.

If the ground-state spin of Ge^{71} is taken to be $p_{\frac{1}{2}}$, the shell model theory indicates that an isomeric level should be present in Ge^{71} of spin $g_{9/2}$, giving rise to an

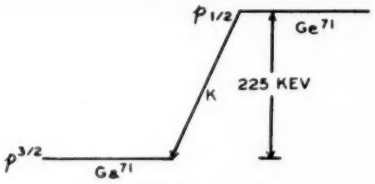

FIG. 5. Decay of Ge^{71}.

$M4$ transition. This gamma ray has apparently not yet been observed.

OSMIUM 193 AND GERMANIUM 77

The gamma rays of Os^{193}($T=32$ hr) have been studied by Swan and Hill,[16] who find a gamma ray at 72.4 kev. Indications of gamma rays at 215, 323, and 460 kev were reported by them,[16] but they were not definitely assigned to Os^{193}. Very recently,[17] Cork *et al.* have re-examined the gamma rays of Os^{193} and found in a magnetic spectrograph nine lines, ranging in energy from 73 kev to 557.8 kev. Three of these reported gamma rays have also been observed in a scintillation spectrometer by the writers. The measured quantum energies were in the interval 200 kev$<E_\gamma<$600 kev at 280, 460, and 560 kev, differing little in energy from the values reported by Cork *et al.*[17]

The gamma rays of Os^{193} were also measured periodically over a time of about 80 hours by the method of coincidence absorption. The hard gamma ray previously reported at 1.58 Mev[18] was again found to be present, but its intensity decayed with a half-period of $\sim$20 hr, suggesting it to be the 1.43-Mev quantum of Ir^{194}.

In the course of studying the gamma rays of As^{77}, the gamma spectrum of the parent element, Ge^{77}, was also noted. The results were essentially the same as those of Smith,[19] except that two high-energy quanta at 2.3 and 2.7 Mev, respectively, unobserved by Smith, were present and decayed in intensity with the 12-hr half-period of Ge^{77}.

ACKNOWLEDGMENT

The writers are indebted to Dr. Walter B. Keighton of Swarthmore College for having carried out the several separations of germanium from arsenic required in the course of these measurements. They also wish to acknowledge the kind interest of Dr. W. F. G. Swann, Director of The Bartol Research Foundation.

[10] P. Morrison and L. I. Schiff, Phys. Rev. **58**, 24 (1940); J. M. Jauch, Oak Ridge National Laboratory Report 1102 (1951).
[11] Bradt, Gugelot, Huber, Medicus, Preiswerk, Scherrer, and Steffen, Helv. Phys. Acta **19**, 222 (1946); D. Maeder and P. Preiswerk, Phys. Rev. **84**, 595 (1951).
[12] Bell, Janch, and Cassidy, Science **115**, 12 (1952).
[13] C. E. Anderson, Phys. Rev. **87**, 668 (1952).
[14] J. S. Campbell, Nature **131**, 204 (1933).
[15] M. G. Mayer, Phys. Rev. **78**, 16 (1950).
[16] J. B. Swan and R. D. Hill, Phys. Rev. **88**, 831 (1952).
[17] Cork, LeBlanc, Nester, Martin, and Brice, Phys. Rev. **90**, 444 (1953).
[18] Mandeville, Scherb, and Keighton, Phys. Rev. **74**, 888 (1948).
[19] Alan B. Smith, Phys. Rev. **86**, 98 (1952).

Radiations of Ra^{227}†

J. P. Butler and J. S. Adam
Chemistry Branch, Atomic Energy of Canada Limited, Chalk River, Ontario, Canada
(Received May 4, 1953)

Ra^{227} has been prepared by the slow neutron irradiation of Ra^{226} in the NRX reactor. Ra^{227} is a β^- emitter with a half-life of 41.2±0.2 minutes and with a β^- end point of 1.31±0.02 Mev. Gamma rays of 291 and 498 kev were observed with a scintillation spectrometer. The cross section for the reaction $Ra^{226}(n,\gamma)Ra^{227}$ was found to be 23 barns.

INTRODUCTION

Ra^{227} has been previously prepared by Peterson[1] by the neutron irradiation of Ra^{226}; however, he did not isolate Ra^{227} but only its daughter Ac^{227}.

In order to determine whether it would be possible to isolate Ra^{227}, it was necessary to predict the nuclear properties of Ra^{227}. The β^- disintegration energy of Ra^{227} was calculated from the following closed decay cycle:

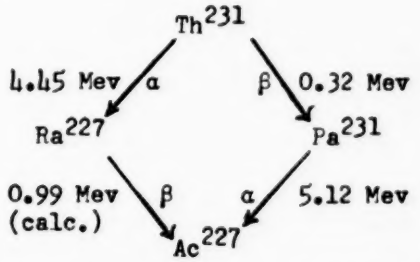

The β^- disintegration energy of Th^{231}(UY) was obtained from the data of Freedman *et al.*[2] The α disintegration of Th^{231} was estimated to be 4.45 Mev by extrapolating the appropriate line on an α-energy *vs* mass number curve.[3] In this manner, the β^- disintegration energy of Ra^{227} was calculated to be 0.99 Mev. The β^- decay of Ra^{227} was expected to be first-order forbidden and thus this energy would lead to a β^- decay half-life of about 30 minutes. Therefore it seemed possible that Ra^{227} could be observed by a short irradiation of Ra^{226} in a high-neutron flux in the NRX nuclear reactor followed by a rapid chemical separation of radium.

EXPERIMENTAL

The Ra^{226} used in these experiments was analyzed spectrographically and was shown to contain 0.2 percent barium, 0.2 percent calcium, 0.1 percent iron, and traces of magnesium and boron.

Before irradiating the Ra^{226}, it was freed from its decay products by boiling the solution of $RaCl_2$ for a few minutes. This removed the 3.85-day Em^{222}. The other decay products, Po^{218}, Pb^{214}, and Bi^{214}, which have short half-lives, were allowed to decay away. A sample of the Ra^{226} solution was then evaporated in a small silica tube and irradiated for 30 to 50 minutes in a thermal neutron flux of 4×10^{13} neutrons/cm² sec.

After the irradiation, the sample was returned to the laboratory through a pneumatic tube. With this arrangement, targets were received 20 seconds after the end of the bombardment. The silica tube was smashed and the radium chloride was dissolved in 0.2*N* hydrochloric acid containing barium, bismuth, and lead carriers. The sulfides of bismuth and lead were precipitated in order to free the radium from the decay products of Ra^{226} which had grown in during the irradiation. Iron sulfide was then precipitated to remove other undesirable impurities. The radium was further purified by precipitating it as the carbonate and then as the chloride, using barium as a carrier. The chemical separation of the radium was completed in about 15 minutes.

The β^- decay of the purified radium was observed with an end-window Geiger counter, using a 5.9-mg/cm² aluminum absorber to prevent α particles from Ra^{226} and its decay products from entering the counter. A half-life of 41.2±0.2 minutes was observed and attributed to Ra^{227}. A typical decay curve is shown in Fig. 1. By subtracting the counts due to Pb^{214} and Bi^{214} which grow in from Ra^{226} with a 3.8-day half-life, it was possible to follow the decay of Ra^{227} through eleven half-lives. In the decay of the sample of Ra^{227} no other components were observed.

The (n,γ) cross section of Ra^{226} was determined in four irradiations. A value of 23 barns with a standard deviation of 1 barn was obtained after making the proper corrections for backscattering and counter window absorption. Since Ra^{226} could be used as a tracer for the Ra^{227}, it was not necessary to know either the initial amount of Ra^{226} irradiated or the chemical yield in order to calculate this cross section. The integrated flux was obtained by measuring the activity produced in a sample of gold which was irradiated

† Paper presented at the Royal Society of Canada Meeting, Quebec, Canada, June, 1952.

[1] S. Peterson, *The Transuranium Elements: Research Papers* (McGraw-Hill Book Company, Inc., New York, 1949), Paper 19.9, p. 1393. National Nuclear Energy Series, Plutonium Project Record, Vol. 14B, Div. IV.

[2] Freedman, Wagner, Jaffey, and May, Argonne National Laboratory Report ANL-4613 (unpublished).

[3] Perlman, Ghiorso, and Seaborg, Phys. Rev. **77**, 22 (1950).

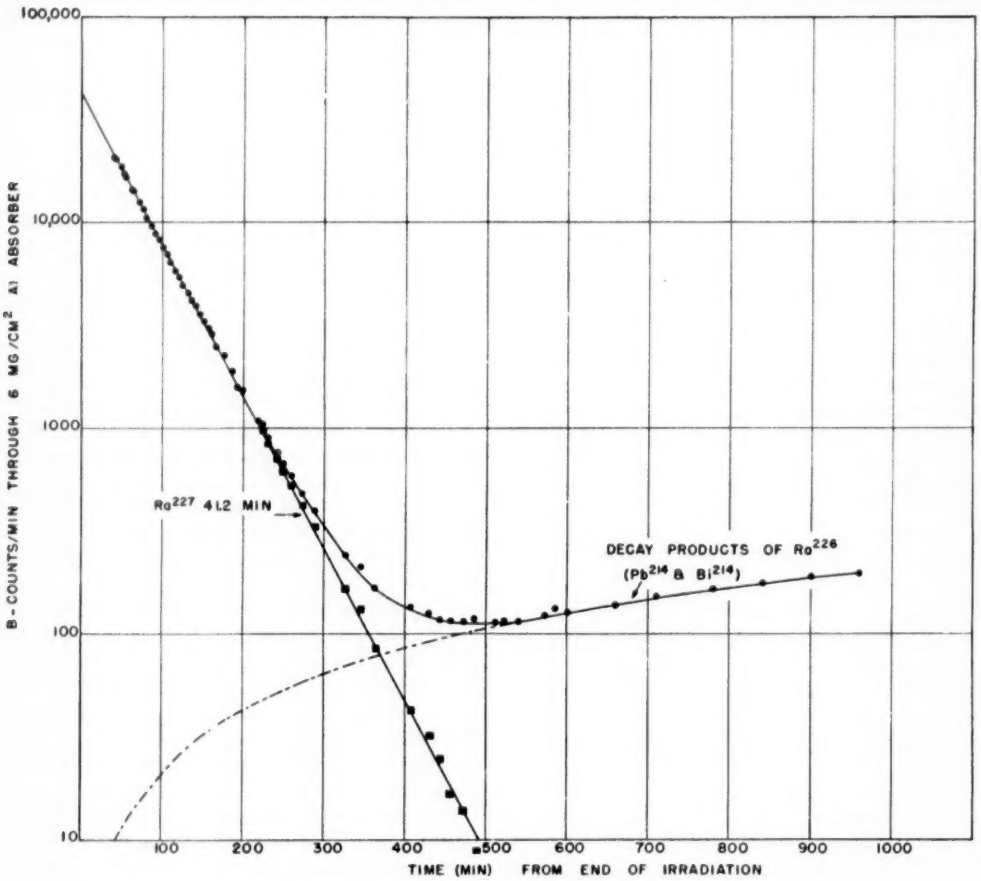

FIG. 1. Decay of Ra fraction from neutron-irradiated Ra^{226}.

simultaneously with the Ra^{226}. The gold cross section was taken as 98 barns.

An aluminum absorption curve of the radiations from Ra^{227} was taken using a sample mounted on a thin polystyrene film (1.5 mg/cm²) (Fig. 2). The absorption curve showed the presence of two components both of which decayed with a 41-minute half-life. The hard component C which was attributed to soft γ rays was subtracted from curve A to give curve B. From curve curve B the soft component, β^- radiation, was shown to have a range equal to 578 mg/cm² of aluminum. This range was obtained both visually and by carrying out a Feather-type analysis using P^{32} as a standard. Using the range-energy relationship,

$$E=(R+0.133)/0.542,$$

given by Glendenin and Coryell,[4] the maximum energy of the β^- particle was calculated to be 1.31 ± 0.2 Mev. This value is 0.3 Mev greater than the predicted value which was calculated from the closed decay cycle.

The γ rays occurring in the β^- decay of Ra^{227} were studied with sodium iodide (thalliated) scintillation spectrometer. The pulses from the R.A.C. 5819 photomultiplier tube were fed into a linear amplifier, then into a cut amplifier and from thence into a twenty-four channel pulse analyzer. The scintillation spectrometer had been calibrated with the 60-kev line of Am^{241}, 364-kev line of I^{131}, 411-kev line of Au^{198}, and 662-kev line of Cs^{137}. From the observed γ spectrum of Ra^{227} plus Ra^{226}, the γ spectrum of Ra^{226} was subtracted. The resulting spectrum decayed with a 41-minute half-life and showed three γ rays with energies of 92, 291, and 498 kev. The numbers of quanta per 100 β^- disintegrations were 3.1, 4.0, and 0.6, respectively. The 92-kev line is most probably a mixture of K_α and K_β x-rays of actinum. These K x-rays presumably arise from the internal conversion of 291- and 498-kev γ rays.

[4] L. E. Glendenin and C. D. Coryell, *Radiochemical Studies, The Fission Products* (McGraw-Hill Book Company, Inc., New York, 1946), Paper 2.12, National Nuclear Energy Series, Plutonium Project Record, Vol. 9B, Div. IV.

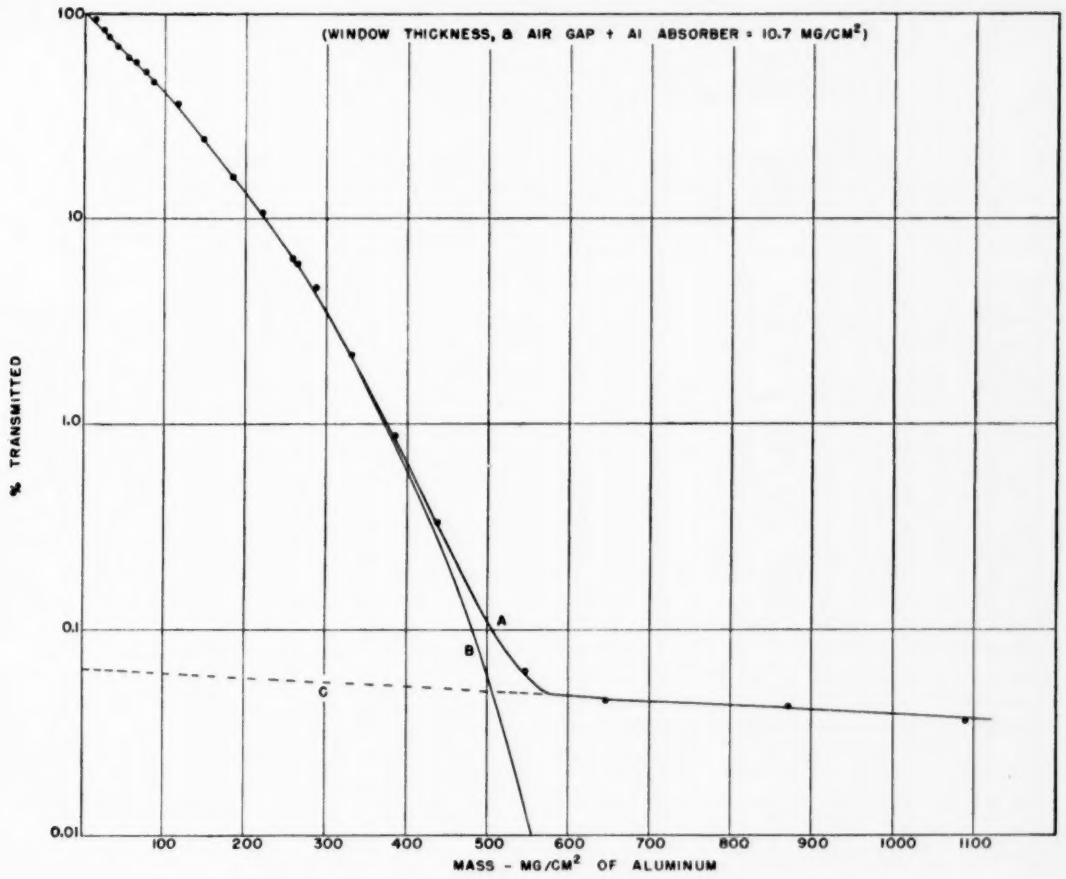

FIG. 2. Absorption curve of Ra^{227}.

DISCUSSION

Since the number of quanta of electromagnetic radiation in the decay of Ra^{227} is small, the 1.31-Mev β^- transition very probably goes to the ground state of Ac^{227}. Thus the β^- disintegration energy of Ra^{227} is 1.31 Mev. This value introduces a discrepancy of about 0.3 Mev in the decay cycle (see above). The decay of both Pa^{231} and Th^{231} (UY) has been studied by several investigators[5,2,6] and it is extremely unlikely that either the α disintegration energy of Pa^{231} or the β^- disintegration of Th^{231} are in error by this amount. Thus, the extrapolated value for the α disintegration of Th^{231} is the only logical decay to account for this discrepancy. The results of this experiment therefore indicate that the α disintegration of Th^{231} is 4.13 Mev. This value is only slightly greater than the α disintegration of Th^{232}.

ACKNOWLEDGMENT

We wish to thank Mr. P. B. Aitken for his design of the pneumatic tube which was used to carry out these experiments.

[5] Rosenblum, Cotton, and Bouissières, Compt. rend. **229**, 825 (1949).
[6] G. B. Knight and R. L. Macklin, Phys. Rev. **75**, 34 (1949).

Neutron Diffraction by Liquid Helium

D. G. HENSHAW AND D. G. HURST
Chalk River Laboratory, Atomic Energy of Canada Limited, Chalk River, Ontario, Canada
(Received May 8, 1953)

Preliminary results of a measurement of the angular distribution of 1.08A neutrons scattered by liquid helium at 4.2°K over the angular range 3.8° to 31° are reported. A maximum in the scattering occurs at 21.3°±1°, corresponding to a peak at 3.6A in the radial distribution of density about any atom in the liquid.

RECENTLY we undertook an investigation of neutron scattering by liquid helium. As this work has been interrupted, it seems worthwhile to publish the results already obtained. In a single run of short duration, the angular distribution of 1.08A neutrons scattered from liquid helium at a temperature of 4.2°K was measured over the angular range 3.8° to 31°.

The geometry of the scattering chamber was similar to that used by Hurst and Alcock[1] in their study of neutron scattering by deuterium gas. The present chamber was larger, having a diameter of 5 inches. Details of the scattering chamber will be published in a forthcoming paper on other liquids.

The results, corrected for background and effective scattering volume, are shown in Fig. 1, the statistical accuracy of the points being ±7 percent. Background was measured without the helium, and should possibly be reduced in part by the attenuation through the helium. This reduction would have a negligible effect at the larger angles and has not been applied owing to the uncertainty in the fraction of the background affected. Corrections for double scattering and instrumental resolution are small compared to the statistical errors and have not been applied. Measurements of the transmission by the helium gave a cross section of 0.8 barn±20 percent.

The main feature of the pattern is the peak at 21.3° ±1° where the limits ±1° were set by inspection of Fig. 1. On the simple picture of scattering applicable to x-rays, the peak is attributable to a maximum at 3.6A in the radial variation of density about any chosen atom in the liquid. The peak in the helium pattern is relatively lower and broader than the corresponding peak in the liquid argon pattern.[2] This could mean that the degree of order in helium is less than in liquid argon and that the number of neighbors at 3.6A is probably somewhat less than the 8.2 found for argon.

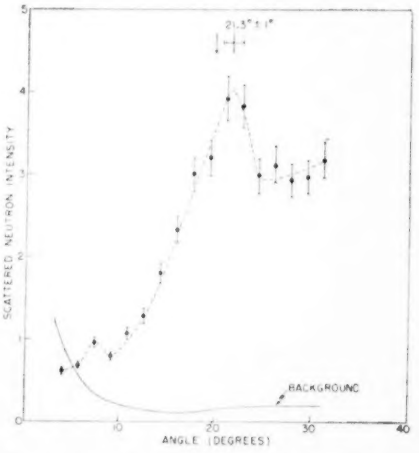

FIG. 1. The angular distribution of 1.08A neutrons scattered by liquid helium at 4.2°K. The background as measured without the helium is also shown. An arrow at 19.5° marks the predicted position of a 1.08A x-ray peak based on the published position of the peak at 28° for 1.54A x-rays with helium at 2.15°K.

Keesom and Taconis[3] and Reekie[4] measured the scattering of Cu$K\alpha$ x-rays from liquid helium at slightly lower temperatures (2.4°K and 2.15°K, respectively). A broad maximum in the scattering was found at an angle of 28°. Changing this to the angle predicted for 1.08A according to the usual diffraction formula ($\sin\theta/\lambda$=constant) gives 19.5° to be compared with the angle 21.3°. If a correction is made for change in density between the two temperatures, the difference between the x-ray and neutron results is increased by approximately one degree.

[1] D. G. Hurst and N. Z. Alcock, Can. J. Phys. **1**, 36 (1951).
[2] Henshaw, Hurst, and Pope (to be published).
[3] W. H. Keesom and K. W. Taconis, Physica **5**, 270 (1938).
[4] J. Reekie, Proc. Cambridge Phil. Soc. **36**, 236 (1940).

The Branching Ratio of Potassium 40†

R. D. Russell, H. A. Shillibeer, R. M. Farquhar, and A. K. Mousuf
Geophysics Laboratory, Department of Physics, University of Toronto, Toronto, Canada
(Received April 30, 1953)

The branching ratio of potassium 40 has been measured by determining the argon and potassium content of potassium feldspars of accurately known ages. The results obtained for five samples differing in age by more than a factor of five are all consistent within the limits of error with a branching ratio of 0.060 ± 0.006 when a total decay constant of 0.54×10^{-9} year^{-1} is assumed. The authors feel that the results obtained indicate that loss of argon from these samples during geological time is unlikely.

THE total radioactive decay constant λ of potassium 40 is the sum of two partial decay constants λ_β and λ_K, the former describing the rate of decay by β emission to calcium, and the latter describing the rate of decay by K-electron capture to argon. The ratio λ_K/λ_β is called the branching ratio. The average of the best available measurements[1] of λ_β is $(0.506\pm0.027)10^{-9}$ year^{-1}, but λ_K is less precisely known and values for the branching ratio have been reported from "less than 0.07" to 1.9 by x-ray measurements,[2] from 0.04 to 0.15 by gamma-ray measurements,[3] and from 0.02 to 0.10 by measurements of the argon content of old potassium minerals.[4]

In order to fix the value of λ_K more closely the authors have measured the radiogenic argon content of five potassium minerals of which the ages have also been determined. The samples were heated with metallic sodium to 850°C in a high-vacuum system in order to release the argon, which was then purified by means of a calcium furnace and measured in a McLeod gauge. Mass spectrometric analyses were made to determine the proportion of radiogenic argon. All argon samples contained less than 10 percent atmospheric argon and some less than 1 percent. Tests with atmospheric argon showed that the method of purification did not alter the A^{40}/A^{36} ratio. The results obtained are given in Table I.

Microcline samples No. 1 to No. 4 were obtained from the same or neighboring pegmatites as uraninite specimens I to IV, respectively, which have been dated in this laboratory by the lead isotope-ratio method with the results shown in Table II. The ages obtained from uraninite samples I and II have been averaged and used to date both microcline samples No. 1 and No. 2.

Microcline specimen No. 5 was obtained from a pegmatite in the Spruce Pine district, as was the uraninite for which a chemical analysis has been published by Føyn.[5] That uraninite contained 74.20 percent uranium, 2.70 percent thorium and 3.64 percent lead, indicating an age of 340 million years. Although no isotopic analysis was made, results published recently indicate that pegmatitic uraninites usually contain

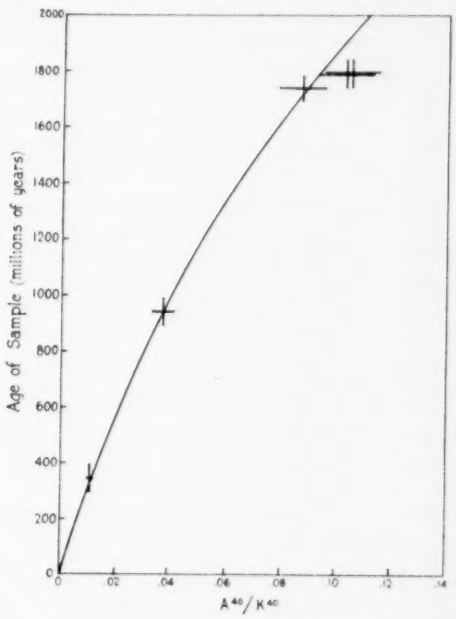

FIG. 1. Comparison of measured values with theoretical curve calculated for a branching ratio of 0.06 and a decay constant of 0.54×10^{9} years^{-1}.

† This investigation has been made possible by financial assistance from the National Research Council of Canada and the Ontario Research Council.

[1] T. Graf, Phys. Rev. **74**, 1199 (1948); O. Hirzel and H. Wäffler, Phys. Rev. **74**, 1553 (1948); J. J. Floyd and L. B. Borst, Phys. Rev. **75**, 1106 (1949); R. W. Stout, Phys. Rev. **75**, 1107 (1949); W. R. Faust, Phys. Rev. **78**, 624 (1950); G. A. Sawyer and M. L. Wiedenbeck (2 results), Phys. Rev. **79**, 490 (1950); F. W. Spiers, Nature **165**, 356 (1950); C. F. G Delaney, Phys. Rev. **81**, 158 (1951).

[2] E. Bleuler and M. Gabriel, Helv. Phys. Acta **20**, 67 (1947); Ceccarelli, Quarcini, and Rostagni, Phys. Rev. **80**, 909 (1950); T. Graf, Arkiv Fysik **3**, 171 (1951); G. A. Sawyer and M. L. Wiedenbeck, reference 1.

[3] For example: J. J. Floyd and L. B. Borst, reference 1; G. A. Sawyer and M. L. Wiedenbeck, Phys. Rev. **76**, 1535 (1949); W. R. Faust, reference 1; Smaller, May, and Freedman, Phys. Rev. **79**, 940 (1950); F. W. Spiers, reference 1; and earlier results.

[4] L. T. Aldrich and A. O. Nier, Phys. Rev. **74**, 876 (1948); Inghram, Brown, Patterson, and Hess, Phys. Rev. **80**, 916 (1950); A. K. Mousuf, Phys. Rev. **88**, 150 (1952).

[5] E. Føyn, Report of the Committee on the Measurement of Geologic Time, National Research Council, Washington, D. C., p. 23, September, 1939.

TABLE I. Radiogenic A^{40}/K^{40} for microcline specimens of known age.

No.	Sample	Origin[a]	Number of runs averaged	% by weight radiogenic argon $\times 10^6$	K_2O%	A^{40}/K^{40} [b]
1	Pink microcline	Charlebois Lake, Saskatchewan; three miles from Row Group uraninite occurrence.	2	12.0	11.5	0.105 ±0.010
2	Pink microcline	Charlebois Lake, Saskatchewan; from pegmatite on island about a half mile from Row Group uraninite occurrence.	2	13.1	12.8	0.103 ±0.010
3	Pink microcline	Lee Lake, Lac La Ronge, Saskatchewan.	3	10.3(3)	12.0	0.087 ±0.009
4	Pink microcline	Bessner Mine, Lot 5, Con. B., Henvey Township, Ontario.	4	4.15	11.3	0.037 ±0.004
5	White perthite	Meadow Mine pegmatite, Spruce Pine District, Avery County, North Carolina, U.S.A.	2	1.34	12.8	0.0106±0.0010

[a] Sample No. 5 was collected by Dr. J. L. Kulp of Columbia University. Samples No. 1, No. 2, and No. 3 were collected by Dr. J. B. Mawdsley and Mr. G. L. Cumming of the University of Saskatchewan. Sample No. 4 was collected by the authors.
[b] The ratio for each sample has been assigned a possible error of ±10 percent, which includes possible errors in potassium analyses as well as in argon measurements. Argon measurements on any specimen were repeatable with much better precision.

TABLE II. Ages of uraninites calculated from radiogenic Pb^{207}/Pb^{206}.

No.	Mineral and locality[a]	Pb^{204}	Pb^{206}	Pb^{207}	Pb^{208}	Ratio radiogenic Pb^{207}/Pb^{206}%	Age (million years)
I	Uraninite, Charlebois Lake, Saskatchewan. Nuzone (channel) showing.	0.044±0.004	85.66	9.83	4.47	10.78±0.06	1780±50
II	Uraninite, Sickle Lake, Saskatchewan; four miles south of Charlebois Lake.	0.071±0.005	84.36	10.18	5.37	10.93±0.04	1800±50
III	Uraninite, Lee Lake, Lac La Ronge, Saskatchewan.	0.036±0.004	87.06	9.83	3.34	10.50±0.06	1740±50
IV	Uraninite, Bessner Mine, Lot 5, Con. B, Henvey Township, Ontario.	0.021±0.007	91.86	6.71	1.44	7.09±0.10	940±50

[a] Sample I was collected by Dr. S. C. Robinson of the Geological Survey of Canada, and is published with the kind permission of the Survey. Samples II and III were collected by Dr. J. B. Mawdsley, University of Saskatchewan. Sample IV was collected by the authors.

less than 1 percent–2 percent common lead.[6] A possible error of 50 million years has been assigned to this age.

Figure 1 shows the ages of the samples plotted against the ratio of radiogenic A^{40} to K^{40}. On the same graph a theoretical curve is shown, calculated for a decay constant of 0.54×10^{-9} year^{-1} and a branching ratio λ_K/λ_β of 0.060. It can be seen that the calculated curve lies within the assigned limits of error of the experimental values. The results of this experiment show that the branching ratio of K^{40} is 0.060±0.006 if the samples have been dated correctly and have not lost a significant amount of argon. That there has been little or no loss of argon during geological time is strongly suggested by the consistency of the results obtained for samples differing in age by as much as a factor of five. Preliminary measurements, not yet reported, on muscovite and feldspar from the same pegmatite agreed within the limits of experimental error, also suggesting that loss of argon is unlikely.

A more detailed report of this investigation, together with data from additional samples will be published shortly.

The authors are grateful to Mr. D. A. Moddle of the Ontario Department of Mines for making the chemical analyses of potassium. They would also like to acknowledge the assistance and advice of Professors E. A. Allin, W. H. Watson, and J. T. Wilson. Thanks are due to Miss D. Perryman and to Mr. W. J. Kenyon and Mr. D. E. Beuk for technical assistance.

[6] A. O. Nier, Phys. Rev. 55, 150 (1939).

Bremsstrahlung from P^{32} Betas

M. GOODRICH, J. S. LEVINGER, AND W. PAYNE
Physics Department, Louisiana State University, Baton Rouge, Louisiana
(Received May 1, 1953)

A NaI scintillation spectrometer has been used to study the spectral distribution of bremsstrahlung from P^{32} betas stopped in brass. Experimental measurements are compared with calculations based on the theoretical photon distribution, corrected for the response of the crystal. The experimental and calculated curves agree within 10 percent for photon energies from 50 to 1100 kev.

INTRODUCTION

THE energy distribution of photons emitted as bremsstrahlung in beta decay is of theoretical interest and also of practical importance, as it provides some of the background in studies of nuclear gammas. Recently Wyard[1] has made an approximate calculation of the spectrum of bremsstrahlung from P^{32} betas. Wyard checked his calculated energy spectrum by absorption measurements, and found reasonable agreement. We have made a more accurate check of Wyard's calculated spectrum, by the use of a NaI scintillation spectrometer. In the next section we describe the equipment used and the experimental results. We then discuss Wyard's approximation for the photon spectrum, the effect of inner bremsstrahlung, and the calculation of the pulse-height spectrum for our NaI crystal. In the last section we compare the experimental results with the calculations; and also set an upper limit on the intensity of nuclear gammas from P^{32}.

EXPERIMENTAL MEASUREMENTS

The P^{32} was produced by neutron activation of KH_2PO_4 in the Oak Ridge pile, and photon spectra from several samples were studied using a NaI scintillation spectrometer. Sample A showed humps in the photon spectrum due to nuclear gammas.[2] Sample B was purified further (see Appendix A) thus greatly reducing the radioactive contamination. Sample A was measured 39 days after the end of neutron activation; while sample B was measured 12 days subsequently. The samples were measured as $Cu_3(PO_4)_2$ in a brass box 1.1 g/cm^2 thick to stop the betas. The brass box was placed directly on the aluminum cover of the NaI crystal, giving a source-crystal distance of about 0.2 cm.

The NaI scintillation spectrometer is quite similar to that used by Jordan, Bell, and associates.[3] It consists of a NaI crystal 1½ in. diameter, 1 in. long, activated with Tl, and enclosed in a 0.01 in. Al light-shield. The light was measured with a Dumont K1186 photomultiplier. The pulse-height spectrum was measured using a single channel differential pulse-height analyzer, with a constant narrow window. The linear energy scale was calibrated using nuclear gammas from Cs^{137} (661 kev) and Ba^{131} (122 kev, 220 kev, 369 kev, and 496 kev).

The data on number of pulses *vs* pulse energy for energies from 40 to 1400 kev is presented in Fig. 1, normalized to 100 at an energy of 300 kev. For sample B, the counting rate at 300 kev was 73 counts/sec. Statistical rms errors are shown in the figure for energies greater than 1100 kev; statistical errors were 1 percent at lower energies. At 1400 kev the counting rate due to the sample was about equal to the background of 0.03 count/sec.

CALCULATIONS

Wyard[1] approximated the Bethe-Heitler-Sommerfeld thin-target bremsstrahlung spectrum[4] for electrons of energy E' by

$$I(k)=4-3k/E', \quad 0\leqslant k\leqslant E', \tag{1}$$

where $I(k)$ is the intensity of photons of energy k. He then calculated the thick target bremsstrahlung spectrum for electrons of energy E, assuming an energy loss per cm independent of electron energy:

$$I'(k)=E[4(1-k/E)-3(k/E)\ \ln(E/k)]. \tag{2}$$

Finally he used this thick-target spectrum combined numerically with the allowed form of the beta spectrum for P^{32} (end point 1.70 Mev) to give the intensity distribution for external bremsstrahlung produced by stopping betas from P^{32}. The approximations seem reasonably good for electron and photon energies from a fraction of a Mev to several Mev. The intensity distribution for the external bremsstrahlung is almost independent of the atomic number of the stopping material. The distribution would have to be recalculated, using Eq. (2), for beta spectra of greatly different form than P^{32}; but for only moderate changes in end-point energy it should still be valid if the energy scale is adjusted appropriately.

We find the photon distribution for external bremsstrahlung by taking Wyard's intensity distribution divided by the energy per photon. The resulting distribution is given as curve EB in Fig. 1; and is also given in Table I.

[1] S. J. Wyard, Proc. Phys. Soc. (London) **A65**, 377 (1952); and private communication.
[2] Goodrich, Levinger, and Payne, Bull. Am. Phys. Soc. **28**, No. 3, 31 (1953).
[3] W. H. Jordan and P. R. Bell, Nucleonics **5**, No. 4, 30 (1949); W. H. Jordan, *Annual Review of Nuclear Science* (Annual Reviews, Inc., Stanford, 1952), Vol. 1, p. 207.
[4] W. Heitler, *Quantum Theory of Radiation* (Oxford, University Press, London, 1944), second edition, Sec. 17.

TABLE I. Bremsstrahlung spectra from P^{32} betas. The table gives the calculated photon spectra for external bremsstrahlung (EB) and inner bremsstrahlung (IB) from P^{32} betas, both normalized at 300 kev; or photon energy/beta endpoint $= k/E_0 = 0.175$. The EB spectrum is calculated by Wyard (reference 1 of this paper, and private communication); the IB spectrum is calculated by the KUB equation (references 5 and 6).

k/E_0	0.1	0.2	0.3	0.4	0.5	0.6	0.7	0.8	0.9	1.0
EB	261	77.4	30.3	12.5	5.1	1.97	0.64	0.16	0.02	0
IB	223	81.	36.	17.	8.3	3.8	1.4	0.33	0.02	0

The photons from P^{32} betas consist of both external bremsstrahlung (EB) due to stopping the betas, and inner bremsstrahlung (IB) emitted in the act of beta creation. The IB spectrum has been calculated by Knipp and Uhlenbeck[5] and by Bloch[6] (KUB); and recently confirmed experimentally for P^{32} from 30- to 250-kev photon energy by Bolgiano, Madansky, and Rasetti,[7] and by Novey.[8] The IB photon distribution is given as curve IB in Fig. 1, and also in Table I. Both the EB and IB photon spectra are normalized to 100 at 300 kev.

We agree with Wyard's calculation that for P^{32} betas stopped in brass the relative total energy of EB to IB is 4:1 (see Appendix B). Within the accuracy of the absorption techniques he used it was not necessary to correct the EB distribution for this small fraction of IB of rather similar spectral distribution; while we should use the correct proportion of EB and IB. (The efficiency of EB production is proportional to Z, while the IB intensity is independent of Z; the present experiment using a brass absorber for the betas was designed, following Wyard, to emphasize the EB, but not to use such a high Z that photon absorption by the absorber would be of great significance.)

The pulse-height distribution given as curve P in Fig. 1 was calculated from this mixture of EB and IB photon spectra taking into account the response curve of the NaI crystal, and absorption and degradation of photons by the brass and aluminum. Some details of the calculation are given in Appendix B.

DISCUSSION

The agreement between the measurements for the purified sample B and the calculated pulse-height distribution (curve P) shown in Fig. 1 is considered good. The experimental points agree with the calculated curve within an accuracy of 10 percent for photon energies from 50 to 1100 kev, or a factor of over 3000 in the counting rate. Sample A shows a nuclear gamma of 600 kev which was removed in the purifications for sample B. The deviations seen for sample B above 1100 kev may be traces of the higher energy nuclear gammas in the contaminant of sample A; but our statistical accuracy is not sufficient for any definite determination of the source of these high energy deviations. We have thus confirmed the usefulness of Wyard's approximations for external bremsstrahlung; though clearly a more direct confirmation of the Bethe-Heitler-Sommerfeld calculation, and Wyard's approximation to it, would be desirable using monoenergetic electrons, and preferably thin-target bremsstrahlung spectra.

We made no measurements on the intensity of the bremsstrahlung relative to that of the beta source. However, in Appendix B we calculate a bremsstrahlung yield of 0.05 photon of energy greater than 50 kev, per beta. The photon distribution from the P^{32} source is quite sensitive to the presence of nuclear gammas—either those due to some contaminant as in sample A; or those due to nuclear gammas of very low intensity present in P^{32}. While it is generally agreed that P^{32} emits no nuclear gammas, we have found no definite statements in the literature as to an upper limit on P^{32} nuclear gammas. We can state an upper limit by comparison with the calculated bremsstrahlung yield, using the resolution of the scintillation spectrometer, and assuming that a deviation from the smooth bremsstrahlung curve of 15 percent would be detected. This upper limit varies greatly with the energy of the assumed nuclear gamma, since bremsstrahlung are comparatively plentiful at low energies, and quite rare at high energies. The upper limit for nuclear gammas from P^{32} at three different energies is: 6×10^{-4} at 200 kev; 2×10^{-4} at 500 kev; and 3×10^{-5} at 900 kev. It is clear that these upper limits could be reduced by studying a P^{32} source emitting fewer *EB*. Either the betas could be stopped in a material of lower Z, or the geometrical arrangement of Bolgiano, Madansky, and Rasetti,[7] and Novey,[8] might be used.

Note added in proof:—Recent measurements here of *IB* give a pulse distribution from 50 kev to 900 kev in good agreement with the KUB calculations. We can now lower the upper limit for nuclear gammas by a factor of about 5.

ACKNOWLEDGMENT

We gratefully acknowledge the assistance of J. Scandrett in performing some of the measurements; of Col. R. B. Emerson for performing the chemical purifications, and discussions concerning the chemistry; of S. J. Wyard for a private communication concerning his calculations; and of P. R. Bell for the use of his data on the efficiency of his NaI scintillation counter.

APPENDIX A. CHEMICAL SEPARATIONS

Sample A was purified as follows: (1) the activated KH_2PO_4 was dissolved in water; (2) the solution was made very slightly alkaline with NaOH; (3) $Cu(NO_3)_2$ solution was added; (4) the $Cu_3(PO_4)_2$ precipitate was washed with water; (5) the precipitate was extracted several times with alcohol to removed $Cu(OH)_2$ and

[5] J. K. Knipp and G. E. Uhlenbeck, Physica **3**, 425 (1936).
[6] F. Bloch, Phys. Rev. **50**, 272 (1936).
[7] Bolgiano, Madansky, and Rasetti, Phys. Rev. **89**, 679 (1953).
[8] T. B. Novey, Phys. Rev. **89**, 672 (1953).

other impurities; (6) the sample was dried and mounted on Scotch tape.

Sample *B* was purified starting with the first 4 steps for sample *A*. The $Cu_3(PO_4)_2$ precipitate was then dissolved in dilute HCl, and steps 2, 3, and 4 above were repeated. This further purification was repeated two more times; and the sample dried and mounted.

We have not investigated carefully to determine the identity of the radioactive contaminant giving the 600-kev gamma in activated KH_2PO_4 from Oak Ridge. The following information might be of use in future work to identify the impurity: (1) the energy is 620 ± 40 kev; (2) the half-life is appreciably longer than that of P^{32} (14.8 days); (3) for sample *A*, 39 days after the end of neutron activation, the intensity was roughly one 600-kev gamma per 600 beta-disintegrations of P^{32}; (4) samples were prepared following a procedure like that of sample *A*, except that the phosphorus was precipitated as $Mg_3(PO_4)_2$ in one case and $Ba_3(PO_4)_2$ in another case. The four precipitates arranged in order of decreasing intensity of 600-kev gamma per beta are: $Cu_3(PO_4)_2$ (sample *A*); $Ba_3(PO_4)_2$; $Mg_3(PO_4)_2$; and $Cu_3(PO_4)_2$ (sample *B*).

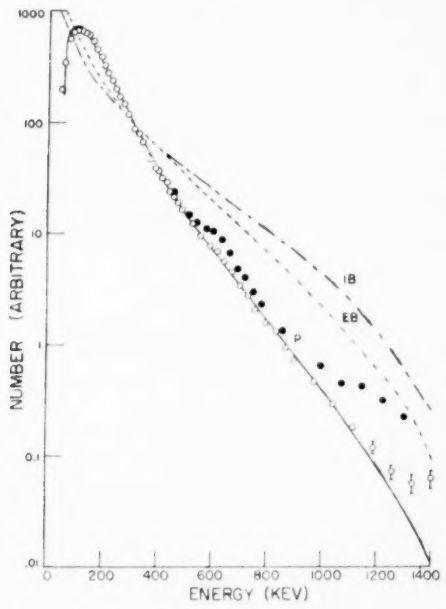

FIG. 1. Energy spectrum of P^{32} bremsstrahlung. The dashed curve is the normalized energy spectrum for external bremsstrahlung (EB) photons from P^{32}, as calculated by Wyard reference 1; the center-line is the normalized energy spectrum for inner bremsstrahlung (IB) photons from P^{32}, as calculated by KUB references 5 and 6; the solid line *P* is the calculated pulse-height distribution for our NaI crystal, for a mixture 80 percent EB with 20 percent IB. The solid circles are for sample *A* (not shown below 400 kev, where they are in substantial agreement with the open circles); the open circles are for the purified sample *B*. The vertical lines for the last four points for sample *B* show the rms statistical error. For the other experimental points the statistical error is smaller than the size of the points.

APPENDIX B. CALCULATIONS OF THE PULSE-HEIGHT DISTRIBUTION

Table I gives the calculated photon spectra for external and inner bremsstrahlung from P^{32} betas. These spectra are also plotted as curves EB and IB in Fig. 1.

The relative intensity of EB and IB can be calculated from the relative energies contained in the two forms of bremsstrahlung. The energy of EB produced by stopping an electron of energy W (including the rest energy) is approximately

$$E_{EB}=1.5N_0\alpha r_0^2(Z^2/A)[W^2-(mc^2)^2]$$
$$=6.8\times10^{-3}[W^2-(mc^2)^2]. \quad (3)$$

Here N_0 is Avogadro's number; α is the fine structure constant; the energies are given in Mev, and the numerical result is given for brass. This equation is based on two approximations: the radiative cross section ϕ_{rad} and the electron energy loss per cm are assumed to be independent of energy. (See reference 4, Fig. 15.) These same two assumptions are made in Wyard's calculation of the EB spectrum.

The energy radiated as EB for betas with an allowed form and end-point W_0 is proportional to their mean square energy $\langle W^2\rangle_{Av}$ which we have calculated as

$$\langle W^2\rangle_{Av}=[8W_0^6-10W_0^4-39W_0^2-64$$
$$+105(W_0/p_0)\ln(W_0+p_0)][14(2W_0^4-9W_0^2-8)$$
$$+210(W_0/p_0)\ln(W_0+p_0)]^{-1}. \quad (4)$$

Here

$$p_0=(W_0^2-1)^{\frac{1}{2}}.$$

The numerical result applies to P^{32}, $W_0=4.35\ mc^2$ (kinetic energy 1.70 Mev). Substituting in Eq. (3), we find that the EB energy is 9.3 kev per beta, or 0.55 percent of the beta disintegration energy, for P^{32} betas stopped in brass.

Bloch[6] calculates the IB energy, giving 0.17 percent as the ratio of IB energy to beta disintegration energy for P^{32}. However, this was based on too high a value for the end-point energy for P^{32}. If we use 1.70 Mev, and Bloch's formula, we find 0.14 percent or one-quarter the value of the EB energy, confirming Wyard's result.[1]

Using Wyard's photon spectrum for EB, together with the value given above for the EB energy, we calculate the ratio of EB photons to betas. The total number of EB photons of energy greater than 50 kev is 0.042 per beta. At 300 kev there are 4.0×10^{-5} EB photons/kev per beta. These figures should be increased by 25 percent because of the IB.

The pulse-height distribution for the NaI crystal was calculated using the photon distribution for 80 percent EB plus 20 percent IB, as given in Table I, and taking into account the effects of the brass and aluminum absorbers, and of the response curve of the NaI crystal. The main contribution to the counting rate is found

to be

$$C(k)=S(k)T(k)\epsilon_p(k). \quad (5)$$

Here $S(k)$ is the photon spectrum (see Table I); $T(k)$ is the transmission for the brass and aluminum for photons of energy k, and $\epsilon_p(k)$ is the efficiency of detection in the photopeak by the NaI crystal. $T(k)$ was determined from the absorption coefficients given in Compton and Allison[9] and Heitler.[4] $\epsilon_p(k)$ was determined as the product of the over-all crystal efficiency $\epsilon(k)$ times the fraction of the pulses that appear in the photopeak. We determined $\epsilon(k)$ by combining Bell's experimental values[10] of the absorption coefficient of NaI with the calculations by the Oak Ridge Mathematics Panel[10] for a $1\frac{1}{2}$ in.$\times$1 in. NaI crystal. The fraction of pulses in the photo-peak (either due to photoeffect in the crystal, or Compton scattering, with subsequent absorption of the scattered gamma[11]) was also taken from Bell's data.[10] The value for Cs^{137} (661 kev) was confirmed within 10 percent by measurements in our laboratory.

We made corrections to $C(k)$ for degradation of photons in the brass and aluminum absorbers, and for Compton pulses in the NaI crystal. Since each correction was rather small (maximum of 15 percent for energies above 150 kev), simple analytic approximations were made in the calculation of these corrections.

Degradation was calculated assuming: (1) that there was at most a single Compton scattering in the absorber; (2) that the energy of the Compton-scattered photon was uniformly distributed from zero to the incident energy; and (3) that the scattered photon was detected by the photopeak in the crystal.

Compton pulses in the crystal[11] were calculated by: (1) approximating the Compton part of the crystal response curve for monoenergetic photons by a curve of uniform height from zero to the maximum energy for a Compton recoil electron, and adjusting this height to give the experimental value[10] for Compton pulse to total pulse ratio; (2) approximating the photon distribution by an exponential with suitably chosen exponent.

At pulse-height energies above 150 kev, both corrections are rather small. The degradation correction is small since the absorber thickness is much less than a mean-free-path for Compton scattering. The crystal Compton pulse correction is small since a Compton pulse of energy W must be due to a photon of energy $W+B$, or greater (where B, about 200 kev, is the energy difference between the photon energy and the maximum energy of a recoil electron). Such photons are relatively rare, due to the rapid decrease of the photon spectrum with increasing energy, as shown in Table I and Fig. 1. At 50 kev the effect of Compton pulses in the crystal is relatively large [90 percent of $C(k)$], since the 50-kev photons detected in the photopeak are strongly absorbed, while the more energetic photons detected as Compton pulses in the crystal are only weakly absorbed in the brass and aluminum absorbers.

We also estimated the effect of the finite width of the photopeak for our NaI crystal, and found that this gave negligible effect (the order of 1 percent) on the pulse-height distribution for the bremsstrahlung photon spectrum.

[9] A. H. Compton and S. K. Allison, *X-rays in Theory and Experiment* (D. Van Nostrand Company, Inc., New York, 1935), Appendix IX.

[10] P. R. Bell and Oak Ridge Mathematics Panel (private communications).

[11] W. H. Jordan, reference 3, pp. 218–226.

Triton-Induced Activities in Magnesium and Aluminum*†

ERIC IWERSEN AND W. S. KOSKI, *Department of Chemistry*

AND

FRANCO RASETTI, *Department of Physics,*
The Johns Hopkins University, Baltimore, Maryland

(Received May 25, 1953)

Triton bombardment of Al^{27} and Mg^{26} gave a 6.5-min aluminum activity as a result of $Al^{27}(t, p)Al^{29}$ reaction and 21.8-hr activity of magnesium produced by the $Mg^{26}(t, p)Mg^{28}$ reaction.

Studies of the gamma-ray spectrum of Mg^{28} showed that a 391 ± 5-kev gamma ray and possibly two more gamma rays with energies 0.95 and 1.35 Mev were associated with the decay of this isotope.

A search was made for a $P^{31}(t, p)P^{33}$ reaction but negative results were obtained.

INTRODUCTION

A RELATIVELY large number of (d, p) reactions have been investigated, and certain aspects of such reactions have been explained in terms of the polarization of the deuteron by the Coulomb field of the nucleus.[1] On the other hand, it is expected that the same type of process may occur with tritons; however, relatively few such reactions have been demonstrated experimentally.[2] We have recently had occasion to examine triton-induced activities in magnesium and aluminum realized by the (t, p) reaction. This type of reaction is of interest not only from the theoretical but also from the experimental point of view, since it enables one to produce radioisotopes which are two neutrons removed from the nearest stable isotope and thereby confirm in some instances uncertain mass assignment of such isotopes and in other instances to produce new isotopes.

EXPERIMENTAL

The bombardment of magnesium and aluminum was accomplished by the use of tritons from the $d-d$ and $Li^6(n, t)He^4$ reactions. In general, it was found most convenient to incorporate the deuterium or lithium in a chemical compound with the atoms to be bombarded. In the case of aluminum, $LiAlD_4$ was bombarded with deuterons from our electrostatic generator and in the case of magnesium, some experiments were made with $MgSO_4 \cdot 6D_2O$. In general, deuteron bombardment of these compounds gave low yields of the (t, p) reaction products and is being utilized only in case of short-lived isotopes. In the case of isotopes of moderately long life such as Mg^{28}, it was found to be more convenient to bombard, with pile neutrons, a Li-Mg alloy formed by heating a 2–1 mole ratio of Li to Mg at 700°C. In both the accelerator and pile irradiations, more than one activity is produced in general, necessitating chemical processing of the target material. In the case of aluminum, the $LiAlD_4$ was dissolved in HCl and carriers of NO_3^- and Mg^{++} were added to remove N^{13} formed by $C^{12}(d, n)N^{13}$ and Mg^{27} formed by $Al^{27}(n, p)Mg^{27}$. The C^{12} which is the source of N^{13} arises from diffusion pump oil vapor. The Mg separation was realized by making the solution sufficiently basic with NaOH so that the Al would dissolve but the Mg would precipitate as the hydroxide. This procedure repeated twice was sufficient to remove interfering activities. The aluminum was removed from solution by precipitating as $Al(OH)_3$. After washing, the precipitate was dissolved in HCl and counted in a dip counter.

The Li-Mg alloy after irradiation was dissolved in HCl to which carriers of Cu, Ni, Fe, Co, Mn, and Na which were suspected impurities were added. The Cu, Ni, etc., were separated from the Mg by hydrogen sulfide precipitation. This process was repeated several times and then the Mg was precipitated as the hydroxide which was liberally washed with water containing NaOH. A portion of this precipitate was used for half-life measurements with an end-window Geiger-Mueller counter and the remainder for gamma-ray measurements. As a confirmation of the mass assignment of the magnesium activity, Al^{28} activity was milked out by precipitating the magnesium as the hydroxide in a strongly basic NaOH solution. The $Mg(OH)_2$ was then centrifuged and the supernatant liquid was examined for Al^{28} activity using a dip counter.

The gamma-ray spectrum of a Mg^{28} source was analyzed by means of an NaI(Tl) crystal scintillation spectrometer. The source was enclosed in an Al container 6 mm thick to absorb all the beta rays, including those of the daughter nucleus Al^{28}, and placed immediately above a crystal of dimensions 2.1 cm×2.1 cm×1.1 cm. The pulse-size spectrum was determined by means of an Atomic Instrument Company linear amplifier and single-channel analyzer. The source intensity was sufficient to yield good readings in one or a few minutes. Curves were taken at various photomultiplier voltages in order to explore the spectral region from 0.05 to 2 Mev. The resolution of the

* This work was supported by the U. S. Atomic Energy Commission.

† Abstracted in part from a dissertation to be submitted by Eric Iwerson in partial fulfillment for the degree of Doctor of Philosophy in The Johns Hopkins University.

[1] J. R. Oppenheimer and M. Phillips, Phys. Rev. **48**, 500 (1935).

[2] D. N. Kundu and M. L. Pool, Phys. Rev. **73**, 22 (1948).

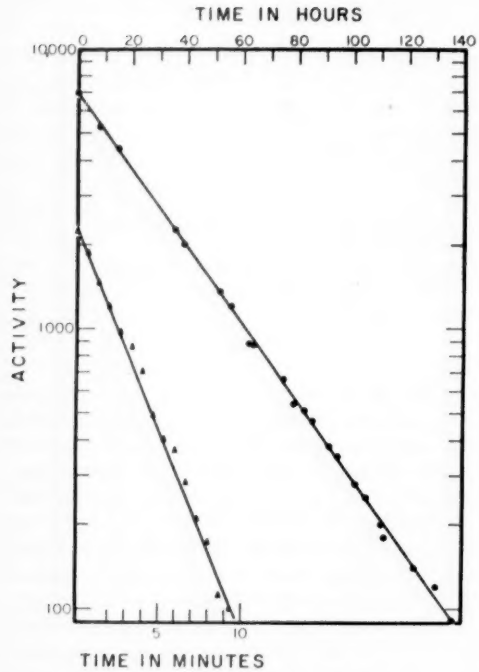

FIG. 1. The decay of Mg^{28} is given by the upper curve. The lower curve gives the decay of Al^{28} milked from an equilibrium mixture of Mg^{28} and Al^{28}.

spectrometer corresponded to 27 percent full width at half-maximum for the Cd^{109} line at 88 kev. Energy calibration was supplied by the photoelectric peaks of several known lines, expecially the annihilation radiation, the Na^{22} line at 1.28 Mev and the ThC″ line at 2.62 Mev. In some experiments, a qualitative picture of the spectrum was obtained by photographing the pulses from the linear amplifier on a synchroscope screen.

RESULTS AND DISCUSSION

Triton-Induced Activity in Magnesium

The decay of the Mg^{28} as a function of time is given in Fig. 1. A half-life of $21.8_5 \pm 0.32$ hr, where the 0.32 hr is the standard deviation, was obtained for Mg^{28}; this is in good agreement with the half-life reported by Sheline and Johnson.[3]

The correctness of the mass assignment of this activity is further confirmed by the Al^{28} milking experiments, the result of which is given by the lower plot in Fig. 1. The half-life obtained here is 2.1 ± 0.2 min which, to within our experimental error, is the generally accepted value. These results, therefore, indicate that Mg^{28} was produced by the $Mg^{26}(t, p)Mg^{28}$ reaction.

Mg^{28} will probably find wide use as a tracer in certain chemical, geological, and biological problems. For many of these applications pile production of Mg^{28} offers some advantages over the accelerator-produced material because of the wider availability of the pile irradiation and because considerably greater yields of the radioisotope are possible. Mg^{28} as produced by the (t, p) reaction is isotopic with the target material, and consequently this method would not be used for producing the isotope carrier-free.

[3] R. K. Sheline and N. R. Johnson, Phys. Rev. **89**, 520 (1953).

Gamma-Ray Spectrum of $Mg^{28} - Al^{28}$

Preliminary exploration indicated a strong gamma-ray photoelectric peak near 0.4 Mev. To perform an energy determination, this peak was compared with the 238.6-kev line of ThB and the annihilation radiation, other experiments having shown that the scale was accurately linear in this region at the voltage employed. The result was 391 kev, with an error estimated at ± 5 kev.

A complete differential pulse-size spectrum in the region 0.25–1.8 Mev is shown in Fig. 2. The photoelectric peak at 1.8 Mev due to the Al^{28} line is not well resolved from the Compton continuum. At lower energies the curve shows several maxima which cannot be entirely assigned to the 1.8-Mev line. The most pronounced of these maxima occur at 0.9–1.0 Mev and 1.3–1.4 Mev. They may be due to photoelectric peaks of lines of the corresponding energies. To compare these results with the effects of a monochromatic gamma-ray of 1.8 Mev, a source of Al^{28} was examined under identical conditions. As the short life of this isotope prevented use of the pulse analyzer, the less quantitative method of photographing pulses displayed on the oscilloscope screen was employed. A block of pure aluminum was irradiated with slow neutrons and then placed near the crystal; the exposure time was two half-lives of the Al^{28}. Sufficient intensity was present to yield good photographs of the spectrum. These, both on visual inspection and from densitometer curves, showed a weak but well-resolved photoelectric peak, the Compton distribution, and a pair peak (with escape of the annihilation radiation) at the expected positions.

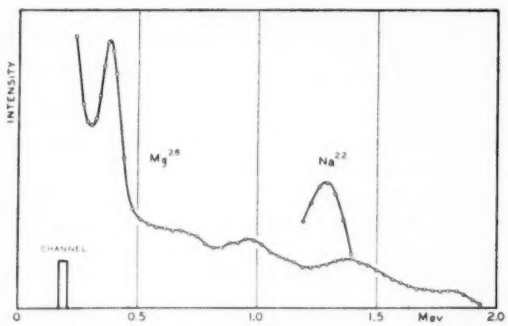

FIG. 2. Pulse size spectrum from a Mg^{28} source. The width of the channel is indicated by a rectangle. The photoelectric peak of the Na^{22} line at 1.28 Mev was used for energy calibration.

Hence it seems certain that the maxima observed near 1.35 and 0.95 Mev are not due to the Al^{28} line, but represent additional lines of Mg^{28}. From our experiments, the energies of these lines cannot be accurately determined, owing to the low intensity of the photoelectric peaks obtained with the relatively thin crystal employed.

The decay of the 391-kev line was followed for 4 half-lives by setting the spectrometer to cover its photoelectric peak. The decay curve thus obtained was exponential within the limit of experimental error and yielded a half-life of 22 hours, in agreement with other determinations.

After our experiments had been completed, Sheline and Johnson[4] reported gamma-ray lines of Mg^{28} at 0.40, 0.95, and 1.35 Mev. The low-energy line agrees well with our determination; the others also agree with the low maxima observed on our curve.

Triton Induced Activities in Aluminum

The aluminum activities obtained by deuteron bombardment of $LiAlD_4$ are indicated in Fig. 3. Aluminum activities of 2.5-min and 6.5-min half-lives are observed, corresponding to the accepted values of Al^{28} and Al^{29}, respectively. Although the yield of Al^{29} is lower than might be desired, there does not seem to be much question as to its presence, which indicates the realization of the $Al^{27}(t, p)Al^{29}$ reaction here.

Search for (t,p) Reaction in Phosphorus

The phosphorus activity produced by pile irradiation of lithium phosphate was examined for evidence of the $P^{31}(t, p)P^{33}$ reaction. The activity was followed for six half-lives and no deviation was obtained from the accepted half-life of P^{32}, indicating that very little or no P^{33} was formed. A possible explanation for this behavior may be the fact that the compound nucleus formed by incorporation of two neutrons from the triton is in an excitation state whose energy is appreciably greater than the binding energy of the neutron, thereby resulting in a "boiling off" of the neutron and production of P^{32}.

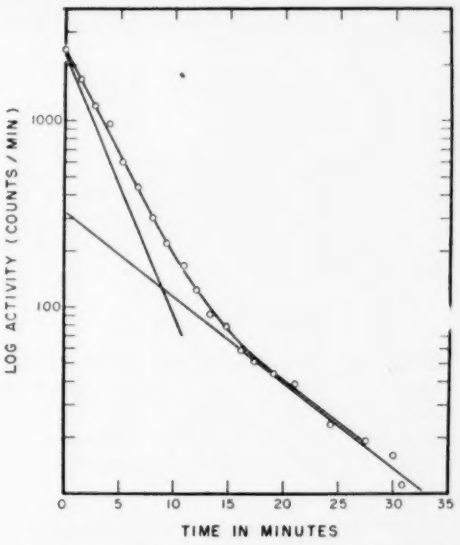

FIG. 3. Aluminum activities produced by bombardment of $LiAlD_4$ with deuterons.

We are indebted to Dr. V. W. Cohen and members of the Isotope Branch of the Brookhaven National Laboratory for the various pile neutron irradiations that were made during the course of work reported here.

[4] R. K. Sheline and N. R. Johnson, Phys. Rev. **90**, 325 (1953).

Cross Terms in Allowed Shape β Spectra*

J. P. DAVIDSON AND D. C. PEASLEE
Columbia University, New York, New York
(Received March 30, 1953)

A statistical analysis is made of allowed shape β spectra to determine the magnitude of any $1/W$ terms that may be present. Both allowed and first forbidden spectra are analyzed; only the allowed spectra are discussed here. It is concluded that the (T, A) mixture in β decay is $\lesssim 4$ percent. Unfortunately only one measurement can be used for the (S, V) mixture, and it does not limit the mixture to less than ~ 10 percent. For neither (T, A) nor (S, V) is the mixture significantly different from zero.

I. INTRODUCTION

THE object of the present note is to determine the maximum admixture of β-decay interactions $(S+V)$ or $(T+A)$ that is consistent with the observed absence of $1/W$ terms in allowed spectrum shapes.

In allowed β decay, the spectrum shape is given by a unique function,

$$N(W, W_0)dW = F_0(Z, W)(W_0-W)^2 p dW, \quad (1)$$

where p, W are the electron momentum and energy in mc^2 units, W_0 is the spectrum end-point energy, and $F_0(Z, W)$ is a specific function[1] of charge and energy. It is customary to plot the quantity $n=(N/pF)^{\frac{1}{2}}$ as a function of W, obtaining a straight line that extrapolates to the energy W_0.

If the β-decay interaction contains an arbitrary mixture of $SVTA$ terms, Eq. (1) must be modified by writing[2]

$$n=C(W_0-W)\left\{\left|\int 1\right|^2(1+R/W)+\left|\int \boldsymbol{\sigma}\right|^2(1+R'/W)\right\}^{\frac{1}{2}}$$
$$=C'(W-W_0)[1+r/W]^{\frac{1}{2}}, \quad (2)$$

where $\int 1$ and $\int \boldsymbol{\sigma}$ are the Fermi and Gamow-Teller matrix elements, including the respective coupling constants. Here

$$R=-2(1-\alpha^2Z^2)^{\frac{1}{2}}\lambda_S\lambda_V[\lambda_S^2+\lambda_V^2]^{-1},$$
$$R'=-2(1-\alpha^2Z^2)^{\frac{1}{2}}\lambda_A\lambda_T[\lambda_A^2+\lambda_T^2]^{-1}, \quad (3)$$

where the λ's are coupling constants.

II. NUMERICAL ANALYSIS

For the analysis of spectrum shapes, the standard plot of n is rather insensitive because of the dominant (W_0-W) term. When this factor is divided out, deviations from linearity as well as the experimental fluctuations are greatly magnified. The experimental quantity used for the analysis is therefore

$$m(W)=[n/(W_0-W)]^2=(a+b/W). \quad (4)$$

A particular spectrum is fitted by minimizing $\sum_j(a+b/w_j-m_j)^2$ with respect to a and b, whence

$$r=b/a=(MK-NJ)/(NK-ML),$$
$$J=\sum_j 1, \quad K=\sum_j 1/W_j, \quad L=\sum_j 1/W_j^2, \quad (5)$$
$$M=\sum_j m_j, \quad N=\sum_j m_j/W_j.$$

The summation in (5) over j includes all the experimental points considered in a given spectrum. Usually m_j deviate badly at both ends of the spectrum for experimental reasons, and some criterion is necessary for selecting the points to be used. The following procedure is adopted here: after discarding by inspection values of m_j differing by an order of magnitude from the average of any spectrum, the mean value $\langle m_j\rangle_{Av}$ of the remaining points is computed. From the center of the spectrum, which is experimentally most reliable, is selected the largest continuous range in which no individual point m_j deviates by more than a prescribed amount x from $\langle m_j\rangle_{Av}$:

$$(1-x)\langle m_j\rangle_{Av}\leq m_j\leq(1+x)\langle m_j\rangle_{Av}. \quad (6)$$

The quantity x is always taken so that the adopted range includes the majority of the spectrum. For most of the spectra analyzed, this could be achieved with $x=10$ percent, which was taken as a standard figure; for one or two exceptional cases, however, larger values of x were necessary. Such preselection improves the consistency of the data used at the expense of the total number of independent points in $\sum_j$, thereby reducing the statistical reliability of the fit (5).

The error in the estimate (5) for n comes from the errors Δ_j in the original points n_j, and the error Δ_0 in the choice of W_0 to convert the data from n_j to m_j. Considering these errors as all independent and assuming a constant fractional error for the points $\Delta_j=\gamma n_j$, we have

$$\Delta_r^2=Q^2\{\gamma^2\textstyle\sum_j m_j^2(N-M/W_j)^2$$
$$+(\Delta_0/W_0)^2[\textstyle\sum_j m_j'(N-M/W_j)]^2\}$$
$$Q=(K^2-JL)/(NK-ML)^2, \quad (7)$$
$$m_j'=-m_jW_0/(W_0-W_j).$$

The calculations for a number of allowed-shape spectra are summarized in Table I. About half the cases considered are presumably 1st forbidden tran-

* Work performed under the research program of the U. S. Atomic Energy Commission.
[1] E. Fermi, Z. Physik **88**, 161 (1934).
[2] M. Fierz, Z. Physik **104**, 553 (1937).

sitions.† The column Δ_r in Table I is computed by assuming $\gamma=2$ percent, $\Delta_0/W_0=1$ percent; the column Δ_r' has $\gamma=0.5x$, $\Delta_0/W_0=0.2x$.

III. DISCUSSION

We discuss only the allowed transitions, which form the first part of Table I. Using the error Δ_r', we have

$$\Delta_r' \gtrsim |r| \tag{8}$$

for all members of the table. That is, by assuming generous but not unreasonable errors (the points used were all read off published graphs) we conclude that none of the values of r is significantly different from zero.

Consider the $\Delta I=1$ transitions, which contain only the Gamow-Teller terms T and A and comprise all but the first case in Table I. Deviations in the spectrum shape caused by the finite size of the nucleus[3] contribute an effective $r\approx\pm0.01$ in the cases considered and can be neglected here. Screening corrections[4] are of the same order of magnitude for the β^- emitters but are an order of magnitude larger for the β^+ spectrum of Cu^{64}. The Gamow-Teller cases in Table I that do not require substantial corrections and have small straggling of the experimental points ($x=0.10$) are P^{32}, $Cu^{64\,d,f}(\beta^-)$. The mean of these cases weighted with Δ_r is

$$r=0.00\pm0.08. \tag{9}$$

The lower limit of our knowledge of r is set by the error term in (9); comparing with (3), we may say that the (T, A) mixture in the β-decay interaction is at most about 4 percent.

To obtain similar information on the mixture of S and V, we must use transitions with $\Delta I=0$, $\Delta T=0$, where T is the total isotopic spin of the nucleus. This second condition rules out cases like S^{35} and in fact restricts us to mirror level transitions. These are generally high-energy positron emitters of short lifetime, which are therefore difficult to measure. Only the N^{13} spectrum is available, from which

$$r\approx0.1\pm0.1. \tag{10}$$

This r combines that of the Fermi term and the Gamow-Teller term, which is also present. For this $p_{\frac{1}{2}}$ transition, however, the Gamow-Teller contribution is considerably smaller than the Fermi part, so that the (S, V) mixture is specified by (10).‡

Measurements of additional mirror level transitions in odd A nuclei would be helpful in reducing this upper limit for the (S, V) mixture. High precision is essential, especially in determining W_0. The most favorable transitions are those with small values of the Gamow-Teller matrix element $\int\boldsymbol{\sigma}$, as discussed in relation to the Fermi term in $\beta-\nu$ correlation.[5]

The numerical calculations of Table I were largely performed on IBM punched card machines through the courtesy of the Watson Scientific Computing Laboratory. The authors wish to thank Professor M. Deutsch and Dr. M. E. Rose for constructive criticism.

TABLE I. Analysis of $1/W$ terms in allowed shape spectra.

Decay	E_0 (Mev)†	x	r	Δ_r	Δ_r'
(A) Allowed transitions					
N^{13} [a]	+1.200	0.10	0.25	0.27	0.53
He^{6} [b]	3.500	0.25	0.66	0.24	1.24
P^{32} [c]	1.698	0.10	−0.07	0.09	0.19
Cu^{64} [d]	0.582	0.10	0.14	0.17	0.34
Cu^{64} [e]	0.582	0.15	−0.07	0.03	0.12
Cu^{64} [f]	0.571	0.10	0.18	0.24	0.49
Cu^{64} [d]	+0.661	0.15	−0.31	0.24	0.74
Cu^{64} [f]	+0.657	0.10	−0.08	0.16	0.36
(B) First forbidden transitions					
Ba^{139} [g]	2.270	0.10	0.22	0.11	0.24
Pr^{143} [h]	0.932	0.10	0.01	0.11	0.23
Pm^{147} [i]	0.227	0.10	−0.22	0.47	0.96
Hf^{181} [j]	0.404	0.10	0.38	0.36	0.71
Hf^{181} [k]	0.412	0.10	−0.21	0.19	0.43
Re^{186} [l]	1.073	0.15	0.13	0.15	0.46
Re^{186} [c]	1.063	0.10	0.07	0.16	0.32
Au^{198} [m]	0.975	0.10	0.38	0.48	0.97
Au^{198} [c]	0.956	0.10	−0.10	0.08	0.17

‡ Energies with a + sign indicate β^+ decay.
[a] W. F. Hornyak and T. Lauritsen, Phys. Rev. **77**, 160 (1950).
[b] Wu, Rustad, Perez-Mendez, and Lidofsky, Phys. Rev. **87**, 1140 (1952).
[c] L. M. Langer and H. C. Price, Jr., Phys. Rev. **76**, 641 (1949).
[d] Langer, Moffat, and Price, Phys. Rev. **76**, 1725 (1949).
[e] Same as d, but with thicker source.
[f] G. E. Owen and C. S. Cook, Phys. Rev. **76**, 1726 (1949).
[g] L. R. Shepard and J. M. Hill, Nature **162**, 566 (1948).
[h] Feldman, Lidofsky, Macklin, and Wu, Phys. Rev. **76**, 1888 (1949).
[i] Lidofsky, Macklin, and Wu, Phys. Rev. **76**, 1888 (1949).
[j] K. Y. Chu and M. L. Wiedenbeck, Phys. Rev. **75**, 226 (1949).
[k] C. Y. Fan, Phys. Rev. **87**, 252 (1952).
[l] Beach, Peacock, and Wilkinson, Phys. Rev. **76**, 1585 (1949).
[m] Steffen, Huber, and Humbel, Helv. Phys. Acta **22**, 167 (1949).

† These are discussed in a separate publication, D. C. Peaslee, Phys. Rev. (to be published).
[3] M. E. Rose and C. L. Perry, Phys. Rev. **90**, 479 (1953).
[4] J. R. Reitz, Phys. Rev. **77**, 10 (1950).

‡ The quantity r expresses directly the mixture of interactions, according to (3). If the square of this quantity is used as a measure of the mixture [H. M. Mahmoud and E. J. Konopinski, Phys. Rev. **88**, 1266 (1952)], the mixture parameter becomes $\lesssim0.2$ percent for (T, A) and is of order 1 percent for (S, V).
[5] D. C. Peaslee, Phys. Rev. **89**, 1148 (1953).

The Half-Life of Thallium-204†

GARMAN HARBOTTLE
Chemistry Department, Brookhaven National Laboratory, Upton, New York
(Received May 26, 1953)

A determination of the half-life of thallium-204 has given the value 4.0±0.1 years.

THE half-life of the long-lived isotope of thallium formed by neutron capture has been reported to be 2.7 years[1] and 3.5 years.[2] In this note we wish to report an additional determination of the half-life.

A sample of active thallium was obtained as thallous nitrate which had been irradiated with neutrons in the Oak Ridge Reactor, and had cooled for 2.2 years. The thallous nitrate was dissolved, scavenged twice with ferric hydroxide, oxidized to thallic hydroxide, washed and dissolved in perchloric acid. The trivalent thallium was finally extracted from a perchlorate-chloride solution into ether.

A few drops of the ethereal solution were evaporated to dryness in the center of an aluminum plate; the radioactive deposit was covered with a coating of "Glyptal" which was baked on when dry, and the varnish was covered with a layer of "Aquadag" to prevent charging effects.

The resultant source, which had a highly reproducible counting rate of about 19 000 counts per minute, was counted at frequent intervals in a "Nucleometer" (methane-flow proportional counter) over a period of about 2.9 years. The source was oriented reproducibly in the counting chamber, a million or more counts were usually recorded, and a standard was counted each day as a check on the operation of the "Nucleometer." At all counting rates employed in this experiment the coincidence loss was well under 1 percent and consequently no correction for coincidence loss was made.

A least-squares fit of the results, plotted as log (Tl^{204} counting rate corrected for background) *versus* time, yields a half-life of 4.02±0.12 years. This half-life is not far from the earlier value of 3.5 years but is entirely inconsistent with the later values of 2.7 years.

The author is indebted to Mrs. William Ryan for the purification of the thallium used in this source, and to Mrs. Hugh Campbell for much of the counting.

† Research carried out under the auspices of the U. S. Atomic Energy Commission.

[1] A. F. Voigt, private communication listed in "Table of Isotopes" by Hollander, Perlman and Seaborg, December, 1952 [Revs. Modern Phys. **25**, 469 (1953)]; and E. E. Lockett and R. H. Thomas, Nucleonics **11**, No. 3, 14 (1953).

[2] K. Fajans and A. F. Voigt, Phys. Rev. **60**, 619 (1941).

π^- and μ^- Meson-Induced Fission*

W. JOHN AND W. F. FRY†
Radiation Laboratory, Department of Physics, University of California, Berkeley, California, and Department of Physics, University of Chicago, Chicago, Illinois
(Received May 26, 1953)

Meson-induced fission has been studied in uranium-loaded Ilford C-2 emulsions exposed to the π^- and μ^- meson beams of the University of Chicago cyclotron. 3762 π^- endings were studied including 16 fission events. 3573 μ^- endings were studied including 7 fission events. The probability of a π^- meson ending in fission is found to be $(4.3\pm1.5)\times10^{-3}$ in C-2 emulsion containing 0.052 g cm^{-3} of uranium. The corresponding probability for μ^- mesons is found to be $(1.7\pm0.7)\times10^{-3}$. Assuming that the emulsion is a homogeneous mixture and that the atomic capture probability is proportional to Z, it is found that (37±13) percent of π^- absorptions in uranium produce fission and (15±6) percent of μ^- absorptions produce fission. If the emulsion is considered to be composed of AgBr and gelatin with the uranium in the gelatin, the corresponding percentages are found to be (18±6) percent and (7±3) percent.

INTRODUCTION

THE probability that a π^- meson stopping in uranium-loaded emulsion will cause a fission event is the product of the probability that the meson will be absorbed in an uranium nucleus and the probability that a π^- meson absorption by the uranium nucleus causes fission. Experimental data on π^- absorption in uranium-loaded emulsion can be used to calculate these probabilities if certain assumptions are made. π^- absorption in uranium-loaded emulsions was previously studied by Al-Salam.[1] The present investigation takes

* This work was performed under the auspices of the U. S. Atomic Energy Commission.

† Present address, Department of Physics, University of Wisconsin, Madison, Wisconsin.

[1] S. G. Al-Salam, Phys. Rev. **84**, 254 (1951).

TABLE I. Measurements of π^- induced fissions.

Event number	Total range of fission track in microns	Ratio of ranges of fission fragments
1[a]	29	1.1
2	26	1.0
3	30	1.4
4	19	1.0
5	26	1.2
6	26	1.1
7	24	1.0
8	23	1.0
9	27	~1.1
10	29	1.3
11	24	1.1
12	24	1.6
13	24	1.1
14	24	1.3
15	28	1.1
16	27	1.3

[a] Third particle emitted from the fission.

advantage of the much improved conditions of observation made possible by the use of the meson beam at Chicago. The present study also includes the study of μ^- absorption in uranium-loaded emulsions.

EXPERIMENTAL DETAILS

200-micron Ilford C-2 emulsions were loaded with uranium. The plates were presoaked in water for about 30 minutes, then soaked in a solution of uranium acetate for an hour and a half. The plates were allowed to dry for three hours and then exposed for one hour to slow π^- mesons from the external meson beam of the University of Chicago cyclotron. The plates were soaked in developer at 8°C and developed at 29°C. Total elapsed time from the uranium solution soaking to fixing was about seven hours. The plates for the study of μ^- capture were treated as above except that they were exposed to the slow μ^- beam of the cyclotron.[2]

The emulsions were scanned at a magnification of 270×. Fission events were studied at 1400×. Fields of view were taken sufficiently far apart to eliminate the possibility of overlap. The concentration of uranium in the emulsion was determined by counting the uranium alphas in a given volume. Allowance was made for the gradation of uranium density with depth. Only the top $\frac{2}{3}$ of the emulsion was scanned. The effective concentration of uranium in the π^- plates was found to be 0.052 g cm^{-3} corresponding to 4.63×10^6 alphas hr^{-1} cm^{-3} of dry emulsion. The uranium concentration in the μ^- plates was 1.15 times higher.

APPEARANCE OF EVENTS

The plates were relatively free of background tracks except for uranium alphas. A fission event appears as a "hammer" track at the meson ending. The two prongs are collinear and approximately equal in length. The fission track is about 26μ long and somewhat heavier than the uranium alpha tracks which are about 22μ long. The fission events are fairly characteristic in appearance, however, in each case the event was carefully checked in detail at high magnification.

RESULTS OF π^- INDUCED FISSION

A total of 3762 π^- endings were studied. Sixteen fission events were seen. One fission was accompanied by the ejection of a third particle at 27° to the fission track. This third track lay completely in the emulsion with a total range of 309μ and was identified as a proton from the grain count. The range corresponds to that of a 7-Mev proton, making the third particle a possible knock-on proton. The measurements of the fission events are given in Table I. The probability of a π^- meson ending in fission is found to be $(4.3\pm1.5)\times10^{-3}$ in C-2 emulsion containing 0.052 g cm^{-3} of uranium before development. The error is estimated from the statistics and the uncertainty in uranium concentration.

RESULTS OF μ^- INDUCED FISSION

A total of 3573 μ^- endings were studied, including 7 fission events. Measurements of the fission events are given in Table II. The probability of a μ^- meson ending in fission in C-2 emulsion containing 0.052 g cm^{-3} of uranium before development is found to be $(1.7\pm0.7)\times10^{-3}$.

DISCUSSION OF π^- INDUCED FISSION

Let us denote by P_a the probability that a π^- meson stopping in uranium-loaded emulsion will be absorbed in an uranium nucleus and by P_f the probability that a π^- meson absorption by the uranium nucleus causes fission. Then the probability P that a π^- meson stopping in uranium-loaded emulsion will cause a fission event is given by $P=P_aP_f$. Unfortunately, neither P_a nor P_f is known from experiment.

We have calculated P_a in two different ways. First it was assumed that the emulsion was a homogeneous mixture. The atomic capture probability, that is, the probability that a π^- meson is captured into an orbit about a nucleus, was taken to be proportional to the atomic number of the capturing nucleus in accordance with the calculation by Fermi and Teller.[3] Then, using the known composition of Ilford C-2 emulsion, the percentage weight/atomic weight for each element was

TABLE II. Measurements of μ^- induced fissions.

Event number	Total range of fission track in microns	Ratio of ranges of fission fragments
1	29	1.4
2	25	1.1
3	24	1.3
4	23	1.1
5	27	~1.1
6	27	1.1
7	25	1.2

[2] W. F. Fry, Phys. Rev. **85**, 676 (1952).

[3] E. Fermi and E. Teller, Phys. Rev. **72**, 399 (1947).

weighted by Z to find P_a. Hydrogen was omitted from the calculation in accordance with the observation by Panofsky *et al.*[4] that π^- mesons are rarely absorbed by hydrogen in compounds. However, the omission of hydrogen has little effect on the calculation. P_a is found to be 11.5×10^{-3}. Taking P from the experimental data, one finds P_f is (0.37 ± 0.13).

P_a was also calculated under the assumption that the emulsion consists of grains of AgBr imbedded in gelatin and that the uranium is dissolved in the gelatin fraction only. Fry[2] has estimated from μ-electron decay that 39 percent of the slow μ^- mesons stopping in emulsion stop in the gelatin and 61 percent in AgBr. This is also in agreement with a rough calculation based on stopping powers. P_a is then given by 0.39 times the probability that a meson ending in the gelatin is absorbed by an uranium nucleus. The latter probability was found by taking the percentage weight/atomic weight of the elements of the gelatin including uranium but omitting hydrogen and weighting by Z. P_a is found to be 23.8×10^{-3}, and finally P_f is 0.18 ± 0.06. The assumptions of this calculation seem more applicable than the homogeneous mixture assumption, although the resulting P_f seems low considering observations of photofission and fast neutron fission.

We have also calculated the Z dependence of P_a assuming that $P_f=1$. The percentage weight/atomic weight of the various elements (omitting hydrogen) were weighted by Z^n. Both the homogeneous mixture and the AgBr-gelatin assumptions give about the same results. It is found that $n=0.1$ to 0.5 agrees with our data. Our experimental result for the number of fissions per π^- meson ending is about one-half of the figure found by Al-Salam.[1] However, the values overlap when the probable errors are considered. Al-Salam[1] concluded that essentially all π^- mesons entering uranium cause fission on the basis of a homogeneous mixture calculation. It should be pointed out that, on the AgBr-gelatin assumption, the P_f calculated from Al-Salam's data is somewhat less than 0.5.

The μ^- contamination on the π^- plates is estimated to be less than 1 percent.

DISCUSSION OF μ^- INDUCED FISSION

The prong distribution for $1516\mu^-$ endings is given in Table III. The distribution is in agreement with that obtained by Morinaga and Fry[5] in a study of μ^- stars on plates exposed under similar conditions. Morinaga and Fry estimate that this prong distribution corresponds to a π^- contamination of less than 3 π^- per 1000 meson endings. One would expect about 0.02 fission per 1000 endings from this π^- contamination. We observed about 100 times this number of fissions per 1000 endings. Hence we conclude that most of the fission events on the μ^- plates were induced by μ^- mesons.

TABLE III. Prong distribution of 1516 stars on μ^- plates.

Number of prongs	Number of events
0	1459
1	43
2	6
3	6
4	2

The study of μ^- stars in emulsions by Morinaga and Fry[5] showed that μ^- capture frequently gives rise to a nuclear excitation of 25 Mev. The calculations of Tiomno and Wheeler[6] gave nuclear excitations of the order of 15 Mev. The compound nucleus formed when a μ^- meson is captured by $_{92}U^{238}$ is $_{91}Pa^{238}$. In estimating the fission threshold of $_{91}Pa^{238}$, we note that the fission parameter Z^2/A for $_{91}Pa^{238}$ has nearly the same value as that for $_{90}Th^{234}$. The photofission threshold for $_{90}Th^{234}$ has been measured and found to be 5.4 Mev.[7] In addition, the μ^- meson must supply the mass difference between $_{91}Pa^{238}$ and $_{92}U^{238}$, which is about 2 Mev.

If the atomic capture probability is taken to be proportional to Z, the homogeneous-mixture calculation gives 0.15 ± 0.06 as the probability of a μ^- meson absorption in the uranium nucleus causing fission. The AgBr-gelatin calculation gives 0.07 ± 0.03. Both of the results are in agreement with the upper limit of 0.25 set by Galbraith and Whitehouse.[8]

The observed number of fissions per μ^- ending in emulsion of a given uranium loading appears to be about one-half the number of fissions per π^- ending, although the uncertainties are large. π^- capture would give an excitation energy of the compound nucleus of about 140 Mev. As the nucleus evaporates particles it loses excitation; after each evaporation there is a certain probability that fission will take place, until finally the excitation of the nucleus is below the fission threshold. μ^- capture leaves the compound nucleus with a much lower excitation than in the case of π^- capture, perhaps of the order of 15 Mev. Fewer particles need to be evaporated before the excitation is below the fission threshold. Hence in this interpretation the overall probability of fission in the case of μ^- capture would be smaller.

The authors thank Professor E. Segrè for suggesting this investigation and for his interest in the work. We are indebted to Professor H. L. Anderson for the use of the cyclotron and to Professor M. Schein for the use of the facilities of the Cosmic Ray Laboratory. We also wish to thank Miss Greta Kemp for her assistance with the scanning work.

[4] Panofsky, Aamodt, and Hadley, Phys. Rev. **81**, 565 (1951).
[5] H. Morinaga and W. F. Fry, Nuovo cimento **10**, 308 (1953).
[6] J. Tiomno and J. A. Wheeler, Revs. Modern Phys. **21**, 153 (1949).
[7] Koch, McElhinney, and Gasteiger, Phys. Rev. **77**, 329 (1950).
[8] W. Galbraith and W. J. Whitehouse, Phil. Mag. **44**, 77 (1953).

Large Angle Scattering of Negative Pions in Aluminum, Copper, and Lead

HARRY H. HECKMAN AND L. EVAN BAILEY
Radiation Laboratory, Department of Physics, University of California, Berkeley, California

(Received May 25, 1953)

The total cross sections for backscattering of 32±10 Mev negative pions in Al, Cu, and Pb have been measured. A stripped emulsion was embedded in a semi-infinite absorber, and exposed to an incident beam of π^- mesons. The positions and direction of mesons stopping in the emulsion were recorded. The cross sections are proportional to the ratio of the backward flux to incident flux, both of which are observed on the same strip of emulsion. The conclusions of this investigation are: (a) the scattering is consistent with energy independence in the region of 32±10 Mev; (b) the angular distribution has a maximum at 180°; (c) the cross section for backscattering is proportional to the mass number A. The total nuclear backscattering cross sections (elastic and inelastic) for negative pions in Al, Cu, and Pb are 59.6±11 mb, 192±27 mb, and 577±80 mb, respectively.

I. INTRODUCTION

ONE of the most direct ways to gather information on the nature of the pion-nucleon interaction is to study the magnitude and angular distribution of pion scattering by nuclei. Previous experiments investigating the scattering of π^- mesons by nuclei have included measurements of total and differential scattering cross sections from hydrogen[1–4] and heavier elements.[5–9] Some of the earliest information about the negative pion-nuclei interaction was obtained by the use of nuclear track emulsions.[10–15] The pion energies for these experiments have been between 30 and 150 Mev.

The present experiment studies the large angle scattering of negative pions of about 30 Mev in pure substances. The method does not differentiate between elastic and inelastic scattering, but does exclude star formation and charge exchange in the calculation of the scattering cross sections, which attenuation experiments do not. The method is adaptable most easily to elements that have a large stopping power, which precludes the use of the very light elements. For this reason, we have chosen for our study the elements aluminum, copper, and lead.

II. EXPERIMENTAL METHOD

The experimental arrangement, Fig. 1, was placed on a cart and rolled through a port into the tank of the 184-inch synchrocyclotron. The π^- mesons were produced in a $\frac{1}{4}$-inch×$\frac{1}{4}$-inch beryllium target and separated from the positively charged particles by the magnetic field. The distance between the target and the scatterer-absorber established an energy spectrum for the negative pions that had a minimum energy cutoff

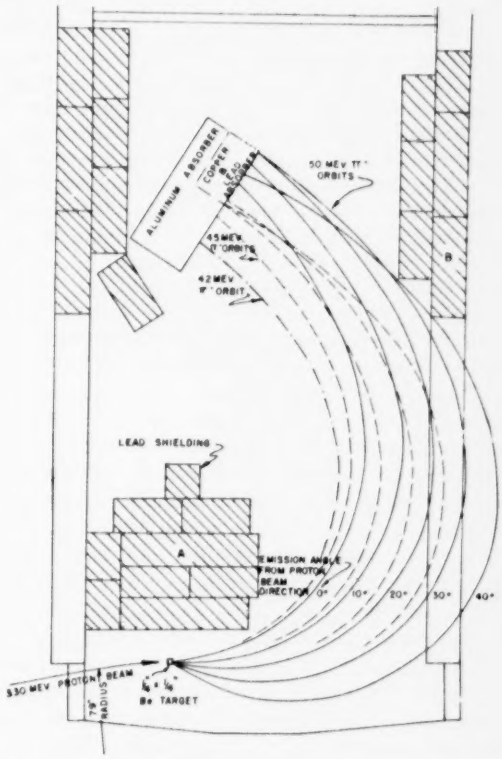

FIG. 1. Schematic drawing of experimental arrangement. Several typical π^- meson orbits of 42, 45, and 50 Mev leaving the Be target at 0 to 40 degrees from the proton beam are shown.

[1] Chedester, Isaacs, Sachs, and Steinberger, Phys. Rev. **82**, 958 (1951).
[2] Shutt, Fowler, Miller, Thorndike, and Fowler, Phys. Rev. **84**, 1247 (1951).
[3] Anderson, Fermi, Long, Martin, and Nagle, Phys. Rev. **85**, 934 (1952).
[4] Anderson, Fermi, Nagle, and Yodh, Phys. Rev. **86**, 793 (1952).
[5] R. L. Martin, Phys. Rev. **87**, 1052 (1952).
[6] Camac, Corson, Littauer, Shapiro, Silverman, Wilson, and Woodward, Phys. Rev. **82**, 745 (1951).
[7] A. M. Shapiro, Phys. Rev. **83**, 874 (1951).
[8] Byfield, Kessler, and Lederman, Phys. Rev. **85**, 718 (1952).
[9] Byfield, Kessler, and Lederman, Phys. Rev. **86**, 17 (1952).
[10] H. Bradner and B. Rankin, Phys. Rev. **80**, 916 (1950).
[11] H. Bradner and B. Rankin, Phys. Rev. **87**, 547 (1952).
[12] Bernardini, Booth, Lederman, and Tinlot, Phys. Rev. **80**, 924 (1950).
[13] Bernardini, Booth, Lederman, and Tinlot, Phys. Rev. **82**, 105 (1951).
[14] Bernardini, Booth, and Lederman, Phys. Rev. **83**, 1075 (1951).
[15] Bernardini, Booth, and Lederman, Phys. Rev. **83**, 1277 (1951).

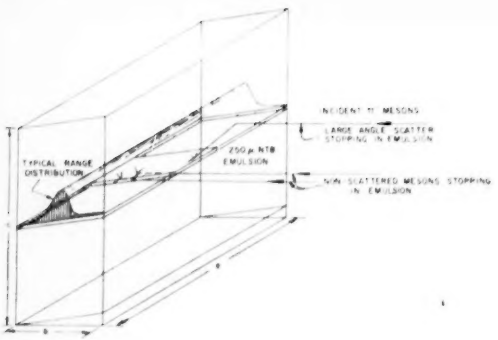
INCIDENT π MESONS
LARGE ANGLE SCATTER STOPPING IN EMULSION
TYPICAL RANGE DISTRIBUTION
250 μ NTB EMULSION
NON-SCATTERED MESONS STOPPING IN EMULSION

FIG. 2. Isometric sketch of aluminum absorber-scatterer showing principle of detection of large angle scattered π^- mesons.

at 42 Mev. Suitable arrangement of the lead shielding allowed no energy greater than 70 Mev to reach the scatterer regardless of the angle of emission from the target.

Figure 2 is an isometric sketch of the aluminum absorber which shows schematically how the incident flux and large angle scatters are detected. Most of the incident π^- mesons, upon entering normally to the surface of the scatterer, lose energy by ionization and come to rest after traversing a range appropriate to their energy. A small fraction of the incident mesons will suffer a nuclear interaction, such as a large angle scatter, and will come to rest at smaller depths of penetration. To sample the distribution of π^- endings, a 250 micron NTB stripped nuclear emulsion is embedded in the scatterer. The figure gives an example of an incident particle that has suffered a large angle scatter and has stopped in the emulsion. Also shown are two examples of nonscattered particles coming to rest in the emulsion at their appropriate ranges. To insure that the mesons traverse the absorber, rather than the emulsion, before entering and stopping in the emulsion, the plane of the emulsion is tilted $7\frac{1}{2}$ degrees from the perpendicular to the scatterer face. After the scattering assembly was placed in the meson beam, the stripped emulsion was removed and developed with Kodak D:19 developer and fixed. After washing, the emulsion was mounted on glass plates to facilitate scanning.

After leaving the target, mesons could possibly scatter from parts of the cyclotron, cart, or shielding, and arrive at the scatterer with reduced energies. To exclude this background, only mesons that were observed to enter the emulsion at angles greater than 90° to the direction of the incident meson beam were used to evaluate the scattering cross sections. An unknown amount of μ^- meson contamination was expected from the decay of π^- mesons while in flight. For this reason, only meson endings in both the forward and backward flux that resulted in nuclear stars were classified as negative pions.

III. THEORETICAL DISTRIBUTION OF BACKSCATTERED PIONS ENDING IN A SEMI-INFINITE ABSORBER

A particle of total range R enters normally to the absorber at 0 and scatters, elastically or inelastically, at x_1, in an interval dx_1, between θ and $\theta+d\theta$. The ending is observed between x and $x+dx$ (Fig. 3). The number of backscattered mesons that can be expected to stop between x and $x+dx$ is given by

$$D(x)dx=2\pi nNdx\int_{f=0}^{f=1}\pi(f)df\int_{90°}^{180°}\frac{\sigma(\theta)\sin\theta}{1-f\cos\theta}d\theta, \quad (1)$$

for $R<R_{\min}$. The range of a pion with an energy of about 42 Mev, the lower energy limit of the incident flux, defines $R_{\min}$. Multiple small angle scattering and range straggling are neglected, although the effect of multiple small angle scattering upon the experimental data will be considered in Sec. IV. N = the number of incident pions; $\sigma(\theta)$ = the differential cross section for

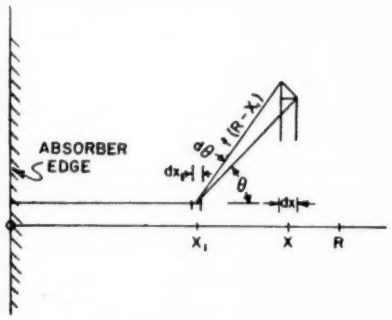

FIG. 3. Geometrical model of scattering used in theoretical analysis.

backscattering; f = the fraction of the residual range $(R-x_1)$ retained after scattering (this describes the inelastic scattering); $\pi(f)df$ = the probability that f lies between f and $f+df$; and n = the density of scattering centers.

If $\pi(f)$ and $\sigma(\theta)$ are energy independent, the integrals of Eq. (1) are independent of x, and $D(x)dx$ is a constant. The distribution can then be written as:

$$D(x)dx=kNn\sigma dx, \quad (2)$$

where

$$k=\int_{f=0}^{1}\pi(f)df\int_{90°}^{180°}\frac{K(\theta)\sin\theta}{1-f\cos\theta}d\theta, \quad (3)$$

and $\sigma(\theta)=\sigma/2\pi K(\theta)/2\pi$. $K(\theta)$ is a function of θ only, and σ is the total cross section for backscattering. k can be interpreted as the probability that a backward scattered meson will remain in the absorber, and is equal to the efficiency of the embedded emulsion for detecting backscattered mesons.

Although the contribution of inelastic scattering events is small,[10–15] the effect of inelastic scattering upon

the detection efficiency, k, is now considered. To evaluate the detection efficiency for observing inelastic backscatterers, the distribution of pion energy loss as well as the angular distribution of the inelastic scatters must be known. By studying the nuclear collisions of 60- to 90-Mev negative pions in photographic emulsions, Bernardini *et al.*[15] were able to measure the approximate initial and final energies of the inelastically scattered pions. The number of events was too small to show any definite structure in the energy loss distribution, but it was consistent with a flat distribution. The data of Lederman *et al.*[9] indicates that the angular distribution of inelastically scattered 60 Mev negative pions from carbon may be isotropic. These results form the basis for our assumptions that the probability for energy loss of inelastically scattered pions of about 30 Mev is a constant and that the angular distribution is spherically symmetric.

$P(E)dE=(\text{constant})\cdot dE$ transforms to $\pi(f)df=mf^{m-1}df$, using the empirical range-energy relation $E_{\text{Mev}}=c(R-x_1)^m$. When m is taken as 0.60 for Al, Cu, and Pb, the detection efficiency, Eq. (3), for inelastic isotropic collisions becomes 0.863. This factor is the fraction of backscattered pions that would remain in the absorber if all scattering events were inelastic and the distribution of the energy loss is described by the function $P(E)=\text{constant}$.

TABLE I. The geometrical detection efficiencies for backscattered pions in a semi-infinite absorber. $\pi(f)$ describes the inelastic nuclear scattering, where f is the fraction of the residual range retained by an inelastically scattered pion. $K(\theta)$ is the angular distribution.

$K(\theta)$	$\pi(f)$	Description	Detection efficiency k[a]
any	$\delta(f-0)$	Completely inelastic, $f=0$	1.000
1	mf^{m-1}	Inelastic isotropic scattering	0.863
1	$\delta(f-1)$	Elastic isotropic scattering	0.693
$\cos^2\theta$	$\delta(f-1)$	Elastic scattering, $\cos^2\theta$ distribution	0.580

[a] Fraction of backscatters that remain in absorber.

Table I gives numerical values of k for several distributions of $K(\theta)$ and $\pi(f)$. In the order listed in the table, the combinations of the distributions chosen for $K(\theta)$ and $\pi(f)$ become more favorable for backscattering out of the absorber. Consequently, the fraction of backscatters that remain in the absorber decreases. This behavior is characterized by the values of k. When no particles escape the absorber, as would be expected for highly inelastic scatters, the value of k is one, the upper limit. The lower limit is 0.50. This would occur if all scatters were elastic and $\theta=180°$, since all particles of range R that were backscattered at a depth of penetration less than $R/2$ would be able to escape the absorber.

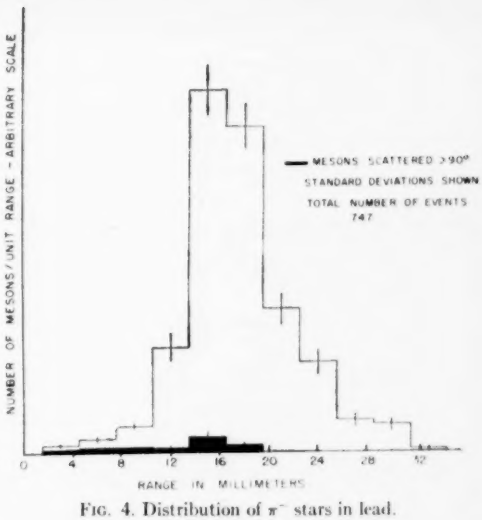

FIG. 4. Distribution of π^- stars in lead.

IV. ANALYSIS AND RESULTS OF EXPERIMENTAL DATA

The total scattering cross section is given by Eq. (2):

$$\sigma=\frac{1}{k_{\text{eff}}n}\frac{D(x)}{N},$$

where $D(x)$ is the observed number of backscatters per cm and N is the total number of particles observed in the incident flux. $D(x)$ and N are determined by scanning the nuclear emulsions from near the leading edges to the range of 70-Mev mesons in each absorber. Five to ten scans through the complete range spectrum were sufficient to determine N. The scanning effort was then turned to finding backscattered pions that stopped in the emulsion at smaller depths of penetration. The data taken for each meson ending observed were (a) depth of penetration, (b) projected angle of entrance into the emulsion, (c) approximate range in the emulsion, (d) type of ending—σ (star-forming) or ρ (non-star-forming), and (e) the number of prongs if a σ-type meson.

Figure 4 is a histogram showing a typical distribution of the pions ending in an absorber. The dark areas represent backscattered pions. Figures 5(a), (b), and (c) show the distribution of backscatters ending in the range intervals 2 to 26 mm in aluminum, 2 to 11 mm in copper, and 1.5 to 10.5 mm in lead. Figure 5(d) is the combined data for all backscatters. From geometrical consideration (employing the incident energy spectrum and the range-energy relations), the deduced scattering energies are 30.7 ± 7.0 Mev in aluminum, and 33.2 ± 8.6 Mev in copper and lead. Statistical tests applied to the spatial distributions of backscattered pions, Fig. 5, showed these distributions were consistent with a straight line of zero slope. This justifies the assumption of energy independence in the energy region of 32 ± 10 Mev in Sec. III.

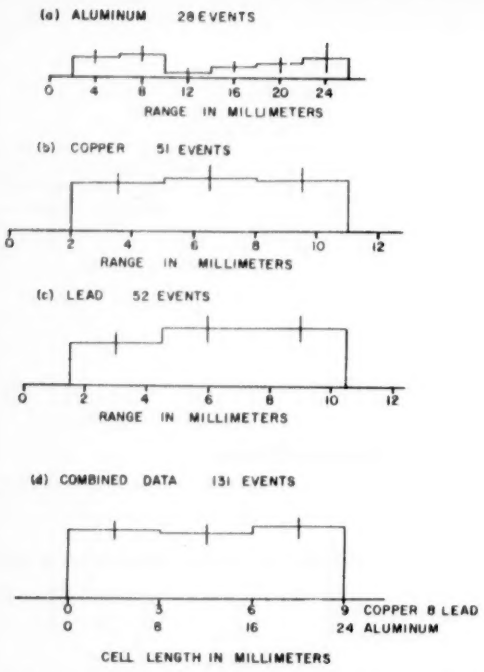
(a) ALUMINUM 28 EVENTS
0 4 8 12 16 20 24
RANGE IN MILLIMETERS
(b) COPPER 51 EVENTS
0 2 4 6 8 10 12
RANGE IN MILLIMETERS
(c) LEAD 52 EVENTS
0 2 4 6 8 10 12
RANGE IN MILLIMETERS
(d) COMBINED DATA 131 EVENTS
0 3 6 9 COPPER & LEAD
0 8 16 24 ALUMINUM
CELL LENGTH IN MILLIMETERS

FIG. 5. Distribution of backscattered negative pion endings in aluminum, copper, and lead. Also combined data.

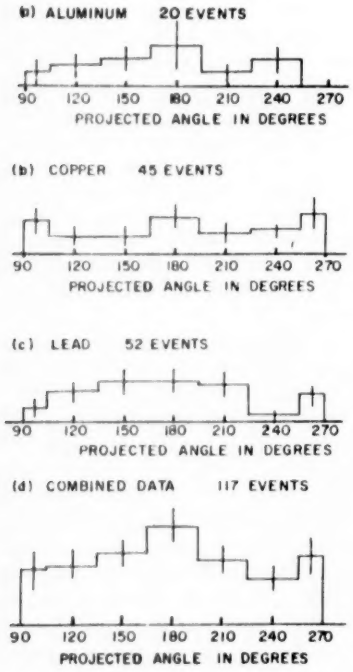
(a) ALUMINUM 20 EVENTS
90 120 150 180 210 240 270
PROJECTED ANGLE IN DEGREES
(b) COPPER 45 EVENTS
90 120 150 180 210 240 270
PROJECTED ANGLE IN DEGREES
(c) LEAD 52 EVENTS
90 120 150 180 210 240 270
PROJECTED ANGLE IN DEGREES
(d) COMBINED DATA 117 EVENTS
90 120 150 180 210 240 270
PROJECTED ANGLE IN DEGREES

FIG. 6. Horizontal projection of entrance angles greater than 90° for negative pions into emulsion from aluminum, copper, and lead.

1. Effective Detection Efficiency

The effective detection efficiency, k_{eff}, depends upon the angular distribution of the backscattering as well as the amounts of elastic and inelastic scattering. Since the fraction of inelastic scattering present cannot be ascertained from the data, we can refer to the work of Bradner and Rankin[10,11] and Bernardini *et al.*[12–15] From their results an estimate for the fraction of inelastic

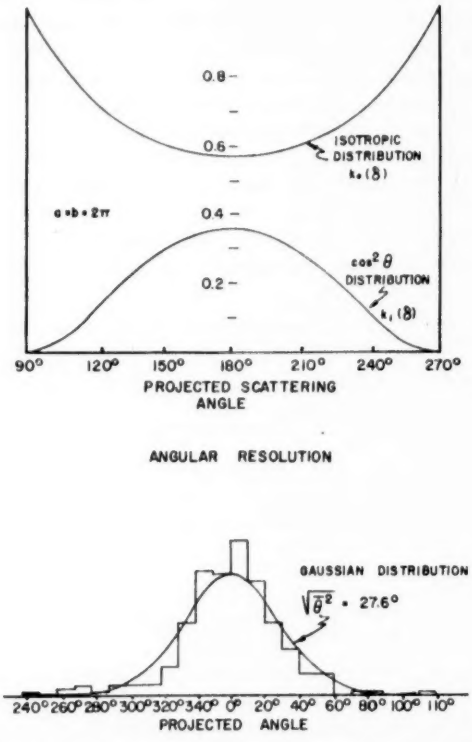

FIG. 7. (a) Horizontal projection of angular distribution, $(a+b\cos^2\theta)/(1-\cos\theta)$; (b) Angular resolution for backscattered pions.

backscattering between negative pions of about 30 Mev and complex nuclei, to one-place accuracy, is $0.2\pm0.1=\sigma_{\text{in}}/\sigma$.

Figure 6 shows the projected entrance angles of star-forming pions that entered the emulsion 90° or greater to the direction of incident flux. After eliminating the contribution of inelastic scattering to the combined angular distribution, Fig. 6(d), the coefficients a_{el} and b for elastic backscattering were determined by least squares fitting. The angular distribution for the elastically backscattered pions that stop in the embedded emulsion is, from Eq. (3), assumed to be

$$k(\theta)d\theta=\frac{(a_{\text{el}}+b\cos^2\theta)}{1-\cos\theta}\sin\theta d\theta.$$

Since a reasonable fit is obtained with the two parameters, no additional terms are used to fit the distribution empirically. To compare this angular distribution with the experimental data, $k(\theta)d\theta$ is expressed as $k(\delta)d\delta$, the projected angular distribution. When the experimental angular distribution is folded into $k(\delta)$, the theoretical angular distribution can be applied to the experimental data to determine the coefficients a_{el} and b.[16]

Figure 7(a) shows $k_0(\delta)d\delta$, the projected angular distribution which corresponds to an isotropic distribution in θ, and $k_1(\delta)d\delta$, the horizontal projection of a $\cos^2\theta$ angular distribution. The angular resolution for the backscatters, Fig. 7(b), was determined by measuring the projected entrance angles of the pions that made up the incident flux. Figure 8 is the fold of the distribution $k_0(\delta)$ and $k_1(\delta)$ and the experimental angular resolution. A least squares analysis of the data gives the best fit when $b=5.54\pm2.4a_{el}$. The fractions of the backscattered pions that contribute to the following modes of scattering are thus:

(1) $0.2\pm0.1=a_{\text{in}}$ for isotropic inelastic scattering,
(2) $0.28\pm0.09=a_{\text{el}}$ for isotropic elastic scattering,
(3) $0.52\pm0.15=b/3$ for $\cos^2\theta$ elastic scattering.

TABLE II. Observed ratios of the numbers of backscattered pions per cm to the total number incident upon the aluminum, copper, and lead absorbers. The mean values are used to evaluate the total backscattering cross sections.

		Aluminum	Copper	Lead
$\frac{D(x)}{N}$	Observer A	$2.26\pm0.22\times10^{-3}$	$12.13\pm3.04\times10^{-3}$	$15.07\pm4.3\times10^{-3}$
	Observer B	2.55 ± 0.83	10.20 ± 1.72	12.64 ± 2.1
	Mean	2.33 ± 0.44	10.73 ± 1.51	13.15 ± 1.83

The value of k_{eff} is given by

$$k_{\text{eff}}=\sum(\text{probability of type of scatter})(\text{detection efficiency})$$
$$=a_{\text{in}}(0.863)+a_{\text{el}}(0.693)+\tfrac{1}{3}b(0.580)$$
$$=0.66\pm0.025.$$

2. Scanning Efficiencies

Table II tabulates the ratio of $D(x)/N$ obtained by the two observers. The weighted mean is used to calculate the total backscattering cross sections, Eq. (2). If the scanning efficiencies of the observers are the same for $D(x)$ and N, the ratio $D(x)/N$ obtained is the true ratio. The relative efficiencies of the observers for finding π^- stars was 75 ± 5 percent. A direct check on the relative efficiencies for finding backscatters was not possible due to the fact that these events were extremely rare. In the areas scanned for backscatters, however, there were enough low energy background particles, principally μ mesons, from which an estimate of the relative efficiencies for the detection of backscatters could be made. Within statistical limits, it was concluded that efficiencies of the observers for finding $D(x)$ and N were the same. The percentage of star forming backscatters was observed to be 72.8 ± 6.0 percent. This agrees well with the accepted value of 72.2 ± 2.0.[17] This agreement suggests that all backscatters observed were pions, and indicates also that the scanning technique was not biased towards many pronged stars.

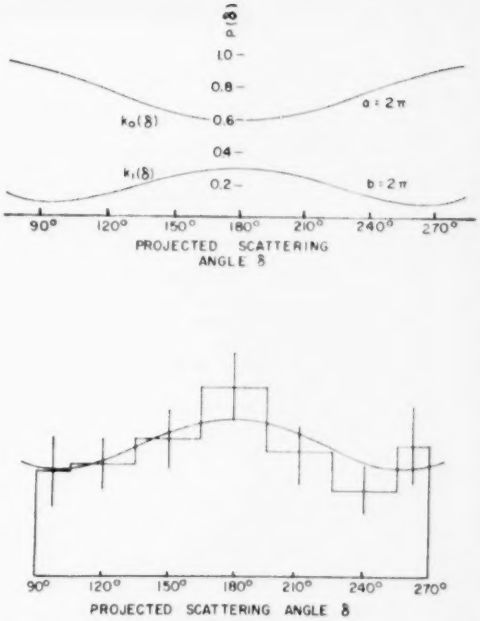

FIG. 8. (a) Folded angular distributions $k_0(\delta)$ and $k_1(\delta)$; (b) Least squares fit to experimental angular distribution.

In lead, Fig. 4, 2.3 percent of the pions detected in the incident flux, at depths of penetration greater than 13.5 mm, entered the emulsion at angles greater than 90° to the beam direction. This percentage of backscatters in the main flux is consistent with the number expected from multiple small angle scattering while the energy is degraded from 50 to 4 Mev. The correction to be applied to $D(x)/N$ for this Coulomb contamination in lead is -4.5 percent. The corrections for this effect in copper and aluminum are negligible. The correction to $D(x)/N$ for aluminum due to flux deviations at the surface of the absorber amounts to $+1.6$ percent.

3. Cross Sections

Using the effective detection efficiency, 0.66 ± 0.025, and including the above corrections, the total cross sections for large angle scattering of negative pions in aluminum, copper, and lead are as follows:
The backscattering cross sections *vs* A are plotted in Fig. 9.

[16] The fold $f(\delta)$ of the function $k(\delta)$ and $g(\delta)$ is defined by the formula $f(\delta)=\int_{-\infty}^{\infty}k(t)g(t-\delta)dt$.

[17] Frank Adelman, University of California Radiation Laboratory Report UCRL-530, 1950 (unpublished).

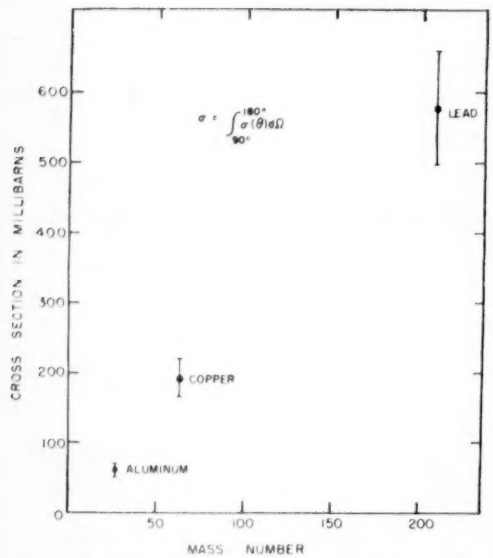

FIG. 9. Backscattering cross sections vs mass number A.

V. DISCUSSION

The conclusions obtained from the experimental results can be summarized as follows.

(a) The scattering of negative pions from complex nuclei is consistent with energy independence in the region of 32±10 Mev.

(b) The angular distribution for backscattering indicates that both the S and P waves contribute to the backscattering.

(c) The cross section for backscattering is proportional to the mass number, A.

The flatness of the combined data, Fig. 5(d), supports, in general, the argument for the energy independence of backscattering. If it were assumed that the energy dependence for backscattering is proportional to E^n, i.e., $\sigma(E)\sim E^n$, then the backscattered pions would be distributed as $(R-x)^{0.6n}$, where R is the total range of the particle and x is the depth of penetration. To estimate the limit of energy dependence, a least squares fit to the combined data gives for the exponent n, (-0.2 ± 0.8). Of the individual elements, aluminum is the only one in which there is an indication that the scattering may have a greater dependency upon energy. The distribution, however, is still consistent with energy independence.

Of particular interest is the indication that the cross section for backscattering may vary as A, and not as $A^{\frac{2}{3}}$. A possible interpretation of this result is outlined in the following argument. Small angle pion-nuclei scattering are collisions which, in general, involve small momentum transfers. These small angle collisions can be thought of as arising from the interactions between pions and whole nuclei since small momentum transfers correspond to large impact parameters. With the whole nucleus entering into the scattering process, one would expect the scattering cross section in this case to vary as $A^{\frac{2}{3}}$. Conversely, one must identify with large angle scattering large momentum transfers between pions and nuclei. For this to occur, the pion must approach the nucleus so closely that the interaction may now take place between the pion and a single nucleon. Under these circumstances, one may expect to observe scatters that actually arise from pion-nucleon collisions within the nucleus and, therefore, the cross section to vary as A, the number of nucleons in the nucleus.

The lowest pion energy used to study π-proton scattering has been approximately 50 Mev. At this energy the total cross sections are about 4 mb for π^- mesons[2] and 20 mb for π^+ mesons.[3] The total cross sections rise rapidly with increasing energy. In this investigation, the average backscattering cross section per nucleon, σ/A, for 32±10 Mev π^- mesons is 2.66±0.24 mb per nucleon.

The interpretation of the apparent proportional relationship between the backscattering cross sections and A as an indication of pion-nucleon collisions, while cogent, is not conclusive. It is observed that the scattering process is essentially energy independent between 20 and 40 Mev. This seems to be inconsistent with the assumption of pion-nucleon collisions, which are highly dependent upon energy. This contradiction, however, arises from the assumption that the property of strong energy dependence of pion-nucleon collisions can be extrapolated to energies below 50 Mev, well below the observed resonant scattering energy of about 150 Mev.

TABLE III. Cross sections for backscattering.

Element	σ(elastic + inelastic) $\approx \int_{90°}^{180°} \sigma(\theta)d\theta$ Cross section in millibarns	Cross section per nucleon, σ/A, in millibarns
Aluminum	59.6±11	2.22±0.41
Copper	192 ±27	3.00±0.42
Lead	577 ±80	2.78±0.38

The same relation between σ and A would result if the nucleus were partially transparent to low-energy pions of about 30 Mev. The observed total cross sections per nucleon for backscattering are indicative of small total interaction cross sections per nucleon for negative pions at this energy. Under these circumstances, light nuclei, such as aluminum, would be highly transparent, enabling the pion to "see" all the nucleons in the nucleus. It is surprising that the results indicate that this argument is apparently valid for the heavier elements, copper and lead. In these cases, less transparency might be expected, and the cross sections would conduce to an $A^{\frac{2}{3}}$ relationship.

We wish to express our sincere appreciation to Dr. Walter H. Barkas for his continued interest throughout the experiment. We are grateful to Professor R. L. Thornton and Dr. J. V. Lepore for their helpful comments. Finally we wish to thank Mr. J. Vale and the cyclotron crew for their aid in making the bombardments.

PHYSICAL REVIEW VOLUME 91, NUMBER 5 SEPTEMBER 1, 1953

The Number of Feynman Diagrams

ROBERT J. RIDDELL, JR.
Radiation Laboratory and Department of Physics, University of California, Berkeley, California
(Received March 20, 1953)

The Feynman-Dyson formulation of a perturbation expansion for quantum field theory allows one to give a general combinatorial treatment to the Feynman diagrams involved. A very simple analysis for the total number of such diagrams, $T(n, \epsilon, \rho)$, in quantum electrodynamics, leads to:

$$T(n, \epsilon, \rho)=\frac{(n!)^2}{(\epsilon!)^2(n-\epsilon)!}\cdot\frac{n!}{\rho!\left[\frac{1}{2}(n-\rho)\right]!2^{\frac{1}{2}(n-\rho)}},$$

in which n is the order of the perturbation and ϵ, ρ are the number of external electron and photon lines, respectively. The first factor is the number of different diagrams using only the electron lines and the second is that for the photon lines. In this total set of diagrams are many undesired ones; these are removed by means of generating functions. Relations which these functions satisfy are obtained, and from them one may readily find the exact numbers of diagrams desired, for not too large n. The generating functions are also used to find the asymptotic dependence on n, and it is found that this dependence is essentially unaffected by removing any specific type of graph. The sign alternations of the matrix elements in quantum electrodynamics are also considered in terms of similar generating functions. The generalization of the analysis to other types of interactions is also discussed.

I. INTRODUCTION

THE Feynman-Dyson formulation of quantum field theory in terms of the S matrix yields a straightforward method for obtaining the matrix elements corresponding to a particular physical process by means of a perturbation expansion in powers of the coupling constant. In this theory it has been shown that each matrix element may be uniquely represented by a linear graph called a Feynman diagram. The problem of performing a calculation to a given order then separates into two parts: (a) the combinatorial problem of obtaining the number of Feynman diagrams of a particular type which there are; and (b), the actual evaluation of the associated matrix elements. It is the purpose of this paper to investigate problem (a) in some detail. In addition to finding the exact number of diagrams, one may also ask for the asymptotic behavior as the order, n, of the perturbation becomes large. Evidently it is the asymptotic behavior (together with the asymptotic properties of the associated matrix elements) which will be of interest in determining the ultimate convergence or divergence of the perturbation expansion. The question of the asymptotic behavior has been investigated by Hurst[1] using a different method from the one employed here; however, the author feels that the present method is somewhat simpler and more conventional, and also that it provides more insight into the structure of the graphs than does the former.

Due to the fact that certain diagrams may either have matrix elements which are equal to zero, or which identically cancel with others, these diagrams should be removed from consideration in the number of contributing diagrams. In addition, other graphs have infinite parts which must be removed by the renormalization technique, and so these, too, should not be counted. In the present study generating functions will be derived from which the desired number of the remaining reduced diagrams for any process can readily be obtained.

[1] C. A. Hurst, Proc. Roy. Soc. (London) **A214**, 44 (1952).

II. THE TOTAL NUMBER OF DIAGRAMS

A method for obtaining the various Feynman diagrams contributing to the S matrix for a particular process for a given order of perturbation theory has been given by Dyson[2] and Wick.[3] In brief, one finds that the S matrix is composed of terms which are ordered products of the interaction Hamiltonian, which in turn is a sum of products of creation and annihilation operators. To obtain the Feynman diagrams for a specific process, one begins by choosing an annihilation operator for each of the initial particles which interact and a creation operator for each final one produced. The remaining operators are "used up" in vacuum fluctuations. In the nth order of perturbation theory, the Feynman diagrams contain n "points of interaction" since the interaction Hamiltonian appears in the product n times. The diagrams are obtained by drawing external lines from outside the diagram to the points of interaction, representing the incoming and outgoing particles. The vacuum fluctuations due to successive creations and annihilations are represented by internal lines between points of the diagram.

As an example, let us now consider quantum electrodynamics, for which the interaction Hamiltonian is

$$H^I(x)=-(e/c)\bar{\psi}\gamma_\mu\psi A_\mu.$$

It will be simple to generalize to other interactions from the results of this case. For the total number of diagrams, the electron and photon lines may connect the n points independently of each other, so that each

[2] F. J. Dyson, Phys. Rev. **75**, 486 (1949).
[3] G. C. Wick, Phys. Rev. **80**, 268 (1950).

may be considered separately and the total number is the product of the two.

(A) The Number of Electron Diagrams

Since the interaction Hamiltonian is bilinear in the creation and annihilation operators for the electron, each point of the diagram has one electron line coming to it, and one leaving it. From this it is evident that for each line coming onto the paper, there is also one which must leave it; thus such lines will form open polygons. Let the number of such free electron lines (at infinity) be ϵ. In order to find the total number of diagrams, given ϵ, we may consider that a line is drawn *from* each point. It is then necessary to make sure that each line then ends on any other point such that only one line goes *to* a given point. To begin the formation of an electron diagram, we simply choose ϵ points from the total of n points and let lines proceed to infinity from them. Each remaining point must then have a line drawn from it to some point on the paper (only one line is allowed to go to each point, of course). Then, to complete the diagram each of the ϵ remaining points which has no line coming to it must be joined to a line from off the paper. Thus we find that the total number of ways, $N^e(n, \epsilon)$ to connect lines to the electrons is:

$$N^e(n,\epsilon)=\frac{n!}{(n-\epsilon)!\epsilon!}\cdot n(n-1)\cdots(\epsilon+1),$$

$$=\frac{(n!)^2}{(\epsilon!)^2(n-\epsilon)!}, \tag{1}$$

in which the first factor is the number of ways to choose the ϵ points for the external lines, and the second is the number of ways to connect the $(n-\epsilon)$ points internally to the n points to which they may go.

This result may also be obtained in a somewhat more illuminating fashion by considering the precise ways in which the points are joined by electron lines. Evidently the electron lines will form ϵ open polygons, and in addition there may be any number of closed loops. Let ϵ_i be the number of open polygons of i points, and λ_j the number of closed loops of j points. With this specification of a diagram, we may form the electron diagrams in

$$\frac{n!}{\prod_i \epsilon_i!(i!)^{\epsilon_i}\prod_j \lambda_j!(j!)^{\lambda_j}}\prod_i (i!)^{\epsilon_i}\prod_j[(j-1)!]^{\lambda_j}$$

different ways. The first factor is the number of ways that we can choose the points to be placed on the various lines, while the second is the number of ways that these points can then be arranged on the lines or loops. Since we have to do with directed lines, any permutation of points on the open polygons is different, while for the closed loops cyclic permutations of a configuration give nothing new whereas any other permutation gives a new diagram.

To find the total number of diagrams, we must now sum over all possible choices of the ϵ_i, λ_j with the restrictions that the number of external lines is ϵ and the total number of points is n. Thus we have

$$N^e(n,\epsilon)=\sum_{(\epsilon_i,\lambda_j)}{}'' \frac{n!}{\prod_i \epsilon_i!\prod_j (j)^{\lambda_j}\lambda_j!},$$

in which the sum is to be taken over all ϵ_i, λ_j with the restrictions (indicated by the double prime):

$$\textstyle\sum_i \epsilon_i=\epsilon, \quad \sum_i i\epsilon_i+\sum_j j\lambda_j=n.$$

To remove the restrictions and allow easier summations we may multiply the equation by $x^{\sum i\epsilon_i+\sum j\lambda_j}\cdot y^{\sum\epsilon_i}$, after which we can sum over all ϵ_i, λ_j independently, choosing only the coefficient of $x^n y^\epsilon$ in the final result. Thus:

$N^e(n,\epsilon)=$ coeff. of $x^n y^\epsilon$ in:

$$n!\sum_{(\epsilon_i,\lambda_j)}\prod_i\frac{(x^i y)^{\epsilon_i}}{\epsilon_i!}\prod_j\frac{1}{\lambda_j!}\left(\frac{x^j}{j}\right)^{\lambda_j} \tag{2}$$

$=$ coeff. of $x^n y^\epsilon$ in:

$$n!\exp[\textstyle\sum_i (x^i y)+\sum_j (x^j/j)] \tag{3}$$

$=$ coeff. of $x^n y^\epsilon$ in:

$$n!(1-x)^{-1}\exp[xy/(1-x)]. \tag{4}$$

One readily finds that the coefficient of $x^n y^\epsilon$ from this generating function agrees with Eq. (1).

(B) The Photon Lines

From the interaction Hamiltonian we see that each point should have one undirected photon line connected to it. To construct a diagram for these, we choose ρ points for the external lines while the remaining points, of which there are $n-\rho$, which must be an even number, are joined in pairs. Thus for the total of the photon diagrams we find

$$N^p(n,\rho)=\frac{n!}{\rho!(n-\rho)!}\frac{[\frac{1}{2}(n-\rho)(n-\rho-1)]\cdots[\frac{1}{2}(2)\cdot(1)]}{[\frac{1}{2}(n-\rho)]!},$$

where the first factor is again the number of ways to choose the ρ points for the external lines, while the second is the number of ways that $n-\rho$ points may be joined in pairs. Thus we have

$$N^p(n,\rho)=\frac{n!}{\rho![\frac{1}{2}(n-\rho)]!2^{\frac{1}{2}(n-\rho)}}. \tag{5}$$

The total number of diagrams $T(n, \epsilon, \rho)$ is the product of Eqs. (1) and (5):

$$T(n,\epsilon,\rho)=\frac{(n!)^2}{(\epsilon!)^2(n-\epsilon)!\rho![\frac{1}{2}(n-\rho)]!2^{\frac{1}{2}(n-\rho)}}.$$

If one introduces the Sterling approximation into this expression, it is found that $T(n, \epsilon, \rho)/n! \sim n^{3n/2}$ as $n \to \infty$.

It is perhaps worth mentioning that one can form simple generating functions for $N^e(n, \epsilon)$ and $N^p(n, \rho)$ as:

$$\sum_{\epsilon} \frac{N^e(n, \epsilon)}{n!} y^\epsilon = L_n(-y),$$

$$\sum_{\rho} \frac{N^p(n, \rho)}{n!} z^\rho = \frac{1}{(i\sqrt{2})^n} H_n(-i\sqrt{2}z).$$

in which $L_n(x)$ and $H_n(x)$ are the nth order Laguerre and Hermite polynomials, respectively.[4] Using the well-known generating function for the Laguerre polynomials one can easily form the "grand generating function" for the electron lines, Eq. (4).

If one wishes to generalize these results to cases in which the interaction Hamiltonian involves factors of the type ϕ^k, it is only necessary to note that one may consider each point as consisting of a set of k subpoints, since each of the k operators, ϕ, may create or annihilate independently. Thus we need only consider the number of photon-like diagrams of $k \cdot n$ instead of n points in such a case. Evidently as k increases from unity with fixed large n, the number of diagrams increases very rapidly.

III. REMOVAL OF UNWANTED DIAGRAMS

The counting scheme of Sec. II for the total number of diagrams must now be modified in order to remove certain graphs for which the matrix elements either give no contribution, or must be removed by renormalization. In these categories we have graphs involving:

(a) Odd electron loops. For quantum electrodynamics, Furry's theorem states that such matrix elements will cancel in pairs.

(b) Closed parts. Dyson[5] has shown that these only multiply the S-matrix by a constant factor.

(c) Self-energy parts for electron or photon lines. Both must be renormalized.

(d) Vertex parts. These lead to the self-charge divergence and must also be renormalized. The removal of (d), (e) leaves one with the number of "irreducible" graphs.[5]

(e) Separated parts with one external electron and one external photon line. These matrix elements vanish since energy and momentum cannot be conserved.

We will remove these various diagrams in order; however, it will be evident that any step may be omitted in case one wishes to retain such elements, as, for instance, in a case in which Furry's theorem does not apply so that one would like to retain the odd loops.

In order to remove the odd loops, it is only necessary to sum over the even j's in Eq. (2), with the result that

$$N_1^e(n, \epsilon) = \text{coeff.} x^{n-\epsilon} \text{ in: } n!(1-x^2)^{-\frac{1}{2}} \exp[xy/(1-x)],$$

and so

$$N_1^e(n, \epsilon) = \text{coeff.} x^{n-\epsilon} \text{ in: } \frac{n!}{\epsilon!}(1-x)^{-(\epsilon+\frac{1}{2})}(1+x)^{-\frac{1}{2}}.$$

For large n this may be estimated as follows. Using the binomial expansion for the two factors, we have

$$N_1^e(n, \epsilon) = \frac{n!}{\epsilon!} \sum_{k=0}^{\infty} \binom{\epsilon+k-\frac{1}{2}}{k} \binom{n-\epsilon-k-\frac{1}{2}}{n-\epsilon-k} (-1)^{n-\epsilon-k},$$

and using the expressions for the binomial coefficients, we find

$$N_1^e(n, \epsilon) = (-1)^{n-\epsilon} \frac{n!}{\epsilon!} \sum_k \frac{\Gamma(\epsilon+k+\frac{1}{2})}{k!\Gamma(\epsilon+\frac{1}{2})} \frac{\Gamma(n-\epsilon-k+\frac{1}{2})}{(n-\epsilon-k)!\Gamma(\frac{1}{2})} (-1)^k.$$

If the integral representations for the gamma functions are introduced and a change of integration variables is made, one obtains

$$N_1^e(n, \epsilon) = \frac{(-1)^{n-\epsilon}}{\Gamma(\epsilon+\frac{1}{2})\Gamma(\frac{1}{2})2^{\epsilon-1}} \binom{n}{\epsilon} \int_0^{\infty} u^n e^{-u} du \times \int_{-1}^{1} dx (1-x)^{\epsilon-\frac{1}{2}} x^{n-\epsilon} (1+x)^{-\frac{1}{2}}.$$

The first integral gives $n!$ Evidently, as $n \to \infty$ the major contribution to the second integral comes near $x = \pm 1$, and for $\epsilon > 0$, we need only consider the region about $x = -1$. If we replace $(1-x)$ by 2 in this region, the remaining integral from 0 to 1 is a beta function so that we find

$$N_1^e(n, \epsilon) \cong \binom{n}{\epsilon} \frac{\sqrt{2}n!}{\Gamma(\epsilon+\frac{1}{2})} \frac{(n-\epsilon)!}{\Gamma(n-\epsilon+\frac{3}{2})}. \tag{6}$$

Using the Stirling approximation, one sees that the order of electron graphs is thus reduced by $n^{\frac{1}{2}}$ compared to Eq. (1).

To remove the graphs with closed parts, we note that every diagram will consist of a subdiagram (which may be the diagram itself) which has no closed parts, and a remainder which is made up of one or more closed parts with no external lines.

Thus we have

$$T(n, \epsilon, \rho) = \sum_{n_1, n_2}{}' \frac{n!}{n_1! n_2!} T(n_1, 0, 0) F(n_2, \epsilon, \rho),$$

in which $F(n, \epsilon, \rho)$ is the number of diagrams with no closed parts, and the sum is over all n_1, n_2 with the restriction that $n_1 + n_2 = n$. The summand simply represents the number of ways that one can make up diagrams from their constituent parts, given n_1, n_2. If

[4] H. Margenau and G. M. Murphy, *The Mathematics of Physics and Chemistry* (D. Van Nostrand Company, Inc., New York, 1943).

[5] F. J. Dyson, Phys. Rev. **75**, 1736 (1949).

we again use the generating functions, we find:

$$\mathfrak{F}(x,\epsilon,\rho)=\frac{\mathfrak{T}(x,\epsilon,\rho)}{\mathfrak{T}(x,0,0)}, \tag{7}$$

where

$$\mathfrak{T}(x,\epsilon,\rho)=\sum_n \frac{T(n,\epsilon,\rho)}{n!}x^n,$$

$$\mathfrak{F}(x,\epsilon,\rho)=\sum_n \frac{F(n,\epsilon,\rho)}{n!}x^n,$$

and in which $T(0,0,0)$ is defined to be equal to 1 for convenience.

The next problem to be considered is that of the number of irreducible diagrams. Before doing this, however, it should be remarked that if one had the exact propagation functions for electrons and photons it would only be necessary to consider the irreducible diagrams. Nevertheless, for the purposes of calculation the renormalized functions are not known, and the only way in which they can be obtained is by obtaining the matrix elements related to the reducible diagrams, removing the divergent parts order by order. For this purpose it is useful to have those graphs from which only the self energies in the external lines have been removed. To calculate this number, we see that a diagram may have a central part of n' points together with n_i external electron lines of i points in self energy graphs, and n_j external photon lines of j points in self energy parts. The total number of graphs is then:

$$F(n,\epsilon,\rho)=\sum_{(n_i,n_j)}{}''' \frac{n!}{n'!\prod_i (i!)^{n_i}n_i!\prod_j (j!)^{n_j}n_j!}$$
$$\times(2\epsilon)(2\epsilon-1)\cdots(2\epsilon-n''+1)$$
$$\times\rho(\rho-1)\cdots(\rho-n'''+1)2^{n'''}$$
$$\times[F(i,1,0)]^{n_i}[F(j,0,2)]^{n_j}G(n',\epsilon,\rho).$$

The sum is to be carried over all arrangements of points in groups, with the restrictions that $n=\sum_i in_i+\sum_j jn_j+n'$, $n''=\sum_i n_i$, and $n'''=\sum_j n_j$. $G(n',\epsilon,\rho)$ is the number of diagrams with no self-energy parts in the external lines. The factors involving $(2\epsilon)\cdots(2\epsilon-n''+1)$ and $\rho\cdots(\rho-n'''+1)$ represent the number of ways in which the electron and photon self energies may be inserted in the external portions of the lines, and $2^{n'''}$ is due to the fact that each photon self energy may be inserted in two different ways. Evidently the number of electron self-energy diagrams of n points is $F(n,1,0)$, and the number for photons in $F(n,0,2)$. If we introduce x to keep track of the first restriction, ξ for the second, and η for the third, we find

$$\mathfrak{F}(x,\epsilon,\rho)=\sum_{n'',n'''}\frac{(2\epsilon)!}{(2\epsilon-n'')!}\frac{\rho!}{(\rho-n''')!}\mathfrak{G}(x,\epsilon,\rho)$$
$$\times\text{coeff.}\,\xi^{n''}\eta^{n'''}\text{ in: }\exp\{\xi\mathfrak{F}(x,1,0)+2\eta\mathfrak{F}(x,0,2)\},$$

so that:

$$\mathfrak{F}(x,\epsilon,\rho)=\mathfrak{G}(x,\epsilon,\rho)\sum_{n'',n'''}\binom{2\epsilon}{n''}[\mathfrak{F}(x,1,0)]^{n''}$$
$$\times\binom{\rho}{n'''}[2\mathfrak{F}(x,0,2)]^{n'''}.$$

Thus,

$$\mathfrak{G}(x,\epsilon,\rho)=\frac{\mathfrak{F}(x,\epsilon,\rho)}{[1+\mathfrak{F}(x,1,0)]^{2\epsilon}[1+2\mathfrak{F}(x,0,2)]^{\rho}}. \tag{8}$$

To find the number of irreducible diagrams, $I(n,\epsilon,\rho)$, we proceed similarly, removing self-energy parts in any of the electron or photon lines and in addition removing all vertex parts. In this case we construct the reducible diagrams by choosing an irreducible diagram of n_0 points and then putting in the various possible additional parts at the vertices or in the lines. The number of vertex parts of n points is $F(n,1,1)$. Thus, we have

$$F(n,\epsilon,\rho)=\sum_{(n_v,n_e,n_p)}{}'''' \frac{n!}{\prod_v (v!)^{n_v}n_v!\prod_e (e!)^{n_e}n_e!\prod_p (p!)^{n_p}n_p!}$$
$$\times I(n_0,\epsilon,\rho)\times\prod_v[G(v,1,1)]^{n_v}\prod_e[F(e,1,0)]^{n_e}$$
$$\times\prod_p[F(p,0,2)]^{n_p}\times(n_0+\epsilon)(n_0+\epsilon-1)\cdots$$
$$\times(n_0+\epsilon-n'+1)[\tfrac{1}{2}(n_0+\rho)][\tfrac{1}{2}(n_0+\rho)-1]\cdots$$
$$\times[\tfrac{1}{2}(n_0+\rho)-n''+1]2^{n''}, \tag{9}$$

in which the first two factors represent the number of ways to choose the points and form the subgraphs among the set of n_v vertex parts of v points, n_e electron self-energy parts of e points, and n_p photon self-energy parts of p points. The remaining factors represent the number of ways that the self-energy parts can be inserted in the $n_0+\epsilon$ electron lines and the $\frac{1}{2}(n_0+\rho)/2$ photon lines. The sum is carried over all n_i's, with the restrictions that $n=\sum vn_v+\sum en_e+\sum pn_p$, $n_0=\sum n_v$, $n'=\sum n_e$, and $n''=\sum n_p$. Note that all points in the diagram are in one of the subgraphs, and the number of ways to put the vertex parts on the irreducible graph is just the number that we are seeking. $G(v,1,1)$ is chosen for the vertex parts rather than $F(v,1,1)$ in order that we only count a self energy subgraph in a line once. Using the generating function method again, we find that Eq. (9) becomes

$$\mathfrak{F}(x,\epsilon,\rho)=\sum_{n_0,n',n''}\frac{I(n_0,\epsilon,\rho)(n_0+\epsilon)![\tfrac{1}{2}(n_0+\rho)]!}{(n_0+\epsilon-n')![\tfrac{1}{2}(n_0+\rho)-n'']!}2^{n''}$$
$$\times\text{coeff.}\,\xi^{n_0}\eta^{n'}\zeta^{n''}\text{ in: }\exp\{\xi\mathfrak{G}(x,1,1)$$
$$+\eta\mathfrak{F}(x,1,0)+\zeta\mathfrak{F}(x,0,2)\},$$

and so

$$\mathfrak{F}(x,\epsilon,\rho)=\sum_{n_0,n_1,n_2}\frac{I(n_0,\epsilon,\rho)}{n_0!}\binom{n_0+\epsilon}{n'}\binom{\frac{1}{2}(n_0+\rho)}{n''}$$
$$\times[\mathfrak{G}(x,1,1)]^{n_0}[\mathfrak{F}(x,1,0)]^{n'}[2\mathfrak{F}(x,0,2)]^{n''}$$
$$=\sum_{n_0}\frac{I(n_0,\epsilon,\rho)}{n_0!}\{\mathfrak{G}(x,1,1)[1+\mathfrak{F}(x,1,0)]$$
$$\times[1+2\mathfrak{F}(x,0,2)]^{\frac{1}{2}}\}^{n_0}\times[1+\mathfrak{F}(x,1,0)]^{\epsilon}$$
$$\times[1+2\mathfrak{F}(x,0,2)]^{\rho/2}.$$

Thus we find for the generating function:

$$\mathfrak{J}(\phi(x),\epsilon,\rho)=\frac{\mathfrak{F}(x,\epsilon,\rho)}{[1+\mathfrak{F}(x,1,0)]^{\epsilon}[1+2\mathfrak{F}(x,0,2)]^{\rho/2}},\quad(10)$$

in which

$$\phi(x)=\mathfrak{G}(x,1,1)[1+\mathfrak{F}(x,1,0)][1+2\mathfrak{F}(x,0,2)]^{\frac{1}{2}}.$$

In order to find $I(n,\epsilon,\rho)$, we must invert the series $\phi=\phi(x)$ and find $x=x(\phi)$. This is then substituted into the right-hand side of Eq. (10), and a comparison of equal powers in ϕ gives the desired result.

To remove the graphs with separated parts of only one external electron and one photon line, we again write the equation satisfied by such diagrams:

$$F(n,\epsilon,\rho)=\sum_{(n_v)}{}'''\frac{n!}{n'!\prod_v(v!)^{n_v}n_v!}$$
$$\times H(n',\epsilon',\rho')\prod_v[F(v,1,1)]^{n_v},$$

in which the restrictions on the sum are $n=n'+\sum_v vn_v$, $\epsilon=\epsilon'+\sum_v n_v$, and $\rho=\rho'+\sum_v n_v$. This equation is treated as before, and one finds

$$\mathfrak{H}(x,y,z)=\mathfrak{F}(x,y,z)\exp[-yz\mathfrak{F}(x,1,1)],$$

in which $\mathfrak{F}(x,y,z)$ is the "grand generating function" for the number of diagrams:

$$\mathfrak{F}(x,y,z)=\sum_{\epsilon,\rho}\mathfrak{F}(x,\epsilon,\rho)y^{\epsilon}z^{\rho},$$

and

$$\mathfrak{H}(x,y,z)=\sum_{n,\epsilon,\rho}\frac{H(n,\epsilon,\rho)}{n!}x^ny^{\epsilon}z^{\rho}.$$

IV. CONCLUSION

From the generating functions, Eqs. (7) and (8), one may readily show that the removal of closed parts and self-energy parts in the external lines does not affect the asymptotic behavior of the number of matrix elements. The treatment of Eq. (10) is more difficult, but Hurst[1] has shown that the asymptotic number of irreducible diagrams of a particularly simple subset is also $\sim n^{3n/2}$ so that the asymptotic behavior is unchanged. If one now considers the sum of all the elements, it is evident that in order to obtain convergence the average element must decrease at least as rapidly as $n^{-n/2}$, since $(n!)^{-1}$ multiplies the nth order terms of the expansion. This extremely rapid decrease seems to put a severe restriction on any field theory. It has been shown in fact that the perturbation expansion for the simple case of a boson field coupled to itself by a ϕ^3 contact interaction diverges.[6] One may also remark that the size of the coupling constant seems to have little to do with the convergence of the theory (although in an *asymptotic* expansion its size would determine the usefulness of the theory).

With regard to the convergence of the expansion, we must still notice that the signs of the various matrix elements are not necessarily alike, and there is still the possibility that judicious cancellations could produce a sufficiently rapid decrease in the average of the elements, even though the average magnitude remains large. For quantum electrodynamics such a sign alternation is associated with the various electron diagrams. It has been shown by Dyson[2] that each matrix element carries an intrinsic sign which is given by $(-1)^p$, in which p is the number of open electron polygons containing an even number of points plus the number of even loops. Although the factor which this multiplies is not necessarily positive we can attempt to estimate the effect of such cancellations by evaluating the sum of the numbers of matrix elements with this sign included, either with all loops allowed or with the odd ones removed. In the first case, we multiply the summand in Eq. (2) by the sign factor and then sum as before. We may let

$$p=\sum(i-1)\epsilon_i+\sum(j-1)\lambda_j,$$

since the odd parts in i, j will not contribute to the sign; and due to the restrictions on ϵ_i, λ_j we find:

$$p=n-\epsilon+\sum\lambda_j.$$

If we multiply the terms in Eq. (2) by this factor and then sum, we find:

$$S^{\epsilon}(n,\epsilon)=\text{coeff.}x^n y^{\epsilon}\text{ in:}$$
$$(-1)^{n-\epsilon}n!(1-x)\exp[xy/(1-x)],$$
$$=(-1)^{n-\epsilon}\frac{n!}{\epsilon!}\binom{n-2}{n-\epsilon}.\quad(11)$$

where $S^{\epsilon}(n,\epsilon)$ is the sum over all the electron diagrams with the above choice of signs. Equation (11) differs from Eq. (1) only by the factor $\epsilon(\epsilon-1)/n(n-1)$. If one removes the odd loops, then he finds:

$$S_1^{\epsilon}(n,\epsilon)=\text{coeff.}x^n y^{\epsilon}\text{ in:}$$
$$n!(-1)^{n-\epsilon}(1-x^2)^{\frac{1}{2}}\exp[xy/(1-x)].$$

[6] C. A. Hurst, Proc. Cambridge Phil. Soc. **48**, 625 (1952); and W. Thirring, Helv. Phys. Acta **26** 33 (1953).

This may be estimated as was $N'^{\epsilon}(n, \epsilon)$ in Sec. IV, with the result that

$$S_1^{\epsilon}(n, \epsilon) \cong (-1)^{n-\epsilon} \frac{n!}{\epsilon!} \frac{(n-4)!}{\Gamma(\epsilon-\frac{1}{2})\Gamma(n-\epsilon-\frac{1}{2})2^{5/2}},$$

which is of order n^{-2} times Eq. (6). These numbers are still exceedingly large, and the convergence would seem doubtful. Nevertheless, there is so much cancellation of terms that one would need an extremely good estimate of the individual elements in order to give a rigorous proof of the convergence or divergence of the theory. This cancellation does not occur for interacting bosons since the integrands may be made positive definite for sufficiently low energies.

Finally, one may remark that the Dyson formulation for the S matrix represents a double series in n and the elements associated thereto. If the perturbation theory converges it seems likely that the cancellations among elements would be essential, and hence that absolute convergence would not obtain. Thus pattern type approximations based on rearrangements of this series seem of doubtful validity.

The author would like to express his appreciation to Professor G. E. Uhlenbeck for suggesting this investigation, and to Drs. J. V. Lepore and Maurice Neuman for interesting discussions during the course of this study. This work was performed under the auspices of the U. S. Atomic Energy Commission.

PHYSICAL REVIEW VOLUME 91, NUMBER 5 SEPTEMBER 1, 1953

Graphical Method for Obtaining Phase Shifts from the Experimental Data on Meson-Nucleon Scattering*

JULIUS ASHKIN AND SEYMOUR H. VOSKO
Carnegie Institute of Technology, Pittsburgh, Pennsylvania

(Received May 18, 1953)

A graphical method is used for obtaining scattering phase shifts from the experimental data on meson-nucleon scattering. The method is based on the observation that the imaginary part of the amplitude for coherent forward scattering is proportional to the total cross section for the meson scattering. The results are in agreement with a complete numerical analysis of the problem made by Fermi with the help of the high-speed electronic computer at Los Alamos.

1. INTRODUCTION

FERMI[1] has recently shown that the present experimental data on meson-nucleon scattering are consistent with the assumptions that the meson-nucleon interaction is charge independent and that (for the energy range below 135 Mev) only the waves of orbital angular momentum $L=0$ and $L=1$ are appreciably scattered. The assumption of charge independence can be expressed as conservation of total isotopic spin. Thus, the meson-nucleon states may be classified by their eigenvalues for total isotopic spin, total angular momentum, and orbital angular momentum. There are accordingly six states involved in the scattering, each with its appropriate scattering phase shift. These are the three states with total isotopic spin $T=\frac{3}{2}$ and angular momentum $S_{\frac{1}{2}}$, $P_{\frac{1}{2}}$, $P_{\frac{3}{2}}$ and the corresponding states with $T=\frac{1}{2}$. The expressions for the cross sections [Eqs. (2), (3), and (4)] of the various possible scattering processes in terms of the phase shifts are rather complicated, and there is no simple algebraic method for obtaining the phase shifts. A very rapid and accurate numerical method for finding the six phase shifts which "best" represent the data has recently been given by Fermi[2] with the help of the high-speed computer at Los Alamos. The purpose of this report is to describe a less accurate, but convenient, graphical method for finding the phase shifts. This graphical technique cannot really compete with the numerical procedure. It is unable to provide the "best" set of phase shifts without prohibitive labor. Nevertheless it may give some insight into the structure of the phase fitting problem and be useful for rough estimations.

2. SCATTERING FORMULAS

Expressions for the scattering cross section in terms of the above-mentioned phase shifts have been derived by Fermi.[1] There are three distinct types of scattering:

$$\pi^+ + p = \pi^+ + p, \tag{1a}$$

$$\pi^- + p = \pi^- + p, \tag{1b}$$

$$\pi^- + p = \pi^0 + n. \tag{1c}$$

The π^+ scattering is described by three phase shifts of total isotopic spin $T=\frac{3}{2}$. The π^- scattering cross sections contain all six phase shifts. The expressions for

* Supported by U. S. Army Office of Ordnance Research.

[1] Anderson, Fermi, Martin, and Nagle, Phys. Rev. **91**, 155 (1953). See also Proceedings of the Third Annual Rochester Conference on High-Energy Physics, December 18–20, 1952 (Interscience Publishers, New York, 1953).

[2] E. Fermi and N. Metropolis, Los Alamos Report LA-1492, November 19, 1952 (unpublished).

the differential scattering cross sections are:

$$\frac{d\sigma(+)}{d\Omega}=\left|\frac{1}{2ik}A+\frac{1}{2ik}B\cos\theta\right|^2+\left|\frac{1}{2ik}C\sin\theta\right|^2 \quad (2)$$

$$=a_++b_+\cos\theta+c_+\cos^2\theta, \quad (2a)$$

$$\frac{d\sigma(-)}{d\Omega}=\frac{1}{9}\left|\frac{1}{2ik}X+\frac{1}{2ik}Y\cos\theta\right|^2+\frac{1}{9}\left|\frac{1}{2ik}Z\sin\theta\right|^2 \quad (3)$$

$$=a_-+b_-\cos\theta+c_-\cos^2\theta, \quad (3a)$$

$$\frac{d\sigma(0)}{d\Omega}=\frac{2}{9}\left|\frac{1}{2ik}P+\frac{1}{2ik}Q\cos\theta\right|^2+\frac{2}{9}\left|\frac{1}{2ik}R\sin\theta\right|^2 \quad (4)$$

$$=a_0+b_0\cos\theta+c_0\cos^2\theta, \quad (4a)$$

where k is the wave number in the c.m. system.

$$A=\exp(2i\alpha_{\frac{1}{2}}{}^0)-1,$$
$$B=2\exp(2i\alpha_{\frac{1}{2}}{}^1)+\exp(2i\alpha_{\frac{3}{2}}{}^1)-3,$$
$$C=\exp(2i\alpha_{\frac{1}{2}}{}^1)-\exp(2i\alpha_{\frac{3}{2}}{}^1),$$
$$X=A+2\exp(2i\beta_{\frac{1}{2}}{}^0)-2,$$
$$Y=B+4\exp(2i\beta_{\frac{1}{2}}{}^1)+2\exp(2i\beta_{\frac{3}{2}}{}^1)-6,$$
$$Z=C+2\exp(2i\beta_{\frac{1}{2}}{}^1)-2\exp(2i\beta_{\frac{3}{2}}{}^1),$$
$$P=\tfrac{3}{2}A-\tfrac{1}{2}X,$$
$$Q=\tfrac{3}{2}B-\tfrac{1}{2}Y,$$
$$R=\tfrac{3}{2}C-\tfrac{1}{2}Z.$$

Note: $T=\frac{3}{2}$ phase shifts are $\alpha_J{}^L$; $T=\frac{1}{2}$ phase shifts are $\beta_J{}^L$.

The experimental angular distribution for each of the possible reactions is fitted to the form $a+b\cos\theta+c\cos^2\theta$. Experiments therefore provide in all nine coefficients a, b, and c, three for each of the three processes.

The first term on the right-hand side of Eq. (2) represents scattering of π^+ without spin flip of the nucleon (i.e., pure elastic scattering). The first term on the right-hand side of Eq. (3) has the same physical meaning for the π^- scattering. In this case there is also the possibility of exchange scattering which is given by Eq. (4).

3. EXPLANATION OF METHOD

The problem can be stated as follows: given the nine experimental quantities a, b, c, which, within the experimental error, will represent the data, determine, if possible, *six* phase shifts. The success or failure of this attempt to fit nine experimental quantities with six phase shifts provides a test of the basic assumptions. The method to be described below depends on first obtaining the expressions A, B, and C, which describe the π^+ scattering, and using these values with the other experimental data to obtain the other phase shifts. The analysis of the π^+ data will be described in detail, and the obvious extension of the π^- case will be sketched briefly.

By equating coefficients of powers of $\cos\theta$ in Eq. (2) and Eq. (2a) we have

$$a_+=\left(\frac{1}{4k^2}\right)(|A|^2+|C|^2), \quad (5a)$$

$$b_+=\left(\frac{1}{4k^2}\right)(AB^*+A^*B), \quad (5b)$$

$$c_+=\left(\frac{1}{4k^2}\right)(|B|^2-|C|^2). \quad (5c)$$

Therefore,

$$|A+B|^2=4k^2(a_++b_++c_+), \quad (6a)$$

$$|A-B|^2=4k^2(a_+-b_++c_+). \quad (6b)$$

In Eq. (6a) and Eq. (6b) we have two relations between the complex numbers A and B and the experimental quantities a, b, c. A third relation is obtained from the general connection between the total scattering cross section and the amplitude for elastic scattering in the forward direction[3] (the so-called "Optical Theorem"),

$$\sigma_{\text{total}}=(4\pi/k)\,\text{Im}(\text{forward elastic scattering amplitude}),$$

where Im means "imaginary part." Integrating Eq. (2a) over angles and applying the theorem gives

$$4\pi(a_++c_+/3)=-(4\pi/k)\cdot(1/2k)\,\text{Re}(A+B), \quad (7)$$

where Re means "real part." The three relations Eq. (6a), Eq. (6b), and Eq. (7) plus a knowledge of the general form of A and B are sufficient to determine the three phase shifts for the π^+ scattering.

Draw two circles of radii $|A+B|$ and $|A-B|$ in the complex plane with center at the origin O (see Fig. 1). Erect a line perpendicular to the real axis through the point $\text{Re}(A+B)$. This line has at most two intersections with the circle $|A+B|$. Either intersection gives a possible point $(A+B)$ in the complex plane. We choose one intersection as the point $(A+B)$. The other intersection leads to the complex conjugate solution with all phase shifts reversed in sign. Draw any line through the point $(A+B)$ intersecting the circle $|A-B|$ at the points P and P'. Then possible positions for the point A are the midpoints M and M' of the segments from $(A+B)$ to P and P', respectively. Hence the point A lies on the locus of the midpoint from $(A+B)$ to the circle $|A-B|$. This locus is obviously a circle with radius $\frac{1}{2}|A-B|$ and center O_1 halfway between $(A+B)$ and O. Another locus for A is obtained from the fact that A is of the form $[\exp(2i\alpha_{\frac{1}{2}}{}^0)-1]$. Hence A lies on a circle of unit radius and center -1 on the real axis. The intersections of this unit circle with the circle of M and M' establish the possible positions of A. In general there are two intersections A_1 and A_2. Together with the point $(A+B)$ this gives two

[3] See for example M. Lax, Phys. Rev. **78**, 306 (1950). The "Optical Theorem" can of course be verified directly from the expression in Eq. (2) of the scattering cross section in terms of the phase shifts.

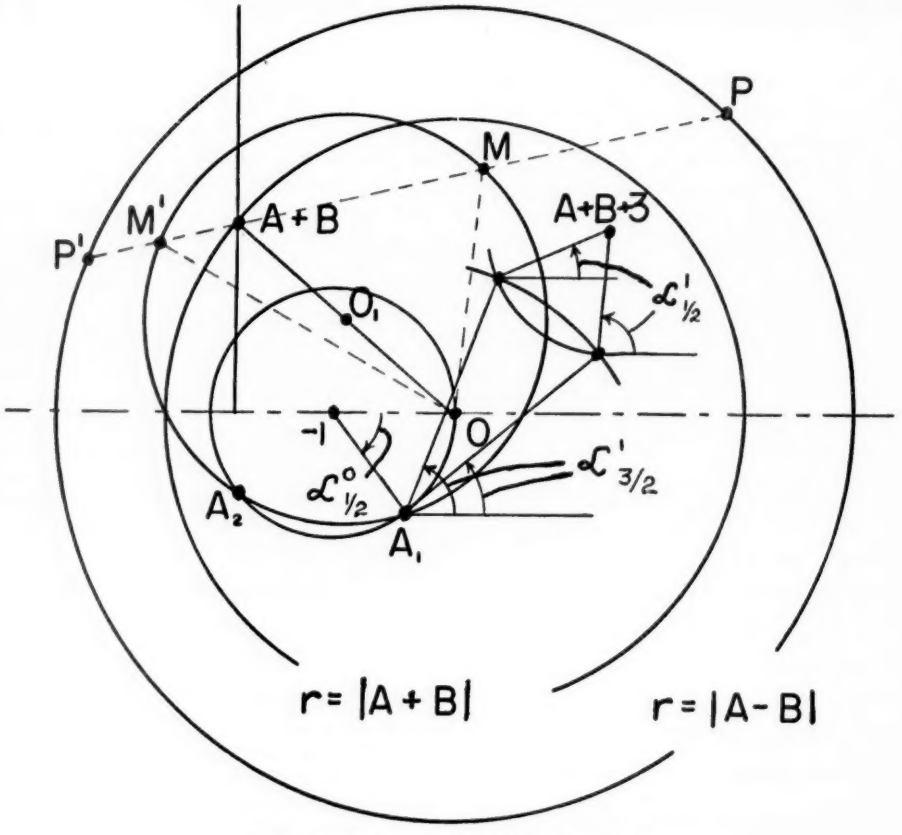

FIG. 1. Graph for Fermi's 135-Mev π^+ scattering.

possibilities for B which are designated as B_1 and B_2. B, however, is of the form

$$B=2\exp(2i\alpha_{\frac{1}{2}}{}^1)+\exp(2i\alpha_{\frac{3}{2}}{}^1)-3.$$

Therefore the complex number representing the line from A to $(A+B+3)$ must have the form $2\exp(2i\alpha_{\frac{1}{2}}{}^1)+\exp(2i\alpha_{\frac{3}{2}}{}^1)$. Thus a solution for $\alpha_{\frac{1}{2}}{}^1$ and $\alpha_{\frac{3}{2}}{}^1$ exists only if the distance from A to $(A+B+3)$ is less than 3 units. For the case shown in Fig. 1 (Fermi's data for π^+ at 135 Mev) A_1 is satisfactory, while A_2 is not. The phase shifts $\alpha_{\frac{1}{2}}{}^1$ and $\alpha_{\frac{3}{2}}{}^1$ can be obtained by drawing a circle of radius 2 with A_1 as center and a circle of radius 1 with $(A+B+3)$ as center, the intersections giving the possible phase shifts. Evidently there are two sets with the relation that the difference,

$$\alpha_{\frac{1}{2}}{}^1-\alpha_{\frac{3}{2}}{}^1,$$

has opposite signs for the two sets. The phase $\alpha_{\frac{1}{2}}{}^0$ is obtained directly from the point A_1.

Thus there are two distinct sets of phases which give exactly the same π^+ cross sections and the same complex numbers A and B.[4] It should be noted that C is not determined uniquely and that there are two possible values for C which have the same absolute magnitude (not complex conjugates). However, only the absolute value of C occurs in the formula for the π^+ cross section [see Eq. (2)]. A unique determination of C which in effect distinguishes between the two sets of $\alpha_{\frac{1}{2}}{}^1$ and $\alpha_{\frac{3}{2}}{}^1$ should come from the π^- data.

The extension to the π^- case is straightforward. The quantities analogous to A and B are X and Y which are related to a_-, b_-, and c_- by

$$|X+Y|^2=9(4k^2)(a_-+b_-+c_-), \tag{8a}$$

$$|X-Y|^2=9(4k^2)(a_--b_-+c_-). \tag{8b}$$

However, the "Optical Theorem" must be applied with care since the total π^- cross section must include the exchange scattering. Therefore

$$4\pi\left(a_-+\frac{c_-}{3}+a_0+\frac{c_0}{3}\right)=\frac{-4\pi}{k}\frac{1}{6k}\,\mathrm{Re}(X+Y). \tag{9}$$

The construction for determining $(X+Y)$ and the locus of X is identical with the π^+ case. The two possibilities of $(X+Y)$ must be used because they now give different results.

[4] The existence of such an alternative set of phase shifts was first noted by C. N. Yang in a private communication to E. Fermi.

TABLE I. Comparison of graphical and numerical procedures.[a]

Lab. deg.	Cross sec.	Measured values	Numerical procedure Fermi 1st	Fermi 2nd	Graphical procedure 1	2	3	4	5	6	7	8
45	$\sigma(-)$	0.87±0.37	1.07	1.07	1.56	1.19	1.52	1.41	1.08	1.18	1.15	1.54
90	$\sigma(-)$	0.65±0.35	0.40	0.37	0.51	0.55	1.03	0.87	0.41	0.55	0.52	1.04
153	$\sigma(-)$	0.87±0.20	0.93	0.93	0.95	0.97	1.15	1.10	0.92	0.97	0.97	1.16
45	$\sigma(+)$	5.66±2.18	6.40	6.69	6.25	—	—	—	—	—	—	—
90	$\sigma(+)$	6.75±2.14	6.49	6.51	6.24	—	—	—	—	—	—	—
135	$\sigma(+)$	21.64±3.55	22.10	22.34	22.08	—	—	—	—	—	—	—
45	$\sigma(\gamma)$	6.50±1.00	5.58	5.61	5.16	5.11	4.03	4.31	5.31	5.12	4.76	4.08
90	$\sigma(\gamma)$	6.70±0.90	6.68	6.46	6.44	6.38	6.26	6.57	6.61	6.40	7.09	6.31
135	$\sigma(\gamma)$	12.80±0.90	12.68	12.76	12.38	12.34	11.62	11.84	12.50	12.35	12.20	11.66
	M		1.90	2.16	6.00	3.52	14.14	9.91	2.54	3.43	4.80	14.39
	Phase shifts											
	$\alpha_{\frac{1}{2}}^{0}$		21.2	20.3	21.5	21.5	21.5	21.5	21.5	21.5	21.5	21.5
	$\beta_{\frac{1}{2}}^{0}$		−2.7	−2.4	−1.5	−1.5	−8.8	−8.8	−1.5	−1.5	−8.8	−8.8
	$\alpha_{\frac{3}{2}}^{1}$		−37.9	−21.2	−21.1	−21.1	−21.1	−21.1	−37.3	−37.3	−37.3	−37.3
	$\alpha_{\frac{1}{2}}^{1}$		−11.5	−48.7	−46.5	−46.5	−46.5	−46.5	−12.5	−12.5	−12.5	−12.5
	$\beta_{\frac{3}{2}}^{1}$		16.8	15.1	16.4	9.0	14.5	0.9	16.4	9.0	14.5	0.9
	$\beta_{\frac{1}{2}}^{1}$		3.8	9.0	5.4	20.1	−6.9	22.1	5.4	20.1	−6.9	22.1

[a] Cross sections are in 10^{-27} cm²/sterad in the center-of-mass system. Phase shifts are in degrees.

From its form X must lie on a circle of radius 2 and center $(A-2)$ not necessarily on the real axis. Each $(X+Y)$ gives two possible X's one of which is rejected since it leads to an incompatible Y. The point $(X+Y-B+6)$ must be within 6 units of the point X, that is,

$$Y-B+6=4\exp(2i\beta_{\frac{1}{2}}^{1})+2\exp(2i\beta_{\frac{1}{2}}^{1}).$$

For each Y there are two sets of phases $\alpha_{\frac{1}{2}}^{1}$ and $\alpha_{\frac{3}{2}}^{1}$ which in general give different values. Thus there are four sets of β's and each may be combined with one of the two α sets giving a total of eight possibilities.

Thus there are eight distinct sets of six phase shifts which reproduce exactly the six linear combinations of the nine coefficients a, b, c given by Eqs. (6a), (6b), (7), (8a), (8b), and (9). This leaves three remaining linear relations among the a, b, c against which each set of six phases is to be tested. In practice the nine coefficients a, b, c are obtained experimentally from measurement of the differential cross sections at three angles (45°, 90°, and 135° in the lab system) for each of the three scattering processes. The most direct way of testing a proposed set of six phase shifts is therefore to compare the measured cross sections at these angles with those calculated from the phase shifts. As a measure of the extent to which the calculated cross sections represent the data, it is useful to calculate the least-squares sum M defined as

$$M=\sum_{i=1}^{9}\frac{(\sigma_{\text{calc}}-\sigma_{\text{exp}})_i^2}{(\delta_i)^2},$$

where δ_i is the quoted experimental error in the ith cross section. The best set of phase shifts is that which minimizes M.

A complete numerical analysis of the phase shift fitting problem has recently been made by Fermi.[2] A comparison of the accurate numerical analysis with the approximate graphical method is given in Table I. The nine experimental quantities[5] for the center-of-mass cross sections of the three processes (1a), (1b), and the exchange scattering leading to γ rays (from the π^0 decay), are tabulated together with the cross sections calculated from the phase shifts listed in the lower part of the table. Fermi found two sets of phase shifts labeled 1st and 2nd which provide local minima of the quantity M with respect to changes of the phases. For the sake of comparison, and to give an indication of the accuracy obtainable in a fairly rough drawing, we have applied the graphical method to a set of initial cross sections equal to those obtained from Fermi's first set of phases rather than to the experimental cross sections themselves. If the drawing were performed with infinite accuracy, one of the eight sets of phases to be tested should coincide exactly with Fermi's first set. The "graphical" set labeled (5) evidently corresponds to Fermi's first set and the "graphical" set (2) corresponds to Fermi's second. The least squares sum M for each of the eight "graphical" sets is also listed in the table. Although none of the eight graphical sets gives a local minimum for M, it is clear that sets (2), (5), and (6) are not band and are about equal in their reproduction of the experimental data. This gives some idea of the order of magnitude of the uncertainties in the phase shifts obtained with the present data.

It is of interest to note that *a priori*, the total number of "graphical" sets of phase shifts that may have to be tested may be as large as 32. There are in general two possibilities for the complex number A, each leading to two sets of α phases. For each value of A there are *a priori* 4 possible values of X, each with two sets of β phases. All together this makes $2\times2\times4\times2=32$. The experimental data thus far exclude 24 of the 32 possibilities immediately.

[5] The data used in these calculations are not the most recent obtained in Chicago. For the most recent experimental results see the report of the Rochester Conference quoted in reference 1.

The Theory of Finite Displacement Operators and Fundamental Length

B. T. DARLING, *Department of Physics and Astronomy, Ohio State University, Columbus, Ohio*

AND

P. R. ZILSEL, *Department of Physics, University of Connecticut, Storrs, Connecticut*

(Received January 12, 1953)

The general finite displacement operator in an n-dimensional complex continuum is defined as an arbitrary superposition of exponential Taylor operators (a Taylor operator yields a Taylor's series). On restriction to the space-time continuum and four-dimensional time-like intervals of constant length ω, the corresponding finite displacement operator may be considered as an ordinary function of the operators u_σ (the partial derivative with respect to x_σ), and must satisfy a Klein-Gordon type equation in u space. This equation possesses relativistic invariant and four-vector solutions that in the limit $\omega\to 0$ reduce to 1 and u_σ, respectively. These operators are combined with the Compton wavelength k and the Dirac or Duffin γ_σ, respectively, to produce a relativistically invariant correspondence type finite-displacement operator generalization of the Dirac-Duffin equation. If the fields are charged, the electromagnetic potentials may be introduced in a manner which leaves the mass spectrum unaltered. The relationship to other nonlocal theories and to the reciprocity theory of Born is briefly considered.

INTRODUCTION

THE purpose of this paper is to give a new mathematical formulation of a theory of fundamental length first proposed in a preceding paper.[1] The approach taken in the present paper arises out of a recent observation of E. Schrödinger, kindly called to our attention by Freistadt,[2] that our scalar averaging operator, Eq. (8), considered as a function of the variables u_σ, is a solution of the Klein-Gordon equation (2). No knowledge of the former mathematical methods is required in order to follow those used here, since the latter methods are entirely independent of the former. Furthermore, because of the great dissimilarity of the methods it seems desirable to restate the necessary basic postulates of the theory and to make the development from them *ab initio*. We also treat briefly the relationship of this theory to some proposed by others. However, general field theoretic questions will be left for a later paper.

For the present purposes, it is appropriate to take as our point of departure the following set of postulates:[1]

A. *One* new fundamental real constant ω with the dimensions of length shall be introduced into the theory; we shall call it a fundamental length.

B. The usual differential laws (field equations) shall be replaced by finite displacement laws such that the field equations at *any* given point involve the field quantities at only those points whose "distance" from the given point satisfies the time-like condition

$$\Sigma_\sigma \Delta x_\sigma^2+4\omega^2=0.$$

C. There shall be a *correspondence principle* such that in the limit as ω approaches zero the new laws reduce to the old differential laws (in which only the infinitesimal neighborhood of any given point enters the laws).

D. The laws shall be relativistically invariant.

With regard to postulate B, we must emphasize that we use a continuum and not a lattice or any other quantization of space. This continuum is the space-time continuum of special relativity, and we shall label its points by x_σ ($\sigma=1$ to 4), where x_k ($k=$ 1 to 3) are the usual space coordinates and are purely real, while $x_4=ix_0=ict$ is purely imaginary, and t is the time. The wave function $\psi(x_\sigma)$ satisfies a certain infinite-order differential equation (9) at all points of the space-time continuum. It is shown in Sec. I that in virtue of postulate B the infinite-order differential operators, $D(u_\lambda)$, which we call finite-displacement operators, by means of which the wave equation (9) is constructed, must be solutions of Eq. (3), *viz.*,

$$[\sum \Delta x_\sigma^2+4\omega^2]D(u_\lambda)=0;$$

in this equation $D(u_\lambda)$ is to be treated as an ordinary function of the independent variables u_λ, and the Δx_σ are symbolic notations for the operators $\partial/\partial u_\sigma$, i.e., $\Delta x_\sigma=\partial/\partial u_\sigma$ in (3). We write (3) in this form to bring out the intimate connection between (1) and (3), which is such that by setting $\Delta x_\sigma=\partial/\partial u_\sigma$ in (1), it becomes the operator on $D(u_\lambda)$ in (3). Any solution of (3) furnishes us with a differential operator on replacing the u_σ by $\partial/\partial x_\sigma$. For the formulation of the theory, then, we may replace postulate B by the postulate that the finite-displacement operators are solutions of Eq. (3).

According to postulates C and D, we seek relativistic scalar and four-vector solutions of (3), $f(u)$ and $g(u)u_\sigma$, respectively, to combine with the scalar $k(=mc/h)$ and the Dirac or Duffin matrices γ_σ to form the wave equation,

$$[\gamma_\sigma g(u)u_\sigma+kf(u)]\psi=0,$$

which in the limit $\omega\to 0$ reduces to the usual differential laws,

$$(\gamma_\sigma u_\sigma+k)\psi=0.$$

This is carried out in Sec. II, where it is shown that the above postulates uniquely determine the form of the wave equation [see Eq. (9)]. The functions $f(u)$

[1] B. T. Darling, Phys. Rev. **80**, 460 (1950).
[2] H. Freistadt, Compt. rend. **235**, 23 (1952).

and $g(u)$ are even functions of u, where

$$u^2=\sum_{\sigma=1}^{4}\frac{\partial^2}{\partial x_\sigma{}^2}=\sum_{k=1}^{3}\frac{\partial^2}{\partial x_k{}^2}-\frac{\partial^2}{\partial x_0{}^2}.$$

The wave equation (9) of Sec. II possesses a mass spectrum in virtue of the time-like intervals assumed in postulate B.[1] That a spectrum of masses results may perhaps be expected from the uncertainty principle $\Delta E\Delta t\cong h$ which, for an essential uncertainty in the proper time, $\Delta\tau=\omega/c$, reduces to $\Delta m\Delta\tau\cong h/c^2$.

In the case of a charged field, the electromagnetic potentials are introduced so as not to disturb the mass quantization, and the u_σ are replaced with $u_\sigma-(ie/\hbar c)A_\sigma$ as usual.

I. FINITE DISPLACEMENT OPERATORS

Let x_σ $(\sigma=1,\cdots n)$ be the coordinates of a point in an n-dimensional space; this space is assumed to be a *continuum* and may in general be *complex*. The individual x_σ may range over all complex numbers, or some may be confined to purely real numbers while others may be confined to purely imaginary numbers, etc. Such restrictions will not invalidate the argument of this section. Consequently the derivations will then be immediately applicable to the case of the space-time continuum for which the space coordinates x_σ $(\sigma=1, 2, 3)$ are purely real, while x_4 $(\sigma=4)$ is purely imaginary since we set $x_4=ix_0=ict$ where t is the time.

Now let Δx_σ be the components of some finite vectorial displacement of this space on itself, so that every point x_σ is displaced to another point $x_\sigma+\Delta x_\sigma$. Let $F(x_\sigma)$ be a function defined throughout this space. Then the value of the function at any subsequent position may be expressed in terms of the value of the function at the corresponding former position by means of Taylor's theorem, which we express in the well-known operator form

$$F(x_\sigma+\Delta x_\sigma)=\exp(\Delta x_\sigma u_\sigma)F(x_\sigma),$$

where $u_\sigma=\partial/\partial x_\sigma$ denotes the partial derivative with respect to x_σ, and the summation convention of repeated index is understood. We shall speak of $\exp(\Delta x_\sigma u_\sigma)$ as the finite displacement operator corresponding to the displacement Δx_σ. More generally, any linear combination of such operators corresponding to different displacements Δx_σ will be spoken of as a finite displacement operator; in particular, this combination may consist of a continuous distribution of displacements. With these definitions it is to be understood that the functions are defined throughout the space, and that the operators may be applied to them at every point.

In the case of one-dimension, consider the following two finite displacement operators f_ω and g_ω:

$$f_\omega\psi(x)=[\psi(x+\omega)+\psi(x-\omega)]/2,$$

and

$$g_\omega\psi(x)=[\psi(x+\omega)-\psi(x-\omega)]/2\omega,$$

associated with the displacements $\Delta x=+\omega$ and $\Delta x=-\omega$. It is clear that the averaging operator f_ω and the differencing operator g_ω have the properties

$$\lim_{\omega\to 0}f_\omega=1,\quad \lim_{\omega\to 0}g_\omega=u=d/dx,$$

and that

$$f_\omega=[e^{\omega u}+e^{-\omega u}]/2=\cosh(\omega u)$$
$$g_\omega=[e^{\omega u}-e^{-\omega u}]/2\omega=\sinh(\omega u)/\omega.$$

The operators g_ω and f_ω are related by

$$g_\omega=(1/\omega^2)df_\omega/du,$$

where the derivative of f_ω on the right side is to be taken in the ordinary way considering f_ω as a function of u. Both f_ω and g_ω considered as functions of u are solutions of

$$[d^2/du^2-\omega^2]D(u)=0.$$

Returning to the general case, let the displacement Δx_σ satisfy

$$\sum_\sigma \Delta x_\sigma{}^2+4\omega^2=0, \tag{1}$$

where ω is a constant (in general complex). Then the finite displacement operator $e^{\Delta x_\sigma u_\sigma}$ corresponding to Δx_σ, when considered as a function of the u_σ treated as independent variables, is such that

$$\sum_\sigma\frac{\partial^2}{\partial u_\sigma{}^2}e^{\Delta x_\lambda u_\lambda}=\sum_\sigma \Delta x_\sigma{}^2e^{\Delta x_\lambda u_\lambda}=-4\omega^2e^{\Delta x_\lambda u_\lambda}.$$

This result makes it apparent that any linear combination $D(\boldsymbol{u})$ of operators corresponding to displacements satisfying (1), when considered as a function of the independent variables u_σ, must obey the equation

$$[\textstyle\sum_\sigma \partial^2/\partial u_\sigma{}^2+4\omega^2]D(\boldsymbol{u})=0. \tag{2}$$

Here $\boldsymbol{u}$ is the vector with components u_σ. The last equation takes a more suggestive form if we convert the left side of the equation (1) into an operator by the identification $\Delta x_\sigma\to\partial/\partial u_\sigma$, whence (1) is replaced by (2) in the form

$$[\textstyle\sum_\sigma \Delta x_\sigma{}^2+4\omega^2]D(\boldsymbol{u})=0. \tag{3}$$

Thus Eq. (1), defining the finite displacements, Δx_σ, is at the same time the operational form of Eq. (3) which the corresponding finite displacement operators must satisfy.

From now on we shall be concerned only with the space-time continuum, for which x_σ $(\sigma=1, 2, 3)$ are purely real while x_4 is purely imaginary. It is clear now that if there are to be any finite displacement laws in physics involving one new fundamental constant ω in accordance with postulates A and B, they must be formed from finite-displacement operators $D(\boldsymbol{u})$ operating on $\psi(x_\sigma)$ defined over the space-time continuum of special relativity, and the $D(\boldsymbol{u})$ must be solutions of

(2). From now on the constant ω in (1) will also be understood to be a positive real number. On setting $\Delta x_4 = i\Delta x_0$, Eq. (1) takes the familiar form

$$\Delta x_0^2 - \sum_{k=1}^{3} \Delta x_k^2 = 4\omega^2, \tag{4}$$

from which it is apparent that the intervals are time-like as required for mass quantization.

II. COVARIANT FINITE DISPLACEMENT OPERATORS AND THE GENERALIZED LAWS OF MOTION

The operator in the Dirac-Duffin-Kemmer equation, which we seek to generalize in accordance with the postulates A to D, may be written

$$\gamma_\sigma u_\sigma + k. \tag{5}$$

It consists of the sum of two scalars k and $\gamma_\sigma u_\sigma$, the latter consisting of the scalar product of the 4-vector differential operator, $u_\sigma = \partial/\partial x_\sigma$, with the Dirac or Duffin matrices denoted indifferently by the γ_σ which, of course, must satisfy the appropriate commutation relations for the respective cases. In order to convert (5) into a finite displacement operator over the time-like intervals defined by (1), we must seek a scalar and vector solution of (2) with the properties:

(a) The scalar operator $f(u)$ shall be relativistically invariant and shall satisfy the correspondence requirement $\lim_{\omega \to 0} f(u) = 1$.

(b) The vector operator $g(u)u_\sigma$ shall be a 4-vector and $\lim_{\omega \to 0} g(u)u_\sigma = u_\sigma$.

We shall see that the conditions (a) and (b) uniquely determine the operators.

(a) The Scalar Finite-Displacement Operator

It is a well-known fact that the only Lorentz invariant functions of u_σ are functions of $u = [\sum_\sigma u_\sigma^2]^{\frac{1}{2}}$ alone.[3] Consequently our scalar operator is a function $f(u)$ of u alone. On substituting $f(u)$ into the differential equation (2) there results the ordinary differential equation,

$$f'' + (3/u)f' + 4\omega^2 f = 0, \tag{6}$$

in which the primes denote first and second derivatives of $f(u)$ with respect to u. By changing the independent variable to $z = 2\omega u$ and setting $f = J(z)/z$, we find that J satisfies Bessel's differential equation,

$$J'' + (1/z)J' + (1 - 1/z^2)J = 0, \tag{7}$$

for Bessel's functions of order one, the primes now denoting derivatives with respect to z. The correspondence condition limits J to the solution regular at the origin and we find

$$f(u) = 2J_1(z)/z, \tag{8}$$

where $J_1(z)$ is the usual Bessel's function of order one.[4] Thus we see that Lorentz invariance and the correspondence limit alone uniquely determine $f(u)$.

(b) The Vector Finite-Displacement Operator

Just as the finite difference operator g_ω of Sec. I is related to the averaging operator f_ω for the one-dimensional case, so here the vector operator satisfying (2) is related to the scalar operator deduced under (a) in the same way. Thus

$$-\frac{1}{\omega^2}\frac{\partial f}{\partial u_\sigma} = \frac{8J_2(z)}{z^2}u_\sigma$$

satisfies (2) and is such that

$$\lim_{\omega \to 0} \frac{8J_2(z)}{z^2}u_\sigma = u_\sigma,$$

as required by the correspondence principle. Again the relativistic property, together with the correspondence requirement, uniquely determines the solution. It may be mentioned that the scalar and vector operators and the relationship between them are precisely the same as obtained in the first paper.

We may sum up the considerations thus far in the following theorem:

> The only finite displacement operators that can be combined with the scalar k and the four-vector γ_λ to form the invariant law of motion in which the displacements Δx_σ are bound by the time-like relation,
>
> $$\sum_\sigma \Delta x_\sigma^2 + 4\omega^2 = 0,$$
>
> involving the introduction of *one* new fundamental (real) constant ω having the dimensions of a length, are the relativistic scalar and vector solutions of
>
> $$[\sum_\sigma \Delta x_\sigma^2 + 4\omega^2]D(u) = 0,$$
>
> where $\Delta x_\sigma = \partial/\partial u_\sigma$; the correspondence principle that $\omega \to 0$ yield the Dirac-Duffin-Kemmer equation restricts the operators to the regular solutions, and we obtain, uniquely, the generalized wave equation
>
> $$\left[-\frac{1}{\omega^2}\gamma_\sigma\frac{\partial}{\partial u_\sigma} + k\right]\frac{2J_1(z)}{z}\cdot\psi = 0, \tag{9}$$
>
> where $z = 2\omega u$, $u = [\sum u_\sigma^2]^{\frac{1}{2}}$, and $u_\sigma = \partial/\partial x_\sigma$.

The wave equation (9) may be written (on remembering $\Delta x_\sigma = \partial/\partial u_\sigma$) in the form

$$[-\gamma_\sigma \Delta x_\sigma + k\omega^2]f(z)\cdot\psi = 0, \tag{10}$$

where $f(z) = 2J_1(z)/z$ is the scalar solution of

$$[\sum_\sigma \Delta x_\sigma^2 + 4\omega^2]f(z) = 0, \tag{11}$$

[3] H. Weyl, *The Classical Groups* (Princeton University Press, Princeton, 1939), first edition, p. 27.

[4] E. Schrödinger, Proc. Roy. Irish Acad. **47A** 1 (1941).

and satisfies

$$\lim_{\omega\to 0} f(z)=1.$$

The dot in (9) and (10) indicates that the operations are to be performed on $f(z)$ first and then the result converted to an operator on ψ by the identification $u_\sigma=\partial/\partial x_\sigma$.

III. INTRODUCTION OF THE ELECTROMAGNETIC POTENTIALS

When we come to introduce the electromagnetic potentials into Eqs. (9) and (10) in case the fields are charged, two conditions presumably should be satisfied. First, the resulting wave equation should be gauge invariant because of the well-known arbitrariness of the electromagnetic potentials under gauge transformations; and second, it should not interfere with the quantization of the mass. The gauge invariance is obtained in the usual manner by replacing u_σ by $U_\sigma=u_\sigma-(ie/\hbar c)A_\sigma$. Whereas, the invariance of mass quantization is achieved by replacing $z=2\omega u$ in the operator of Eqs. (9) or (10) by $z=-2\omega\gamma_\lambda u_\lambda$. That this is so may be seen by noting that the operator in (9) or (10) is then a function of z alone. Indeed, either equation after carrying out the indicated operations and trivial multiplications or divisions by ω may be written

$$D(z)\psi=0, \tag{12}$$

with

$$D(z)=[-2J_2(z)+\bar{k}J_1(z)]/z, \tag{13}$$

in which $z=-2\omega\gamma_\lambda u_\lambda$ and $\bar{k}=\omega k=\beta e^2/\hbar c$.[5] The dimensionless quantity β is defined by setting $\omega=\beta e^2/mc^2$ and is of order unity. If we define an operator Z by setting $Z=-2\omega\gamma_\lambda U_\lambda$, then the wave equation including the potentials and satisfying all requirements is

$$D(Z)\psi=0. \tag{14}$$

It is apparent that if z_n (a real number)[6] is a root of $D(z_n)=0$, and if ψ_n is a solution of $(Z-z_n)\psi_n=0$, then ψ_n is also a solution of Eq. (14).

IV. RELATION TO OTHER THEORIES

It has been proposed at various times to make up operators by taking finite or infinite products of Dirac operators (5) with any arbitrarily chosen spectrum of masses, or by introducing (arbitrarily or by other means) transcendental functions of $\gamma_\lambda u_\lambda$.[7] Obviously, in the first type of theory there does not exist a correspondence principle. It is furthermore apparent that there is no means of fixing upon any spectrum of masses—this being left arbitrary. But more important, both types of theories cannot be considered as theories of fundamental length as such, for they consist of introducing not just one new fundamental constant length, but rather, as we shall see, a whole spectrum of lengths specified by a weight function. In still other theories[8] smearing functions of various quantities are introduced. Here also a spectrum of lengths specified by an arbitrary function is introduced.

Where smearing functions are used, it is usually apparent on simple inspection of the function that a spectrum of lengths is involved, with the smearing function itself playing the part of the weight function. In other cases we may express them as Fourier-Bessel integrals over ω of the averaging operator (8). We may then forthwith turn our attention to the first-mentioned theories.[7]

We shall find it convenient to feature the dependence of the $D(z)$ of Eq. (13) on ω. Let $x=-\gamma_\lambda u_\lambda$, then $z=\omega x$, and

$$D(z)=D(\omega x)=[-2J_2(\omega x)+\bar{k}J_1(\omega x)]/\omega x. \tag{15}$$

Since no correspondence limit $\omega\to 0$ will be involved in the following we may hold $\bar{k}$ fixed at its value $\beta(e^2/\hbar c)$. Our problem then is to express an operator $g(x)$ of one of the above theories in the form

$$g(x)=\int_0^\infty h(\omega)D(\omega x)d\omega. \tag{16}$$

The weight function, $h(\omega)$, specifying the spectral composition of the lengths ω involved in the operator $g(x)$, may be found by means of Mellin transforms.[9] If $G(s)$ is the Mellin transform of $g(x)$, then

$$G(s)=\int_0^\infty g(x)x^{s-1}dx, \tag{17}$$

and

$$g(x)=\frac{1}{2\pi i}\int_{c-i\infty}^{c+i\infty} G(s)x^{-s}ds. \tag{18}$$

In the latter integral the path of integration is along a line parallel to the imaginary axis and at some suitably chosen distance c to the right of that axis. Taking the transform of (16) and reversing the order of integra-

[5] We wish to call attention to an error in footnote (25) of the first paper, which incorrectly set $z=2\omega\gamma_\lambda u_\lambda$ and gives an incorrect sign to the J_2 term of Eq. (13) above.

[6] It is not difficult to prove that $J_{\nu+1}(z)+kJ_\nu(z)=0$, where k is real and ν is real and greater than minus one, has only real roots.

[7] F. Bopp, Ann. Physik **38**, 345 (1940); Z. Naturforsch. **1**, 53 (1946). A. Landé and L. H. Thomas, Phys. Rev. **60**, 121, 514 (1940); **65**, 175 (1944). B. Podolsky and C. Kikuchi, Phys. Rev. **62**, 68 (1942); **65**, 228 (1944). D. Blokhinzev, J. Phys. U.S.S.R. **11**, 72 (1947). D. J. Montgomery, Phys. Rev. **69**, 117 (1947). A. Green, Phys. Rev. **72**, 628 (1947). B. Podolsky and P. Schwed, Revs. Modern Phys. **20**, 40 (1948). L. de Broglie, Compt. rend. **229**, 157, 269, 401 (1949). A. Pais and G. E. Uhlenbeck, Phys. Rev. **79**, 145 (1950). W. Heisenberg, Z. Naturforsch. **5a**, 251, 367, 373 (1950).

[8] F. Bopp, Ann. Physik **42**, 573 (1943). R. P. Feynman, Phys. Rev. **74**, 939 (1948). R. Peierls and H. McManus, Proc. Roy. Soc. (London) **A195**, 323 (1948). J. Irving, Proc. Phys. Soc. (London) **A62**, 780 (1949).

[9] E. C. Titchmarsh, *Introduction to the Theory of Fourier Integrals* (Clarendon Press, Oxford, 1937), first edition, pp. 7 and 315.

tions, we obtain

$$G(s)=\int_0^\infty h(\omega)d\omega\int_0^\infty x^{s-1}D(\omega x)dx.$$

On changing the variable x to $v=\omega x$, this becomes

$$G(s)=\int_0^\infty h(\omega)\omega^{-s}d\omega\int_0^\infty v^{s-1}D(v)dv.$$

From the form of (17) we see that

$$G(s)=H(1-s)\mathfrak{D}(s), \tag{19}$$

where

$$H(s)=\int_0^\infty h(\omega)\omega^{s-1}d\omega,$$

and

$$\mathfrak{D}(s)=\int_0^\infty D(v)v^{s-1}dv,$$

are the Mellin transforms of h and D. Solving (19) for H and making use of (18) we have

$$h(\omega)=\frac{1}{2\pi i}\int_{c-i\infty}^{c+i\infty}\frac{G(1-s)}{\mathfrak{D}(1-s)}\omega^{-s}ds,$$

the desired solution.

The Mellin transform of $D(v)$ may be obtained by use of a formula from the theory of Bessel functions,[10]

$$\int_0^\infty\frac{J_\nu(t)dt}{t^{\nu-\mu+1}}=\frac{\Gamma(\frac{1}{2}\mu)}{2^{\nu-\mu+1}\Gamma(\nu-\frac{1}{2}\mu+1)},$$

valid when $0<\mathrm{R}(\mu)<\mathrm{R}(\nu)+\frac{1}{2}$, where R means the real part. By straightforward application of this formula we find

$$\mathfrak{D}(s)=-\frac{2\Gamma[(s+1)/2]}{2^{2-s}\Gamma[(5/2)-(s/2)]}+\bar{k}\frac{\Gamma(s/2)}{2^{2-s}\Gamma(2-\frac{1}{2}s)},$$

valid when $0<\mathrm{R}(s)<\frac{3}{2}$. The constant c in (18) must of course be chosen in this range.

We next turn our attention to the reciprocity theory of Born.[11] His position is that the basic laws of physics are self-reciprocal between coordinate and momentum space, a self-reciprocal function being defined in two different not exactly equivalent ways[12] as either functions that are their own Fourier transforms or eigenfunctions $F(p)$ of

$$S(x,p)F(p)=sF(p),$$

where

$$S(x,p)=S(p,-x)$$

is a reciprocal invariant and $x_k\rightarrow-i\partial/\partial p_k$. The basic reciprocal invariant function which he introduces is the eight-dimensional distance in phase space,

$$S=x_kx^k+p_kp^k, \tag{20}$$

which we may write in our notation as

$$\sum\Delta x_\sigma^2-\sum\Delta u_\sigma^2,$$

since $p_k=-i\Delta u_k$. Note that the x and p in (20) are dimensionless quantities (see later).

At this point it is clear that our operator (15) is not self-reciprocal in either sense and that while the so-called "reciprocal" Klein-Gordon equation (3) plays an important role in the theory of fundamental length, it is not reciprocally invariant. We treat the coordinate space on an entirely different footing than the momentum space. This divergence between the theories becomes more apparent when we proceed further. For, contrary to determining a finite displacement operator in the manner we do from Eq. (1), Born determines an operator $F(p)$ from the eigenvalue problem,[13]

$$[-\partial^2/\partial p_k\partial p^k+p_kp^k]F_l(p_\lambda)=s_lF_l(p_\lambda).$$

Thus, the eight-dimensional distance (20) takes on a spectrum of eigenvalues s_l with their corresponding eigenoperators F_l. Consequently, Born's theory in our opinion is not a theory of fundamental length, but is rather a spectral theory of "distance" in phase space.

Finally, in Born's theory there is no correspondence principle such as our $\omega\rightarrow0$ limit. The x and p in formula (20) are dimensionless quantities in terms of a length a and momentum b, where $ab=h$. The masses are given by

$$\mu=bk/c=hk/ac,$$

where c is the velocity of light and $k=(p_\lambda p^\lambda)^{\frac{1}{2}}$ is a root of $F_l(p_\lambda)=0$. Then as $a\rightarrow0$ (corresponding to our $\omega\rightarrow0$) all $\mu\rightarrow\infty$. The electron is treated on a different footing in Born's theory and, so to speak, stands outside his mass quantization procedure.

We conclude this section with the mention of a theory of Landé[14] which makes use of time-like intervals obeying the form (1). However, he makes use of (1) in an entirely different manner than we do, with the consequence that his theory leads to a spectrum of charges with one mass whereas we obtain a spectrum of masses with one charge.

ACKNOWLEDGMENT

We wish to thank Dr. E. Schrödinger for his valuable advice and criticism in the preparation of this paper.

[10] G. N. Watson, *Theory of Bessel Functions* (University Press, Cambridge, 1922), second edition, p. 391.
[11] M. Born, Revs. Modern Phys. **21**, 463 (1949).
[12] E. Schrödinger, Proc. Roy. Irish Acad. **55A2**, 29 (1952).
[13] One should consult the paper of Schrödinger (reference 12) for a careful consideration of this eigenvalue problem as well as the problem of Fourier reciprocity.
[14] A. Landé, J. Franklin Inst. **229**, 767 (1940).

Fourth-Order Radiative Corrections to Atomic Energy Levels*†

J. WENESER,‡§ R. BERSOHN,‖ AND N. M. KROLL
Columbia University, New York, New York

(Received May 19, 1953)

In this paper the fourth-order radiative corrections to the elastic scattering of an electron in the field of a fixed potential are examined, using the Dyson S-matrix formulation of quantum electrodynamics. The result can be represented as an addition to the interaction energy density of the electron with the external potential:

$$-ie\bar{\psi}(x)\gamma_\mu\psi(x)\Box^2/\kappa^3 A_\mu^e(x)[(\alpha^2/4\pi^2)(0.52\pm0.21)],$$

plus the anomalous magnetic moment already known. The contributions that arise from the vacuum-polarization currents are omitted. This term calculated contributes to the level shift in a hydrogenic atom an energy of

$$(\alpha^4Z^4/n^3)\ \mathrm{Ry}\delta_{l0}[(4/\pi^2)(0.52\pm0.21)].$$

For the $2S$ level of hydrogen this is 0.24 ± 0.10 Mc/sec.

INTRODUCTION

EVIDENCE that fourth-order terms may well be of experimental significance comes from the recently completed precise measurements of the fine structure of the $n=2$ levels in hydrogen and deuterium. The application of the second order of quantum electrodynamics to the interpretation of atomic energy level shifts has met with very great success. The more precise measurements make possible a more severe test of the theory.

A crude estimate of the order of magnitude to be expected is easily obtained. The main part of the second order level shift is given by the term[1]

$$(\alpha^3Z^4/n^3)\ \mathrm{Ry}\ \ln(mc^2/\bar{E}).$$

The leading term of the fourth-order contribution may be expected to be of the form

$$(\alpha^4Z^4/n^3)\ \mathrm{Ry}\ \ln(mc^2/\bar{E}),$$

or simply

$$(\alpha^4Z^4/n^3)\ \mathrm{Ry},$$

according as there is or is not a logarithm.[2] Thus the fourth-order effect might amount to a part in a hundred or a part in a thousand of the second-order effect, and these are experimentally significant magnitudes.

METHOD OF CALCULATION

In the evaluation of second-order radiative corrections to atomic energy levels two approaches have been used. One of these consists of an evaluation of a formula for the self energy obtained in a straightforward manner from second-order perturbation theory, while the other consists of an evaluation of the second-order radiative corrections to elastic scattering, from which one infers the level shift. The relationship between the two methods is quite apparent if one compares the formulas of French and Weisskopf[3] with those of Feynman.[4] Thus, for the intermediate states of the electron, French and Weisskopf use plane waves corrected by a single Born approximation rather than the exact states of the external potential. This approximation corresponds essentially to the scattering approximation. For transitions involving low-energy photons both the scattering approximation and, accordingly, the above-mentioned treatment of intermediate states fail in the second-order calculation. This failure manifests itself in the appearance of an infrared catastrophe, and makes necessary a modified treatment for the low energy photons.

The scattering method, while possibly less straightforward, is actually much the simpler of the two, particularly for the higher-order corrections. Accordingly, this paper will be devoted to a discussion and evaluation of the fourth-order radiative corrections to elastic scattering in first Born approximation. It is easily seen that the result may be represented as a modification in the interaction energy density of the electron with the external potential of the form:

$$C_1\bar{\psi}(x)\sigma_{\mu\nu}\psi(x)\int f_1(x-x')F_{\mu\nu}^e(x')d^4x'$$

$$+C_2\left(-ie\bar{\psi}(x)\gamma_\mu\psi(x)\Box^2\int f_2(x-x')A_\mu^e(x')d^4x'\right)$$

$$\int f_1(x-x')d^4x'=\int f_2(x-x')d^4x'=1. \quad (1)$$

* The results of this calculation have been reported previously by Bersohn, Weneser, and Kroll, Phys. Rev. **86**, 596 (1952).

† Publication assisted by the Ernest Kempton Adams Fund.

‡ Holder of a U. S. Atomic Energy Commission Predoctoral Fellowship.
§ Now at Brookhaven National Laboratory, Upton, New York.
‖ Now at Cornell University, Ithaca, New York. This author wishes to thank Professor W. E. Lamb, Jr. for his hospitality at Columbia University, and much guidance and inspiration.
Columbia University Fellow, summer of 1951.

[1] H. Bethe, Phys. Rev. **72**, 339 (1947).

[2] An investigation of the fourth-order level shift using nonrelativistic electrodynamics is relatively simple and indicates that there is no logarithm.

[3] J. B. French and V. F. Weisskopf, Phys. Rev. **75**, 1240 (1949).

[4] R. P. Feynman, Phys. Rev. **74**, 1430 (1948).

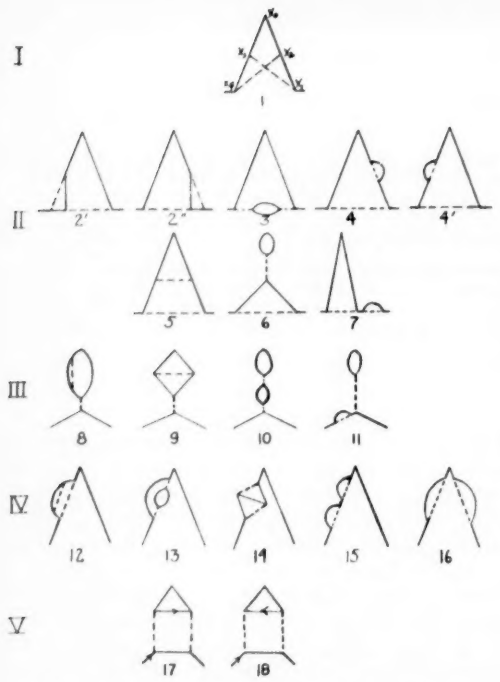

FIG. 1. The Feynman diagrams corresponding to $U_1^{(4)}$.

Expressed as in Eq. (1), the two terms correspond to an extra magnetic moment interacting with a modified external field and the interaction of the electron current with a modified external potential. The level shift may be obtained by including Eq. (1) in the interaction energy of the bound electron and evaluating its effect using first-order perturbation theory. The scattering approximation is expected to be valid to order α^4Z^4 Ry, at least for high energy photons. The functions $f_1(x-x')$, $f_2(x-x')$ are characterized by a range of the order of the electron's Compton wavelength, and will be replaced by δ functions. The effect on the level shift of this replacement is at most of order α^7Z^5 Ry. In view of the approximation involved in the use of the scattering method, a more precise representation of these functions is, in fact, unwarranted.

The evaluation of the fourth-order level shift requires, therefore, merely the calculation of the constants C_1 and C_2. C_1 represents the fourth-order contribution to the anomalous moment and has already been calculated. We shall be concerned here with the closely related but considerably more involved problem of evaluating C_2. It should be mentioned that C_2 turns out to be finite in the infrared. This suggests that for the fourth-order corrections the scattering approximation is valid to order α^4Z^4 Ry even for the low-energy photons.[5]

[5] An explicit proof that the fourth-order level shift is given correctly to order α^4Z^4 Ry by the scattering approximation has been given by one of the authors (NK) and R. L. Mills. The corrections to the scattering approximation are of order α^5Z^5 Ry. A note on this subject is in preparation.

THE SCATTERING CALCULATION

The calculation was carried out using the Dyson S-matrix formulation of quantum electrodynamics and the Dyson renormalization program.[6] We are here concerned only with the fourth-order, single-interaction with the external field, one-electron part of the S-matrix. This has been discussed by Karplus and Kroll,[7] and called by them $U_1^{(4)}$.

The Feynman diagrams that describe $U_1^{(4)}$ are repeated in Fig. 1. The sum of the diagrams 17 and 18 is just zero by Furry's theorem. The diagrams of group IV and diagram 7 give rise only to renormalizations of lower order scattering processes, and so can be dropped from further consideration. The diagrams of class III are vacuum-polarization effects; these terms have been calculated by Baranger, Dyson, and Salpeter.[8] This leaves the diagrams 1 through 6, and it is seen later that only 1 through 5 actually contribute.

The integrals corresponding to diagrams 1 through 6 are, in fact, given explicitly by Karplus and Kroll. The procedure for reducing these expressions to integrals over Feynman's auxiliary variables has been fully discussed and will be reviewed only briefly. The essential problem here is one of organizing the calculations in such a way as to keep the computational labor involved within manageable limits. Therefore, in the discussion to follow, emphasis will be placed upon the procedure used. As the procedure differs from diagram to diagram, the various diagrams will be discussed separately. Diagram 1, being irreducible, is the best organized and so the easiest to discuss. It is also the most complicated one to evaluate, and, therefore the one for which organization is most necessary. Therefore, we consider it first and in some detail.

The Evaluation of the Irreducible Diagram

Diagram 1 (see Fig. 1 for the labeling) gives rise, immediately on application of Dyson's prescription, to the integral

$$M_1=-\frac{e}{\hbar c}\frac{\alpha^2\pi^2}{4}\int_{-\infty}^{+\infty}d^4x_0d^4x_1d^4x_2d^4x_3d^4x_4$$
$$\times\{A_\mu^e(x_0)D_F(x_3-x_1)D_F(x_4-x_2)\bar{\psi}(x_1)$$
$$\times\gamma_\nu S_F(x_2-x_1)\gamma_\lambda S_F(x_0-x_2)\gamma_\mu S_F(x_3-x_0)$$
$$\times\gamma_\nu S_F(x_4-x_3)\gamma_\lambda\psi(x_4)\}. \quad (2)$$

On inserting the Fourier transforms and carrying out

[6] F. J. Dyson, Phys. Rev. **75**, 486, 1736 (1949).
[7] R. Karplus and N. M. Kroll, Phys. Rev. **77**, 536 (1950).
[8] Baranger, Dyson, and Salpeter, Phys. Rev. **88**, 680 (1952).

the trivial integrations, M_1 becomes

$$M_1=(e/\hbar c)(\alpha^2/\pi^2)\int d^4k d^4k' d^4p_1 d^4p_2 A_\mu^e(p_1-p_2)$$
$$\times\frac{\bar\psi(p_1)\gamma_\nu[i\gamma\cdot(p_1-k)-\kappa]\gamma_\lambda[i\gamma\cdot(p_1-k-k')-\kappa]\gamma_\mu[i\gamma\cdot(p_2-k-k')-\kappa]\gamma_\nu[i\gamma\cdot(p_2-k')-\kappa]\gamma_\lambda\psi(p_2)}{[(p_1-k)^2+\kappa^2][(p_1-k-k')^2+\kappa^2][(p_2-k-k')^2+\kappa^2][(p_2-k')^2+\kappa^2][k^2+\lambda^2][k'^2+\lambda^2]}. \quad (3)$$

A photon rest-mass has been used to control the infrared divergence; it will be considered later. Denominators are combined by the Feynman identity

$$\frac{1}{abcdef}=5!\int_0^1\frac{duzdzw^2dwx^3dxy^4dy}{[(a-b)yxwzu+(b-c)yxwz+(c-d)yxw+(d-e)yx+(e-f)y+f]^6}. \quad (4)$$

The form of the final integrals over the auxiliary variables u, z, w, x, y depends on the choice of assignment of denominators in this identity. The assignment used here—and by Karplus and Kroll in the magnetic moment calculation—is

$$\begin{aligned} a&=[(p_2-k-k')^2+\kappa^2], & d&=[k^2+\lambda^2],\\ b&=[(p_1-k-k')^2+\kappa^2], & e&=[(p_2-k')^2+\lambda^2], \\ c&=[(p_1-k)^2+\kappa^2], & f&=[k'^2+\lambda^2]. \end{aligned} \quad (5)$$

This choice of a and b, together with the fact that $a=b$ for $p_1=p_2$, will be seen later to make one of the auxiliary variable integrations, the u integration, trivial. Then

$$M_1=120\left(\frac{e}{\hbar c}\right)\left(\frac{\alpha^2}{\pi^2}\right)\int d^4k d^4k' d^4p_1 d^4p_2 A_\mu^e(p_1-p_2)\int_0^1 duzdzw^2dwx^3dxy^4dy$$
$$\times\frac{\bar\psi(p_1)\gamma_\nu[i\gamma\cdot(p_1-k)-\kappa]\gamma_\lambda[i\gamma\cdot(p_1-k-k')-\kappa]\gamma_\mu[i\gamma\cdot(p_2-k-k')-\kappa]\gamma_\nu[i\gamma\cdot(p_2-k')-\kappa]\gamma_\lambda\psi(p_2)}{\{k^2xy+k'^2(1-xy+xywz)+2k\cdot(-\Delta pyxwzu-p_1yxw} \quad (6)$$
$$+2k\cdot k'yxwz+2k'\cdot(-\Delta pyxwzu-p_1yxwz-p_2y+p_2xy)+\lambda^2(1-y+xy(1-w))\}^6$$

with $\Delta p=(p_2-p_1)$, where use has been made of $p_1^2+\kappa^2=p_2^2+\kappa^2=0$.

Further manipulation is greatly facilitated by introducing new variables K, K', linearly related to the k, k', that diagonalize the denominator to the form[9]

$$\{\alpha K^2+\beta(K')^2+\gamma\kappa^2+\delta(\Delta p)^2+\epsilon\lambda^2\}, \quad (7)$$

where α, β, γ, δ, ϵ are

$$\alpha=xy,$$
$$\beta=[1-xy(1-wz+w^2z^2)],$$
$$\gamma=w^2xy+y^2\frac{[1-x+xwz(1-w)]^2}{[1-xy(1-wz+w^2z^2)]},$$
$$\delta=w^2xyuz(1-uz)+y^2xwz\frac{[1-x+uxwz(1-w)][1-w-u(1-wz)]}{[1-xy(1-wz+w^2z^2]},$$
$$\epsilon=1-y+xy,$$

and where further use has been made of $p_1^2+\kappa^2=p_2^2+\kappa^2=0$. In terms of these new variables, K and K', the numerator can be brought into the form:

$$\bar\psi(p_1)\{(\ )(K')^4\gamma_\mu+(\ )K^2(K')^2\gamma_\mu+(\ )K^2\kappa^2\gamma_\mu+(\ )\kappa^4\gamma_\mu$$
$$+(\ )(K')^2(\Delta p)^2\gamma_\mu+(\ )K^2(\Delta p)^2\gamma_\mu+(\ )\kappa^2(\Delta p)^2\gamma_\mu$$
$$+(\ )K^2\kappa\sigma_{\mu\nu}\Delta p_\nu+(\ )(K')^2\kappa\sigma_{\mu\nu}\Delta p_\nu+(\ )\kappa^3\sigma_{\mu\nu}\Delta p_\nu$$
$$+(\ )\kappa\sigma_{\mu\nu}\Delta p_\nu(\Delta p)^2+(\ )\gamma_\mu(\Delta p)^4+(\ )K^2\kappa\Delta p_\mu$$
$$+(\ )(K')^2\kappa\Delta p_\mu+(\ )\kappa^3\Delta p_\mu\}\psi(p_2)A_\mu^e, \quad (8)$$

where the factors are functions of the auxiliary variables. Terms containing K, K' to odd powers have been dropped since they vanish on integration over K, K'.

On separating off the renormalizations and carrying out the K, K' integrations, the result immediately takes the form:

$$\bar\psi(p_1)\{f((\Delta p/\kappa)^2)A_\mu^e(\Delta p)\sigma_{\mu\nu}\Delta p_\nu/\kappa$$
$$+g((\Delta p/\kappa)^2)\gamma_\mu A_\mu^e(\Delta p)(\Delta p)^2/\kappa^2$$
$$+h((\Delta p/\kappa)^2)\Delta p_\mu A_\mu^e(\Delta p)$$
$$+j((\Delta p/\kappa)^2)\sigma_{\mu\nu}\Delta p_\nu(\Delta p)^2A_\mu^e(\Delta p)$$
$$+l((\Delta p/\kappa)^2)\gamma_\mu(\Delta p)^4A_\mu^e(\Delta p)\}\psi(p_2). \quad (9)$$

In this calculation terms of higher order in $(\Delta p/\kappa)$ than the second are discarded. This corresponds to replacing the functions $f_1(x_1-x_2)$, $f_2(x_1-x_2)$ appearing in Eq. (1) by δ functions, as previously discussed. This leaves the

[9] Note that the definition of δ, γ is such that $(\delta/\gamma)\leq 1$. This means that after the K, K' integration an expansion in $\Delta p/\kappa$, for small $(\Delta p/\kappa)$, is valid for all values of the auxiliary variables.

terms

$$\bar{\psi}(p_1)\{f(0)A_\mu^e(\Delta p)\sigma_{\mu\nu}\Delta p_\nu/\kappa+g(0)\gamma_\mu A_\mu^e(\Delta p)(\Delta p/\kappa)^2 +h(0)(\Delta p_\mu/\kappa)A_\mu^e(\Delta p)\}\psi(p_2). \quad (10)$$

Now, the term $h(0)\Delta p_\mu/\kappa A_\mu^e(\Delta p)$ is gauge variant; it is, then, to be expected that if all terms of this form are carefully collected, the coefficient, $h(0)$, will vanish. In this problem $A_\mu^e=(0,0,0,V(r))$, and so $\Delta p_\mu A_\mu^e(\Delta p)=0$ in any case. The $f(0)A_\mu^e(\Delta p)\sigma_{\mu\nu}\Delta p_\nu/\kappa$ term is just the fourth-order contribution to the anomalous moment of the electron.[5] The problem here is to calculate the $g(0)$.

The terms in the numerator, (8), that contribute to $g(0)$ are those in which Δp appears as $(\Delta p)^0$ or $(\Delta p)^2$. The terms contributing to $f(0)$ are the significantly less populous group involving only the terms $\kappa K^2\sigma_{\mu\nu}\Delta p_\nu$, $\kappa(K')^2\sigma_{\mu\nu}\Delta p_\nu$, $\kappa^3\sigma_{\mu\nu}\Delta p_\nu$. The various spinor products appearing originally in the numerator are reduced to the form Eq. (8) using a number of identities, of which a particularly simple example is

$$\bar{\psi}(p_1)\gamma_\nu\gamma\cdot p_1\gamma_\mu\gamma\cdot p_2\gamma_\nu\psi(p_2) =\bar{\psi}(p_1)\{-2\kappa^2\gamma_\mu-2\gamma_\mu(\Delta p)^2\}\psi(p_2).$$

In obtaining these identities free use has been made of the fact that $\bar{\psi}(p_1)$, $\psi(p_2)$ are free particle spinors; all terms depending on Δp otherwise than as $(\Delta p)^0$ or $(\Delta p)^2$ have been dropped.

As written, $g(0)$ is a sum of integrals over the five auxiliary variables, and is a function of λ, the photon mass. The result is of physical interest only in the limit $\lambda\to 0$. In the very great majority of integrals, called group g', there is convergence uniform with respect to the λ. In these terms it is, then, quite correct to put $\lambda\equiv 0$; in doing this, only terms that go to zero as λ goes to zero are dropped. However, in a particular group of integrals, putting $\lambda\equiv 0$ makes the integrals divergent; these are discussed later, calling this group g''.

The set of integrals g' is discussed first. A particular system of classification was used; this classification appeared to us to be crucial to the feasibility of the calculation. The g' can be written—after the trivial integration—as

$$g'=\Sigma c(k,m,n,s,t)I(k,m,n,s,t), \quad (11)$$

where the c's are numerical factors and

$$I(k,m,n,s,t)=\int_0^1 dzdwdxdy\frac{z^{s+1}w^{t+2}x^{n+2k-3-m}y^{n+2k-2}}{\beta^{n+k}\gamma^k}[1-x(1-wz+w^2z)]^m$$
$$=\int_0^1 dzdwdxdy\frac{z^{s+1}w^{t+2}x^{n+2k-3-m}y^{n+k-2}[1-x(1-wz+w^2z)]^m}{[1-xy(1-wz+w^2z^2)]^n[w^2x+y\{(1-x+xwz(1-w))^2-w^2x^2(1-wz+w^2z^2)\}]^k}, \quad (12)$$

with k, m, n, s, t positive integers such that $0\le m\le n+2k-3$. Terms that actually appeared are given by

$k=1$	$n=1\{m=0\dagger$	$n=2\{m=1$ $m=0\dagger$	$n=3\{m=1$ $m=0\dagger$	$n=4\{m=1^*$ $m=0^*$	
$k=2$	$n=0\{m=0\dagger$	$n=1\{m=1\dagger$ $m=0\dagger$	$n=2\{m=2\dagger$ $m=1\dagger$ $m=0$	$n=3\{m=3\dagger$ $m=2\dagger$ $m=1$	$n=4\{m=3^*$ $m=2^*$
$k=3$	$n=-1\{m=0$	$n=0\{m=2$ $m=1$	$n=1\{m=2$ $m=1$	$n=2\{m=3$ $m=2$	various higher n

each with a range of values for s, t.

This system of classification in terms of the I's was first used by Karplus and Kroll in their magnetic moment calculation; in the terms marked by † the expressions after the x, y integrations were furnished us by these authors. It is not surprising that the same type of integrals appear in $g(0)$ as appear in $f(0)$. However, the evaluation of $g(0)$ is a much more formidable task than that of $f(0)$. First, there are simply a greater number of terms present after the K-space integration that must be rearranged into this classification system. We have already seen that the magnetic-moment terms came from a smaller group of terms in Eq. (8). The second and more important source of difficulty is the appearance of terms in $g(0)$ of higher k, n than are present in $f(0)$. For given k, n the labor involved in evaluating I increases sharply with decreasing m. There is an even sharper increase with increase of k and n. The appearance of increased difficulties can be seen directly from Eq. (7). The terms

$$(K')^2(\Delta p)^2\gamma_\mu,\quad K^2(\Delta p)^2\gamma_\mu,\quad \kappa^2(\Delta p)^2\gamma_\mu,$$

will give rise to I's of k equal to those arising from

$$(K')^2\kappa\sigma_{\mu\nu}\Delta p_\nu,\quad K^2\kappa\sigma_{\mu\nu}\Delta p_\nu,\quad \kappa^3\sigma_{\mu\nu}\Delta p_\nu.$$

However, in addition there are the other terms that contribute to $g(0)$. Thus, $\kappa^4\gamma_\mu$ terms are the $k=3$ integrals. The $(K')^2\kappa^2\gamma_\mu$, $K^2\kappa^2\gamma_\mu$ give rise to $k=2$ integrals as compared to the $k=1$ integrals coming from the $(K')^2(\Delta p)^2\gamma_\mu$, $K^2(\Delta p)^2\gamma_\mu$. Further, even when the two terms being compared give integrals of equal k the coefficients are much more complicated in the terms associated with $g(0)$. Also, even for equal k, $g(0)$ contains I's of higher n, lower m. Finally, the appearance of the higher s, t terms multiplies the labor.

The I's are computed by carrying out the integrations in the order x, y, z, w. Actually, it was found sufficient to carry out the x, y integration; there then remain for any I a small number of double integrals. A series of tables for these double integrals then completes the evaluation.[10] The values of a large number of I's for the k, n m indicated were obtained and are available. All of the integrals can be evaluated analytically and can be expressed in terms of the same set of transcendentals as those of Karplus and Kroll.

The integrals marked by an * were not evaluated. Instead the terms that contained these I's were estimated by *rigorous* upper and lower bounds. This was done for the I's of higher k, n, lower m where the labor was very large and the computed contributions quite small. The fact that these quantities were not evaluated exactly leads to a small uncertainty in the final result; the stated uncertainty represents outside limits; the actual error is probably much less.

[10] These tables coincide in part with those developed by Karplus and Kroll, and these parts were made available to us.

Next the set g'' is discussed. All the terms that are λ-divergent come from the quantity obtained on putting k, k' equal to zero in the numerator of Eq. (5); after the removal of the renormalization terms and integration over the photon momenta, this gives rise to the integral

$$\int_0^1 dwdzdxdy\left\{\frac{2zw^2xy^2}{\{w^2xy+y^2([1-x+xwz(1-w)]^2-w^2x^2[1-wz(1-wz)])+\lambda^2(1-y+xy)[1-xy(1-wz+w^2z^2)]\}^2}\right.$$
$$\left.\times\frac{-4zw^2xy^2\int_0^1 du[uzw^2(1-uz)xy][1-xy(1-wz+w^2z^2])+xwzy^2[1-u-w(1-uz)][1-x+xwzu(1-w)]}{\{w^2xy+y^2([1-x+xwz(1-w)]^2-w^2x^2[1-wz(1-wz)])+\lambda^2(1-y+xy)[1-xy(1-wz+w^2z^2]\}^3}\right\}. \quad (13)$$

A deficiency in powers of z and w makes the integrals divergent if we put $\lambda\equiv 0$. The presence of the λ makes evaluation appreciably more difficult, as the above discussed procedure fails. However, a more roundabout procedure proved sufficiently simple to be carried out. Thus, writing the integrals as

$$\int_0^1 dx\int_0^1 dy\int_0^1 dz\int_0^1 dwF(x, y, z, w, \lambda/\kappa), \quad (14)$$

the identity

$$\int_0^1 dx\int_0^1 dy\int_0^1 dz\int_0^1 dwF(x, y, z, w, \lambda/\kappa)$$
$$=\int_0^1 dx\int_0^1 dy\int_0^1 dz\int_{(\lambda/\kappa)}^1 dwF(x, y, z, w, 0)$$
$$+\int_0^1 dx\int_0^1 dy\int_0^1 dz\int_{(\lambda/\kappa)}^1 dw\{F(x, y, z, w, \lambda/\kappa)$$
$$-F(x, y, z, w, 0)\}+\int_0^1 dx\int_0^1 dy\int_0^1 dz\int_0^{(\lambda/\kappa)} dw$$
$$\times F(x, y, z, w, \lambda/\kappa)$$

provides a useful separation. The first term is easily integrated over x, y, z by the same procedure that was used in the I's. The remaining w integration is also easily carried through, since, as can be shown rigorously, it is correct to put $\lambda=0$ throughout except for the integration of a simple rational fraction. It is only this first term that gives a λ-divergent dependence. The second and third terms give a result that is finite as λ goes to zero. For these terms it is very useful to use the new variables

$$w=(\lambda/\kappa)W, \quad 1-x=(\lambda/\kappa)X.$$

The explicit dependence on λ occurs in two ways: λ still appears in the integrand after cancelling out common powers of λ between numerator and denominator, and λ appears in the limits as κ/λ. It can be rigorously shown that it is correct to put $\lambda=0$ in both places simultaneously. There is left, then, only a definite integral without any dependence on parameters. It is possible to carry these integrals out more or less straightforwardly. Only terms that go to zero with λ have been dropped in this whole procedure.

The final result for this diagram is

$$M_1=-8\pi^2\left(\frac{e}{\hbar c}\right)\alpha^2\int d^4p_1d^4p_2\bar{\psi}(p_1)\gamma_\mu A_\mu^e(\Delta p)$$
$$\times(\Delta p/\kappa)^2\psi(p_2)m_1,$$
$$m_1=-(13/9)\ln\lambda-4.24\pm 0.10.$$

The Evaluation of the Reducible Diagrams

The other diagrams are all reducible; these require the use of the modified $\bar{S}_F$, $\bar{D}_F$, or $\bar{\Gamma}_\mu$ functions. Since the form of the modified functions is sufficiently more complex than that of S_F, D_F, γ_μ, the organization of the terms is less unified. This tends to prevent a simple description of the calculations. Since only diagram 2 is of appreciable difficulty, further comments are limited to a few remarks on this diagram.

The diagrams $2'$ and $2''$ lead to equal contributions and we understand M_2 to mean $2M_{2'}$. Then:

$$M_2=8\pi i\left(\frac{e}{\hbar c}\right)\alpha\int d^4p_1d^4p_2A_\mu^e(\Delta p)\int d^4k$$
$$\times\bar{\psi}(p_1)\gamma_\nu\frac{i\gamma(p_1-k)-\kappa}{(p_1-k)^2+\kappa^2}\gamma_\mu\{\Gamma_\mu(p_1-k, p_2-k)\}\frac{1}{k^2+\lambda^2}\psi(p_2). \quad (15)$$

The quantity in the brackets is the contribution of the corner vertex, the renormalization term having already been removed. This modified function is obtained explicitly in Karplus and Kroll.[11]

The prescription of the choice of factors in the denominator combination identity cannot be given simply here. However, by

[11] There is a transcription error in Karplus and Kroll Eq. (31); the definition of K_μ should read:

$$K_\mu(p', p''; u, v)$$
$$=(1-u)(i\gamma\cdot p'+\kappa)\gamma_\mu(i\gamma\cdot p''+\kappa)$$
$$-(i\gamma\cdot p'+\kappa)[\kappa(1-u^2)\gamma_\mu+i(1-u)(1-uv)(p'+p'')_\mu$$
$$-i(1-u+2uv)(1-uv)(p'-p'')_\mu]$$
$$-[\kappa(1-u^2)\gamma_\mu+i(1-u+uv)(1-u)(p'+p'')_\mu$$
$$+i(1-u+uv)(1+u-2uv)(p'-p'')_\mu](i\gamma\cdot p''+\kappa)$$
$$-(1-u)\gamma_\mu[(p'^2+\kappa^2)(1-uv)+(p''^2+\kappa^2)(1-u+uv)]$$
$$-i\kappa(p'-p'')_\mu u(1+u)(1-2v)+\gamma_\mu(p'-p'')^2[1-u+u^2v(1-v)]$$
$$+\kappa\sigma_{\mu\nu}(p'-p'')_\nu u(1-u).$$

suitable choices of the order of the factors and by suitable simple transformations, the auxiliary variable integrals can be made to fall into a useful classification system. Again, in the great majority of integrals it is correct simply to put $\lambda=0$. In those integrals in which λ must be kept, the procedure outlined for the analogous integrals of diagram 1 is applicable here; no further discussion of these is necessary. Of the remaining integrals, with $\lambda=0$, the group containing almost all the integrals can be written as

$$\Sigma c(k, m, n, s, t)J(k, m, n, s, t),$$

where the c's are constants and J is given by

$$J(k, m, n, s, t)=\int_0^1 du\int_0^1 dv\frac{u^s v^t}{(1-uv)^{n+k-m}}$$
$$\times\int_0^1 dx\int_0^1 dy\frac{y^n x^{n+k-1-m}(1-ux(1-v)(1-uv))^m}{[yv(1-ux(1-v)/(1-uv))^2+ux/(1-uv)]^k}; \quad (16)$$

the k, m, n, s, t are positive integers such that $0\leq m\leq n+k-1$. The integrals that actually occurred are given by

$k=1^*$,
$k=2$, $n=1^*$, 2, 3,
$k=3$, $n=$ 2^*, 3, 4.

Those marked by an asterisk were evaluated before this system of classification was devised; the others are available. There is a very great simplification brought about by this system of classification, especially for the higher k. The use of a more naive system—say, according to powers of x in the numerator, rather than the $x^{n+k-1-m}[1-ux(1-v)/(1-uv)]^m$ is almost prohibitively laborious. The I's are easily evaluated by integrating in the order y, x, u, v; after the y, x integrations the u, v functions are of the same form as the two-variable integrals met with in diagram 1, and the tables used there are immediately applicable here.

Not all the integrals fit into this classification. A few integrals are found in which the power of x in the numerator is greater than $(n+k)$. The simple program of integrating in the order y, x, u, v is then stopped after the y integration by the presence of the integral:

$$(\text{function of } u, v)\int_0^1 dx\frac{1}{ax+b}\ln(cx+d);$$

a, b, c, d are functions of u and v. Since the result of the x integration is not expressible in terms of elementary functions, a more roundabout and much more laborious technique of integration must be used. While these integrals can again be carried through and expressed in terms of the previously mentioned set of transcendentals, the smaller terms of this kind were in fact estimated by means of rigorous upper and lower bounds.

The final result for diagram 2 is

$$m_2=-\tfrac{2}{3}(\ln\lambda)^2-(1/18)\ln\lambda+4.86\pm0.11.$$

The diagrams 3, 4, 5 were carried out easily and exactly. The integrals were sufficiently few and simple so that no system of classification was required. The calculations in these diagrams were not much more difficult than the analogous magnetic moment calculations; in the case of the diagrams 1 and 2 the tasks were of a different order of magnitude. The integrals that were λ dependent were more difficult here than in the magnetic moment case; however, the procedure discussed above is efficacious here too.

Diagram 6 is easily dismissed. It consists of two second-order pieces joined by a photon line. Since the photon part is proportional to $(\Delta p/\kappa)^2$, the vertex part to $(\Delta p/\kappa)$ at least, the diagram as a whole cannot contribute terms of order $(\Delta p/\kappa)^2$.

The results for the five diagrams are

$$M=-8\pi^2\left(\frac{e}{\hbar c}\right)\alpha^2\int d^4p_1d^4p_2\bar{\psi}(p_1)\gamma_\mu A_\mu^*(\Delta p)$$
$$\times(\Delta p/\kappa)^2\psi(p_2)m,$$
$$m=\sum m_i;$$
$$m_1=-(13/9)\ln\lambda-4.24\pm0.10,$$
$$m_2=-\tfrac{2}{3}(\ln\lambda)^2-(1/18)\ln\lambda+4.86\pm0.11,$$
$$m_3=-(77/432)\pi^2+(1009/648)=-0.06,$$
$$m_4=\tfrac{2}{3}(\ln\lambda)^2+(1/18)(\ln\lambda)-(17/36)\pi^2+1109/864$$
$$=\tfrac{2}{3}(\ln\lambda)^2+(1/18)\ln\lambda-3.38,$$
$$m_5=(13/9)(\ln\lambda)+(91/216)\pi^2-(355/432)$$
$$=(13/9)(\ln\lambda)+3.34,$$
$$m=0.52\pm0.21. \quad (17)$$

Note that the sum of the five diagrams is infrared convergent; the use of the λ can now be regarded as completely formal.

This result corresponds to an addition to the interaction-energy-density

$$-\tfrac{1}{2}ie\bar{\psi}\gamma_\mu\psi[\Box^2/\kappa^2A_\mu^e][(\alpha^2/2\pi^2)m].$$

Such a perturbation contributes to the level shift in a hydrogenic atom an energy:

$$\alpha^4Z^4/n^3\ \mathrm{Ry}[(4/\pi^2)m]\delta_{L0}.$$

For the $2S$ level of hydrogen this is

$$0.24\pm0.10 \text{ megacycle per second.}$$

Again it should be remarked that the error indicated arises from the fact that some of the integrals were estimated, using rigorous upper and lower bounds, instead of being evaluated exactly. The error stated represents the outside limits; the actual error is probably much smaller.

The result obtained is somewhat small in terms of the order-of-magnitude estimates given in the introduction. There does not seem to be any particular reason for anticipating a small coefficient. In the corresponding calculation of the fourth-order magnetic moment, the coefficient was large.

For completeness we note that the fourth-order magnetic moment contributes -0.70 Mc/sec to the $2S_{\frac{1}{2}}$, $+0.24$ Mc/sec to the $2P_{\frac{1}{2}}$ level, and -0.12 Mc/sec to the $2P_{\frac{3}{2}}$ levels in hydrogen.

Logical Relations among the Principles of Statistical Mechanics and Thermodynamics*

JOHN S. THOMSEN
Radiation Laboratory, The Johns Hopkins University, Baltimore, Maryland
(Received May 29, 1953)

Five propositions used in thermodynamics and statistical mechanics are formulated: detailed balance, microscopic reversibility, the ergodic hypothesis, the Second Law, and a restriction on the transition probabilities which will be termed the "λ hypothesis." It is shown that the last three propositions are equivalent. The ergodic hypothesis and detailed balance together are proved to be equivalent to microscopic reversibility. This shows that microscopic reversibility is a stronger condition that the Second Law. The results are discussed in connection with Onsager's principle.

INTRODUCTION

THERMODYNAMICS and statistical mechanics have been developed from a number of different starting points. Classical thermodynamics is a theory of equilibrium based on the First and Second Laws, while statistical theories of equilibrium have depended largely on the ergodic hypothesis. Statistical theories of irreversible processes, on the other hand, have generally made use of the principle of microscopic reversibility in some form. The macroscopic theory of irreversible processes also depends to a great extent on this principle, which is the basis of Onsager's reciprocal relations. Examples are found in the work of Cox,[1] de Groot,[2] Denbigh,[3] Onsager,[4] and Prigogine.[5]

At first glance these assumptions appear quite different, but a number of logical relations between them can be demonstrated. In the present paper, five basic propositions employed in statistical mechanics and thermodynamics will be formulated, and all possible relations between them will be investigated. Some of the resulting theorems are rather obvious when properly formulated, and several have been previously proved. However, all are included for the sake of a complete but concise summary of the possible relations.

I. DEFINITIONS

The following definitions will apply.

(1) *System.*—The system under consideration will be taken as one of an ensemble of N identical systems. Each one is considered isolated and each has the same energy E.

(2) *States.*—Each system is assumed to have W possible quantized states accessible to it. Since the energy is fixed, W may be taken as finite.

(3) *Probabilities.*—The probability that a system chosen at random will be in state i will be denoted by p_i where $1 \leq i \leq W$. The probabilities must, of course, satisfy the restriction:

$$\sum_i p_i = 1. \tag{1}$$

(4) *Transition Probabilities.*—λ_{ij} will denote the conditional transition probability per unit time of a system going from state i to state j, i.e., $p_i\lambda_{ij}dt$ is the probability of a system originally being in state i and going to state j within the small time interval dt. λ_{ii} will be defined as zero for all i. The λ_{ij}, taken collectively, may be considered as a transition matrix. All λ_{ij} are assumed to be *independent of time.*

From this definition it follows that the probability of some transition out of state i in time dt is found by summing $p_i\lambda_{ij}dt$ over all j. Similarly the probability of a transition into state i is obtained by summing $p_j\lambda_{ji}dt$ over all j. Thus the net change in p_i is

$$dp_i = \sum_j p_j\lambda_{ji}dt - \sum_j p_i\lambda_{ij}dt.$$

Hence

$$\dot{p}_i = \sum_j (p_j\lambda_{ji} - p_i\lambda_{ij}). \tag{2}$$

(5) *Equilibrium.*—The necessary and sufficient condition for equilibrium is that all $\dot{p}_i$ vanish. By Eq. (2) it follows that

$$\sum_j (p_j\lambda_{ji} - p_i\lambda_{ij}) = 0 \text{ at equilibrium}, \tag{3}$$

for every i.

(6) *Entropy.*—The usual statistical definition of entropy[6] will be used, namely,

$$S = -k\sum_i p_i \ln p_i, \tag{4}$$

where k is the Boltzmann constant. It might be possible to argue that this definition applies at equilibrium, but does not properly describe irreversible phenomena. However, this possibility will not be explored further, and Eq. (4) will henceforth be considered axiomatic. An expression for $\dot{S}$ may easily be obtained from Eq. (4).

$$\dot{S} = -k\sum_i \dot{p}_i \ln p_i - k\sum_i \dot{p}_i.$$

* Based on a thesis submitted in partial fulfillment of the requirements for the degree of Doctor of Philosophy at The Johns Hopkins University.

[1] R. T. Cox, Revs. Modern Phys. **22**, 238 (1950).

[2] S. R. de Groot, *Thermodynamics of Irreversible Processes* (North Holland Publishing Company, Amsterdam; Interscience Publishing Company, New York, 1951).

[3] K. G. Denbigh, *The Thermodynamics of the Steady State* (Methuen and Company, Ltd., London, 1951).

[4] L. Onsager, Phys. Rev. **37**, 405 (1931); **38**, 2265 (1931).

[5] I. Prigogine, *Étude thermodynamique des phenomenes irreversibles* (Desoer, Liege, Belgium, 1947).

[6] See, for example, R. T. Tolman, *The Principles of Statistical Mechanics* (Oxford University Press, London, 1938), Sec. 122, for a discussion of this definition.

The last term vanishes, since Eq. (1) holds identically for all time. Thus

$$\dot{S}=-k\sum_i \dot{p}_i \ln p_i. \tag{5}$$

(7) *Interconnection of States.*[7]—Two states will be said to be interconnected if it is possible to go from one to the other in both directions. (This does not mean that all λ_{ij} are non zero. For example, although λ_{ij} may vanish, it will be possible to go from i to j if $\lambda_{ik}\neq 0$ and $\lambda_{kj}\neq 0$.) In the systems to be considered it will be assumed that all states are interconnected. Mathematically this is equivalent to saying that the states of each system form an irreducible Markov chain.

II. PROPOSITIONS

Five logical propositions will now be stated; these will be denoted by letters to distinguish them from ordinary equations. It should be noted that there are some discrepancies among various authors as to the meanings of the terms used, e.g., microscopic reversibility.

(1) *Microscopic Reversibility.*—(**M**) states that the transition probabilities between two states are the same in either direction, i.e.,

$$\lambda_{ij}=\lambda_{ji} \tag{M}$$

for every i and j. This means that the transition matrix is symmetric. The definition is the same as that employed by Cox.[1]

(2) *Detailed Balance.*—(**D**) requires that transitions between any two states take place with equal frequency in either direction at equilibrium. Thus, for every i and j,

$$p_i\lambda_{ij}=p_j\lambda_{ji} \text{ at equilibrium.} \tag{D}$$

This principle is also referred to as microscopic reversibility by some authors, but in the present paper it is important to distinguish it from (**M**) as given above.

(3) *The Ergodic Hypothesis.*—(**E**) assumes that all states are equally probable at equilibrium, i.e., for every i,

$$p_i=1/W \text{ at equilibrium.} \tag{E}$$

(4) *The Second Law of Thermodynamics.*—(**S**) states that the entropy of an isolated system never decreases, i.e.,

$$\dot{S}\geq 0. \tag{S}$$

(5) *The* λ *Hypothesis.*—(**L**) assumes that the sum of all elements in a given row of the transition matrix is equal to the sum of the elements in the corresponding column.[8] This means that, for every i and j,

$$\sum_j\lambda_{ij}=\sum_j\lambda_{ji}. \tag{L}$$

Two simple lemmas, to be denoted by ($\mathbf{L}_1$) and ($\mathbf{L}_2$), will now be proved. These follow directly from (**L**) and may be used wherever (**L**) is assumed. Let f_i be any factor or product of factors which depends only on the index i. Then, by (**L**),

$$\sum_j f_i\lambda_{ij}=f_i\sum_j\lambda_{ij}=f_i\sum_j\lambda_{ji}.$$

Hence

$$\sum_j f_i\lambda_{ij}=\sum_j f_i\lambda_{ji}. \tag{$\mathbf{L}_1$}$$

Consider next a double summation and apply ($\mathbf{L}_1$).

$$\sum_i\sum_j f_i\lambda_{ij}=\sum_i\sum_j f_i\lambda_{ji}.$$

Interchanging the summation indices on the right gives

$$\sum_i\sum_j f_i\lambda_{ij}=\sum_i\sum_j f_j\lambda_{ij}. \tag{$\mathbf{L}_2$}$$

The above propositions appear quite different at first glance. They may be placed in three categories. (**D**) and (**E**) give symmetry conditions involving the equilibrium probabilities; (**L**) and (**M**) imply certain symmetry relationships satisfied by the transition matrix; (**S**) is a thermodynamic statement of irreversibility.

III. THEOREMS

The various possible logical relationships between the above propositions will now be considered. It will first be shown that (**E**), (**L**), and (**S**) are equivalent propositions. It will then be proved that (**M**) is equivalent to (**D**) and (**E**) taken together. Finally, counter examples will be given to show that neither (**D**) nor (**E**) by itself implies (**M**). These relations may be represented schematically as follows:

$$(\mathbf{E})\rightleftarrows(\mathbf{L})\rightleftarrows(\mathbf{S}),$$
$$(\mathbf{M})\rightleftarrows[(\mathbf{E})+(\mathbf{D})].$$

Theorem 1: (**E**) implies (**L**). At equilibrium there are W equations of the form of Eq. (3), i.e.,

$$\sum_j(p_j\lambda_{ji}-p_i\lambda_{ij})=0.$$

However, (**E**) requires that all probabilities are equal to $1/W$ at equilibrium. Hence

$$(1/W)\sum_j(\lambda_{ji}-\lambda_{ij})=0.$$

It follows that

$$\sum_j\lambda_{ji}=\sum_j\lambda_{ij}. \tag{L}$$

This proves the theorem.

Theorem 2: (**L**) implies (**S**). An extreme value of $\dot{S}$ will first be found subject to the normalization condition of Eq. (1). This will be done by the method of Lagrange multipliers, which gives W equations of the form

$$\frac{\partial\dot{S}}{\partial p_r}+\mu\frac{\partial}{\partial p_r}\Big(\sum_i p_i-1\Big)=0.$$

[7] It will be noted that this restriction is used only in Theorems 2, 3, and 5; actually it is not essential in Theorem 2.

[8] See W. Feller, *An Introduction to Probability and its Applications* (John Wiley and Son, New York, 1950), p. 327 for a discussion of doubly stochastic matrices, which are closely related to (**L**). Let A be a matrix which gives the probabilities at time $t+\Delta t$ in terms of those at t, i.e., $p_i(t+\Delta t)=\sum_j A_{ij}p_j(t)$. For small Δt, it may be shown that $A_{ij}=\lambda_{ji}\Delta t+\delta_{ij}(1-\sum_k\lambda_{ik}\Delta t)$. If (**L**) holds, then $\sum_j A_{ij}=1=\sum_j A_{ji}$, which is the definition of a doubly stochastic matrix. The converse holds also under appropriate conditions.

With the help of Eq. (5), this becomes

$$-k\sum_i \frac{\partial \dot{p}_i}{\partial p_r}\ln p_i - \frac{k\dot{p}_r}{p_r} + \mu = 0. \tag{6}$$

Since $\dot{p}_i$ is given by Eq. (2), it follows that

$$-k\sum_i(\lambda_{ri}-\delta_{ri}\sum_j\lambda_{ij})\ln p_i - (k/p_r)\sum_j(p_j\lambda_{jr}-p_r\lambda_{rj}) + \mu = 0. \tag{7}$$

Rearranging the first term and applying $(\mathbf{L}_1)$ to the second gives

$$-k\sum_i\lambda_{ri}\ln p_i + k\sum_j\lambda_{rj}\ln p_r - (k/p_r)\sum_j(p_j\lambda_{jr}-p_r\lambda_{jr}) + \mu = 0.$$

When the first summation index is changed to j, μ is given by

$$\mu = k\sum_j\left[\lambda_{rj}\ln\left(\frac{p_j}{p_r}\right) + \left(\frac{p_j}{p_r}-1\right)\lambda_{jr}\right]. \tag{8}$$

Assume for the moment that all probabilities are not equal when $\dot{S}$ attains its extreme value. Let P be the probability of the most probable state or states. Since all states are assumed to be interconnected, there must be at least one state with this probability connected to a state of lesser probability. In other words, there must be an r such that $p_r = P$, $\lambda_{rj} \neq 0$ for at least one j with $p_j < P$. When this p_r is substituted in Eq. (8), $(p_j/p_r) \leq 1$ for all j, and thus μ is clearly nonpositive. However, there is at least one j described above for which $\lambda_{rj}\ln(p_j/p_r) < 0$. Thus $\mu < 0$.

The state or states of minimum probability may be treated similarly. At least one p_r can be found which gives $\mu > 0$. Thus a contradiction is reached unless all probabilities are equal to $1/W$ at the extreme value. In this case Eq. (8) gives $\mu = 0$ for every r, and the Lagrange condition is satisfied. Hence at most one extreme value exists.

When all probabilities are equal and $(\mathbf{L})$ holds, Eq. (2) shows that all $\dot{p}_i$ vanish. It is then clear from Eq. (5) that $\dot{S} = 0$; it only remains to show that this value of $\dot{S}$ is a minimum.

To investigate the region near equilibrium let the probabilities be given by

$$p_i = (1/W)(1+\Delta_i), \tag{9}$$

with the provision that $|\Delta_i|_{\max} \ll 1$. Then $\ln p_i$ may be approximated by

$$\ln p_i \approx -\ln W + \Delta_i.$$

Substitution in Eq. (5) gives

$$\dot{S} = -k\sum_i \dot{p}_i[-\ln W + \Delta_i].$$

Since $\ln W$ is independent of i and $\sum_i \dot{p}_i = 0$ as a consequence of Eq. (1), this reduces to

$$\dot{S} = -k\sum_i \dot{p}_i\Delta_i. \tag{10}$$

Successive use of $(\mathbf{L}_1)$ and Eq. (9) in Eq. (2) yields

$$\dot{p}_i = \sum_j(p_j - p_i)\lambda_{ji} = (1/W)\sum_j(\Delta_j - \Delta_i)\lambda_{ji}.$$

This expression is now substituted in Eq. (10); thus

$$\dot{S} = -(k/W)\sum_i\sum_j(\Delta_j\Delta_i - \Delta_i^2)\lambda_{ji}.$$

Application of $(\mathbf{L}_2)$ to the second term yields

$$\dot{S} = -(k/W)\sum_i\sum_j(\Delta_j\Delta_i - \Delta_j^2)\lambda_{ji}.$$

The last two equations are now added to obtain

$$\dot{S} = (k/2W)\sum_i\sum_j(\Delta_i - \Delta_j)^2\lambda_{ji} \geq 0. \tag{11}$$

Consequently the only extreme value is a minimum and $\dot{S} = 0$ at this point. Thus the Second Law $(\mathbf{S})$ results.[9]

Theorem 3: $(\mathbf{S})$ implies $(\mathbf{E})$. Equation (5) shows that $\dot{S} = 0$ at equilibrium since all $\dot{p}_i$ vanish. It follows from $(\mathbf{S})$ that $\dot{S}$ must have an extreme value at equilibrium. The method of Lagrange multipliers may again be used; Eq. (6) applies since it was obtained without making any use of $(\mathbf{L})$. The extreme value occurs at equilibrium; hence all $\dot{p}_r$ vanish and it follows that

$$-k\sum_i \frac{\partial \dot{p}_i}{\partial p_r}\ln p_i + \mu = 0.$$

This can be evaluated as in the last theorem, yielding

$$\mu = k\sum_j \lambda_{rj}\ln\left(\frac{p_j}{p_r}\right). \tag{12}$$

Assume now the probabilities are not all equal, and let r be a state of maximum probability. Then it is evident that $\mu \leq 0$. By the same argument previously used, based on the interconnection of states, it is clear that at least one p_r can be found which gives $\mu < 0$. Similarly, there is at least one p_r for a state of minimum probability for which $\mu > 0$. Thus a contradiction is reached unless all probabilities are equal and $\mu = 0$. Thus all $p_r = 1/W$ at equilibrium and (E) holds.

Corollary: Propositions $(\mathbf{E})$, $(\mathbf{L})$, and $(\mathbf{S})$ are equivalent.

By Theorems 1–3, $(\mathbf{E})$ implies $(\mathbf{L})$, $(\mathbf{L})$ implies $(\mathbf{S})$, and $(\mathbf{S})$ implies $(\mathbf{E})$. It follows that any one of them implies any other; thus they are completely equivalent.[10]

[9] A more general form of this theorem, using the concept of a doubly stochastic matrix, is given in Hardy, Littlewood, and Pólya, *Inequalities* (Cambridge University Press, Cambridge, 1952), pp. 88–91; Messenger of Mathematics **58**, 145 (1929).

[10] The equivalence of $(\mathbf{E})$ and $(\mathbf{L})$ is also proved in Feller (reference 4) p. 327 and in M. Fréchet, *Traité du calcul des probabilités et ses applications*, Émile Borel, Tome I, Fascicule III, Second Livre, *Théorie des événements en chaine dans le cas d'un nombre fini d'états possibles* (Gauthier-Villars, Paris, 1938), p. 37. It is obvious that $(\mathbf{E})$ furnishes a possible equilibrium solution if $(\mathbf{L})$ holds. However, the uniqueness of this solution involves a longer argument based on the interconnection of states. Since Theorems 2 and 3 furnish an indirect proof, the direct one will be omitted.

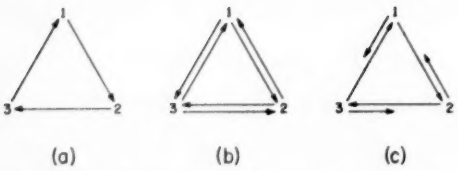

FIG. 1. Types of equilibrium for a system with three states) (Length of arrows represents number of transitions per unit time.. (a) Equilibrium given by Eq. (14), a special case of (**L**). (b) Equilibrium required by (**M**). (c) General type of equilibrium permitted by (**L**).

Theorem 4: (**E**) and (**D**) together imply (**M**). (**D**) states that $p_i\lambda_{ij}=p_j\lambda_{ji}$ at equilibrium. However, the probabilities are equal at equilibrium by (**E**); hence $\lambda_{ij}=\lambda_{ji}$ and (**M**) holds.

Theorem 5: (**M**) implies (**E**) and (**D**). (**M**) is clearly a special case of (**L**). However, (**L**) is equivalent to (**E**); hence (**M**) implies (**E**). Since all probabilities are thus equal at equilibrium and $\lambda_{ij}=\lambda_{ji}$ by (**M**), it follows that

$$p_i\lambda_{ij}=p_j\lambda_{ji} \text{ at equilibrium.} \qquad (\mathbf{D})$$

This proves the theorem.

The relations stated at the beginning of this section have now been proved. It might still be thought that there are other relations which have been overlooked. Such a possibility will be disproved by means of counter examples in the two succeeding theorems.

Theorem 6: (**D**) does not imply (**M**). Let $p_1=\frac{1}{2}$, $p_2=\frac{1}{3}$, and $p_3=\frac{1}{6}$, and let the transition matrix be

$$\lambda=\begin{bmatrix}0 & 2 & 1\\ 3 & 0 & 1\\ 3 & 2 & 0\end{bmatrix}. \qquad (13)$$

Equation (3) is satisfied, showing that the distribution represents a condition of equilibrium. (**D**) is seen to hold, but (**M**) is obviously not satisfied. Actually it will be possible to find a λ matrix which satisfies (**D**) for any given set of equilibrium probabilities; (**M**) will not hold true unless the probabilities in this set are all equal.

Theorem 7: (**L**) does not imply (**M**). Consider the transition matrix:

$$\lambda=\begin{bmatrix}0 & 1 & 0\\ 0 & 0 & 1\\ 1 & 0 & 0\end{bmatrix}. \qquad (14)$$

Each row and column adds to unity, thus satisfying (**L**). However, obviously (**M**) does not hold.

CONCLUSIONS

It is interesting to compare the types of equilibrium given by (**M**) and (**L**) respectively. It has been shown that (**E**) holds in both cases. If the matrix of Eq. (14) is taken as an example of (**L**), the equilibrium picture will be that indicated in Fig. 1(a), with all transitions occurring in the same direction. This equilibrium, which may be termed "circular," has been discussed by Onsager[4] and Denbigh.[11]

A symmetric matrix, i.e., one which satisfies (**M**), will give detailed balance (**D**), as proved in Theorem 5. The equilibrium situation for three states is shown in Fig. 1(b). If a symmetric λ matrix is added to that of Eq. (14), (**L**) is still satisfied by the sum. This gives the most general type of equilibrium consistent with (**L**) and is represented in Fig. 1(c).

Obviously (**M**) is a stronger requirement than (**L**) or (**S**) and may thus yield valuable information not obtainable from classical thermodynamics. Microscopic reversibility is frequently referred to as an auxiliary to the First and Second Laws.[12] However, when (**M**) is stated in the form given here, it includes (**S**) as a consequence, without involving any additional assumption except the statistical definition of entropy.[13] Clearly, it is also possible to postulate (**S**) and (**D**) and reach the same conclusions as obtained by assuming (**M**).

There is one disconcerting question raised by these results. It might appear, on the basis of quantum mechanics, that (**M**) should hold under all circumstances.[14] (Since the definitions employed are not necessarily valid for all quantum-mechanical problems, this conclusion may not always be true.) According to Onsager,[5] microscopic reversibility as he defines it cannot be expected to hold in the presence of a magnetic or Coriolis field. It is not obvious just how this feature of Onsager's principle is to be reconciled with quantum mechanics. This point may be discussed further in a future paper.

The author wishes to thank Professor Richard T. Cox of The Johns Hopkins University for suggesting the problem discussed here and for giving many hours of help toward the preparation of this paper. He is also indebted to Professor Theodore H. Berlin, Dr. Albert J. Novikoff, and Mr. David B. Lowdenslager, all of The Johns Hopkins University, for advice and assistance.

[11] Reference 3, pp. 31–34.
[12] See, for example, reference 3, p. 96.
[13] See Cox, reference 1, for a more direct proof of this statement.
[14] See, for example, P. A. M. Dirac, *Quantum Mechanics* (Oxford University Press, London, 1947), third edition, pp. 172–74.

PHYSICAL REVIEW VOLUME 91, NUMBER 5 SEPTEMBER 1, 1953

S Matrix and Causality Condition. II. Nonrelativistic Particles

N. G. VAN KAMPEN
Institute for Advanced Study, Princeton, New Jersey
(Received May 20, 1953)

The application of the "causality condition" to the S matrix for nonrelativistic particles encounters several difficulties: (a) there is no maximum velocity; (b) the interference of ingoing and outgoing waves has to be taken into account; (c) wave packets with a sharp front do not exist. The condition is therefore reformulated as follows: At any time the total probability of finding the particle outside the scattering center shall not be greater than 1, for every form of the incident wave packet. From this follows for spherical waves that S, as a function of the momentum p, is analytic and holomorphic in the first quadrant and that $e^{2iap}S(p)$ (where a is the radius of the scattering center) has an imaginary part $\leqslant 1$. That suffices to give an explicit integral representation and a product expansion for S, but these permit a more general form for S than is usually envisaged. If, however, the usual symmetry relation $S(-p)=S(p)^*$ is assumed in addition to the causality condition, more specific equations can be derived, which are direct generalizations of those in Part I. In particular, integral relations between the real and imaginary parts of S, and the properties that Wigner found for the R matrix can be deduced.

I. FORMULATION OF THE CAUSALITY CONDITION

IN part I[1] the consequences of the causality condition for the scattering of a Maxwell field by a fixed scattering center or "core" of finite size were investigated. It was assumed that outside a sphere with radius a the free-field equations hold but that nothing is known about the interior of the sphere. The causality condition was formulated as follows: If at a large distance r_1 from the center of the sphere the ingoing wave packet is zero for all $t<t_1$, then the outgoing wave packet shall be zero at r_1 for all $t<t_1+2(r_1-a)/c$.

Obviously, for nonrelativistic particles a modification is necessary, since no maximum velocity exists, and one is inclined to postulate: If at any distance r_1 the ingoing wave packet is zero for all $t<t_1$, then the outgoing wave packet must also be zero for $t<t_1$. This would have to be true for all $r_1\geqslant a$, but it is sufficient to take the strongest form, namely $r_1=a$. This formulation of the causality condition was indeed used by Schützer and Tiomno,[2] who treated the same problem. However, as mentioned in I, there is a serious objection.

The difficulty is that *there are no ingoing or outgoing wave packets that are rigorously zero up to a certain time*, as can be seen as follows. All (spherically symmetrical) superpositions of ingoing waves have the form

$$r\psi_{\text{in}}(r,t)=\int_0^\infty A(p)e^{-ipr-iEt}dp, \tag{1}$$

where $E=p^2/2m$, $h=1$, and $A(p)$ is an arbitrary square integrable function. At a given point $r=r_1$ this is a Fourier expansion of $r\psi_{\text{in}}(r_1,t)$ with respect to t, but the frequency E only runs from 0 to ∞. This puts a severe restriction on ψ_{in} as a function of t, and in particular it can be shown that $\psi_{\text{in}}(r_1,t)$ cannot be zero over any length of time.[3] This difficulty can be overcome by formulating the causality condition in the following way: The probability of finding an outgoing particle at r_1 prior to t_1 cannot be greater than the probability of finding an ingoing particle at r_1 prior to t_1.

A second difficulty, however, arises. At any finite distance r_1 the total probability cannot be uniquely decomposed into an ingoing and an outgoing part, because there is an interference term corresponding to a rapidly oscillating probability current. In the case of relativistic particles this second difficulty can be overcome by letting r_1 go to infinity, but that is not possible for nonrelativistic particles. For, owing to the absence of a maximum velocity, the above condition becomes weaker as r_1 increases; and if it is only postulated for $r_1=\infty$, it leads to practically no restrictions on the S matrix. One is thus forced to the following formulation: The outgoing probability current, integrated from $t=-\infty$ to $t=t_1$, cannot exceed the integrated ingoing current by more than the absolute value of the integral of the interference term. The presence of the interference term makes the condition considerably weaker than in the electromagnetic case and will turn out to be the reason why the S matrix can now have singularities on the positive imaginary axis.

The condition can be given a more familiar form by considering the behavior of ψ as a function of r rather than of t. It is then readily seen to be equivalent to postulating that *if the ingoing wave packet is so normalized as to represent at $t=-\infty$ one incident particle, the total probability at $t=t_1$ of finding a particle outside of any sphere of radius $r_1\geqslant a$ cannot be greater than 1.*

[1] N. G. van Kampen, Phys. Rev. **89**, 1072 (1953). This paper will be referred to as I; the formulas contained in it are denoted by (I, ··).

[2] W. Schützer and J. Tiomno, Phys. Rev. **83**, 249 (1951). The difficulty becomes apparent in their Eq. (7), in which the lower limit of integration should be 0 instead of $-\infty$.

[3] According to (1) ψ is analytic in the lower half of the complex t plane; if it were zero in an interval on the real axis, it could be continued by Schwarz's reflection principle [E. C. Titchmarsh, *The Theory of Functions* (Clarendon Press, Oxford, 1939), second edition], which would give an analytic function vanishing in an interval. For this simple proof I am indebted to Professor N. Levinson; a more general result is mentioned in L. Bieberbach, *Lehrbuch der Funktionentheorie*, Vol. 2 (B. G. Teubner, Leipzig, 1931), second edition, p. 159.

Clearly we get the strongest condition by choosing $r_1=a$ and do not lose anything by taking $t_1=0$. Our final form of the causality condition thus becomes

$$\int_a^\infty 4\pi r^2|\psi_{\rm in}(r,0)+\psi_{\rm out}(r,0)|^2dr\leqslant 1, \tag{2}$$

ψ being normalized by

$$\int_a^\infty 4\pi r^2|\psi_{\rm in}(r,-\infty)|^2dr=1. \tag{3}$$

Obviously this condition is satisfied whenever it is possible to define a probability density (obeying a conservation law) in the interior of the core.

The scattering process is described by an S matrix in the usual way. We shall assume that the core is spherically symmetric and we consider only s waves. Then, similarly to Eq. (1),

$$r\psi_{\rm out}(r,t)=-\int_0^\infty B(p)e^{ipr-iEt}dp, \quad (a<r<\infty), \tag{4}$$

and $S(p)$ is defined by

$$B(p)=S(p)A(p) \quad (0<p<\infty). \tag{5}$$

The ingoing probability current, integrated with respect to t from $-\infty$ to $+\infty$, is

$$8\pi^2\int_0^\infty |A(p)|^2dp, \tag{6}$$

and, of course, the same value is found for (3). This is the physical reason for imposing on $A(p)$ the restriction of square-integrability. The integrated outgoing current is given by the same expression with $B(p)$ instead of $A(p)$; as we shall assume that no particles can be absorbed by the core, both expressions must be equal, so that S must be unitary:

$$|S(p)|=1 \quad (0<p<\infty). \tag{7}$$

It should be emphasized that in physically meaningful scattering states only positive values of p occur, so that any extension of the definition of $S(p)$ to negative p is purely conventional. One may postulate, for example, the familiar equation

$$S(-p)=S^*(p), \tag{8}$$

or, alternatively, one may define $S(-p)$ as the analytic continuation of $S(p)$ (if it exists and is unique). It is known[4] that if the interaction inside the core can be described by a potential field, both these definitions lead to the same values for $S(-p)$ but there is no reason to assume that they will also coincide in the general case treated here. We shall therefore consider $S(p)$ as a function defined *a priori* for real positive p only.

[4] R. Jost, Helv. Phys. Acta **20**, 256 (1947).

We now use (6) for the right-hand side of (2) and substitute (1) and (4) on the left. On inverting the order of integration such terms occur as

$$\int_a^\infty e^{i(p-p')r}dr=2\pi e^{i(p-p')a}\delta_+(p-p')$$
$$=e^{i(p-p')a}\left\{\frac{1}{-i(p-p')}+\pi\delta(p-p')\right\}.$$

The terms with the δ functions cancel owing to (7) and only the principal-value terms remain. The exponentials can be absorbed in A and B by putting

$$\begin{aligned} &e^{-ipa}A(p)=A_a(p), \quad && e^{+ipa}B(p)=B_a(p),\\ &B_a(p)=S_a(p)A_a(p), \quad && S_a(p)=e^{2ipa}S(p). \end{aligned} \tag{9}$$

One is then left with

$$\int_0^\infty\int_0^\infty \frac{B_a(p)B_a^*(p')-A_a(p)A_a^*(p')}{i(p-p')}dpdp'$$
$$\geqslant\int_0^\infty\int_0^\infty \frac{B_a(p)A_a^*(p')-A_a(p)B_a^*(p')}{i(p+p')}dpdp'. \tag{10}$$

The causality condition requires that this inequality be satisfied for all square integrable functions $A_a(p)$, the function $B_a(p)$ being related to $A_a(p)$ by (9).

From this condition we shall deduce in Sec. II that S has an analytic continuation without singularities in the first quadrant of the complex p plane and in Sec. III that the imaginary part of this analytic function is bounded from above. These results are used in Sec. IV to derive the integral representation (24) and the product expansion (28), which, however, still contain the undetermined functions $\tilde\beta$ and α. In Sec. V the consequences of the additional assumption (8) are investigated, and the representations (30) and (35) are derived. In that case it is possible to find integral equations and sum rules similar to those in Part I and to derive the properties of Wigner's R matrix. Some of these equations are not new and others might have been conjectured as generalizations of the results in I. The purpose of the present work, however, is to show that they actually follow rigorously from general assumptions. Unfortunately, the use of some rather unfamiliar theorems about complex functions is inevitable. It has been attempted to present the mathematical arguments in no more detail than is necessary to make a reconstruction of the rigorous proofs possible. In Sec. VI the physical significance of the resulting equations is discussed, and it is emphasized that the use of the analytic continuation of S should be regarded merely as a mathematical procedure, which happens to be the adequate tool for treating certain properties of the physically significant function $S(p)$ on the positive

real axis, and not for instance as a means of computing bound states.

II. ANALYTIC CONTINUATION OF S

An essential difference with the electromagnetic case shows up in the range of integration in (10), which is now $(0, \infty)$ rather than $(-\infty, +\infty)$. This makes it impossible to cope with the integral kernel $i(p-p')^{-1}$ by using the theory of Hilbert transforms, but fortunately it is still possible to find its eigenfunctions. Indeed, one easily verifies

$$\int_0^\infty \frac{(p')^{i\tau-\frac{1}{2}}}{i(p'-p)}dp' = (\pi \tanh\pi\tau)p^{i\tau-\frac{1}{2}},$$

whence it follows that $p^{i\tau-\frac{1}{2}}$ $(-\infty<\tau<+\infty)$ are improper eigenfunctions with eigenvalues $\pi\tanh\pi\tau$. The expansion in eigenfunctions amounts to a Mellin transformation[5]:

$$\begin{aligned} A_a(p) &= \int_{-\infty}^{+\infty} \mathfrak{A}(\tau)p^{i\tau-\frac{1}{2}}d\tau, \\ \mathfrak{A}(\tau) &= (1/2\pi)\int_0^\infty A_a(p)p^{-i\tau-\frac{1}{2}}dp. \end{aligned} \tag{11}$$

This establishes a one-to-one correspondence of all functions $A_a(p)$ of the class[6] $L_2(0, \infty)$ with all functions $\mathfrak{A}(\tau)$ of the class $L_2(-\infty, +\infty)$, and

$$\int_0^\infty |A_a(p)|^2 dp = 2\pi\int_{-\infty}^{+\infty} |\mathfrak{A}(\tau)|^2 d\tau. \tag{12}$$

When $B_a(p)$ is similarly transformed,

$$B_a(p) = \int_{-\infty}^{+\infty} \mathfrak{B}(\tau)p^{i\tau-\frac{1}{2}}d\tau,$$

the relation (5) between the ingoing and outgoing waves takes the form

$$\mathfrak{B}(\tau) = \int_{-\infty}^{+\infty} \mathfrak{S}(\tau-\tau')\mathfrak{A}(\tau')d\tau'. \tag{13}$$

The inequality (10) can now be transformed; using the identity

$$\int_0^\infty \frac{(p')^{i\tau-\frac{1}{2}}}{i(p+p')}dp' = \frac{-\pi i}{\cosh\pi\tau}p^{i\tau-\frac{1}{2}},$$

one finds

$$\begin{aligned} &\int_{-\infty}^{+\infty} \tanh\pi\tau\{\mathfrak{B}(\tau)\mathfrak{B}^*(\tau)-\mathfrak{A}(\tau)\mathfrak{A}^*(\tau)\}d\tau \\ &\quad \geqslant \int_{-\infty}^{+\infty} \frac{i}{\cosh\pi\tau}\{\mathfrak{A}(\tau)\mathfrak{B}^*(\tau)-\mathfrak{A}^*(\tau)\mathfrak{B}(\tau)\}d\tau. \end{aligned} \tag{14}$$

If $\mathfrak{A}(\tau)$ and $\mathfrak{B}(\tau)$ are L_2 functions connected by (13), the same is true for $\mathfrak{A}(\tau-\mu)$ and $\mathfrak{B}(\tau-\mu)$, for any real constant μ. Hence one may write $\tanh\pi(\tau+\mu)$ and $\cosh\pi(\tau+\mu)$ in (14). Also one may subtract from the left-hand side,

$$\int_{-\infty}^{+\infty} \{|\mathfrak{B}(\tau)|^2-|\mathfrak{A}(\tau)|^2\}d\tau,$$

which vanishes according to (12) and (7). The result is[7]

$$\begin{aligned} &\int_{-\infty}^{+\infty} \frac{e^{-2\pi(\tau+\mu)}}{1+e^{-2\pi(\tau+\mu)}}\{|\mathfrak{A}(\tau)|^2-|\mathfrak{B}(\tau)|^2\}d\tau \\ &\quad \geqslant 2\int_{-\infty}^{+\infty} \frac{e^{-\pi(\tau+\mu)}}{1+e^{-2\pi(\tau+\mu)}}\mathfrak{I}[\mathfrak{A}^*(\tau)\mathfrak{B}(\tau)]d\tau. \end{aligned} \tag{15}$$

This inequality must be satisfied by any square integrable $\mathfrak{A}(\tau)$ and for all real μ. We choose for $\mathfrak{A}(\tau)$ a function that vanishes so fast for $\tau\to-\infty$ that $e^{-\pi\tau}\mathfrak{A}(\tau)$ is also square integrable, and let μ tend to $+\infty$. The first term on the left can be written

$$e^{-2\pi\mu}\int_{-\infty}^{+\infty} \frac{|e^{-\pi\tau}\mathfrak{A}(\tau)|^2}{1+e^{-2\pi(\tau+\mu)}}d\tau,$$

and is of order $e^{-2\pi\mu}$ because the integral is clearly bounded. Similarly, the right-hand side of (15) becomes

$$2\mathfrak{I}e^{-\pi\mu}\int_{-\infty}^{+\infty} \frac{e^{-\pi\tau}\mathfrak{A}^*(\tau)\mathfrak{B}(\tau)}{1+e^{-2\pi(\tau+\mu)}}d\tau$$

and is therefore of order $e^{-\pi\mu}$. The remaining term must also be of order $e^{-\pi\mu}$, i.e.,

$$\int_{-\infty}^{+\infty} \frac{|e^{-\pi\tau/2}\mathfrak{B}(\tau)|^2}{\cosh\pi(\tau+\mu)}d\tau$$

must be bounded. Consequently, for any positive T, the expression

$$\frac{1}{\cosh\pi T}\int_{-\mu}^{-\mu+T} |e^{-\pi\tau/2}\mathfrak{B}(\tau)|^2 d\tau$$

must be bounded, which implies that there is a constant K depending on T such that

$$\int_{\tau_1}^{\tau_2} |e^{-\pi\tau/2}\mathfrak{B}(\tau)|^2 d\tau \leqslant K|\tau_2-\tau_1| \quad \text{for} \quad |\tau_2-\tau_1| \geqslant T.$$

[5] See, for instance, E. C. Titchmarsh, *Introduction to the Theory of Fourier Integrals* (Clarendon Press, Oxford, 1937). The formulas in the text can also be found by putting $p=e^x$.

[6] That is the class of functions for which the square integral in the interval $(0, \infty)$ exists (in the Lebesgue sense); see Titchmarsh, reference 3.

[7] $\mathfrak{I}$ denotes the imaginary part, $\mathfrak{R}$ the real part.

From this it follows that

$$\int_{-\infty}^{+\infty} |e^{-\theta\tau}\mathfrak{B}(\tau)|^2 d\tau < \infty \quad \text{for} \quad 0 \leqslant \theta < \tfrac{1}{2}\pi.$$

This result has to be translated in terms of $A_a(p)$ and $B_a(p)$ by means of the transformation (11). If both $\mathfrak{A}(\tau)$ and $e^{-\pi\tau}\mathfrak{A}(\tau)$ are L_2,

$$A_a(pe^{i\theta}) = e^{-i\theta/2} \int_{-\infty}^{+\infty} \mathfrak{A}(\tau) e^{-\theta\tau} p^{i\tau - \frac{1}{2}} d\tau$$

exists and is square integrable over p, for every value of θ between 0 and π. Moreover, the square integral has a uniform bound for $0 \leqslant \theta \leqslant \pi$:

$$\int_0^\infty |A_a(pe^{i\theta})|^2 dp = 2\pi \int_{-\infty}^{+\infty} |\mathfrak{A}(\tau) e^{-\theta\tau}|^2 d\tau$$
$$\leqslant 2\pi \int_0^\infty |\mathfrak{A}(\tau)|^2 d\tau + 2\pi \int_{-\infty}^0 |\mathfrak{A}(\tau) e^{-\pi\tau}|^2 d\tau,$$

so that $A_a(\lambda)$ is a regular analytic function of $\lambda = pe^{i\theta}$ for $0 < \theta < \pi$ and tends to the boundary function $A_a(p)$ for almost all p as θ goes to zero.[8] Conversely, when $A_a(\lambda)$ has these properties $e^{-\theta\tau}\mathfrak{A}(\tau)$ is $L_2(-\infty, +\infty)$ for $0 \leqslant \theta \leqslant \pi$. Thus the above theorem becomes: *When $A_a(p)$ is the boundary function of a function $A_a(\lambda)$ analytic in the angle $0 < \theta < \pi$ and satisfying*

$$\int_0^\infty |A_a(pe^{i\theta})|^2 dp \leqslant M \quad \text{for} \quad 0 \leqslant \theta \leqslant \pi,$$

then $B_a(p)$ is the boundary function of a function $B_a(\lambda)$ analytic in the angle $0 \leqslant \theta < \frac{1}{2}\pi$ and satisfying

$$\int_0^\infty |B_a(pe^{i\theta})|^2 dp \leqslant N_\delta \quad \text{for} \quad 0 \leqslant \theta \leqslant \tfrac{1}{2}\pi - \delta,$$

with arbitrary positive δ. By a slightly more sophisticated argument one can show that it is sufficient to assume for $A_a(\lambda)$ the same properties as are concluded for $B_a(\lambda)$, *viz.*, regularity for $0 < \theta < \frac{1}{2}\pi$ and uniform square integrability for $0 \leqslant \theta < \frac{1}{2}\pi - \delta$.

It is now possible to define the analytic continuation $S(\lambda)$ of $S(p)$ in the first quadrant by means of

$$B_a(\lambda) = S_a(\lambda) A_a(\lambda) = e^{2i\omega\lambda} S(\lambda) A_a(\lambda).$$

It has no singularities and the behavior at infinity can be specified as follows. One may choose

$$A_a(\lambda) = (\lambda + i\beta)^{-1};$$

since the corresponding outgoing wave packet,

$$B_a(\lambda) = S_a(\lambda)/(\lambda + i\beta),$$

must be square integrable, it follows that for large $|\lambda|$,

$$S_a(\lambda) = e^{2i\omega\lambda} S(\lambda) = o(|\lambda|) \tag{16}$$

in the angle $0 < \arg\lambda < \frac{1}{2}\pi$. The analytic continuation can be extended to the fourth quadrant by putting

$$S(\lambda^*) = [S(\lambda)]^{*-1},$$

which reduces to (7) for real positive λ. The only possible singularities are poles corresponding to the zeros above the real axis. *In this way $S(\lambda)$ is defined as a meromorphic function in the right half of the complex λ plane, excluding the imaginary axis.*

III. BEHAVIOR OF S ON THE IMAGINARY AXIS

The fact that a part of the boundary of the domain in which S could be continued analytically had to be excluded, makes it impossible to arrive at a product expansion and integral relations by a method similar to that in I. Our next task is therefore to find more information about the behavior of $S(\lambda)$ on the imaginary axis. It may be expected that the interference term on the right of (15) is important for this purpose, because that was the term which prevented us from extending the analytic continuation of S beyond the i axis. The result will be that ϑS_a is bounded from above, which in Sec. IV will be seen to contain implicit information about the behavior on the boundary and to be as useful as a more explicit specification.

Let us choose for $\mathfrak{A}(\tau)$ a function such that, for some $\Delta > 0$,

$$e^{-\theta\tau}\mathfrak{A}(\tau) \quad \text{is} \quad L_2 \quad \text{for} \quad 0 \leqslant \theta \leqslant \tfrac{1}{2}\pi + \Delta. \tag{17}$$

According to the result in the previous section one then has certainly

$$e^{-\theta\tau}\mathfrak{B}(\tau) \quad \text{is} \quad L_2 \quad \text{for} \quad 0 \leqslant \theta \leqslant \tfrac{1}{2}\pi - \Delta.$$

Because of (17) the first term on the left in (15) is of order $e^{-(\pi+2\Delta)\mu}$, whereas the second term may be omitted since it is negative. After multiplying through by $e^{\pi\mu}$ and putting $\mu = +\infty$, one finds for the right-hand side of (15) the condition

$$\vartheta \int_{-\infty}^{+\infty} e^{-(\pi/2+\Delta)\tau}\mathfrak{A}^*(\tau) \cdot e^{-(\pi/2-\Delta)\tau}\mathfrak{B}(\tau) d\tau \leqslant 0,$$

which by means of (11) and (5) can be written

$$\vartheta e^{-i\Delta} \int_0^\infty [A_a(ipe^{i\Delta})]^* A_a(ipe^{-i\Delta}) S_a(ipe^{-i\Delta}) dp \leqslant 0. \tag{18}$$

It is clear that the special choice,

$$A(\lambda) = (\lambda + z^*)^{-1}$$

(z^* complex conjugate of a point $z = x + iy$ in the first quadrant), satisfies the restriction (17), provided Δ is taken less the $\frac{1}{2}\pi - \arg z$. With this choice, (18) can be

[8] On substituting $\lambda = e^z$ these assertions reduce to well-known theorems about analytic functions in a strip, see, e.g., R. E. A. C. Paley and N. Wiener, *Fourier Transforms in the Complex Domain* (American Mathematical Society, New York, 1934).

written

$$\Re\int_0^{\infty\exp[i(\pi/2-\Delta)]}\frac{S_a(\lambda)d\lambda}{(\lambda+z^*)(-\lambda+z)}\geqslant 0.$$

On shifting the integration path to the real axis, the integral becomes[9]

$$\int_0^\infty\frac{S_a(p)dp}{(p+z^*)(-p+z)}+2\pi i\frac{S_a(z)}{z+z^*}.$$

Hence we get

$$\begin{aligned}\frac{\pi}{x}-\vartheta S_a(z)&\leqslant\Re\int_0^\infty\frac{S_a(p)dp}{(p+z^*)(-p+z)}\\&\leqslant\left\{\int_0^\infty\left|\frac{S_a(p)}{p+z^*}\right|^2dp\cdot\int_0^\infty\frac{dp}{|p-z|^2}\right\}^{\frac12}\\&\leqslant\int_{-\infty}^{+\infty}\frac{dp}{p^2+y^2}=\frac{\pi}{y},\end{aligned}$$

so that

$$\vartheta S_a(z)\leqslant x/y. \tag{19}$$

This shows that the imaginary part of $S_a(z)$ is bounded from above in any angle $0<\delta\leqslant\arg z<\frac12\pi$. Now consider the function,

$$F(z)=\exp[-iS_a(z)],$$

in an angular region $0\leqslant\arg z\leqslant\theta$, where $0<\theta<\frac12\pi$. It has an upper bound e on the real axis, and on the radius $\arg z=\theta$ it is bounded by $\exp(\cot\theta)$. Also

$$\int_0^\theta\log^+|F(pe^{i\theta'})|\cdot\sin(\pi\theta'/\theta)d\theta'$$

is bounded as $p\to\infty$, so that according to Phragmén-Lindelöf's theorem[10] $|F(z)|$ attains its maximum value on the boundary of the region. By letting θ go to $\frac12\pi$ one thus finds $|F|\leqslant e$ in the whole quadrant, or

$$\vartheta S_a(z)\leqslant 1\quad\text{for}\quad 0\leqslant\arg z<\tfrac12\pi. \tag{20}$$

This result will be used in the next section to derive an integral representation and a product expansion, but we remark here that it implies that $|S_a|$ is bounded, except in the neighborhood of the i axis. Indeed, since (20) followed from the causality condition for a core with radius a, it must also be fulfilled for any $a'>a$, i.e.,

$$\vartheta e^{2ia'z}S_a(z)\leqslant 1\quad\text{for}\quad a'\geqslant 0.$$

Or, if $\Phi=\arg S_a$,

$$e^{-2a'y}|S_a(z)|\sin(2a'x+\Phi)\leqslant 1.$$

For each value of x, y it is possible to choose an a' between 0 and π/x for which the sine takes the value 1, so that

$$|S_a(z)|\leqslant e^{2\pi y/x}. \tag{21}$$

We summarize the results: $S_a(\lambda)$ *is meromorphic in the right half-plane* $\Re\lambda>0$. *In the first quadrant it is regular and its imaginary part has the upper bound 1* (which is attained only on the positive real axis). *The absolute value* $|S_a(\lambda)|$ *is bounded in every angle* $0\leqslant\arg\lambda\leqslant\frac12\pi-\delta$.

IV. EXPLICIT REPRESENTATIONS OF S

For the derivation of an integral representation it is convenient to use the variable $w=\frac12\lambda^2$, which on the real axis reduces to the energy $E=\frac12p^2$ (we put from now on $m=1$). The function $S_a(w)-i$ is regular in the upper half-plane, and its imaginary part is $\leqslant 0$. According to a remarkable theorem of Herglotz,[11] this entails the validity of the Poisson integral

$$S_a(w)-i=\Theta-\int_{-\infty}^{+\infty}\frac{1+Ew}{E-w}d\beta(E), \tag{22}$$

where Θ is a real constant and $\beta(E)$ is some *bounded nondecreasing* real function. β is connected with the boundary values of the imaginary part of S_a by[12]

$$\vartheta S_a(E)-1=-\pi(1+E^2)\beta'(E). \tag{23}$$

This equation is valid for all (real) E for which S_a is analytic and therefore certainly for $E>0$. For $E<0$, however, $\beta(E)$ may have discontinuities with a positive jump:

$$\beta_n=\beta(E_n+0)-\beta(E_n-0)>0.$$

As β is bounded, the E_n form a denumerable set and $\Sigma\beta_n<\infty$. Denoting by $-\tilde\beta(-E)$ the continuous function that remains after subtracting the jumps, one obtains

$$\begin{aligned}S_a(w)-i=\Theta&+\frac1\pi\int_0^\infty\frac{1+Ew}{E-w}\frac{\vartheta S_a(E)-1}{1+E^2}dE\\&+\Sigma\beta_n\frac{1+E_nw}{w-E_n}+\int_0^\infty\frac{Ew-1}{E+w}d\tilde\beta(E).\end{aligned} \tag{24}$$

[9] That there is no contribution from the circular arc at infinity can be shown in much the same way as for functions in a strip (Paley and Wiener, reference 8). The origin too has to be cut off by a small arc, but there is no difficulty in showing that this contribution also vanishes.

[10] This formulation of the theorem is due to F. and R. Nevanlinna, see, e.g., L. Bieberbach, reference 3, p. 129. ($\log^+x$ is defined as $\log x$ for $x>1$, and 0 for $x<1$.) In order to apply it to the present case the right half-plane had to be mapped onto the angle $0\leqslant\arg z\leqslant\theta$, which is the reason why $\sin(\pi\theta'/\theta)$ appears rather than $\cos\theta'$.

[11] A. Herglotz [Ber. Verhandl. K. sächs. Ges. Wiss. Leipzig, Math.-phys. Kl. **63**, 501 (1911)] proved this theorem for functions in the unit circle; see also M. H. Stone, *Linear Transformations in Hilbert Space* (American Mathematical Society, New York, 1932), p. 570. W. Cauer [Bull. Am. Math. Soc. **38**, 713 (1932)] and J. A. Shohat and J. D. Tamarkin [*The Problem of Moments*, American Mathematical Society, New York, 1943] applied it to functions in a half-plane; J. S. Toll [thesis, Princeton, 1952] used it in connection with the causality condition for the propagation of light in a medium. In the actual theorem an additional linear term $\Theta'w$ appears on the right, but since $\Theta'=\lim S_a(w)/w$ for $|w|\to\infty$, $\delta\leqslant\arg w\leqslant\pi-\delta$ (see Shohat and Tamarkin), it follows from (16) or (21) that in our case $\Theta'=0$.

[12] This can be found directly from (22) by letting w approach a point E on the real axis (see J. S. Toll, reference 11).

The third term on the right exhibits the poles of $S_a(w)$ on the negative real axis with the positive residues[12] $b_n=\beta_n(1+E_n^2)$. There can be no E_n equal to zero, because $S_a(E)$ is bounded for $E>0$. Hence this term can also be written

$$\Sigma b_n\left\{\frac{1}{w-E_n}+\frac{1}{E_n}\right\}-\Sigma\frac{\beta_n}{E_n}, \tag{25}$$

which is a Mittag-Leffler expansion with respect to the poles E_n. The finite constant $\Sigma\beta_n/E_n$ can be absorbed in Θ.

As will be shown in Sec. V, the fourth term on the right stems from the fact that we have not assumed the symmetry relation (8). It may contain additional singularities in $S_a(w)$ on the negative real axis, but they give rise to a slower increase than the poles.[14] It thus follows from (24) that $S(\lambda)$ can have no poles of higher order than the first on the $+i$ axis, which can also be concluded directly from (20).

Although the integral representation (22) or (24) lends itself for the study of the behavior of S on the boundary, it has two serious disadvantages. It contains the arbitrary constant a implicitly in the Θ and β, and it disregards the information that $|S(E)|=1$ for $E>0$. We proceed to derive a product expansion, which does not suffer from these shortcomings, and therefore seems to be a more natural representation for S.

In order to apply more readily some theorems in function theory, it is convenient to map the first quadrant of the λ plane onto the unit circle by putting

$$\zeta=(i\lambda^2+1)/(i\lambda^2-1).$$

The integral (22) then becomes

$$S_a(\zeta)=\Theta_1-2i\zeta\int_0^{2\pi}\frac{d\beta(\theta)}{e^{i\theta}-\zeta},$$

where Θ_1 is now a complex constant. It has been shown[15] that one may conclude from this that $S_a(\zeta)$ belongs to the so-called Hardy class[16] H_p for every $p<1$, which means that, for each such p,

$$\int_0^{2\pi}|S_a(\rho e^{i\varphi})|^p d\varphi$$

is bounded as $\rho\to 1$.

The importance of this result lies in the fact that for functions of that type a canonical representation is known.[17] They can be decomposed in two factors, $S_a(\zeta)=b(\zeta)f_a(\zeta)$, where

$$b(\zeta)=\prod_n|\zeta_n|\frac{1-\zeta/\zeta_n}{1-\zeta\zeta_n^*}$$

is the "Blaschke-product" containing all zeros ζ_n inside the unit circle, and $f_a(\zeta)$ can be represented as follows

$$f_a(\zeta)=\exp\int_0^{2\pi}\frac{e^{i\varphi}+\zeta}{e^{i\varphi}-\zeta}d\alpha_a(\varphi), \tag{26}$$

$\alpha_a(\varphi)$ being some function of bounded variation. Since $|S_a(\lambda)|=1$ on the positive real axis, $|f_a(\zeta)|=1$ on the arc $\pi<\varphi<2\pi$ of the unit circle and hence $d\alpha_a(\varphi)=0$ for $\pi<\varphi<2\pi$. Translating (26) back to the variable λ one thus finds, putting $\cot(\varphi/2)=s^2$,

$$f_a(\lambda)=\exp\left[i\Theta'\lambda^2-i\int_0^\infty\frac{s^2\lambda^2-1}{s^2+\lambda^2}d\alpha_a(s)\right]. \tag{27}$$

The constant Θ' has to be added, as mentioned in footnote 11, to allow for a possible discontinuity of $\alpha_a(\varphi)$ at $\varphi=0$ (or $\varphi=2\pi$).

The factor $e^{2ia\lambda}$ contained in $S_a(\lambda)$ can be written in the same form (27) and may therefore be combined with $f_a(\lambda)$. *Hence we obtain for $S(\lambda)$ the canonical representation*

$$S(\lambda)=\prod\frac{1-\lambda^2/\lambda_n^2}{1-\lambda^2/\lambda_n^{*2}}\times\exp\left[i\Theta'\lambda^2-i\int_0^\infty\frac{s^2\lambda^2-1}{s^2+\lambda^2}d\alpha(s)\right]. \tag{28}$$

This is the counterpart of (I, 16). The right-hand side does not involve a but is uniquely determined by $S(\lambda)$. It has been derived only for the first quadrant but it is clearly valid for all λ in the half-plane $\Re\lambda>0$.

The Blaschke product in (28) contains only the zeros and poles on the right of the imaginary axis. The poles on the imaginary axis itself arise from the (logarithmic) discontinuities of $\alpha(s)$; that they do not appear explicitly is reasonable, because they have no special role among all the singularities that may occur in the half-plane $\Re\lambda\leqslant 0$. From the fact that the product converges one finds a sum rule for the λ_n; in terms of the corresponding energies $w_n=u_n+iv_n=\frac{1}{2}\lambda_n^2$ (u_n resonance energy, $2v_n$ level width) it takes the same form as in I:

$$\Sigma v_n/|w_n|^2<\infty.$$

The exponential factor in (28) corresponds to some sort of potential scattering. Instead of the single con-

[12] That the residue must be positive is well known for potential fields, see C. Møller, Kgl. Danske Videnskab. Selskab, Mat.-fys. Medd. **22**, No. 19 (1946).

[14] Let $w=E+iv(E<0, v>0)$ and $v\to 0$; then it can be shown that the last term in (24) is $o(1/v)$, owing to the continuity of β. This term may also be singular at E_n, in which case E_n is not just a pole of $S_a(w)$.

[15] V. J. Smirnoff, J. Soc. Phys.-Math. Léningrade **2**, 22 (1929).

[16] F. Riesz, Math. Z. **18**, 87 (1923).

[17] See references 15 and 16. I am indebted to Professor A. Beurling for the remark that this is a special case of Nevanlinna's theorem for "beschränktartige" functions [R. Nevanlinna, *Eindeutige Analytische Funktionen* (J. Springer, Berlin, 1936)], because $\{S_a(\zeta)-2i\}^{-1}$ is bounded in the unit circle.

stant α in (I, 16) it contains an undetermined function $\alpha(s)$ and in addition the constant Θ', owing to our ignorance about the analytic behavior in the left half-plane. They are not completely arbitrary but have to be such that (20) is satisfied. We shall not derive the explicit form of this restriction, but mention only that Θ' must not be negative, as can also be seen from (21). The physical meaning of Θ' is clear from (4): Combined with the time factor e^{-iEt} it gives $\exp[-\frac{1}{2}p^2(t-2\Theta')]$, so that it simply delays the outgoing wave packet—which does not violate the causality condition.

V. THE SYMMETRY PROPERTY

In this section we shall show how the above results can be simplified if the symmetry relation (8) is assumed. More precisely, it is assumed that $S(\lambda)$ has a unique analytic continuation across the positive imaginary axis, which on the negative real axis assumes the values defined by (8). This analytic continuation must satisfy

$$S(-\lambda^*)=[S(\lambda)]^*, \tag{29}$$

and it is therefore a regular function in the second quadrant and meromorphic for $\Re\lambda<0$. On the imaginary axis $S(\lambda)$ is real at all points except the singularities.

We shall now make the additional assumption that there are no other than isolated singularities on the imaginary axis. Then there can only be simple poles. For poles of higher order were already shown to violate (20); if a branch point occurred the analytic continuation would not be unique; and essential singularities can also be shown[18] to be incompatible with (20). Because of (7) there can be no pole at $\lambda=0$, so that (29) yields $S(0)=\pm 1$. For brevity we shall confine ourselves to the case $S(0)=1$. In the literature only S functions of this restricted class have been envisaged (for pure scattering), and, indeed, Wigner[19] showed that S must be of this form if the interaction can be described by some self-adjoint Hamiltonian. On the other hand, these additional properties cannot be derived from our causality condition, as is shown by the following example. Let α, β, γ be positive constants and $\beta>\alpha$. Then

$$S(\lambda)=\frac{(\lambda+\gamma+\alpha i)(\lambda+\gamma-\beta i)}{(\lambda+\gamma-\alpha i)(\lambda+\gamma+\beta i)}$$

does not satisfy (29) and even has a pole $-\gamma+\alpha i$ in the second quadrant, but it can be verified by direct calculation that it satisfies our basic inequality (10) (with $a=0$).

With these additional assumptions the integral relation (24) can be simplified considerably. When w tends to a point $E<0$ (which does not happen to be one of the poles E_n), one obtains according to (23)

$$1=\pi(1+E^2)\tilde{\beta}'(-E).$$

On substituting this in (24), the last term cancels the $-i$ on the left and the -1 in the remaining integral on the right. Furthermore this integral can be rewritten in a fashion similar to (25), because $\Im S_a(0)=0$. The new constant Θ is then obviously $S_a(0)=1$, so that the final form becomes

$$S_a(w)-1=-\frac{1}{\pi}\int_0^\infty\left(\frac{1}{w-E}+\frac{1}{E}\right)\Im S_a(E)\cdot dE + \Sigma b_n\left(\frac{1}{w-E_n}+\frac{1}{E_n}\right). \tag{30}$$

This equation is valid in the whole complex plane, but it gives only one branch of the two-valued function $S_a(w)$. It is therefore preferable to use the variable λ; (30) then takes the form

$$\frac{S_a(\lambda)-1}{\lambda^2}=\frac{2}{\pi}\int_0^\infty\frac{\Im S_a(p')}{p'(p'^2-\lambda^2)}dp'-\Sigma\frac{2b_n}{\kappa_n^2(\kappa_n^2+\lambda^2)}, \tag{31}$$

where $\kappa_n^2=-2E_n$. If now λ tends to a real value p, one finds a relation between real and imaginary parts of S:

$$\Re S_a(p)=1+\frac{2p^2}{\pi}\int_0^\infty\frac{\Im S_a(p')}{p'(p'^2-p^2)}dp' - 2p^2\Sigma\frac{b_n}{\kappa_n^2(\kappa_n^2+p^2)} \tag{32a}$$

(principal value at $p'=p$). By inverting this equation one obtains

$$\Im S_a(p)=-\frac{2p}{\pi}\int_0^\infty\frac{\Re S_a(p')}{p'^2-p^2}dp'+2p\Sigma\frac{b_n}{\kappa_n(\kappa_n^2+p^2)}. \tag{32b}$$

These equations are generalizations of Eqs. (I, 30).

A *product expansion* for $S(\lambda)$ in the present case cannot be obtained simply as a specialization of the general representation (28), because the latter is essentially restricted to the right half of the λ plane, e.g., it involves zeros $-\lambda_n$ which are not zeros of $S(\lambda)$. Instead, $S(\lambda)$ should now be considered as a meromorphic function defined in the whole upper half-plane, for which a product expansion with respect to the zeros *and* the poles has to be found.

We shall first construct a product containing all the

[18] If $i\kappa$ is an isolated singularity, $S(\lambda)$ can be split up according to Laurent's theorem (see Titchmarsh, reference 3) into two terms: $S=g_1+g_2$, where g_1 is regular in the neighborhood of $i\kappa$ and g_2 is regular everywhere but in $i\kappa$. Moreover, both are real on the i axis. Hence $\Im g_1(x+iy)\leqq Cx$ in the neighborhood, and the same is true for g_2 because of (19). Put $\lambda=i\kappa-i/\zeta$ and $g_2(\lambda)=g(\zeta)$, so that g is an entire function. Then $\Im g(\xi+i\eta)\leqq C(-\eta)/(\xi^2+\eta^2)$ in the lower half of the ζ plane and therefore $\Im g(\zeta)<0$, since it cannot have a maximum. It has been proved in I that from this follows $g(\zeta)=\alpha_1\zeta+\alpha_2$, which means that $S(\lambda)$ has a simple pole at $i\kappa$. Instead of (19) one can also use (20) and the Phragmén-Lindelöf theorem.

[19] E. P. Wigner, Phys. Rev. **70**, 15 and 606 (1946).

poles. Since $S(iy)$ is a real function of y, having poles at $y=\kappa_n$ whose residues are all of the same sign, there must be at least one zero ν_n between κ_n and κ_{n+1}. The product

$$\prod_{n=1}^{\infty}\frac{1+\lambda/i\kappa_n}{1-\lambda/i\kappa_n}\frac{1-\lambda/i\nu_n}{1+\lambda/i\nu_n} \tag{33}$$

contains all the poles of S_a in the upper half-plane, has modulus 1 on the real axis, and can readily be shown to be convergent. For[20] the (absolute) convergence of the product depends on the convergence of the sum

$$\sum\left|\frac{1}{\kappa_n}-\frac{1}{\nu_n}\right|\leqslant\sum\left(\frac{1}{\kappa_n}-\frac{1}{\kappa_{n+1}}\right)\leqslant\frac{1}{\kappa_1}.$$

Now put

$$g_N(\lambda)=S_a(\lambda)\Big/\prod_{n=1}^{N}\frac{1+\lambda/i\kappa_n}{1-\lambda/i\kappa_n}\frac{1-\lambda/i\nu_n}{1+\lambda/i\nu_n}.$$

This function is regular in the first quadrant, and its imaginary part is not greater than 1 on the boundaries. By applying Phragmén-Lindelöf's theorem to $e^{-ig_N(\lambda)}$, one finds $\Im g_N(\lambda)\leqslant 1$ in the whole quadrant. Consequently the limiting function $S_a^0(\lambda)=\lim g_N(\lambda)$, which is regular in the upper half plane and of modulus 1 on the real axis, has also an imaginary part $\leqslant 1$ in the first quadrant. Hence it satisfies an equation of the type (30) or (31) without the term containing the poles:

$$\frac{S_a^0(\lambda)-1}{\lambda}=\frac{1}{\pi}\int_{-\infty}^{+\infty}\frac{\Im S_a^0(p')}{p'(p'-\lambda)}dp'.$$

From this it follows, as in I, that $S_a^0(\lambda)=O(|\lambda|)$ and therefore necessarily bounded,[21] and subsequently, that $S_a^0(\lambda)$ can be expanded into a product of the form

$$S_a^0(\lambda)=e^{+2i\alpha'\lambda}\prod_n\frac{1-\lambda/\Lambda_n}{1-\lambda/\Lambda_n^*}\frac{1+\lambda/\Lambda_n^*}{1+\lambda/\Lambda_n}\prod_m\frac{1-\lambda/iL_m}{1+\lambda/iL_m}, \tag{34}$$

where again $\alpha'\geqslant 0$.

The iL_m are the zeros of $S(\lambda)$ on the imaginary axis that were not yet included in the ν_n. As the distinction between the zeros $i\nu_m$ and iL_m depends on an arbitrary choice, it is desirable to write the expansion of $S(\lambda)$ in a unique way, e.g., as follows:

$$S(\lambda)=e^{-2i\alpha\lambda}\prod\frac{1-\lambda/\Lambda_n}{1-\lambda/\Lambda_n^*}\frac{1+\lambda/\Lambda_n^*}{1+\lambda/\Lambda_n}\prod\frac{1-\lambda/iP_m}{1+\lambda/iP_m}. \tag{35}$$

Here $\alpha\leqslant a$ and iP_m runs over all zeros on the imaginary axis, taken in the order of increasing absolute value of P_m; a positive P_m corresponds to a zero on the positive imaginary axis, a negative P_m to a pole.

This product expansion is the direct generalization of (I, 16). The same formulas for the cross section in the neighborhood of resonance follow from it. The sum rule (I, 19) carries over:

$$\sigma(0)=4\pi\left\{-\alpha+2\Sigma\frac{\Gamma_n}{|\Lambda_n|^2}+\Sigma\frac{1}{P_m}\right\}^2,$$

provided the signs of the P_m are taken into account. The generalization of the integral relations in I has been given above. The relation (I, 25), for the case $\alpha=0$, goes over into

$$\eta(\infty)-\eta(0)=\pi(2N+M-K),$$

where N is again the number of zeros Λ_n in the first quadrant, and M and K are the numbers of zeros and poles on the $+i$ axis. However, Levinson[22] showed that, if the interaction is caused by a potential field, $\eta(0)-\eta(\infty)=\pi K$, so that necessarily $N=M=0$. But this cannot be true, because there must be a zero between any two successive poles on the imaginary axis. Consequently it is not possible for a potential field of finite range that $\alpha=0$ in (35).[23]

We shall again derive for the R matrix

$$R(w)=\frac{1}{i\lambda^*}\frac{S_a(\lambda)-1}{S_a(\lambda)+1}\quad(w=\tfrac{1}{2}\lambda^2), \tag{36}$$

the general properties by which Wigner[24] defined the class of "R functions." It is clear that R is meromorphic and real both for $w>0$ and $w<0$. We proceed to show that $R(w)$ is holomorphic in the upper half-plane, i.e., that $S_a(\lambda)+1$ has no zeros in the first quadrant.

First let $\alpha'=0$ in (34) and let the products consist of N and L factors, respectively, and let (33) consist of K factors. Then S_a is a rational function of order $2N+2K+L$ and has the limit $+1$ at infinity (because L is necessarily even). Hence it assumes the value -1 in $2N+2K+L$ points of the λ plane. Now on the imaginary axis S_a is real and has $2K$ poles whose residues have the same sign, so that it takes the value -1 at least $2K$ times. On the real axis S has modulus 1 and the phase changes $2N+L$ times 2π, so that it takes the value -1 at least $2N+L$ times. There can be no other points where $S_a(\lambda)+1=0$. In the second place let $\alpha'>0$ in (34). Take a large rectangle in the λ plane whose vertical sides intersect the real axis at $\pm\pi h/\alpha'$, where h is some large integer. The variation of the phase of $S_a(\lambda)+1$ around the rectangle will be the same as for $e^{2i\alpha'\lambda}+1$, that is $2h\cdot 2\pi$, since the rational factor in $S_a(\lambda)$ tends

[20] This proof seems somewhat shorter than the one given by P. I. Richards, Duke Math. J. **14**, 777 (1947).

[21] This point was treated too summarily in I, because it does not follow from (I, 39) that $(\lambda+i\beta)^{-1}S(\lambda)$ is ***uniformly*** bounded in the upper half-plane. Rather than the ordinary Phragmén-Lindelöf theorem one should therefore use Nevanlinna's formulation (see reference 10).

[22] N. Levinson, Kgl. Danske Videnskab. Selskab, Mat.-fys. Medd. **25**, No. 9 (1949).

[23] A similar argument shows that α must be positive; for examples see C. Møller (reference 13) and D. ter Haar, Physica **12**, 501 (1946).

[24] E. P. Wigner, Ann. Math. **53**, 36 (1951).

to 1. That means that the factor $e^{2i\alpha'\lambda}$ gives rise to $2h$ new zeros of $S_a(\lambda)+1$; but they lie necessarily on the real axis, because the phase between $-\pi h/\alpha'$ and $+\pi h/\alpha'$ now changes $2N+L+2h$ times 2π. Finally let N, K, and L tend to infinity: according to a theorem of Hurwitz (see Titchmarsh[3]) the zeros of the limiting function must also lie on either the real or the imaginary axis. Hence in the w plane $R(w)$ can only have poles on the real axis.

To show that $\mathfrak{I}R(w)>0$ for $\mathfrak{I}w>0$ let us first return to the case N, K, L finite, $\alpha'=0$. In a point on the $+i$ axis of the $\lambda=x+iy$ plane where $S_a(iy)+1$ vanishes, one must have $dS_a(iy)/dy>0$, because otherwise there would be at least three zeros of $S_a(\lambda)+1$ between the neighboring poles, which would result in more than $2N+2K+L$ zeros in total. It then follows from (36) that $R(w)$ has here a simple pole with negative residue. The same is true for the poles on the positive real axis of λ, because there one must have $d\eta_a/dx>0$. Consequently all poles in the w plane may be cut off from the upper half-plane by small semicircles on which $\mathfrak{I}R>0$. Moreover, for large $|w|$ one has $R(w)\sim\lambda^{-2}$ so that $\mathfrak{I}R(w)$ vanishes uniformly at infinity. It thus follows that $\mathfrak{I}R$ is nowhere negative, since it cannot have a minimum. If now $\alpha'>0$ there is an infinity of poles on the real axis, but by using a large rectangle as before, one can prove the same result. Finally, if N, K, and L tend to infinity, $\mathfrak{I}R(w)$ cannot, of course, become negative; neither can it become zero in any point, because that would be a minimum.

This completes the proof that the properties of the S matrix which were found from the causality condition (2) together with the symmetry relation (8), imply the known properties of the R matrix. In another paper (to be published in Rev. Mex. Fis.) we shall show that the converse is also true.

VI. DISCUSSION

The representations (24) and (28) of S, which followed from our causality condition alone, contain an undetermined function and are therefore of little practical use. Only by making the additional assumption (8) was it possible to obtain the more specific representations (31) and (35), which are similar to those in the electromagnetic case, but for the presence of poles in the upper half-plane. The main effect of these poles is that $S(\lambda)$—for complex λ—is no longer expressed in its values on the real axis alone, but one also needs the poles and their residues in (31). This seems a poor result, because an analytic function is already determined by its values in an arbitrarily small interval, but the following has to be borne in mind.

When two analytic functions take the same values in a small interval, they are identical throughout the region where they are defined. However, if one only knows that their difference in the interval is less than ϵ, then, no matter how small ϵ is, their values in any other point of the region may vastly differ. In other words, if the function $S(p)$ is given in a small interval on the real axis, its analytic continuation $S(\lambda)$ does not depend on the given values in a continuous way. It follows from this remark that it is impossible to express $S(\lambda)$ explicitly in terms of the values in a certain interval on the real axis. Nor is it possible to find an algorithm for computing the values in the complex plane. Although $S(\lambda)$ is unique when $S(p)$ is given, the problem to construct the actual values of $S(\lambda)$ from $S(p)$ is not a correctly set problem.[25]

On the other hand, if a function is holomorphic in a region, the problem of finding its values in the interior from its values on the boundary (or even only from its real or its imaginary part on the boundary) is correctly set and an explicit expression is possible, namely the Cauchy integral (respectively, the Poisson integral). If this region is the upper half-plane, the values on the whole real axis are required and in addition some information about the behavior at infinity; this was the basic idea of I. In the present article $S(\lambda)$ may have poles, but if they are known together with their residues, they can be subtracted and the remaining holomorphic function can again be expressed by means of a Poisson integral in terms of its imaginary part on the boundary. This is the underlying idea of (31); the roundabout derivation was necessary because of the infinite region and the infinite number of poles.

An interaction that decreases rapidly with increasing distance is physically not very different from an interaction of finite extent. But our mathematical derivation is no longer valid; in fact even an exponentially decreasing potential field can give an S with other singularities than just simple poles.[4] Let such an interaction be cut off at some large distance; that may alter the values of S in the complex plane considerably, but not the values on the real axis, because they are directly connected with physically measurable quantities. It can therefore be asserted that equations like (32), connecting physical quantities, are approximately correct if the interaction is approximately zero beyond a certain distance. One might even say that they are as correct as the whole idea of an S matrix, because applying S matrix theory to any actual experiment implies that one regards the scattered particles as free when they reach the observing apparatus.

It has been suggested that the bound states can be found from the scattering data by analytic continuation of the S matrix.[26] That turned out to be true if the interaction is caused by a field of finite extent, but not for instance for the potential e^{-r}. This distinction between sharply cut-off and rapidly decreasing potentials

[25] Actually the only way to give the values of $S(p)$ in the interval with infinite precision is by means of some analytic representation. It is a common procedure to use that representation (or a derived one) for an explicit definition of the analytic continuation. However, this has to be done for each case separately and does not solve the problem of finding a generally valid explicit expression of $S(\lambda)$ in terms of $S(p)$.

[26] W. Heisenberg, Z. Naturforsch. **1**, 608 (1946).

seems unnatural to a physicist. According to the above considerations it has, indeed, no physical meaning, because the analytic continuation is not determined in a constructive way so that it is *never* possible to compute the energies of the bound states from the phase shift.

Jost and Kohn[27] showed that the potential can be calculated from the scattering phase shift, when, in addition, the energies and the normalization factors of the bound states are given. If it is known *a priori* that the potential has a finite extent, these constants are already determined by the analytic continuation of the scattering phase shift. Nevertheless, there is again no abrupt difference between the case of potential fields of finite extent and rapidly decreasing potentials, because the constants are determined in a nonconstructive way, so that for actual calculations they still have to be given explicitly.

When the interaction at large distances arises from a potential that does not fall off rapidly, Eqs. (32) are still practically valid, as mentioned above, provided that a is chosen very large. However, for large a all terms on the right tend to zero except the contribution of the singularity in the integral, and the equation reduces to a triviality. It is therefore preferable to solve the wave equation explicitly as far as possible and enclose in the sphere with radius a only the interaction which is unknown or cannot be treated explicitly. That amounts to replacing $e^{\pm ipr}$ with the explicit solutions in the outer region, in the manner of Wigner and Eisenbud.[28] It will then be possible to generalize the present treatment, provided the analytic behavior of these solutions (as functions of p) has roughly the same features as that of $e^{\pm ipr}$. Presumably a sufficient condition is that the potential is a regular analytic function of r for $|r|>a$, including the point $r=\infty$. A special case is the centrifugal potential $l(l+1)/r^2$ which comes in when the higher multipole waves are treated.

ACKNOWLEDGMENT

I am indebted to Professor E. P. Wigner, Professor V. Bargmann, and to members of the Institute for Advanced Study for valuable discussions.

[27] R. Jost and W. Kohn, Kgl. Danske Videnskab. Selskab, Mat.-fys. Medd. **27**, No. 9 (1952).

[28] E. P. Wigner and L. Eisenbud, Phys. Rev. **72**, 29 (1947).

Letters to the Editor

PUBLICATION of brief reports of important discoveries in physics may be secured by addressing them to this department. The closing date for this department is five weeks prior to the date of issue. No proof will be sent to the authors. The Board of Editors does not hold itself responsible for the opinions expressed by the correspondents. Communications should not exceed 600 words in length and should be submitted in duplicate.

The Band Width of the *F* Band in KBr at 78°K†

IRVING L. MADOR, JORDAN J. MARKHAM,* AND REUEL T. PLATT, JR.
Applied Physics Laboratory, Johns Hopkins University, Silver Spring, Maryland
(Received July 6, 1953)

THE *F* band in alkali halide crystals is known to have a frequency and half-width depending on the material and temperature of measurement. The half-width *W* also may be affected by the interaction of the *F* centers with other imperfections or dislocations in the lattice. An understanding of this effect would be of particular interest in view of certain bleaching experiments on *F* bands in KBr at low temperatures where the optical instability was determined to be a function of the mode and temperature of formation of the *F* centers.[1] The effect was interpreted as a result of the recombination of electron surplus and hole centers existing in high concentrations in the vicinity of lattice imperfections.

There is a rather large spread in the values for *W* reported in the literature. For example, for KBr at approximately 78°K, *W* has been reported as 0.20[2] and 0.23 ev.[3] Since such differences are greater than can be accounted for considering variations in temperature and resolving power, a study has been made to determine the reproducibility of *W* in a given sample.

The experimental techniques have been described before.[2] The measurements were made with a Beckman Model DU Spectrophotometer at a slit width of 0.06 mm corresponding to a band pass of 27A at 600 mμ. Under these conditions of measurement the apparent broadening of the band contour due to slit width can be neglected.

The contribution of the broad *F'* band to the intensity of the *F* band was eliminated by optically bleaching the *F'* band. A small optically stable *K* band (also called V_0) at 530 mμ also overlaps the *F* band. The *K* band contribution was estimated by evaluating the dissymmetry introduced into the *F* band envelope. This approximation showed that in ignoring the contribution of the *K* band, the error in the value of *W* was less than ¼ mμ or 0.001 ev.

Table I gives measurements of *W* in five specimens cleaved from a single additively colored Harshaw crystal.[4]

In Table II are summarized the results on several samples: samples 2 and 4 were cleaved from the same Harshaw crystal, sample 3 was from a different Harshaw crystal, and sample 5 was from a crystal[5] shown to be particularly pure.[1] Each measurement was made on an individual specimen. The values of $\log_{10}(I_0/I)$ for the x-rayed samples varied in the range 0.400 to 0.850.

TABLE I. Half-width in additively colored KBr at 78°K.

Specimen No.	$\log_{10}(I_0/I)$	Half-width in ev
1	1.516	0.208_8
2	0.670	0.209_4
3	0.737	0.208_7
4	1.172	0.208_2
5	1.550	0.208_2
	Mean	0.208_6
	Probable error	0.000_2

TABLE II. Summary of half-widths at 78°K.

Sample No.	Half-width in ev	Probable error	Number of measurements
1. KBr additively colored	0.208_6	0.000_2	5
2. KBr (Harshaw) x-rayed at 300°K	0.201_8	0.000_4	6
3. KBr (Harshaw) x-rayed at 300°K	0.195_7	0.000_9	3
4. KBr (Harshaw) x-rayed at 78°K	0.200_0	0.000_8	4
5. KBr (Schulman) x-rayed at 300°K	0.201_1	0.000_7	3

Table II indicates that *W* can be measured to 0.001 ev. The dependence of *W* on the mode of formation of the *F* centers is not certain. Although the values of *W* for the x-ray colored crystals are appreciably lower than for the additively colored, only a single sample of the latter was available for measurement. The variation in *W* for crystals colored by x-radiation is greater than the probable error of the measurement. No correlation is observed between *W* and concentration of *F* centers, or between *W* and susceptibility to optical bleaching.

† This research was supported by the Bureau of Ordnance, U. S. Navy.
* Now at Zenith Radio Corporation, Research Division, 6001 W. Dickens Avenue, Chicago, Illinois.
[1] Markham, Platt, and Mador (to be published).
[2] W. H. Duerig and J. J. Markham, Phys. Rev. **88**, 1043 (1953).
[3] E. Mollwo, Z. Physik **85**, 56 (1933).
[4] This crystal was additively colored by A. B. Scott of Oregon State College.
[5] This crystal was prepared by J. H. Schulman of the Naval Research Laboratory.

Relation between the de Haas-van Alphen Effect and the Magnetoresistance in Bismuth

TED G. BERLINCOURT
Naval Research Laboratory, Washington, D. C.
(Received June 12, 1953)

FROM magnetoresistance and magnetic susceptibility data on bismuth monocrystals at low temperatures de Haas and van Alphen[1] concluded that "a connection exists between this resistance and magnetization perpendicular to it," but the nature of this "connection" was not ascertained. Recently, Alers and Webber[2] compared their new low-temperature magnetoresistance data on bismuth with Shoenberg's[3] magnetic susceptibility data and noted certain correlating features. In order to clarify and extend this correlation, low-temperature magnetic susceptibility measurements were undertaken in fields up to 25 kilogauss using the same bismuth single crystal (*7b*) used by Alers and Webber in their magnetoresistance measurements. Only the section between the potential leads (obtained by cleaving in liquid nitrogen) was used, however.

Inasmuch as this investigation utilized the torision balance method,[3] the exact geometry employed in the magnetoresistance measurements (*viz.*, *H* perpendicular to the trigonal or 3-axis and one binary or 1-axis) could only be approximated.[4] However, in the case of bismuth, with small angles ϕ between the bisectrix or 2-axis and *H* and for the 1-axis perpendicular to *H*, the susceptibility difference $\chi_3-\chi_2$ yielded by the torsion balance method may be treated in the same manner as $-\chi_2$ in comparing susceptibility and magnetoresistance data. For example, if $\phi=\pm5°$ the oscillation periods (or positions of maxima and minima) in $\chi_3-\chi_2$ differ by less than 3 percent from those in $-\chi_2$ for $\phi=0$.

According to the electronic scheme proposed by Shoenberg[3] for bismuth the pertinent constant energy surfaces in momentum space consist of three long thin ellipsoids (two of which are obtainable from the other by rotations about the 3-axis of 120° and 240°) such that the susceptibility will in general contain three oscillating terms whose amplitudes and periods depend upon the orientation of the crystal with respect to the field. For small ϕ and for *H* perpendicular to the 1-axis, two of these terms are

approximately equivalent such that a term having a period P and two terms having a period $\approx P\cos 60°$ in H^{-1} exist in the susceptibility. However, if, as was actually the case in this study, H differs from perpendicularity to the 1-axis by a small angle δ as a result of inexact orienting techniques, then the observed periods will be given approximately by $P\cos\delta$ and $P\cos(60°\pm\delta)$.

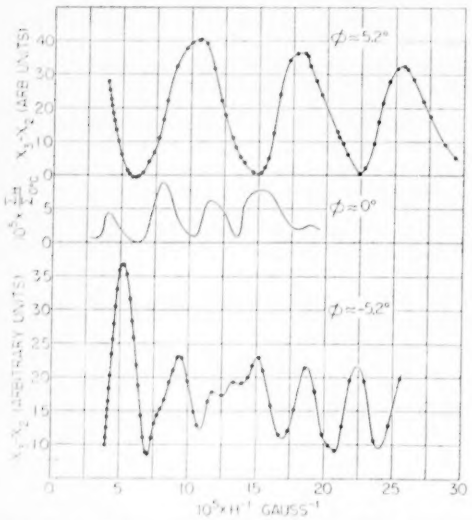

FIG. 1. The oscillating portion of the conductivity (as observed by Alers and Webber for $\phi = 0$) and $\chi_3 - \chi_2$ plotted as functions of H^{-1} for $T = 4.2°$K.

In Fig. 1 the susceptibility data (which show essential agreement with Shoenberg's[3] lower field measurements) obtained at 4.2°K are plotted along with the data for the oscillating portion of the conductivity as observed by Alers and Webber also at 4.2°K. In the susceptibility curves the long period term ($P\cos\delta$)

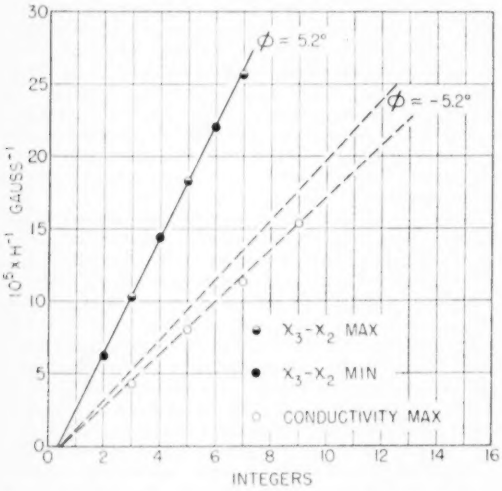

FIG. 2. Values of H^{-1} for which susceptibility and conductivity maxima and minima occur plotted against odd and even integers, respectively. The dashed lines represent the short period susceptibility oscillations.

is most important for $\phi \approx 5.2°$, while two shorter period terms ($P\cos[60°\pm\delta]$) predominate for $\phi \approx -5.2°$. A more illuminating means of comparison is provided in Fig. 2. The solid line is obtained by plotting values of H^{-1} for which maxima and minima in $\chi_3 - \chi_2$ occur in the long period term for $\phi \approx 5.2°$ against odd and even integers, respectively, and the dashed lines are obtained for the two short period terms derived from an analysis of the susceptibility curve for $\phi \approx -5.2°$. (This analysis also yielded a value of $\delta \approx 2.5°$ illustrating the sensitivity of the short period oscillations to slight errors in orientation.) The open circles represent values of H^{-1} for which Alers and Webber (see Table II of reference 2) observed maxima in the oscillating portion of the conductivity. The proximity of these points to the dashed lines despite slightly different geometries supports the belief that the magnetoresistance oscillations have the same period as the short period susceptibility oscillations, and that both phenomena arise from a common electronic structure. Exact correlation would require that the open circles fall midway between the dashed lines. Then for H along the 2-axis a maximum in diamagnetism would correspond to a maximum in conductivity in the 3-direction. In the case of the long period term the conductivity data do not justify critical comparison, and it appears that effort toward a more rigorous correlation might profitably be devoted to an investigation of graphite in which the relevant de Haas-van Alphen electronic structure is less complicated.

I wish to express my thanks to Mr. P. B. Alers and Dr. R. T. Webber for the bismuth crystal and much helpful discussion.

[1] W. H. de Haas and P. M. van Alphen, Proc. Acad. Sci. Amsterdam **33**, 1106 (1930); Commens. Kamerlingh Onnes Lab. Univ. Leiden **212a** (1930).
[2] P. B. Alers and R. T. Webber, Phys. Rev. **91**, 1060 (1953).
[3] D. Shoenberg, Proc. Roy. Soc. (London) **A170**, 341 (1939).
[4] The notation is that of Shoenberg in reference 3. The 1, 2, and 3 axes are orthogonal.

Lyman-Alpha Radiation in the Solar Spectrum

E. T. BYRAM, T. CHUBB, H. FRIEDMAN, AND N. GAILAR
U. S. Naval Research Laboratory, Washington, D. C.
(Received June 29, 1953)

THE intensity of the Lyman-alpha line of hydrogen (λ1216A) in the solar spectrum was measured by means of photon counters flown in three Aerobee rockets at the White Sands Proving Grounds, New Mexico, during May 1952. Each flight provided a continuous telemetered record of the intensity *versus* altitude up to about 128 kilometers. A preliminary study[1] of the data showed that HL_α was first detected[2] at approximately the same altitude in each flight, 74±2 km (18°–20° sun elevation). From the variation of intensity with residual air path, an absorption coefficient was computed, 0.046 cm^{-1} (base e, NTP) which compares well with 0.063 cm^{-1} obtained in laboratory measurements of the attentuation of HL_α in dry air at low pressures.[3,4] The discrepancy between these two absorption coefficients is equivalent to an altitude error of 2.2 kilometers or a 27 percent difference in pressure. Pressure data were taken from the Rocket Panel report[5] and are estimated to have a probable error of ±15 percent in the neighborhood of 80 kilometers.

The photon counters used in these flights were sensitive to a narrow band of wavelengths from 1180A to 1300A. Although the spectral sensitivity curve between these limits had a jagged appearance due to the absorption lines of chlorine gas, which was one of the gas components in the photon counter, the sensitivity over a range of several angstroms in the immediate neighborhood of HL_α was fairly constant. The conversion from counting rate to flux of incident energy was obtained by comparison with the response of photomultiplier tubes coated with sodium salycilate or vacuum pump oil,[6,7] which were in turn compared with a calibrated mercury lamp at λ2536A. By a stroke of good fortune, the photon counter tube used in the most satisfactory flight was recovered undamaged. It was subjected to careful recalibration during the past year and no significant drift in characteristics from its preflight calibration was detected. The measured solar intensity based on this tube was 0.10±0.02 erg cm^{-2} sec^{-1} at the top of the atmosphere. No unusual solar activity was observed

during the flight. The present result is lower than the 0.4 ergs cm^{-2} sec^{-1} previously reported by Tousey, Watanabe, and Purcell[8] based on exposure of a thermoluminescent powder, responsive to the wavelength band 1050–1240A. Pietenpol *et al.*[9] recently reported photographic detection of HL_α in a flight that exceeded 80 km and estimated the intensity to be of the order of magnitude of 0.3 erg cm^{-2} sec^{-1}.

The straight line character of the plot of logarithm of intensity *versus* residual air path shown in Fig. 1, is evidence for the monochromatic nature of the radiation that was measured. Hopfield's spectrograms[10] revealed the existence of a deep window in the O_2 absorption spectrum at HL_α and Watanabe, Marmo, and Inn[3] recently published quantitative measurements of the absorption coefficients in the neighborhood of this window. Within ± 1.0A on either side of HL_α, the absorption coefficient increased by at least 200 percent. The constancy of the measured absorption coefficient over the entire altitude range of the rocket therefore indicates that the breadth of the solar emission line must certainly be less than one angstrom unit. Pietenpol[9] judged the width of his photographed line to be about 6A. In view of the narrowness of the O_2 window, such an observed line width at 80 km would be difficult to explain except as instrumental broadening.

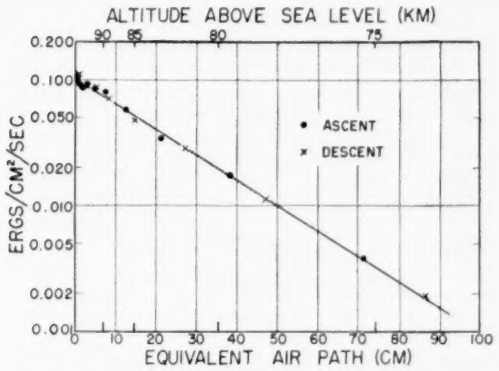

FIG. 1. Log incident energy *versus* the equivalent air path at NTP traversed by solar radiation as measured with a photon counter sensitive in the 1180–1300A region.

At the peak of the flight, 128 km, the rocket was above the molecular oxygen atmosphere. Figure 1 does not indicate all the data points obtained near the top of the flight. The rocket spent 140 seconds above 105 kilometers during which time the roll of the rocket exposed the photon counter to the sun 28 times. The rms deviation of the counting rates measured for these 28 exposures was ± 6 percent, and the average value of the intensity fell within one percent of the straight line plot of Fig. 1. Any appreciable intensity outside the HL_α wavelength would have appeared in excess of the intercept of the HL_α characteristic at zero residual air path. It may be concluded from these observations and the spectral sensitivity curve of the photon counter that the continuous solar emission background in the neighborhood of 1200A must have been less than 0.01 erg cm^{-2} sec^{-1} per 100A. This is equivalent to a black body temperature less than 4600 degrees K.

It has been suggested that absorption of HL_α by NO may provide the observed *D*-layer ionization.[11,12] The present rocket data do not exclude this possibility. Although the rocket data have been explained by attributing all the absorption to O_2, a weak absorption due to nitric oxide or water vapor could have been present within the experimental error. If we assume that the contribution of H_2O or NO to the absorption observed in the rocket experiment was less than ten percent, the maximum concentrations relative to air must have been less than 1.6×10^{-6} and 9.4×10^{-6}, respectively, using absorption coefficients[3,4] of 390 cm^{-1} and 67 cm^{-1} for H_2O and NO. The latter concentration is equivalent to an upper limit of 0.007 cm (NTP) of NO above 75 km, well below the value of 0.02 cm (NTP) given by Migeotte and Neven[13] as the maximum possible abundance based on their studies of the solar spectrum in the infrared. Watanabe *et al.*[3] have found that approximately 50 percent of the absorption of NO at the wavelength of HL_α leads to photoionization. If only one percent of the HL_α intensity observed in the rocket experiment were absorbed by NO, the rate of ion production in the *D* layer would average about 15 ion pairs cm^{-3} sec^{-1}, which is of the order of magnitude required to produce the *D* layer.[11]

[1] Byram, Chubb, Friedman, and Lichtman, J. Opt. Soc. Am. **42**, 876 (1952).
[2] About one percent of intensity incident at top of atmosphere.
[3] Watanabe, Marmo, and Inn, Phys. Rev. **90**, 155 (1953).
[4] W. M. Preston, Phys. Rev. **57**, 887 (1940).
[5] The Rocket Panel, Phys. Rev. **88**, 1027 (1952).
[6] Johnson, Watanabe, and Tousey, J. Opt. Soc. Am. **41**, 702 (1951).
[7] K. Watanabe and E. C. Y. Inn, J. Opt. Soc. Am. **43**, 32 (1953).
[8] Tousey, Watanabe, and Purcell, Phys. Rev. **83**, 792 (1951).
[9] Pietenpol, Rense, Walz, Stacey, and Jackson, Phys. Rev. **90**, 156 (1953).
[10] J. J. Hopfield, Astrophys. J. **104**, 208 (1946).
[11] D. R. Bates and M. J. Seaton, Proc. Phys. Soc. (London) **B63**, 129 (1950).
[12] M. Nicolet, Mém. roy. met. inst. Belgium **19**, 1 (1945).
[13] M. Migeotte and L. Neven, Mém. soc. roy. sci. Liège **12**, 165 (1952).

The Shape of Exchange Narrowed Paramagnetic Resonance Lines*

R. T. WEIDNER AND C. A. WHITMER
Department of Physics, Rutgers University, New Brunswick, New Jersey
(Received July 15, 1953)

THE theory of Anderson and Weiss[1] on exchange narrowing in paramagnetic resonance absorption predicts that the line shape in the case of large exchange interaction is of the resonance or Lorentz type in the observable center of the line. Organic free radicals, having very narrow absorption lines, are suitable substances for testing the validity of the line shape prediction. Measurements at 3.2-cm wavelength do indeed show that the diphenyl picryl hydrazyl absorption follows the resonance line shape.

The absorption curves were derived from recorder tracings which were made by a procedure that has been described.[2] The

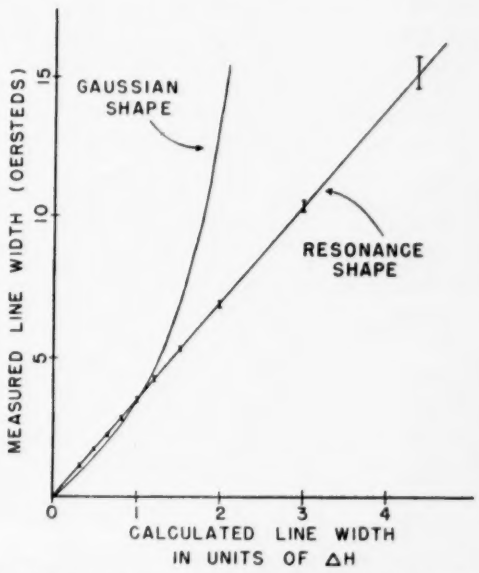

FIG. 1. Shape analysis of diphenyl picryl hydrazyl resonance at 4.2°K and 3.2-cm wavelength.

resonance shape may be written as $f=(1+x^2)^{-1}$, $x=2(H-H_0)/\Delta H$, where f is the fractional absorption relative to the peak absorption at a magnetic field H, H_0 is the field at the resonance peak, and ΔH is the full line width at $f=\frac{1}{2}$. The shape analyses were made by measuring the full line widths for various values of f and plotting the measured line widths against the calculated line widths for corresponding values of f, i.e., against $(1/f-1)^{\frac{1}{2}}$.

Figure 1 shows the results for the hydrazyl radical at 4.2°K, where the data for a number of runs, taken under various conditions of sample cavity mismatch and without saturation effects, are summarized. For comparison, the curve to be found under the assumption of a Gaussian line shape, which is predicted for the case of negligible exchange effects, is also shown, the fit with the measured widths being made at half-maximum absorption. The data are clearly incompatible with the Gaussian shape, particularly in the wings of the line. (The extreme plotted data correspond to $f=0.05$.) The value of ΔH for 4.2°K is found to be 3.46 ± 0.04 oersteds, with $g=2.0025\pm0.0003$. At room temperature the shape is also found to be of the resonance type with $\Delta H=2.70\pm0.02$ oersteds and $g=2.0036\pm0.0002$; at 77°K, $\Delta H=2.36\pm0.02$ oersteds and $g=2.0036\pm0.0003$.

These results are in qualitative agreement with those of Singer and Spencer,[3] who find at 25 Mc/sec a substantial increase in line width and a 0.10 ± 0.05 percent decrease in g in going from room temperature to 4.2°K. Our data fail to show a bulge on the low-field side of the resonance line, as observed by Hutchison, Pastor, and Kowalsky;[4] this can be attributed to differences in the preparation of the samples. The effect of the anisotropy in g value, found for single crystals,[4] was essentially eliminated by the use of finely powdered samples. The hyperfine structure, which is revealed when the hydrazyl radical is sufficiently diluted in benzene, makes no important contribution to the line shape in the undiluted sample, inasmuch as the nearest satellite lines rise from the wings of the central line at a field separation of about 10 oersteds as the samples are diluted.

* This work has been supported by the U. S. Office of Naval Research, the Rutgers University Research Council, and the Radio Corporation of America.

[1] P. W. Anderson and P. R. Weiss, Revs. Modern Phys. **25**, 269 (1953).
[2] R. T. Weidner and C. A. Whitmer, Rev. Sci. Instr. **23**, 75 (1952).
[3] L. S. Singer and E. G. Spencer, J. Chem. Phys. **21**, 939 (1953).
[4] Hutchison, Pastor, and Kowalsky, J. Chem. Phys. **20**, 534 (1952).

A New Thermal Resistivity Maximum in Superconducting Alloys

RONALD J. SLADEK
Institute for the Study of Metals, University of Chicago, Chicago, Illinois
(Received July 9, 1953)

THE thermal conductivity of a series of homogeneous, solid solution indium-thallium alloys with thallium contents up to 50 atomic percent has been measured as a function of magnetic field and temperature in the liquid helium region, the specimens being those for which magnetic and electrical data were previously obtained by Stout and Guttman.[1] Details of the temperature variation of the thermal conductivity in the pure superconducting and pure normal states will be discussed in a later paper. The purpose of this note is to report a new thermal resistivity maximum which accompanies the isothermal destruction of superconductivity by a *longitudinal* magnetic field, at temperatures sufficiently below T_c, in alloys containing between 15 and 50 atomic percent Tl. This effect is illustrated in Fig. 1, where the dependence of the thermal resistivity of a long, single crystal cylinder of 20 atomic percent Tl and 80 atomic percent In upon *longitudinal* magnetic field is compared with the variation of the magnetic induction and electrical resistance found by Stout and Guttman[1] for the same specimen.

The thermal resistivity passes through a sharp maximum within the range $1<H/H_c<4$, where the gradual flux penetration and delayed return of electrical resistance imply the co-existence of both superconducting and normal filaments at fields well above H_c. It seems possible to these additional resistivity responsible for the maximum is due to the scattering of heat carriers at the boundaries between superconducting and normal regions. The scattering of electrons at these boundaries is probably unimportant, since although the electronic thermal conductivity is still appreciable, the electronic mean free path is short ($\sim2\times10^{-6}$ cm in the 20 percent Tl specimen) even compared to the probable thickness of the boundary ($\sim10^{-5}$ cm)[2] between normal and superconducting regions. Phonons, on the other hand, have a much longer mean free path in these alloys, particularly in the superconducting state in which there are fewer normal electrons available to act as scattering centers.[3] In the 20 percent Tl specimen at 1.345°K, for example, the phonon mean free path is estimated from the experimental thermal conductivity corrected for the electronic contribution[3] to be 9.8×10^{-5} cm for the pure normal state and 1.4×10^{-3} cm for the pure superconducting state. Thus, if the average diameter of the normal filaments is comparable with that of the superconducting filaments, boundary scattering of phonons is probably important only in the latter.

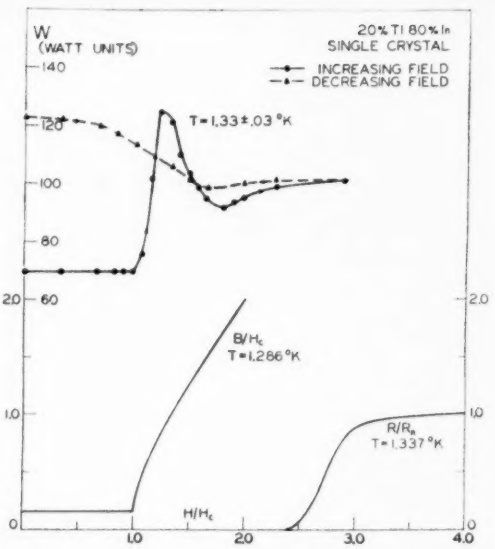

FIG. 1. Thermal resistivity, reduced magnetic induction, and reduced resistance *versus* reduced magnetic field. The induction and electrical resistance data are from Stout and Guttman (reference 1).

With an appropriate separation of the lattice and electronic conductivities[4] and an allowance for the fraction of normal material as derived from the induction curve, the additional resistivity in the superconducting filaments was computed for the maximum of Fig. 1 and for similar maxima at several different temperatures. This resistivity was found to be roughly proportional to T^{-3}, in good agreement with the expected temperature variation for boundary scattering of phonons,[5,6] provided that the filament diameter is itself independent of temperature. If scattering at the boundaries is completely diffuse, the magnitude of the additional resistivity indicates a phonon mean free path of approximately 3×10^{-4} cm, which sets an upper limit to the average filamental diameter and, moreover, satisfies the other boundary scattering condition that the wavelengths of the phonons important in heat conduction[6] ($5\times10^{-7}<\lambda<2\times10^{-6}$ cm in this case) be shorter than the distance between boundaries.

After the magnetic field is removed, the final thermal resistivity is considerably greater than the virgin superconducting or normal state values, presumably due to scattering of phonons at the boundaries of frozen-in normal regions, the presence of which is indicated by the incomplete Meissner effect. The additional lattice

resistivity in this case is again roughly proportional to T^{-3}, with a somewhat larger phonon mean free path (or filamental diameter), 1.1×10^{-3} cm, for diffuse scattering.

It should be mentioned that although thermal resistivity maxima have been reported previously for cylindrical specimens in *transverse* magnetic fields, both for pure metals[7–10] and for dilute alloys,[11–13] no longitudinal field maxima were reported for any of these specimens. In the pure metals these transverse field maxima occur in the intermediate state range $0.5<H/H_c<1.0$ and are probably due to scattering of electrons[7] at the boundaries between superconducting and normal laminas perpendicular to the axis of the cylinder.

I wish to thank Professor John K. Hulm for suggesting this research and for his constant advice, aid, and encouragement.

[1] J. W. Stout and L. Guttman, Phys. Rev. **88**, 703 (1952).
[2] D. Shoenberg, *Superconductivity* (Cambridge University Press, London, 1952), second edition, p. 117.
[3] J. K. Hulm, Proc. Roy. Soc. (London) **A204**, 98 (1950).
[4] J. K. Hulm, National Bureau of Standards Circular **519**, 37 (1952).
[5] H. B. G. Casimir, Physica **5**, 495 (1938).
[6] R. E. B. Makinson, Proc. Cambridge Phil. Soc. **34**, 474 (1938).
[7] R. T. Webber and D. A. Spohr, Phys. Rev. **84**, 384 (1951).
[8] D. P. Detwiler and H. A. Fairbank, Phys. Rev. **88**, 1049 (1952).
[9] J. L. Olsen and C. A. Renton, Phil. Mag. **43**, 946 (1952).
[10] J. K. Hulm, Phys. Rev. **90**, 1116 (1953).
[11] K. Mendelssohn and J. L. Olsen, Proc. Phys. Soc. (London) **A63**, 2 (1950).
[12] K. Mendelssohn and J. L. Olsen, Phys. Rev. **80**, 859 (1950).
[13] J. L. Olsen, Proc. Phys. Soc. (London) **A65**, 518 (1952).

Penetration Depth of Superconductors

M. C. Steele and M. F. M. Osborne
Naval Research Laboratory, Washington, D. C.
(Received July 13, 1953)

We have been considering a model for superconductivity in which the electrons move in parabolic potential wells. This model is quite analogous to Einstein's model in which he put the ions into parabolic wells and obtained the specific heat of the lattice. The parameters of the present model are the number of electrons per well, the number of wells per cc, and the fundamental frequency associated with the well. By choosing parabolic wells we are able to solve for the electronic energy eigenvalues in the presence of a magnetic field without having to use perturbation theory.[1] When appropriate values are assigned to the parameters of the model, it s found to represent the thermodynamic (specific heat and magnetic moment) properties of a superconductor quite nicely.

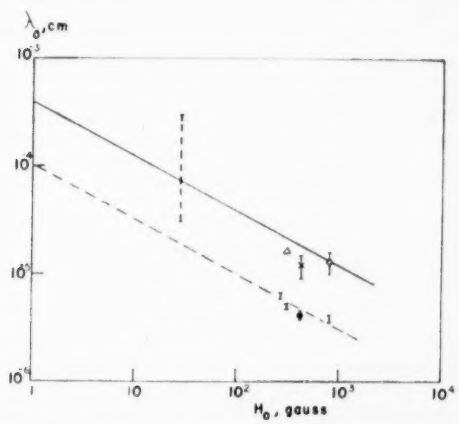

FIG. 1. Logλ_0 vs logH_0. The experimental points are taken from the following sources:
I, (Pb, Sn, In) J. M. Lock, Proc. Roy. Soc. (London) **A208**, 391 (1951).
●, (Hg) E. Laurmann and D. Shoenberg, Proc. Roy. Soc. (London) **A198**, 560 (1949).
○, (Pb) M. C. Steele, Phys. Rev. **78**, 791 (1950).
×, (Hg) Appleyard, Bristow, London, and Misener, Proc. Roy. Soc. (London) **A172**, 540 (1939).
△, (Sn) N. E. Alekseevsky, J. Phys. (U.S.S.R.) **4**, 401 (1941).
⁞, (Cd) M. C. Steele and R. A. Hein, Phys. Rev. **87**, 908 (1952).

If we identify the size of the well (at an energy equal to the Fermi energy) with the penetration depth, we obtain the following relation between λ_0, the penetration depth at $T=0°$K, and H_0, the critical magnetic field at $T=0°$K:

$$\lambda_0=1.6(\hbar c/eH_0)^{\frac{1}{2}}. \tag{1}$$

Here $\hbar$, c, and e have their usual values. Equation (1) is plotted in Fig. 1 as the solid curve, with experimental points from the sources indicated. The dashed curve is drawn parallel to the theoretical curve to fit the data of the Cambridge workers, since their results fall in a separate group. The numerical factor of Eq. (1) has to be 0.41 in order to get the dashed curve. The trend of λ_0 with H_0, as well as the absolute values, are quite well represented.

A relation equivalent to Eq. (1) can also be obtained from a totally different development; namely London's[2] concept of superficial currents whose elemental charges each carry an angular momentum of $\hbar$. Starting from London's[2] equation (4) for the critical surface mass transfer R_c,

$$R_c=(mc/4\pi e)H_0,$$

and, assuming that at $T=0°$K

$$R_c\simeq n\hbar,$$

where n is the number of superconducting electrons per cc, we obtain

$$H_0=4\pi ne\hbar/mc.$$

Combining this with London's[2] equation (6),

$$\lambda_0^2=mc^2/4\pi ne^2,$$

yields

$$\lambda_0=(\hbar c/eH_0)^{\frac{1}{2}},$$

which is just our Eq. (1) with a slightly different numerical factor.

Details of the present model will be given in a subsequent paper.

[1] C. G. Darwin, Proc. Cambridge Phil. Soc. **27**, 86 (1931).
[2] F. London, Revs. Modern Phys. **17**, 310 (1945).

Paramagnetic Resonance in *N*- and *P*-Type Silicon*

F. K. Willenbrock and N. Bloembergen
Division of Applied Science, Harvard University, Cambridge, Massachusetts
(Received July 13, 1953)

We have independently observed the paramagnetic resonance recently reported for *N*-type silicon by Portis, Kip, Kittel, and Brattain[1] and have also observed the resonance for *P* type. Our measurements were made on two samples of *N* type and three samples of *P*-type silicon[2] with impurity concentrations ranging from 5×10^{17} to 5×10^{18} cm^{-3}. The experiment was performed at 9000 Mc/sec at 78°K.

By comparison with the free radical α,α-diphenyl β-picryl hydrazyl,[3] it was established that the g factor for both holes and electrons is 2.00. The line widths at half-maximum absorption are 4 to 5 gauss for both *N* and *P* type. The intensity of the absorption signal is found to be roughly proportional to the impurity concentration. As it has been shown[1] that the resonance is the result of the spin of the free carriers, this implies that the impurities are nearly completely ionized in our samples. Experiments at liquid helium temperatures may give information about the effective mass of the holes.

* This research was assisted in part by the U. S. Office of Naval Research.
[1] Portis, Kip, Kittel, and Brattain, Phys. Rev. **90**, 5, 988 (1953).
[2] Supplied through the courtesy of W. H. Brattain, Bell Telephone Laboratories, Murray Hill, New Jersey.
[3] C. H. Townes and J. Turkevich, Phys. Rev. **77**, 1, 148 (1950).

Electrical Properties of Gold-Germanium Alloys*

W. C. DUNLAP, JR.
General Electric Research Laboratory, Schenectady, New York
(Received July 14, 1953)

RECENT studies[1-3] have shown that zinc, and copper, as well as the third and fifth column elements, can act as activator elements in germanium. The present note deals with gold, which is shown to be an acceptor capable of taking up electrons at two distinct energy levels. The first acceptor level is 0.15 ev above the filled band, the second (trapping) level is 0.20 ev below the conduction band.

Gold-germanium alloys have been made using cp gold wire (exact purity unknown), gold wire (99.96 percent), and gold ingot[4] (purity checked in the G. E. Research Laboratory and found to be 99.99 percent or better). Consistent results were obtained using these materials.

Gold was added during growth of the single crystals in proportions ranging from 0.01 to 0.1 percent. *N*-type crystals showed an increase in resistivity at the point of addition; *p*-type crystals showed a decrease. The segregation coefficient (ratio of gold in the solid to that in the liquid) was found to be about 1.5×10^{-5}, assuming that each gold atom furnished two acceptor states. The solubility of gold appears to be about 10^{15} atoms/cm³.

Figure 1 shows Hall effect data, which also give the density of carriers, for samples cut from a gold-doped germanium ingot. Temperatures of measurement ranged from 77°K to 400°K. The

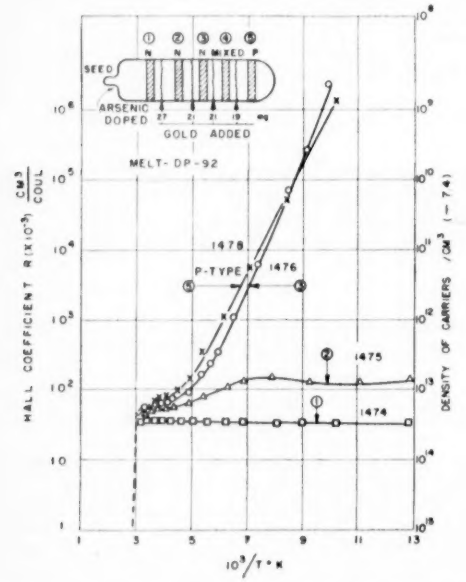

FIG. 1. Hall coefficient vs $1/T$°K for a series of germanium samples cut from wafers containing progressively increasing amounts of gold. The crystal was originally *n*-type before gold was added. Each successive wafer is more *p*-type as the result of the addition of gold, as well as the normal segregation process. The scale at the right represents (1/7.4) times the actual density of carriers.

steep slope is in contrast to the behavior of the usual impurities (including zinc and copper), for which the Hall curve is practically constant in this temperature range. The slopes indicated an ionization energy of ~0.20 ev for the *n*-type samples, ~0.15 ev for the *p*-type sample.

The observed results may be accounted for in terms of the scheme of Fig. 2. Acceptor levels at 0.20 ev below the conduction band and 0.15 ev above the filled band are indicated. The observed

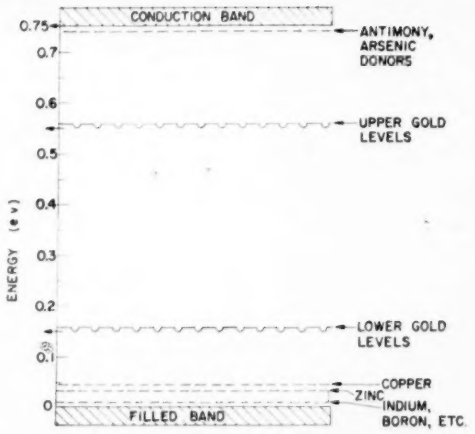

FIG. 2. Impurity level spectrum of germanium, based upon published work to date. Indicated are the acceptor levels of gold, as well as those of zinc and copper and the third column elements. The donor levels are those characteristic of the fifth column elements. The upper gold level is seen in conduction processes mainly as an electron trap, whereas the lower gold levels act both as electron traps and high-ionization energy acceptors.

properties are then determined by the degree to which these levels are filled by electrons from donor impurities. If no such impurities are present, the crystal is *p*-type.

These experiments also showed that the number of upper gold levels was equal to the number of lower gold levels, to within experimental error (±25 percent). This might be accounted for if each gold atom accepts one, then a second electron, to become Au^- and Au^{--}.

Several interesting properties have been discovered in gold-doped germanium at 77°K: (a) a slow-decay component has been found in the photoconductivity following illumination in the infrared; (b) current-pulsing, in some samples, leads to immediate loss of conductivity, followed by its slow reappearance; (c) new photoconductivity bands in the infrared, apparently associated with the levels discussed here, have been found by R. Newman. The phenomena, which will be discussed in detail in later reports, appear to be related to disturbance of the equilibrium between the various traps and the conduction bands.

By proper compensation of impurities, resistivities at 77°K as high as 5×10^7 ohm cm have been obtained. This is an aid in the doing of experiments in which the relatively high conductivity of germanium has been a hindrance.

The high ionization energy of gold in germanium also leads to simplification of the problem of studying germanium in the impurity ionization range, since many of these experiments can now be done in the range 77°K to room temperature.

* Some of these results were presented at the 1953 Durham meeting, American Physical Society [Phys. Rev. **90**, 208 (1953)].

[1] W. C. Dunlap, Jr., Phys. Rev. **85**, 945 (1952).
[2] C. S. Fuller and J. D. Struthers, Phys. Rev. **87**, 526 (1952).
[3] F. J. Morin and J. P. Maita, Phys. Rev. **90**, 337 (1953).
[4] I wish to thank M. D. Fiske for a supply of this gold.

Scintillation Response of Organic Phosphors

G. T. WRIGHT
Department of Physics, Rhodes University, Grahamstown, South Africa
(Received March 23, 1953; revised manuscript received July 14, 1953)

THE scintillation efficiencies and decay times of organic phosphors depend upon the nature and energy of the absorbed particles. From the available experimental data concerning these quantities we may infer the nature of the quenching processes which occur for ionizing particles and calculate the scintillation response of these phosphors.

For fast electrons internal conversion of energy by electronically excited molecules is almost certainly the predominant quenching process. It is consistent with the efficiency being independent of electron energy, and Birks[1] has shown that it can quantitatively explain the low values found. For more heavily ionizing particles the scintillation efficiency may become very small, yet the accompanying decrease in decay time is relatively slight.[2] This indicates that the additional quenching is due to bimolecular processes, e.g., neighboring ionized and electronically excited molecules may interact to form new chemical entities (such as dianthracene in anthracene), excited molecules may be affected adversely by the coulomb fields of neighboring ions and return non-radiatively to the ground state, and interaction between excited molecules may occur leading to non-radiative dissipation of their electronic energy. This latter process is discussed by Black[3] who shows that it can provide an interpretation of the experimental data. This author also considers the effects of migration of energy out of the excitation column. However, due to the rapidity with which the bimolecular processes occur, expansion of the excitation column may be neglected whether taking place by resonance exchange of energy between molecules[4] or by photon emission and reabsorption.[1] Considering then that quenching of fluorescence is due to the combined effect of monomolecular and bimolecular processes in the excitation column, one may readily calculate the scintillation efficiency.

In penetrating a distance Δx the particle loses energy $(dE/dx)\Delta x=\epsilon_0\Delta x$ to the molecules along or near its path. At a time t after absorption the excess electronic energy of the molecules in this length of the excitation column is ϵ, and we have

$$d\epsilon=-(p+k+a\epsilon)\epsilon dt, \tag{1}$$

where $a\epsilon$ = rate of energy dissipation by bimolecular quenching processes, k = rate of energy dissipation by monomolecular quenching processes, and p = rate of energy dissipation by fluorescence emission. The total fluorescence emission from these molecules is

$$dL=p\Delta x\int_0^\infty \epsilon dL=\frac{p}{a}\ln\left(1+\frac{a}{p+k}\cdot\frac{dE}{dx}\right)\Delta x. \tag{2}$$

When dE/dx is small this may be written in the approximate form

$$\frac{dL}{dx}=\frac{p}{p+k}\cdot\frac{dE}{dx}\Big/\left(1+\frac{1}{2}\cdot\frac{a}{p+k}\cdot\frac{dE}{dx}\right), \tag{3}$$

in agreement with the semi-empirical expression proposed by Birks.[5] The total scintillation emission excited by the particle is

$$L=\int_0^z dL=\int_E^0\frac{dL}{dE}\cdot dE. \tag{4}$$

When dE/dx is small, Eq. (4) reduces to $L=pE/(p+k)$; thus the constant $p/(p+k)$ denotes the phosphor efficiency for fast electrons. For the particular case of anthracene the complete integration of Eq. (4) has been performed using a graphical method. The differential energy loss dE/dx was calculated from the theoretical stopping formula, except for alpha particles with energies below 10 Mev for which a semi-empirical method based on the range-energy curves for air was used;[6] the constant $p/(p+k)$ is 0.05 for anthracene, and the ratio a/p was determined from the data for 5-Mev protons to be 0.23. The curves obtained are illustrated in Fig. 1 and compared with the experimental data.[7,8] The agreement is very satisfactory, and since the response of all organic phosphors is very similar we may expect this in other cases.

A point of interest concerns the decay time of fluorescence, which is longer when excited with particles than with ultraviolet quanta. This has been interpreted as the result of additional absorption and emission processes undergone by fluorescence photons emitted from initially ionized molecules;[1] an alternative explanation is that particle excitation involves an effective delay in the emission of fluorescence by ionized molecules due to the finite time of ion recombination. It is hoped that measurements of decay times and efficiencies of fluorescence excited by radiations in the wavelength range 3000A to 100A will resolve this question; such measurements are in progress in this laboratory.

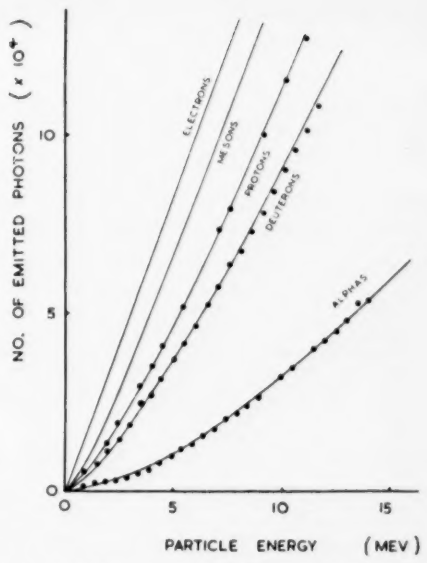

FIG. 1. Scintillation response of anthracene to ionizing particles. ——— theoretical curves; ● experimental observations.

[1] J. B. Birks, *Scintillation Counters* (Pergamon Press, London; McGraw-Hill Book Company, Inc., New York, 1953).
[2] Bittman, Furst, and Kallman, Phys. Rev. **87**, 83 (1952).
[3] F. A. Black, Phil. Mag. **44**, 263 (1953).
[4] G. T. Wright, Proc. Phys. Soc. (London) (to be published).
[5] J. B. Birks, Proc. Phys. Soc. (London) **A64**, 874 (1951).
[6] G. T. Wright, Ph.D. thesis, University of Birmingham, 1952 (unpublished).
[7] Taylor, Jentschke, Remley, Eby, and Kruger, Phys. Rev. **84**, 1034 (1951), and private communication.
[8] Frey, Grim, Preston, and Gray, Phys. Rev. **82**, 372 (1951).

Variable Activation Energy and the Motion of Lattice Defects*

G. J. DIENES
Brookhaven National Laboratory, Upton, New York
(Received June 30, 1953)

IN a recent paper, Overhauser[1] successfully analyzed isothermal annealing curves of irradiated copper on the basis of a variable activation energy, i.e., an activation energy which depends on the number of disturbances left in the lattice. The writer was concerned with the analysis of this type of annealing kinetics in another connection[2] and arrived at some general conclusions on the basis of a simple example. It is the purpose of this note to summarize the results briefly.

Let n denote the number of lattice disturbances present at any time t, and assume that over the range of interest the activation energy, E, decreases linearly with increasing n. This simple case can be handled analytically. The source of this functional dependence of E on n is most likely the strains introduced in the lattice by the disturbances, particularly interstitial atoms.[1,3] A linear dependence is a reasonable approximation to the relation derived by Overhauser[1] on the basis of lattice strains. E is expressed, therefore, as

$$E/k=E_0/k-\alpha n/k, \tag{1}$$

and the general rate equation for the disappearance of n is

$$dn/dt=-\nu n^\gamma e^{-E_0/kT}e^{\alpha n/kT}. \tag{2}$$

Integrating formally gives

$$\int_{n_0}^{n} \frac{e^{-bn}}{n^{\gamma}} dn = -\nu t e^{-E_0/kT}, \tag{3}$$

where $b=\alpha/kT$. The integrals of (3) are expressible in terms of the exponential integral for any integer γ. At a fixed value of n one may write

$$t = K' e^{E_0/kT} e^{-\alpha'/kT}, \tag{4}$$

where K' is a constant and $\alpha'=\alpha n$. Thus, a plot of log$t$ *versus* $1/T$ obtained at a fixed n is linear just as in the simple case of constant activation energy but the effective activation energy, $E_{eff}=E_0-\alpha'$, depends on the value chosen for n; i.e., the phenomenologically determined activation energy[4] varies systematically with n.

The influence of a variable activation energy on the nature of the annealing curve is best discussed on the basis of an actual example. n *versus* t curves were calculated at a fixed temperature (250°C) for $n_0=0.10$; $E_0/k=15\,000$ with $\alpha/k=25\,000$; $E_0/k=12\,500$ with $\alpha=0$; $\nu=10^{13}$, for $\gamma=2$ and 3. For $\gamma=2$, Eq. (3) integrates to

$$\frac{e^{-bn_0}}{n_0}-\frac{e^{-bn}}{n}+b[\mathrm{Ei}(-bn_0)-\mathrm{Ei}(-bn)]=-\nu t e^{-E_0/kT} \tag{5}$$

(using the notation of Jahnke and Emde). By simple integration by parts the integral for any γ may be obtained. The results obtained are shown in Fig. 1. (The semi-log plot is used for convenience only.) From the curves of Fig. 1 it is clear that a variable

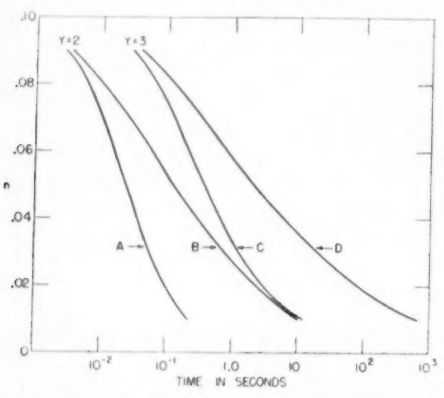

FIG. 1. Relaxation of n at 250°C. Comparison of constant and variable activation energy. A and C: $E_0/k=12\,500$, $\alpha/k=0$. B and D: $E_0/k=15\,000$, $\alpha/k=25\,000$.

activation energy which increases with decreasing n has the effect of lengthening the time scale for any given isothermal annealing curve. A rather small variation of E with n leads to a very large change in the time scale. Figure 1 also shows that an increase in the order of reaction (from $\gamma=2$ to $\gamma=3$ in Fig. 1) has a qualitatively similar effect to that of an E increasing with decreasing n. Computations showed that an annealing curve characterized by a given γ and a variable E can often be fitted by a constant E but a higher and not necessarily integer value of γ. This conclusion is in accord with Overhauser's experimental results.[1]

The results of this study may be summarized as follows:

1. A variable activation energy leaves the nature of the plot of log$t$ *vs* $1/T$, taken at any fixed n, unchanged but manifests itself in a systematic change of the slopes of these lines as a function of the amount of anneal at which E is being determined.

2. A rather small variation of E with n leads to a very large change in the time scale for the relaxation of n.

3. An annealing curve of low γ and variable E is very similar in character to a reaction of higher order (not necessarily integral) and of constant E.

4. More complex expressions of $E=f(n)$ may be required in specific cases. As long as E is a decreasing function of n the above conclusions are qualitatively valid.

* Under contract with the U. S. Atomic Energy Commission.
[1] A. W. Overhauser, Phys. Rev. **90**, 393 (1953).
[2] G. J. Dienes (unpublished).
[3] G. J. Dienes, Phys. Rev. **86**, 228 (1952).
[4] Parkins, Dienes, and Brown, J. Appl. Phys. **22**, 1012 (1951).

Determination of the Neutron-Proton Capture Cross Section

G. VON DARDEL AND A. W. WALTNER*
AB Atomenergi, Department of Physics, Stockholm, Sweden
(Received June 15, 1953)

A DIRECT determination of the neutron-proton capture cross section has been made by a measurement of the mean life of neutrons in water, as first done by Manley, Haworth, and Luebke.[1] In the present method, which is capable of high precision, the diffusion correction which was the main source of uncertainty in their investigation has been avoided by making the measurements in a large tank, of dimensions $97\times97\times107$ cm, with the modulated neutron source, a stainless steel target bombarded by deuterons from a 150-kv accelerator, in the center. The decay of the neutron intensity at a number of positions was analyzed by a multichannel time analyzer, the detectors being cylindrical brass counters, 1 cm in diameter and filled to 600 mm of BF_3, which extended through the entire depth of the tank and thus automatically performed an integration of the neutron intensity in the vertical direction. By subsequent integration of the data in the radial direction the decay of the total number of neutrons in the tank was obtained and found to be accurately exponential apart from a small constant background.

The period of the exponential decay of the neutrons was found from 3 complete runs to be 206.6 ± 1.5 μsec, the estimated uncertainty being due mostly to the uncertainty of the correction for the constant background, since the statistical accuracy and consistency of the measurements was much better. A small correction of -0.4 μsec for counting losses in the time analyzer has been included in this result. The result has to be corrected for the influence of the counters on the neutron distribution. Since the brass counters used in the experiment have a larger capture cross section than the corresponding amount of water, the decay in the counters will be more rapid than in the water. This effect was investigated by comparing the decay curves obtained at three positions in the tank with the brass counters and with aluminum counters filled to such pressure of BF_3 that they have the same absorption cross section per volume as water. This measurement yielded a correction of $+5.5$ μsec with an uncertainty of 2 μsec. Because of the absence of moderating nuclei in the counter, a depression in neutron density will develop during the first intervals of time when the neutrons are being slowed down. As soon as the neutrons have become thermal this hole will, however, quickly fill up by diffusion. The effect of the absence of scattering in the counter once the neutrons have become thermal should be proportional to the Laplacian of the neutron density and will disappear in the integration over the whole tank. These considerations were verified by comparing the decay curves measured with two aluminum counters of different volume, both having the same absorption as water. The presence of a depression in the larger counter during the first intervals of time after the neutron burst from the source was clearly visible, but after about 50 μsec the decay curves became identical. In calculating the period, the initial part of the decay curve is therefore discarded.

For the corrected mean life in distilled water at 22.6°C, we thus obtain 212 ± 3 μsec, and the corresponding neutron-proton capture cross section for a neutron velocity of 2200 m/sec is 0.321 ± 0.005 barns, in satisfactory agreement with the most recent determinations by quite different methods of Hamermesh, Ringo, and Wexler,[2] 0.329 ± 0.004 barn, and of Muehlhause *et al.*,[3] 0.332

± 0.007 barn. The uncertainty is almost entirely the result of the background correction and the correction for counter absorption and should be decreased considerably in future measurements.

The controversial results of recent determinations of the cross section of boron,[4-7] which has been in widespread use as a standard for cross sections, makes a more reliable standard desirable. The knowledge of the neutron-proton capture cross section with considerable accuracy would make water well suited as a primary standard, due to its general availability, well defined nuclear properties, and the ease with which it can be produced in a pure state. For applications where the low absorption and high scattering cross section of water is a disadvantage, secondary standards of boron or other highly absorbing compounds can be prepared by relative measurements.[8] We have prepared such a secondary standard in the form of a solution of 8.83 g borax per liter of water and have for this solution measured a neutron mean life of 74.5 ± 0.5 μsec, corresponding to a cross section of 0.0610 ± 0.0004 cm^2 per cm^3 solution. If necessary, the solution may be concentrated by evaporation if account is taken of the change in cross section due to the evaporated water. In the measurements on the borax solution the counters were chosen to have the same absorption as the solution and should thus not give rise to any depression in the neutron density. The major uncertainty is the result of the background correction. The measured value corresponds to a boron absorption cross section of 708 ± 12 barns, where account has been taken in the probable error of the uncertainty of the chemical analysis of the solution, which was about 1 percent. While this value is in good agreement with some of the old values for the cross section,[4] it disagrees with the more recent determinations[6,7] which give much higher values. It is proposed to investigate this problem in more detail by making comparison measurements between our standard solution and samples of the boron used by other investigators.

* On leave from North Carolina State College, Raleigh, North Carolina.
[1] Manley, Haworth, and Luebke, Phys. Rev. **61**, 152 (1942).
[2] Hamermesh, Ringo, and Wexler, Phys. Rev. **90**, 603 (1953).
[3] C. O. Muehlhause *et al.* (to be published).
[4] Fermi, Marshall, and Marshall, Phys. Rev. **72**, 193 (1947).
[5] L. J. Rainwater and W. W. Havens, Jr., Phys. Rev. **70**, 136 (1946).
[6] *Neutron Cross Sections*, U. S. Atomic Energy Commission Report, AECU-2040 (1952).
[7] H. Pomerance, Oak Ridge National Laboratory Reports, ORNL-577 and ORNL-366 (unpublished).
[8] W. J. Whitehouse and G. A. R. Graham, Can. J. Research **A25**, 261 (1947).

The Construction of Potentials in Quantum Field Theory

ABRAHAM KLEIN*
Physics Department, University of Rochester, Rochester, New York
(Received July 16, 1953)

IN a paper with the above title, Brueckner and Watson[1] have given a method for constructing scattering kernels in quantum field theories by means of an inductive technique starting from the Lippmann-Schwinger integral equation.[2] We wish to show that the same results can be achieved quite simply by a specified method of successive elimination of the components of the state vector from the usual Schrödinger equation.

We use the notation of reference 1. For the sake of simplicity, we limit ourselves here to the case of a coupling linear in the meson variables and without nucleon pair production. The Schrödinger equation is

$$a\psi = H'\psi. \tag{1}$$

Let $\psi = \psi_e + \psi_o$, where ψ_e contains only amplitudes for an even number (including zero) of mesons and ψ_o only amplitudes for an odd number. In virtue of the properties of H', we can write in place of Eq. (1),

$$\begin{aligned} a\psi_e &= H'\psi_o, \\ a\psi_o &= H'\psi_e. \end{aligned} \tag{2}$$

Eliminating ψ_o (thinking of the two-nucleon problem for definiteness), we obtain the equation

$$a\psi = H'a^{-1}H'\psi = \Delta_0\psi, \tag{3}$$

having dropped the subscript on ψ.

Again we divide the remaining ψ into an even and an odd part, the even part consisting now of the amplitudes for $4l$ mesons ($l=0, 1, 2\cdots$), the odd part embracing the remaining amplitudes. The effective interaction,[1] Δ_0, has both a diagonal part V_0 and an off-diagonal part U_0. Equation (3) then becomes

$$\begin{aligned} (a-V_0)\psi_e &= U_0\psi_o, \\ (a-V_0)\psi_o &= U_0\psi_e, \end{aligned} \tag{4}$$

or, after elimination of the odd part,

$$(a-V_0)\psi = [U_0(a-V_0)^{-1}U_0]\psi = \Delta_1\psi. \tag{5}$$

This procedure can be repeated any number of times. After the first step the amplitude for no mesons is coupled only to the amplitude for two mesons, after the nth step only to the amplitude for 2^n mesons. In the limit as n increases indefinitely, we obtain an ordinary Schrödinger equation,

$$a\psi = V\psi, \tag{6}$$

where V is the infinite (nonperturbation) series diagonal in occupation numbers defined in reference 1.

The same method can be applied to non-linear interactions and to nucleon-pair production. As soon as one departs from the case of a Hamiltonian linear in creation and absorption operators, however, the resulting solution is only a formal one, since the energy denominators of the "potential" are still nondiagonal in occupation numbers.[1] This corresponds to the fact that in the general case, at any stage of elimination, a given amplitude is coupled to members of both the even and odd set. In any practical calculation, where one includes only a few amplitudes, the most suitable procedure is to work directly with the coupled equations and eliminate alternate components. This yields an effective potential diagonal in occupation numbers which can be obtained from the formal solution only by additional manipulation of the latter.

Finally, we wish to point out that the method of integral equations proposed by Lévy[3] can also be expressed simply by the symbolic means used in this note. The relationship between the different methods will be pursued further in a more complete communication.

* On leave for the summer of 1953 from the Society of Fellows, Harvard University.
[1] K. A. Brueckner and K. M. Watson, Phys. Rev. **90**, 699 (1953).
[2] B. Lippmann and J. Schwinger, Phys. Rev. **79**, 469 (1950).
[3] M. M. Lévy, Phys. Rev. **88**, 72 (1952).

Deficiency of the Phenomenological Theory of the Lamb Shift

FREDERICK J. BELINFANTE
Department of Physics, Purdue University, Lafayette, Indiana
(Received July 15, 1953)

DR. W. E. Lamb has kindly drawn my attention to the fact that Eqs. (1) and (2) with (17) of Bethe, Brown, and Stehn[1] do not give the complete dependence of the Lamb shift on the atomic number Z. Instead of

$$\delta E_{nlj} = (Z^4\alpha^3 Ry/\pi n^3)\cdot\{c_{lj}/(2l+1) + (8/3)[\ln(Ry/k_{nl}) + 10.0988\delta_{l,0}]\} + \text{corrections}, \tag{1}$$

with $c_{lj} = (-1)^{l-j+\frac{1}{2}}/(j+\frac{1}{2})$ and with

$$\ln|Ry/k_{nl}| \approx -2.812\delta_{l,0}, \tag{2}$$

as derived from these equations,[2] the correct quantum-electrodynamical formula for the Lamb shift is

$$\delta E_{nlj} = (Z^4\alpha^3 Ry/\pi n^3)\cdot\{c_{lj}/(2l+1) + (8/3)[\ln(Ry/k_{nl}) + (10.0988 - 2\ln Z)\delta_{l,0}]\} + \text{corrections}. \tag{3}$$

For the Lamb shift $(\delta E_{2S\frac{1}{2}}-\delta E_{2P\frac{1}{2}})$ for He^+, Eq. (1) gives approximately 16 900 Mc/sec, and Eq. (3) gives about 13 880 Mc/sec, while the experimental value for this quantity as found by Lamb and Skinner[3] is around 14 020 Mc/sec. This shows the correctness of the quantum-electrodynamical formula (3) in the approximation used and the nonvalidity of Eq. (1).

Some time ago, I proposed a phenomenologic theory of the Lamb shift,[2] in which self-interactions were completely "forbidden," and in which the Lamb shift was due to some assumed direct interaction between electron and proton and between the spins and the electromagnetic field. This theory led to Eq. (1) with Eq. (2) substituted. It is hard to see how this theory could ever be made to yield the additional term with $-2(\ln Z)\delta_{l,0}$ by any simple modification of the interactions proposed. Therefore the experimental evidence on He^+ rules out the explanation of the Lamb shift by such direct interactions, and thus yields new evidence for the reality of the finite part of the quantum-electrodynamical self-interaction of the electron.

As regards the attempts to postulate the nonexistence of self-interactions, this evidence shows that such a postulate would have to be modified in such a way as to leave at least such part of the self-interaction as corresponds to the finite part of the self-energy leading to the Lamb shift, thus removing the necessity of *ad hoc* assumed direct interactions. Other restrictions to be imposed on this postulate of nonexistence of part of the self-interactions have been discussed by me earlier.[4]

[1] Bethe, Brown, and Stehn, Phys. Rev. **77**, 370 (1950).
[2] F. J. Belinfante, Phys. Rev. **84**, 949 (1951).
[3] W. E. Lamb and M. Skinner, Phys. Rev. **78**, 539 (1950).
[4] F. J. Belinfante, Phys. Rev. **85**, 468 (1952).

The Nuclear Magnetic Moment of Cr^{53} and Sr^{87}

C. D. Jeffries and P. B. Sogo
Physics Department, University of California, Berkeley, California
(Received July 15, 1953)

FROM the hyperfine structure of the paramagnetic resonance absorption of a magnetically dilute single crystal, Bleany and Bowers[1] have observed the spin of Cr^{53} to be $\frac{3}{2}$ and the magnetic moment to be $|\mu|=(0.5\pm0.1)$ nm, the sign being undetermined. Using a nuclear induction spectrometer, we have observed the nuclear magnetic resonance of Cr^{53} at a frequency of 2.40 Mc/sec in a field of 10 000 gauss. The nuclear induction signals have been observed in a 1.1-molar aqueous solution of Na_2CrO_4 in which the Cr has been isotopically enriched to 90 percent Cr^{53}. The signals have also been observed, with reduced amplitude, in a saturated solution of natural abundance Na_2CrO_4. The polarity of the Cr^{53} nuclear induction signal is opposite to that of Na^{23}, indicating that Cr^{53} has a negative magnetic moment. In the same magnetic field the ratio of the nuclear resonance frequency of Cr^{53} to that of D^2 in a sample of D_2O containing 1 molar of $MnCl_2$ has been observed to be $\nu(Cr^{53})/\nu(D^2)=0.36820\pm0.00003$. From this we find for the magnetic moment of Cr^{53}, without diamagnetic correction, $\mu(Cr^{53})=-(0.47351\pm0.00007)$ nm, where we have used in this calculation the spin $\frac{3}{2}$ of Cr^{53} as observed by Bleany and Bowers,[1] the ratio $\mu(D^2)/\mu(H)=0.307015$ as given by Mack,[2] and $\mu(H)=2.7925$ nm as determined by Bloch and Jeffries.[3]

From optical hyperfine structure measurements Heyden and Kopfermann[4] have determined the spin of Sr^{87} to be 9/2 and the magnetic moment to be $\mu=-1.1$ nm. Using a saturated aqueous solution of $SrBr_2$, we have observed a nuclear induction signal at a frequency of 1.84 Mc/sec in a field of 10 000 gauss. We have enhanced the signal amplitude and also verified that this is indeed the magnetic resonance of Sr^{87} by using a 3.1-molar aqueous solution of $SrBr_2$ in which the Sr had been enriched to 60-percent Sr^{87}. The polarity of the Sr^{87} signal was observed to be opposite to that of Br^{79}, verifying that the magnetic moment of Sr^{87} is negative. We have detected no "chemical shift"[5] between the resonance frequencies of Sr^{87} in $SrBr_2$ and SrI_2. Using the enriched sample, we have observed that, in the same magnetic field, the ratio of the nuclear resonance frequency of Sr^{87} to that of D^2 in D_2O containing 1-molar $MnCl_2$ is $\nu(Sr^{87})/\nu(D^2)=0.28232\pm0.00003$. From this we find for the magnetic moment of Sr^{87}, without diamagnetic correction, $\nu(Sr^{87})=-(1.0892\pm0.00015)$ nm, where we have used a spin of 9/2 for Sr^{87} as measured by Heyden and Kopfermann[4] and the values of $\mu(D^2)/\mu(H)$ and $\mu(H)$ as quoted above.

The authors gratefully acknowledge the assistance of Mr. Charles Cook in the preparation of the enriched Cr sample and the loan of the enriched isotopes by the Stable Isotopes Division of the U. S. Atomic Energy Commission.

[1] B. Bleaney and K. D. Bowers, Proc. Phys. Soc. (London) **A64**, 1135 (1951). K. D. Bowers, Proc. Phys. Soc. **A65**, 860 (1952).
[2] J. E. Mack, Revs. Modern Physics, **22**, 64 (1950).
[3] F. Bloch and C. D. Jeffries, Phys. Rev. **80**, 305 (1950).
[4] M. Heyden and H. Kopfermann, Z. Physik **108**, 232 (1938).
[5] W. C. Dickinson, Phys. Rev. **81**, 717 (1951).

Lower Limit for the Lifetime of the 665-kev Excited State of Mo^{97}†

F. R. Metzger and W. B. Todd
Bartol Research Foundation, of the Franklin Institute, Swarthmore, Pennsylvania
(Received July 15, 1953)

ACCORDING to Goldhaber and Hill[1] the 665-kev gamma ray emitted in the decay of Nb^{97} is probably a magnetic dipole transition between states with orbitals $g_{7/2}$ and $d_{5/2}$. As the Nb^{97} decay involves a rather energetic beta ray which can compensate for the gamma-ray recoil, Nb^{97} seemed to be a favorable case for a lifetime measurement using resonance scattering.[2]

A measurement of the nuclear resonance scattering of a gamma ray is a determination of the width of the initial nuclear level involved in the transition. The resonance scattering technique is especially well suited for lifetimes of the order of 10^{-13} second and shorter (widths$\geq 6\times10^{-3}$ ev). This is just the region into which, according to Weisskopf's lifetime formula,[3] the magnetic dipole transitions of $\approx mc^2$ energy should fall. The only $M1$ transition in this energy range whose lifetime is known is the 478-kev transition in Li^7. From an observation of the Doppler broadening due to the motion of the Li^{7*} nucleus in the $B(n,\alpha)$ reaction, Elliott and Bell[4] deduced a lifetime of 7×10^{-14} second, which is even somewhat shorter than expected from Weisskopf's formula. On the other hand, the lifetimes of several low-energy $M1$ transitions have been measured by Graham and Bell[5] using delayed coincidence techniques. Most of these lifetimes were found to be $\sim$100 times longer than predicted from Weisskopf's formula. If the 665-kev Mo^{97} gamma ray belonged to this "slow" group, resonance scattering would not be observable with our present means; if, however, the 665-kev gamma ray followed Weisskopf's formula, a large nuclear resonance scattering effect could be expected.

Ten milligrams of ZrO_2 enriched[6] in Zr^{96} were bombarded in the Brookhaven pile and yielded a 0.3-millicurie source of Zr^{97} and its daughter Nb^{97}. The gamma rays from this source were scattered alternately from Mo and Zr scatterers. The scattered radiation was observed with a scintillation spectrometer which accepted only pulses corresponding to the 665-kev photoelectron line. As the difference in atomic number between Zr and Mo is small, Rayleigh scattering from the two scatterers was almost the same. The small difference in Rayleigh scattering was determined in a separate experiment using the 663-kev gamma ray from Cs^{137}.

After correcting for the difference in Rayleigh scattering the counting rates for the Nb^{97} source with the Mo and Zr scatterers were identical, the experimental uncertainty being two percent.

If one assumes the contribution of the resonance scattering from the Mo scatterer to be two percent of the counting rate (i.e., equal to the uncertainty), and if one takes into account that only a small percentage of the gamma rays is emitted while the nucleus still has the momentum imparted to it by the beta ray,

one arrives at an upper limit for the width of the 665-kev excited state of Mo^{97}, $\Gamma \leq 5\times10^{-4}$ ev, and at a lower limit for the lifetime of this state of 1.5×10^{-12} second. This lifetime is one order of magnitude longer than the one expected from the Weisskopf formula. Thus, the $M1$ transition in Mo^{97} shows the same behavior as the low-energy $M1$'s.

It should be mentioned that the Mo^{97} transition, as well as most of the low-energy transitions measured by the Canadian group, involve a change of two units of orbital angular momentum, whereas the Li^7 gamma ray presumably leads from a $p_{\frac{1}{2}}$ to a $p_{\frac{3}{2}}$ state.

† Assisted by the joint program of the U. S. Office of Naval Research and the U. S. Atomic Energy Commission.

[1] M. Goldhaber and R. D. Hill, Revs. Modern Phys. **24**, 179 (1952).
[2] W. Kuhn, Phil. Mag. **8**, 625 (1929); P. B. Moon, Proc. Phys. Soc. (London) **63**, 1189 (1950).
[3] V. Weisskopf, Phys. Rev. **83**, 1073 (1951).
[4] L. G. Elliott and R. E. Bell, Phys. Rev. **76**, 168 (1949).
[5] R. L. Graham and R. E. Bell, Can. J. Phys. **31**, 377 (1953).
[6] Obtained from Y-12 Plant, Carbon and Carbide Corporation, Oak Ridge, Tennessee.

Production of V_1^0 Particles by Negative Pions in Hydrogen*

W. B. Fowler, R. P. Shutt, A. M. Thorndike, and W. L. Whittemore
Brookhaven National Laboratory, Upton, New York
(Received July 16, 1953)

THE photograph reproduced in Fig. 1 is one of two obtained in a hydrogen-filled diffusion cloud chamber exposed to a beam of 1.5-Bev negative pions (π^-) from the Cosmotron. The hydrogen was at a pressure of 18 atmospheres, and a field of 11 000 gauss was applied. The picture is believed to represent the production of a V_1^0 particle by a π^- interaction with a proton. Track a is the incident π^-, the end point of which is to be called A. Tracks b and c are the decay products of the V_1^0. A single neutral heavy meson also may have been produced at A, which would travel in the direction indicated by d.[1]

Since track a is short, its momentum can only be estimated to lie near the nominal π^- beam momentum of 1.63 Bev/c. This track is parallel to the other beam tracks and thus probably is not due to a secondary particle. The line connecting point A with the vertex of b and c, to be called G, forms an angle of 26° with a. The distance between A and G is 0.65 cm. Tracks a, b, and c are coplanar, while only coplanarity of A, b, and c is necessary for the tracks to be associated. In addition, the components of momentum of b and c perpendicular to line AG balance. Track b forms an angle of 16° with a; b is caused by a positive particle with a measured momentum of 480±80 Mev/c and an estimated ionization density of 3×minimum. Thus b is identified as a proton track. The angle between b and c is 37°. Track c is negative, with a momentum of 210±70 Mev/c and estimated ionization density of less than 1.5×minimum. An upper limit of 410 m_e is inferred for its mass, indicating a π^-. Assuming that b and c represent the decay of a $V_1^0(\rightarrow p+\pi^-+Q)$, one finds a Q-value of 51 Mev from these data.[2] Assuming the generally accepted Q of 37 Mev one would find that, for the given angles, the momenta should be 460 Mev/c for the proton and 180 Mev/c for the π^-. These values fall within the errors given for the measured values and have been used for the further computations. The lifetime of this V_1^0 is 4×10^{-11} sec.

The total energy of the V_1^0 is 1.26 Bev, and its momentum is 610 Mev/c. To conserve energy and momentum at least one other neutral particle must start at A. Assuming a single particle, its total energy would have to be 1.31 Bev and its momentum 1.11 Bev/c, leading to a mass of 1350±70 m_e for a kinetic energy of 1.5 Bev for the incident π^-. For an energy of 1.2 Bev instead of 1.5 Bev one would obtain a value of 1150 m_e. However, such a low value for the incident energy is improbable. In any case, if only one other particle had been produced in addition to the V_1^0, this would have to be a heavy meson. Its direction of flight is indicated by d in Fig. 1, and its lifetime must have been longer than 4×10^{-10} sec since no decay was observed in a path of 23 cm in the chamber. A threshold energy of 870 Mev is necessary for the process discussed, while 1.06 Bev were available for a 1.5-Bev incident π^- (including the rest mass of the π^-).

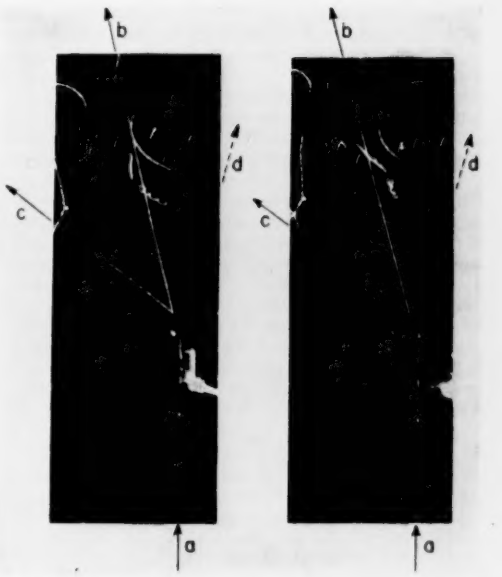

FIG. 1. Stereoscopic photograph of a V_1^0 (tracks b and c) produced in hydrogen by a negative pion (track a) of an energy of 1.5 Bev. If one heavy meson of a mass of about 1350m_e has been produced in addition, its line of flight is indicated by d.

The other photograph is quite similar to the one described, except that no momentum measurements can be obtained. However, the measured angles and estimated ionization densities are quite consistent with a V_1^0. Its direction of flight forms an angle of 30° with the incident π^-. If it is assumed to be a V_1^0 one calculates that its total energy is 1.33 Bev, its momentum 745 Mev/c, and is lifetime 3×10^{-11} sec. Assuming again that only one other neutral particle leaves the event, its mass would be 1280±80 m_e (for a 1.5-Bev incident π^-) and its lifetime longer than 3×10^{-10} sec.

Of course, instead of one heavy particle several lighter ones (for instance two π^0's, or a π^0 and a V_2^0) could originate from the events in addition to the V_1^0. However, the present results are consistent with the possibility of production of V_1^0 together with one other heavy unstable particle.[3]

* Work performed under the auspices of the U. S. Atomic Energy Commission.
[1] It is not likely that the interaction of the π^- at A involved carbon or oxygen in the alcohol rather than H_2, since (1) there is at most one molecule of alcohol per 800 molecules of H_2 and (2) an interaction with C or O would most probably give rise to charged prongs.
[2] Leighton, Wanlass, and Anderson, Phys. Rev. **89**, 148 (1953).
[3] A. Pais, Phys. Rev. **86**, 663 (1952). References to previous work are cited in this article.

Effect of the Electric Quadrupole Interaction on the $\gamma-\gamma$ Directional Correlation in Cd^{111}. III

H. Albers-Schönberg, K. Alder,* O. Braun, E. Heer, and T. B. Novey†
Swiss Federal Institute of Technology, Zürich, Switzerland
(Received July 16, 1953)

IN previous letters[1,2] we showed the effect of an interaction between the nuclear electric quadrupole moment of the intermediate state and an extranuclear inhomogenous electric field on

the angular correlation of the Cd^{111} $\gamma-\gamma$ cascade. Since it is not possible to produce artificial inhomogenous electric fields of sufficient strength we used metallic indium single crystals containing active In^{111} as sources. Our preliminary experiments proved that quadrupole interaction with the crystalline field occurs and we pointed out that the investigation of this interaction can yield the electric quadrupole moment of the first excited state of Cd^{111}.

Meanwhile, careful quantitative experiments have been made and the theory of the influence of external fields on the angular correlation of a $\gamma-\gamma$ cascade has been developed and treated in detail for the case of axial symmetric fields.[3] The correlation function depends in a complicated way upon the orientation of the symmetry axis **c** of the field with respect to the two counters. To simplify the formulas we restricted ourselves to the measurement of the anisotropy $\epsilon=W(\pi)/W(\pi/2)-1$, and we chose the arrangement where the **c** axis lay in the plane of the two counters (experiment 1 and arrangement 1 of references 1 and 3, respectively). The orientation of the **c** axis is characterized by the angle ϑ between the vector $\mathbf{k}_1$ and the **c** axis. For this case the anisotropy can be written as

$$\epsilon=\Sigma_n d_n \cos^n\vartheta/\Sigma_n e_n \cos^n\vartheta, \tag{1}$$

if the undisturbed correlation is $W(\theta)=A_{kk}P_k(\cos\theta)$. The coefficients d_n and e_n are of the form

$$d_n=\Sigma_\mu \sigma_{n\mu}{}^{k_1k_2}A_{k_1k_2}G_\mu{}^{k_1k_2}, \tag{2}$$
$$n,\ k_1,\ k_2 \text{ even}; \qquad \mu<k_1,\ k_2.$$

The $A_{k_1k_2}$ describe the correlation function and can be taken from the tables of Rose.[4] The attenuation factors $G_\mu{}^{k_1k_2}$ describe the mechanism and the strength of the interaction. For pure electric interaction they are defined as the sums:

$$G_\mu{}^{k_1k_2}=\sum_m s_{m\mu}{}^{k_1k_2}\frac{1}{1+(mx)^2}. \tag{3}$$

The numerical factors $s_{m\mu}{}^{k_1k_2}$ and $\sigma_{n\mu}{}^{k_1k_2}$ are tabulated in reference 3. x measures the strength of the interaction and is, for half-integer spin values:

$$x=\frac{eQ}{2h}\frac{\partial E_z}{\partial z}\frac{6}{(2I-1)I}\tau. \tag{4}$$

τ is the mean life of the intermediate state, Q the quadrupole moment of the nucleus, and $\partial E_z/\partial z$ the interacting field gradient.

For our experiments we used metallic indium single crystals. The crystals are tetragonal and we assume the symmetry axis to be identical with the crystalline **c** axis. The orientation of the **c** axis was obtained from x-ray rotating crystal diagrams. The anisotropy $\epsilon(\vartheta)$ was measured as a function of the angle ϑ, and the interaction strength x was found by a least-squares fit. This fit had to take into account the finite solid angle of the detectors and the finite resolving time of the coincidence circuit.

Two independent runs with two different single crystals have been made; the results are:

crystal 1, $x=1.57\pm0.03$;
crystal 2, $x=1.60\pm0.02$;
mean value, $x=1.59\pm0.02$.

One of the results is shown in Fig. 1. With the known spin (5/2) and mean life $[\tau=(1.23\pm0.06)\times10^{-7}$ sec] of the 247-kev level of Cd^{111} one gets:

$$(eQ/h)(\partial E_z/\partial z)=(6.86\pm0.4)\text{ Mc/sec},$$
$$Q\partial E_z/\partial z=(2.84\pm0.18)\times10^{-8}\text{ volt}.$$

The sign of $Q\cdot\partial E_z/\partial z$ cannot be obtained by this experiment as can be seen from Eq. (3).

Three additional methods have been used to determine the value of x. Another geometrical arrangement (experiment 2 of reference 1) gave $x=1.85\pm0.2$. Polycrystalline metallic sources gave the result $x=1.4\pm0.2$. In a third experiment we oriented the crystalline **c**-axis perpendicular to the plane of the two counters and applied a magnetic field in the same direction.[5] The result was $x=1.6\pm0.2$. The arrangement 1 is, however, much more sensitive than the others.

To determine the value of Q from these measurements one must know the magnitude of $\partial E_z/\partial z$. Calculations are very difficult, but crude estimations give $\partial E_z/\partial z=5.85\times10^{16}$ v cm^{-2} and $Q\sim5\times10^{-25}$ cm^2. It is planned to measure $\partial E_z/\partial_z$ by nuclear induction experiments in which the known quadrupole moment of In^{115} would serve as a reference standard.[6] This experiment would yield $Q(In^{115})\ \partial E_z/\partial z$. An angular correlation experiment with the same crystal containing In^{111} atoms gave $Q(Cd^{111})\ \partial E_z/\partial z$. One could in this way measure the quadrupole moment of Cd^{111} (247 kev) in units of the quadrupole moment of In^{115}, assuming the field gradients in both cases to be equal. One difficulty remains for all methods of determination of $\partial E_z/\partial z$: one does not know to what extent the K- capture of the In^{111} and the following γ-decay (recoil) changes the field at the nucleus.

We also hope to study the quadrupole interaction in other single crystals. This would give other values for x and provide a better basis for obtaining the quadrupole moment.

We thank Prof. P. Scherrer for his continued interest and help, Dr. W. Känzig and R. Kern for their help with the growing and orientation of the single crystals, the cyclotron group for the many irradiations carried out for these experiments, and R. Leidenix for the calculation of the field gradient.

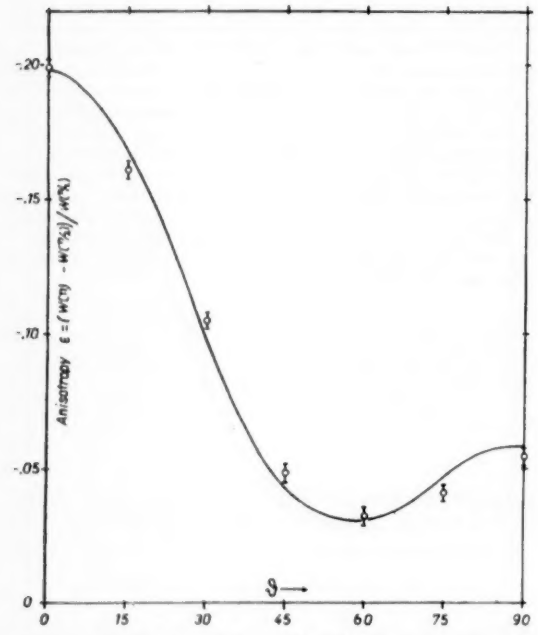

FIG. 1. Result for single crystal 2. $\epsilon=W(\pi)/W(\pi/2)-1$ is plotted against the angle ϑ between the direction of the fixed counter and the **c** axis. The curve shows $\epsilon(\vartheta)$ for $x=1.60$ obtained by a least-squares fit.

* C. E. R. N., European Council for Nuclear Research, Theoretical Study Group at the Institute for Theoretical Physics, University of Copenhagen.
† National Science Foundation Postdoctoral Fellow, on leave from Argonne National Laboratory.

[1] Albers-Schönberg, Hänni, Heer, Novey, and Scherrer, Phys. Rev. **90**, 322 (1953).
[2] Albers-Schönberg, Heer, Novey, and Rüetschi, Phys. Rev. **91**, 199 (1953).
[3] Alder, Albers-Schönberg, Heer, and Novey, Helv. Phys. Acta (to be published).
[4] L. C. Biedenharn and M. E. Rose, Revs. Modern Phys. (to be published).
[5] Albers-Schönberg, Alder, Heer, Novey, and Scherrer, Proc. Phys. Soc. (London) (to be published).
[6] A. K. Mann and P. Kusch, Phys. Rev. **77**, 427, 435 (1950).

The Scattering of 40-Mev Positive Pions by Hydrogen*,†

J. P. PERRY AND C. E. ANGELL
Department of Physics, University of Rochester, Rochester, New York
(Received July 8, 1953)

DIFFERENTIAL scattering cross sections of hydrogen for 40 ±3-Mev positive pions have been measured at laboratory angles of 45, 60, 90, 120, and 140 degrees.

After analysis and focusing both by the cyclotron fringing field and by a deflecting magnet, the pion beam was further defined and counted by a double coincidence telescope consisting of the scintillation counters 1 and 2 shown in Fig. 1. The beam so defined was quite parallel but contained a 3 percent muon-electron contamination, as was determined from range measurements, and a 1 percent contribution due to random coincidences between counters 1 and 2. Polyethylene and carbon scatterers were placed behind counter 2 and a larger counter, 5 the pulses of which were in anticoincidence with those from the defining telescope, was placed behind the scatterers. Since the energy of pions scattered by hydrogen is a function of the scattering angle, different scatterer thicknesses were used at each angle, and the geometries

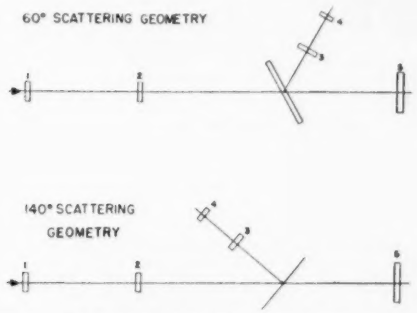

FIG. 1. Elevation drawings of the 60° and the 140° setups illustrating the transmission geometry used in the forward hemisphere and the reflection geometry used in the backward hemisphere.

illustrated by Fig. 1 were used. The scatterers were made sufficiently thin so that the scattered pions had enough energy to traverse the detecting telescope which consisted of the counters 3 and 4.

Because of the large background counting rate due to elastic scattering and star production by carbon, the pulse heights in counter 3, corresponding to particles passing through the detecting telescope in time coincidence with a pion in the incident beam, were recorded. By restricting the CH_2-carbon subtraction to that region of pulse height in which hydrogen-scattered pions were expected, reasonable signal-to-noise ratios were attained.

The results, corrected for beam contamination and for the inefficiency of a fast coincidence circuit used, are given in Table I. θ_0 is the nominal scattering angle; θ_{max} and θ_{min} are, respectively, the maximum and minimum scattering angles accepted by the detecting telescope; and Ω_{eff} is the effective solid angle which was

TABLE I. The results expressed in the laboratory system and in the center-of-mass system. θ_{max} and θ_{min} give the total angular spreads and Ω_{eff} is the effective solid angle.

Scattering angles laboratory θ_0 (deg)	θ_{min} (deg)	θ_{max} (deg)	c.m. Θ (deg)	Ω_{eff} (sterad)	Hydrogen cross section (10^{-27} cm²/sterad) laboratory	c.m.
45	35	58	53	0.0773	0.14±0.43	0.11±0.34
60	48	73	69	0.0942	0.49±0.18	0.42±0.15
90	76	110	100	0.110	0.89±0.34	0.91±0.35
120	101	135	129	0.0863	1.18±0.30	1.44±0.37
140	125	150	147	0.0702	1.63±0.55	2.20±0.74

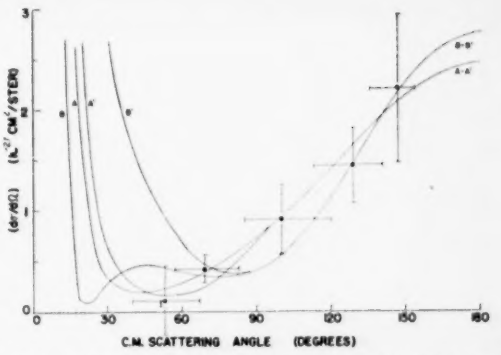

FIG. 2. The center-of-mass angular distribution of $\pi^+ + p \to \pi^+ + p$ at 40 Mev. For Curve A the phase shifts are $\alpha_3 = -5.7°$, $\alpha_{33} = +4.1°$, $\alpha_{31} = -0.1°$. For Curve B: $\alpha_3 = -2.0°$, $\alpha_{33} = +6.0°$, $\alpha_{31} = +0.7°$. Curves A' and B' correspond, respectively, to A and B with reversed signs of the phases.

calculated taking into account the known distribution of incident beam intensity across the scatterer. The errors are standard deviations and include uncertainties in the corrections and in the solid angles as well as those due to counting statistics.

Because of the large uncertainties, the data can be reproduced by several sets of phase shifts. The curves of Fig. 2 represent two such sets: Curve A, $\alpha_3 = -5.7°$; $\alpha_{33} = +4.1°$; $\alpha_{31} = -0.1°$; Curve B: $\alpha_3 = -2.0°$; $\alpha_{33} = +6.0°$; $\alpha_{31} = +0.7°$. α_3, α_{33}, and α_{31} are, respectively, the phase shifts for the $S_{\frac{1}{2}}$, $P_{\frac{1}{2}}$, and $P_{\frac{3}{2}}$ states. The curves A' and B' correspond, respectively, to A and B with reversed signs. The Coulomb interference was calculated from the equation given by Van Hove[1] to lowest order in his expansion of the Coulomb amplitude. It is apparent that if the magnitude of α_{33} is large compared to α_3 (Curves B and B') that the negative sign for α_3 is favored by the data. The test is not so crucial when α_3 and α_{33} are about equal in magnitude (Curves A and A'), but again the set with negative α_3 gives a somewhat better fit.[2]

The integrated total cross section is $(10.9\pm3)\times10^{-27}$ cm², in agreement with the most recent value[3] reported by this laboratory from an attenuation measurement.

We are indebted to Professor S. W. Barnes for his guidance, to Professor R. E. Marshak for discussion, and to Mr. D. T. Nelson for assistance in taking the data.

* This work was performed under the auspices of the U. S. Atomic Energy Commission.
† Based upon a thesis submitted to the Graduate School of the University of Rochester by one of the authors (JPP) in partial fulfillment of their requirements for the degree of Doctor of Philosophy.
[1] L. Van Hove, Phys. Rev. **88**, 1358 (1952).
[2] See R. E. Marshak and A. E. Woodruff (to be published).
[3] C. E. Angell and J. P. Perry, Phys. Rev. **90**, 724 (1953).

Evidence for a Region of Extra Nuclear Stability between the 82- and 126-Neutron Shells*

BENJAMIN G. HOGG† AND HENRY E. DUCKWORTH
McMaster University, Hamilton, Ontario, Canada
(Received July 13, 1953)

A NUMBER of new atomic mass measurements have been made in this laboratory in the region $82<N<126$. These masses have been used to study nuclear stability in this region. A previous study[1] of nuclear stability, in the region $28<N<50$ and $28<Z<40$, indicated no unusual stability; especially lacking was the existence of subshell effects in this lighter region.

A useful method of representing the data in order to locate mass effects is to plot the neutron number against the difference between the semi-empirical mass values of Metropolis and Reitweisner[2] and the experimental masses. Since the semi-empirical mass formula has no compensating factors which allow for shell

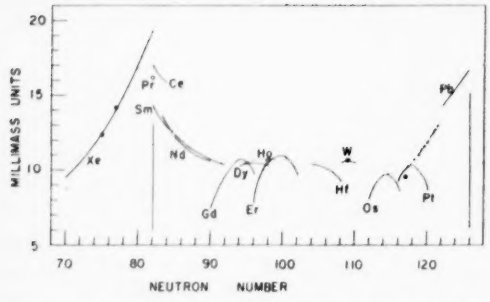

FIG. 1. A plot of experimental deviation from the semi-empirical masses *versus* neutron number. The solid curves are the best fit for points belonging to even-A, even-Z nuclei. The closed circles represent odd-A, even-Z nuclei, and the open circles represent odd-Z, odd-A nuclei.

structure, large mass differences appear at regions of higher stability. This method of representing the data is more sensitive for detecting small variations than the conventional plot of binding energy per nucleon.

Figure 1 shows a plot of the data which are obtained from forty experimentally-determined masses in the region $82<N<126$. The uncertainty in an individual measurement is from one-half to one millimass unit. No stability effects associated with a particular neutron number are noticed, but rather there is a broad general increase in stability between the 82- and 126-neutron shells.

It has been pointed out to us by Goldhaber that this stability may be the result of the mixing of configurations,[3] an effect which is greatest in the region between shells, and which is a possible explanation for the previously noted[4,5] lowering of the first excited states of the heavier rare-earth nuclei. It is interesting to notice that the region of depression of the first excited states agrees very well with the region of depression of the ground state, as shown by the rise in Fig. 1.

A detailed report on these experiments will appear in the Canadian Journal of Physics. The authors are indebted to Dr. M. Goldhaber for helpful suggestions concerning interpretation of the data and to Dr. F. H. Spedding for supplying the pure rare-earth metals which made the experiments possible.

* Work supported by the U. S. Air Research and Development Command, the National Research Council of Canada, and the Research Council of Ontario.

† National Research Council of Canada Fellow.

[1] B. G. Hogg and H. E. Duckworth, Can. J. Phys., September (1953).
[2] N. Metropolis and G. Reitweisner, Table of Atomic Masses, 1950 (unpublished).
[3] A. de Shalit and M. Goldhaber (to be published).
[4] P. Preiswerk and P. Stähelin, Helv. Phys. Acta **24**, 623 (1951).
[5] G. Scharff-Goldhaber, Phys. Rev. **90**, 587 (1953).

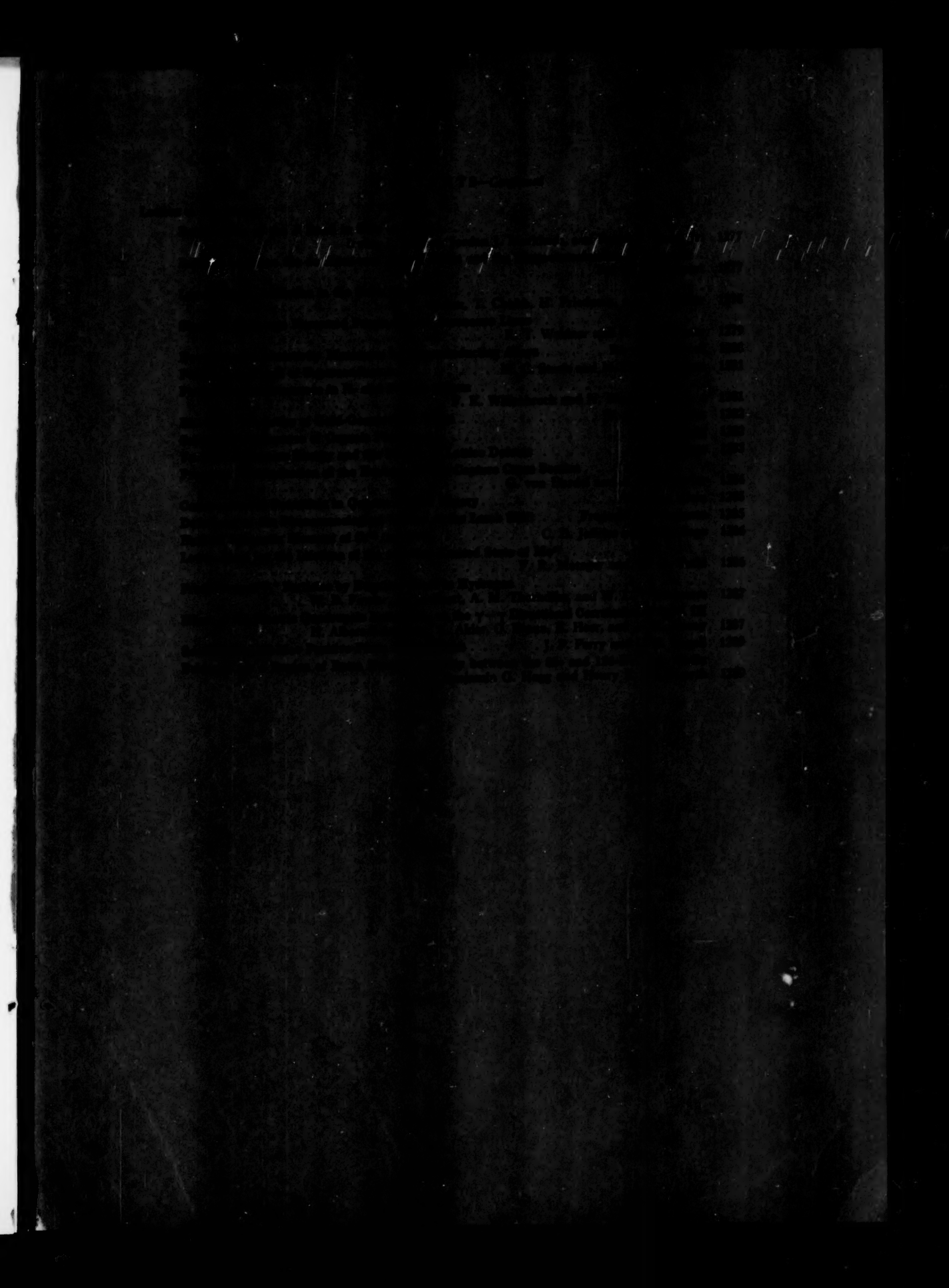

CONTENTS

THE PHYSICAL REVIEW SECOND SERIES, VOLUME 91, NO. 5 September 1, 1953

Two-Fluid Models of Superconductivity with Application to Isotope Effects. . . . . Paul M. Marcus and E. Maxwell 1035
Field Emission Initiated Vacuum Arc. I. Experiments on Arc Initiation . . . . . W. P. Dyke, J. K. Trolan, E. E. Martin, and J. P. Barbour 1043
Field Emission Initiated Vacuum Arc. II. The Resistively Heated Emitter . . . . . W. W. Dolan, W. P. Dyke, and J. K. Trolan 1054
Rapid Separation of He^3 from He^4 by the "Heat Flush" Method . . . . . T. Soller, W. M. Fairbank, and A. D. Crowell 1058
Magnetoresistance of Bismuth Crystals at Low Temperatures . . . . . P. B. Alers and R. T. Webber 1060
Electronic Structure of *F* Centers: Hyperfine Interactions in Electron Spin Resonance . . . . . A. F. Kip, C. Kittel, R. A. Levy, and A. M. Portis 1066
Electronic Structure of *F* Centers: Saturation of the Electron Spin Resonance . . . . . A. M. Portis 1071
Electron Multiplication in Silicon and Germanium . . . . . K. G. McKay and K. B. McAfee 1079
Sublattice Effects in Magnetic Resonance . . . . . Roald K. Wangsness 1085
Mobility of Interstitial Atoms in a Face-Centered Metal . . . . . H. B. Huntington 1092
Electronic and Lattice Specific Heats in W, Mo, and Re . . . . . M. Horowitz and J. G. Daunt 1099
Mechanism of Transition in Magnetite at Low Temperatures . . . . . H. J. Williams, R. M. Bozorth, and Matilda Goertz 1107
Deformation of Copper Single Crystals at 300°K and 78°K . . . . . T. H. Blewitt 1115
Computation of Mean Debye Temperature of Cubic Crystals from Elastic Constants . . . . . S. L. Quimby and Paul M. Sutton 1122
Deflection of High-Energy Electrons in Magnetized Iron . . . . Stephan Berko and Frank L. Hereford 1127
New Approximation Method for Order-Disorder Problems . . . Lloyd D. Fosdick and Hubert M. James 1131
Changes in the Electrical, Thermal, and Thermoelectrical Properties of Monovalent Metals by Lattice Distortions . . . . . A. W. Sáenz 1142
Electrical Resistance of Graphite at Low Temperatures . . . . . J. M. Reynolds, H. W. Hemstreet, and T. E. Leinhardt 1152
Photoionization Cross Section of Nitric Oxide . . . K. Watanabe, F. F. Marmo, and Edward C. Y. Inn 1155
Broadening of Microwave Absorption Lines Due to Wall Collisions . . . . . Michael Danos and Stanley Geschwind 1159
Polarizability of the Deuteron . . . . . N. F. Ramsey, B. J. Malenka, and U. E. Kruse 1162
Electric Scattering of the Polarizable Deuteron . . . . B. J. Malenka, U. E. Kruse, and N. F. Ramsey 1165
Exchange Scattering of an Electron by the Hydrogen Atom . . . . . Saul Altshuler 1167
Shift of the 1^1S State of Helium . . . . . S. Chandrasekhar, Donna Elbert, and G. Herzberg 1172
Excitation of Molecular Rotations and Vibrations in Inelastic Scattering Processes . Edward H. Kerner 1174
Complex Amplitudes for Electron Scattering by Atoms . . . . . Jean A. Hoerni and James A. Ibers 1182
Ionization Energy Losses of Relativistic μ Mesons in Gases . J. E. Kupperian, Jr., and E. D. Palmatier 1186
Gamma-Ray Spectrum of As^{77} . . . . . F. Rasetti and E. C. Booth 1192
Photoionization of Molecules in the Vacuum Ultraviolet . . . . . Edward C. Y. Inn 1194
Accurate Determinations of Nuclear Reaction Energies . . . . . K. F. Famularo and G. C. Phillips 1195
Radiations from Zr^{89} . . . . . F. J. Shore, W. L. Bendel, H. N. Brown, and R. A. Becker 1203
Decay of K^{42} . . . . . Bernd Kahn and W. S. Lyon 1212
Complementarity in Angular-Momentum States . . . . . B. A. Lippmann 1213
Radiations from Arsenic 77 and Germanium 71 . . . . . B. L. Saraf, J. Varma, and C. E. Mandeville 1216
Radiations of Ra^{227} . . . . . J. P. Butler and J. S. Adam 1219
Neutron Diffraction by Liquid Helium . . . . . D. G. Henshaw and D. G. Hurst 1222
Branching Ratio of Potassium 40 . R. D. Russell, H. A. Shillibeer, R. M. Farquhar, and A. K. Mousuf 1223
Bremsstrahlung from P^{32} Betas . . . . . M. Goodrich, J. S. Levinger, and W. Payne 1225
Triton-Induced Activities in Magnesium and Aluminum . Eric Iversen, W. S. Koski, and Franco Rasetti 1229
Cross Terms in Allowed Shape β Spectra . . . . . J. P. Davidson and D. C. Peaslee 1232
Half-Life of Thallium-204 . . . . . Garman Harbottle 1234
π^- and μ^- Meson-Induced Fission . . . . . W. John and W. F. Fry 1234
Large Angle Scattering of Negative Pions in Aluminum, Copper, and Lead . . . . . Harry H. Heckman and L. Evan Bailey 1237
Number of Feynman Diagrams . . . . . Robert J. Riddell, Jr. 1243
Graphical Method for Obtaining Phase Shifts from the Experimental Data on Meson-Nucleon Scattering . . . . . Julius Ashkin and Seymour H. Vosko 1248
Theory of Finite Displacement Operators and Fundamental Length . . . B. T. Darling and P. R. Zilsel 1252
Fourth-Order Radiative Corrections to Atomic Energy Levels . J. Weneser, R. Bersohn, and N. M. Kroll 1257
Logical Relations among the Principles of Statistical Mechanics and Thermodynamics . John S. Thomsen 1263
S Matrix and Causality Condition. II. Nonrelativistic Particles . . . . . N. G. van Kampen 1267

(continued on cover three)

LANCASTER PRESS, INC., LANCASTER, PA.